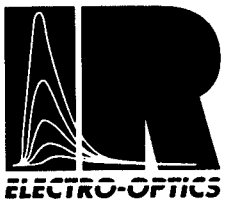

The Infrared & Electro-Optical Systems Handbook

VOLUME 5

Passive Electro-Optical Systems

Stephen B. Campana, *Editor*

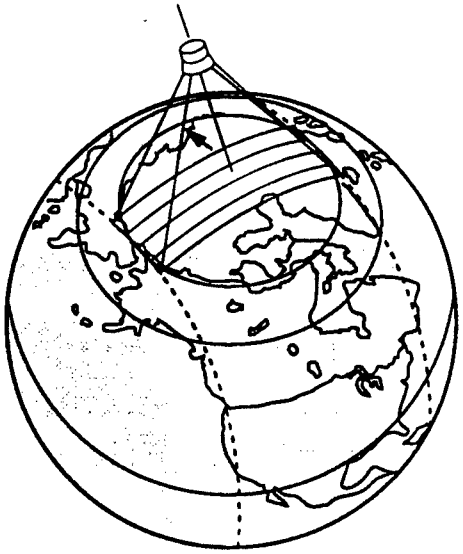

Passive Electro-Optical Systems

VOLUME 5

The Infrared and Electro-Optical Systems Handbook

The Infrared and Electro-Optical Systems Handbook

Joseph S. Accetta, David L. Shumaker, *Executive Editors*

Chapter 3. Optomechanical System Design, Daniel Vukobratovich
Chapter 4. Infrared Imaging System Testing, Gerald C. Holst
Chapter 5. Tracking and Control Systems, Robert E. Nasburg
Chapter 6. Signature Prediction and Modeling, John A. Conant, Malcolm A. LeCompte

■ **VOLUME 5.** **Passive Electro-Optical Systems,**
Stephen B. Campana, *Editor*

Chapter 1. Infrared Line Scanning Systems, William L. McCracken
Chapter 2. Forward-Looking Infrared Systems, George S. Hopper
Chapter 3. Staring-Sensor Systems, Michael J. Cantella
Chapter 4. Infrared Search and Track Systems, Joseph S. Accetta

■ **VOLUME 6.** **Active Electro-Optical Systems,** Clifton S. Fox, *Editor*

Chapter 1. Laser Radar, Gary W. Kamerman
Chapter 2. Laser Rangefinders, Robert W. Byren
Chapter 3. Millimeter-Wave Radar, Elmer L. Johansen
Chapter 4. Fiber Optic Systems, Norris E. Lewis, Michael B. Miller

■ **VOLUME 7.** **Countermeasure Systems,** David Pollock, *Editor*

Chapter 1. Warning Systems, Donald W. Wilmot, William R. Owens, Robert J. Shelton
Chapter 2. Camouflage, Suppression, and Screening Systems, David E. Schmieder, Grayson W. Walker
Chapter 3. Active Infrared Countermeasures, Charles J. Tranchita, Kazimieras Jakstas, Robert G. Palazzo, Joseph C. O'Connell
Chapter 4. Expendable Decoys, Neal Brune
Chapter 5. Optical and Sensor Protection, Michael C. Dudzik
Chapter 6. Obscuration Countermeasures, Donald W. Hoock, Jr., Robert A. Sutherland

■ **VOLUME 8.** **Emerging Systems and Technologies,**
Stanley R. Robinson, Editor

Chapter 1. Unconventional Imaging Systems, Carl C. Aleksoff, J. Christopher Dainty, James R. Fienup, Robert Q. Fugate, Jean-Marie Mariotti, Peter Nisenson, Francois Roddier
Chapter 2. Adaptive Optics, Robert K. Tyson, Peter B. Ulrich
Chapter 3. Sensor and Data Fusion, Alan N. Steinberg
Chapter 4. Automatic Target Recognition Systems, James W. Sherman, David N. Spector, C. W. "Ron" Swonger, Lloyd G. Clark, Edmund G. Zelnio, Terry L. Jones, Martin J. Lahart
Chapter 5. Directed Energy Systems, Gary Golnik
Chapter 6. Holography, Emmett N. Leith
Chapter 7. System Design Considerations for a Visually-Coupled System, Brian H. Tsou

Copublished by

Infrared Information Analysis Center
Environmental Research Institute of Michigan
Ann Arbor, Michigan USA

and

SPIE OPTICAL ENGINEERING PRESS
Bellingham, Washington USA

Sponsored by

Defense Technical Information Center, DTIC-DF
Cameron Station, Alexandria, Virginia 22304-6145

Passive Electro-Optical Systems

Stephen B. Campana, *Editor*
Naval Air Warfare Center

VOLUME 5

The Infrared and Electro-Optical Systems Handbook

Joseph S. Accetta, David L. Shumaker, *Executive Editors*
Environmental Research Institute of Michigan

Library of Congress Cataloging-in-Publication Data

The Infrared and electro-optical systems handbook / Joseph S. Accetta, David L. Shumaker, executive editors.
p. cm.
Spine title: IR/EO systems handbook.
Cover title: The Infrared & electro-optical systems handbook.
Completely rev. ed. of: Infrared handbook. 1978
Includes bibliographical references and indexes.
Contents: v. 1. Sources of radiation / George J. Zissis, editor — v. 2. Atmospheric propagation of radiation / Fred G. Smith, editor — v. 3. Electro-optical components / William D. Rogatto, editor — v. 4. Electro-optical systems design, analysis, and testing / Michael C. Dudzik, editor — v. 5. Passive electro-optical systems / Stephen B. Campana, editor — v. 6. Active electro-optical systems / Clifton S. Fox, editor — v. 7. Countermeasure systems / David Pollock, editor — v. 8. Emerging systems and technologies / Stanley R. Robinson, editor.
ISBN 0-8194-1072-1
1. Infrared technology—Handbooks, manuals, etc. 2. Electrooptical devices—Handbooks, manuals, etc. I. Accetta, J. S. II. Shumaker, David L. III. Infrared handbook. IV. Title: IR/EO systems handbook. V. Title: Infrared & electro-optical systems handbook.
TA1570.I5 1993
621.36'2—dc20 92-38055
CIP

Copublished by

Infrared Information Analysis Center
Environmental Research Institute of Michigan
P.O. Box 134001
Ann Arbor, Michigan 48113-4001

and

SPIE Optical Engineering Press
P.O. Box 10
Bellingham, Washington 98227-0010

PRINTED IN THE UNITED STATES OF AMERICA

Preface

The Infrared and Electro-Optical Systems Handbook is a joint product of the Infrared Information Analysis Center (IRIA) and the International Society for Optical Engineering (SPIE). Sponsored by the Defense Technical Information Center (DTIC), this work is an outgrowth of its predecessor, *The Infrared Handbook,* published in 1978. The circulation of nearly 20,000 copies is adequate testimony to its wide acceptance in the electro-optics and infrared communities. *The Infrared Handbook* was itself preceded by *The Handbook of Military Infrared Technology.* Since its original inception, new topics and technologies have emerged for which little or no reference material exists. This work is intended to update and complement the current *Infrared Handbook* by revision, addition of new materials, and reformatting to increase its utility. Of necessity, some material from the current book was reproduced as is, having been adjudged as being current and adequate. The 45 chapters represent most subject areas of current activity in the military, aerospace, and civilian communities and contain material that has rarely appeared so extensively in the open literature.

Because the contents are in part derivatives of advanced military technology, it seemed reasonable to categorize those chapters dealing with systems in analogy to the specialty groups comprising the annual Infrared Information Symposia (IRIS), a Department of Defense (DoD) sponsored forum administered by the Infrared Information Analysis Center of the Environmental Research Institute of Michigan (ERIM); thus, the presence of chapters on active, passive, and countermeasure systems.

There appears to be no general agreement on what format constitutes a "handbook." The term has been applied to a number of reference works with markedly different presentation styles ranging from data compendiums to tutorials. In the process of organizing this book, we were obliged to embrace a style of our choosing that best seemed to satisfy the objectives of the book: to provide derivational material data, descriptions, equations, procedures, and examples that will enable an investigator with a basic engineering and science education, but not necessarily an extensive background in the specific technology, to solve the types of problems he or she will encounter in design and analysis of electro-optical systems. Usability was the prime consideration. In addition, we wanted each chapter to be largely self-contained to avoid time-consuming and tedious referrals to other chapters. Although best addressed by example, the essence of our handbook style embodies four essential ingredients: a brief but well-referenced tutorial, a practical formulary, pertinent data, and, finally, example problems illustrating the use of the formulary and data.

The final product represents varying degrees of success in achieving this structure, with some chapters being quite successful in meeting our objectives and others following a somewhat different organization. Suffice it to say that the practical exigencies of organizing and producing a compendium of this magnitude necessitated some compromises and latitude. Its ultimate success will be judged by the community that it serves. Although largely oriented toward system applications, a good measure of this book concentrates on topics endemic and fundamental to systems performance. It is organized into eight volumes:

Volume 1, edited by George Zissis of ERIM, treats sources of radiation, including both artificial and natural sources, the latter of which in most military applications is generally regarded as background radiation.

Volume 2, edited by Fred Smith of OptiMetrics, Inc., treats the propagation of radiation. It features significant amounts of new material and data on absorption, scattering, and turbulence, including nonlinear propagation relevant to high-energy laser systems and propagation through aerodynamically induced flow relevant to systems mounted on high-performance aircraft.

Volume 3, edited by William Rogatto of Santa Barbara Research Center, treats traditional system components and devices and includes recent material on focal plane array read-out electronics.

Volume 4, edited by Michael Dudzik of ERIM, treats system design, analysis, and testing, including adjunct technology and methods such as trackers, mechanical design considerations, and signature modeling.

Volume 5, edited by Stephen Campana of the Naval Air Warfare Center, treats contemporary infrared passive systems such as FLIRs, IRSTs, IR line scanners, and staring array configurations.

Volume 6, edited by Clifton Fox of the Night Vision and Electronic Sensors Directorate, treats active systems and includes mostly new material on laser radar, laser rangefinders, millimeter-wave systems, and fiber optic systems.

Volume 7, edited by David Pollock, consultant, treats a number of countermeasure topics rarely appearing in the open literature.

Volume 8, edited by Stanley Robinson of ERIM, treats emerging technologies such as unconventional imaging, synthetic arrays, sensor and data fusion, adaptive optics, and automatic target recognition.

Acknowledgments

It is extremely difficult to give credit to all the people and organizations that contributed to this project in diverse ways. A significant amount of material in this book was generated by the sheer dedication and professionalism of many esteemed members of the IR and EO community who unselfishly contributed extensive amounts of precious personal time to this effort and to whom the modest honorarium extended was scarcely an inducement. Their contributions speak elegantly of their skills.

Directly involved were some 85 authors and editors from numerous organizations, as well as scores of technical reviewers, copyeditors, graphic artists, and photographers whose skill contributed immeasurably to the final product.

We acknowledge the extensive material and moral support given to this project by various members of the managements of all the sponsoring and supporting organizations. In many cases, organizations donated staff time and internal resources to the preparation of this book. Specifically, we would like to acknowledge J. MacCallum of DoD, W. Brown and J. Walker of ERIM, and J. Yaver of SPIE, who had the foresight and confidence to invest significant resources in the preparation of this book. We also extend our appreciation to P. Klinefelter, B. McCabe, and F. Frank of DTIC for their administrative support during the course of this program.

Supporting ERIM staff included Ivan Clemons, Jenni Cook, Tim Kellman, Lisa Lyons, Judy Steeh, Barbara Wood, and the members of their respective organizations that contributed to this project.

We acknowledge Lorretta Palagi and the publications staff at SPIE for a professional approach to the truly monumental task of transforming the manuscripts into presentable copy and the patience required to interact effectively with the authors.

We would like to pay special tribute to Nancy Hall of the IRIA Center at ERIM who administrated this at times chaotic project with considerable interpersonal skill, marshaling the numerous manuscripts and coordinating the myriad details characteristic of a work of this magnitude.

We properly dedicate this book to the people who created it and trust it will stand as a monument to their skills, experience, and dedication. It is, in the final analysis, a product of the community it is intended to serve.

Joseph S. Accetta
David L. Shumaker
Ann Arbor, Michigan

January 1993

Notices and Disclaimer

This handbook was prepared by the Infrared Information Analysis Center (IRIA) in cooperation with the International Society for Optical Engineering (SPIE). The IRIA Center, Environmental Research Institute of Michigan, is a Defense Technical Information Center-sponsored activity under contract DLA-800-C-393 and administrated by the Defense Electronics Supply Center, Defense Logistics Agency.

This work relates to the aforementioned ERIM contract and is in part sponsored by the Department of Defense; however, the contents do not necessarily reflect the position or the policy of the Department of Defense or the United States government and no official endorsement should be inferred.

The use of product names does not in any way constitute an endorsement of the product by the authors, editors, Department of Defense or any of its agencies, the Environmental Research Institute of Michigan, or the International Society for Optical Engineering.

The information in this handbook is judged to be from the best available sources; however, the authors, editors, Department of Defense or any of its agencies, the Environmental Research Institute of Michigan, or the International Society for Optical Engineering do not assume any liability for the validity of the information contained herein or for any consequence of its use.

Contents

CHAPTER 1

Infrared Line Scanning Systems

William L. McCracken
Radiance Engineering
Wayland, Massachusetts

CONTENTS

1.1 INTRODUCTION

1.1.1 Symbols, Nomenclature, and Units

Table 1.1 lists symbols, nomenclature, and units, and Table 1.2 gives acronyms used in this chapter.

1.1.2 Infrared Line Scanner Definition

An infrared line scanner (IRLS) is an imaging device that forms images by successive scans of a rotating mirror. The scans are transverse to the line of flight of the vehicle carrying the IRLS. The second scan needed for a two-dimensional image is provided by forward motion of the vehicle along its flight path. Figure 1.1 shows a typical IRLS and Fig. 1.2 gives the scan pattern and the coordinates used. In the special case of infrared imaging from space, the vehicle could be a satellite and the flight path could be the satellite orbit. IRLS devices have been adapted for use as FLIR-type scanners for ground testing and for various special purposes. The second scan is then provided by adding a separate means of optical scanning, such as a nodding mirror, or by panning the entire scanner. Satellite IRLS imagers have been ground tested in this manner. Panoramic imagery of California was produced by Hughes Aircraft with the ERTS scanner, and of Colorado by Martin Denver with the S-192 NASA Multispectral Scanner made by Honeywell. The scanners in these tests viewed horizontally with a nominal azimuth scan. In the S-192 Denver imagery the entire scanner was panned vertically at a slow rate. Early infrared line scanners have been turned 90 deg to scan horizontally. Vertical scanning means were then added to convert the IRLS to early forms of FLIR because IRLS technology predated that of FLIR.

1.1.3 Airborne Reconnaissance with IRLS Systems

An IRLS in a high-speed reconnaissance aircraft is one of the most efficient means ever invented for gathering pictorial information. Modern reconnaissance aircraft can typically travel 600 nmi in 1 h. Just 10 min of IRLS data collection at this velocity provides a strip map covering 100 nmi of terrain.

1.1.3.1 High Data Rates Generated by IRLS. If an IRLS has an across-track (transverse) scan field of view of 120 deg (FOV = 120 deg) and a 0.5 mrad constant angular resolution (its IFOV, or instantaneous field of view), the number of IFOV per scan line in the across-track (ACT or x) direction is

$$N_{\mathrm{ACT}} = \frac{(120 \text{ deg per line})\ (\pi/180)}{(0.5 \times 10^{-3} \text{ rad per IFOV})} = 4189 \text{ IFOV per line} \ .$$

At 2000-ft altitude, the IFOV subtense δS at nadir will be

$$\delta S = h(\mathrm{IFOV}) = (2000)\ (0.5 \times 10^{-3}) = 1 \text{ ft} \ .$$

This is also the along-track ground width of one scan line. A 100-nmi strip map of contiguous scan lines will thus contain

Table 1.1 Symbols, Nomenclature, and Units

Symbols	Nomenclature	Units
A_d	Area of detector	cm^2
c	Velocity of light	$m\ s^{-1}$
C_1	First radiation constant, $C_1 = 1.19106 \times 10^4$	$W\ cm^2\ sr^{-1}$
C_2	Second radiation constant, $C_2 = 14{,}388.33$	$\mu m\ K$
D	Optical density of film	density unit
D	Detectivity (reciprocal NEP)	W^{-1}
D^*	D-star	$cm\ Hz^{1/2}\ W^{-1}$
D^*_{BB}	Blackbody D-star	$cm\ Hz^{1/2}\ W^{-1}$
D^*_λ	Spectral D-star	$cm\ Hz^{1/2}\ W^{-1}$
D^*	In-band average spectral D-star	$cm\ Hz^{1/2}\ W^{-1}$
D^*_{PK}	Spectral D-star at peak D-star wavelength	$cm\ Hz^{1/2}\ W^{-1}$
D^*_{BLIP}	Spectral D-star when background limited	$cm\ Hz^{1/2}\ W^{-1}$
D^{**}	Double-D-star, D-double-star	$cm\ Hz^{1/2}\ W^{-1}$
d_c	Approximate diameter of comatic spot	rad
e	Base of Napierian logarithms, $e = 2.718281828$	–
E	Film exposure	$J\ m^{-2}$
f_e	Electrical frequency	Hz
f	Optics focal length	cm
f_s	Spatial frequency	cycles/rad
f_c	Cutoff spatial frequency	cycles/rad
$f/\#$	Ratio of focal length to working aperture	–
g	Acceleration of gravity at earth equator	$g\ cm\ s^{-2}$
h	Altitude above ground level (AGL)	ft, m
I_b	Detector bias current	A
IFOV	Instantaneous FOV	mrad
$(IFOV)_{REQ}$	Required IFOV to accomplish a given imagery discrimination task	mrad
J_0	Zero-order Bessel function	–
k	Noise bandwidth estimation factor	–
K	Kelvin temperature	K
MTF_D	MTF of IRLS aperture diffraction	–
n_f	Number of spin-mirror facets	–
N	Infrared radiance	$W\ cm^{-2}\ sr^{-1}$
N_λ	Spectral radiance	$W\ cm^{-2}\ sr^{-1}\ \mu m^{-1}$
$(N_{max})_{\Delta\lambda}$	In-band maximum radiance	$W\ cm^{-2}\ sr^{-1}$
N_{ALT}	Number of parallel detectors per scan	–
N_{ACT}	Number of IFOV per scan line in ACT	–
NEN	Noise equivalent radiance	$W\ cm^{-2}\ sr^{-1}$
$(NEN)_{\Delta\lambda}$	In-band NEN	$W\ cm^{-2}\ sr^{-1}$
NEP	Noise equivalent pwer	W
nmi	Nautical mile (US and Int.)	nmi
N_{PIX}	Number of pixels in ACT scan line image	–
N_{TOT}	Total number of pixels in an image	–

Table 1.1 *(continued)*

Symbols	Nomenclature	Units
NETD	Noise equivalent temperature difference	°C, K
P_C	Probability of correctness in imagery discrimination task	–
P_D	Probability of detection	–
P_I	Probability of identification	–
P_n	Noise power	W
P_R	Probability of recognition	–
P_S	Signal power	W
Q_B	Background IR photon flux	photons/s
$(Q_W)_{\Delta\lambda}$	In-band photon radiant exitance	photons s^{-1} cm^{-2}
R	Detector responsivity	V W^{-1}
R_λ	Detector spectral responsivity	V W^{-1} μm^{-1}
R_e	Earth mean radius	m
r_L	Bias load resistance	Ω
r_m	Mirror reflectance	–
R_{MAX}	Maximum slant range to target	m, ft
r_{sc}	IRLS scan rate	scans/s
r_{sp}	Spin-mirror rotation rate	rps, rpm
T	Temperature	°C, K
T	Transmission of film or optical element	–
T	Interscan period of IRLS	s
V_b	Detector bias voltage	V
V_{SOT}	Satellite suborbital track velocity	m s^{-1}
V/H	Velocity-to-height ratio	rad s^{-1}
α	Atmospheric attenuation coefficient	km^{-1}
α	Angular separation of two resolved sources in Rayleigh criterion	rad
δf	Electrical signal bandwidth	Hz
δf_n	Electrical noise bandwidth	Hz
δS	IFOV footprint at target, normal to IRLS line of sight	ft, m
ΔN	Radiance contrast	W cm^{-2} sr^{-1}
ΔT	Temperature difference or contrast	°C, K
ε	Graybody emissivity	–
ϕ	Cone angle of cold shield	deg
Φ_{ALT}	ALT FOV	mrad
λ	Wavelength	m, μm
σ	Normalized angular radius of Gaussian spot containing the fraction P of power	cycles/rad
τ_a	Transmission of atmospheric path	–
τ_o	Transmittance of optics	–
τ_w	Transmittance of IR window	–
$(IFOV)_x$	IFOV in x axis	mrad
$(IFOV)_y$	IFOV in y axis	mrad
Ω_{IFOV}	Solid angle of IFOV	sr

Table 1.2 Acronyms and Abbreviations

Acronym or Abbreviation	Meaning
ACT	Across-track axis of IRLS scan, x axis, transverse axis
AGERD	Aerospace ground equipment requirements document
AGL	Above ground level
ALT	Along-track axis of IRLS scan, y axis, parallel to flight
APC	Armored personnel carrier
AR	Antireflection (coating)
BAe	British Aerospace and Electronics
CAD	Computer-aided design
CAL	Calibration
CCC = C^3	Communication, Command, and Control
CCD	Charge-coupled device
CNVEO	U.S. Army Center for Night Vision and Electro-Optics
ECR	Electronic combat and reconnaissance (mission)
ERTS	Earth Resources Technology Satellite
FLIR	Forward-looking infrared imaging device
FOV	Field of view
GAF	German Air Force
GRD	Ground-resolved distance
GSE	Ground-support equipment
IFOV	Instantaneous field of view
IR	Infrared
IRLS	Infrared line scanner
LP	Line pair (in an image)
LRU	Line replaceable unit
LWIR	Long-wavelength infrared
MDTD	Minimum detectable temperature difference
MRTD	Minimum resolvable temperature difference
MTBF	Mean time between failure
MTF	Modulation transfer function
NA	Numerical aperture
NEN	Noise equivalent radiance
NEP	Noise equivalent power
NFOV	Narrow FOV of IRLS
NIIRS	National Imagery Interpretability Rating Scale
PC	Photoconductive
Pixel	Picture element
PV	Photovoltaic
RAF	Royal Air Force (UK)
RECCE	Reconnaissance (airborne usually)
RH	Relative humidity
RMS	Reconnaissance management system
rms	Root mean square

Table 1.2 *(continued)*

Acronym or Abbreviation	Meaning
RPV	Remote piloted vehicle
SNR	Signal-to-Noise ratio
SON	Statement of Need (USAF planning document)
TAC RECCE	Tactical reconnaissance (airborne)
USAF	United States Air Force
WFOV	Wide FOV of IRLS

$$N_{ALT} = (100 \text{ nmi})\,(6076.12 \text{ ft nmi}^{-1}) = 607{,}612 \text{ lines} .$$

If each square IFOV sample is to be represented by a discrete pixel, the total number of pixels in the 100-nmi strip map image is

$$N_{TOT} = N_{ACT}N_{ALT} = (4189)(607{,}612) = 2.545 \times 10^9 \text{ pixels} .$$

If the analog signals were to be digitized prior to recording, then digital oversampling requirements would further increase the high data rate.

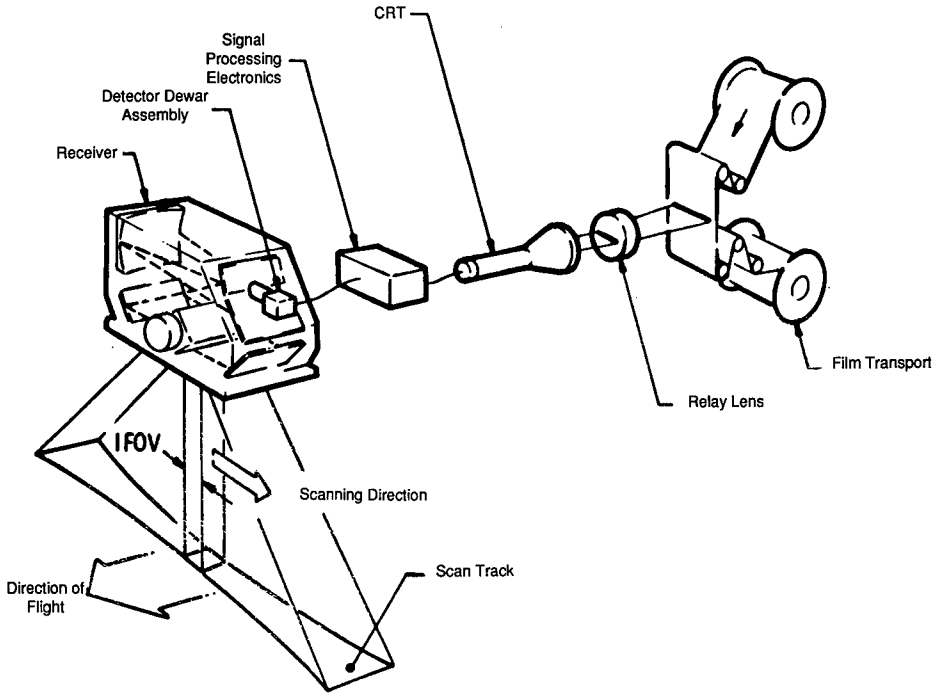

Fig. 1.1 Typical IR reconnaissance set.

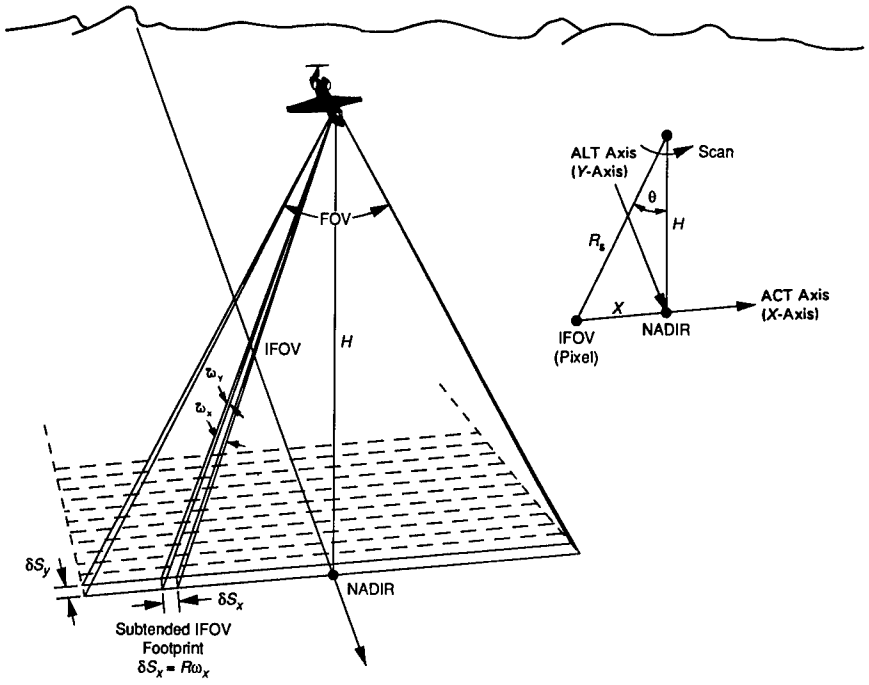

Fig. 1.2 IRLS scan pattern and coordinates. (Note: IRLS systems usually scan several lines in parallel during each scan. For clarity of illustration only one line is shown.)

Processing, storage, distribution, and interpretation of high-data-rate imagery is a challenge. IRLS systems must often interface with reconnaissance management systems (RMSs) and with data links and ground stations. At each interface there is a potential for loss of image quality and for loss of part of the imagery because of limitations in each piece of equipment. Interface specifications and measurement of IRLS image quality become very important. Such measurement criteria as modulation transfer function (MTF), noise equivalent temperature difference (NETD), and minimum resolvable temperature difference (MRTD) ensure that overall image quality reaches the end user.

1.1.3.2 Fundamental Scanning Relations in IRLS Design. The velocity-to-height ratio (V/H) is one of the dominant parameters in IRLS design because it determines the scan rates, the number of detectors scanned in parallel, and the electrical signal bandwidth. In particular, the maximum value $(V/H)_{MAX}$ is used to start the design trade-off process. The V/H ratio describes the angular rate of motion of the scene with respect to the moving platform and, hence, the resulting motion of the image in the focal plane. Its units are rad s^{-1}. The simplest approach to IRLS design assumes that continuous rotation of a scan mirror is to provide a contiguous set of scan lines across some transverse FOV. The IRLS may scan with a single detector or it may use n detectors in parallel in the along-track (y) axis to keep the mirror rotation rates to practical values. The required scan rate N_{SC} for contiguous scans at nadir is

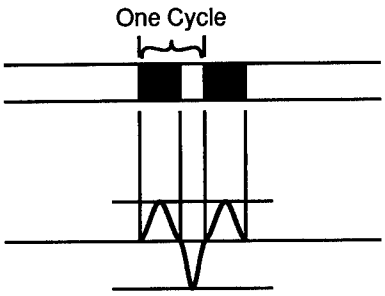

Fig. 1.3 One cycle of spatial frequency equals two pixels.

$$N_{SC} = \frac{(V/H)_{MAX}}{n(IFOV)_y} \quad [\text{scans/s}] \ , \tag{1.1}$$

where n detectors are scanned in parallel to the along-track (ALT or y) axis with each detector subtending an ALT angle $(IFOV)_y$. The across-track IFOV scan rate is

$$N_{(IFOV)_x} = \frac{N_{SC}\,\pi}{(IFOV)_x} \quad [\text{IFOV/s}] \tag{1.2}$$

because there are π rad in a 180-deg scan.

The electrical signal bandwidth is one-half the IFOV scan rate because there are two IFOV in one cycle, as shown in Fig. 1.3:

$$\delta f = \frac{N_{(IFOV)_x}}{2} = \frac{N_{SC}\,\pi}{2(IFOV)_x} = \frac{\pi(V/H)_{MAX}}{2n(IFOV)_x(IFOV)_y} \quad [\text{Hz}] \ . \tag{1.3}$$

The required spin mirror rotation rate depends on the number of facets. If n_f facets are scanned per each mirror revolution, the spin rate is

$$r_{sp} = \frac{N_{SC}}{n_f} \quad [\text{rps}] \ . \tag{1.4}$$

1.1.4 Types of IRLS

1.1.4.1 Axehead Scanners. The earliest IR line scanners used an axehead design, so-called because of the chisel-like appearance of their scan mirrors. The most common axehead scanner uses a single-facet scan mirror set at a 45-deg angle to the shaft. A scanned beam from the scene is reflected 90 deg to an optical telescope. Figure 1.4 shows this type of single-facet axehead scanner, configured here as an absolute imaging radiometer. This type is still favored in the scientific community for imaging radiometers. Some advantages and disadvantages of single-mirror scanners are given in Table 1.3.

Early single-facet axehead scanners had poor scan efficiency. Mirror rotation rates were limited by windage and flexure distortions. Attempts were made to improve performance by redesign of the spin mirror. The new axehead scanner types (b) and (c) of Fig. 1.5 were successful in that the spin mirror

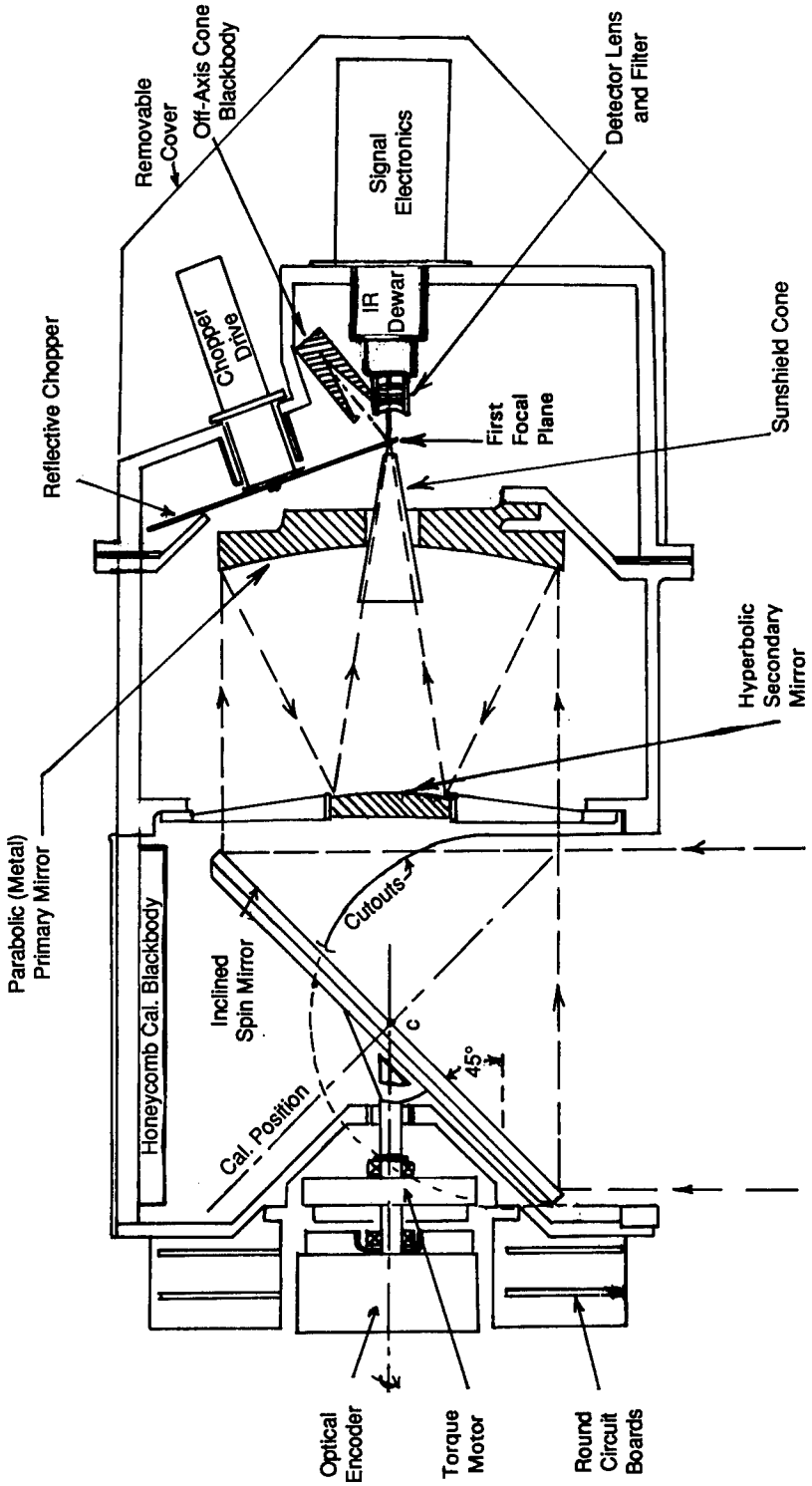

Fig. 1.4 Single-facet axehead scanner configured as a radiometer.

Table 1.3 Single-Facet Axehead Scanner: Advantages and Disadvantages

Advantages	Disadvantages
1. Simple, reliable, and proven design. 2. Large aperture in small cylindrical volume. Fits in most pods, RPVs where the vehicle or pod cross section is a critical concern. 3. Constant large aperture over 180-deg scan gives good sensitivity and high optical transfer function. 4. Adaptable to wide variety of folded optical telescopes. 5. Preferred for IR radiometers: a. Easy to insert choppers and beam splitters for multispectral IR radiometry (see Fig. 1.4). b. Easy to include ac zero clamp via rotating chopper. c. Calibration is viewed once each scan without data interruption. d. Does not cause polarization errors.	1. Image rotates 180 deg (±90 deg) for a 180-deg scan. Distortions occur in the final image when a linear array of detectors is used. 2. Windage and flexure problems of large scan mirror limit scan rate and prevent use for high velocity-to-height (V/H) ratios. 3. Wide cutout slot needed for 180-deg scan causes structural problems in pods, RPVs. 4. Low scan efficiency (1 scan/rev). 5. Works best with only a single detector on-axis, where the image rotation is not a problem.

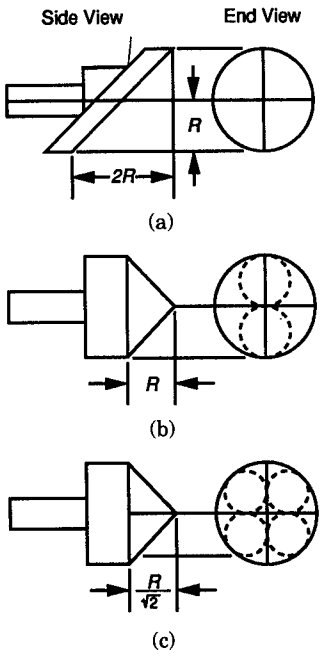

No. Facets On Spin Mirror	Telescope Required Diameter	Effective Aperture Area	Diffraction Aperture Diameter
1	$2R$	πR^2	$2R$
2	$2R$	$\frac{\pi R^2}{4}$	R
4	$2R$	$\frac{\pi R^2}{4\sqrt{2}}$	$\frac{R}{\sqrt{2}}$

Fig. 1.5 Three types of spin mirror for axehead scanner.

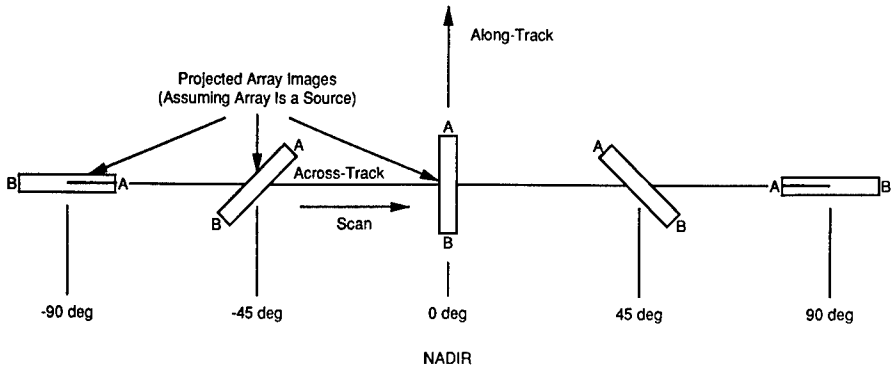

Fig. 1.6 The projected image of the array rotates 180 deg during one 180-deg scan of a single-facet axehead scanner.

was given greater stiffness and less windage, but there was a reduction in optical aperture compared to single-facet designs. The scan efficiency increased but volume efficiency was less.

All forms suffer from image rotation distortion. There is a possibility of optical image interference in the use of the facets, when beams from two successive facets both reflect into the telescope. Optical design of types (b) and (c) can become complex when linear detector arrays are used to permit higher *V/H* values. Parallel scanning of several lines in axehead scanners is complicated by image rotation in the focal plane. For convenience of depiction, one can consider that the projected image of the array rotates on the ground during the scan and is parallel to the flight track only at nadir. Rotation of the array's ground projection is shown in Fig. 1.6. Early axehead scanners were limited to low *V/H* ratios because of the reasons noted here.

Axehead scanners have recently been reconsidered for high *V/H* missions. Modern semiconductor random access memories (RAM) used with large linear detector arrays now allow real-time electronic correction of image rotation distortion. The image rotation can even be exploited to give a constant ground footprint across the scan. This image processing allows design of a compact, wide field-of-view IRLS for high *V/H* applications when the scanner must fit within the small cylindrical envelope usually occurring in small RPV or pod installations.

1.1.4.2 Split-Aperture Scanners. Military needs for higher *V/H* values led to development of the split-aperture scanners, which can go to very high *V/H* values. Most deployed military IRLS systems now use a split-aperture design.

Several split-aperture scanners were patented by H. V. Kennedy of Texas Instruments.[1] Versions with both three- and four-sided spin mirrors are shown in Figs. 1.7 through 1.9. The prismatic spin mirror typically presents two facets to incoming radiation and at nadir scan position each facet has equal aperture. As the spin mirror turns off-nadir, the projected aperture of one facet narrows while the projected aperture of the other facet widens. The combined ACT aperture tends to remain constant over a wide scan angle. The ALT aperture remains constant throughout the scan because it is not scanned except by the aircraft motion. The relatively small spin-mirror cross section allows high

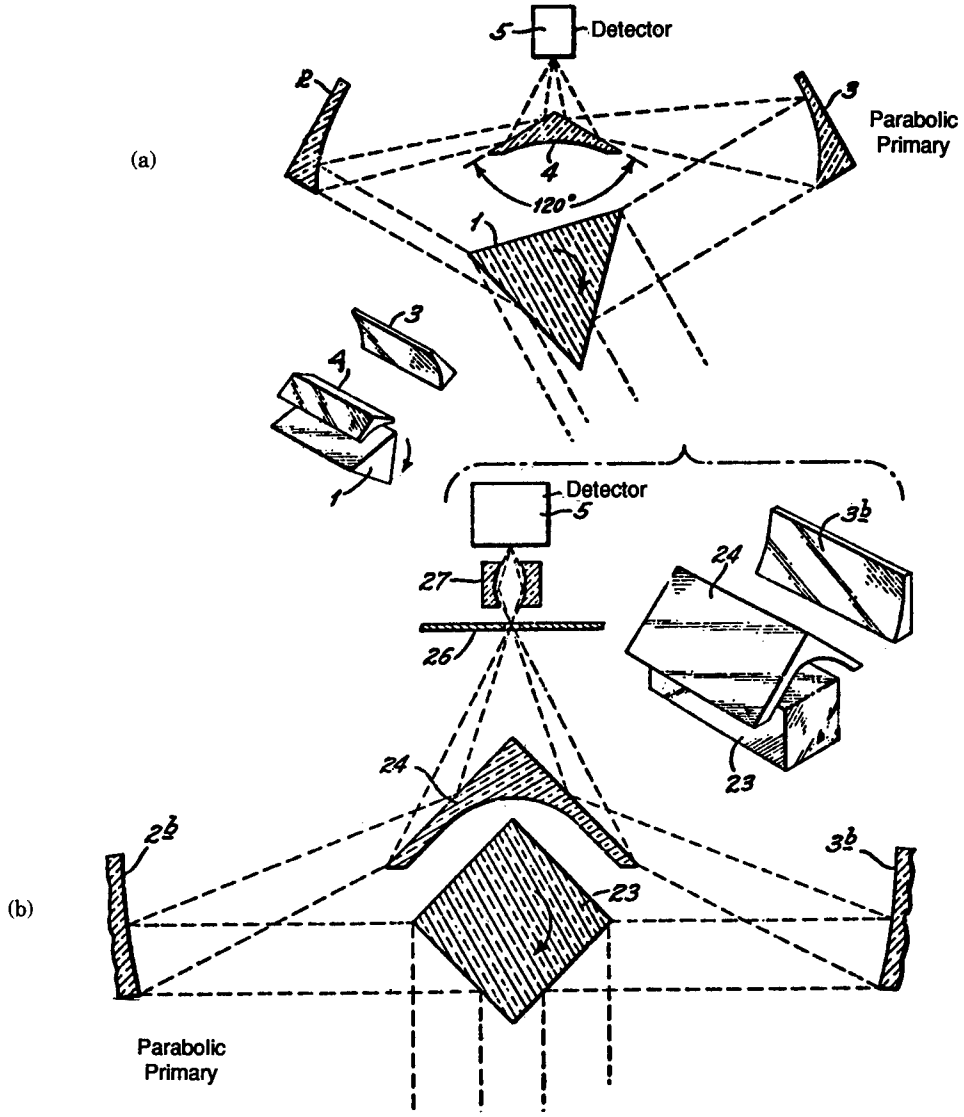

Fig. 1.7 Kennedy split-aperture scanners[1]: (a) triangular and (b) square spin mirror version.

rotation rates, which are needed for the desired high *V/H* capability. The remaining optics of the Kennedy scanner designs fold, focus, and combine the two separate beams into a single image at the focal plane. Figures 1.8 and 1.9 show rugged and simple forms of split-aperture scanner that are easier to adjust and focus than the dual-parabola designs of Figs. 1.7(a) and 1.7(b).

A spin mirror with a square cross section does not allow 180-deg scanning. For 180-deg scans with a split aperture, the spin mirror must have a triangular cross section. This permits the folding mirrors to be set high enough to clear the horizon aperture of the spin mirror, as shown in Figs. 1.7(a), 1.8, and 1.10.

The British Aerospace and Electronics (BAe) Linescan 2000 IRLS is shown schematically in Fig. 1.10. The main advantage of the outboard placement of the parabolic mirrors is that the scanner is more compact in height as compared to the central-parabola Kennedy design shown in Figs. 1.8 and 1.9. The two

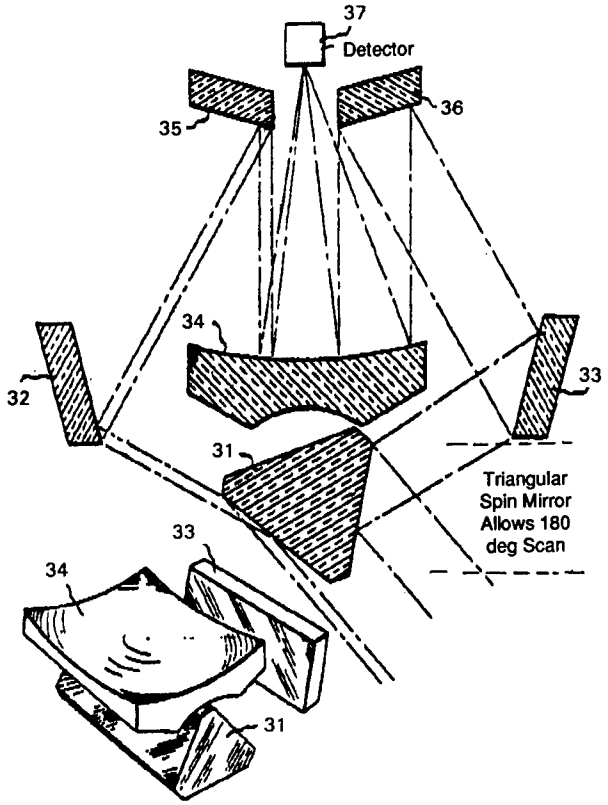

Fig. 1.8 Single-parabola Kennedy scanner.[1]

parabolic mirrors used are more difficult to align and focus than a single on-axis parabolic mirror.

A design used for several airborne platforms is shown in Fig. 1.11. The optical paths are folded so as to keep some advantages of the single-parabola design yet give a reduced scanner height in a rugged package.

1.1.4.3 Narcissus Reduction. The split-aperture design of Fig. 1.11 has an unwanted narcissus path that is uncovered when the spin-mirror apex turns away from its lowest position when nadir is viewed. The lowest spin-mirror apex climbs to reveal a narcissus strip of width W, within which the detector has a view of itself. Because the detector array and its surrounding substrate are at a temperature of less than 90 K, a negligible number of photons are received while viewing this area. This causes an undesirable lowering of the average video signal level. In the design of Fig. 1.11 this defect was corrected by a reduction in the aperture of the lower right fold mirror M4. A rectangular strip was cut from its bottom so that the two ACT apertures are no longer equal. The right ACT aperture is 0.88 of that on the left. Another disadvantage of this design, and of similar four-facet spin-mirror designs, is that the two lower outboard fold mirrors must be set level with the spin mirror. Also, they must be placed wide apart so that their reflected optical beams clear the spin

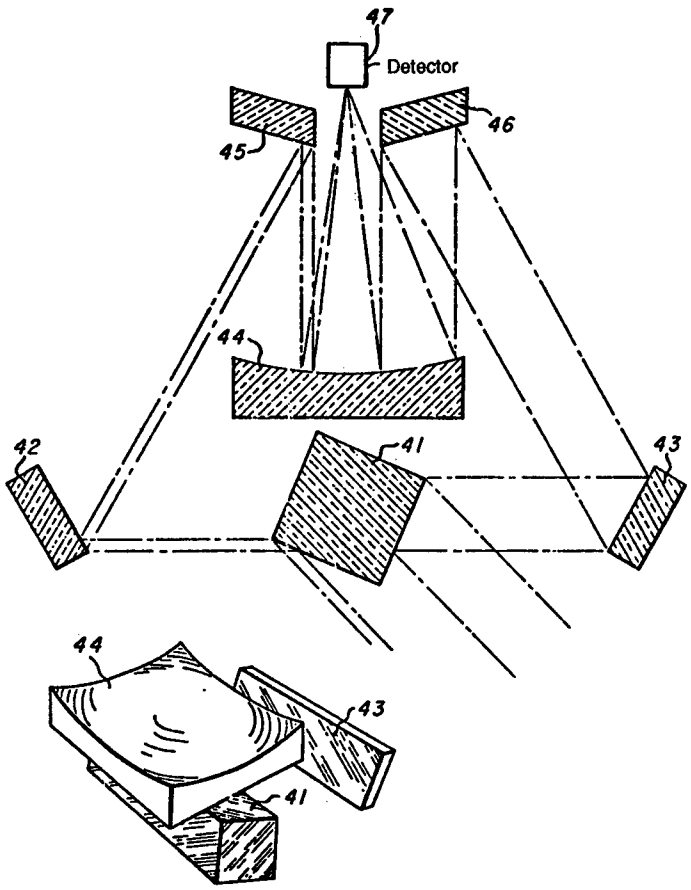

Fig. 1.9 Single-parabola Kennedy scanner.[1]

mirror and its shield. These two requirements cause the receiver to be approximately rectangular in cross section, while many of the small RPVs and pods require a more circular cross section.

1.1.4.4 Combined Split-Aperture IRLS and FLIR. A combined IRLS/FLIR built for automatic guidance and homing of a proposed autonomous vehicle[2] is shown in Figs. 1.12 and 1.13. An inertial navigation system was to obtain periodic updates to correct drift by flying over known checkpoints on the flight path. The on-board computer was to be provided with abstracted ground images of the checkpoints so that offset errors could be measured via map matching. The IRLS/FLIR views the checkpoint area in the downward (IRLS) mode. Once the autonomous vehicle arrives at its target, the IRLS converts rapidly to FLIR mode and homes using correlation guidance. Conversion to FLIR operation occurs by rotation of a lightweight hemicylindrical metal shutter, as shown in the figures. The elevation scanning mirror ran continuously in either mode. It was servo-controlled to provide the added functions of pitch axis pointing

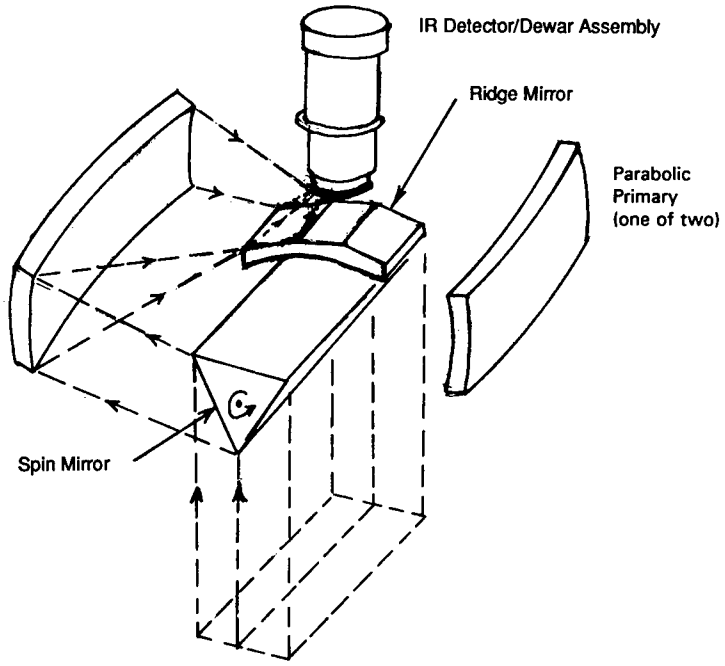

Fig. 1.10 BAe Linescan 2000 IRLS.

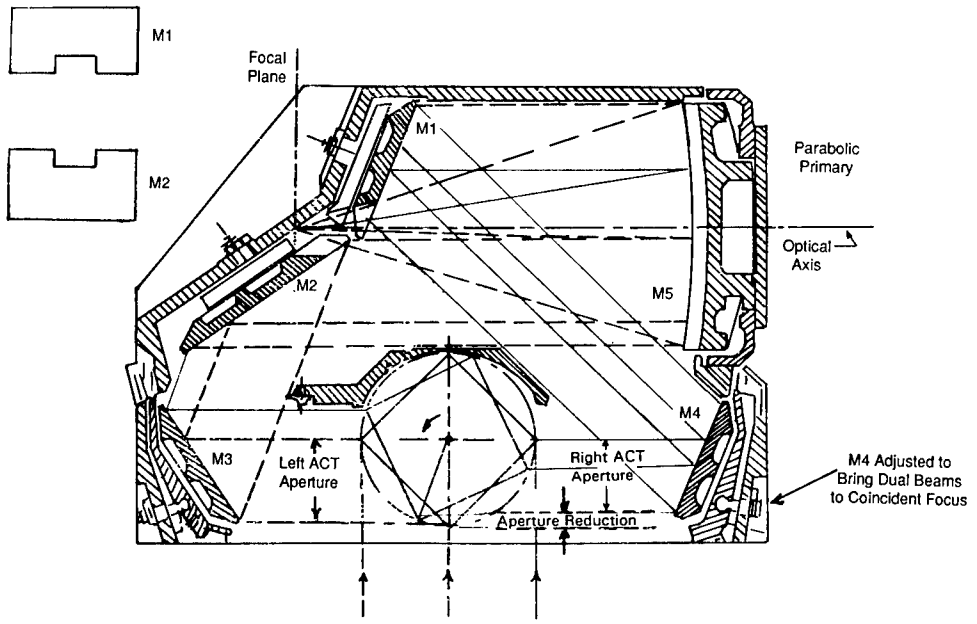

Fig. 1.11 Reduced-height receiver layout.

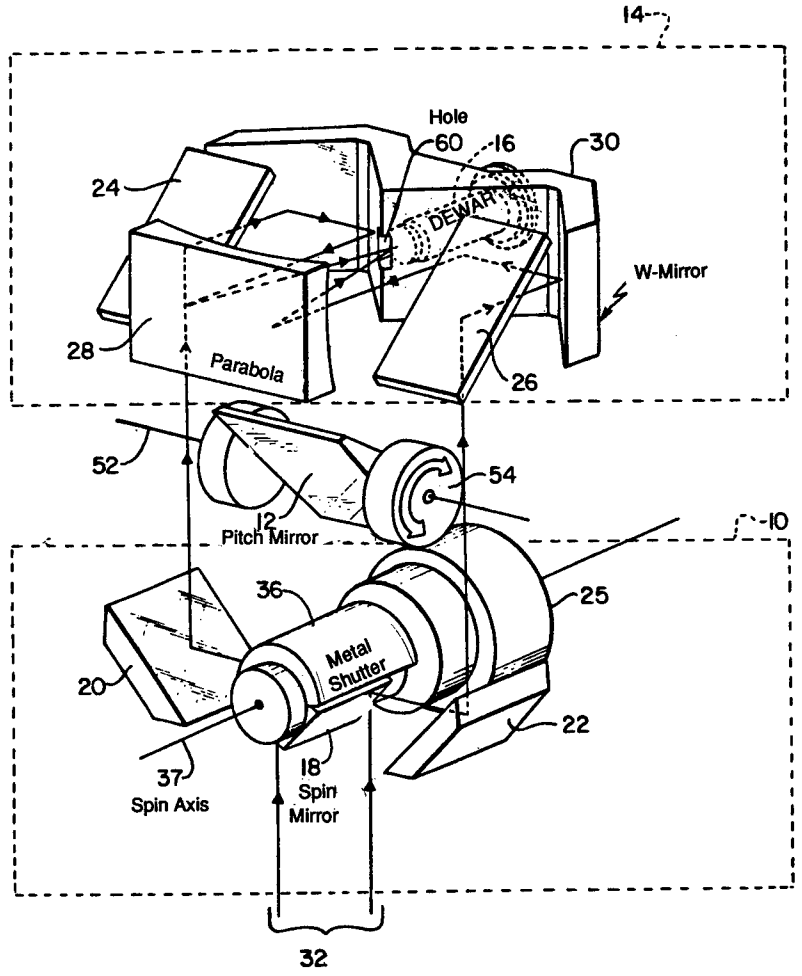

Fig. 1.12 Dual IRLS/FLIR in downward mode.[2]

and pitch stabilization using reference signals from an IRLS internal rate gyro package. The dual optical paths of the split-aperture sensor were folded to the rear via the two upper fold mirrors and then forward to a central parabolic primary via a W-shaped mirror. The compact sensor fit on a two-axis gimbal. The pitch mirror servo acted as a third virtual gimbal to stabilize the FLIR mode in all three axes. In downward mode the sensor used both electronic and mechanical stabilization plus offset pointing in the roll axis only.

1.1.4.5 Conical Scanners and IRLS Imaging from Spacecraft. Several instances of line scanning from unmanned and manned satellites are interesting. Of these, the ERTS Scanner and the NASA S-192 Multispectral Scanner for Skylab are examples. The ERTS used a rectangular FLIR-type scan but the S-192 scanner used the conical scan pattern shown in Fig. 1.14. This scanner used silicon detectors for spectral channels 1 through 12, while channel 13 operated in the 10.2- to 12.5-μm LWIR band using photoconductive mercury

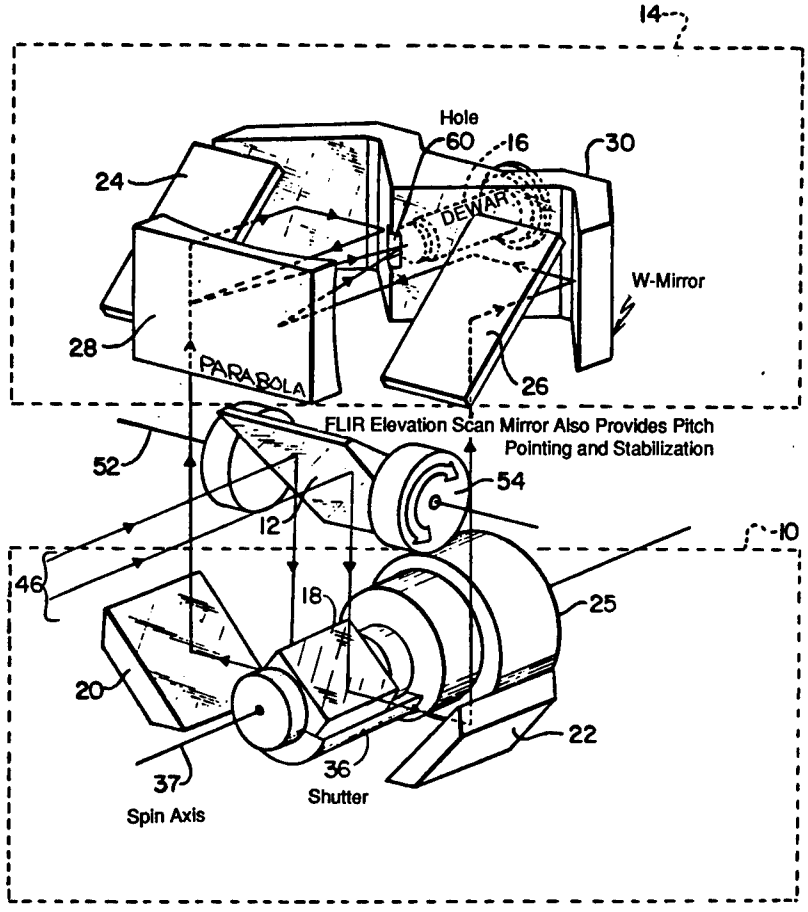

Fig. 1.13 Dual IRLS/FLIR in targeting mode.[2]

cadmium telluride. The conical scan pattern was formed by giving the scanner a 9-deg forward tilt from nadir. Scanning was accomplished by a small flat fold mirror that rotated on an arm to scan a circular zone of the image in the first focal plane of the telescope. The primary was a 20-in.-diameter spherical mirror. The image thus contained spherical aberration, symmetric about the optical axis. The scan mirror scanned a zone of this known constant spherical aberration, which was subsequently corrected by the refocusing optics. A well-corrected image was obtained over a wide spectral band, yet the high cost of a large parabolic primary mirror was avoided.

The data were tape recorded as conical scan arcs that required computer rectilinearization prior to imagery display on raster-scanned TV monitors.

1.1.4.6 Pushbroom Scanners. Occasionally, pushbroom scanners are recommended for airborne reconnaissance. Design studies have shown that the goal of a simpler scanner with no moving parts is not cost effective when compared to a conventional optomechanical scanner. Table 1.4 lists a few problems of pushbroom scanners. Pushbroom scanners, however, can be cost effective in satellites or for pointable scanners.

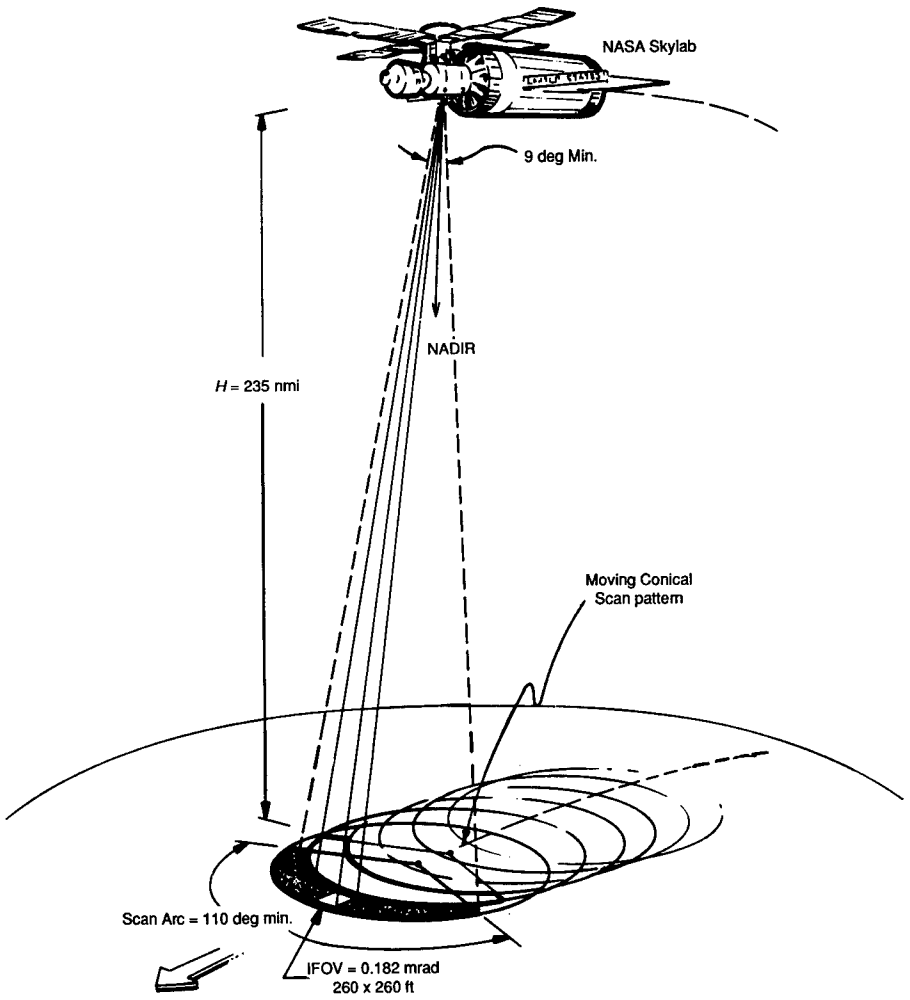

Fig. 1.14 Scan pattern of S192 multispectral scanner.

Table 1.4 Problems of Pushbroom Scanners

1. For 180-deg FOV at least six windows and telescopes are needed if a telescope field of 30 deg is optimistically assumed.
2. Means must be found to obtain a warm and a cold reference signal for stabilization of the ac signal. Usually this will require oscillation of a chopper mirror to interrupt the scene radiation.
3. A large multiplexed detector array is needed. The array must follow the curved focal plane of the multiple telescopes. Multiple detector dewars will be needed and cryogenic cooling will be difficult.

1.2 PRELIMINARY SCANNER DESIGN

A preliminary scanner design study assesses practicality of a proposed IRLS scanner design. Performance, size, weight, and cost trade-offs are made to assure a viable solution to imposed requirements. Sections 1.2 and 1.3 discuss some important aspects of preliminary design, starting with the scanner.

1.2.1 Diffraction-Limited Resolution

Before the requirements analysis and system design studies of Secs. 1.2 and 1.3 are started, it is wise to estimate whether the desired angular resolution can be achieved within the confines of a given envelope and with a given type of scanner. The angular resolution of an IRLS is determined by the aperture diffraction and by the detector size. The Rayleigh criterion used for estimating diffraction-limited resolution must distinguish between two aperture types:

1. for round apertures:

$$\alpha = 1.22 \frac{\lambda}{D} \text{ rad}$$

2. for rectangular apertures:

$$\alpha = \frac{\lambda}{D} \text{ rad} ,$$

where λ is the wavelength, D is the aperture diameter for circular apertures (or the aperture width for rectangular apertures), and α is the angle separating the two point or line sources in object space. The criterion of resolution is when the first null of one diffraction pattern in the focal plane falls on the peak of the other. In split-aperture line scanners the limiting aperture is that of a single ACT aperture. The two beams are not correlated because optical path lengths differ for each aperture. Hence, one cannot add the two apertures together to calculate diffraction effects. The diffraction-limit estimate should use the wavelength of peak energy for the spectral band chosen. Consider, for example, a split-aperture IRLS design in which the smaller of the two rectangular apertures has a width of 3 cm at nadir. At 10-μm peak energy wavelength, the Rayleigh criterion is

$$\alpha_{ACT} = \frac{10 \times 10^{-6} \text{ m}}{3 \times 10^{-2} \text{ m}} = 3.333 \times 10^{-4} \text{ rad} = 0.333 \text{ mrad} .$$

Obviously, with this scanner design it would be unwise to expect resolution of 0.2 mrad in the ACT axis where this 3-cm aperture applies. Resolution in the ALT axis depends on the length of the spin mirror. If, in our example, this length is 10 cm, the Rayleigh criterion gives

$$\alpha_{ALT} = \frac{10 \times 10^{-6} \text{ m}}{10 \times 10^{-2} \text{ m}} = 1 \times 10^{-4} \text{ rad} = 0.100 \text{ mrad} .$$

These estimates are first done for nadir viewing when both across-track apertures are nominally equal in split-aperture scanners but must be also done at higher scan angles if the ACT aperture is smaller at these angles.

1.2.2 *f*/Number and Detector Size

Most IRLS scanners have optics designs at $f/\# = 1$, where $f/\#$ is defined simply as focal length divided by aperture width. Because split-aperture scanners have two narrow rectangular apertures, the $f/\#$ used in scanner design does not apply to the two scan apertures, but rather to the total aperture projection on the primary mirror. The $f/\#$ is a parameter used in determining the cone angle of all rays that the detector must accept. Figure 1.15 gives the angular convergence of the rays in terms of cone angle ϕ for various $f/\#$ values. Most IRLS designs use $f/1.0$ parabolas ($f/\# = 1.0$) to minimize detector noise. Detector noise is proportional to the linear size of the detector, so a minimum $f/\#$ is desirable. Faster systems with fractional $f/\#$ are rare because the rays converge to the detector at oblique angles that are difficult to couple into the detector.

Because split-aperture designs have two rectangular primary apertures on the focusing parabola, there is a possibility of two separate $f/\#$ values and a nonsquare detector. Usually, $f/\#$ is determined from the diagonal of the rectangular aperture and a square detector is used. In our example, the spin mirror is 10 cm long in the along-track (y) dimension. The primary aperture used is a 10- $\times$ 10-cm square with a diagonal of $10\sqrt{2}$ cm = 14.14 cm. For

$$f/\# = \frac{\text{Effective Focal Length}}{\text{Aperture Width}} = \frac{f}{D}$$

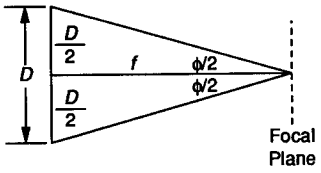

$$\tan\frac{\phi}{2} = \frac{D}{2f} = \frac{1}{2(f/\#)}$$

$$\frac{\phi}{2} = \tan^{-1}\left[\frac{1}{2(f/\#)}\right]$$

f/#	φ/2 (deg)	φ/2 (rad)	φ (deg)	φ (rad)
0.75	33.69	0.59	67.38	1.18
1.00*	26.57	0.46	55.13	0.93
1.50	18.43	0.32	36.87	0.64
2.00	14.04	0.24	28.07	0.49

*Most IR Line Scanners Use $f/\# = 1.00$ to Minimize Detector Size for a Given IFOV

The Detector Size for an IFOV of ω is Simply $s = f\omega$, where s = Detector Size, f = Focal Length, ω = IFOV (rad)

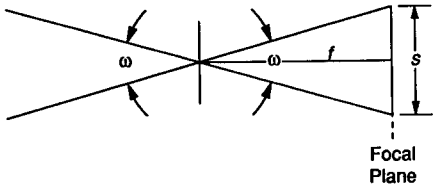

Fig. 1.15 Simplified use of $f/\#$ in line scanners.

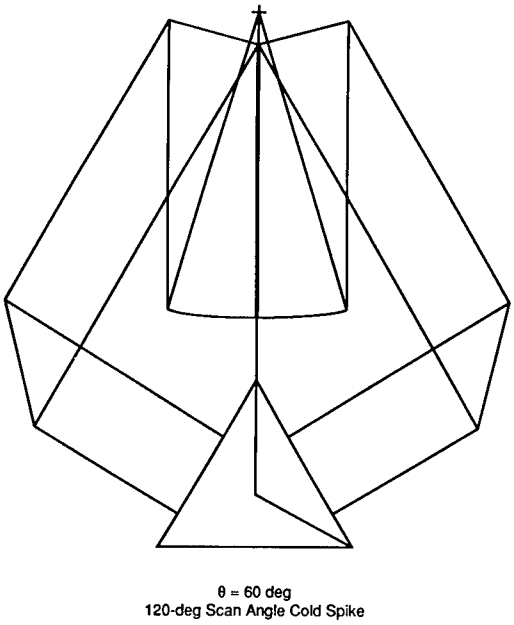

Fig. 1.16 Example of a printout from a CAD cold-spike preliminary study.

an $f/\# = 1$ system the focal length must be 14.14 cm. The detector size (see Fig. 1.15) for a specified IFOV of 0.33 mrad would then be

$$s_x = s_y = f(\text{IFOV}) = (14.14 \text{ cm})(0.33 \times 10^{-3} \text{ rad})$$

$$= 4.67 \times 10^{-3} \text{ cm} = 1.84 \text{ mil} .$$

1.2.3 Layout Drawings and Graphical Ray Tracing

After the preliminary estimates show that use of the chosen size of IR line scanner is practical, a rough layout and preliminary graphical ray-trace sketches are made. Computer-aided design (CAD) ray-trace studies are then usually done to disclose any obvious problems in the following areas of concern:

1. scanner overall envelope
2. scanner installation in allocated space
3. scanner ACT field of view
4. stray radiation and narcissus problems
5. roll effects on FOV and wing or pod interferences
6. cold-spike location and total number per revolution.

Figure 1.16 is an example printout from a CAD cold-spike analysis. This work interacts with the requirements analysis of Sec. 1.3.1.

1.3 REQUIREMENTS ANALYSIS

Any new IRLS development or new IRLS application needs a comprehensive requirements analysis. The proposed IRLS equipment is considered in the full

context of its intended use. It is vital to involve the following people or disciplines at the earliest possible stages of the development: users, IRLS designers, aircraft/avionics designers, parts suppliers, reliability, logistics, and financial and program planners.

A USAF document called a Statement of Need (SON) defines basic needs and requirements for the proposed IRLS, including

1. altitude range
2. *V/H* range
3. scan field of view (transverse scan field)
4. resolution
5. aircraft or platform
6. deployment considerations.

After review and modification the SON can lead to a detailed USAF procurement specification. Other services and users usually follow a similar process.

1.3.1 Mission Requirements

Table 1.5 lists some mission types using IRLS sensors in both manned and unmanned vehicles. Mission altitudes range from the very low altitudes used in penetration reconnaissance to the satellite altitudes used for earth observations and meteorological data collection. This wide range of altitudes corresponds to a wide range of *V/H* values. The *V/H* range for a given IRLS has a great influence on its design. At the lowest reconnaissance altitudes the *V/H* ratio is very high and rapid scanning is required to provide contiguous imagery. At satellite altitudes the *V/H* ratio is very low and redundant scans of the same scene object usually occur even with a single detector channel.

Table 1.5 IRLS Mission Types for Manned and Unmanned Vehicles

Tactical Reconnaissance
1. Mid-altitude general reconnaissance
2. Low-altitude penetration of high-threat areas
3. Mid-altitude standoff reconnaissance
Surveillance
1. Low- and mid-altitude oblique viewing of border areas
2. Low-altitude overflight of specific targets or zones such as suspected nuclear sites and mountain passes
3. Ocean and coastal zone patrol, including antisubmarine patrol
4. Forest-fire patrol and coal-mine fire patrol
Special Missions
1. Radiometric surveys of specific ground targets such as factories
2. Economic and ecological surveys such as crop health, crop size
3. Pollution monitoring in waterways such as effluent monitoring, oil slick detection, and vegetation damage
4. Meteorological and scientific studies such as atmospheric sounding and cloud-cover imaging
5. Autonomous navigation of cruise missiles and navigational checkpoint determination in manned aircraft

A mission requirements analysis helps determine such important IRLS design choices as

1. scan field (transverse coverage versus altitude)
2. scan rate versus number of parallel detector channels per scan
3. spatial resolution
4. thermal sensitivity
5. imagery display means, real-time viewing, and recording means.

1.3.2 Scan Field of View

As an example of determination of scan FOV requirements from a typical mission analysis, consider the use of an IRLS for low-level penetration reconnaissance. By flying very low and fast the aircraft is masked by terrain while defending radar is confused by the ground clutter. The aircraft *V/H* rate is so high that ground-based antiaircraft defense equipment has severe difficulty in locking on and tracking. Both the penetration and data collection runs are made at high speed and very low altitude, which requires that the entire flight be precisely and carefully planned. Most targets will be preassigned with their locations known to be in specific designated zones. The flight path is chosen to minimize aircraft exposure and to minimize time spent within the defended high-threat zones. The impact on the IRLS is that the aircraft will usually have to fly to the right or to the left of a target zone or between two target zones for the data collection. There may be a few dangerous instances where targets are overflown, but typical low-level reconnaissance will require offset viewing, as shown in Fig. 1.17.

Figure 1.18 compares the very-wide-FOV requirements of the low-level penetration missions to that of more conventional IRLS systems. The very low flight altitudes and the need to view targets on both sides of the flight track simultaneously require that the IRLS have a 180-deg FOV for nominally flat terrain. If the aircraft flies in a valley at low altitude, or if the terrain rises on one side, the $\pm$ 90-deg scan will intercept the ground on one side and the horizon will not be seen. Figure 1.19 shows terrain effects in offset viewing during low-level missions. In IRLS designs using only electronic roll stabilization within the collected video information, aircraft roll motions must be studied to determine if a given target will be seen in the chosen transverse scan.

1.3.3 Coverage Versus Altitude

Simple trigonometry determines ground coverage for a nominally flat earth once the FOV is chosen. Figure 1.20 gives relations for slant range R and offset distance X at aircraft altitude H.

1.3.4 *V/H* Range, Scan Rate, and Number of Parallel Channels

The *V/H* ratio can vary widely depending on altitude. If a military aircraft flies at a constant velocity of 1000 ft s^{-1} over an altitude range of 300 to 30,000 ft, the *V/H* varies from 3.33 to 0.0333 rad s^{-1}. Both the spin-mirror rotation rate and the number of parallel channels used can be varied to accommodate this wide *V/H* range. Usually, the spin-mirror rotation rate is changed in fixed

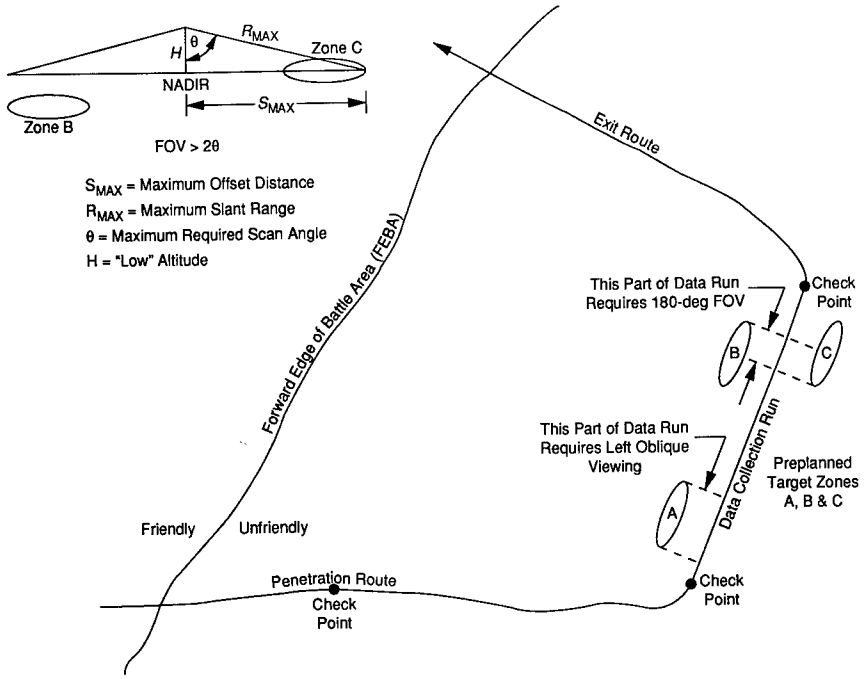

Fig. 1.17 Penetration mission requires wide-scan coverage.

increments. One IRLS design uses a 2:1 speed change for the higher *V/H* values encountered at lower altitudes and uses automatic selection of from 1 to 12 parallel detector channels as the *V/H* varies within each of the two altitude zones. The aircraft inertial navigation system provides the IRLS with a *V/H* signal used by the automatic channel selection logic. Overlap writing on film is possible at certain *V/H* values, and the amount of overlap used is also an automatic decision of the logic circuits. Other IRLS designs use similar means to accommodate the *V/H* range.

1.3.5 Spatial and Thermal Resolution Requirements

Mission objectives will determine spatial and thermal resolution requirements. In tactical airborne reconnaissance, primary interest is in detection, classification, recognition, and identification of specific military targets. Detection of military activity is also an important outcome of imagery interpretation. As an example of activity we note that it is important to be able to distinguish active armored vehicles from inactive ones or from burned out hulks. Warships and factories can be inactive or they can be idle. Adequate spatial and thermal resolution allows fulfilling the four main imagery interpretation tasks:

1. *Detection:* the process of establishing that a valid military target is present in the image at a specific location
2. *Classification:* the determination that the detected target falls within

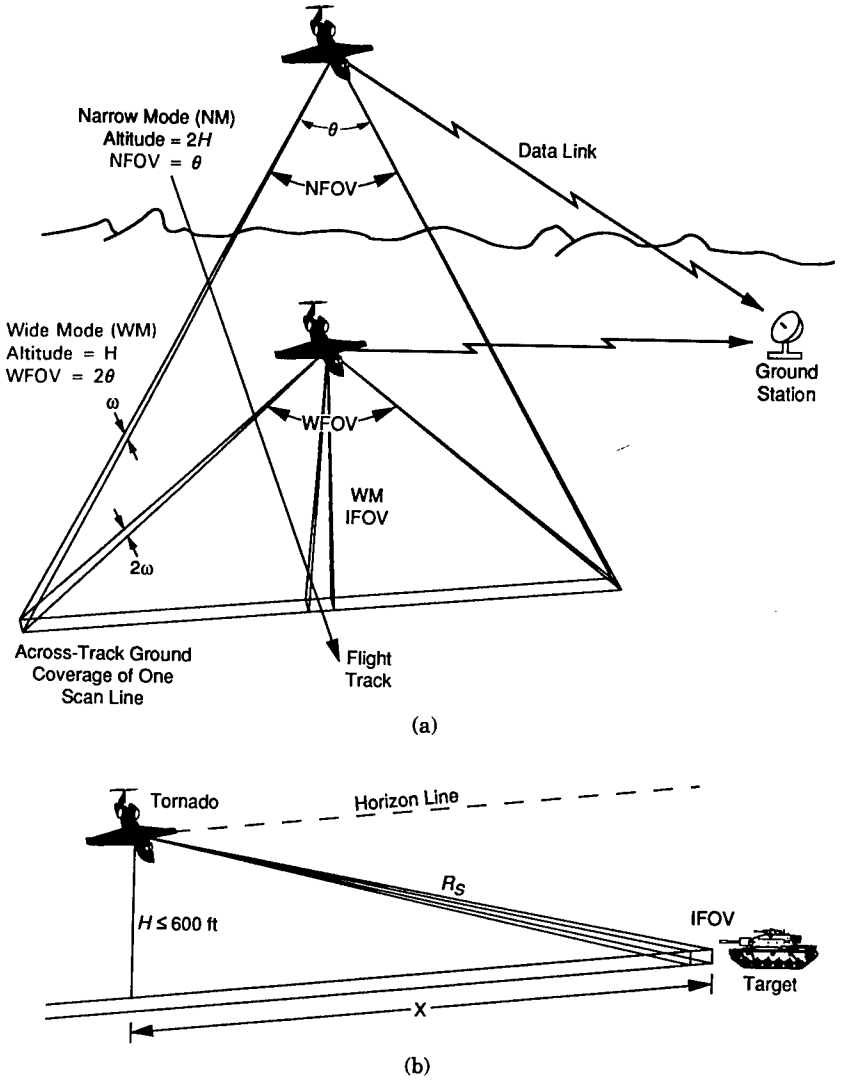

Fig. 1.18 (a) Centered narrow- and wide-FOV reconnaissance. (WM = wide mode; altitude = H, FOV = 2θ; since IFOV = 2ω and WMFOV = 2 NFOV, the signal bandwidth and imagery format are the same in either FOV mode.) (b) Oblique viewing in low-level penetration mission. (At very low altitudes, a 180-deg scan is needed.)

a general target class such as "tracked armored vehicle," "towed artillery piece," etc.

3. *Recognition:* the process of establishing the specific class of target, such as determining that the target is not only in the general class "tracked armored vehicle," but that it falls within the specific class "tank" as opposed to "armored personnel carrier"
4. *Identification:* the process of establishing the specific type or model of the target. An example would be identification of M-60 as the specific tank model.

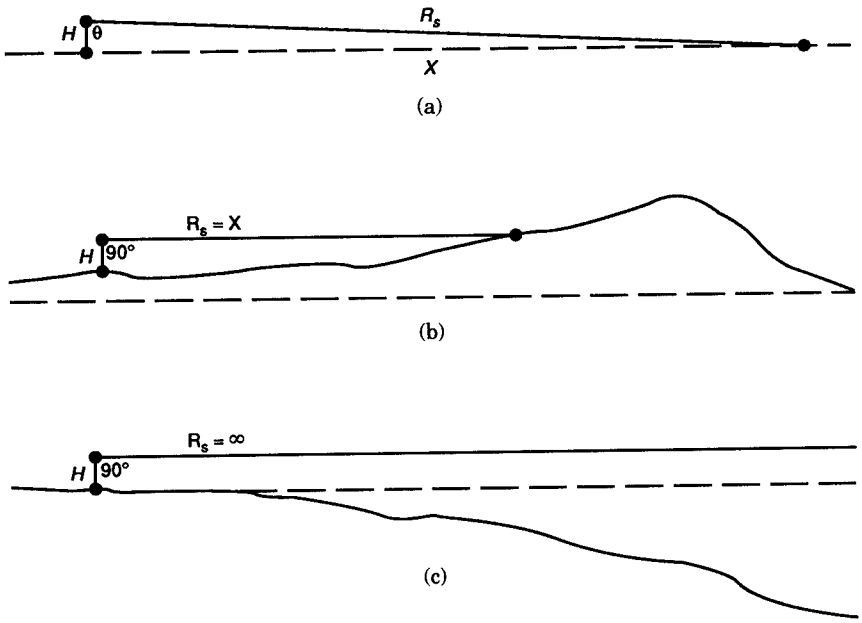

Fig. 1.19 Terrain effects in low-level missions: (a) flat earth; (b) rising terrain limits offset distance (defocus effect must be considered); (c) falling terrain causes view of sky in imagery.

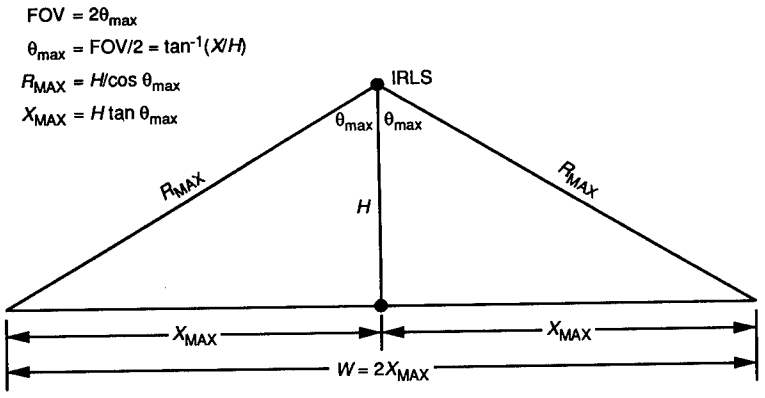

Fig. 1.20 IRLS coverage versus altitude.

These four tasks are graded here in order of difficulty. Increased spatial resolution is needed as difficulty increases. Thermal resolution also is important because accomplishment of each task requires a specific perceived signal-to-noise ratio.

1.3.6 Spatial Resolution Requirements

The determination of IRLS spatial resolution requirements is similar to that for FLIR sensors and is based on research performed by the US Army, the US

Navy, and others. The standard used is the work done at the US Army Center for Night Vision and Electro-Optics (CNVEO). Johnson and Lawson[3] give probability of detection P_D, probability of recognition P_R, and probability of identification P_I versus number of spatial cycles n placed across the critical target dimension for army vehicles. Figure 1.21 is a graph based on the work of Johnson and coworkers. It shows the probability of successfully performing the specified task versus normalized spatial frequency (f/f_0). In this figure, f_0 is that spatial frequency placed across the critical target dimension that gives 50% probability of success for that task. The frequency f is the spatial frequency capability of the sensor. For army vehicles, the values of spatial resolution required for the tasks of detection, recognition, and identification are given in Tables 1.6, 1.7, and 1.8, respectively. Data for the classification task can be obtained by averaging the requirements for detection and recognition. Tables 1.6 and 1.7 are taken from "Night Vision Laboratory static performance model for thermal viewing systems."[4] Ratches *et al.* applied the data to FLIR systems, but IRLS systems also produce thermal imagery. IRLS designers routinely use the same criteria and requirements of spatial resolution. The title of this document includes the words "static performance," which is valid for IRLS imagery. Tables 1.6 through 1.9 are thus useful for IRLS imagery displayed on CRT monitors, and when film recordings are viewed on a light table for

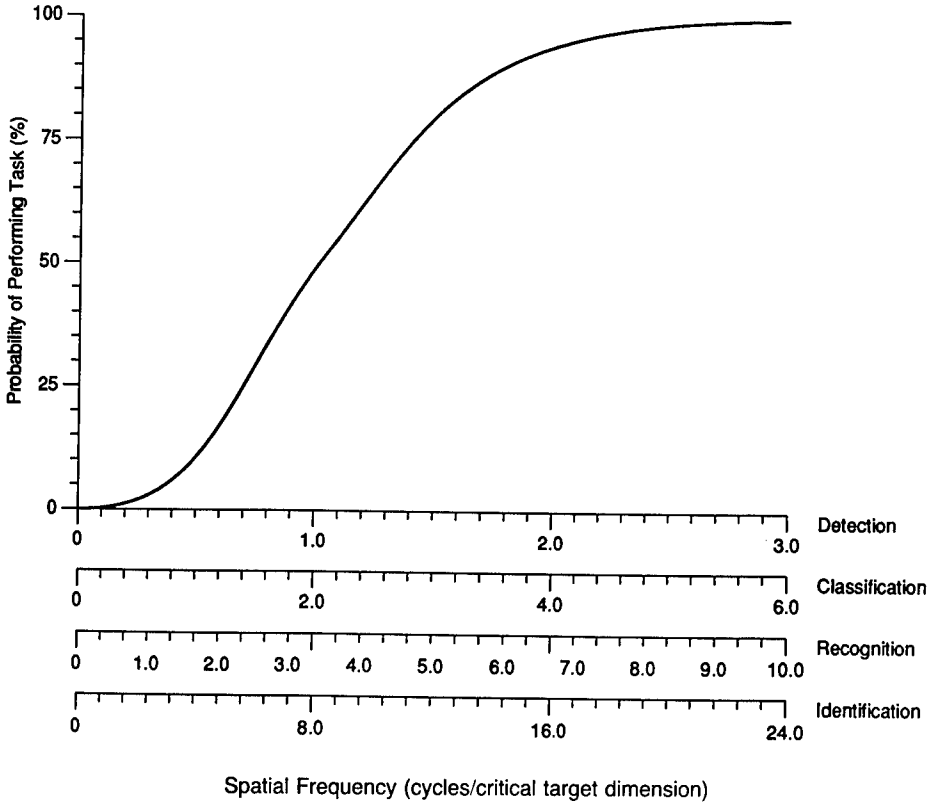

Fig. 1.21 Detection and recognition criteria in terms of probability of accomplishing task.

Table 1.6 Probability of Detection Versus Number of Cycles Placed across Critical Target Dimension for Army Vehicles

Probability of Detection P_D	Number of Cycles	Number of Pixels (one IFOV/pixel)
1.0	3	6
0.95	2	4
0.80	1.5	3.0
0.50	1.0	2.0
0.30	0.75	1.50
0.10	0.50	1.00
0.02	0.25	0.50
0	0	0

Table 1.7 Probability of Recognition as a Function of Number of Cycles across Critical Target Dimension for Army Vehicles

Probability of Recognition P_R	Number of Cycles across Critical Target Dimension		
	Pessimistic	Optimistic	Average
1.0	12	9	10.5
0.95	8	6	7
0.80	6	4.5	5.25
0.50	4	3	3.5
0.30	3	2.25	2.63
0.10	2	1.5	1.75
0.02	1	0.75	0.88
0	0	0	0

Table 1.8A Probability of Identification as a Function of Number of Cycles across Critical Target Dimension for Army Vehicles (Approximate Suggested* Values for Film Viewing on a Light Table with IRLS Imagery)

Probability of Identification P_I	Number of Cycles	Number of Pixels
1.0	18	36
0.95	12	24
0.80	9	18
0.50	6	12
0.30	4.5	9
0.10	3	6
0.02	1.5	3
0	0	0

*Numbers are approximate because the identification process exploits known characteristic features of the target type. Features vary in size and location. A target may be identified, for example, by a peculiar type of flash hider on its cannon. Another may be identified by cannon barrel length. Experience improves results considerably. Values given here are not supported by any studies of interpreter performance but are used in IRLS design with good results.

Table 1.8B Probability of Identification Versus Number of Cycles across Critical Target Dimension for Army Vehicles To Be Used for IRLS Viewing on CRT Monitors (adapted from Ref. 5)

Probability of Identification P_I	Number of Cycles	Number of Pixels
1.0	24	48
0.95	16	32
0.80	12	24
0.50	8	16
0.30	6	12
0.10	4	8
0.02	2	4
0	0	0

Table 1.9 Probability of Detection of Open Ocean Targets* Versus Number of Cycles across the Target Critical Dimension

Probability of Detection P_D	Number of Cycles	Number of Pixels (one IFOV/pixel)
1.0	1.5	3.0
0.95	1.0	2.0
0.80	0.75	1.5
0.50	0.50	1.0
0.30	0.375	0.75
0.10	0.25	0.50
0.02	0.125	0.25
0	0	0

*Open ocean targets are almost always ships. Barges, submarines, oil-drilling platforms, or offshore oil-loading platforms could occasionally be objects to be detected. Open ocean targets present difficulties for the longer oblique ranges in standoff reconnaissance because of the humid air paths encountered.

interpretation the tables are used even though the experimental justification is for FLIRs. The light table film imagery is much brighter, has less surface reflections, and does not flicker compared to a CRT. Formation of a complete image from a CRT moving spot requires integration by the observer.

Table 1.6 gives probability of detection P_D versus number of cycles across the critical target dimension for army vehicles. The critical target dimension in most cases is the minimum viewed dimension. In plan view this would be the vehicle width, while in a front or rear or side aspect it would be the nominal vehicle height.

A pixel is the representation of an IFOV in the imagery. One cycle of spatial frequency in the imagery contains two pixels. In tests this will be one bar and one space of a four-bar test target. Each cycle is rendered in a positive image as a dark and a light pixel, and vice versa for a negative image.

In Table 1.7 the probability of recognition P_R is given versus the number of cycles across the critical target dimension. The number of required cycles is given in pessimistic, optimistic, and average values because the spread in the measured data allows some design choice. Table 1.8 gives the more stringent resolution requirements for the identification task.

Table 1.9 gives requirements for detection of open ocean targets, including ships, barges, surfaced submarines, and oil well platforms. Open ocean targets are seen against a clear background and differ from army vehicles in that higher spatial resolution is needed for recognition and identification. For example, in recognizing warships on the open sea with long-range standoff (oblique) viewing, a destroyer class ship can be mistaken for a cruiser class warship at longer range. Warships vary significantly within the same class or even within the same type. Naval reconnaissance is interested in determining if specific modifications have been made to a given ship class. Determination of these modifications is critical for identification. High resolution is needed to see structural details used for discrimination and identification. Because required resolution for open ocean targets is dependent on the specific ship in the case of identification, no tables are given for ship recognition and identification. IRLS designers use a safety factor compared to the requirements for army vehicles. The exact factor is a matter of end-user choice. For a given IRLS resolution the tasks of recognition and identification could be accomplished by flying close to the target. In combat this is not usually an option. The required resolution is then a function of the required standoff range.

1.3.6.1 NIIRS Rating. The NIIRS rating system is a convenient aid in determining spatial resolution requirements. NIIRS is an acronym for National Imagery Interpretability Rating Scale. It is a means of rating photographic military reconnaissance imagery and gives imagery rating categories from 0 through 9. Rating category 7 is shown in Table 1.10 as an example. The

Table 1.10 National Imagery Interpretability Rating Scale Example

Rating Category 7
Ground-resolved distance—20 to 40 cm (8 to 16 in.)
Identify radar equipment
Identify major electronics by type on a KILDIN DD or KASHIN DD
Identify command and control headquarters
Identify nuclear weapon components
Identify land mine fields
Identify the general configuration of an SSBN/SSGN submarine sail to include relative placement of bridge periscope(s) and main electronics/navigation equipment
Identify pitot tubes on fighter aircraft (e.g., FLAGON)
Identify a strategic missile transporter/erector when not in a known missile area
Identify a T 54 tank by the presence of a turret ventilator
Identify a T 55 tank by the absence of a turret ventilator
Perform technical analysis on ports and harbors
Perform technical analysis on railroad yards and shops
Perform technical analysis on roads

NIIRS scale is self-explanatory except certain acronyms are included, such as DD: destroyer and SSBN, SSGN: submarine types. When NIIRS categories are used for IRLS requirements, the ground-resolved distance (GRD) is assumed to be the subtense of the IFOV at the target.

1.3.6.2 Contextual Cues and Clues. In using both the NIIRS scale and the Johnson criteria to determine IRLS resolution requirements it is wise to remember that contextual cues, observer training, experience, and innate skill also play an important role in interpretation. Ship identification criteria are different for open ocean targets as opposed to the same ships in a harbor or tied up at a pier or in a dry dock. Contextual clues in the latter cases can usually help determine size, type, activity, and even the ship's name in some cases. There are many instances of infrared contextual cues and clues. Well-disguised Communication, Command, and Control (CCC) stations can be identified as much by the heat from their power units as by the image of the installation itself. CCC installations are often underground with only a whip antenna showing. Evidences of traffic to and from the buried entrance may also be noted by terrain scarring, vehicle tracks, and footprints, which change soil emissivity.

1.3.6.3 Requirements for Oblique Viewing. The low-altitude penetration missions demand imaging at highly oblique scan angles. Targets will be seen at aspects that approximate side views rather than the plan views seen near nadir. Figure 1.22 compares two target situations to which the Johnson spatial resolution criteria can be applied. Figure 1.22(a) shows low-level oblique viewing. Figure 1.22(b) shows plan viewing, which occurs near nadir. Spatial resolution is defined by the IFOV subtense δS at the target:

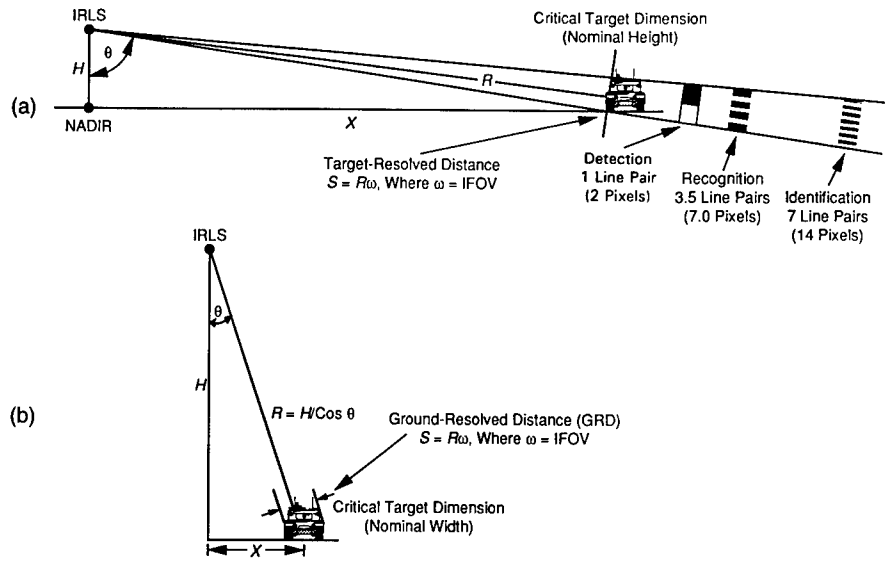

Fig. 1.22 Comparison between oblique and plan viewing: (a) oblique viewing where $\theta >$ 60 deg; (b) plan viewing where $\theta \leq 60$ deg.

$$\delta S = R(\text{IFOV}) \quad [\text{ft or m}] \ , \tag{1.5}$$

where R is the slant range and the IFOV is the detector subtense in radians. We can therefore determine the required IRLS angular resolution from the mission requirement to recognize a tank at a specified range R. For example, the mission requirement may be to recognize a NATO standard tank target with 50% probability of success ($P_D = 0.5$) at a slant range of 1 km during low-altitude oblique viewing for standoff reconnaissance. From Fig. 1.22(a) we have a required footprint δS of

$$\delta S = \frac{2.3 \text{ m}}{7} = 0.3286 \text{ m} = 1.08 \text{ ft.}$$

The required angular resolution is then

$$\text{IFOV} = \frac{\delta S}{R} = \frac{0.3286}{1000} = 0.3286 \times 10^{-4} \text{ rad} = 0.33 \text{ mrad} \ .$$

If the mission requirement is to achieve the same recognition performance at a 2-km slant range, the resolution would need improvement by a factor of two so that the required IFOV would be 0.164 mrad. This is too fine a resolution for many small split-aperture IRLS designs because of limitations from aperture diffraction. Under the poor atmospheric transmission conditions often encountered in long slant paths near the ground, the signal-to-noise ratio could also be poor. In low-altitude missions the near-nadir portions of the scanned scene will be viewed at much shorter ranges, and at nadir the range to the ground is simply the altitude. If the aircraft flies at an altitude of 200 m, for example, the nadir range is 200 m, while at a 84.26-deg scan angle the range is 2000 m = 2 km, as shown in Fig. 1.23. The number of required cycles of spatial frequency across the critical target dimension to accomplish a given task (such as recognition) remains constant throughout the scan. For the 10:1 range variation in the scan example of Fig. 1.23, a 10:1 variation in angular resolution requirement also occurs. This reduction in angular resolution requirements for the close-in ranges has two important consequences.

First, almost all IR line scanners use fixed-focus simple optical designs. Varying the focus dynamically during the few milliseconds available during a scan is both undesirable and impractical. Fixed-focus telescopes set at infinity will be considerably out of focus at the shorter ranges and design-value angular

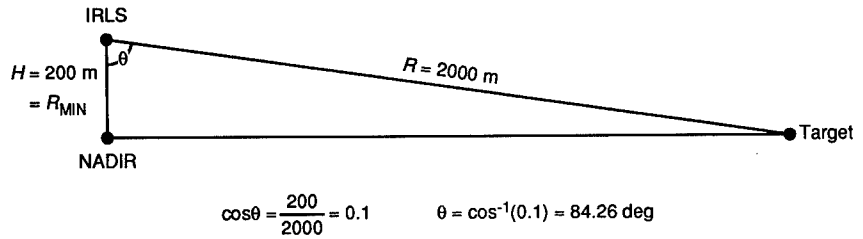

Fig. 1.23 Wide variation in slant range with low-altitude oblique viewing.

resolution will not be achievable. This defocus effect has the tendency to produce a more constant footprint at a target regardless of location within the scan. Imagery is difficult to interpret if resolution varies widely within a single scan. Unimportant details are resolved in the central region of the scan, yet resolution rapidly degrades as the scan proceeds toward the horizon.

Second, if high resolution is specified in terms of a constant angular resolution across the scan, an impractically high data rate results. For a high *V/H* and a high resolution, many detectors are needed. Electrical bandwidth per signal channel becomes excessive. This creates data recording, transmission, and display problems. For example, specifying 0.22 mrad constant angular resolution for a 180-deg low-altitude scan forces the number of IFOV per 180-deg scan line to be

$$N_{\text{IFOV}} = \frac{\pi \text{ rad per scan}}{0.22 \text{ mrad per IFOV}} = 1.428 \times 10^4 \text{ IFOV/line} .$$

Even very-high-quality military CRT monitors seldom produce more than 1000 pixels per horizontal line. A high-capacity film recorder with 5-in.-wide aerial reconnaissance film has a 4.55-in. format width. Even with a 1.0-mil spot diameter, only a maximum of $N_{\text{PIX}} = 4.55/0.001$, or 4550 pixels per line, could be recorded. If magnetic tape recording is to be used, the electronic bandwidth and recording rate limits will be exceeded.

1.3.6.4 Constant Footprint Processing. The defocus effect plus electronic data processing is used in many IRLS systems to provide a constant footprint across a scan and to reduce signal bandwidth to manageable proportions. Constant footprint processing has the desirable feature of rendering same-sized targets as same-sized images regardless of position in the scan. Perspective is thus corrected. A 20-ft-long truck is depicted as the same size in the image at all scan positions. The target footprint, $\delta S = R(\text{IFOV})$, follows a cosine θ_{SC} law because the slant range R varies as the cosine of the scan angle θ_{SC}, giving

$$\delta S = R(\text{IFOV}) = \frac{h(\text{IFOV})}{\cos\theta_{\text{SC}}} \quad [\text{m (for altitude } h \text{ in m)}] . \tag{1.6}$$

A constant footprint across the scan changes the number of pixels per scan to be recorded or displayed. In a constant angular resolution design, one simply divides the scan FOV by the IFOV to obtain the number of pixels per line (N_{IFOV} = FOV/IFOV). Table 1.11 gives the number of pixels for several FOV values in constant angular resolution IRLS systems for a 0.25 mrad IFOV.

In constant-footprint IRLS systems the pixels in a scan line are counted differently. The counting is done for only half the symmetrical scan, and then the total for the line is obtained by doubling the count. Since the target footprint δS is constant throughout the scan, it is possible to divide the half-scan into a nested series of right triangles, as shown in Fig. 1.24. From the figure, the maximum scan angle θ_{max} can be computed using simple trigonometry as follows:

$$X_{\text{max}}^2 = R_{\text{max}}^2 - H^2 . \tag{1.7}$$

Here, R_{max} is the maximum slant range at which the target is to be recognized or identified and is a specific mission requirement. The altitude H is either a specific mission requirement or is to be varied over a limited range (such as 100 to 1000 ft in steps of 100 ft). Thus, for each altitude there will be a specific value of X_{max}. The maximum scan angle is

$$\theta_{max} = \tan^{-1}\left(\frac{X_{max}}{H}\right) . \tag{1.8}$$

Table 1.11 Number of Pixels Per Line Versus Scan FOV for Constant Angular Resolution IRLS Systems with IFOV = 0.25 mrad

FOV (deg)	Number of Pixels/Line = FOV/IFOV
60	4189
90	6283
120	8378
140	9774
160	11170
180	12566

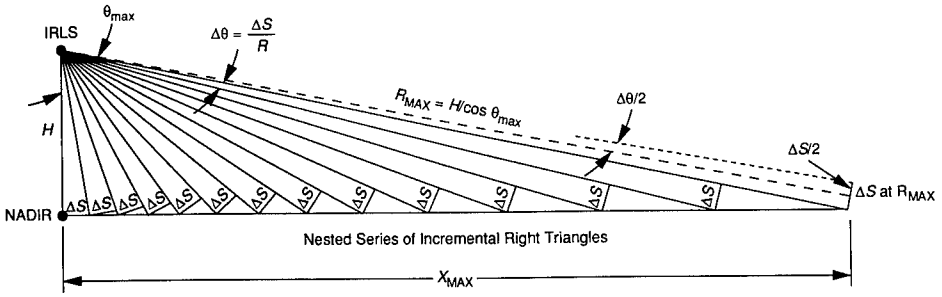

$$\tan\theta = \frac{X}{H}$$

$$X = H\tan\theta$$

$$R = \frac{H}{\cos\left(\theta_i + \frac{\Delta\theta}{2}\right)}$$

$$\tan\left(\frac{\Delta\theta}{2}\right) = \frac{\frac{\Delta S}{2}}{R} = \left(\frac{\Delta S}{2}\right)\frac{\cos\left(\theta_i + \frac{\Delta\theta}{2}\right)}{H}$$

$$\Delta\theta = 2\tan^{-1}\left\{\left(\frac{\Delta S}{2}\right)\left[\frac{\cos\left(\theta_i + \frac{\Delta\theta}{2}\right)}{H}\right]\right\}$$

where θ_i = Generalized Scan Angle Incremented in Computer Program

Fig. 1.24 Computing the number of pixels per line in an IRLS system that provides a constant ground footprint across the line scan.

In general, from Fig. 1.24 we have

$$\tan\theta = \frac{X}{H} , \tag{1.9}$$

so that

$$X = H \tan\theta , \tag{1.10}$$

$$R = \frac{H}{\cos(\theta + \delta\theta/2)} , \tag{1.11}$$

$$\tan\left(\frac{\delta\theta}{2}\right) = \frac{(\delta S/2)}{R} = \frac{\delta S}{2}\frac{\cos(\theta + \delta\theta/2)}{H} , \tag{1.12}$$

so that

$$\delta\theta = 2\tan^{-1}\left[\frac{\delta S}{2H}\cos\left(\theta + \frac{\delta\theta}{2}\right)\right] . \tag{1.13}$$

A closed-form solution giving the number of pixels per line has been given.[6] Equations (1.14) and (1.15) give NPIX, the pixels per line, directly. It should be remembered that in analog IRLS systems there are no discrete pixels per se in the ACT dimension, but in digitally sampled IRLS data the digital sampling switch will produce a discrete number of samples that should approximate NPIX. The two equations are

$$f_0 = \frac{H}{2\delta S} , \tag{1.14}$$

$$\text{NPIX} = 4f_0 \ln\left[\tan\left(\frac{\theta_{\max}}{2} + 45\right)\right] , \tag{1.15}$$

where f_0 is the spatial frequency at the nadir point of the scan in cycles per radian, H is the altitude, and δS is the IFOV footprint at the target. In an IRLS for low-altitude missions we wish to have δS constant across the scan as the scan angle θ is varied on either side of nadir. In Eq. (1.15) $\theta_{\max}$ is the maximum value of the scan angle. NPIX is the total number of pixels in a line. The factor 4 includes doubling the pixels calculated for a single side.

1.3.7 Thermal Resolution Requirements

Thermal resolution of an IRLS or FLIR can be expressed in several ways:

1. noise equivalent temperature difference (NETD)
2. system minimum resolvable temperature difference (MRTD)
3. system minimum detectable temperature difference (MDTD)
4. thermal resolution on film for IRLS systems using film recording.

Equations for NETD and MRTD are given in Sec. 1.4.

Often in the literature the word "difference" is omitted since it is understood that in thermal imaging systems the temperature difference of a target from the background is the main concern. We thus encounter NET, MRT, and MDT. Of these four performance measures, the NETD is the most commonly used means of rating IRLS performance. It is convenient for rating IRLS sensitivity in a laboratory environment but it does not predict target detection or recognition in actual tactical reconnaissance imagery. The NETD is obtained by a measurement of signal-to-noise ratio at the output of the scanner, usually at the output of the detector preamplifier. If the scanner is a separate line replaceable unit (LRU), the NETD serves as a convenient means of rating the LRU performance but other parts of the IRLS system are ignored. For FLIRs, the prediction and assessment of system performance is usually based on the system MRTD. The MRTD involves both spatial resolution, as measured by the system MTF, and thermal sensitivity, as measured by NETD. MRTD has not been often used for IRLS systems because film was heretofore the chief display medium, where objective film microdensitometer measurements can be made rather than relying on the very subjective MRTD measurements. Recently, some IRLS systems have included an MRTD requirement in their specifications. MDTD has not been popular for IRLS systems since the objective measurement of thermal resolution on film was possible using microdensitometry. NETD and MRTD for IRLS use are based on scanning a four-bar (square-wave) target [Fig. 1.25(a)], while the MDTD uses a square target against a uniform background [Fig. 1.25(b)]. Both target types are useful for IRLS tests.

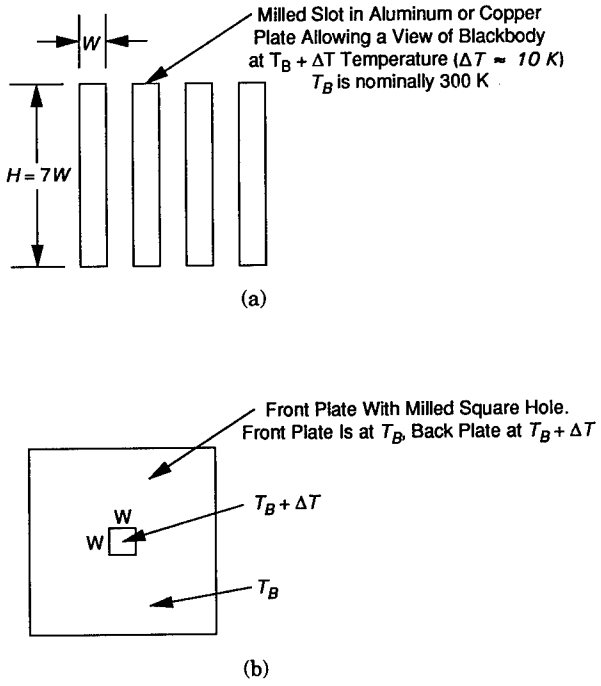

Fig. 1.25 IRLS test targets: (a) four-bar target for IRLS NETD and MTF measurements; (b) square target for IRLS MRTD and thermal resolution tests. A separate four-bar slot set is cut for each of seven or eight spatial frequencies. $T_B + \Delta T$ is controlled for constant ΔT above background.

Table 1.12 Probability of Detection Versus Signal-To-Noise Ratio (from Refs. 5 and 7)

Probability of Detection P_D	SNR
1.0	5.5
0.9	4.1
0.8	3.7
0.7	3.3
0.6	3.1
0.5	2.8*
0.4	2.5
0.3	2.3
0.2	2.0
0.1	1.5
0	0

*A value of SNR = 2.25:1 has now been widely accepted for $P_D = 0.5$. SNR = 2.25 is used in the US Army Static Performance Model for Thermal Imaging Systems[4] and is also widely used in IRLS design.

Square-wave targets are used for testing thermal resolution on film in those IRLS systems using film recording. In our example low-altitude penetration mission, we used a square NATO Standard Tank Target 2.3 m on a side. From this target we determined spatial resolution requirements needed to see this target at various slant ranges.

The thermal resolution requirements can also be based on this target. The thermal resolution requirement arises from the need to have a minimum signal-to-noise ratio to accomplish a specified imagery interpretation task such as detection, recognition, or identification. Rosell and Wilson[7] studied probability of detection as a function of signal-to-noise ratio, with results given in Table 1.12.[5,7] Subsequent experience by IR workers has shown that Table 1.12 is pessimistic and that SNR $\geqslant$ 2.25 is sufficient for a 50% probability of accomplishing the required task of detection or recognition. This SNR is applied to FLIRs in the US Army static performance model[4] and is conservative for IRLS imagery. IRLS imagery is easier to interpret in almost all comparable weather situations for the following reasons:

1. IRLS imagery covers a much wider FOV than FLIR imagery, so more contextual cues will be present.
2. IRLS imagery is static, while airborne FLIR imagery is very dynamic. IRLS images can be studied for as long as necessary. An airborne RMS could have a frame-freeze capability that would allow the FLIR image to be studied as a static image like an IRLS frame.
3. IRLS film imagery used for ground-station interpretation is viewed on a light table with continuous, bright, even illumination over all the image, while a CRT provides only a rapidly moving bright spot of

illumination. The average brightness of the light table is therefore superior and less tiring to the eye and no field flicker occurs. IRLS imagery displayed on airborne cockpit monitors does not have these advantages.

1.3.8 Target Temperature Contrast

In a requirements analysis, target contrast with the background is of interest. All thermal imagers depict variations in apparent infrared radiance. Radiance variations occur from both temperature and emissivity variations as modified by the atmospheric transmission. Emissivity of a given object is a result of two effects, inherent surface properties and gross three-dimensional surface geometry. These effects are difficult to predict beforehand, so most IRLS system calculations assume unity emissivity. The scene is assumed to consist only of temperature variations. This is an acceptable procedure because most natural objects have high values of emissivity. The assumptions of a simple temperature contrast and no atmospheric attenuation are useful in preliminary performance estimates. Later, with a given IRLS design, atmospheric transmission and emissivity of special targets can be studied as required. Table 1.13 gives[4] average target ΔT and dimensions for some military targets in a summer field test.

In determining required thermal resolution, the usual practice is to assume unity emissivity. If an SNR = 2.25 is accepted for 50% probability of detection ($P_D = 0.5$), then the thermal resolution with these assumptions is found by first calculating the radiance contrast ΔN:

$$\Delta N = N_T - N_B \ , \tag{1.16}$$

where N_T is the target radiance at target temperature $T_T = T_B + \delta T$, where δT is the specified target temperature contrast, and N_B is the background radiance at temperature T_B. Both N_T and N_B are calculated by solution of the

Table 1.13 Target Average Temperature Contrast and Target Area for Summer Field Test Conditions

Target	ΔT_{av} (°C) above Summer Background	Area (m × m)
Tank (side)	5.25	2.7 × 5.25
Tank (front)	6.34	2.7 × 3.45
2½-ton truck (side)	10.40	0.83 × 4.22
2½-ton truck (front)	8.25	2.03 × 1.67
APC[a] (side)	4.67	1.8 × 4.80
APC (front)	5.65	1.8 × 2.09
Man (erect, front)	8.00	0.5 × 1.5
NATO Std. Tank (avg.)[b]	2.00	2.3 × 2.3

[a]APC = armored personnel carrier

[b]Since the time of collection of the data, the NATO Standard Tank Target has been widely used for IRLS specifications.

Planck radiation equation. Once ΔN is known for the specified target temperature contrast, the required noise equivalent radiance $(\text{NEN})_{\text{REQ}}$ is

$$(\text{NEN})_{\text{REQ}} = \frac{N_T - N_B}{2.25} = \frac{\Delta N}{2.25} \ . \tag{1.17}$$

Once the required NEN is determined for the specified target temperature contrast, the IRLS system NEN can be calculated from Eq. (1.33) in Sec. 1.4.2 to see whether the IRLS design meets the requirement. This calculation will not be done here. The required IRLS system NETD is

$$(\text{NETD})_{\text{REQ}} = \frac{(\text{NEN})_{\text{REQ}}}{(\delta N/\delta T)} \ . \tag{1.18}$$

The NETD equation is derived in Sec. 1.4.2 as Eqs. (1.35) and (1.36). Here, $\delta N/\delta T$ is the radiance derivative with respect to temperature and is discussed in Sec. 1.4.3. It is obtained by solution of the differentiated Planck equation. If atmospheric effects are to be included, the required NEN must improve by the atmospheric attenuation ratio. For preliminary simplified system calculations, an attenuation coefficient of $\alpha = 0.25$/km is often used. The atmospheric transmission is then

$$\tau_a = e^{-\alpha R} = e^{-0.25R} \ , \tag{1.19}$$

where R is the slant range in km. In our low-altitude penetration mission example, $R = R_{\max} = 1.8$ km, so $\tau_a = 0.638$. The required NEN then becomes

$$(\text{NEN})'_{\text{REQ}} = 0.638(\text{NEN})_{\text{REQ}} \ . \tag{1.20}$$

The required NETD also changes accordingly. For recognition tasks, a higher SNR is required. Preliminary IRLS requirements calculations often use a value of SNR ≥ 10 as a means of arriving at NEN and NETD requirements. IRLS specifications for some airborne platforms have requirements imposed on both NETD and thermal resolution on film.

The NETD applies to the receiver only and does not involve the recorder or any other LRU. NETD is therefore not a useful means of measuring IRLS thermal performance in the final imagery. It is, rather, a useful quality-control tool that is easy to measure and that immediately discloses system problems. The thermal resolution, or thermal sensitivity, is the specification intended to control thermal performance in the final imagery.

The thermal resolution specified is that of the entire system, including the means of recording or display. It is measured on film for 1 × IFOV-sized targets, or larger, viewed against a uniform background temperature of 300 K. For some applications, with 1 × IFOV-sized targets, or larger, the thermal resolution has been required to be 7.5 times the NETD. For 2 × IFOV targets, or larger, the target thermal resolution has been required to be 2.5 times the NETD, or better, when measured against a uniform 300 K background. The thermal resolution change was required to produce a film density change

of +0.15 from a reference film density of 0.65 ± 0.15. Film density is defined as

$$D \equiv \log_{10}\left(\frac{1}{T}\right) , \tag{1.21}$$

where T is the transmission of the film. Density values are read by means of a transmission densitometer. Prediction of density requires a knowledge of the film and its development as characterized by the H&D (Hurter & Driffield), or D-log$E$, curve, which plots density versus the logarithm of the exposure in energy density units. The exposure is under the control of the IRLS film recorder designer since the CRT brightness is made to be proportional to the IR signal. For a requirements analysis, it is sufficient to define SNR requirements, the dynamic range, and the recording parameters to assure that thermal resolution requirements are met. This involves the transfer curves of each element of the signal processing chain, including the CRT and the film and its development.

For IRLS systems in which the imagery is displayed on a CRT, specification of thermal resolution is omitted as such and use is made of system MRTD, which involves both system MTF and NETD. The predominant MRTD used in IRLS systems is an objective MRTD in that a human operator/observer is not needed for each MRTD test. Subjective MRTD testing is best performed during the early stages of IRLS development. This establishes that the desired performance with human operators is indeed achieved by the design. Once this has been established, the specifications for the objective MRTD can be refined. During production, the IRLS and its LRUs can be tested and accepted solely on the basis of the objective MRTD and related objective tests, such as CRT spot brightness. Objective MRTD production tests save time and avoid any variability caused by testing with so-called standard human observers. Details of testing NETD, MRTD, MDTD, and thermal resolution are given in Sec. 1.6.

1.3.9 Wavelength and Detector Trade-offs

Earlier IRLS systems used the 3- to 5-μm IR atmospheric window band when practical photoconductive indium antimonide (InSb) detectors became readily available in the 1960s. InSb detectors were adequate, but most infrared scenes have peak radiance in the 8- to 14-μm band. Hot targets, however, can have high radiance values in the 3- to 5-μm band. The peak radiance can be estimated from the Wien displacement law:

$$\lambda_{pk} = \frac{2897.82}{T} \quad (\mu m) , \tag{1.22}$$

where T is the scene or target temperature in kelvin. Table 1.14 gives peak wavelengths for various blackbody temperatures.

Table 1.14 does not tell the whole story. If we look at atmospheric transmission for a horizontal path at sea level with variable water content, we see that the longer wavelength band has a transmission advantage in many types

Table 1.14 Wavelength of Peak Radiance at Various Blackbody Temperatures

Temperature (K)	λ_{pk}	Spectral Band
280	10.349	8- to 14-μm band favored
285	10.168	
290	9.992	
295	9.823	
300	9.659	
350	8.279	
400	7.245	
450	6.440	
500	5.796	
550	5.629	
600	4.830	3- to 5-μm band favored
700	4.140	
800	3.622	
900	3.220	

of humid air. This advantage persists until the water-vapor content exceeds approximately 50-mm precipitable water. In reasonable weather, such as 25°C temperature and 60% RH, precipitable water is 4.2 mm per kilofoot (13.8 mm km^{-1}). If we have a horizontal slant range of 2 km as the maximum range for a low-altitude, high-V/H mission in the temperature zone, the maximum amount of precipitable water is 2 km × 13.8 mm km^{-1} = 27.6 mm. Therefore, under these conditions the 8.0- to 13.0-μm band would be superior for such a mission. Higher humidity air such as 25°C air at 80% RH will have 18.0 mm precipitable water per km, so a 2-km slant range will have 36 mm precipitable water and the 8.0- to 13.0-μm band is only slightly superior to the 3- to 5-μm band.

For most missions using low-altitude oblique viewing at long slant ranges, the 8.0- to 13.0-μm band is to be preferred unless there are definite advantages in detector technology such as the use of focal-plane arrays with CCD readout such that several (n) rows of redundant detectors each view the same point. In that case the SNR improvement is $\sqrt{n}$ and the shorter-wavelength band could have a definite advantage. Figure 1.26 shows the transmission of the 8.0- to 14.0-μm band together with the wavelength response of a mercury cadmium telluride photoconductor (PC HgCdTe) optimized for this band. HgCdTe can be optimized for other bands such as the 3- to 5-μm band by varying the stoichiometric ratio (the ratio of mercury to cadmium) in the ternary alloy.

In choosing an atmospheric window band it is important to remember the following points:

1. There are numerous absorption notches within both these bands such that transmission varies considerably within the band.
2. The band edges on the long-wavelength end of the 8- to 14-μm band between 13 and 14μm contain water-vapor absorption notches. Therefore, the long-wavelength edge of the band moves toward shorter wavelengths with increasing water-vapor content. In humid air or light drizzle it is prudent to assume that the band cuts off at 12.5 μm. The short-wavelength end is also sensitive to water vapor. For preliminary calculations one can assume the band starts at 8.0 μm and that water vapor is the dominant atmospheric effect. However, this is not always true.

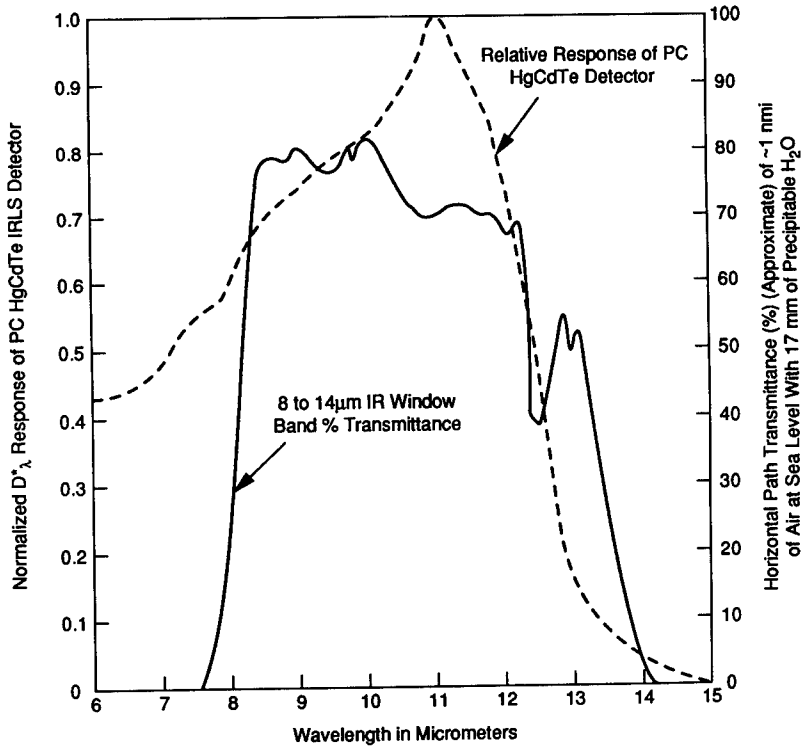

Fig. 1.26 HgCdTe detector response compared to typical 8- to 14-μm window transmission at sea level.

3. The PC HgCdTe detectors in production typically show a peak response wavelength near 12.5 μm when designed for the 8- to 13-μm band.
4. Dust clouds from tracked armored vehicles, smokes, and battlefield chemical clouds all attenuate infrared radiance. The 8- to 13-μm band has better transmission than the 3- to 5-μm band in such conditions.

For these reasons, most presently deployed military IRLS systems favor the 8.0- to 12.5-μm band. Light haze or drizzle conditions are common in Europe and in parts of North America. If the purpose of the IRLS is to detect hot targets against sky, water, or other natural backgrounds, then the 3- to 5-μm band is useful.

The trade-off between IRLS operating wavelength band and detector choice is complex if many climates and atmospheric conditions are to be encountered. For precise calculations the available atmospheric transmission computer codes should be used.

1.3.10 Vehicle Installation

Most IRLS systems are designed for tactical reconnaissance in high-speed reconnaissance aircraft. Many installations are in a forward compartment of the aircraft. A protective door opens to expose a viewing slot for scanner use. In certain aircraft this causes aerodynamic problems so the installation re-

quires an infrared window. IR windows are expensive, heavy, and require careful handling. High-speed flight in heavy rain or sandstorms at desert airfields can cause erosion or pitting and damage to the protective and anti-reflection coatings on the outer window surface. F/A-18 reconnaissance aircraft fly with the IRLS behind a ZnS/ZnSe window having appropriate AR and protective coatings. The earlier RF-4 series aircraft fly with only a protective door. Some F-16 reconnaissance aircraft use a center-mounted pod. Table 1.15 gives some IRLS installation and application possibilities but is not meant to be comprehensive. For example, many of the earlier axehead scanners are still flying in a variety of aircraft installations and have found a niche in many nonmilitary uses such as the monitoring of crops, forest fires, and mine fires, and for search and rescue. IRLS systems have been found effective for pollution monitoring. Airborne IR and UV line scanners have been used for oil-slick detection in ocean and coastal regions, but UV sensors are limited to daylight hours. The nonmilitary aircraft used for these missions have a free choice of altitudes and need not fly at high *V/H* values. The smaller and lighter civilian aircraft are often less stable in flight and are seldom equipped with the elaborate avionics available on military aircraft. The high-accuracy inertial navigation systems, radar altimeters, MIL-STD-1553 BUS, flight computers, etc., are costly and not usually available on civilian aircraft. Hence, it is common to accept the consequences of aircraft roll or pitch motions in small civilian aircraft.

Table 1.15 Some Vehicle and IRLS Installation Possibilities

Platform	Location	Door/Window	Application
RF-4	Forward gun compartment	Door	TAC RECCE[a]
RF-111	In fuselage	Door	RECCE
F-14	TARPS pod under fuselage	Door	RECCE
F/A-18R	Forward nose section	ZnS/ZnSe 3-piece window	TAC RECCE
TRA RPV	In RPV fuselage	Ge window	RECCE
Beech 1900	In cabin with real-time display	Door	Oil slick monitoring
Skyeye RPV	Forward fuselage	Ge window	RECCE
Tornado	Fuselage	Door	TAC RECCE
Hawk 200	Wing pod	Optional	TAC RECCE
Tornado	Fuselage	Door	ECR[b]
Various	Various	Various	Scientific/economic
Cruise missile	Missile nose cone (pod simulation)	Ge 3-piece IRLS window + Ge FLIR window	Nav. and homing (IRLS/FLIR)
NASA SKYLAB	Wall of multiple docking adapter	Ge & quartz windows	Scientific

[a]TAC RECCE means tactical reconnaissance.

[b]ECR means electronic combat and reconnaissance.

Table 1.16 LRU Complement for a Typical IRLS

LRU Name [a]	Function
Infrared receiver	Infrared scanner, detector/dewar, preamps
Power supply	Power and filtering to all LRUs
Control indicator	Control and indication of IRLS status, mode
Recorder	Signal conditioning, CRT film recording, most signal electronics
Film magazine	Contains and servo-transports aerial reconnaissance film in proportion to a *V/H* signal

[a]In addition to the LRUs, a set of interconnection cables and two mounting yokes are required for the installation.

1.3.11 LRU Concept

Most US and other services require that equipment be furnished in line replaceable units (LRUs). An LRU is a self-contained module providing one or more distinct system functions. Each LRU has its own set of specifications and drawings so that it may be separately procured and stocked. As an example, the LRU structure of a typical IRLS is shown in Table 1.16.

1.3.12 Installation Requirements

Volume and weight are always at a premium in aircraft. Effort is needed to minimize size and weight of each LRU. Size is often restricted in one dimension and freer in another. In RPV and pod installations, fore and aft room is freer than the cross section. LRU shape, especially receiver shape, must comply with these restrictions. This leads to a preference for smaller IRLS designs even if spatial and thermal resolution is sacrificed. There are mounting and installation problems with wide-FOV and 180-deg-FOV scanners:

1. The receiver must be located as low as possible in the fuselage or pod so as to minimize the required viewing slot or window.
2. The aircraft rolls during flight as much as ± 30 deg. If an unvignetted 120-deg FOV is demanded, then a slot covering an angle of 120 deg + 60 deg = 180 deg is needed. Often, some amount of roll vignetting is allowed on the downwing side and in many installations a pod or a weapon is in the FOV anyway.

If a 180-deg scanner is to be mounted in a pod or a small RPV, a 180-deg viewing slot cut in the vehicle may be precluded by the structure. RPVs and pods often have a backbone "upside-down keel" type of structure that may allow better clear viewing, but vehicle plumbing, wiring, and control cables may interfere.

1.3.13 Windows for Certain IRLS Installations

For wide-FOV IRLS installations a three-piece window is appropriate, as shown in Fig. 1.27. For certain portions of the scan the incoming beam will be vignetted (partially interrupted) by the joint obscuration between adjoining sections. By careful exploitation of the index of refraction of the window material(s) it is possible to minimize the joint obscuration. This is especially true

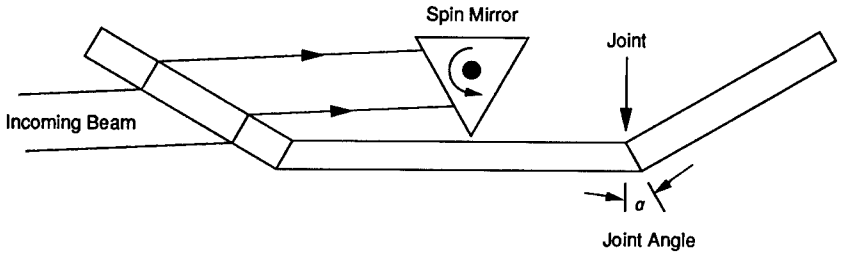

Fig. 1.27 Three-piece IRLS window for wide-FOV designs.

for germanium windows because Ge has a nominal index of 4, which allows the refraction angle to equal the joint angle as shown in the figure. The refracted ray thus parallels the joint for minimum joint obscuration. The Ge three-piece window used for the PATHS IRLS was designed in this manner and little shift in the signal level was noted when the scan passed over the joints. With the more popular Zn/ZnSe sandwich windows the index is less favorable to the joint angle. Thus, some projected joint width is seen as the scan passes by and a signal level shift might require electronic correction. This correction is possible because the joint locations are known and repeat their time position each scan period. With CAD traces, an electrical level shift control gate pulse can be located easily. The time constants and signal level in the automatic gain control (AGC) and the automatic level control (ALC) must be considered, however.

The window can reflect unwanted local IR sources into the scanner. The window can also cause a partial narcissus reflection unless it is tilted fore or aft with respect to the nadir line so that narcissus rays cannot return to the detectors. Appropriate shields and baffles are used to keep some IR noise sources (such as motors) from the FOV.

All IR windows require antireflection coating on both outer and inner surfaces. In addition, a hard coating is required to protect the outer surface from erosion and mechanical damage. In some instances after extensive flight programs it has been necessary to restore the outer surface by repolishing and recoating. This is very costly and time consuming.

Water condensation on the flat portions of IRLS windows is a concern when the vehicle descends suddenly from prolonged high-altitude flight (20 min or longer) into low-altitude humid ambient air. In some installations the window has 165°F heated air blown across it to preclude condensation. The window can become heated and its self-emission can lower IRLS thermal sensitivity.

Ideally, dried conditioned air can be blown through the IRLS compartment, but in RPVs and in most aircraft this is seldom available.

1.3.14 Vibration and Shock Isolation

Vibration and shock protection must be provided by the LRU mounting for the receiver and the recorder as a minimum. Other LRUs, such as the power supply, often may be hard-mounted. The scanner requires particular care. Figure 1.28 shows a typical IRLS mounting. The IRLS mounting design must also withstand landing/launch shocks and crash safety shock levels. Also, each

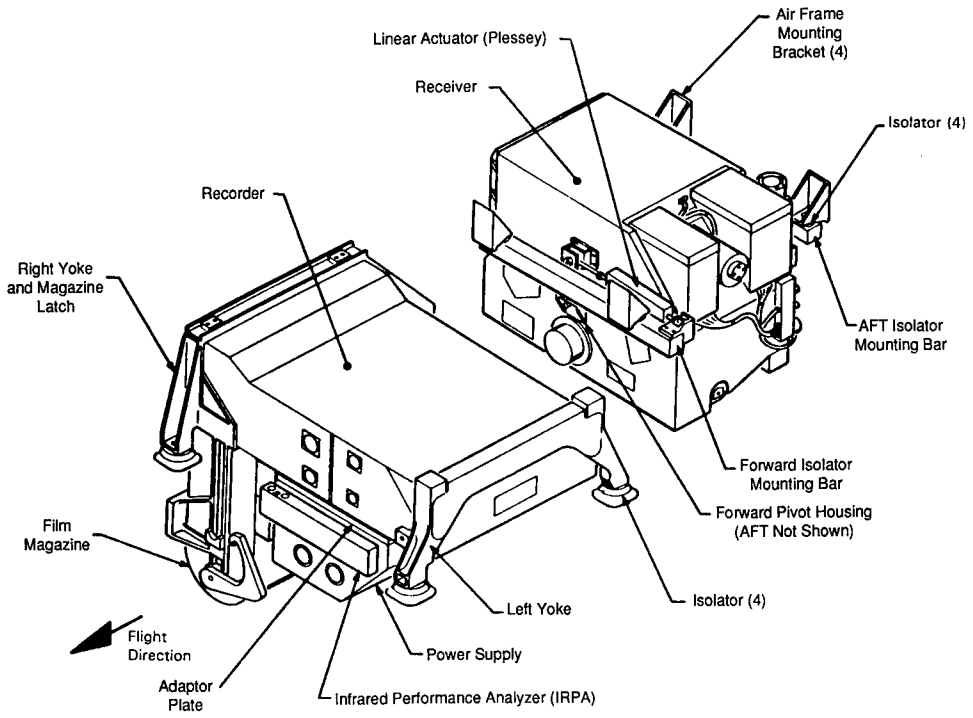

Fig. 1.28 Equipment mounting design.

LRU in its shipping container must withstand transportation and handling levels of shock and acceleration.

Vibration isolation and IRLS boresight specifications are mutually antagonistic. Imposition of an IRLS boresight specification that has very tight limits is useless unless the scanner is gimbal-mounted so that all vibrations can be isolated. The motivation for boresight specifications is the hope that target coordinates can be taken from an IRLS target cuer/display cursor and then used for immediate weapon aiming. These hopes are usually simplistic because the IRLS can derive two-dimensional image coordinates accurately enough but the target is part of a three-dimensional world. Terrain altitude variations are sufficient to destroy an accurate target location unless both accurate slant range and altitude data are given to the cuer. If map coordinates are to be computed accurately, the inertial drift (INS drift) must also be removed by flying over a known check point in the vicinity of the target. This measurement task could be accomplished by the IRLS working with the flight computer.

1.3.15 Ambient Air and Temperature Control

Temperature control of IRLS systems is often a problem. Cooling air is usually required. In IRLS installations with open door viewing the scanner will be exposed to outside air temperatures. Wind buffeting can occur. If the aircraft descends rapidly from a high altitude to low-altitude humid air, there can be condensation on the IRLS optics until sufficient time is allowed for temperature

stabilization. Dry air blown into the scanner compartment at a slight overpressure can prevent entry of the humid low-altitude air. In systems using a window there must be a vent to equalize pressure slowly and the window must be protected from condensation by blowing dry warm air across the inner window surface. If on-board thermal development of dry silver film is included in the installation, the developer heat must be dissipated by supplying adequate cooling air.

1.3.16 Electrical Power and Electromagnetic Noise

IRLS systems require conditioned and filtered power because the raw aircraft power is too noisy and variable. The IRLS detectors and preamplifiers are very susceptible to most sources of conducted and radiated interference. Signal wires should be well shielded and shield grounding must be studied for each separate installation and then revised after flight trials. Competing on-board systems such as radar and TACAN may cause streaks in the IRLS imagery, often ruining the image. It is recommended that such systems be inoperative during any IRLS data collection. For power-supply design, typical required regulation is 1% on +5-V and ± 15-V supplies, while higher dc voltages could be relaxed to 5%. Ripple should be below 50 mV peak-to-peak. Any 115-V, 400-Hz power supply must be isolated from aircraft line transients by a transformer and filter.

1.3.17 Acoustic Noise

IRLS spin mirrors are a source of high decibel acoustic noise. Most procurement specifications impose limits on this noise to protect air crews and technicians working with the equipment during ground testing. These are sometimes difficult specifications to meet. Hearing protection is required when scanners are operated in small, closed laboratories. The spin mirrors are sirens and some three-sided mirrors at speeds of 6000 to 12,000 rpm can be dangerously loud and painful to the ear.

1.3.18 Imagery Stabilization

IRLS imagery must be stabilized against aircraft roll motions because high roll rates and large roll excursions of reconnaissance aircraft will interfere with image interpretation or cause loss of a target image. Roll angles can be up to ± 30 deg at high roll rates and accelerations. Pitch and yaw stabilizations are usually omitted for simplicity because these motions occur over much smaller angles and at much lower rates. They are not very damaging to the imagery interpretation process. Two- and three-axis stabilization has been used with IRLS systems, however, and is used when vehicle motion is severe as in RPVs and light aircraft. Two- and three-axis stabilization is best done by mechanically stabilizing the entire scanner on a platform. The larger, heavier reconnaissance aircraft (RF-4, F-14, F-16, F/A-18(RC), RF-111, TORNADO, etc.) are sufficiently stable that yaw stabilization can be ignored. There has been interest in pitch-axis stabilization because the rapid pitch motions from terrain avoidance systems on such aircraft as TORNADO or RF-111 can cause line-to-line compression or expansion in the imagery. Most systems, however,

do not have pitch compensation or control because of its difficulty and expense. In certain slow-flying RPV types, such as AQUILA, a maneuver known as jinking is used to confuse enemy defenses to enhance vehicle survival. This maneuver causes sudden side slips and rolls so that two- or three-axis IRLS stabilization is required even when it is awkward in the small confines of the RPV. The cost impact must also be considered since the RPV has a shorter lifetime than a manned aircraft.

1.3.19 Roll Compensation

Across-track roll compensation is the most versatile and cost-effective means of IRLS imagery stabilization. Mechanical roll stabilization is used in the Texas Instruments 720 series scanners. Mechanical compensation in the 720 series of scanners uses rotation of an optical relay element in the scanner/recorder so that the proper roll-corrected scan data are recorded on the film. All-electronic stabilization can be used in systems that have a CRT film recorder. Using a roll signal from the aircraft inertial navigation system (INS), a display unblank gate is developed and shifted in time to trigger the CRT sweep only when the roll-corrected video occurs. If a roll-corrected 60-deg FOV is needed when the aircraft roll is ± 20 deg, then 60 deg + 40 deg = 100 deg or more of video must be collected. The CRT display unblank pulse is shown in Fig. 1.29 for a roll of 20 deg. Roll-correction accuracy to better than one pixel at very high roll rates and roll accelerations can be handled. The same all-electronic roll-compensation method has been used with IRLS magnetic-tape recording. The CRT "display unblank pulse" is renamed a "data unblank pulse." Two cautions are necessary in IRLS roll compensation:

1. If the IRLS is located in a wing pod or other location remote from the aircraft center of roll, then a local roll measurement must be made with a rate gyro package internal to the IRLS.
2. If the aircraft cannot furnish a dedicated wire from the INS or offers to furnish the roll signal on a Mil-Std-1553 Bus, this will require a local rate gyro package because most modern reconnaissance aircraft will have such high roll rates and accelerations that the Mil Bus roll signal will have an unacceptable latency error by the time the Bus gives the interrupt signal. A gyro package is also needed in the IRLS if the vehicle lacks an accurate INS.

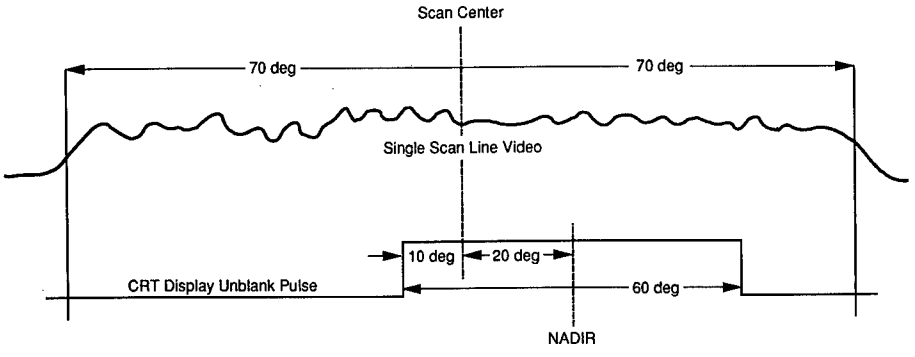

Fig. 1.29 Electronic roll compensation.

The wing, wing pods, or weapons can obscure the IRLS FOV at high roll angles, especially in wide-body aircraft such as the TORNADO. Any such obscuration is dependent on the placement of the scanner. The spin mirror must be as low as possible, and in some aircraft a curved bubble can be fitted to the bottom of the fuselage for 180-deg scanners. Close cooperation with the aircraft designers is essential and the earlier, the better. IRLS requirements cannot be expected to drive the aircraft design very far, but in the early stages of development some accommodations might be made. Cooling air and humidity control, doors versus windows, etc., can be considered together with the possibility of a dedicated roll signal line.

1.3.20 *V/H* Compensation

IRLS systems require a *V/H* signal from the aircraft INS so that the film or tape-recording rate follows the *V/H*. This signal can arrive on a Mil Bus because latency is not a problem in the ALT axis. The *V/H* signal also permits channel selection in multichannel designs. For example, in some airborne platforms there are a total of 12 detectors in the ALT direction. At maximum *V/H* in wide mode all 12 detectors are used to provide contiguous coverage. As *V/H* decreases, fewer channels are needed. A design choice occurs at certain values of *V/H*, i.e., to select only those channels necessary to maintain coverage, or to allow overlapped (repeat) scans of the same line to occur. Channel select logic provides overlap coverage at certain *V/H* values. This gives contiguous imagery at all *V/H* for a constant scan speed yet allows overlaps to improve the signal-to-noise ratio. In the selecting of channels to be recorded, the logic allows anywhere from zero overlap (one exposure) to three overlaps (four exposures). Up to a factor of $\sqrt{4} = 2$ improvement in SNR results in better NETD and MRTD at these *V/H* values. At maximum *V/H*, the range is short and SNR improvement is not needed. Variable *V/H* can also be accommodated by spin-mirror rate control, either continuously or in a stepped manner.

BAe line scanners achieve high *V/H* rates by scanning at 12,000 rpm, giving 600 scans/s with a three-sided scan mirror. *V/H* variations are handled by channel selection (one to four parallel SPRITE detectors), by allowing overlap, and by exploiting the defocus effect.

1.3.21 *V/R* Compensation within the Scan

In some recently developed high-*V/H* line scanners for low-altitude penetration missions, there is a need for oblique viewing at high scan angles using a 180-deg scan FOV. Within a single scan from horizon to horizon the *V/R* varies dramatically. It increases nonlinearly from almost zero at the highest scan angles to a maximum at nadir and then decreases again. For example, let the aircraft velocity be

$$V = 600 \text{ knots} = 1012.7 \text{ ft s}^{-1} \quad [1 \text{ knot} = 1 \text{ nmi h}^{-1} \text{ and } 1 \text{ nmi}$$

$$= 6076.103 \text{ ft (U.S. and International)}] \ .$$

Let H = 300 ft AGL:

$$R = \frac{\mathrm{H}}{\cos\theta}\ , \text{ so } \frac{V}{R} = \left(\frac{V}{H}\right)\cos\theta = \left(\frac{1012.7}{300}\right)\cos\theta\ .$$

At nadir, $\theta = 0$ and $V/H = V/R$ because $H = R$ at this point:

$$\left(\frac{V}{H}\right)_{\mathrm{MAX}} = \left(\frac{1012.7}{300}\right)(1) = 3.376 \text{ rad s}^{-1}\ .$$

The large variation in V/R within the scan increases the difficulty of forming an image without ALT distortion. One solution is to use constant-footprint processing where the ALT imaging of the ground follows a cosine θ law, as shown in Fig. 1.30. We note that $R = H/\cos\theta$, while the subtended ALT footprint at the target δS is determined by the IFOV at the slant range R:

$$\delta S = (\mathrm{IFOV})R = \frac{H(\mathrm{IFOV})}{\cos\theta}\ . \tag{1.23}$$

If the IFOV is made to be a function of the scan angle θ for a constant δS, we have

$$\mathrm{IFOV} = (\delta S)\frac{\cos\theta}{H}\ , \tag{1.24}$$

where IFOV now varies across the scan. The variable IFOV is achieved by exploitation of the defocus effect at short ranges using fixed-focus optics, and by allowing the detector to sample the defocused image of an IFOV in the ALT dimension. The sampling strategy follows the cosine θ law and the defocus effect as it varies within the scan.

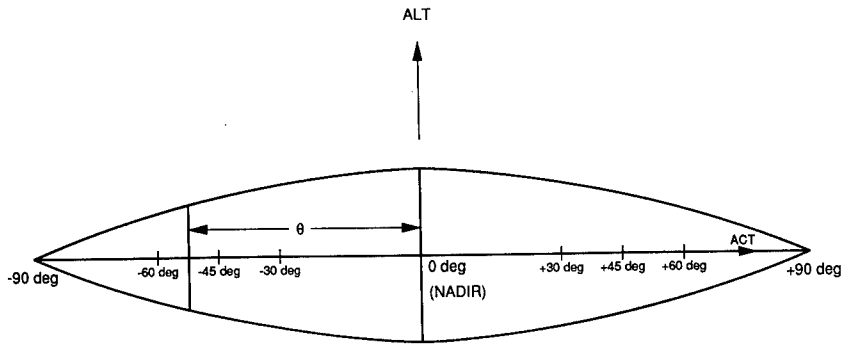

Fig. 1.30 Cosine law gives desired angular subtense in ALT axis for continuous coverage and provides a constant ALT ground swath width ΔY throughout 180 deg of scan.

1.3.22 Defocus Effect

In low-altitude missions, the image will be out of focus throughout much of the scan because the scanner uses a fixed-focus telescope set for infinity focus. This variable defocus effect is an aid in achieving a uniform swath width in the ALT dimension. The defocus effect is readily shown by a few simple examples. Consider a split-aperture line IRLS with its two rectangular apertures as shown in Fig. 1.31. The scanner is shown at nadir where the apertures are nominally equal. The length L in the ALT dimension is the same for both apertures and does not change during the scan. The length L is made larger than the ACT width W of either aperture because the video signal results only from ACT scanning. This allows electronic signal boosting to be done in the ACT axis to compensate the MTF roll-off resulting from ACT aperture diffraction. There is no equivalent simple way to compensate for the MTF roll-off of the ALT aperture because there is no ALT scanning. The ALT aperture is thus made longer to give a better diffraction MTF. This partially compensates for lack of boost but increases the amount of defocus in the ALT axis.

For rectangular apertures the defocus effect can be simply analyzed by projecting the aperture on the ground (see Fig. 1.32). The ALT length of the aperture projection on the ground is the IFOV footprint of the scanner. In our example, the aperture is $L = 6$ in. and quasi-collimated rays that originate within this rectangular aperture are focused to a single detector. There is no possibility of resolving finer detail in the ALT axis than this 6-in. footprint. The ACT defocus effect is less because each ACT aperture is smaller. In preliminary IRLS studies the ACT defocus is ignored. During the detailed optical design process the computer optical analysis program can analyze both axes thoroughly. The ALT defocus has a direct impact on IRLS design and so must guide the array layout, the sampling strategy, and the channel-switching logic. Assume that $(V/H)_{MAX} = (V/R)_{MAX} = 3.376$ rad s^{-1} at nadir. We must keep up with the maximum value because at other scan angles the V/R is less.

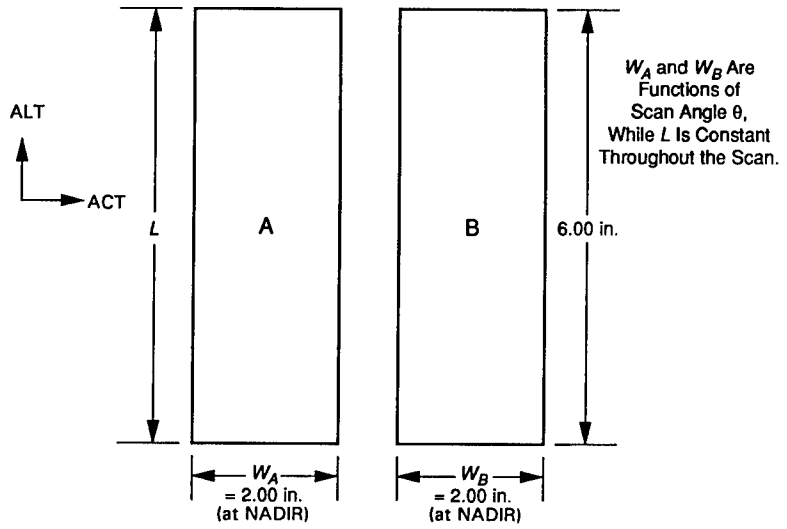

Fig. 1.31 Example split rectangular aperture at nadir.

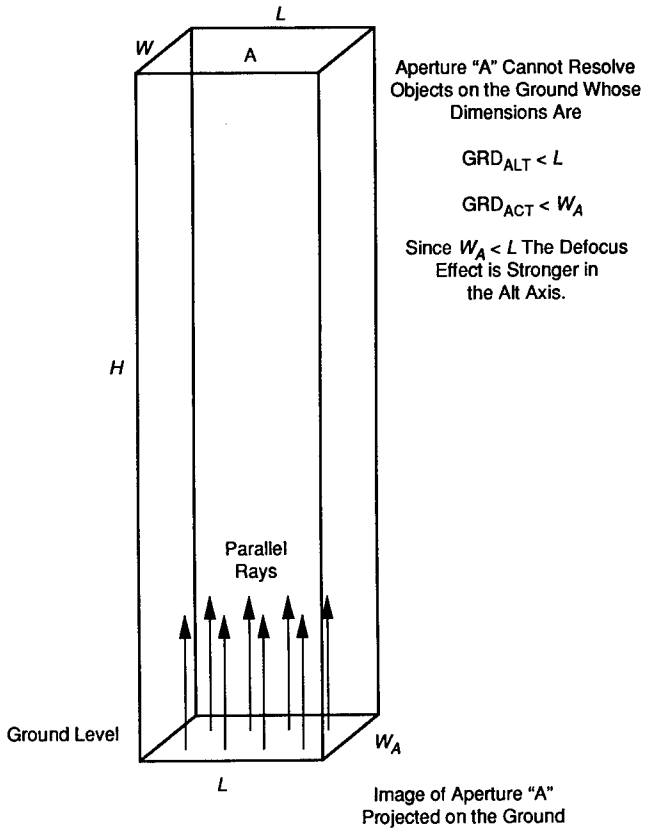

Fig. 1.32 Useful approximation for estimating defocus.

Suppose further that we wish to use six parallel channels that are fed by selecting from an array of N parallel detectors, as shown in Fig. 1.33. Each of the signal channels will contain samples that follow a cosine law as shown in the figure. The total ALT angular coverage at nadir must be

$$\Phi_{ALT} = \frac{(V/H)_{MAX}}{N_{sc}} \quad \text{[rad/scan]} \ , \tag{1.25}$$

where N_{sc} is the scan rate in scans/s, given by

$$N_{sc} = \left(\frac{\text{rpm}}{60}\right)k \tag{1.26}$$

where k is the number of spin-mirror facets.

There is a trade-off between Φ_{ALT} and rpm. Usually one wishes to use an even number of detectors and sometimes a simple round number of rpm such as 6000 or 9000. If we use a three-sided spin mirror and 6000 rpm, we get n = 300 scans/s. Therefore, Φ_{ALT} = 3.376/300 = 0.01125 rad = 11.25 mrad. We have chosen to sample only six pixels at any instant, so we sample six defocus

patterns (projected images of one aperture), as shown in Fig. 1.33. For the value of V/H chosen, each of the six pixels should have an angular ALT subtense of

$$(\text{IFOV})_{\text{ALT}} = \frac{\Phi_{\text{ALT}}}{6} = \frac{11.25}{6} = 1.875 \text{ mrad} .$$

The example aperture of 6 in. (0.5 ft) at a vehicle altitude of 300 ft will subtend an ALT angle

$$\Phi_y = \frac{0.5}{300} = 0.001667 \text{ rad} = 1.67 \text{ mrad} .$$

To adjust the mismatch, one could increase the aperture length. There are many such trade-offs in a preliminary design. If we wish to recognize a 3-m target at a maximum slant range of 1500 m, for example, the required angular resolution for 50% P_R is

$$(\text{IFOV})_{\text{REQ}} = \frac{(3\text{m}/7)}{R_{\text{MAX}}} = \frac{0.4286}{1500} = 0.000286 \text{ rad} = 0.286 \text{ mrad} .$$

We have established two resolution requirements:

1. $(\text{IFOV})_y = 0.286$ mrad at $\theta_{\max} = \pm \cos^{-1} (H/R_{\text{MAX}})$
2. $(\text{IFOV})_y = 1.67$ mr at nadir.

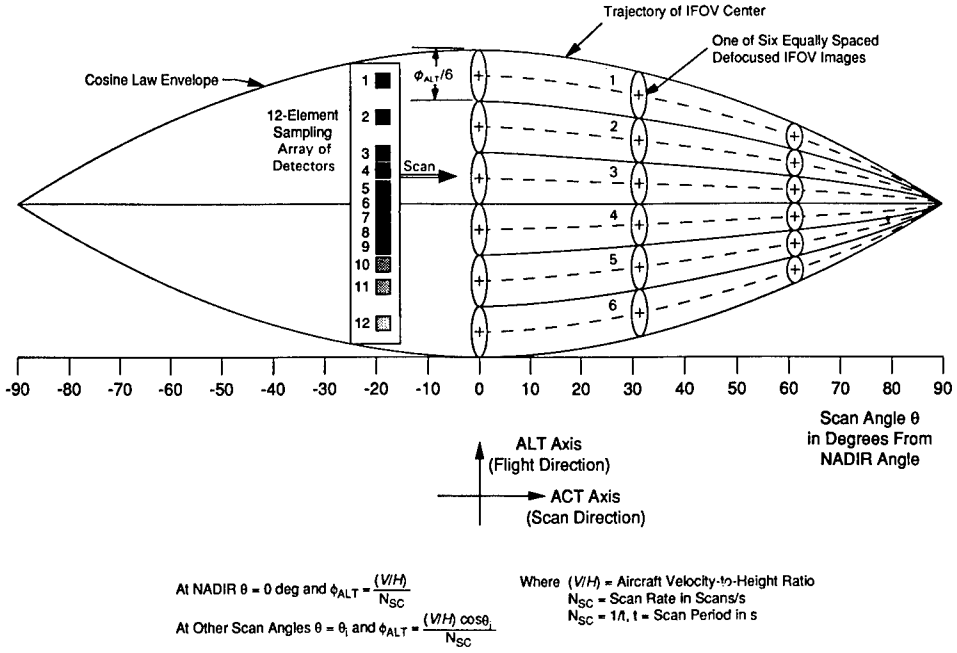

Fig. 1.33 Angular subtense of defocused IFOV images varies as the cosine of the scan angle.

We can see from Fig. 1.33 that between these two extremes the resolution should taper gradually from either side of nadir. The sampling strategy must be determined so as to form a correct image. For our example, three strategies are possible:

1. Use a linear array of 0.286 mrad detectors covering the required Φ_{ALT}. There would have to be $m = \Phi_{ALT}/0.286 = 11.25/0.286 = 39.3$ detectors in the array. The coarser resolution at nadir could be synthesized by adding six adjacent detector signals to cover an angle of $6 \times 0.286 = 1.716$ mrad. For intermediate scan angles similar approximations will hold.
2. Use an array with several different detector sizes, arranged symmetrically about the optic axis. This leads to an array with $1\times$, $2\times$, $4\times$, $8\times$, etc., sized detectors, where $1\times$ is the smallest size for the innermost detectors used at maximum slant range and the largest detectors are placed on the array edges. At nadir the smaller detectors are summed to synthesize a large detector for six equal samples of the ALT coverage. Detector switching chooses a correct combination for a series of closely spaced ACT sampling steps.
3. Use an array of 12 equal-sized detectors in an open sampling pattern shown in Fig. 1.33. The array detectors are closely spaced near the optic axis and are spaced progressively farther apart as their position departs from the center. In the nadir regions of the scan the distance is short and the defocused IFOV is large so that the SNR is more than adequate. We can sample the larger IFOV with a small detector and adjust the gain to restore the signal level. The IFOV radiance distribution is reasonably flat in the center portion of the pattern, as shown in Fig. 1.34. The sampling patterns are controlled by PROM-driven switches that act on the following input information:

   a. altitude
   b. number of channels (six)
   c. scan angle (encoder data)
   d. computation of nearest detector
   e. known detector coordinates in the array.

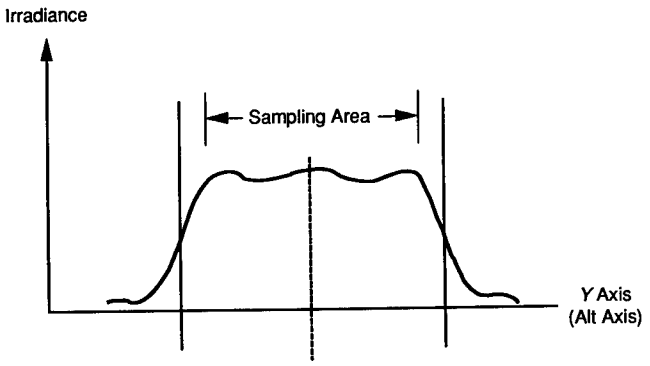

Fig. 1.34 ALT defocused image in focal plane.

The computation of nearest detector uses the known detector coordinates and compares with the trajectory coordinate for each of the six channels at each scan sampling angle. The output of the chosen detector is then connected to the appropriate channel until the next sample period. The sample periods can be evenly spaced or they can be adjusted so that a square sample is always taken. The advantage of this method is that the array is simpler and cheaper than the arrays for the other two methods.

All three sampling methods and others have been implemented in IRLS systems. Exact details are proprietary and the examples here are hypothetical.

1.3.23 Delay and Add

Delay and add, or time delay integration (TDI), is a technique to improve the SNR by repetitively scanning the same IFOV with different detectors and then summing the resulting signals in time registration. Since repetition involves a delay in time, the earlier signals must be delayed appropriately so that all signals are in time registration. This is an obvious extension of taking many measurements of physical quantities and averaging the results to improve the accuracy. Since noise, or uncertainty of the measurements, is random, it is uncorrelated with other measurements while the signals themselves are correlated. Adding the signals then follows the well-known statistical law that the noise adds in root sum square while the signals add directly. The net result, as previously noted, is that the SNR improves by $\sqrt{n}$, where n is the number of measurements. This technique has been used in infrared imaging, in early IRLS systems by Texas Instruments, and in other early IRLS designs. There are several ways to include TDI in an IRLS. The BAe line scanners use SPRITE (Signal Processing within The Element) detectors. A SPRITE detector is roughly equivalent to a horizontal array of discrete horizontal detectors connected to delay lines, as shown in Fig. 1.35. In the 12-element serially scanned array of Fig. 1.35, there are 12 signal voltages and 12 noise voltages so that the SNR improves by a factor of $\sqrt{12}$. The price paid in the discrete array technique is that we need 12 detectors, 12 bias supplies (for PC detectors), 11 delay lines, and 12 preamplifiers, all for a single channel. The SPRITE detector uses only a single bias supply and a single preamplifier to accomplish the same result. The SPRITE detector was developed only after mercury cadmium telluride material with a sufficiently long carrier lifetime became available. A long lifetime is needed to prevent recombination of the conductive charge cloud IFOV image before it reaches the collection electrode.

To use SPRITE detectors in IRLS systems it is necessary to scan at a high rate in order to prevent recombination, even with the noted increase in carrier lifetime. By adjusting the bias field in the SPRITE, the photoconductive charge-carrier image of an IFOV is swept to the other electrode at the same rate as the IRLS scan. The photocarrier cloud is thereby continuously reinforced by photons from the same point on the ground. The BAe line scanners therefore use a 12,000 rpm spin rate. Using a three-sided spin mirror gives 600 scans/s. The interscan period for a 180-deg scan is $t_{sc} = 1/600 = 1.667$ ms. This period is short enough for good SPRITE operation. There is a trade-off of length versus resolution at a given scan speed with these detectors. Longer elements theo-

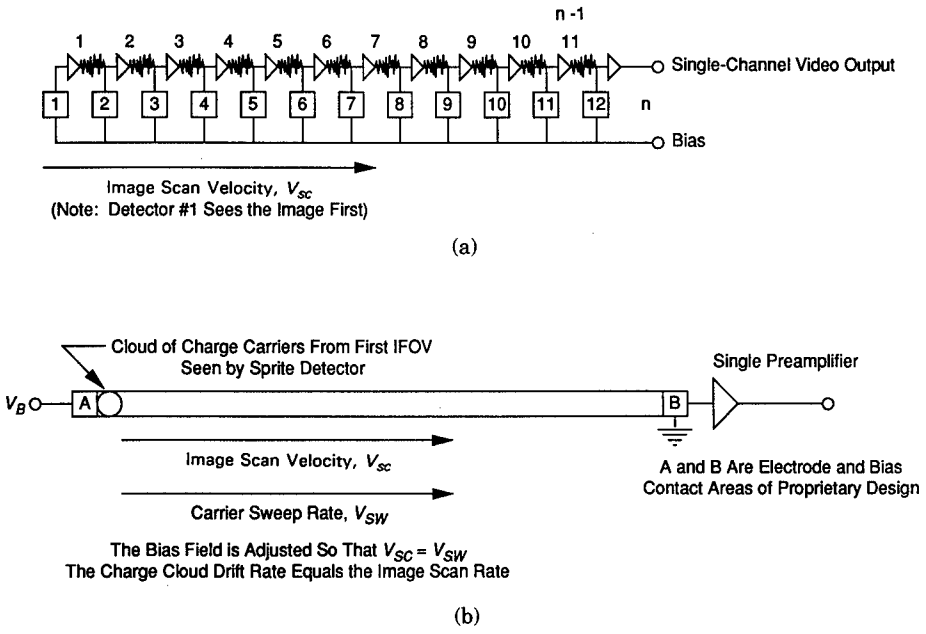

Fig. 1.35 Comparison of discrete horizontal array with SPRITE detector: (a) horizontal array of n discrete detectors with n preamplifiers and $n - 1$ delay lines; (b) SPRITE detector with single preamp is equivalent to n-element discrete array.

retically give better SNR, but charge-cloud diffusion limits ACT axis MTF. A benefit of the high spin rate used with SPRITE detectors is that high V/H values can be achieved with only a few SPRITEs in parallel. Consider our example of $(V/H)_{MAX} = 3.376$ rad s^{-1} at 300-ft altitude. The required ALT angular coverage was

$$\Phi_{ALT} = \frac{(V/H)_{MAX}}{n} = \frac{3.376}{600} = 0.00563 \text{ rad} = 5.63 \text{ mrad}$$

for each scan. This is to be compared with the earlier example of 6000 rpm where $\Phi_{ALT} = 11.25$ mrad. Acceptable mapping with SPRITE detectors seldom needs more than a maximum of four detectors in parallel.

1.3.24 Reliability, Logistics, and Cost of Ownership

Reliability and logistics have a large impact on a program, and most IRLS procurements now include extensive requirements for analysis of all aspects of reliability, logistics, and cost of ownership. Certain choices made in the initial requirements analysis influence reliability and cost of ownership and ultimate practicality of the IRLS. A well-known example is the choice of a wet-processed film as an IRLS recording medium for military reconnaissance. The pace and geographic scope of modern conflict now forces nations to consider long-range strike forces and rapid-deployment forces. Airborne reconnaissance may be needed on short notice anywhere in the world. To expect rapid airborne

deployment of wet photofilm processing equipment in desert, arctic, or equatorial regions is clearly impractical, especially when one considers that the wet film processors require fairly large amounts of pure temperature-controlled water and a reliable logistical supply of processing chemicals. In addition, the reconnaissance film requires refrigeration. It is also an urgent user concern that IRLS imagery be exploited as soon as possible by interpreters. With highly mobile targets this is imperative. The development time of wet-processed film is not the problem because the film can arrive at the ground station almost at the same time as the reconnaissance crew for debriefing. The problem is to get the information immediately after collection. Thus, a real-time output of imagery is essential. For these reasons the trend of tactical reconnaissance has been to record on analog and digital magnetic tape (or both) or to use thermally developed dry silver film and to use data links where possible.

1.3.25 Specific Reliability Concerns

There are several components in IRLS systems for which extra reliability emphasis and control must be made. These are listed here in no particular order of importance:

1. mirror coatings
2. spin motor
3. spin motor speed control and bearings
4. cryogenic refrigerator [lowest mean time between failure (MTBF) of system]
5. spin motor shaft encoder and its coupling
6. IR/detector dewar assembly (high-cost item)
7. IR windows (if used) and their coatings and mounting
8. in CRT recorders, the CRT and its high-voltage (18 kV) supply
9. film transport mechanism, if used, and its servo system
10. built-in test equipment resistance to false alarms from electrical transients and EM noise pulses
11. high-density tape recorders (high-cost, complex items)
12. thermal environment in electronics.

1.3.26 Logistics and Training

Logistics should be considered early in an IRLS development. There is a useful USAF planning document called an AGERD (Aerospace Ground Equipment Requirements Document). This document assists in planning for ground-support equipment such as AGE test benches and the support equipment to go with the benches for field, depot, and factory maintenance and repair. The US Navy has specific requirements for repair and maintenance items on its carriers. Decisions on replacement of modules, circuit cards, major assemblies, and LRUs must be made and maintenance manuals written. Logistics planning is also essential to any upgrade and modification program.

1.3.27 Documentation

The following documents are critical to any IRLS development:

1. IRLS system specification
2. individual LRU specifications
3. interface specifications
4. installation and outline drawings
5. electrical interface specifications
6. critical item component specifications, e.g., IR detector/dewar, optical elements, IR window, tape recorders, etc.
7. aerospace ground equipment (AGE) test bench specifications
8. built-in test (BIT) specifications
9. AGE test set specifications
10. qualification test plan and specifications
11. acceptance test plan and test procedures
12. maintenance manuals (formal)
13. operation and maintenance manual (informal O&M manual).

Documentation should be written so that individual items can be either separately procured, or procurement of the total IRLS system is possible. This aids logistics. An informal O&M manual has been found to be invaluable in training new factory technicians and engineers and can be updated as the need arises. The military manuals require formal publishing procedures, including extensive validation by skilled military maintenance technicians.

1.4 SYSTEM EQUATIONS AND RELATIONSHIPS

1.4.1 General Overview

This section gives equations for evaluating radiometric and imaging performance in terms of noise equivalent radiance (NEN), noise equivalent temperature difference (NETD), and radiance contrast (ΔN). Infrared blackbody functions are discussed. Prescriptions for estimating system electrical bandwidth and the filtering effects of signal processing and display elements of the system are given. Component equations and procedures for calculating system modulation transfer function, $(\mathrm{MTF})_{\mathrm{SYS}}$, are given, plus means to calculate the summary measure of IRLS performance, the minimum resolvable temperature difference (MRTD). Cautions in the use of MRTD as a merit figure are noted.

1.4.2 Noise Equivalent Radiance (NEN) and Noise Equivalent Temperature Difference (NETD)

Both these concepts use the definition of detectivity D^*. In rating early infrared detectors, noise equivalent power (NEP) was used. The NEP is simply the value of signal power P_S when it just equals the noise power P_N. In this case SNR = 1:

$$\frac{P_S}{P_N} = 1, \text{ so NEP} = P_S = P_N \quad [\mathrm{W}] \ .$$

In comparing two different IR detectors, the detector with the lowest NEP is superior, all other parameters being equal. Some people felt that bigger should be better, so they inverted the NEP to create detectivity (D) or reciprocal NEP:

$D \equiv 1/\text{NEP W}^{-1}$. This figure of merit was found to be simplistic because the noise-collection bandwidth and the measurement wavelengths were not included. It was also found that detector area and shape influenced performance. It was then decided to normalize to unit bandwidth and unit area. The noise is random and uncorrelated so it adds as the root sum square (rss). It is proportional to the square root of detector area ($A_d^{1/2}$) and to the square root of the electrical bandwidth ($\delta f_n^{1/2}$) within which it is measured. The $A_d^{1/2}$ noise dependency is a result of the fact that the number of collected photons depends on the area of the detector. With normalizations to unit area and unit bandwidth we can define the merit factor D^* as

$$D^* \equiv \frac{A_d^{1/2}\delta f_n^{1/2}}{\text{NEP}} \quad [\text{cm Hz}^{1/2}\,\text{W}^{-1}] \ . \tag{1.27}$$

Several cautions must be observed in interpreting D^*, however:

1. Frequency of chopping modulation used in measuring D^* must be stated.
2. Cell shape must not deviate too far from a square (rectangle length must not exceed seven times width).
3. Wavelengths of measuring radiation must be specified.
4. Detector temperature must be specified.
5. Bias current or bias field (if used) must be specified.
6. Cell thickness, electrode contacting method, cell surface treatment, and surface quality can influence $1/f$ noise.

Usually some of these parameters are included in the specification of D^* in parentheses following the value. For example, we write

$$D^*_{\text{BB}}\ (500,\ 1000)\ \text{cm Hz}^{1/2}\,\text{W}^{-1}$$

for a 500 K blackbody measurement of D^* at 1000-Hz chopping frequency. Alternatively, we can write $D^*_\lambda(\lambda,f)$, where λ is the specific wavelength used for the D^* measurement and f is the chopping frequency. One further caution is necessary. The value of D^*, whether blackbody or λ type, depends on the detector field of view. Most D^* data are given for a 180-deg (π steradian) FOV. In IRLS detector dewars, a cold shield is always used to limit the solid angle of arriving photons to those leaving the last focusing optical element. The cold shield improves the D^* by the factor $(\pi/\Omega)^{1/2}$. Here, Ω is the solid angle of the cold shield. The D^* for a hemispherical FOV is sometimes called D^{**}, or D-double-star, defined as

$$D^{**} \equiv \left(\frac{\Omega}{\pi}\right)^{1/2} D^* \ . \tag{1.28}$$

If the cold shield forms a rotationally symmetric cone of rays about the optical axis, we can express the angular flare of the cone in terms of the cold-shield angle, as shown in Fig. 1.36. Using the ordinary angle θ instead of the solid angle Ω gives

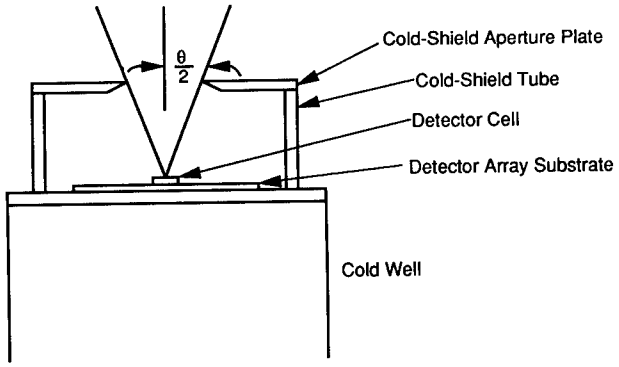

Fig. 1.36 Cold shield and cold-shield angle.

$$D^* = \frac{D^{**}}{\sin(\theta/2)} \ . \tag{1.29}$$

For rectangular cones, the solid angle Ω of the defining equation should be used instead of Eq. (1.29).

1.4.3 NEN and NETD Derivations

The NEN equation is derived from the definition of D^*:

$$D^* = \frac{A_d^{1/2}\delta f_n^{1/2}}{(\text{NEP})} \ , \text{ so NEP} = \frac{A_d^{1/2}\delta f_n^{1/2}}{D^*} \quad [\text{W}] \ . \tag{1.30}$$

The infrared radiance N is measured in W cm^{-2} sr^{-1}. We thus divide the NEP by the IRLS collecting area A_o in square centimeters and by the IFOV subtended solid angle $\Omega = (\text{IFOV}_x)(\text{IFOV})_y$ in steradians to get

$$\text{NEN} = \frac{\text{NEP}}{A_o(\text{IFOV})_x(\text{IFOV})_y}$$

$$= \frac{A_d^{1/2}\delta f_n^{1/2}}{A_o(\text{IFOV})_x(\text{IFOV})_y D^*} \quad [\text{W cm}^{-2}\ \text{sr}^{-1}] \ . \tag{1.31}$$

The IRLS optics are not 100% efficient, so we must divide by the optics transmission τ_o to give

$$\text{NEN} = \frac{A_d^{1/2}\delta f_n^{1/2}}{A_o\tau_o(\text{IFOV})_x(\text{IFOV})_y D^*} \quad [\text{W cm}^{-2}\ \text{sr}^{-1}] \ . \tag{1.32}$$

Atmospheric transmission τ_a is handled by dividing in the same way:

$$\text{NEN} = \frac{A_d^{1/2}\delta f_n^{1/2}}{A_o\tau_o\tau_a(\text{IFOV})_x(\text{IFOV})_y D^*} \quad [\text{W cm}^{-2}\,\text{sr}^{-1}] \; . \tag{1.33}$$

Usually, radiance is integrated across the spectral band of interest using D^*_λ. For simplified calculations, one uses in-band spectral averages:

$\overline{D}^*_\lambda, \bar{\tau}_o, \bar{\tau}_a, \overline{\text{NEN}}$, etc.,

where the average is taken across the spectral band.

The NETD equation is derived from the NEN equation by dividing by the radiance derivative with respect to temperature:

$$\text{NETD} = \frac{\text{NEN}}{(\delta N/\delta T)} \quad [\text{K}] \; . \tag{1.34}$$

Units of $\delta N/\delta T$ are W cm^{-2} sr^{-1} K. The radiance derivative is obtained by solving the differentiated Planck radiation equation using engineering units of radiance. We substitute the entire NEN expression [Eq. (1.33)] for NEN in Eq. (1.34) to get

$$\text{NETD} = \frac{\text{NEN}}{(\delta N/\delta T)} = \frac{A_d^{1/2}\delta f_n^{1/2}}{(\delta N/\delta T)(\text{IFOV})_x(\text{IFOV})_y A_o\tau_o\tau_a D^*} \; . \tag{1.35}$$

Usually we want the NETD over the specific infrared band of interest, such as the 8.0- to 12.5-μm band. We can then show the integration as

$$(\text{NETD})_{\Delta\lambda} = (\text{NETD})_{8\text{–}12.5}$$

$$= \frac{A_d^{1/2}\delta f_n^{1/2}}{(\text{IFOV})_x(\text{IFOV})_y A_o \displaystyle\int_8^{12.5} \tau_{o\lambda}\tau_{a\lambda} D^*_\lambda (\delta N/\delta T)_\lambda \, d\lambda} \; , \tag{1.36}$$

or, for simplified calculations use the in-band average parameters,

$$(\text{NETD})_{\Delta\lambda} = \frac{A_d^{1/2}\delta f_n^{1/2}}{(\text{IFOV})_x(\text{IFOV})_y A_o\bar{\tau}_o\bar{\tau}_a\overline{D}^*_\lambda \displaystyle\int_{\lambda_1}^{\lambda_2} (\delta N/\delta T)_\lambda \, d\lambda} \; . \tag{1.37}$$

The integral of the in-band radiance derivative is found by computer solution of the differentiated Planck equation. The remaining parameters in the NETD equation are discussed here in sequence.

1.4.3.1 Detector Noise Term $A_d^{1/2}$. The detector area for a square detector is $A_d = s^2 = s_x s_y$, where size s is $s_x = f(\text{IFOV})_x$ or $s_y = f(\text{IFOV})_y$. IFOV must be in radians and the focal length f must be in centimeters. In most IRLS

designs the parabolic mirror is the only element with optical power, so f is simply the focal length of this parabola. It should be noted that the approximation

$$\Omega_{\text{IFOV}} \approx (\text{IFOV})_x(\text{IFOV})_y \tag{1.38}$$

is accurate enough for all calculations. The correct expression for a solid angle is obtained by integration over a unit sphere to give

$$\Omega_{\text{SQ}} = (\text{IFOV})_x \sin(\text{IFOV})_y \ . \tag{1.39}$$

The two expressions are comparable for small values of the IFOV up to 200 mrad. Likewise, the approximations $S_x \approx f(\text{IFOV})_x$ and $S_y \approx f(\text{IFOV})_y$ are sufficiently accurate for all IRLS calculations.

1.4.3.2 Equivalent Noise Bandwidth $\delta f_n^{1/2}$. The equivalent noise bandwidth (often called the noise equivalent bandwidth, or NEB) is derived from the required signal bandwidth δf. The signal bandwidth is equal to one-half the IFOV scan rate, $N_{(\text{IFOV})_y}$, given in Sec. 1.1.3. The required line scan rate is

$$N_{\text{sc}} = \frac{(V/H)_{\text{MAX}}}{\Phi_{\text{ALT}}} = \frac{(V/H)_{\text{MAX}}}{n(\text{IFOV})_y} \quad [\text{lines/s}] \ , \tag{1.40}$$

where Φ_{ALT} is the ALT field of view, which is just the number of detectors n scanned in parallel multiplied by the ALT IFOV. The IFOV scanning rate $N_{(\text{IFOV})_x}$ is, from Sec. 1.1.3,

$$N_{(\text{IFOV})_x} = \frac{N_{\text{sc}}\pi}{(\text{IFOV})_x} = \frac{(V/H)_{\text{MAX}}\pi}{n(\text{IFOV})_x(\text{IFOV})_y} \quad [\text{IFOV/s}] \ . \tag{1.41}$$

The signal bandwidth δf is one-half the IFOV scan rate because there are two pixels per cycle, as shown in Fig. 1.3. This ignores any subsequent signal sampling scheme. Therefore, the analog signal bandwidth is

$$\delta f = \frac{N_{(\text{IFOV})_x}}{2} = \frac{\pi(V/H)_{\text{MAX}}}{2n(\text{IFOV})_x(\text{IFOV})_y} \quad [\text{Hz}] \ . \tag{1.42}$$

The equivalent noise bandwidth is found from the signal bandwidth δf by applying an equivalent filter factor k:

$$\delta f_n = k\delta f \ . \tag{1.43}$$

The factor k depends on the envelope of the equivalent bandpass of the total system, including any display or recorder. IRLS system designers usually use a k value of $\pi/2 = 1.57$ for a conservative preliminary estimate of noise equivalent bandwidth and a value of $k = 1.18$ for those systems using a CRT for display or film recording. The smaller k value is appropriate for these systems because the CRT spot acts as a low-pass filter that prevents passage of high-spatial-frequency noise. One can also plot the system power frequency response

curve, measure its area, then plot an equivalent area rectangular ("brick-wall") envelope to determine the equivalent noise bandwidth.

1.4.3.3 Net Optics Collecting Area A_o. The value A_o used here is the effective collecting aperture of the IR scanner. The gross area of the scanner aperture is not used because scanner optical paths are usually folded. This creates an effective hole in the aperture. In addition, one must account for the obscuration of any baffles and for possible reductions in aperture used to prevent unwanted narcissus views. Scanners with dual rectangular apertures will have equal apertures at nadir (scan angle $\theta = 0$ deg) unless they are made unequal because of the aforementioned narcissus control efforts. Figure 1.37 is an example of a Kennedy-type scanner that shows various influences on scanner aperture. As the spin mirror rotates off-nadir by an angle α, the scan angle θ is equal to 2α because of mirror angle doubling. The two half-apertures vary with α because the projection of the reflecting facet of the mirror narrows on one side and widens on the other. The total unobscured collecting aperture is the sum of both half-apertures so that it stays approximately constant over a wide scan angle. This is a primary advantage of the Kennedy-type split-aperture scanner. The angular range of constant aperture and the value of the total aperture at each scan angle θ are geometric functions of a particular scanner design. The aperture and the ray illumination footprint on each reflecting surface are calculated using the versatile and powerful ray-trace programs now available to the IRLS designer. It is best to evaluate the line-scan performance at ± 5- or ± 10-deg increments over the full scan angle. The ray-trace study should give the following outputs versus spin-mirror angle:

1. aperture on each side
2. ray pattern footprint (projected area) on each mirror face
3. stray radiation ray traces
4. unwanted scene look angles ("sneak paths")
5. narcissus paths where the detector sees its own cold-finger area
6. stray reflections from machined surfaces (e.g., mirror cutouts, baffles)
7. baffle placement analysis
8. focal-plane spot diagrams and energy density patterns.

Preliminary NETD analyses usually are based on nadir performance. Most performance testing and specifications are written for performance at nadir because it is easy to set the receiver LRU for a nadir view of an IR target. High values of the scan angle θ can have reduced aperture. NETD testing at these angles is recommended. Loss of aperture gives fewer photons and, hence, lower SNR, but at certain scan angles there can also be a loss in across-track MTF as ACT aperture width decreases. Both effects influence measured NETD.

1.4.3.4 Transmission of the Optics τ_o. The various obscurations and aperture limitation have already been accounted for in A_o, the net collecting aperture. In an all-reflective scanner design using the same type of high-reflectivity coating, the optics transmission is

$$\tau_o = r_m^n \ , \tag{1.44}$$

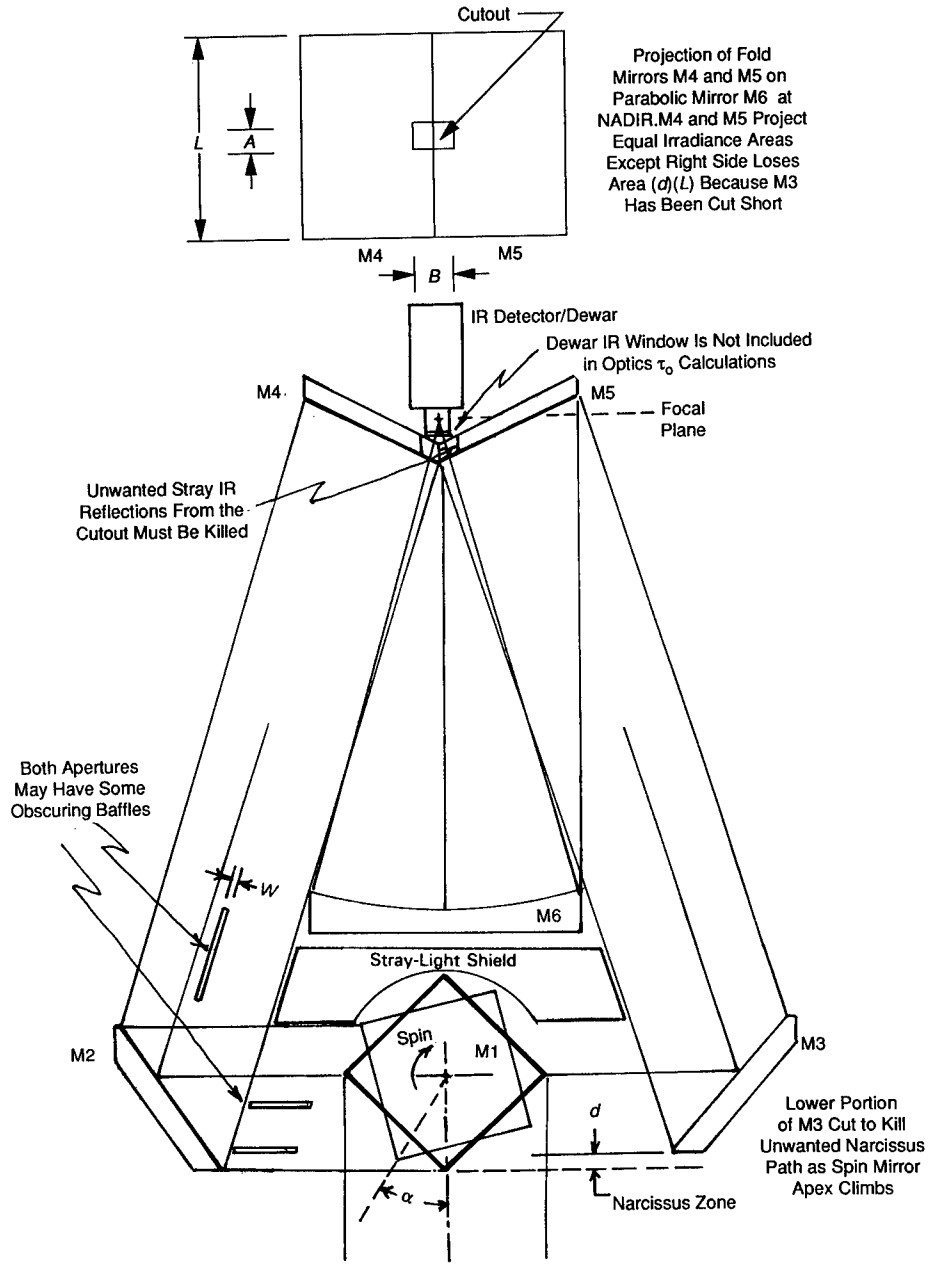

Fig. 1.37 Kennedy scanner as example of method of calculating area of collection at nadir position and optics transmission calculations.

where r_m is the mirror coating reflectance and n is the number of mirror reflections in tandem for any one ray. If one uses a different coating on one mirror, such as the spin mirror, then

$$\tau_o = r_{\text{sm}} r_m^{n-1} , \tag{1.45}$$

where r_{sm} = spin-mirror reflectance. If the scanner is catadioptric (has both mirrors and lenses), or uses a window,

$$\tau_o = r_m^n \tau_w \tau_1 \tau_2 \tau_3 \ldots , \tag{1.46}$$

where τ_o is the coated window transmission as measured or as specified and $\tau_1, \tau_2, \tau_3 \ldots$ are coated IR lens transmissions. If there is wavelength dependence within the spectral band of interest (3 to 5 μm or 8 to 13 μm), then an integration must be made and NETD computed using Eq. (1.36). The transmission of the IR window of the IR detector/dewar assembly should not be included in the computation of overall optics transmission τ_o. It is already included in the D^* measurement, which is necessarily performed with the window while the detector is at cryogenic operating temperature in its dewar.

1.4.3.5 Transmission of the Atmosphere τ. Atmospheric transmission varies widely with local weather conditions and with scan angle θ. It is usually ignored in all preliminary IRLS design calculations for NETD except in low-altitude, wide-FOV missions where offset viewing at the longer slant ranges is a vital requirement. Several examples of low-altitude oblique offset viewing were given in Sec. 1.3. In such preliminary requirements analyses the NETD and the MRTD (which includes NETD) can be estimated using a very simple atmospheric attenuation model based on uniform mixing of attenuating conditions and an essentially horizontal slant path. This is simplistic, but convenient. For example, one could assume

$$\tau_a = e^{-\alpha R} , \tag{1.47}$$

where α is the attenuation coefficient per kilometer and R is the slant range in kilometers. The value of α could be chosen for haze or light drizzle in a temperate climate. For recognition of a target at 1.5 km, for example,

$$\tau_a = e^{-0.25(1.5)} = e^{-0.375} = 0.687 .$$

These estimates are easily done with a hand calculator. Detailed calculations can be made via large batch calculation programs such as LOWTRAN, SELBY, etc. In using these comprehensive programs one can input such parameters as latitude zone, aerosols, weather, altitude, and slant-path angle (relates to scan angle). As with any large computer code it is easy to become inundated with data. For IRLS applications it should be remembered that most weather and most obscurants lie in the first few hundred feet of altitude. This is especially true of ground fogs in the early morning, battlefield dust, and chemical weapons. Worst case atmospheric attenuation will be found in low-altitude, wide-FOV missions at the maximum scan angles. This may drive the IRLS design.

1.4.3.6 Detectivity D^*. The NETD equation most often used for IRLS calculations is Eq. (1.36). It includes spectral D^* because this allows incremental computer approximation of the integral over the spectral band of interest. Figure 1.38 is the wavelength response function of a typical PC HgCdTe detector suitable for IRLS use. The spectral curve is obtained from an infrared

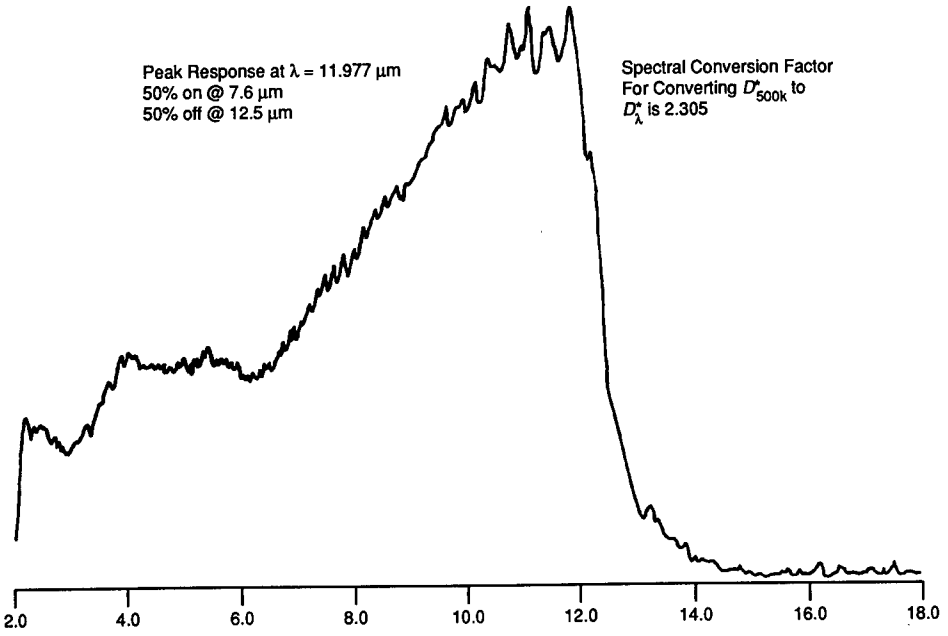

Fig. 1.38 Typical spectral response curve for PC HgCdTe.

spectrometer scan of a 500 K blackbody. The curve is normalized to the peak wavelength and a conversion factor is given for conversion to D^*_λ. (The actual value of peak D^*_λ is not given because it is classified.) The dip in response at approximately 6 μm is caused by absorptions in the AR coating used on the detector. Note that the automatic measurement also gives the 50% response wavelengths on either side of peak. IRLS systems have relied on the following types of detector:

1. PC InSb (3 to 5 μm)
2. PC HgCdTe (8 to 12.5 μm)
3. SPRITE PC HgCdTe (8 to 12.5 μm).

The preference of photoconductive over photovoltaic detectors is partly historic because PC types came first and because photoconductive gain allows for easier preamplifier design. The PV detectors have a $\sqrt{2}$ theoretical advantage in SNR but their higher impedance means that this advantage is harder to realize. With modern PV arrays and microcircuit readouts using CCDs, etc., PV detectors are becoming more appropriate for future systems. The PV types use no bias, or very little bias current if bias is used. Dissipation and the thermal load on the dewar and cryogenics are thus less for large PV arrays.

SPRITE D^* is handled like that of a single detector but the value used is that for the equivalent super-D^* detector with TDI already included.

1.4.3.7 Radiance Derivative ($\delta N/\delta T$). Equation (1.36) uses the wavelength-dependent radiance derivative $(\delta N/\delta T)_\lambda$. This is evaluated by computer using a program such as those given elsewhere in this handbook. The programs

useful in IRLS design should be written in the units needed for IRLS work. The Planck radiation equation and its first derivative, $\delta N/\delta T$, should be calculated using equations written in the engineering units used by IRLS designers. For example,

$$N_\lambda = \frac{\varepsilon C_1 \lambda^{-5}}{\exp(C_2/\lambda T) - 1} \quad [\text{W cm}^{-2}\ \text{sr}^{-1}\ \mu\text{m}^{-1}] \ , \tag{1.48}$$

where

ε = emissivity if we do not have a perfect blackbody
C_1 = 1.19106×10^4 W cm^{-2} sr^{-1}, first radiation constant (engineering units)
C_2 = 14388.33 μm K, second radiation constant (engineering units)
λ = wavelength in micrometers, the engineering unit of wavelength
T = temperature in kelvin.

Constants C_1 and C_2 have these values in engineering CGS units because wavelength is measured in micrometers and length in centimeters. Constant C_1 is the CGS value $3.7415 \times 10^4/\pi$ (to convert to radiance units because there are π steradians in a hemisphere and surfaces radiate into a hemisphere). In Eq. (1.48), N_λ is spectral radiance in W cm^{-2} sr^{-1} μm^{-1}. Differentiation of Eq. (1.48) with respect to temperature gives the radiance derivative

$$\left(\frac{\partial N}{\partial T}\right)_\lambda = \frac{\varepsilon N_\lambda C_2 \exp(C_2/\lambda T)}{[\exp(C_2/\lambda T) - 1]\lambda T^2} \ , \tag{1.49}$$

which is the radiance change per degree kelvin temperature change. Substituting Eq. (1.48) in Eq. (1.49) gives

$$\left(\frac{\partial N}{\partial T}\right)_\lambda = \frac{\varepsilon C_1 \lambda^{-5} C_2 \exp(C_2/\lambda T)}{[\exp(C_2/\lambda T) - 1]^2 \lambda T^2} = \frac{\varepsilon C_1 C_2 \lambda^{-6} \exp(C_2/\lambda T)}{T^2[\exp(C_2/\lambda T) - 1]^2} \ . \tag{1.50}$$

In IRLS calculations, emissivity is usually ignored in calculating NETD because the emissivity of IR test targets and IR scenes is close to unity. The in-band radiance and in-band radiance derivative are used for calculation of NETD using Eq. (1.37). For Eq. (1.37) we need to compute

$$\int_{\lambda_1}^{\lambda_2} \left(\frac{\partial N}{\partial T}\right)_\lambda d\lambda = C_2 \int_{\lambda_1}^{\lambda_2} \frac{N_\lambda \exp(C_2/\lambda T)}{[\exp(C_2/\lambda T) - 1]\lambda T^2} \, d\lambda \ . \tag{1.51}$$

1.4.4 Radiance Contrast and Other Blackbody Functions

Occasionally in IRLS design studies it is useful to compute other quantities besides NETD and MRTD. Radiance contrast is a useful tool in requirements analysis and similar studies. Radiance contrast ΔN is the radiance change for a given temperature contrast:

$$\Delta N = N_{T_1} - N_{T_2} \ . \tag{1.52}$$

In other studies one must occasionally calculate blackbody functions at a specific wavelength instead of integrating over the entire band. The following wavelength-dependent quantities are used in IRLS design:

1. flux (radiance and radiant exitance)
2. spectral radiance derivative at λ
3. spectral radiance contrast at λ for T_1 and T_2
4. photon-noise power density at λ.

It is also useful to be able to express blackbody quantities in either units of power (watts-type units) or photons. The photon radiance is needed to calculate detector performance. For example, the background photon radiant exitance is used to calculate the background photon noise $Q_B^{1/2}$, where Q_B is the total number of background photons reaching the detector. The background, acting as a blackbody, contributes an in-band photon radiant exitance $(Q_W)_{\Delta\lambda}$ [photons s^{-1} cm^{-2}], so that for a detector of area A_d the total background photon count will be

$$Q_B = (Q_W)_{\Delta\lambda} A_d \quad [\text{photons s}^{-1}] \tag{1.53}$$

and the photon noise is simply $Q_B^{1/2}$ because the photons arrive randomly in accordance with Poisson statistics. These quantities are easily calculated as subroutines in a program solving the Planck equation.

1.4.5 Signal-Processing Effects on Noise Bandwidth

Section 1.4.3 gave a prescription for estimating system noise equivalent bandwidth δf_n based on a simple multiplier k. In preliminary estimates $k = 1.57$ is used. This gives a conservative approximation for δf_n. In designs using a CRT and other system elements that act as filters, $k = 1.18$ is often used. A goal in IR design is to make the system "detector-noise-limited," where the detector is the dominant noise source. The signal processing chain of Fig. 1.39 contains, as a minimum, the elements shown. The total noise is

$$P_n = (P_D^2 + P_{PA}^2 + P_A^2)^{1/2} , \tag{1.54}$$

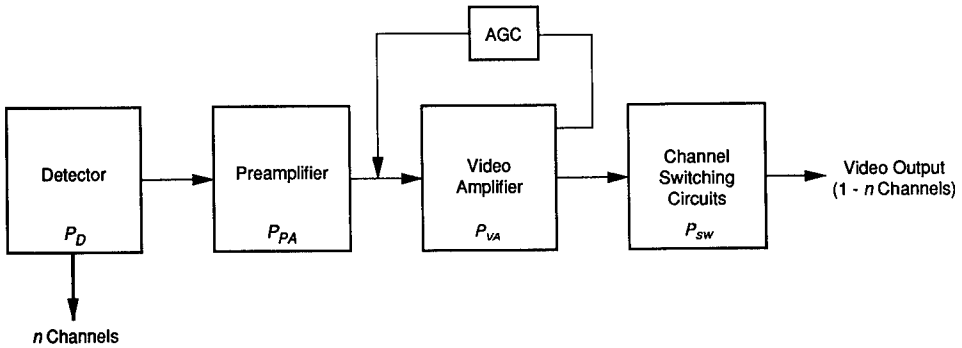

Fig. 1.39 Dominant noise sources in IRLS analog signal channel. (Detector noise predominates. Video amplifier noise is important at low AGC levels because detector and preamp noises are then attenuated.)

where P_D is detector noise power, P_{PA} is preamplifier noise power, and P_A is the amplifier noise power. In all preliminary IRLS calculations only the two noise sources are considered, namely, the detector and preamplifier. In IRLS systems using PC detectors, the photoconductive gain works to advantage and even the preamplifier noise can be ignored in early calculations. The preamplifier can be designed for low noise using proper biasing and such techniques as parallel input stages. When small sources are rss combined with larger sources, the smaller sources become unimportant. For these reasons the NETD equations [Eqs. (1.35), (1.36), and (1.37)] all assume detector noise only.

1.4.6 Recorder and Display Noise

As previously noted, the NETD equations assume that detector noise dominates. In infrared technology the NETD has usually been measured at the output of the preamplifier, but in IRLS systems made up of LRUs it is convenient to measure NETD at the output of the receiver LRU. This is useful in separate procurement and acceptance testing or when the receiver LRU must interface directly with a reconnaissance management system (RMS) that does further processing of the IRLS video data. In such instances or when digital processing or tape recorders are used, it is necessary to account for digitization noise and other noise sources in assessing total IRLS performance.

1.4.7 IRLS Dynamic Range

Video average level control and IRLS dynamic range are both important to image quality and utility. The analog video from a well-designed IRLS has a wide dynamic range that can vary with the type of scene and the type of targets to be depicted in the scene. With the present state of technology it is not possible to render all the dynamic range in a linear manner. Some nonlinear compression is inevitable. If the detector and preamplifier are linear over a 10^4 dynamic range, it is not possible to record this range on film or to display it on a CRT monitor, as shown in Figs. 1.40(a) and (b). If analog tape recorders are used, their dynamic range is also limited, and if digital processing is used with digital tape recording, even a 10-bit digitization cannot guarantee that inherent IRLS thermal resolution can be preserved over the entire dynamic range. The dynamic range of the detector and preamplifier can be estimated using the concepts of target radiance and IRLS noise equivalent radiance (NEN). The signal voltage dynamic range is

$$\text{D.R.} = \frac{V_{\text{MAX}}}{V_{\text{MIN}}} , \tag{1.55}$$

where

$$V_{\text{MAX}} = \text{RP}_{\text{MAX}} = R[N_{\text{MAX}} A_o \tau_o \tau_a (\text{IFOV})_x (\text{IFOV})_y] , \tag{1.56}$$

$$V_{\text{MIN}} = RP_{\text{MIN}} = R(\text{NEP})_{\Delta\lambda} = R\left(\frac{A_d^{1/2} \delta f_n^{1/2}}{D^*_\lambda}\right) , \tag{1.57}$$

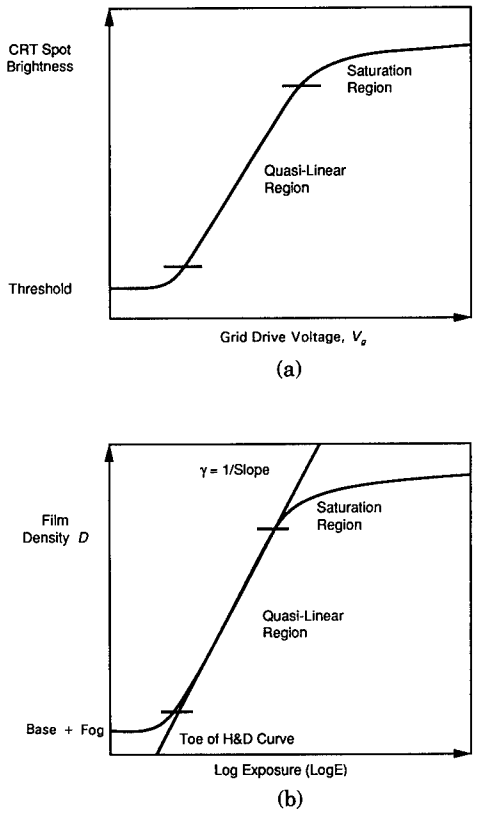

Fig. 1.40 Saturation effects of CRT and film: (a) CRT transfer curve; (b) D versus log$E$, or Hurter and Driffield curve, for film.

R = detector responsivity in volts per watt, N_{MAX} = maximum scene radiance (for hottest object in the scene), $(IFOV)_x$ and $(IFOV)_y$ are the detector subtense in the ACT and ALT axes, and

$$(NEP)_{\Delta\lambda} = \frac{A_d^{1/2}\delta f_n^{1/2}}{\overline{D}^*_\lambda} \quad . \tag{1.58}$$

Thus, to compute the signal voltage dynamic range

1. Decide on the hottest scene object temperature in kelvin.
2. Compute N_{MAX} using an appropriate blackbody program.
3. Compute V_{MAX} with Eq. (1.56) with known values A_o, τ_o, τ_a, $(IFOV)_x$, $(IFOV)_y$ from the IRLS design and R from the detector data.
4. Compute V_{MIN} using Eq. (1.57) with known values $A_d^{1/2}$, $\delta f_n^{1/2}$, and in-band average D^*_λ (obtained from plot of detector response versus wavelength).
5. Divide V_{MAX} by V_{MIN} to get dynamic range.
6. Include this together with bandwidth and input noise and gain requirements, etc., in the preamplifier specification.

Table 1.17 IRLS Digitization Problem

Number of Bits n	Dynamic Range = 2^n
8	256
10	1,024
12	4,096
13	8,132
13+	10,000 (typical IRLS)
14	16,384

1.4.8 Digital Signal Dynamic Range

If the signal is digitized, we note a problem as shown by Table 1.17. A good IRLS with as much as 10^4 dynamic range requires 14-bit digitization, yet the analog bandwidth seldom exceeds 2 MHz. If there are up to 12 signal channels (some IRLSs use 2, 4, or 6), the cost and complexity become high. Fortunately, it is not necessary in most applications to provide linearity over the full dynamic range. Some compression is desirable because in most applications it is not necessary to know or to depict exact temperatures of very hot scene objects. Except for IRLS radiometers, it is usually enough to show that the object is significantly hotter than the surroundings.

1.4.9 Analog Signal Compression

Analog compression is used to better match the IRLS video signal to the saturating transfer curves of the CRT and film shown in Figs. 1.40(a) and (b), respectively. This compression is applied at the video processor amplifier, which is given a quasi-logarithmic response or other suitable compression function. This simple compression is sometimes inadequate when the system is operating at full gain and a high contrast target is encountered. This is the situation in some airborne IRLSs when scanning over the open ocean with a calm sea state. The AGC operates on integrated video detail to generate a gain signal that is inversely proportional to the scene detail in the middle band of spatial frequencies. Motivation for this form of AGC was to see better in light fog or haze conditions, which reduce the video contrast. On a clear day on the calm open ocean the system thus selects maximum gain and can saturate when a high-contrast target such as a ship is encountered. The saturation is very undesirable because the deck and superstructure detail are lost and the ship is seen as a silhouette. This problem could be solved by the use of a smarter gain control system. Similar problems occur in the commercial photoprinting industry when it is necessary to print a high-contrast negative on photopaper with a much more limited dynamic range of gray tones. Spatial filtering has been used for many years to reduce the gain of the middle band of spatial frequencies while keeping the gain of the higher spatial frequencies intact. In effect, the detail rides on a pedestal and the pedestal amplitude is reduced. No important scene information is lost. Human vision has a tremendous dynamic range and processes optical data using similar techniques in the visual cortex. The process is shown schematically in Fig. 1.41 because it is applicable

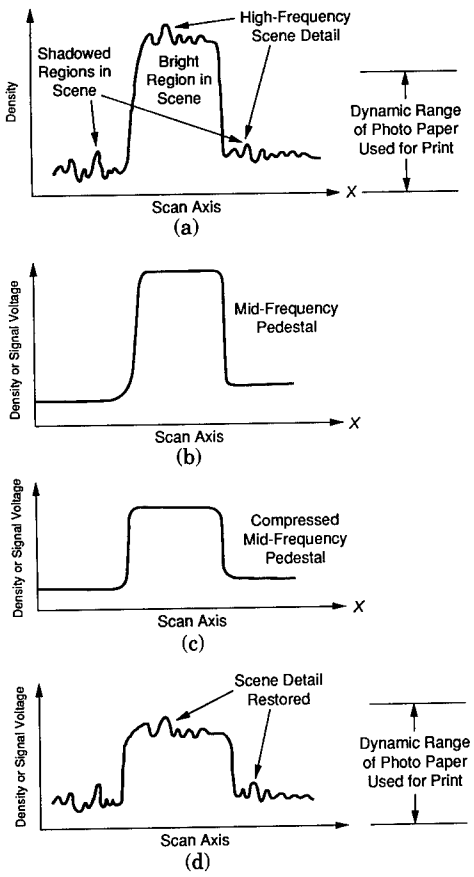

Fig. 1.41 Mid-frequency compression in commercial photo printing is useful for IRLS signal processing. (a) Scene dynamic range is too much for print paper. (b) Extract mid-frequencies by filter. (c) Compress the mid-frequencies. (d) Add mids and highs to restore scene.

to IRLS gain control. The US Army developed a similar technique for FLIRs, called ALFGL (automatic low frequency gain limiting). It is necessary to perform these filtering operations carefully because phase shifts can occur that degrade resolution when the two spatial frequency scene bands are recombined to form the image.

1.4.10 Digital Techniques of Signal Compression

Digital equivalents of this technique of spatial filtering and control have been applied to IRLS image processing and are discussed in Sec. 1.8.1.

1.4.11 Example Dynamic Range Calculation

Let it be desired to linearly depict targets as hot as $T = 600$ K (327°C) against a 273 K winter background. Because such hot targets are the exception, we wish to preserve the inherent noise equivalent radiance (NEN) performance. The dynamic range is

$$\text{D.R.} = \frac{(N_{\text{MAX}})_{\Delta\lambda}}{(\text{NEN})_{\Delta\lambda}} , \tag{1.59}$$

where $(N_{\text{MAX}})_{\Delta\lambda}$ is the in-band spectral radiance in the 8.0- to 13.0-μm band for the 600 K hottest target and $(\text{NEN})_{\Delta\lambda}$ is the in-band noise equivalent radiance. Let the IRLS have the following parameters:

f = 18.0 cm, focal length
A_o = 90 cm^2, optics net collecting area
τ_o = $r_m^4 = 0.98^4$ for four mirror reflections
τ_a = 1 (ignore the atmosphere for this calculation)
$(\text{IFOV})_x = (\text{IFOV})_y = 0.3 \times 10^{-3}$ sr, detector IFOV
$A_d^{1/2}$ = $f(\text{IFOV}) = (18)(0.3 \times 10^{-3}) = 5.4 \times 10^{-3}$ cm, detector size
δf_n = $1.11\delta f = 1.11(1.26 \times 10^6) = 1.4$ MHz equivalent noise bandwidth
D_λ^* = 2.5×10^{10} cm $\text{Hz}^{1/2}$ W^{-1} (hypothetical detector).

Substitution of these values into the $(\text{NEN})_{\Delta\lambda}$ equation gives

$$(\text{NEN})_{\Delta\lambda} = \frac{A_d^{1/2}\delta f_n^{1/2}}{A_o(\text{IFOV})^2\tau_o\tau_a D_\lambda^*} = \frac{(5.4 \times 10^{-3})(1.4 \times 10^6)^{1/2}}{(90)(0.3 \times 10^{-3})^2(0.92)(1)(2.5 \times 10^{10})}$$

$$= 3.43 \times 10^{-5} \text{ W cm}^{-2} \text{ sr}^{-1} .$$

The value of N_{MAX} is obtained from computer solution of the Planck equation in radiance units for T = 600 K and the spectral band λ_1 = 8.0 μm to λ_2 = 13.0 μm, giving

$$(N_{\text{MAX}})_{\Delta\lambda} = 5.6224 \times 10^{-2} \text{ W cm}^{-2} \text{ sr}^{-1} .$$

The IRLS dynamic range is therefore

$$\text{D.R.} = \frac{(N_{\text{MAX}})_{\Delta\lambda}}{(\text{NEN})_{\Delta\lambda}} = \frac{5.6224 \times 10^{-2}}{3.43 \times 10^{-5}} = 1.639 \times 10^3 = 1639 .$$

If this dynamic range is digitized, it would require 11 bits to preserve the NEN of the IRLS within the dynamic range.

1.4.12 Filtering Effects of Signal Processing and Display Elements

IRLS systems use cathode-ray tubes to display the imagery, or, if film is the display medium, a CRT or a moving spot of modulated light is used for recording the video data. With digital signal processing it is necessary to operate a digital sampling switch in each channel. For each of these cases there is an ACT sample size that represents the ACT angular resolution $(\text{IFOV})_x$. It gives the final displayed ACT resolution. This is not always identical to the IFOV of the scanner. Usual IRLS design practice is to match the CRT spot and the ACT

digital sample size to the scanner IFOV. Therefore, one IFOV = one CRT spot width = one ACT sample interval (spatial equivalent) in digital systems. Also, one IFOV = one CRT spot = one TV line in the ALT dimension. Any digital sampling used in the ACT direction should always be at the Nyquist rate or better. One digital sample per IFOV (per half-cycle of spatial frequency) equals one sample per half-cycle of the IFOV electrical frequency f_{IFOV}. Higher frequencies in the scene and higher noise frequencies will not be rendered. The CRT spot width and the phosphor persistence act as a high-frequency cutoff filter. Neither high-frequency noise nor high-frequency aliasing effects will be seen in the display. Cost and complexity considerations usually limit digital sampling to the Nyquist rate, although twice Nyquist would be desirable to preserve MTF.

1.5 SYSTEM MODULATION TRANSFER FUNCTION

The MTF of an infrared system is a useful design tool because it describes the effect on the signal modulation caused by each element of the system. Multiplication (cascading) of the separate MTFs gives the overall IRLS system MTF:

$$\text{MTF}_{\text{SYS}} = (\text{MTF})_1(\text{MTF})_2(\text{MTF})_3 \ldots \quad (1.60)$$

It is worthwhile to review the meaning and limitations of the MTF concept. We start with the concept of modulation. Modulation was originally defined for electrical waves but the concept has been extended to include sinusoidal spatial-frequency distributions of scene radiance or irradiance in a focal-plane image. When these spatial distributions are uniformly scanned, or are uniformly sampled in time sequence, a sinusoidal electrical frequency is obtained after appropriate wave-form reconstruction. The various elements of the system can be considered as processes or "black boxes" that influence the modulation, while the spectrum of Fourier frequencies is considered the carrier of information throughout the chain of processes. Figure 1.42 defines the MTF. Several conditions must be satisfied for the MTF concept to be valid:

1. Sinusoidal inputs and outputs or combinations of sinusoids must be used. Complex wave forms, such as square waves, must be Fourier analyzed by being expressed as a sum of Fourier odd harmonics. Other complex waves have lesser interest to IRLS design analysis.

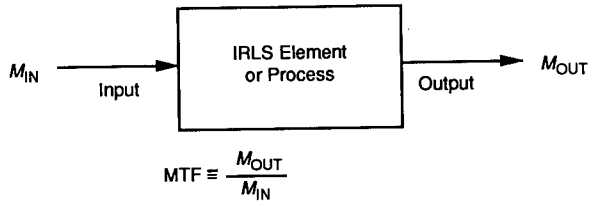

Fig. 1.42 Definition of modulation transfer function (MTF).

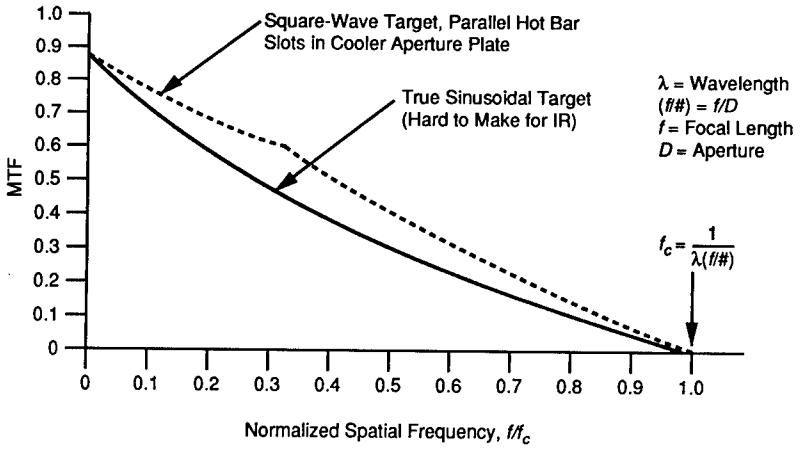

Fig. 1.43 Cutoff frequency for an aberration-free circular aperture (axehead IRLS designs).

2. These Fourier component sinusoidal waves are assumed to be continuous (with no beginning or end). In nature this does not occur. Fortunately, for IRLS analysis we can ignore this requirement.
3. IRLS system elements must be linear in their response to the amplitude variation of their sinusoidal inputs. In an example IRLS we have previously noted several nonlinear response functions, such as
   a. video amplifier saturation (deliberately introduced to compress the video signal dynamic range).
   b. CRT response is nonlinear in the saturation and threshold regions of the S-shaped transfer curve. The central portion, however, can be treated as a linear response. IRLS MTF analysis is applicable to this linear region only.
   c. Film response in film recorders follows a curve called the H&D curve, or density versus log exposure curve, which has a similar threshold region with a linear midrange; hence, the same remarks as No. 2 above apply.
   d. Additional dynamic range compression may be done via digital signal processing if such digital image processing is used in the IRLS.

Care must be used in determining the MTF of such processing. Usually one tries to minimize any processing effects on the IFOV frequency (MTF $\approx$ 1).

The concept of *cutoff frequency* f_c is useful. The cutoff frequency is that frequency where MTF = 0. It can be an optical or an electrical cutoff frequency. Figure 1.43 shows an optical cutoff frequency for an aberration-free circular aperture. The abscissa is normalized spatial frequency f/f_c, where f_c is that frequency where MTF first goes to zero. In optics we can have more than one cutoff.

1.5.1 Across-Track MTF Analysis of IRLS Systems

In IRLS analysis of MTF both the ACT (across-track or x) axis and the ALT (along-track or y) axis must be considered. The IRLS is treated as a cascade

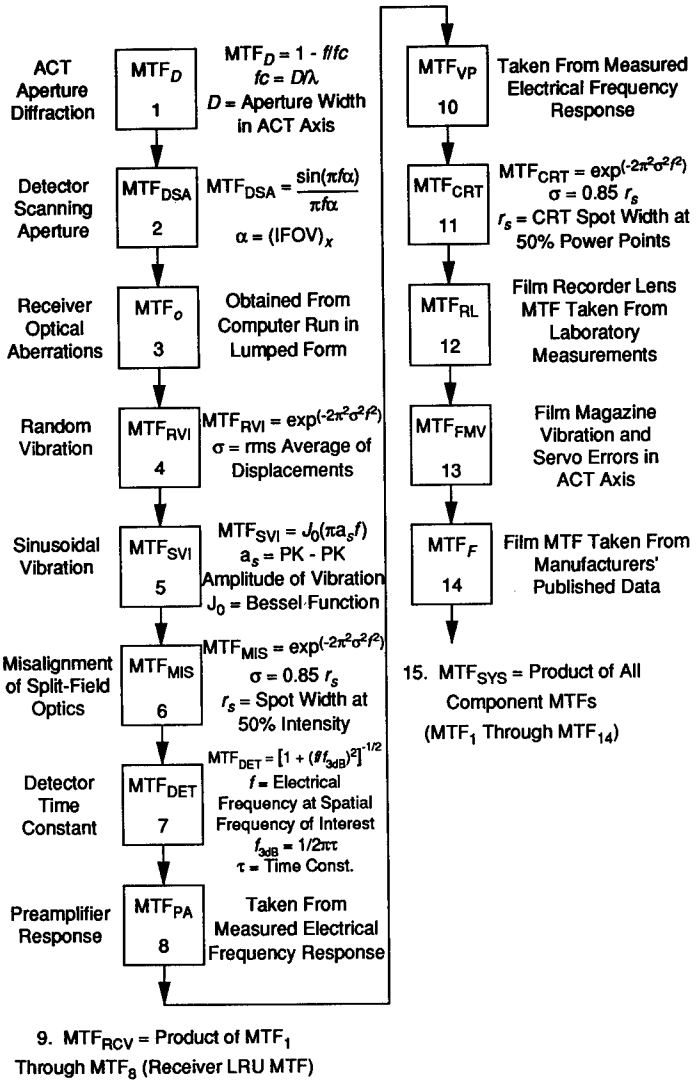

Fig. 1.44 ACT-axis analysis of MTF of a typical IRLS that uses a film recorder.

of process elements starting at the scanner aperture and ending with the CRT display or film (if film is the final display). Figures 1.44 and 1.45 are examples of the MTF analysis used for several airborne IRLS systems. The figures give expressions for each main contributor or indicate how to proceed. Starting with the entrance aperture diffraction, some of these contributors are described below, with emphasis on ACT calculations.

1.5.1.1 ACT Aperture Diffraction, MFT$_D$. Most IRLS systems use either a round aperture or a pair of varying rectangular apertures (split-aperture designs). The MTF of a circular optical aperture with no aberrations is a result of boundary-wave diffraction by the aperture rim interfering with the incoming

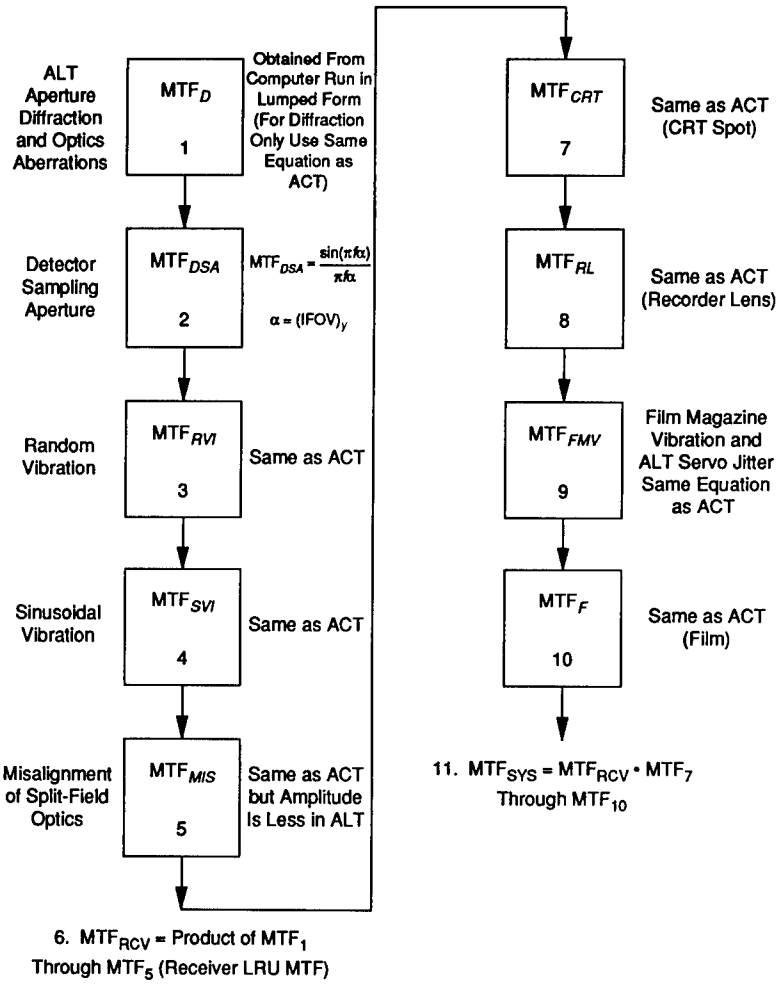

Fig. 1.45 ALT-axis analysis of MTF of a typical IRLS that uses a film recorder.

plane waves from a point source at infinity. Interference of the incoming signal waves with the boundary wave produces the diffraction pattern in the focal plane, which, at the cutoff frequency f_c, destroys the modulation. The MTF of such an aperture is given by

$$\text{MTF}\,(f) = \frac{2}{\pi}\left[\arccos\left(\frac{\lambda f}{2(\text{NA})}\right) - \frac{\lambda f}{2(\text{NA})}\sin\left(\arccos\frac{\lambda f}{2(\text{NA})}\right)\right], \qquad (1.61)$$

where f is the spatial frequency in cycles per radian and NA is the numerical aperture. For IRLS analyses NA = $^1/_{2F}$*.

The reader is referred to any good optical text for a derivation of Eq. (1.61). For a very thorough discussion see Born and Wolf (see Bibliography). For a single rectangular aperture the diffraction MTF is

$$\mathrm{MTF}_D = 1 - \frac{f}{f_c} , \tag{1.62}$$

where f is the spatial frequency and the cutoff frequency $f_c = D/\lambda$, where D is the width of the rectangular aperture in the ACT dimension. In split-aperture scanners there are two separate rectangular apertures that vary in ACT width as the scan progresses. At nadir, the two apertures are at maximum. Each aperture must have its diffraction MTF separately evaluated for any arbitrary scan angle because the radiation passing through each aperture is not correlated with the other aperture. The optical path lengths differ so we cannot consider the diffraction of the total pair. Instead, the weighted MTF must be computed based on the relative widths of the two rectangular apertures at the scan angle of interest. In split-aperture scanners the ALT aperture is constant with scan angle, so the computation of MTF_D is easier for the ALT axis. In preliminary MTF analyses, only the nadir MTF_D is computed. Later, the MTF_D at a series of stepped scan angles is calculated using a desktop or large computer. Using design data and the spin mirror cross section (triangle or square), the aperture widths and MTF_D for each aperture are calculated and combined in a weighted manner for the composite MTF_D as follows:

$$\mathrm{MTF}_D = \mathrm{MTF}_1\left[\frac{D_1}{(D_1 + D_2)}\right] + \mathrm{MTF}_2\left[\frac{D_2}{(D_1 + D_2)}\right] . \tag{1.63}$$

In reality, the weighting is based on relative aperture areas, but, since the ALT dimension is constant, it need not appear in the weighted MTF sum. The ACT width of the left aperture is represented by D_1, and D_2 is the ACT width of the right aperture, and likewise for the MTF subscripts. The circular aperture in axehead scanners does not vary with scan angle. This is one advantage of an axehead scanner. One disadvantage, however, is its poor scan efficiency.

1.5.1.2 The Detector as a Sampling Aperture, $\mathrm{MTF}_{\mathrm{DSA}}$. Most IRLS detectors are rectangular. Future array designs might deviate from this, because focal-plane arrays often use oval or rectangular cells. For convenience, a rectangular detector can be considered to sample the scene when the scene image is scanned across the detector. The detector sampling aperture has a width S_x in the ACT axis and S_y in the ALT axis. The MTF of the detector sampling aperture is

$$\mathrm{MTF}_{\mathrm{DSA}} = \frac{\sin(\pi f\alpha)}{\pi f\alpha} , \tag{1.64}$$

where f is the spatial frequency in cycles/mrad and α = IFOV in mrad. At f_{IFOV} it takes two pixels (2 IFOV) to make one cycle, so $f_{\mathrm{IFOV}} = {}^1/_{2\alpha}$. At f_{IFOV}, the detector scanning aperture MTF is

$$\mathrm{MTF}_{\mathrm{DSA}} = \frac{\sin(\pi f_{\mathrm{IFOV}}\alpha)}{\pi f_{\mathrm{IFOV}}\alpha} = \frac{\sin(\pi\alpha/2\alpha)}{\pi\alpha/2\alpha} = \frac{\sin(\pi/2)}{\pi/2} = 0.637 .$$

1.5.1.3 Optical Aberrations, MTF_o. Several scanner optical aberrations are important, namely, coma, spherical aberration, and astigmatism. The MTFs of these aberrations are evaluated by large digital computers using ray-trace programs such as Code V or ACOS. It is convenient to lump the aberrations together using wave-front analysis and get a combined optics MTF_o for nadir (scan angle $\theta = 0$ deg) and for other values of θ as needed. These large programs will print out tables of MTF_o versus θ very rapidly.

1.5.1.4 Random Vibration, MTF_{RVI}. Vibration effects are often omitted in an MTF analysis unless severe vibration effects are present on any optical element. One must distinguish between vibration-induced motions that are random with respect to x- and y-axis image motion and those that are sinusoidal. Random displacement of a spot image causes the spot to blur to a Gaussian pattern. The MTF from random vibration is therefore

$$\mathrm{MTF_{RVI}} = \exp(-2\pi^2\sigma^2 f^2) \ , \tag{1.65}$$

where σ is the rms amplitude of the vibration displacement.

1.5.1.5 Sinusoidal Vibration, MTF_{SVI}. Sinusoidal vibration can occur when a flat folding mirror vibrates in its mount, causing spot displacements in the ACT axis. This is because there is usually an angle adjustment built into the lower (outboard) fold mirrors of split-aperture scanners. The MTF of such a sinusoidal displacement is

$$\mathrm{MTF_{SVI}} = J_0(\pi a_s f) \ , \tag{1.66}$$

where J_0 is a zero-order Bessel function, a_s is the peak-to-peak amplitude of sinusoidal vibration effect (radians), and f is the spatial frequency (cycles per radian).

1.5.1.6 Misalignment of Split-Field Optics, MTF_{MIS}. Since both paths of a split-aperture scanner must be aligned, there is a residual misalignment in each axis. This can be considered as a Gaussian error, so the MTF is that of a Gaussian. The same form of equation as Eq. (1.65) should be used.

1.5.1.7 Detector Time Constant, MTF_{DET}. The detector has a finite time constant that delays its response to changes in image irradiance as it scans. The time constant MTF is well known and will not be derived here. We have

$$\mathrm{MTF_{DET}} = \left[1 + \left(\frac{f}{f_{3\mathrm{dB}}}\right)^2\right]^{-1/2} \ , \tag{1.67}$$

where f is the electrical frequency of interest and $f_{3\mathrm{dB}}$ is the electrical frequency at which the signal voltage is 3 dB down (50% power) from its dc, or low-frequency, value. The detector is measured in the detector laboratory to determine its $f_{3\mathrm{dB}}$ value or, if its time constant τ is known, $f_{3\mathrm{dB}} = 1/2\pi\tau$. For example, let a detector have a time constant

$$\tau = 200 \text{ ns} = 0.2 \times 10^{-6} \text{ s, so } f_{3\mathrm{dB}} = {}^1/_{2\tau} = \frac{10^6}{2\pi(0.2)} = 796 \text{ kHz} \ .$$

If we have a signal electrical frequency of 500 kHz,

$$\mathrm{MTF_{DET}} = \left[1 + \left(\frac{500}{796}\right)^2\right]^{-1/2} = 0.847 \ .$$

If we have an electrical frequency of $f = 1$ MHz, we have

$$\mathrm{MTF_{DET}} = \left[1 + \left(\frac{1000}{796}\right)^2\right]^{-1/2} = 0.623 \ .$$

1.5.1.8 Preamplifier Response, $\mathrm{MTF_{PA}}$. The response versus frequency curve of the preamplifier is usually peaked near the IFOV frequency to partially compensate for MTF roll-offs from other elements of the IRLS. Figure 1.46 shows a typical preamplifier frequency response curve. The $\mathrm{MTF_{PA}}$ is easily calculated from the preamplifier frequency response curve by reading the gain in dB relative to that at f_R and substituting the gain V_{OUT}/V_{IN} into Eq. (1.68):

$$\mathrm{MTF_{PA}} = \mathrm{GAIN} = \log^{-1}\frac{A}{20} \ , \tag{1.68}$$

where A is the decibel gain at the frequency of interest.

1.5.1.9 Receiver, $\mathrm{MTF_{RCV}}$. If the receiver LRU signal output is taken at the output of the preamplifier, we get the receiver MTF by multiplying all previous MTF values at each frequency:

$$\mathrm{MTF_{RCV}} = \mathrm{MTF_D MTF_{DSA} MTF_O MTF_{RVI} MTF_{SVI} MTF_{MIS} MTF_{DET} MTF_{PA}} \ . \tag{1.69}$$

Equation (1.69) must be evaluated at each spatial frequency. $\mathrm{MTF_{DET}}$ and $\mathrm{MTF_{PA}}$ use electrical frequencies that must be converted to spatial frequencies.

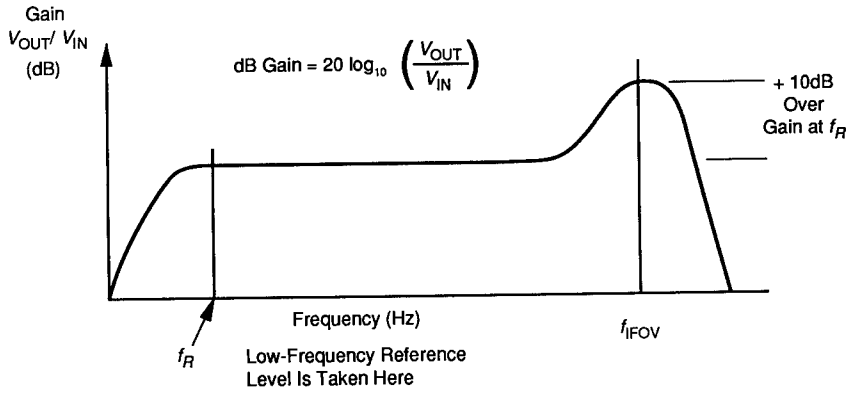

Fig. 1.46 Preamplifier response peaking near f_{IFOV}.

Receiver MTF is useful as a means of predicting performance when the LRU is procured separately.

1.5.1.10 Video Processor, MTF_{VP}. The video processor has several functions:

1. post amplification
2. automatic gain control (AGC)
3. automatic level control (ALC)
4. additional filtering and peaking near the IFOV frequency.

The MTF_{VP} is obtained from the plotted frequency response curve of the video processor in the same manner as for the preamplifier.

1.5.1.11 CRT Spot Size, MTF_{CRT}. In several airborne film recorders the film is exposed by a 12-channel CRT. Each of the spots is capable of being modulated or being cut off. Each spot is Gaussian in shape (see Fig. 1.47), so the modulation transfer function is given by

$$MTF_{CRT} = \exp(-2\pi^2\sigma^2 f^2) \ . \tag{1.70}$$

In Eq. (1.70), σ is the CRT spot width at the 50% intensity level in angular units:

$$\sigma = \frac{r_s}{[\ln(1/1 - p)]^{1/2}} \ , \tag{1.71}$$

where r_s is the radius of the circle containing the fraction p of the spot power. Since we want the 50% power width, $p = 0.5$ and

$$\sigma = \frac{r_s}{[\ln(1/1 - 0.5)]^{1/2}} = \frac{r_s}{(\ln 2)^{1/2}} = 0.85 r_s \ . \tag{1.72}$$

The spot radius r_s is measured using a scanning slit photometer or other suitable means. The following CRT setup parameters are varied to adjust the size of the array of spots and the individual spot size:

1. anode high voltage
2. grid potentials

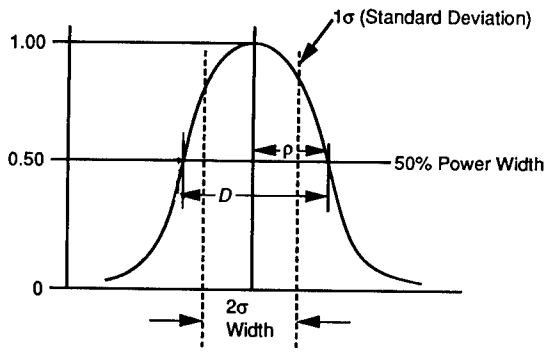

Fig. 1.47 Gaussian CRT spot.

3. focus coil current
4. astigmatism coil current.

Once r_s is known, σ can be computed by multiplying by 0.85, and since f_{IFOV} is equal to ½(IFOV), we can express f in angular units of radians. The recorder spot diameter can be adjusted to give, nominally,

$$D_s = 2r_s \approx 1 \text{ mil for 1 IFOV} ,$$

$$\sigma = 0.85r_s = \frac{0.85(\text{IFOV})}{2} = 0.425(\text{IFOV}) .$$

Substitution in Eq. (1.71) gives $MTF_{CRT} = 0.410$. When the CRT is carefully set up, a 0.9-mil spot width can be achieved giving $MTF_{CRT} = 0.486$. At lower spatial frequencies, MTF_{CRT} improves.

Spot measurements require care. Two different positions of the spot on the CRT screen are usually analyzed together with three different spot sizes. As the spot is scanned to the edge of the screen, electron-beam astigmatism causes the spot to grow from 0.9 mil at the center to 1.0 or 1.1 mil at the edges. Normalized units used in Gaussian MTF expressions must be mastered because the Gaussian MTF occurs for many components of the IRLS system.

1.5.1.12 Recorder Lens, MTF_{RL}. Some recorders use a relay lens to transfer the image from the CRT to the film. The MTF shown in Fig. 1.48 has a scale in line pairs per millimeter (cycles per millimeter) because this is common practice in optics. For IRLS calculations the frequency is converted to cycles per radian. The conversion requires that, in our example, the 1-mil CRT spot equals one IFOV. If the IFOV $= 0.25 \times 10^{-3}$ rad, then the CRT spot width of our example $D_s = (1 \times 10^{-3}$ in.)(25.4 mm/in.) $= 2.54 \times 10^{-2}$ mm corresponds to one IFOV of 0.25 mrad. The conversion factor is then

$$k = \frac{2.54 \times 10^{-2} \text{ mm}}{0.25 \times 10^{-3} \text{ rad}} = 1.016 \times 10^2 = 101.6 \text{ mm/rad} .$$

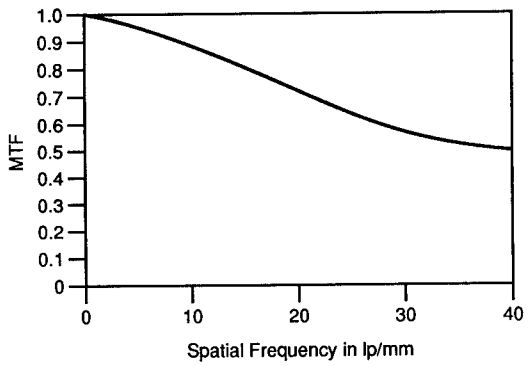

Fig. 1.48 MTF of example recorder relay lens.

The spatial frequency for IFOV = 0.25×10^{-3} rad is f = 2000 cycles/rad or 2 cycles/mrad, so

$$f_{\text{IFOV}} = 2000 \text{ cycles/rad} = \frac{2000}{k} = \frac{2000}{101.6} = 19.685 = 19.7 \text{ cycles/mm} .$$

A different film recorder has no relay lens. Film is transported directly across the CRT fiber optic faceplate. In this instance, MTF_{RL} must be replaced by MTF_{FO}. The MTF of the fiber optics faceplate is measured in the laboratory, either as the MTF of the faceplate alone, or as a part of the complete CRT including the spot MTF.

1.5.1.13 Film, MTF_F. The film used in most IRLS systems is aerial reconnaissance film. MTF_F is read from the manufacturer's curve except that the lowest spatial frequencies given are not used. Instead, the flat part of the MTF curve is extrapolated to the lowest frequencies. Again, line pairs per millimeter units must be converted to IRLS spatial frequency units of cycles/rad. Note that the published MTF data for the film apply only to the specified development. Other film development conditions require new MTF measurements.

1.5.1.14 Other Contributions to MTF. The example systems were used here purely for guidance in an MTF analysis. If the imagery data flow in other paths, the MTF analysis must branch to include each processing path. Possible alternate paths are

1. Data link to ground station with remote operation of film recorder (the same recorder LRU is used but the sync pulses and a *V/H* signal must be transmitted in the scan dead time);
2. Data link to ground station with remote operation of a digital tape recorder followed by replay to digital processor and frame grabber type display;
3. On-board analog tape recording with frame grabber and real-time cockpit CRT display;
4. Handover to reconnaissance management system (RMS) where MTF responsibility rests with the RMS manufacturer but the IRLS designer will still be judged by the quality of the end imagery. Great care is needed in specifying, measuring, and preserving the MTF and MRTD of the IRLS at all interfaces. The RMS and IRLS teams must work closely to preserve the inherent IRLS imagery MTF and general quality for the end viewer.

1.5.2 Along-Track MTF Analysis of IRLS Systems

Figure 1.45 gives the outline of the MTF analysis of the example IRLS in the ALT axis. Because dynamic scanning is absent, analysis in this dimension is considerably simpler than for ACT.

1.5.2.1 ALT Aperture Diffraction, MTF_D. Because the scanner samples in ALT and scans only in ACT there is no possibility for a simple electronic boost to compensate for MTF roll-off near the IFOV frequency. Thus, it is customary in split-aperture scanners to make the ALT aperture much larger than either

of the two ACT apertures. For example, the ALT aperture is set to 7.75 in. while the average of the two ACT apertures is 2.22 in. at nadir. The ALT aperture is constant during a scan and its diffraction MTF is higher than that of the ACT apertures.

1.5.2.2 ALT Film Magazine Servo Jitter, MTF_{FMJ}. Servo jitter is treated in the same way as ACT jitter or other ACT Gaussian effects. Other MTF contributors in the ALT axis may be treated in the same way:

1. detector sampling aperture, MTF_{DSA}
2. receiver random vibration, MTF_{RVI} (not as likely to occur in the ALT dimension because of mirror-mount design)
3. receiver sinusoidal vibration, MTF_{SVI}
4. misalignment of split-aperture optics, MTF_{MIS}
5. CRT spot size, MTF_{CRT}
6. recorder lens, MTF_{RL}.

The film transport moves the film at V/H rates. For low V/H values there is greater possibility of servo jitter from a variety of causes, such as bearing stiction, vibration, and motor cogging. The jitter should be measured in the laboratory at several low V/H values, and a Gaussian MTF should then be used to model the behavior with σ derived from the measured displacement data.

1.6 PERFORMANCE FIGURES OF MERIT

In Sec. 1.4.2 the NEN [Eq. (1.32)] and the NETD [Eqs. (1.35), (1.36), and (1.37)] have been noted as IRLS figures of merit that have their greatest utility as production quality control tools. They tell that the detectors are functioning properly within the operating optomechanical scanner and that the amplifiers are not too noisy. The NETD does not predict image quality or usefulness.

1.6.1 Objective MRTD

For assessing resolution in the image, the system MTF discussed in Sec. 1.5 is essential. By combining MTF and NETD we can obtain an objective measure, called objective MRTD, which is related to the subjective MRTD used with FLIRs. Subjective MRTD was developed for FLIR use by the US Army Center for Night Vision and Electro-Optics. Subjective MRTD is used in their static performance model for thermal imaging systems.[4] Unfortunately, there is no equivalent universally accepted definition of MRTD for IRLS use.[8] Even the MRTD formulations of the FLIR model have been modified by subsequent researchers, e.g., Ref. 9. Their goal was to improve agreement with test measurements in the low-frequency region and to improve modeling of the human eye response. A further complication is that the static performance model[4] is not easily adapted to IRLS use because the FLIR model assumes a round aperture and a TV-type scan frame rate that is identical to the TV display frame rate. This is not always true even for FLIR designs and is a problem when attempting to describe IRLS scan rates. The FLIR model also only treats CRT displays, while IRLS systems have the option of film display on a light table under more favorable viewing conditions. It is also necessary to formulate

an objective MRTD because a modern IRLS must now function with the following additional or auxiliary systems:

1. RMS (reconnaissance management systems)
2. target cuers
3. sensor-fusion image-processing systems at ground stations
4. real-time display systems on-board with frame grabbers or analog magnetic tape "ping-pong" buffer storage
5. narrow-band data links and data compression systems (these alter both the bandwidth and the dynamic range and influence the distribution and phase of spatial-frequency components of the image)
6. correlation or map-matching systems for guidance and navigation.

Instead of concerning ourselves only with subjective performance of a human observer in viewing a CRT monitor, we must now also consider objective IRLS performance and interface specifications for these newer systems. The shortcomings of the FLIR model discussed here are relevant only when the model is applied to IRLS systems where the model was not intended for use. The great pace of development in digital image processing and artificial intelligence technology now requires the new IRLS objective MRTD as an accepted figure of merit. The human eye response and the subjective MRTD can be used, provided objective and subjective MRTD measures can be correlated and validated by both laboratory and field measurements.

There has been an unfortunate tendency to try to use subjective MRTD as an acceptance criterion for 100% of FLIR production systems. This is a very costly, time-consuming, and unreliable practice because the final decision to accept each FLIR system rests on the subjective judgment of a so-called standard observer under standard viewing conditions. The MRTD test is somewhat difficult to perform and human observers vary in their performance from day to day and even within the same day. An observer's skill and familiarity play important roles in performance, but each of these cannot be modeled with any precision. For IRLS testing, the custom with some IRLS programs has been to accept receivers or scanner LRUs based on separate NETD measurements and separate receiver MTF measurements. The acceptance procedure for the complete IRLS system adds, as a minimum, the following to the receiver tests:

1. thermal resolution on film (or equivalent test for tape)
2. uniformity and image quality
   a. distortions
   b. striations (film)
   c. uniformity of density and density control (film)
3. *V/H* following ability
4. MTF on film or tape. IR targets are viewed while scanning and modulation is measured on developed film (or tape) with a scanning microdensitometer (for film) at various spatial frequencies.

If the IRLS system includes other features, such as tape recorders or real-time displays, these are separately tested during acceptance. Development and compatibility tests establish their performance with a complete IRLS system prior to any production. Recent opinion is that both subjective and objective MRTD have their uses for IRLS testing. Several cautions are worth heeding before designing an IRLS test program, however.

Elaborate noise filtering is not needed for IRLS MTF measurements because multiple passes of the scan across a fixed laboratory target can be viewed on an oscilloscope. This allows visual averaging of the multiply viewed signal during MTF measurements where peak-to-peak voltage is to be measured. Several bar targets of different spatial frequencies are used and the MTF plotted. In many IRLS designs the ac zero level is clamped to the housing radiance level once each scan. The ac gain is set by viewing the narcissus cold spike and comparing its signal to that of the housing once each scan. The housing is considered to be a blackbody at a nominal 300 K temperature, but it is not important to know the temperature exactly. It is sufficient to know that it cannot rapidly change. Low-frequency noise is thus filtered by the IRLS system during the MTF measurement.

A separate MRTD formulation and test procedure are needed when IRLS MRTD is to be measured on film using a human observer and a light table as the display device. There will be no frame rate and, hence, the FLIR model is not applicable unless it is modified. With the more favorable film viewing conditions it is expected that MRTD will be better than with a CRT display. Also, MRTD on film with IRLS systems using overlap writing will vary with the number of exposure overlaps (there can be up to a 2× improvement in NETD when three overlaps are used at certain *V/H* values). In such systems the MRTD test would become elaborate. Several *V/H* settings would be needed for each FOV mode, and several different target spatial frequencies would be required. Because MTF varies with scan angle, the test would also require a set of different scan angles and much data would be collected.

The MRTD formulation for CRT viewing of IRLS imagery could be closer to the FLIR model, provided it is modified to IRLS needs.

1.6.2 Objective MRTD Formulation for IRLS Use

Several formulations have been recommended and used for objective MRTD. These can be compared with the FLIR model MRTD equation given by Ratches[4,5] (also see Hepfer[9]):

$$\text{MRTD}\,(f_0) = (0.66)(\text{SNR})(f_0)\frac{\text{NETD}}{\text{MTF}_{\text{SYS}}(f_0)} \times \left(\frac{4}{\pi}\frac{\Delta x \Delta y}{\eta_{\text{OVS}} F_R t_e}\right)^{1/2}\left[4f_0^2(\Delta x)^2 + 1\right]^{-1/4}, \tag{1.73}$$

where η_{OVS} is the overscan ratio, F_R is the frame rate, and t_e is the eye integration time. The last term is usually taken to be unity for most values of spatial frequency f_0. This gives, for $\Delta x = \Delta y = \alpha_D$,

$$\text{MRTD}\,(f_0) = (0.66)(\text{SNR})(f_0)\frac{\text{NETD}}{\text{MTF}_{\text{SYS}}(f_0)}\left(\frac{2}{\pi^{1/2}}\right)\frac{\alpha_D}{(\eta_{\text{OVS}} F_R t_e)^{1/2}}. \tag{1.74}$$

The signal-to-noise ratio recommended by Ratches et al.[4] is SNR = 2.25. For the human eye integration time, $t_e = 0.25$ s is most often used. Equation (1.74)

for an overscan ratio of unity and a frame rate of 30 frames/s then becomes (for $\eta_{OVS} = 1, F_R = 30/\text{s}, t_e = 0.25$ s)

$$\text{MRTD}(f_0) = 0.684\alpha_D f_0 \frac{\text{NETD}}{\text{MTF}_{SYS}(f_0)} , \tag{1.75}$$

where $\alpha_D = \omega_x = \omega_y$ = IFOV, the detector angular subtense in radians, and f_0 is the spatial frequency in cycles per radian.

Recent IRLS systems have used the following formulation of objective MRTD:

$$\text{MRTD}(f_0) = \frac{\pi}{4\sqrt{7}}(\text{SNR})\frac{2\alpha_D f_0}{\sqrt{\eta_{OVS}}} \frac{\text{NETD}}{\text{MTF}_{SYS}(f_0)} , \tag{1.76}$$

where SNR = 2.25 for 50% probability of recognition of vehicle targets. The overscan ratio is taken to be unity for the IRLS. Substituting SNR = 2.25 and overscan ratio of 1 in this objective MRTD equation gives

$$\text{MRTD}_{OBJ} = 1.336\alpha_D f_0 \frac{\text{NETD}}{\text{MTF}_{SYS}(f_0)} \quad \text{(K)} , \tag{1.77}$$

where all parameters are as previously defined. This formulation [Eq. (1.77)] has been used in IRLS testing and acceptance by measuring the MRTD at the output of the receiver LRU prior to any recording and further data processing or display. The MTF of all further processing has been modeled. Appropriate testing is performed on these subsystems separately. To tie objective and subjective MRTD together, validation tests and human eye modeling are needed.

The objective MRTD measure, Eq. (1.77), has been found useful in acceptance testing of IRLS systems and in performance testing at remote sites, such as after installation on the aircraft. Up to the time of this writing, universal agreement has not been achieved in the IR community on an objective MRTD formulation. A series of validation tests would be more expensive than those done with FLIRs because aircraft flights would have to be included and weather is a variable.

1.7 DETECTORS, ARRAYS, DEWARS, AND CRYOGENIC COOLING

Presently deployed IRLS systems chiefly use photoconductive (PC) detectors. Sections 1.2 and 1.3 have discussed some of the uses of PC arrays in IRLS systems. Development of PC HgCdTe SPRITE detectors in Great Britain has led to their use in a family of compact IRLS systems. The PC materials most often used are HgCdTe and InSb, although doped Ge and other detector materials have been used for special purposes, such as longer-wavelength IR radiometry.

1.7.1 Photovoltaic Arrays

Developments in detector array technology raise the possibility of using photovoltaic (PV) detectors in large arrays. As previously noted, the PV detectors have a $\sqrt{2}$ advantage in D^*, which is difficult to realize in practical systems

because of the higher impedance of PV cells. PC cells are noisier but their lower impedance makes it easier to couple the signal to a practical preamplifier. Typical PC HgCdTe detectors have cell impedances as low as 50 Ω, while a PV cell impedance can be hundreds or even thousands of ohms. If the charge from the PV effect can be temporarily stored in a capacitive-type cell that is periodically coupled to a readout preamplifier, the storage device can act as a miniature impedance transformer. Readout arrays of several types, such as a CCD or a CID or various forms of MOSFET array switches have now been applied to PV arrays. In the near-IR band, platinum silicide arrays with silicon readout arrays have provided impressive performance. A large PV array allows the scanner to be operated at a slower scan rate because the required ALT coverage Φ_{ALT} can be achieved even at high V/H values by adding more detectors to the array in the ALT direction. The complexity of extra bias and preamplifiers is minimized by the readout multiplexer (of whatever type). When smaller IRLS scanners are needed for RPVs and pods, these techniques may be used. The lower signal from the smaller aperture is compensated for by the slower scan (longer dwell per IFOV) and by using more detectors per scan. This can be seen in the scan rate equation:

$$N_{sc} = \frac{V/H}{n(IFOV)} \quad \text{scans/s} \ . \tag{1.78}$$

Using n ALT detectors causes increased off-axis aberrations, especially coma. These aberrations can be partially corrected in the scanner optical design. Coma can be roughly estimated in the round-aperture axehead scanners where these large PV arrays might be used. Coma angular diameter d_c is approximately

$$d_c \approx \frac{0.1875u}{(f/\#)^2} \quad \text{rad} \ , \tag{1.79}$$

where u is the field angle between the chief ray to the point of interest in the focal plane and the optical axis and $f/\#$ is the focal length divided by the aperture diameter. Another trade-off results from the defocus effect. The motivation for the extra detectors in the ALT dimension is to keep up with high V/H values in low-altitude operation. The defocus effect prevents any realization of detector-sized resolution when the detectors are sized for the longer slant ranges, as discussed in Secs. 1.2 and 1.3. Their inherent resolution can only be achieved at large scan angles. Falloff of ALT optical resolution as the off-axis angle increases then becomes less of a problem and practical solutions exist. As the scan angle increases from nadir, the outer detectors can be dropped and the center detectors used, as shown in Fig. 1.37.

1.7.2 Detector Dewars

The IR detector/dewar assembly is a costly and important component of any IRLS. Most IRLS dewars are end-looking designs that accept a cold finger from a split-Sterling cryogenic refrigerator. Integral refrigerators are more rugged and several successful designs have been made. Microphonics or IRLS shape restrictions may prohibit their use because they must fit directly on the dewar.

A detector array is fabricated from a slab of semiconductor material called a chip or a clip. Evaporated leads are attached. These must run down the cold well of the dewar to an array of metal leads penetrating the dewar glass via Kovar glass-to-metal seals and ultimately to a connector. Because these leads conduct heat they are a significant contributor to the static heat load of the dewar. The other important heat-load contributors are glass conduction and the static load from all sources. In PC arrays there is the dynamic load of the bias and the incoming signal radiation. PC bias dissipation is significant and is an IRLS design trade-off item. High bias gives more signal but adds to electrical noise and to the dynamic thermal load on the dewar.

The IRLS system engineer, the preamplifier designer, the dewar designer, and the detector array engineer must work closely together to optimize the total array design for minimum thermal load and noise. Cryo-refrigerators are made in various capacities, such as 1/4, 1/2, and 1 W. In most IRLS installations where size, weight, and electrical power are to be minimized, it is undesirable to use a larger cooler than necessary. This can motivate use of PV detectors for large arrays because a PC detector array would have a large bias dissipation and more leads through the glass. Biasing of PC detectors is discussed further in Sec. 1.7.3.

A dewar window of IR-transmitting material (such as Ge or BaF) is attached to the glass by the manufacturer. The window is given an AR coating and an outer protective coating. The array is usually AR coated to improve photon capture in *f*/1 optical systems. Dewar designs have been improved recently to eliminate materials that deteriorate at high storage temperatures. Long shelf lifetimes and high storage and shipping temperatures have become requirements in most procurements.

The detector array is fitted with a metal cold shield to limit, insofar as is practical, the field of view of the detector to only those rays coming off the final focusing element, i.e., the parabolic mirror in most IRLS scanners. Details of cold-shield design are discussed in Sec. 1.7.4.

1.7.3 Biasing of Photoconductors

Each PC detector requires a bias source of current that is modulated by the photoconductivity. Each cell has an impedance and a responsivity R_λ (in volts per watt per micrometer of wavelength):

$$R_\lambda = \frac{V_s}{P_\lambda} = \frac{V_s}{W_\lambda \Delta_d} \quad (\mathrm{V\ W^{-1}\ \mu m^{-1}}) \ , \tag{1.80}$$

where

P_λ = rms signal power per unit wavelength incident on the detector
V_s = rms signal voltage
W_λ = spectral irradiance (in $\mathrm{W\ cm^{-2}\ \mu m^{-1}}$)
A_d = detector area in square centimeters.

Spectral responsivity can be integrated across the spectral band of interest to get the in-band responsivity:

$$R = \frac{V_s}{(WA_d)} \ . \tag{1.81}$$

The bias circuit for a photoconductor may be represented as shown in Fig. 1.49. The signal voltage V_s is simply $V_s = I_b \delta r_c$, where $I_b = V_b/(r_c + r_L)$, r_c is the photoresistance, and r_L is the load resistance in Fig. 1.49. The load resistor is usually chosen to be much larger than the detector impedance (which for PC HgCdTe is approximately 50 Ω) so that r_L may be 2000 Ω. When $r_L \gg r_c$, the detector is operating essentially at constant bias, where

$$I_b \approx \frac{V_b}{r_L} \ . \tag{1.82}$$

For estimates of signal, one solves Eq. (1.80) or (1.81) for V_s. Using in-band values,

$$V_s = RWA_d \ , \tag{1.83}$$

where R is given by the detector manufacturer for the band of interest. If a spectral plot of R_λ is given, then

$$V_s = \int_{\lambda_1}^{\lambda_2} R_\lambda W_\lambda A_d \, d\lambda \ , \tag{1.84}$$

where W_λ is obtained from computer solution using appropriate blackbody programs. The value of signal voltage for various scene temperature changes can be computed if the emissivity of scene objects is known or assumed to be unity. The expected range of signal voltage is needed for the preamplifier design.

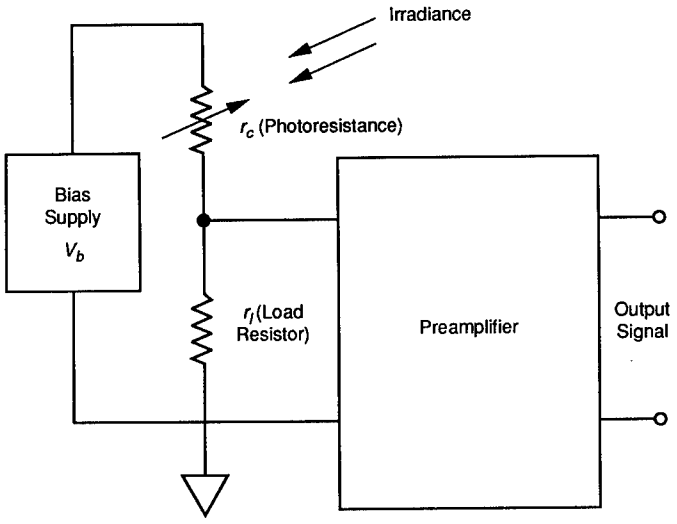

Fig. 1.49 Biasing a photoconductive IR detector.

1.7.4 Cold-Shield Design

The dewar includes a cold shield to limit the acceptance angle of a detector array in each dimension. The ideal cold shield would allow passage of all signal rays and would block all unwanted rays from creating an interfering background. An ideal optical design would place a pupil near the focal plane so that a cold shield placed at the pupil would limit incoming rays to the optical path and block all other rays. An ideal cold shield can be approached for a small single-cell detector but cannot be achieved for a large linear or two-dimensional array. In most IRLS designs the final optical element is the parabolic mirror. This mirror is often rectangular in shape, being wider in the ALT direction. The cold shield must therefore accept all rays from the rectangular aperture footprint on the parabolic mirror and allow them to come to a focus on the detectors. The individual detectors of a typical airborne IRLS are disposed as shown in Fig. 1.50. The larger wide-mode array dominates the required cold-shield angle, as shown in Figs. 1.50 and 1.51. In cases where two different array sizes are used in the same focal plane, there is no need for a symmetrical aperture. Shapes such as that of Fig. 1.51 are more efficient. Detector performance is estimated by integrating the background flux Q_B falling on any given detector using x and y coordinates derived from the detector layout drawing (Fig. 1.50). The value of Q_B is then inserted in

$$D^*_{\text{PK\_BLIP}} = \left(\frac{\lambda_{co}}{2hc}\right) Q_B^{-1/2} , \tag{1.85}$$

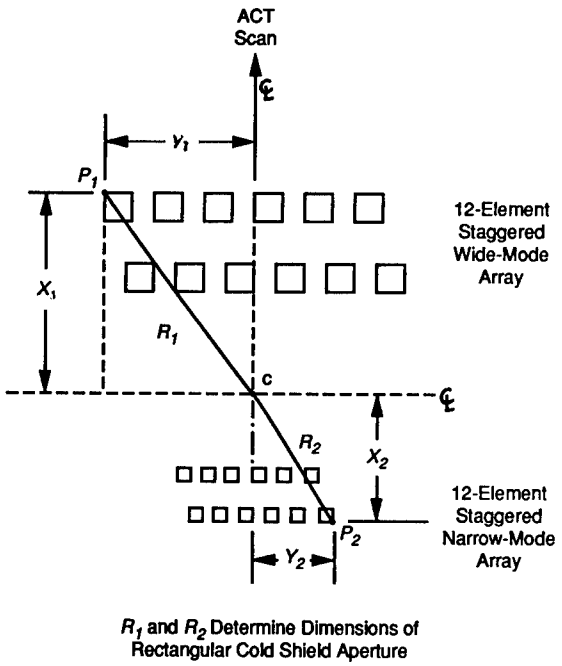

Fig. 1.50 Dual-array focal-plane layout as an example of cold-shield sizing.

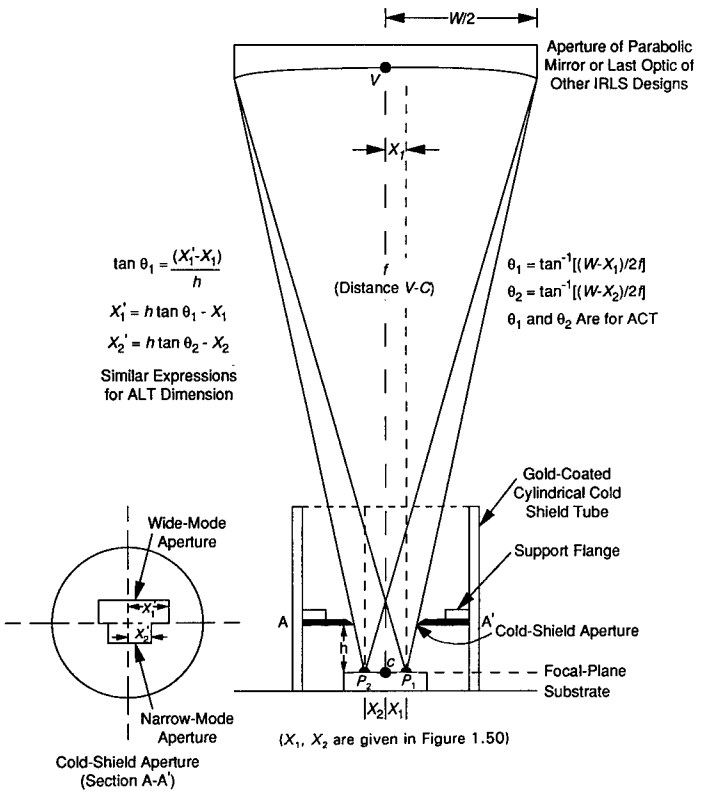

Fig. 1.51 Cold-shield design example for ACT dimension.

where

$D^*_{PK\_BLIP}$ = background-limited peak detectivity (cm $Hz^{1/2}$ W^{-1})
λ_{co} = cutoff wavelength at 50% response in micrometers
h = Planck's constant
c = velocity of light
Q_B = background photon flux on detector area A_d in photons per second.

1.7.5 IR Detector/Dewar Assembly Tests

The IR detector/dewar assembly should be given a carefully written specification that, as a minimum, should include the following tests:

1. D^*_λ on each cell
2. R_λ on each cell
3. impedance on each cell
4. time constant or frequency response on each cell
5. cuton and cutoff wavelengths for each cell
6. biasing and choice of select bias resistors
7. array geometry

8. array uniformity (be careful not to overspecify)
9. spot scans of cell response as required.

These tests are self-explanatory except for the last three. Array geometry is determined both by microscopic visual inspections and by infrared spot scans to assure correct geometry of IR response. The array uniformity test assures that D^*_λ, τ, and R_λ do not deviate beyond the specified limits from the required average or absolute values. It is very important in writing the detector specifications to avoid any overspecification. One can specify for D^* and τ and take whatever responsivity and impedance results, but beware of attempting to put tight controls on both uniformity of D^* and uniformity of responsivity in the same array. The production yield could go to zero or to unacceptable levels. Cost follows yield inversely.

1.7.6 Cryogenic Cooling

Almost all IRLS systems use mechanical cryogenic refrigerators. These fall into four types:

1. Gifford-McMahon (nitrogen cycle)
2. split-Stirling (helium cycle)
3. integral Stirling (helium cycle)
4. Vuilleumier (helium cycle).

The split-Stirling types are the most popular and the split feature allows the cooling head to be separate from the compressor. This helps with packaging and minimizes microphonics in the dewar. Care must be taken to isolate the cold head from the dewar so that mechanical vibrations will not couple to the detector. Microphonics can arise from the following mechanisms:

1. detector lead bending, causing variations in interlead capacitance
2. detector substrate flexure, causing changes in cell photoconductivity
3. changes in contact resistance between the detector and its leads
4. Nitrogen boiling at the end of the cold finger (or pressure waves in Stirling refrigerators), which impact the metal end of the cold finger. This causes changes in detector operating temperature, which alters detector responsivity.

Various proprietary means are used to minimize detector mechanical noise.

The desired operating temperature of the IRLS detector is achieved by balancing the cooling rate with the passive and active thermal loads on the detector/dewar assembly. In some instances, where the cooler has excess cooling capacity, it has been found useful to employ a focal-plane heater to servo-control detector temperature. In such cases there is an auxiliary resistor for temperature-monitoring placed in the dewar. Some designs mount a FLIR minicooler directly on the receiver near the detector/dewar to keep the capillary tube connection between the compressor and the cold head short. The cryogenic refrigerator requires more maintenance and has the shortest MTBF of any unit in the IRLS. Proper getter design preserves the vacuum and gives the IR detector/dewar a long lifetime either in storage or in use.

1.8 SIGNAL PROCESSING AND IMAGE PREPARATION

CRT monitors and television technology are convenient to use and are found both in the cockpit and at ground stations. The nearly instantaneous transmission of frames of reconnaissance imagery to multiple viewing stations is so convenient that the limitations of the CRT as a display medium for IRLS imagery must be accepted. System engineers must find ways to overcome frame limitations so that the tremendous information-gathering capability of the IRLS sensor can be matched to the restricted format of the CRT. A good CRT monitor may be capable of displaying 1000 TV lines horizontal, which is equivalent to 1000 pixels of IRLS imagery. A typical IRLS provides more than 4000 pixels per line with its 12-channel maximum instantaneous data rate of 15.2 MHz. CRT monitors and video recorders can handle approximately 3 MHz in frames of no more than 1000 lines horizontal by 750 lines vertical. In terms of TV frames, a strip section of imagery that covers 750 lines in the ALT direction will require at least

$$N_f = \frac{4000}{1000} = 4 \text{ TV frames side-by-side} .$$

If the TV monitor is only capable of 600 TV lines horizontal, the IRLS would require even more TV frames side-by-side to show a complete section of its imagery. Several strategies have been used by systems engineers to overcome this mismatch in data rate and display format. These have been applied both for airborne and ground-station viewing and are as follows:

1. Video tape recording of incoming imagery using two tape recorders in a "ping-pong" alternation so that frames can be manipulated and viewed while new imagery is being taken without interruption. With this method the user can scroll through recently recorded imagery frames while new data are still being taken. The RAF TORNADO uses a similar system.
2. Systems such as No. 1 that also include a high-density digital tape recorder (HDDTR) as an archival storage medium available to the ground station when required. A data link can be used after data collection while the aircraft is leaving the target area on its exit run. The archival recorder could be film but the trend is away from wet-processed film for the logistic reasons already given.
3. On-board thermal development of dry silver film. Near-real-time viewing is possible with a TV camera pickup system as the developed film is leaving the developer. An operator can view selected pieces of stored imagery by unwinding and scrolling the stored film without interrupting the collection and recording of new imagery. Because the IRLS imagery format is much wider than that of the TV camera, as previously noted, the TV pickup camera must be traversed across the film in the ACT dimension. Scrolling the film gives the other dimension of image scanning.
4. IRLS systems such as No. 1 that have near-real-time viewing and that also provide wet-processed archival film.

5. Data links may be used for remote operation of IRLS film recorders, tape recorders, and real-time display systems. Several IRLS systems have been used with data links while the film recorder operated remotely at a ground station. Other more complex recorders have recorded IRLS data at a ground station using a data link.
6. Data compression has been proposed to reduce the bandwidth requirements for IRLS data links but has not been pursued to the point of flight trials. Laboratory simulation of IRLS imagery data compression on image processing computers has shown that compression of the data is practical and that no apparent information is lost. The low-altitude missions at the highest *V/H* rates have sufficient defocus that the true information content of the scene is not represented by the high-altitude data rate in terms of a constant angular resolution. Therefore, because the aircraft is closer to the ground, the footprint is adequate to meet the desired NIIRS category but the true information rate is less. The compression can be achieved without changing the NIIRS category. Equations (1.14) and (1.15) show that these wide-FOV, low-altitude missions produce fewer recordable pixels per scan because of the constant-footprint processing used in both ALT and ACT axes. Constant-footprint processing resembles data compression but the defocus effect acts to prevent high resolution in the central part of the scan while at the scan edges the full high resolution is needed. The compression algorithms therefore must be applied judiciously.

1.8.1 Data-Compression Experiments with IRLS Imagery

Data-compression experiments have been performed on recorded IRLS and FLIR imagery in an image-processing laboratory. Various data-compression schemes applied to the imagery were evaluated on a CRT monitor. Most data compression involves digitization of the raw video signals followed by compression of the dynamic range. Most of the compression was applied to the middle band of spatial frequencies. Usually, this compression of dynamic range is combined with some form of differential pulse code modulation (DPCM). In these experiments compression ratios between 2:1 and 2.5:1 were shown to have no discernible effect on the displayed imagery at the CRT. Table 1.18 gives some guidelines for compression of IRLS imagery data so that no significant reconnaissance information is lost. Table 1.19 lists some data-compression

Table 1.18 General Guidelines for IRLS Data Compression

1. Combine all redundantly sampled pixels or channels prior to any data compression. If SNR is adequate, drop any redundant pixels.
2. Choose a data-compression method or algorithm that preserves the amplitude and phase of the higher spatial frequencies of the scene.
3. Compress the dynamic range of the low-spatial frequencies a mild amount.
4. Compress the dynamic range and amplitude of the middle band of spatial frequencies without significantly disturbing their phase.
5. Do not be too ambitious. Try only for a data-compression ratio between 2:1 and 3:1. More than this may cause significant loss of scene information.

Table 1.19 Some Useful Data-Compression Methods

1. Pulse code modulation (PCM)
2. Differential pulse code modulation (DPCM)
3. Predictive coding (e.g., Huffman coding)
4. Transform coding (e.g., cosine transform)
5. Hybrid forms
a. DPCM plus Huffman coding
b. Transform plus predictive coding

methods applicable to IRLS use. Predictive coding could be applied to the problem of imaging ships against a calm ocean background. In such cases the IRLS is operating at maximum gain because the AGC uses video detail to decrease the gain. Once a ship is sensed, the gain needs to be reduced in the vicinity of the ship so that its deck and superstructure detail will be seen. This is related to dynamic range compression. In a multielement array an early detector signal could be used to sense the ship and then reduce the gain. This early "look-ahead" detector would be placed off-axis in the ACT direction to give the AGC circuits time to respond.

There is an extensive and lively literature related to image processing and data compression (see Refs. 10 and 11). IRLS imagery is preferably compressed prior to recording, transmission, and display. Compression prior to interfacing with any RMS can help to simplify the interface between IRLS and RMS.

1.9 FUTURE TRENDS AND LIFETIME OF DEPLOYED SYSTEMS

Well-maintained IRLS systems have long useful lifetimes, especially if system upgrades are used to improve performance. Upgrade examples are

1. higher *V/H* capability
2. replacement of older cryogenic cooler designs with those easier to maintain and having higher MTBF
3. resurfacing and recoating of exposed optics with more resistant coatings, especially windows and spin mirrors
4. replacement of IR detector arrays with higher performance designs
5. replacement of separate spin-mirror encoder and shaft coupling with an encoder disk mounted directly on the spin-mirror shaft or replacement of the encoder by an electro-optical synchronization assembly that operates from the spin-mirror facet reflections
6. improvements on AGC and ALC circuits to improve imaging of ships against open ocean backgrounds
7. data compression, including dynamic range control
8. addition of automatic target cueing (ATC) to any existing real-time display subsystem (RTD plus ATC). For IRLS systems interfacing with a reconnaissance management system, the ATC cues could be part of the video signal sent to the RMS. Alternatively, the ATC could be a part of the RMS. An ATC subsystem also can have Nos. 6 and 7 included.

1.9.1 General Improvements

IRLS designs for RPV installations can benefit from the use of composite structural materials. Structural innovations that reduce size, weight, or cost would be welcome. Use of honeycomb or foamed aluminum backs for IRLS mirrors is an example. Diamond machining has been shown to be feasible on composite aluminum/foamed-aluminum mirrors. Adhesive joining and filament-wound reinforced plastics for scanner structures is another example, but changes in dimensions from humidity are a concern.

With appropriate upgrades and good maintenance it is expected that the deployed and soon-to-be-deployed IRLS and RMS systems will be used well beyond the year 2000. There will be opportunities for new IRLS designs that solve special problems, including the ever-present problems of minimizing IRLS size/shape and weight, reducing electrical power consumption, and minimizing the initial cost as well as the cost of ownership.

IRLS systems have been installed in high- and low-flying RPVs both with and without windows. Also, there have been installations in small-diameter pods hung beneath manned aircraft to convert fighter/bombers for reconnaissance or for combined strike/reconnaissance. There is a trend to the use of RMS systems on manned reconnaissance aircraft and an interest in automatic target cueing, as discussed in Sec. 1.9.2.

An IRLS in long-range military aircraft, such as a bomber or a patrol aircraft, can be used at night to update the drift of the inertial navigation system by recognition and location of known check points along the flight path. The similar use of IRLS systems for guidance of autonomous homing vehicles has been noted in Sec. 1.1.4.4.

1.9.2 Automatic Target Cueing (ATC)

There is a great need to reduce the task load of the on-board observer of a two-seat reconnaissance mission by using ATC and other automated aids. In one-man reconnaissance missions this need is self-evident. The pilot is too busy to allow any detailed inspection of IRLS imagery on a cockpit CRT display. ATC from IRLS imagery expedites the target location process. The danger in any such automated system is that some valid targets could be overlooked if the ATC is too simplistic or if wrong target signatures are used in the ATC decision. If, however, the decision threshold is set too low, the false alarm rate becomes unacceptably high. If the decision criteria are strengthened to where only a few targets will be missed yet the false alarm rate is acceptable, the ATC becomes complex and costly. The trade-off between probability of detection and false alarms is difficult and complicated. For example, in a section of IRLS imagery there may be three tank images: (1) yesterday's burned out tank, (2) an inactive but lethal tank that is deliberately powered down, or (3) an active, powered-up tank. The task of automatically discriminating between case (1) and case (2) is difficult, but the active tank can be picked out by the heat from its exhaust or from its hot gun barrel (if firing). Some IRLS designs include a hot-spot detector as a form of target cuer. Whenever a hot target is detected in the video, an LED is illuminated that exposes a triangular mark in the film margin. This works well for the rare isolated hot-spot targets but in urban or industrial areas the hot-spot indicator triggers too frequently. A

Table 1.20 Possible Target Signatures

1. Radiance contrast against average scene radiance
2. Rate of change of radiance contrast
3. Size of object exhibiting radiance contrast
4. Spatial frequencies of object exhibiting radiance contrast (high-frequency edges, etc.)
5. Very hot spot located on target object (smokestacks, vents, vehicle exhaust pipes, gun barrels, etc.)
6. Association of candidate target with nearby candidate targets in a target cluster (missile launch sites, AA batteries, etc.)
7. Correlation with a stored library of known target shapes (very important for ship targets on the open ocean)

more sophisticated decision process using other target signatures beyond simple radiance contrast is required. Table 1.20 lists some possible target signatures to aid the decision process.

Figure 1.52 shows how one form of ATC can aid in locating targets in wide-FOV IRLS imagery generated by low-altitude penetration reconnaissance missions. The advent of very-high-speed integrated-circuit (VHSIC) technology and the availability of large RAM chips makes such an ATC practical and very compact. Some designs of IRLS are provided with a real-time display (RTD)

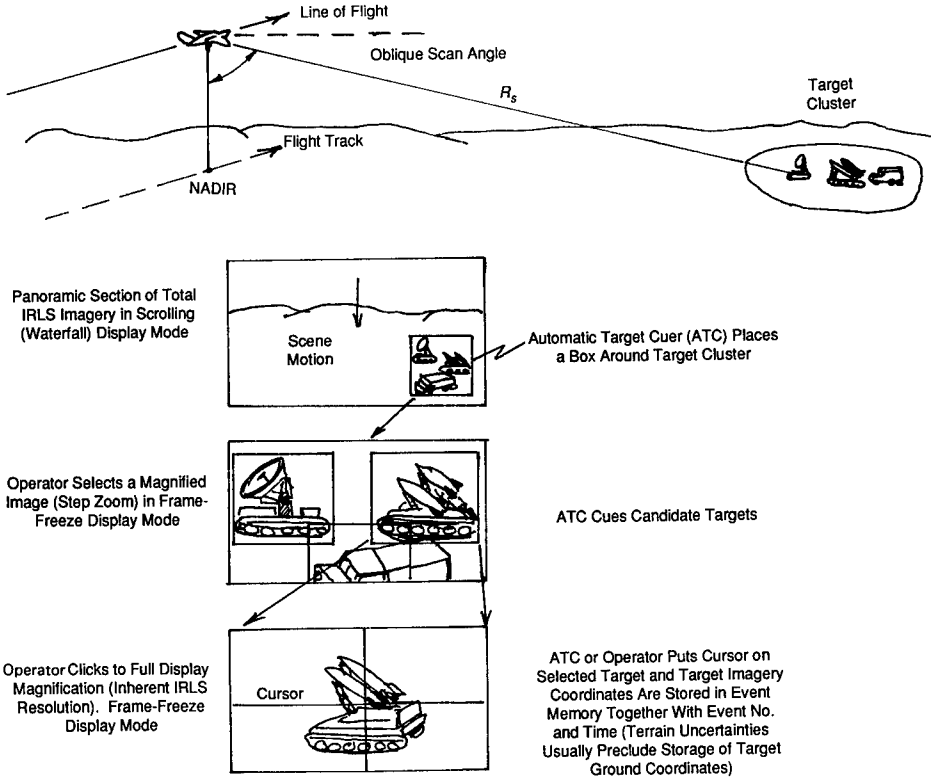

Fig. 1.52 IRLS with real-time display and automatic target cueing.

that allows frames to be selected from panoramic IRLS imagery for further step-zoom display magnification using an operator-controlled pistol grip. ATC algorithms and circuits have been separately developed and laboratory tested but as yet have not been flight demonstrated. Those manufacturers developing RMS systems will also be able to include ATC without extensive development. Best ATC performance occurs when the operator has the final decision responsibility. The task load of sifting through the full IRLS imagery strip map has been greatly reduced by the ATC, but the human operator is left in full control and can study previous frames when necessary. A scrolling waterfall display is very difficult to follow for more than a few minutes. Combat experience has shown that perfectly viewable targets have been missed by operators in flight, yet they immediately detect them on playback of the tape recorder during ground-station debriefing. The ATC subsystem prevents such omissions if its threshold is set low enough to include a few false alarms. In RPV missions, and some fully automated manned missions, imagery can be relayed and played back at the ground station where the target cuer can operate in the same manner as in the airborne example discussed here. In an ATC subsystem, automatically cued candidate target images have their image locations stored in an event-time memory with each candidate numbered to allow rapid access without the need to scroll through the entire tape or film record. Once the candidate target or target cluster is located and the surrounding imagery is brought up on the CRT display, the step-zoom display magnification feature can be used to allow detailed examination. The display magnification does not provide any new information but it effectively matches IRLS resolution to that of the display CRT. Other sensors can be used to enhance the knowledge concerning a given candidate target. Synergism is the intent of the RMS and sensor-fusion efforts are underway in the airborne reconnaissance community. Certain sensors work well with the IRLS on low-level missions. Among these are

1. side-looking radar
2. emitter locators
3. laser rangefinders and laser designators
4. laser three-dimensional active imagers
5. Radar altimeters and laser altimeters
6. E-O imaging sensors (daylight hours mostly)
7. FLIRs for side looks near the two horizons and oblique viewing.

A FLIR combined with an IRLS allows a higher resolution view of a candidate target detected by the IRLS if the FLIR frame is recorded and available. The RAF TORNADO reconnaissance aircraft uses a pair of FLIR-type side-looking IR (SLIR) sensors in this manner. With such a system, the ATC plus IRLS illustrated in Fig. 1.52 would be even more effective. More exotic SLIR sensors have been studied and proposed using focal-plane-array technology with PV detectors and multiplexed readouts. These SLIR sensors could be used to supplement the IRLS zone of coverage from scan angles of ± 75 deg to ± 90 deg (both horizons). In these two zones the IRLS has its poorest signal-to-noise ratio. The higher magnification SLIRs with their limited FOV but much better MRTD would offer a big advantage. The SLIR could use a simple nodding mirror scan to overcome the wide variation in V/R in the SLIR operation zones near the horizons.

References

1. H. V. Kennedy, Texas Instruments, U.S. Patent No. 3,211,046 (1965).
2. L. B. Harkless, W. L. McCracken, and J. A. Colosimo, Honeywell Radiation Center, U.S. Patent No. 4,527,055 (1985).
3. J. Johnson and W. R. Lawson, "Performance modeling methods and problems," in *Proceedings of the IRIS Specialty Group on Imaging* (1974) (Classified Confidential).
4. J. A. Ratches, W. R. Lawson, L. P. Obert, R. G. Bergemann, T. W. Cassidy, and J. M. Swenson, "Night vision laboratory static performance model for thermal viewing systems," Army Electronics Command, Fort Monmouth, NJ (1975). (This useful document is available as AD-AO11 212 from National Technical Information Service, U.S. Department of Commerce.)
5. J. A. Ratches, "Static performance model for thermal imaging systems," *Optical Engineering* **15**(6), 525–530 (1976).
6. W. E. Westell, private communication (1985).
7. F. A. Rosell and R. H. Wilson, "Performance synthesis of electro-optical sensors," AFAL-TR-74-104, Air Force Avionics Laboratory, WPAFB, OH (1974).
8. G. M. Cuthbertson, L. G. Shadrake, and N. J. Short, "A technique for the objective measurement of MRTD," *Proceedings of the SPIE* **590,** 179–192 (1985).
9. K. C. Hepfer, "A new TIS technical performance model," in *Proceedings of the IRIS Specialty Group on Infrared Imaging,* NASA Ames Research Center, Moffett Field, CA, December 2–3, 1981.
10. R. C. Gonzalez and P. Wintz, *Digital Image Processing,* Addison-Wesley, Reading, MA (1977).
11. K.-H. Tzou and H.-M. Hang, Guest Eds., *Optical Engineering,* Special Issue on Visual Communications and Image Processing III, **30**(7) (July 1991).

Bibliography

Born, M., and E. Wolf, *Principles of Optics,* Pergamon Press, Elmsford, NY (1959).

Hudson, R. D., Jr., *Infrared Systems Engineering,* John Wiley & Sons, New York (1969).

Jamieson, J. H., R. H. McFee, G. N. Plass, R. T. Grube, and R. G. Richards, *Infrared Physics and Engineering,* McGraw-Hill, New York (1963).

Jenkins, F. A., and H. E. White, *Fundamentals of Optics,* McGraw-Hill, New York (1957).

Levi, L., *Applied Optics,* John Wiley & Sons, New York (1968).

Lloyd, M., *Thermal Imaging Systems,* Plenum Press, New York (1985).

Mechtly, E. A., "The international system of units, physical constants and conversion factors," 2nd revision, NASA SP-7012, NASA, Washington, DC (1973).

CHAPTER 2

Forward-Looking Infrared Systems

George S. Hopper
Institute for Defense Analyses
Alexandria, Virginia

CONTENTS

2.1 INTRODUCTION

A FLIR is an infrared analog of a visible TV camera. The term FLIR is an acronym for forward-looking infrared originating from the modification of an early 1960s Air Force down-looking infrared mapper to a forward-looking, real-time, infrared imaging system. The name has remained even though today a more appropriate name would be "thermal imaging" or "infrared imaging." The purpose of a FLIR is simply to see in the dark by the detection and appropriate processing of the natural radiation emitted by all material bodies. This radiation is described by various forms of the Planck radiation law. At 300 K, the peak of this radiation occurs at about 10-μm wavelength. Since there is an atmospheric transmission window between 8 and 14 μm, this is a useful region in which to operate. There is also a window between 3 and 5 μm, so operation here is also possible. A system operating anywhere in the 8- to 14-μm region is usually referred to as an LWIR (long-wavelength infrared) FLIR, and one operating anywhere in the 3- to 5-μm region as an MWIR (medium-wavelength infrared) FLIR. The term FLIR usually refers only to systems operating in one or the other of these regions.

It is important to note that FLIR operation is in distinct contrast to the other type of night vision devices that operate in near darkness by amplifying existing visible (or near-visible) external radiation due to moonlight, starlight, sky glow, etc. These systems are quite common and operate very well if there is sufficient external illumination. They cease to operate altogether in absolute darkness or in deep shadows. Also, they do not see as well as FLIRs through smoke, dust, haze, etc. On the positive side, these systems tend to be smaller and less expensive than FLIRs.

The connotation of a FLIR is a system that provides a visible rendition of the invisible infrared radiation scene. The same technology also can be applied to such applications as missile guidance, search and track, threat warning, and various other uses where an actual visible scene is not created for direct interpretation by a human operator, but where some sort of image processing is used to extract the required information. In this chapter we confine the discussion to the man-in-the-loop case. The rationale for this is that a human is just one form of image processor, and the system output can always be thought of as a re-created scene even though it is just a two-dimensional array of values. The system fundamentals up to the point of image processor presentation are the same, and the interested reader is referred to publications dealing with the rapidly growing field of image processing for the logical extension to applications not involving a human operator.

Throughout this chapter there is a peculiar mixing of units. Detector surface dimensions are given in mils (milli-inches), but detector thickness is expressed in micrometers. Wavelength is given in micrometers, while lens aperture is expressed in inches. Resolution is defined in milliradians, while field of view is given in degrees. The field of infrared imaging crosses many technical specialties, each with its own methods and units of description. This blending has resulted in the present situations, and we repeat it by convention. Table 2.1 lists the symbols, nomenclature, and units used in this chapter.

Table 2.1 Symbols, Nomenclature, and Units

Symbol	Nomenclature	Units
$a(f)$	Normalized noise power spectrum	—
A_D	Detector area	cm^2
A_R	System relative aperture	—
c	Speed of light	$m\ s^{-1}$
D_o	IR optics aperture	in.
$D^*(\lambda)$	Spectral specific detectivity	$cm\ Hz^{1/2}\ W^{-1}$
D^*_{BB}	Spectral averaged detectivity	$cm\ Hz^{1/2}\ W^{-1}$
f	Spatial-frequency variable	$cycles\ mrad^{-1}$
f_c	Diffraction-limited frequency	$cycles\ mrad^{-1}$
f_D	Approximate diffraction-limited frequency	$cycles\ mrad^{-1}$
f_0	System reference frequency	$cycles\ mrad^{-1}$
fl	IR optics focal length	in.
$f/\#$	IR optics f-number	—
$(f/\#)_{cs}$	Cold-shield f-number	—
G_0	Magnitude of the noise power spectrum	$°C^2\ mrad^2$
h	Planck's constant	J s
k	Boltzmann's constant	$J\ K^{-1}$
MRT	Minimum resolvable temperature	°C
MTF	Modulation transfer function	—
N	Number of detector elements	—
NEP(λ)	Spectral noise equivalent power	W
NET	Conventional noise equivalence temperature	°C
NET_0	Limiting noise equivalent temperature	°C
NET*	System output noise equivalent temperature	°C
Q	Weighted average noise power spectrum factor	—
R	Target range	km
R_0	Range to $\Delta\theta$ size MRT target	km
S	Overall MRT target size	m
t_D	Detector dwell time	s
T	Temperature variable	K
T_0	Average scene temperature	K
w	Detector element size	mils
Greek:		
β	Atmospheric extinction coefficient	km^{-1}
Δf_r	Reference electrical bandwidth	Hz
ΔT	Effective signal temperature	°C
ΔT_0	Thermodynamic temperature difference	°C
$\Delta\theta$	Detector angular subtense	mrad
$\Delta\phi$	MRT target bar size	mrad
ε_s	Scanner (or chopper) efficiency	—

Table 2.1 *(continued)*

Symbol	Nomenclature	Units
η	Detector quantum efficiency	—
η_{cov}	Detector-array coverage efficiency	—
η_{cs}	Cold-shield efficiency	—
η_s	Total FLIR system efficiency	—
η_0	Effective total detector efficiency	—
λ	Wavelength variable	m
λ_1	Detector cuton wavelength	m
λ_2	Detector cutoff wavelength	m
σ	Stefan-Boltzmann constant	$W\ m^{-2}\ K^4$
σ_o	IR optics design blur	mrad
τ_F	System frame time	—
τ_o	Spectral average optics transmission	—
$\tau_o(\lambda)$	IR optics transmission	—

2.2 PRINCIPLES OF OPERATION

2.2.1 Fundamentals of Thermal Imaging

All material objects above absolute zero radiate electromagnetic radiation. The maximum value of this radiation per unit wavelength is given by the Planck blackbody radiation law,

$$M_e(\lambda,T) = \left(\frac{2\pi hc^2}{\lambda^5}\right)\left[\exp\left(\frac{hc}{\lambda KT}\right) - 1\right]^{-1} \quad [W\ m^{-3}]\ , \tag{2.1}$$

where

c = speed of light in vacuum = 2.997×10^8 m s^{-1}
h = Planck's constant = 6.626×10^{-34} J s
k = Boltzmann's constant = 1.381×10^{-23} J K^{-1}
T = absolute temperature in kelvins
λ = radiation wavelength in meters.

The radiation of a real object is obtained by multiplying the blackbody radiation term by the spectral emissivity of the object $\varepsilon(\lambda)$:

$$[M_e(\lambda,T)]_{\text{actual}} = \varepsilon(\lambda,T)M_e(\lambda,T)\ . \tag{2.2}$$

Equation (2.2) can be considered a definition of emissivity. Since the energy per photon is known to be (hc/λ), Planck's law in terms of photon flux can be written as

$$M_q(\lambda,T) = \left(\frac{\lambda}{hc}\right)M_e(\lambda,T) \quad [\text{photons}\ s^{-1}\ m^{-3}]\ . \tag{2.3}$$

The total power radiated is given by the integration of Eq. (2.1) over all wavelengths, yielding

$$M_e(T) = \sigma T^4 \quad [\mathrm{W\ m-2}] \ , \tag{2.4}$$

where σ = Stefan-Boltzmann constant = 5.67×10^{-8} W m^{-2} K^{-4} . For a blackbody at 300 K, and 1 m^2 area, this corresponds to a total power of about 460 W. The rate of change with temperature of this object is

$$\frac{\partial M_e}{\partial T} = 4\sigma T^3 \tag{2.5}$$

and at 300 K corresponds to about 6 W m^{-2} K^{-1}. If we were to somehow measure the radiation emanating from a typical IR scene consisting of grass, trees, roads, etc., we would find variations from point to point due to variations in temperature and emissivity. It is only this variation in radiance that is useful in image formation. If we operate in the 8- to 14-μm atmospheric window, we will get about a third of Eq. (2.5), or something like 2 W per degree of temperature difference for a 1 m^2 blackbody. Later we will define an equivalent temperature difference in terms of both emissivity and temperature variations. At least for now we might expect to be able to form useful images with only a few degrees variation across the target scene. There has been an ongoing interest in thermal imaging for well over a hundred years, and a rough chronology leading up to the DoD standard common module FLIRs is shown in Table 2.2.

The basic concept of a modern FLIR is to form a real image of the infrared scene, detect the variation in the imaged radiation, and, by suitable electronic processing, create a visible representation of this variation. The common module approach is schematically represented in Fig. 2.1. FLIRs usually use telescopes in the sense that the lens system is focused at a distance very much larger than the focal length. Characteristics such as field of view, resolution

Table 2.2 Chronology of FLIR Development

1848	Sir John Herschel	Lampblack-coated paper soaked in alcohol
1900	Various investigators	IR sensitive photographic films
1930	Czerny *et al.*	"Evapograph," thin membrane immersed in oil in an enclosure
1952	U.S. Army	"Thermograph," single element scanned, recorded on film
1956–1960	Various investigators	Short wavelength, real time, scanned
1962	Texas Instruments	Modified AN/AAS-18 mapper, long wavelength, real time, named FLIR
1962–1972	Various contractors	Progression of improvements, custom designed for each application
1972	Army Night Vision Laboratory and Texas Instruments	Common module FLIR

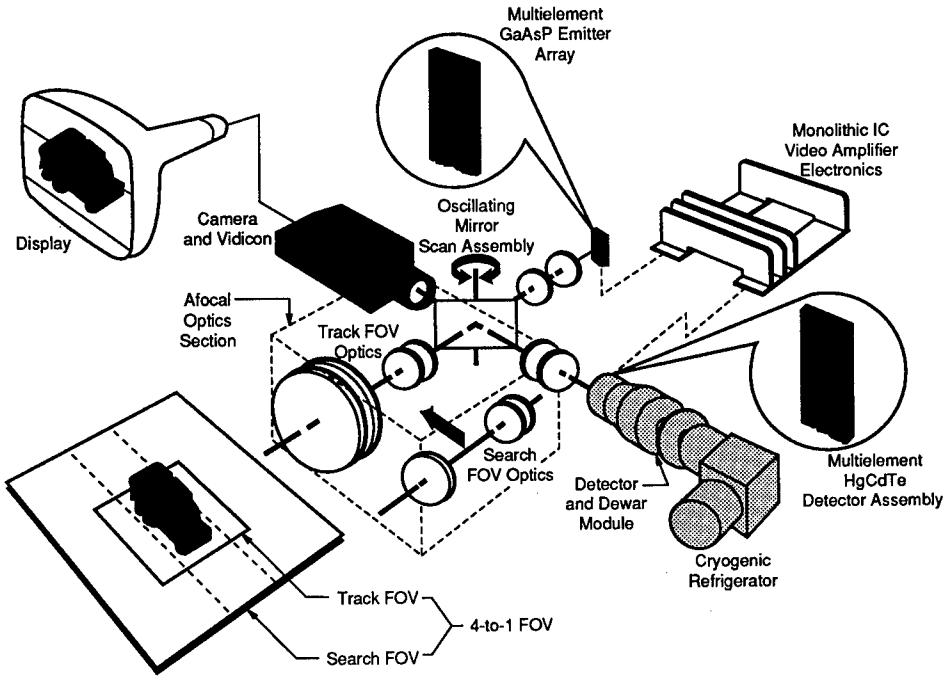

Fig. 2.1 Modular FLIR concept. Common module systems scan an array of IR sensitive detectors across the target scene. The detector outputs are used to drive a geometrically equivalent array of light-emitting diodes to present a visible representation to a television camera.

element size, and spatial frequency are expressed in angular units. By convention, field of view is expressed in degrees, resolution in milliradians, spatial frequency in cycles per milliradian, and noise in units of temperature.

There are unique problems associated with thermal imaging not found in visible imaging systems. The first is the fact that LWIR wavelengths are about 20 times larger than visible wavelengths. This results in FLIR optics being diffraction limited, whereas visible optics are usually optical aberration limited. Second, a FLIR signal is a relatively small variation about a large dc level. In other words, infrared imagery is analogous to a visible image of very low contrast and high illumination. This requires ac coupling (or dc level subtraction by some means) prior to display. Even if an IR-sensitive photocathode existed, it could not be used in the simple visible image intensifier approach of photocathode/electron focusing lens/phosphor. The output would be of too little contrast to be useful. Finally, as we shall see, the fundamental noise limit is related to total photon flux. This is dominated by the large background, and, therefore, the noise is essentially independent of the "signal" level. This is in contrast to visible imaging systems where the noise varies with signal level. FLIR noise is essentially constant.

2.2.2 Functional Elements

The functional elements required for infrared imaging can be grouped into four main categories: (1) image formation, (2) detection, (3) signal processing

(including amplification), and (4) display. All of these are important, and interrelated. However, since the detection function has such an impact on the required characteristics of the others, we start here.

2.2.2.1 Infrared Detection. Infrared radiation can be detected by its interaction with matter either through the process of photon-to-photon exchange-heating effect, or by direct electron absorption/internal photoelectric effect. In the former, the radiation is absorbed as heat, resulting in a temperature rise. Then, some temperature-dependent parameter of the detector is measured. Such devices are referred to as square-law detectors. In the latter process, the valence band (or impurity level) electrons in a band-gap semiconductor are elevated to the conduction band by direct photon absorption. This increase in conduction band electrons can then be measured. These devices are referred to as quantum detectors. The details of operation of either type, as well as the subtleties involved with their fabrication and electric interface, are very complex and outside the purpose of this chapter. We restrict the discussion here to the more important characteristics affecting system design.

2.2.2.2 Quantum Detectors. The most glaring difference between square-law and quantum devices is that the latter must be cooled to cryogenic temperatures. The very small band gaps required for infrared photon energies result in unacceptably high levels of conduction band electrons at temperatures close to ambient and necessitate operation at 80 K or lower. Quantum detectors are very carefully mounted to the cold surface of a cooler (the "cold finger") inside a vacuum enclosure called a dewar. Since the size and power of the cryogenic refrigerator are determined by the cold-finger heat load, great care is taken in dewar design to minimize external heat flow due to conduction of the electrical leads. The interested reader is referred to the chapter dealing with cryogenic coolers, dewars, and infrared detectors for more details. Operationally, there are three common types of quantum detectors: photoconductors, photodiodes, and photocapacitors. They have different electrical interface requirements, and external system complexity, as well as performance, are affected by the choice.

Photoconductors are simply solid-state resistors. They are usually operated in a voltage-divider network configuration. The bias voltage, and individual load resistors, are selected to optimize detector/preamp composite signal-to-noise ratio. Photoconductors are typically low-responsivity (< 20 kV W^{-1}), low-impedance ($< 100\ \Omega$) devices and are far more compatible with bipolar preamps than with MOS. This, combined with the relatively high bias power, almost precludes placing preamps (and other processing circuitry) on the cold finger. The result is that each detector lead must be brought out of the dewar separately. Thus, practical dewar/cooler configurations limit photoconductor arrays to 200 or so elements. On the positive side, photoconductors are relatively easy to build and are the most forgiving of material impurities and defects. For many applications 200 or fewer detectors is more than adequate. They are used in the original DoD standard common module systems. These were the first mass-produced FLIRs, and by the end of 1990 more than 50,000 of them had been deployed.

Photodiodes are the infrared equivalent of silicon photocells. They are usually operated at a small reverse bias to minimize Johnson current noise, and

here the current is almost all photon flux induced. The electrical interface is usually a current amplifier in a virtual ground configuration (a transimpedance amplifier or equivalent). This is compatible with MOS, so preamps, and other processing circuitry, can be on the cold finger. This, plus the lack of bias power, means that it is possible to consider photodiode arrays consisting of many thousands of elements.

Photocapacitors, or MIS detectors, are the infrared equivalent of a single cell in a silicon CCD camera. They are integrating devices, whereas photoconductors and photodiodes are not, and are equivalent to a Schottky barrier photodiode with a built-in integrating capacitor. No bias power is required, and very simple MOS circuitry can be on the cold finger, so large arrays are possible. Since no diode junctions are formed, fabrication is a simple planar process. On the negative side, limited charge integration capacity, tunneling current, and $1/f$ noise may require much better material than photodiodes for equivalent performance.

2.2.2.3 Square-Law Detectors. Uncooled detectors absorb IR radiation as heat and indicate this as a change in some measurable physical parameter caused by the resultant temperature change. The possibilities are almost limitless. The question is not what parameters change with temperature, but what doesn't? Volume, pressure, reflectivity, polarization, Peltier current, resistance, and many other parameters have been used to make a variety of IR detectors since the discovery of electromagnetic energy beyond the visible by Sir William Herschel in 1800. The possibilities are truly almost endless. It is often said that square-law devices are not useful for imaging because they inevitably suffer from poor performance and are too slow. This is not quite correct. In fact, it can be shown that a square-law device suspended in a vacuum in such a way that it can only exchange energy by radiation and absorption from one surface has the same limit of performance as a quantum detector exposed to hemispherical background radiation. In addition, even though the thermal time constant in such a case might be minutes, the fundamental noise also has this same temporal response. Thus, external frequency compensation of the signal will just flatten the noise, and the resulting signal-to-noise ratio will be determined by the final setting of the desired bandwidth (flux integration time)—just as it would for an ideal detector. The real problem here is one of thermal isolations and responsivity: isolation to obtain acceptable detector noise performance and responsivity sufficient to maintain it in the readout device.

Of the many possibilities, one that has been developed and has proved to produce very competitive LWIR imagery at TV frame rates is briefly described as an example. The element used here is a thin ferroelectric material, metallized on opposing surfaces to form a small parallel plate capacitor. Ferroelectrics are characterized by a spontaneous electric polarization that rapidly goes to zero at a characteristic temperature called the Curie point. In addition, the dielectric constant also rapidly changes with temperature in this region. If the device is operated just slightly below this critical temperature, large changes in capacitance with temperature result, and relatively straightforward MOS bias and readout circuitry can be used to provide responsivities greater than photoconductors at 60 Hz. This is adequate for staring arrays—a system

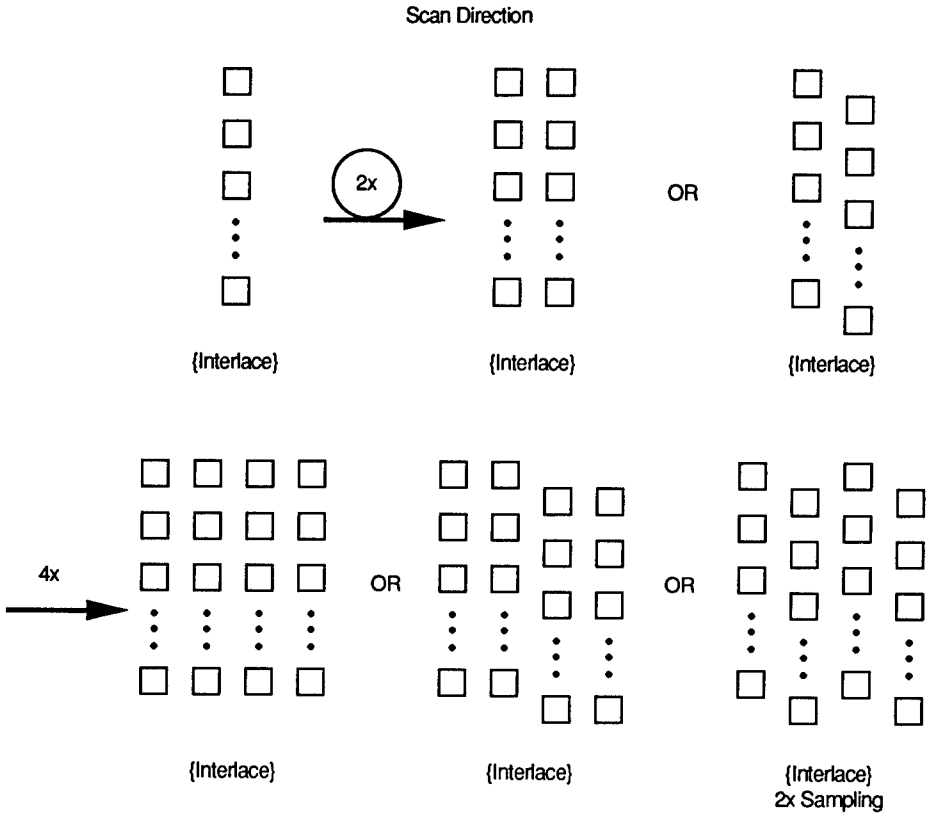

Fig. 2.2 Detector array scanning FPA formats. Parallel system array formats can be used to eliminate interlace or increase the vertical sampling rate.

type to be described later. The required thermal isolation for detector performance is provided by the method of contacting the capacitors to the silicon processor to produce very low thermal conductivity to the temperature-controlled heat sink.

2.2.2.4 Detector Arrays. Detectors are fabricated as single-element devices replicated into arrays of one to many thousands of elements. Element sizes are in the range of one to two mils and are usually square or rectangular in shape. Thicknesses are usually in the range of 10 μm for quantum detectors, and may be up to several times this for ferroelectric devices. The total number of elements in an array directly affects the ultimate sensitivity of the system, as discussed in the section on performance. The geometrical arrangement of the elements (the array format) can be used in a variety of ways for system advantages. Some possibilities are indicated in Fig. 2.2.

2.2.3 Image Formation

Infrared energy is electromagnetic radiation and thus subject to the same laws of reflection, refraction, and diffraction as visible light. All the concepts and analytical techniques are directly applicable, and most visible components

have an IR counterpart. Common visible glasses do not transmit IR radiation, so refractive elements must be made from materials that do. On the other hand, reflective elements are virtually the same. Many materials transmit IR radiation, but practical considerations concerning strength, dispersion, index of refraction, etc., limit the choices. Common IR materials are germanium, TI 1173 (and other chalcogenide glasses), IRTRAN, zinc selenide, and gallium arsenide. FLIR optical systems tend to be larger than comparable field of view visible systems because of diffraction and sensitivity differences. Objective lenses may be ten inches or larger in some cases, and are rarely less than one inch for short-range applications. In optical design terms. FLIR optics are usually much faster than visible systems.

The most common type of system requires an optical scanning subsystem in order to provide full focal-plane coverage with a limited number of detectors. Conceptually, this is accomplished by mechanically scanning the image across the detector array in a prescribed manner. Usually, a flat mirror intersects the optical beam and rotates to provide the required scan. Rotating wedges, prisms, and the like can be, and have been, used, as well as multifaceted rotating mirror assemblies. Simple oscillating flat mirrors are more common. The easiest type to understand is the object-plane scanner. Here, the mirror (or other element) is placed in front of the objective lens, centered on the optical axis, and rotated about an axis perpendicular to it. This causes the imaging system to "point" to different positions in object space determined by the instantaneous mirror angle. The practical problem here is that the mirror must be placed far enough to the left of the objective lens so as not to hit it as it scans. A simple ray trace will show that the mirror must always be larger than the objective—the largest element in the optical train. The mirror can be made much smaller by judiciously placing it somewhere in the internal optical path. Just where depends on the specific design. This type is called an image-plane scanner. The easiest way to see how any type of scanner works, no matter how complicated, is to imagine an individual detector element as a diffuse light source, trace the resulting beam through the optics, and see where it goes in object space. Radiation from object space will traverse this same path in reverse.

Almost all scanning systems use quantum detectors, and performance considerations require reducing the background radiation to the minimum possible. This minimum is just that background flux coming through the optics front aperture. To approach this, the detector array is baffled inside the dewar, typically by placing a metal cap with a hole or slit in it above the surface of the detectors and in contact with the cold finger. This is called cold shielding. The cold-shield baffle must be at a low temperature because, otherwise, it would add back in some or all of the external flux it blocked. The degree to which the background flux is reduced to the ideal is indicated by the cold-shield efficiency. A typical cold-shield arrangement is shown in Fig. 2.3.

Cold shielding and/or scanning complicate optical subsystem design and packaging and usually result in different trade-offs for each application. If no attention is paid to the locations of the various entrance and exit pupils, the input beam that is eventually focused onto an individual detector will wander around on the objective lens, the scan mirror, and the cold-shield aperture. The result would be an oversized and inefficient system. The ideal design would

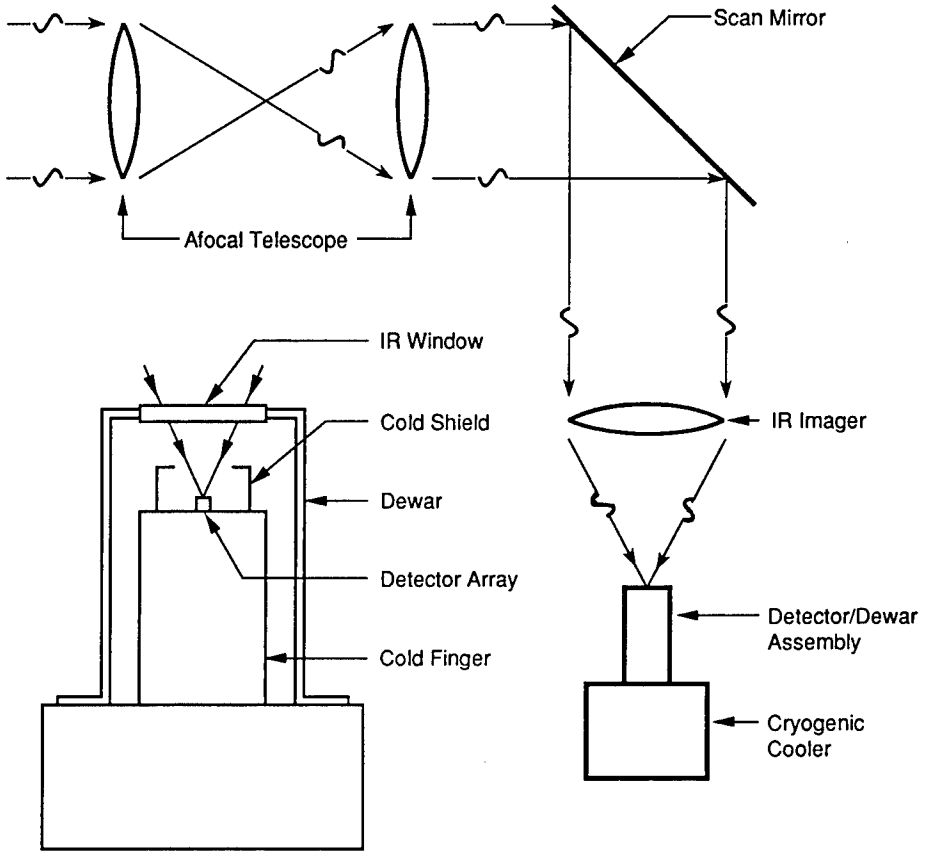

Fig. 2.3 FLIR systems typically use an afocal telescope/IR imager arrangement. This allows scanning a collimated beam as well as allowing the imager and detector array to be used in many different applications by simply changing afocals.

place the primary entrance pupil on the objective lens, an intermediate exit pupil on the scan mirror, and the primary exit pupil on the cold-shield aperture. However, this may require a complicated optical system with many lenses and several intermediate focal planes. Also, packaging, size, weight, cost, and transmission loss can make this an unacceptable choice in some applications.

An additional problem associated with cold focal-plane scanning is referred to as the narcissus effect. The detector array, and the area adjacent to it, lie in the primary focal plane of the imaging system. It is then possible that reflections from the lens elements prior to the scanner can at least partially focus the area around the detector back onto the focal plane. This will result in a variation in the background flux incident on the detector during the scan. If the narcissus is in relatively sharp focus, the result will be a dark streak down the center of the display called cold spike. In poor focus, this spreads to a smooth variation across the entire display called hump. Design practice is to eliminate cold spike altogether and to control lens-surface curvature and location to minimize hump to acceptable levels. Hump is always present to

some degree and can be readily observed by looking at a uniform scene at high system gain.

Fortunately, in spite of all the complications, it is still possible to describe and analyze the impact of the IR optical system on the total FLIR system in very simple terms. After all the critical factors have been prioritized, optical layouts agreed upon, and elements designed, the entire optical system, or any subgroup of elements, can be described in simple, idealized, "thin-lens" terms. One has only to keep in mind that (1) the effective objective aperture may be smaller and of a different shape than the actual objective lens, (2) the scanning element may be larger and less efficient than ideal, (3) cold-shield efficiency may be less than unity, and (4) the image will be blurred a finite amount over and beyond that caused by diffraction, and may be worse at the edges of the field of view than at the center. The overall transmission is determined by the number of surfaces and their respective transmissions or reflectivities and by the bulk absorption of window and lens materials.

A further conceptual simplification can be made by reexamining scanner action. In reality, the action of the scanner is to cause the target image to be optically swept across the detector array in some prescribed manner. Since it is only the relative motion that matters, one can imagine that the image is stationary and the detector sweeps across the image in the reverse direction. Now, conceptually, all lens-system descriptions, scanning or not, reduce to that of a single lens, and the detector array either scans or it does not. We use this single-lens, scanning-array approach in all that follows, but use the actual values for such parameters as cold-shield and scanner efficiency.

Consider a thin circular lens of diameter D_o and focal length fl. If an object of height H_1 is placed at a distance S_1 to the left of the lens (object space), its image will occur at a distance S_2 to the right of the lens (image space), given by

$$S_2 = \frac{fl}{1 - (fl/S_1)} , \tag{2.6}$$

and will be of size H_2, given by

$$H_2 = \left[\frac{fl}{1 - (fl/S_1)}\right]\left(\frac{H_1}{S_1}\right) . \tag{2.7}$$

Now, if the object distance is very large relative to the focal length, Eq. (2.6) says all objects will be focused at the focal length fl, regardless of their distance S_1, and Eq. (2.7) says the image size will be related to the angle subtended by the target at the lens. Furthermore, for a small target angle ϕ,

$$H_2 = fl\left(\frac{H_1}{S_1}\right) \cong fl\phi . \tag{2.8}$$

Conversely, a detector of dimension w will collect energy over an object-plane angle $\Delta\theta$, given by

$$\Delta\theta = \frac{w}{fl} \ . \tag{2.9}$$

Evidently, this angle will be a major factor in determining the resolution capabilities of the system and is a key parameter called the detector instantaneous field of view (IFOV). If the detector is not square, the IFOV will be different in x than it is in y, and the extension of Eq. (2.9) is obvious. If the detectors are confined to a working area of linear dimensions $F_x \times F_y$, then the total object-plane angles that can be used by the system are given by

$$\phi_x = \frac{F_x}{fl} \ ; \quad \phi_y = \frac{F_y}{fl} \tag{2.10}$$

and are referred to as the horizontal and vertical fields of view, respectively.

FLIR focal lengths rarely exceed 20 in., object distances are usually greater than 100 ft, and detector dimensions are typically 2 mils or less, so the small-angle assumption is usually quite good. The only problems that would occur are for very short object distances or for focal-plane linear dimensions comparable to the focal length. In the former case only, the system must be refocused, and in either case, the field of view and perhaps $\Delta\theta$ must be recalculated. We assume small angles for simplicity. Only object-plane angles matter—not target size or distance—and image-plane angles are the same as object-plane angles.

Next, consider a Lambertian surface of linear area A_T at a distance R from the lens. The power collected by the lens from this target, P_c, is then

$$P_c = \left(\frac{M_T A_T}{\pi}\right)\left(\frac{\pi D_o^2}{4R^2}\right) \ , \tag{2.11}$$

where M_T is the emittance of the target in watts/area and D_o is the optics diameter. The first term in Eq. (2.11) is the emittance per unit solid angle, and the second term is the solid angle subtended by the lens. This power is then focused on the image plane and spread out over the image area A_I. The resulting focal-plane irradiance M_I, in watts/area, is thus

$$M_I = \frac{D_o^2 M_T A_T}{4R^2 A_I} = \left(\frac{D_o^2}{4fl^2}\right) M_T \ , \tag{2.12}$$

where we have used the fact that

$$\frac{A_T}{R^2} = \frac{A_I}{fl^2} \ . \tag{2.13}$$

Therefore, the focal-plane power density is linearly related to the object-plane power density by the optics f-number ($f/\#$):

$$M_I = \left[\frac{1}{4(f/\#)^2}\right] M_T \ , \tag{2.14}$$

where

$$(f/\#) = \frac{fl}{D_o} \ . \tag{2.15}$$

Strictly speaking, the derivation of Eq. (2.12) is only approximate and is valid for a system focused at infinity. In any case we define $f/\#$ by Eq. (2.14). Perhaps surprisingly, it can be shown that for a well-designed IR optical system, Eq. (2.15) is true for the effective focal length and aperture. The proof is beyond the purpose here.

Also note from Eq. (2.11) that the power collected per unit target solid angle is

$$\frac{P_c}{\Omega_T} = \left(\frac{D_o^2}{4}\right) M_T \ , \tag{2.16}$$

where

$$\Omega_T = \frac{A_T}{R^2} \ . \tag{2.17}$$

Now, since image- and object-plane angles are the same, the total power P_D collected by a detector of subtense $\Delta\theta_x$, $\Delta\theta_y$ is

$$P_D = \left(\frac{D_o^2 \Delta\theta_x \Delta\theta_y}{4}\right) M_T = \left[\frac{(D_o \Delta\theta_E)^2}{4}\right] M_E \ , \tag{2.18}$$

where

$$\Delta\theta_E = (\Delta\theta_x \Delta\theta_y)^{1/2} \ . \tag{2.19}$$

This suggests that the product of the optics aperture and the detector IFOV, as defined by Eq. (2.19), is a significant quantity. In the section on performance it will be shown that this is indeed the case.

FLIR systems typically use an afocal/IR imager arrangement, as shown in Fig. 2.3. This has the advantage of scanning a collimated beam, rather than a converging beam, and it also allows the scanner and imager to be used in many different applications by changing only the telescope aperture and the afocal ratio.

2.2.4 Signal Processing

The signal-processing function is to condition the detector outputs into a form suitable for interface to the display. This is in contrast to information-processing subsystems, such as target trackers and cuers, whose function is to extract information from the signal-processing output. In general, the subfunctions to be performed (in no particular order except for the first and last) are

1. *preamplify* to raise the detector signal output to a useful level, i.e., make the detector noise larger than any subsequent circuit noise
2. *dc level subtract* to eliminate the large, unwanted, constant output associated with the background radiation
3. *gain and level correct* to normalize the inevitable variations in element-to-element offsets and responsibilities
4. *multiplex* to reduce the numerous detector outputs into a single, or at least a few, lines
5. *scan convert* the detector scan format into the one required by the display
6. *set up* the final display output by establishing the levels, sync signals, etc., required by the display.

A required additional function is that of global gain and level control. This is done either by providing operator accessible dc level and gain control, in which case it is trivial, or by special automatic processing algorithms, which borders on information processing. The need for this is discussed later.

Preamps are intimately associated with detector elements and, in the case of large focal-plane arrays, are physically located on the focal plane. Practical limitations play a major role in determining the suitability of detectors for imaging uses, especially in the case of square-law devices. Photoconductors place the severest requirement on preamps because of their low responsivity and impedance. Common-module systems use bipolar transistors, and the heat load requires them to be external. This limits the number of elements, as previously noted. Photodiodes are next since they require transimpedance amplifiers (or the equivalent). Photocapacitors are probably the easiest. Preamp design is well covered in numerous sources on the amplification of low-level signals, and infrared detectors pose no significant new problems.

Large focal-plane arrays are usually amplified, dc restored, and multiplexed on focal plane. Then, since reformatting always requires at least partial frame storage, the first external process is usually to A/D convert the analog detector assembly outputs so that more or less standard digital-processing techniques and components can be used to perform the functions of gain and level correction, reformatting, and, if needed, automatic global gain and level control. Correction is accomplished by storing offset and gain coefficients for each detector element in the array and then using them to correct the data stream at the appropriate time in the flow.

In common-module systems, each detector lead is brought out of the dewar as a separate output. Analog signal processing is used throughout, one channel per detector. The outputs are capacitively coupled, so no level correction is required. Channel gains are adjusted manually. Multiplexing and reformatting are performed in one subsystem referred to as an electro-optical multiplexer. The output of each channel is used to drive a visible light-emitting diode (LED) in an array geometrically equivalent to the detector array. The diode array is scanned, using the back side of the IR scan mirror, and focused by a visible lens onto a TV camera. The camera can be operated in (almost) any required format—usually 525- or 875-line standard TV. A visible imager can also be used to view the scanning diode array directly. The DoD standard common modules are shown in Fig. 2.4.

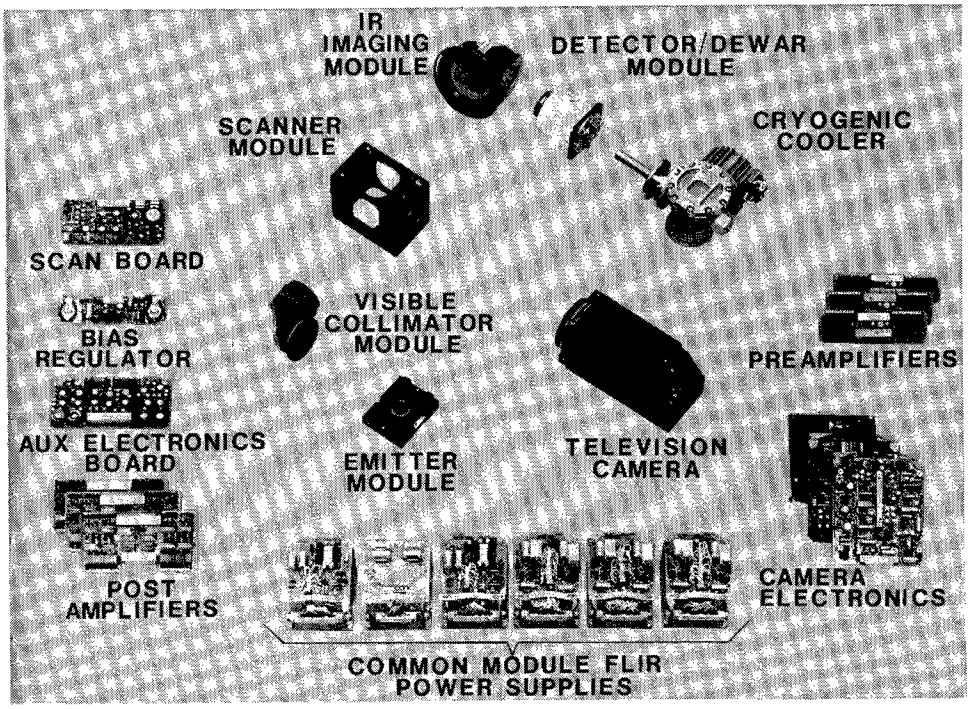

Fig. 2.4 The standard modules used in common-module systems are shown. Through 1990 more than 50,000 systems had been built.

2.2.5 Display

The function of the display is to convert the signal-processor output into a two-dimensional visible-light distribution corresponding to the selected portion of the IR scene. The obvious choice of preference is a standard TV monitor using a cathode-ray tube, or solid-state equivalent. There is a large assortment of auxiliary video equipment readily available—recorders, mixers, test equipment, etc. Also, many applications use multiple sensors or have other uses for the display, so a standard is logical.

Some applications, notably man-portable or other essentially self-contained systems, have no requirement for display sharing and trade standard TV format for reduced signal-processing complexity and/or total system power.

It has been said that any imaging-system design should start with the display. This is certainly true, and a common pitfall is a FLIR sensor design inappropriate for the display situation used. The human eye has a finite resolution, and therefore the angle subtended by the display to the eye is critical to what a human can see. No image will look "sharp" unless it is eye limited, but the more this is the case, the less the amount of sensor information conveyed. On the other hand, too large an angle to the eye will result in a blurred image with glaring scan lines, confusing the operator and reducing information transfer. The trick is to match the sensor to the display such that eye resolution is close to sensor resolution. This means that since the eye resolves one minute

of arc, the viewing distance must be such that each scan line is close to being resolved but is not actually resolved. This sets an optimum viewing distance at which a 525-line display height subtends 8 deg vertically.

Other display parameters affecting performance include signal transfer function (gamma), resolution, useful brightness range, maximum-to-minimum brightness ratio, image distortion, and extraneous noise. Display environment factors include ambient lighting and vibration.

2.2.6 Types of Systems

All imaging systems are describable in terms of amplitude as a function of position and time. This takes at least four dimensions: one for amplitude, two for position in a plane, and one for the time. Color TV requires three for amplitude alone (although only two are sometimes used). It is also possible to determine range, actively (with, say, a laser) or by angular rates if motion is involved. This would require an additional spatial coordinate. Mathematically, the choice of coordinate system is arbitrary, but the final output, at least, must be physically realizable.

In the system descriptions that follow we choose three dimensional Cartesian coordinates, one for amplitude, z, and two for position in a plane, (x,y). This precludes range and spectral (IR "color") information, and ignores time. Ignoring time would appear to limit us to stationary scenes. Scene motion is accounted for by assuming a "framing" sequence at a suitable rate. Edison invented this concept in order to expand still photography to motion pictures. Early experiments indicated that 20 or so frames per second were sufficient for most scene motions of interest to a human, but frame rates of less than about 42 Hz caused the scene to annoyingly "flicker." They settled on a 25-Hz frame rate (just to be safe) and flashed this at a 50-Hz rate by use of a mechanical shutter bar to eliminate flicker. Later, the U.S. television broadcast industry chose the familiar 30/60-Hz frame/field rates so they could lock-in power supplies, oscillators, etc., with the existing 60-Hz electrical power system. They also decided to transmit a frame as a sequence of horizontal lines and that about 500 lines were adequate. They settled on 525 lines to allow for some vertical retrace dead time. The current standard is 0.925 vertical efficiency, which yields 485 usable lines. This is commonly rounded to 480. In addition, the television industry decided that the display width would be four-thirds (4/3) its height for a so-called "aspect ratio" of 4:3.

Assuming no other degradation, we might expect that the minimum vertical dimension discernible on a standard TV display is related to the number of lines. Also, the minimum horizontal dimension should be determined by the video signal bandwidth. If we assume these to be about the same, we can think of a standard image as equivalent to an array, or matrix, of 480×640 contiguous, individually controlled, light sources. Broadcast TV is not this good, nor is most FLIR imagery. However, degradations can be accounted for by allowing correlations among the light sources. We refer to these conceptual sources, or to the signal valves controlling them, as pixels.

FLIR systems are divided into two broad categories: scanning and staring. Scanning systems are further subdivided into the categories of serial and parallel.

2.2.6.1 Staring Systems. As the name suggests, the approach here is simply to fill up the desired focal-plane area with detectors. No scanning is required, although periodic shuttering may be used to produce gain and level-correction coefficients, and as we shall see later, staring systems have very high sensitivity performance potential. A standard system, as defined previously, would require an array of 480 × 640 detectors. Assuming a square cell 2 mils on a side, the array size would be 0.96 × 1.28 in. This is quite large and can easily make the optics more complicated than might otherwise be anticipated, and may result in cryogenic-cooling problems. Also, maximum sensitivity requires cell integration times of 33 ms, and this can be difficult to do for IR quantum detectors interfaced to on-focal-plane MOS circuitry. This particular problem is less for MWIR detectors owing to the lower background flux in this spectral region.

2.2.6.2 Serial Systems. A pure serial system consists of a linear array of one to several detectors, aligned horizontally and scanned sequentially in a two-dimensional rectilinear raster pattern across the focal plane, from the upper-left corner to the lower-right corner, as shown in Fig. 2.5. This is the same pattern as the CRT electron-beam scan used for standard TV display operation. Two scanners are required, rotating about an orthogonal axis. Because of the high scan speed required, the horizontal scanner is usually a continuously rotating multifaceted mirror assembly commonly referred to as a carousel scanner. This is followed by a one-way vertical scan with as fast a retrace as possible. This is the usual order, although the reverse is possible. The two scanners must be very accurately synchronized to maintain a stable scan pattern.

U.S. 525-line TV format can be obtained by running the vertical scan at 60 Hz and the horizontal scan at 15.75 kHz. The number of useful lines, however, will be the vertical scan efficiency times 525, and this will not be correct unless

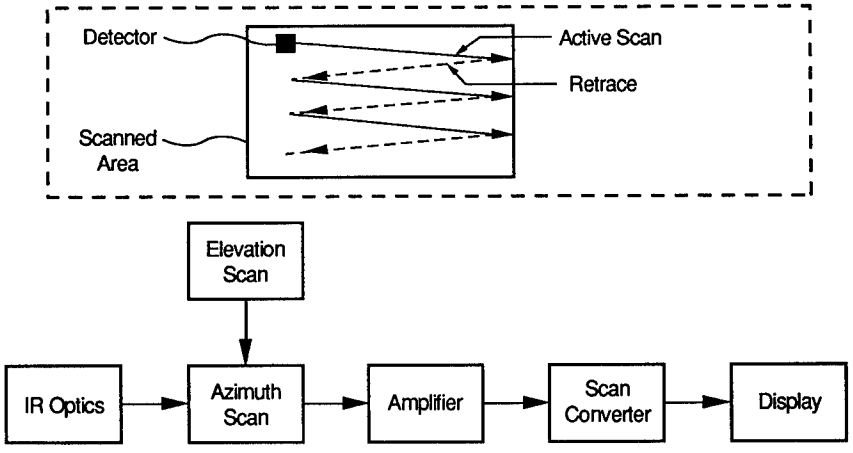

Fig. 2.5 Two-dimensional scanner system single detector. A serial system scans a TV-like raster pattern. It requires a high-speed horizontal scanner synchronized to a low-speed vertical scanner. System performance can be improved by adding detectors in TDI or by adding more rows.

this efficiency is exactly 92.5%. There also is a similar horizontal linewidth problem. The missing lines, and the useless video at the edges of the good lines, are usually blanked out, leaving a black border around the displayed image. Because of this, the pixel matrix is not quite standard, but the format is, so the output can be set up to drive a standard display, or other auxiliary video equipment, with no reformatting.

If more than one detector is used in a serial string, their outputs must be specially processed. Because they all lie along the same horizontal line, every detector may be thought of as generating separate images that are horizontally displaced from each other. If we take the left-most detector image as being correct, the next one is off one unit, the next one to that two units, then three units, and so forth. The amount of this displacement unit is equal to the center-to-center spacing between the elements in focal-plane space, or this distance divided by the linear horizontal focal-plane scan speed, in time. To correct this, the first (left-most) element is not delayed, the second one is delayed one time unit, the third is delayed two time units, and so forth. Then, the resulting outputs are all added together. The result is a single image of enhanced signal-to-noise ratio. The signals from each element add linearly, but the noise, being statistically independent from element to element, adds as root mean square. The result is a detector signal-to-noise-ratio improvement, compared to a single element, equal to the square root of the number of detectors. This technique is almost always used whenever two or more detectors lie along the same scan line in any array format. The process is called time delay and integrate (TDI) and is important to remember and understand.

The main advantage of a serial system is inherent uniformity. Since TDI is equivalent to a single "super" detector, gain and level correction is not required. Reformatting also is not needed (or is at least less complex), but this is offset by the increased complexity associated with the two-dimensional scanner. At least four detectors must be used to obtain reasonable performance for modest uses. Performance is improved by increasing the number, but this is limited by the inherent loss in effective horizontal scan efficiency associated with long arrays in the scan direction. More than one row can be used to increase the number, but this adds some reformatting complexity. Adding many rows begins to approach a parallel-system format.

2.2.6.3 Parallel Systems. A pure parallel system consists of a linear array of contiguous detectors, aligned orthogonally to the scan direction and of sufficient length to entirely cover the field of view in this dimension, as shown in Fig. 2.6. This requires only a one-dimensional scan, which may be either horizontal (the usual case) or vertical. It would require 480 elements scanned horizontally or 640 elements scanned vertically to produce our standard pixel matrix. The scan frequency would be 30 Hz in either case. It is also possible to remove every other detector, run the scanner at 60 Hz, and produce the required pixel format in an interlaced manner by altering the cross-scan position of the scanner by one line on every other scan. Photoconductive array systems, such as the original common modules, use this approach to reduce the number of elements to a manageable number. More than one interlace step is also possible, although rarely used, and the array can be contiguous. In addition, detectors can be added as additional columns or arranged to lie

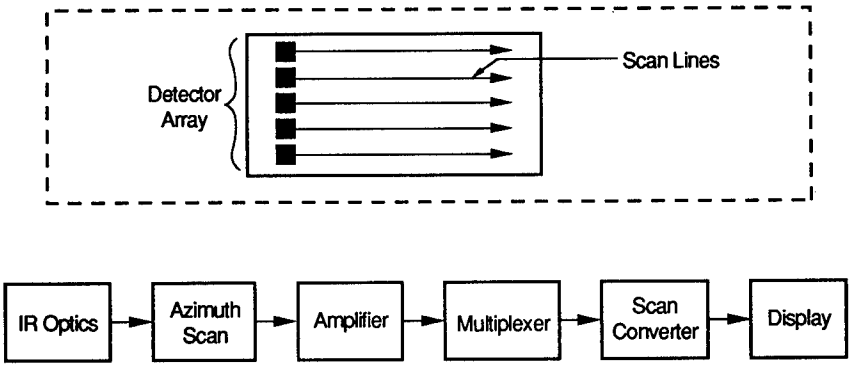

Fig. 2.6 One-dimensional scanner system. A parallel system scans a vertical array horizontally. This allows great flexibility in adding elements for TDI to increase system performance.

along scan lines to produce "super" detectors at each location by TDI. There are many combinations and perturbations. The main advantage here is that numerous detectors can be used without serious efficiency loss, and this is very often needed to meet application requirements. Flexibility of array format and interlacing is also a plus, as well as the reduced mechanical complexity. A disadvantage compared to pure serial scan is gain and (usually) level correction. It has been said that there is also an added complexity because of the need to reformat. This is not necessarily true. If a pure parallel system is scanned vertically at 60 Hz and multiplexed horizontally at 15.75 kHz, the single-line output will be in standard TV format, just like the pure serial-system operation previously described. If the vertical scan mirrors have the same efficiency, the number of useful lines will be the same, but there will be no missing portions at the beginning or end of these lines. In a sense, the function of the serial system high-speed horizontal scan is replaced by electronic multiplexing. Most parallel systems are reformatted, but this is done by choice.

2.3 FLIR SYSTEM PERFORMANCE

2.3.1 Image Fidelity—Resolution

All FLIR systems previously described are sampled data systems in the sense that the continuous input scene is discretely sensed, processed, and displayed. The effects of this are very important, especially at the limits of performance, and must be addressed in system design. The approach here is to start with the assumption of a continuous system and discuss sampling as a perturbation on these results later. The justification for this is that the effects are scene dependent describable in terms of continuous system parameters, and, for a well-designed system, these perturbations are small.

We further assume that the system is linear in the mathematical sense (or at least piecewise so). This assumption allows us to determine uniquely the output function as the convolution of the system impulse response with the

input function. This two-dimensional impulse response (which may be thought of as a "blurring" effect) completely describes the system's ability to re-create fine detail in the output and quantifies such qualitative descriptions as "resolution." It is common to call the area over which there is significant signal correlation as the resolution area, and this is a useful quantitative measure. Each functional element of a system has its own impulse response, and, from linear system theory, the resultant total system response is found by mathematically convolving these together. But, since the Fourier transform of a convolution is the product of the Fourier transforms of the individual functions, it is easier to work in transform space (spatial frequency in cycles per milliradian) than in real space (milliradians). For this reason the commonly used measure of FLIR system image fidelity is defined to be the (normalized) magnitude of the Fourier transform of the system impulse response function. This ignores phase, which can be important. The rationale here is that, unlike real-time-based systems where there is an inherent relationship between amplitude and phase due to causality, imaging systems are space based. In simple terms, there is no reason to require that an impulse response be zero, in, say, the negative x direction. Phase shifts can be introduced, by asymmetry in the optics or display and in the electronic signal processing. For simplicity we assume any such effects to be negligible and ignore phase in all that follows.

The easiest way to obtain the MTF of any subsystem (or the entire system) is to determine the output resulting from an input "point source." This is an input of spatial, or time, dimension very much smaller than any anticipated output dimension, and of amplitude adjusted to size so as to result in unit area. In the limit of zero size and infinite amplitude this reduces to a Dirac delta function. Then, the Fourier transform of this output function is calculated and its magnitude normalized to unity at zero frequency. This normalized magnitude is the MTF of that element. If the magnitude happens to be zero at zero frequency, as would be the case, for example, for an ac-coupled circuit, or indeterminate, as it may be for a dc-restored circuit, then it is customary to normalize the element MTF so that the maximum value of the total system MTF is unity. In the following we restrict derivations to one dimension for simplicity.

2.3.1.1 Image Formation MTF. An optical system with a finite-size entrance pupil will image an object-space point source as a specific image-plane power distribution uniquely determined by the size and shape of this entrance pupil. This distribution is called a diffraction pattern. The resulting MTF for monochromatic radiation can be determined by suitably normalizing the convolution of the aperture with itself, and will be different in each dimension if the pupil is not symmetric. The result for a circular aperture is

$$\mathrm{MTF}_{\mathrm{diff}} = \left(\frac{2}{\Pi}\right)\left\{\arccos\left(\frac{f}{f_c}\right) - \left(\frac{f}{f_c}\right)\left[1 - \left(\frac{f}{f_c}\right)^2\right]^{1/2}\right\}, \tag{2.20}$$

where f is the spatial frequency variable and

$$f_c = \frac{D_o}{\lambda}, \tag{2.21}$$

where D_o is the aperture diameter and λ is the radiation wavelength.

The result for a finite spectral bandwidth is the weighted average of the MTF for each wavelength. However, since we rarely need great precision in MTF, a very good approximation is to use 10 μm (LWIR) and 4 μm (MWIR) for the wavelength in Eq. (2.21). An additional simplification can be made by using the linear approximation of Eq. (2.20):

$$\text{MTF}_{\text{diff}} = 1 - 1.27\left(\frac{f}{f_c}\right) . \tag{2.22}$$

The comparison between Eqs. (2.22) and (2.20) is shown in Fig. 2.7. Equation (2.22) can be rewritten as

$$\text{MTF}_{\text{diff}} = 1 - \left(\frac{f}{f_D}\right) , \tag{2.23}$$

where

$$f_D = \frac{f_c}{1.27} = \frac{D_o}{1.27\,\lambda} . \tag{2.24}$$

By coincidence, f_D for a 1-in. aperture is 2 cycles/mrad (LWIR) and 5 cycles/mrad (MWIR). Therefore, a good rule of thumb is that the diffraction cutoff f_D of the entrance-pupil aperture will be about twice its size in inches (in each dimension) for LWIR and 2.5 times this for MWIR. This has a lot to do with the custom of expressing IR optics dimensions in inches.

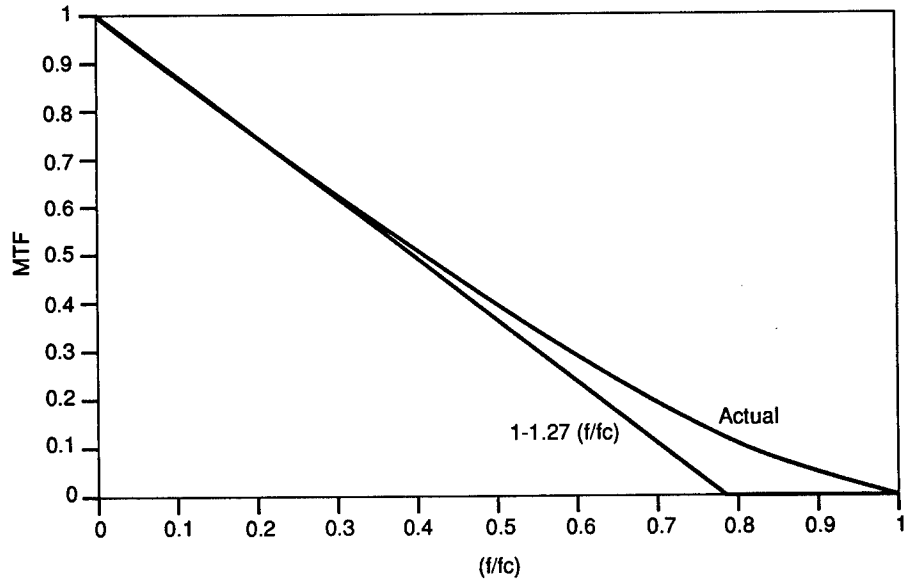

Fig. 2.7 Diffraction MTF circular aperture. The often-used straight line approximation for the diffraction MTF of a circular aperture is accurate over most of the region of interest.

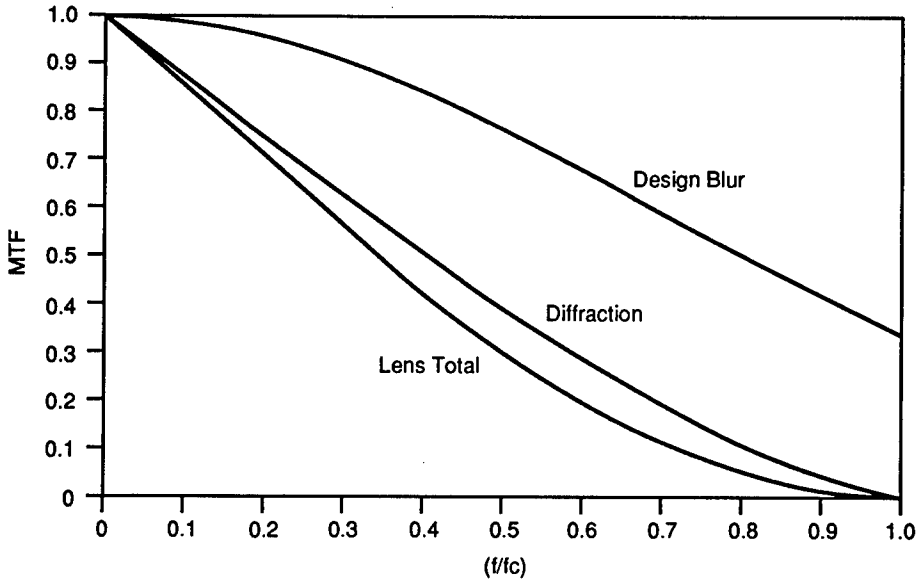

Fig. 2.8 LWIR lens MTF. Design blur σ = IFOV/3. The total lens system MTF is the product of diffraction and geometrical design blur.

As stated previously, IR optical systems are usually diffraction limited, whereas visible systems are usually design blur limited. However, design blur (imperfect geometrical focus) can be a significant factor for FLIR as well. The causes of this are well documented in numerous optics design sources. The result is that the design blur impulse response is approximately a Gaussian shape in two dimensions. The MTF is therefore also Gaussian and is given by

$$\mathrm{MTF}_{\mathrm{design}} = \exp[-\Pi(f\sigma_0)^2] \ , \tag{2.25}$$

where σ_0^2 is the mean square deviation in mrad^2 and f is the spatial-frequency variable in cycles mrad^{-1}. In summary, the optical system MTF is approximately, assuming perfect symmetry,

$$\mathrm{MTF}_{\mathrm{optics}} = \mathrm{MTF}_{\mathrm{diff}}\mathrm{MTF}_{\mathrm{design}} \tag{2.26}$$

and can be approximated by

$$\mathrm{MTF}_{\mathrm{optics}} \cong \left(1 - \frac{f}{f_D}\right) \exp[-\Pi(f\sigma_0)^2] \ , \tag{2.27}$$

with f_D given by Eq. (2.24). The quantity σ_0 can be regarded as a degradation factor associated with the quality of the optical system materials, design, fabrication, and mounting. The total lens system MTF is shown in Fig. 2.8.

2.3.1.2 Infrared Detection MTF. It might appear that the resolution effect associated with the primary detection process depends on the type of system, the array format, the signal processing, and the type of display. While it is

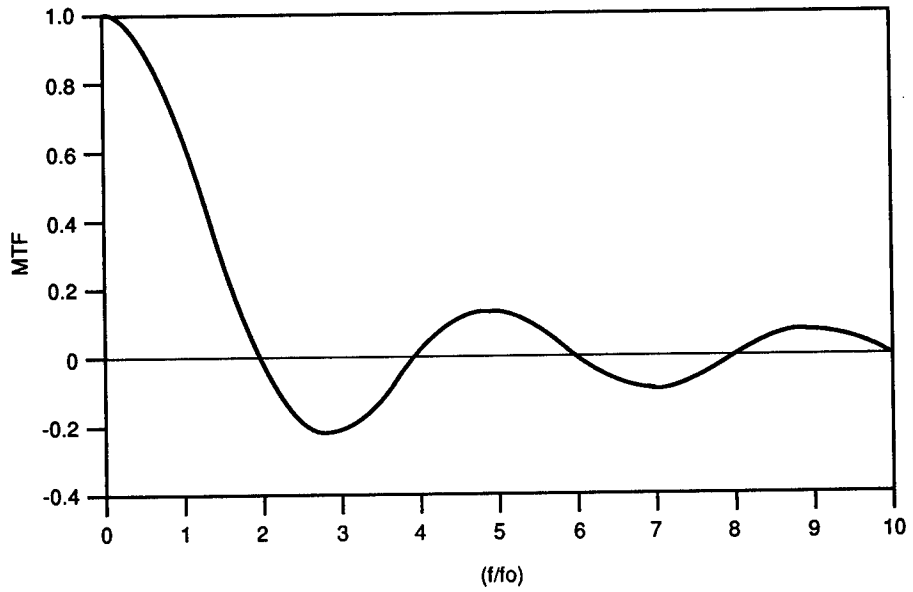

Fig. 2.9 Detector MTF with $f_0 = 1/(2 \times \text{IFOV})$. The spatial integrating effect of an IR detector results in a sinc function MTF for square or rectangular elements.

true that all these factors may contribute to the final system MTF, there will always be a term in this final expression that depends only on the geometrical (and responsivity profile) characteristics of a single detector element. The assumption here that all the detectors in an array are identical is consistent with the mathematical linearity assumption. This unique detector term is inherent to the primary detection process and is a fundamental limit to total system performance. The easiest way to determine detector MTF is to note that at any instant of time, a detector integrates the incident irradiance over its surface. That is, the signal output S (in units of voltage, current, etc.) is given by

$$S \sim \iint J(x,y)\Omega(x,y)\, dx\, dy \ , \tag{2.28}$$

where $J(x,y)$ is the irradiance, $\Omega(x,y)$ is the element responsivity profile, and the integration is over the area of the detector. Expression (2.28) is equivalent to the convolution of J and Ω evaluated at the origin; therefore, the MTF is determined by the Fourier transform of $\Omega(x,y)$. For example, a square detector of uniform responsivity has an MTF given by

$$\text{MTF}_{\text{det}} = \frac{\sin \pi f \Delta\theta}{\pi f \Delta\theta} \ , \tag{2.29}$$

where $\Delta\theta$ is the detector IFOV in one dimension. All detector elements considered here are assumed square, or rectangular. Also, the responsivity profile is usually essentially uniform, so that Eq. (2.29) is at least a very good approximation to the MTF associated with the primary detection process. The detector MTF, relation (2.29), is shown in Fig. 2.9.

2.3.1.3 Signal Processing and Display Effects. The MTF associated with the signal-processing function is difficult to generalize and usually must be evaluated on a case-by-case basis. Fortunately, it is possible to reduce the degradation here to an insignificant level. The primary factor is the temporal frequency response of the analog circuits, preamps, multiplexers, sample-and-hold circuits prior to analog-to-digital conversion, etc., and this can show up as vertical and/or horizontal MTF loss. A common pitfall is to get lost in the flip-flopping back and forth between vertical and horizontal, and in the time-base relationship to spatial frequency. Frequencies can vary from kHz to many MHz within the same processor, and the spatial correspondence must be carefully determined.

The same considerations apply to the display. If it is a single-beam CRT, as commonly used in any TV standard, the effect is almost entirely attributed to the video channel frequency response and to the electron-beam shape and size. The latter usually dominates and is almost always a Gaussian. In this case, it is equivalent to an optics design blur with its own σ.

2.3.1.4 Composite System MTF. The total system MTF is the product of the subsystem functions, so

$$\mathrm{MTF}_{\mathrm{system}} = \left(1 - \frac{f}{f_D}\right) \exp[-\Pi(f\sigma_0)^2] \left(\frac{\sin \pi f \Delta\theta}{\pi f \Delta\theta}\right) \mathrm{MTF_p MTF_D} \ , \qquad (2.30)$$

where

f = spatial frequency coordinate in cycles/mrad
f_D = diffraction cutoff frequency in cycles/mrad
$\Delta\theta$ = detector IFOV in mrad
$\mathrm{MTF_p}$ = MTF of the signal processor
$\mathrm{MTF_D}$ = MTF of the display.

This assumes a circular optical aperture, or that an equivalent one can be defined (almost always the case), and is valid only for $f \leq f_c$. Outside this range, the MTF is zero. A typical FLIR system total MTF for LWIR operation is shown in Fig. 2.10. Figure 2.11 indicates the change in MTF for MWIR operations.

The sinc function in Eq. (2.30) has a first zero when its argument is π. This corresponds to a frequency of

$$f = \frac{1}{\Delta\theta} \ . \qquad (2.31)$$

Since this is almost always less than f_D, it is regarded as the useful frequency limit to FLIR performance. A commonly used reference spatial frequency f_0 is defined to be one-half this value, or

$$f_0 = \frac{1}{2\Delta\theta} \ . \qquad (2.32)$$

For a well-designed sensor and a good display, diffraction and detector MTF dominate. At f_0, diffraction is typically 0.7, detector MTF is 0.64, design blur

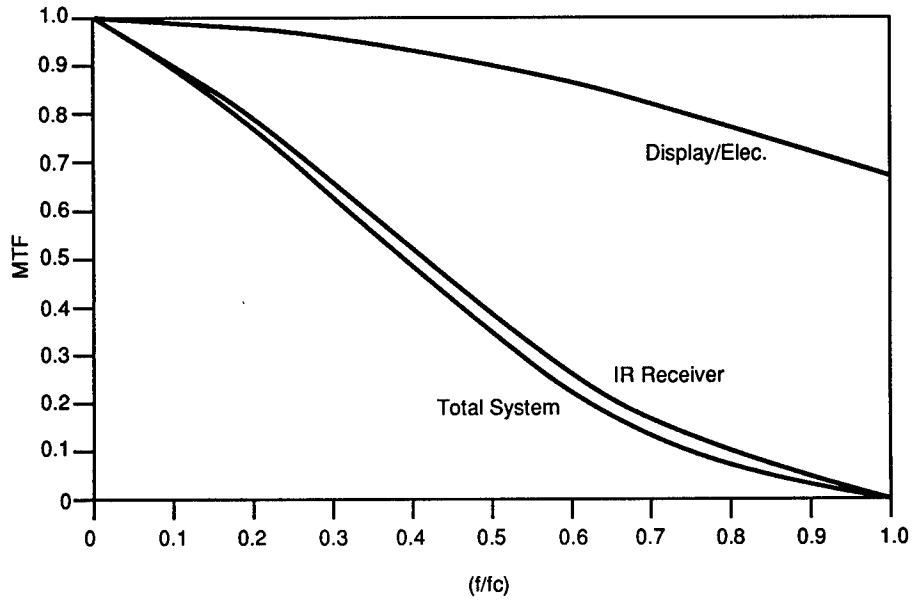

Fig. 2.10 Total FLIR MTF LWIR. The total FLIR system MTF is the product of the display/electronics and the IR receiver. The latter is the result of diffraction, lens design blur, and detector integration.

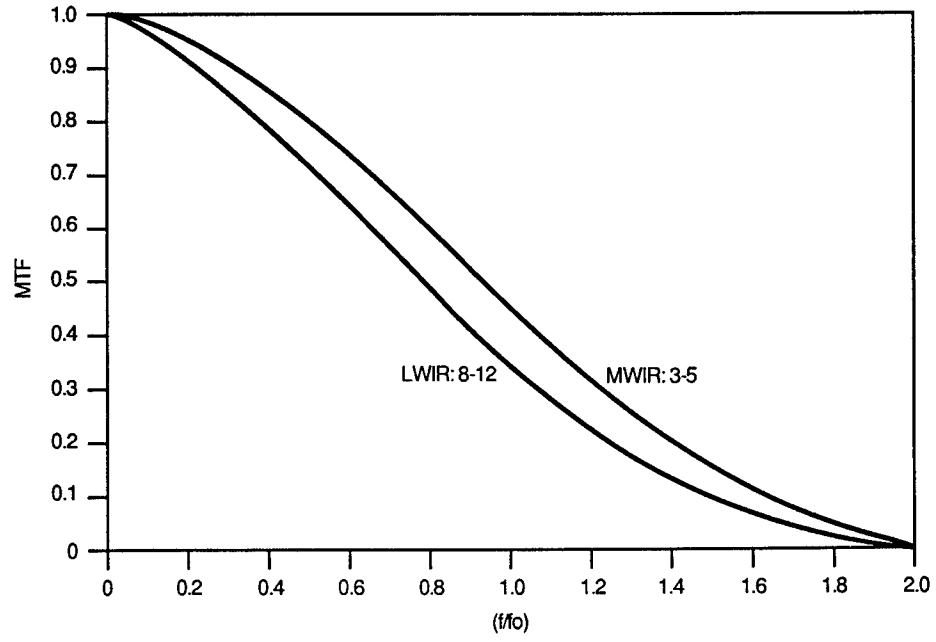

Fig. 2.11 MTF for LWIR and MWIR. MWIR systems have somewhat better MTF response than LWIR systems because of the wavelength dependence of diffraction.

MTF is 0.9, and processor MTF is close to one. The sensor-only MTF is then about 0.4. Displays are difficult to generalize but most achieve at least 0.6 or better. We therefore expect FLIR MTF at f_0 to be in the range of 0.25 to 0.4, which is rather typical.

2.3.2 Image Uncertainty—Sensitivity

The connotation of sensitivity is the minimum value of something that can be reliably measured, and this is always related to the unwanted signal-like responses (noise) associated with the measurement process. There is an inherent noise associated with any photon-detection process, and this sets an upper limit to performance by any criteria. Additional noise sources are always present, to one degree or another, and must also be accounted for. We assume here that all noise sources result from random ergotic processes and are all statistically independent of each other. This, with the linearity assumption, allows us to describe the output scene as a superposition of the target scene, in spatial frequency coordinates, and the "noise" in terms of its noise power spectrum. Then, if we know the transfer function of the final information processor (human operator, target tracker, etc.), and its criteria for "success," we can calculate final performance in terms of those criteria.

By definition, the noise power spectrum is the Fourier transform of the noise autocorrelation function, so its integration over all spatial frequencies is the output mean square variance. The square root of this, expressed in temperature units, is then a sort of display noise equivalent temperature. It also is possible to calculate a noise equivalent temperature (NET) by normalizing the rms noise at some node in the signal-processing subsystem, but, except for simple cases, these two temperature noises will not be the same. Clearly the "electrical" NET is only useful in assessing the relative performance of systems of very similar design. Nevertheless, NET is commonly used (and misused) as a relative measure, so we examine it for a case where it is closely related to display performance. In addition, we also gain other important systems parameters.

2.3.2.1 Single-Detector NET. Consider a single-element serial system scanning a target scene consisting of a single large object of emissivity $\varepsilon(\lambda)$ and temperature T, on a uniform blackbody background at temperature T_0. The resulting continuous analog output signal amplitude in volts is then

$$v_s = \left[\frac{A_D}{4(f/\#)^2}\right] \int_{\lambda_1}^{\lambda_2} \Delta M_e(\lambda)\tau_A(\lambda)\tau_o(\lambda)R(\lambda)\, d\lambda \ , \tag{2.33}$$

where

$$\Delta M_e(\lambda) = \varepsilon(\lambda)M_e(\lambda,T) - M_e(\lambda,T_0) \tag{2.34}$$

A_D = detector area
$\tau_A(\lambda)$ = atmospheric transmission
$\tau_o(\lambda)$ = optical system transmission
$R(\lambda)$ = detector/preamp responsivity in V W^{-1}

and λ_1, λ_2 describe the integration spectral band.

Detector noise is traditionally specified in terms of its noise equivalent power, NEP, such that the total (wavelength-independent) noise V_n is

$$V_n = R(\lambda)\text{NEP}(\lambda) \ . \tag{2.35}$$

Also, a normalized noise measure D^* is defined to be

$$D^*(\lambda) = \frac{(A_D \Delta f)^{1/2}}{\text{NEP}(\lambda)} \ , \tag{2.36}$$

where Δf is the electrical bandwidth over which the rms noise V_n is measured. Then, using Eqs. (2.33), (2.35), and (2.36), we have, for the signal-to-noise ratio,

$$\frac{S}{N} = \left[\frac{1}{4}\left(\frac{A_D}{\Delta f}\right)^{1/2}(f/\#)^{-2}\right]\int_{\lambda_1}^{\lambda_2}[\Delta M_e(\lambda)\tau_A(\lambda)][\tau_o(\lambda)D^*(\lambda)]\,d\lambda \ . \tag{2.37}$$

Relation (2.37) can be considered sort of a master equation from which all subsequent NET analysis evolves. This analysis can be done in a number of ways, all of which ultimately lead to the same result. We proceed in a special way as follows.

We can interpret S/N as the result of multiplying a source term I_S by a response factor I_R. That is,

$$\frac{S}{N} = I_R I_S \ , \tag{2.38}$$

where

$$I_R = \left[\frac{1}{4}\left(\frac{A_D}{\Delta f}\right)^{1/2}(f/\#)^{-2}\right]\int_{\lambda_1}^{\lambda_2} M'_e(\lambda)\tau_o(\lambda)D^*(\lambda)\,d\lambda \ , \tag{2.39}$$

$$I_S = \frac{\displaystyle\int_{\lambda_1}^{\lambda_2}\tau_A(\lambda)D^*(\lambda)\Delta M_e(\lambda)\,d\lambda}{\displaystyle\int_{\lambda_1}^{\lambda_2} M'_e(\lambda)D^*(\lambda)\,d\lambda} \ , \tag{2.40}$$

$$M'_e(\lambda) = \left[\frac{\partial M_e(\lambda,T)}{\partial T}\right]_{T=T_0} \ . \tag{2.41}$$

Now, the source term I_S has the units of temperature, so it is natural to define FLIR input signal in terms of an equivalent temperature differential. The response factor I_R must have the units of inverse temperature, so the reciprocal of I_R must be some sort of equivalent temperature noise. We thus define the spot noise NET_s as the reciprocal of I_R.

Then, defining

$$\tau_o = \frac{\int_{\lambda_1}^{\lambda_2} [M'_e(\lambda)D^*(\lambda)]\tau_o(\lambda)\, d\lambda}{\int_{\lambda_1}^{\lambda_2} M'_e(\lambda)D^*(\lambda)\, d\lambda} , \tag{2.42}$$

$$D^*_{BB} = \left(\frac{1}{4\sigma T_0^3}\right)\int_{\lambda_1}^{\lambda_2} M'_e(\lambda)D^*(\lambda)\, d\lambda , \tag{2.43}$$

we have

$$\mathrm{NET_s} = \left(\frac{\Delta f}{A_D}\right)^{1/2} \frac{(f/\#)^2}{\sigma T_0^3 \tau_o D^*_{BB}} . \tag{2.44}$$

This is a central result and expresses single-element temperature noise in a generalized standard form. The term defined by Eq. (2.42) is the effective optics transmission, and the term defined by Eq. (2.43) is called the blackbody D^*.

The standard definition of NET is that blackbody temperature difference required to produce an S/N of one, over a reference bandwidth, with unity atmospheric transmission. For a blackbody and unity τ_A, we have

$$I_s = \Delta T_0 , \tag{2.45}$$

where ΔT_0 is the true, thermodynamic temperature difference between the target and its background. Therefore, the standard NET is just the $\mathrm{NET_s}$ defined by Eq. (2.44) evaluated at a reference bandwidth Δf_R. This reference bandwidth is usually defined as

$$\Delta f_R = \left(\frac{\pi}{2}\right)\left(\frac{1}{2t_D}\right) , \tag{2.46}$$

where t_D is the detector dwell time, defined as the time required for it to scan a distance equal to its size in the scan direction. For a scanning system this would be

$$t_D = \frac{\Delta\theta}{V_s} , \tag{2.47}$$

where $\Delta\theta$ is the IFOV and V_D is the element scan speed in milliradians per second. Therefore, by definition, the standard NET for a single detector is

$$\mathrm{NET} = \mathrm{NET_s}\Delta f_R , \tag{2.48}$$

with $\mathrm{NET_s}$ given by Eq. (2.44).

Returning now to the source function I_S, it is convenient to define an effective temperature difference ΔT with respect to atmospheric transmission averaged over the spectral bandpass τ_A. That is,

$$I_s = \tau_A \Delta T \tag{2.49}$$

Now, it can be shown that for a background-limited intrinsic photodetector (BLIP),

$$D^*(\lambda) = \eta^{1/2}(\lambda)\left(\frac{\lambda}{hc}\right)E_q^{-1/2} , \tag{2.50}$$

where $\eta(\lambda)$ is the detective (solid-state) quantum efficiency and E_q is the incident photon irradiance in photons s^{-1} cm^{-2}. Most usable detectors at least have this functional form, and Eq. (2.49) can be used by simply scaling η down accordingly to reflect the actual S/N compared to BLIP performance. Then, if η, ε, and τ_A are all slowly varying across the spectral band, we have for small ΔT_0

$$\Delta T \cong \left(\frac{M}{M'}\right)\Delta\varepsilon + \varepsilon\Delta T_0 , \tag{2.51}$$

where

$$M = \int_{\lambda_1}^{\lambda_2} M_q(\lambda)\, d\lambda , \tag{2.52}$$

$$M' = \int_{\lambda_1}^{\lambda_2} M_q'(\lambda)\, d\lambda . \tag{2.53}$$

That is, M is the total photon irradiance and M' is its partial derivative with temperature. The approximation here is quite good in most cases and at least shows the relative importance of emissivity. The ratio M/M' in Eq. (2.51) is about 30 for LWIR and 54 for MWIR, so emissivity variations are important.

2.3.2.2 Generalized Sensitivity Analysis. The standard NET described above is specifically defined for a single-element system, and it is certainly not clear how it relates to displayed noise performance. In fact, there is no reason to assume that the true system noise bandwidth is equal to the reference bandwidth Δf_R used in measuring, or calculating, NET. Also, it is not clear how the concept should be extended for complex focal-plane-array systems of many detectors with overlapping detector scan lines and sampling intervals smaller than the dwell time t_D. For a pure parallel system (one contiguous column of detectors aligned vertically and scanned horizontally, or vice-versa) the extrapolation is straightforward because the detector dwell time is increased by the number of detectors. The reference bandwidth, and hence NET, is thus

reduced by a factor of $N^{1/2}$. One can also argue that for a serial system of N detectors (all aligned in the scan direction), the effect of time delay and integrate (TDI) is to increase the effective system D^* by a factor of $N^{1/2}$. The effect of adding more detectors is the same in both cases, so more detectors should result in more "displayed sensitivity," all else being equal, regardless of the focal-plane arrangement. This is indeed the case, as will become apparent in the following. The key is to develop a generalized expression for the noise power spectrum in two-dimensional display-plane coordinates. This is the ultimate analytical tool to determine the performance of any information processor with a known transfer function and a success criteria. In addition, any number of summary "displayed noise" figures of merit can be unambiguously defined by integrating the noise power spectrum over the corresponding two-dimensional display space bandwidth.

To proceed, it is expedient to first abandon the approach of describing detector performance in terms of D^* in favor of expressing it in terms of photon counting. Quantum detectors respond to photon flux, not power, and the traditional D^* formalism is both cumbersome and unnecessary.

2.3.2.3 Detectors as Photon Counters. Because of the statistical nature of a blackbody radiation field, there is an uncertainty in the number of photons within any given volume. The determination of this is relatively straightforward and is found in numerous texts dealing with quantum statistical mechanics. For infrared wavelengths the rms variation in any photon-counting process is equal to the average number counted. In other words, if $\overline{N}$ is the average value of a large number of individual counts,

$$\overline{\delta N^2} = \overline{N} \ . \tag{2.54}$$

Thus, the small signal-to-noise ratio of any IR detection process cannot exceed

$$\left(\frac{S}{N}\right)_0 = \frac{\Delta N_s}{N_B^{1/2}} \ , \tag{2.55}$$

where ΔN_s is the signal count and N_B is the number of background photons counted. It is therefore convenient to think of IR detectors, plus their intimately associated integrating circuits, as photon counters. Then, their performance can be described as

$$\left(\frac{S}{N}\right)_{\text{actual}} = \eta_D^{1/2}\left(\frac{\Delta N_s}{N_B^{1/2}}\right) = \eta_D^{1/2}\left(\frac{S}{N}\right)_0 \ , \tag{2.56}$$

where we define η_D by Eq. (2.56) and refer to it as the detector efficiency. For a BLIP detector, η_D is equal to the quantum efficiency, and it can be shown that Eq. (2.56) leads directly to the D^* expression (2.49).

2.3.2.4 Display Noise Power Spectrum. Consider an array of N detectors arranged in any geometrical format and scanned, or stepped, or jumped about the focal-plane area in any manner that results in uniform coverage. Then it is conceivable that a signal-processing subsystem can be configured to sort all

this out and produce a displayed image correctly corresponding to the focal-plane image. The normalized transfer function for the image will be the entire system MTF, and the noise power spectrum can be written as

$$G(f_x,f_y) = G_0 a^2(f_x,f_y) \quad [^\circ\mathrm{C}^2\ \mathrm{mrad}^2] \ , \tag{2.57}$$

where $a(f_x,f_y)$ is the normalized transfer function of all elements following the point of noise insertion. This function is essentially determined by the product of the processor and display MTF. In any event, the integral of a^2 over all spatial frequencies is inversely proportional to the area over which the noise is reasonably correlated, and this area will always be less than the resolution area.

Now, consider the signal-to-noise ratio that would result from averaging over the entire display. For a rectangular display of dimension $\phi_x \times \phi_y$, the transfer function for this averaging process would be

$$\mathrm{TF}(f_x,f_y) = \mathrm{sinc}(\pi f_x \phi_x)\ \mathrm{sinc}(\pi f_y \phi_y) \ , \tag{2.58}$$

so the noise must be

$$\overline{\delta T_F^2} = G_0 \int_{-\infty}^{\infty}\int_{-\infty}^{\infty} a^2(f_x,f_y)\mathrm{TF}^2(f_x,f_y)\, df_x\, df_y \ , \tag{2.59}$$

but TF is so sharply peaked about the origin compared to $a(f_x,f_y)$ for any usable system design that Eq. (2.59) reduces to

$$\overline{\delta T_F^2} = (\phi_x\phi_y)^{-1} G_0^{-1} \tag{2.60}$$

for anything that could be considered an imaging system. The display average S/N is then

$$\left(\frac{S}{N}\right)_F^2 = (\phi_x\phi_y)(\overline{\Delta T})^2 G_0^{-1} \ . \tag{2.61}$$

But, from the viewpoint of photon counting, this must be inversely proportional to the total number of background photons counted N_{BT} by all detectors over the entire frame time τ_F. Then, since

$$\Delta N_{\mathrm{ST}} = \sum_{i=1}^{N_1}\left(\frac{\partial N_S}{\partial T}\right)\Delta T_i = N\left(\frac{\partial N_S}{\partial T}\right)\overline{\Delta T} = \left(\frac{\partial N_{\mathrm{ST}}}{\partial T}\right)\overline{\Delta T} \ , \tag{2.62}$$

where ΔN_{ST} is the total signal count, it must be that

$$\left(\frac{S}{N}\right)_F^2 = \eta_D N_{\mathrm{BT}}^{-1}\left(\frac{\partial N_{\mathrm{ST}}}{\partial T}\right)^2 (\overline{\Delta T})^2 \ . \tag{2.63}$$

Thus,

$$G_0 = \eta \bar{D}^1(\phi_x \phi_y)\left[\left(\frac{\partial N_{ST}}{\partial T}\right)^{-2} N_{BT}\right] . \tag{2.64}$$

Now,

$$\frac{\partial N_{ST}}{\partial T} = \frac{\tau_o}{4(f/\#)^2} M_q' N A_D \varepsilon_S \tau_F , \tag{2.65}$$

$$N_{BT} = \frac{1}{4(f/\#)_{cs}^2} M_q N A_D \varepsilon_S \tau_F , \tag{2.66}$$

where $(f/\#)_{cs}$ is the equivalent cold shield $f/\#$ and ε_S is the scanner efficiency.

Then, if we adopt the convention that D_o is always to be regarded as a dimensionless quantity numerically equal to the effective optics aperture in inches and that G_0 is to be scaled to $°C^2$ mrad^2, then, by straightforward manipulation of terms, it can be shown that

$$G_0 = (\eta_s D_o)^{-2} \mathrm{NET}_0^2 \quad [°C^2 \text{ mrad}^2] , \tag{2.67}$$

where

$$\mathrm{NET}_0 = \left(\frac{7.87 \cdot M_q^{1/2}}{M_q' \tau_F^{1/2}}\right) , \tag{2.68}$$

$$\eta_s = \tau_o \varepsilon_s^{1/2} \eta_{cov}^{1/2} \eta_{cs}^{1/2} \eta_D^{1/2} = \text{system efficiency} , \tag{2.69}$$

$$\eta_{cov} = \frac{N A_D}{A_{FP}} = \frac{\text{total detector area}}{\text{focal-plane area}} , \tag{2.70}$$

$$\eta_{cs} = \frac{(f/\#)_{cs}^2}{(f/\#)^2} = \text{cold-shield efficiency} , \tag{2.71}$$

and

τ_o = optics transmission
ε_s = scan/shutter efficiency
η_D = effective detector efficiency.

The expression for G_0, Eq. (2.67), is a central result. It expresses the magnitude of the display noise power spectrum in a remarkably simple form, completely independent of the manner of operation of the system. The parameter NET_0 depends only on the spectral band employed, the ambient temperature T_0, and the frame time τ_F (normally taken as 1/30 s). The numerical factor here converts inches to cm and scales the spectrum to mrad^2. This fundamentally important parameter is shown as a function of temperature for both LWIR and MWIR in Fig. 2.12.

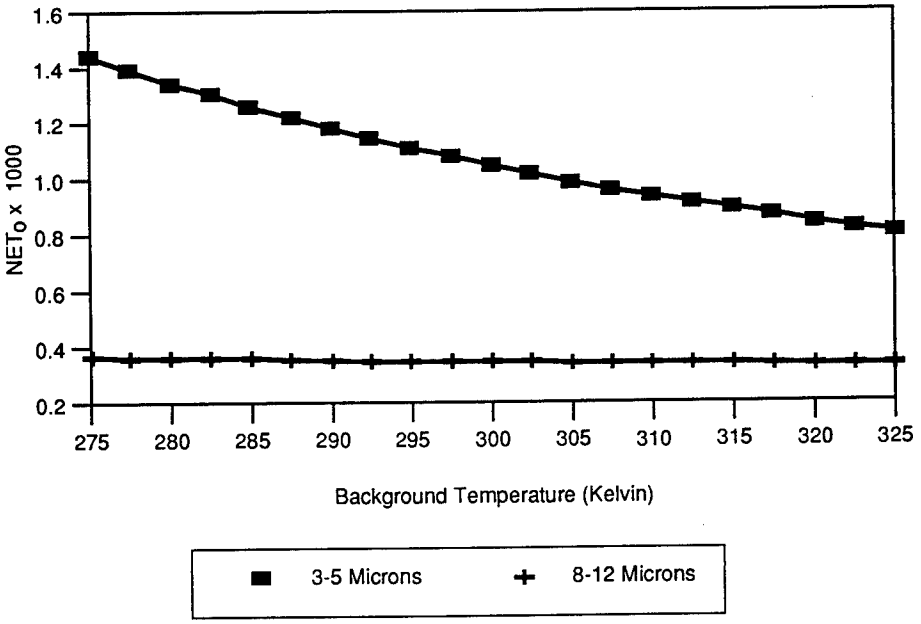

Fig. 2.12 NET_0 versus temperature for MWIR and LWIR. The noise factor NET_0 depends on the spectral region and the background temperature. Note that the value for MWIR is three times greater at 300 K and far more temperature dependent than LWIR. A τ_F of 0.033 is used in the above.

The aperture term D_o is dimensionless and is numerically equal to the optics aperture in inches, as stated. The system efficiency η_s is the product of the five component terms. The new term, η_{cov}, describes the only impact on sensitivity of the number, and area, of the detectors as the ratio of total detector area to the focal-plane area. At any given instant, only this fraction of the total focal-plane irradiance can be detected. The upper limit of this is unity, as it would be for a staring, contiguous array. The optics transmission is the only linear term in Eq. (2.69) because it only affects signal photon count, and not background count. All other terms affect both.

The displayed mean-square variance is thus

$$\overline{\delta T_D^2} = (\eta_s D_o)^{-2} \mathrm{NET}_0^{-2} \int_{-\infty}^{\infty} \int_{-\infty}^{\infty} a^2(f_x, f_y)\, df_x, f_y$$

$$= (\eta_s D_o)^{-2} \mathrm{NET}_0^{-2} \Delta f_s \ , \tag{2.72}$$

where Δf_s is the displayed noise bandwidth. Then, a system term analogous to the electrical term previously discussed, NET_s, is

$$\mathrm{NET}_s^* = [\eta_s^{-1} (D_o^{-1} \Delta f_s^{1/2})] \mathrm{NET}_0 \ . \tag{2.73}$$

A reference bandwidth analogous to that used to define the electrical NET is

$$\Delta f_{SR} = \Delta\theta^{-2} \ , \tag{2.74}$$

where $\Delta\theta$ is the detector IFOV in the scan direction expressed in milliradians.

Then, a meaningful and unambiguous summary noise measure is

$$\text{NET}^* = \eta_s^{-1}(D_o\Delta\theta)^{-1}\text{NET}_0 \ . \tag{2.75}$$

This term is consistent with the original intent of the electrical channel NET. In fact, except for the unnecessary $\pi/2$ factor, it is equal to the electrical NET for a simple serial system with no overlapping scan.

NET* is an easily determined summary noise measure, valid for any system, and is very useful in system design trade-offs.

2.3.3 System Performance Perturbations

In the preceding we have tacitly assumed mathematical linearity, white noise sources, and stationary input scenes. Real systems, however, must process moving scenes, will introduce coherent noise to some degree, and are not mathematically linear. The approach here is to regard these factors as perturbations to the ideal. The system model described so far can be regarded as a first-order term in some sort of Taylor series expansion of the real case. This term is the limit of performance as the perturbations approach zero. Well-designed systems approach this limit quite closely, and in this section we discuss the requirements on these perturbations that make this true.

2.3.3.1 Sampling. Any imaging system utilizing a detector array of discrete elements is inevitably sampled in at least one dimension. The very act of sensing the input scene in a line raster pattern assures this in the cross-line direction even if a continuous detecting medium is used. Large parallel-system focal-plane arrays are also multiplexed in the scan direction, so they are sampled in both dimensions. The effect of sampling is that spatial-frequency components can be introduced into the output spectrum that were not in the input. The consequences of this depend on the input scene and on the system MTF components both before and after the sampling process. As such, there is no known unique sampling effects performance measure. However, it is possible to examine a simple case and determine the general sampling requirements for a FLIR.

Consider a one-dimensional object-plane scene characterized by its Fourier transform $A_{OP}(f)$. The image-plane distribution $A_{IP}(f)$, is then

$$A_{IP}(f) = \text{MTF}_L(f)A_{OP}(f) \ , \tag{2.76}$$

where MTF_L is the transfer function of the entire IR lens system (diffraction and design blur). Let this function be sampled by a detector of width $\Delta\theta$ at equal intervals spaced $\Delta\theta$ apart. Then, it can be shown that the Fourier transform of the system output is related to the input by

$$A_s(f) = a(f) \sum_{l=-\infty}^{\infty} A_0(f - lf_s) \ , \tag{2.77}$$

where

$$A_0(f) = \left[\frac{\sin(\pi f \Delta\theta)}{\pi f \Delta\theta}\right] \mathrm{MTF}_L(f) A_{\mathrm{OP}}(f) \tag{2.78}$$

and f_s is the sampling frequency, given by

$$f_s = \frac{1}{\Delta\theta_s} \,. \tag{2.79}$$

The first three terms of Eq. (2.77) are

$$A_s(f) = a(f)[A_0(f) + A_0(f - f_s) + A_0(f + f_s)] \tag{2.80}$$

and it is noted that unless $A_0(f)$ is zero for frequencies greater than $\frac{1}{2} \cdot f_s$, the terms will overlap, resulting in output components that were not in the input spectrum. This overlapping is referred to as aliasing, and the critical frequency limit, $\frac{1}{2} \cdot f_s$, is called the Nyquist limit. Figure 2.13 is a plot of Eq. (2.80) for three different values of f_s.

Linear reproduction requires both prefiltering of the input scene at the Nyquist limit to eliminate aliasing and postfiltering after sampling to remove all the sideband terms ($l \neq 0$). We note that the lens and detector act as prefilters and that the electronics and display act as postfilters. For typical aperture sizes the input prior to sampling would be essentially zero beyond the detector cutoff frequency, $1/\Delta\theta$. Then, no aliasing of any consequence would occur if the sample interval is $\Delta\theta/2$, and this is said to be 2 to 1 oversampling. Experience has shown, however, that if the oversampling is at least 1.5 to one, the system can be regarded as continuous out to one-half the sampling frequency. However, since a staring system is sampled one to one, caution must be exercised in predicting performance based on linear analysis. Scene motion, or displacing the array a half element every other frame, helps alleviate this problem.

Perfect postfiltering would require that the term $a(f)$ go to zero sharply at $\frac{1}{2}$ the sample frequency, but this is rarely done. This is usually of no consequence to a machine interface; it is primarily a cosmetic factor to a human (if the sampling rate is sufficient for aliasing) and is not a major distraction at normal viewing angles.

2.3.3.2 Scene Motion. A framing system integrates each point in the input scene, in time, over a finite interval, and samples this once per frame time. If there is scene motion, the input at any point varies in time, and the result will be an additional MTF effect due to smearing, or an amplitude aliasing effect, or a combination of the two. For a staring array integrating over most of the frame time, the effect is essentially smearing. For a scanning system, the integration is very small compared to a frame time, so there is essentially no smearing. However, the once-per-frame time sampling means that if the scene motion results in temporal frequencies greater than one-half the frame rate, temporal aliasing will occur. This results in artifacts in the output image. These range from asymmetrical shortening or broadening of objects to jagged

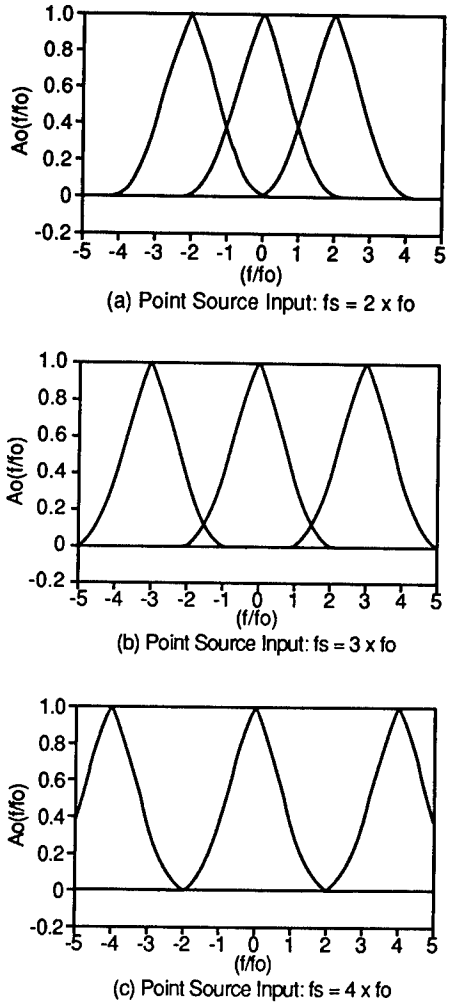

Fig. 2.13 The effects of sampling are determined by the amount of sideband overlap. This overlap decreases to almost zero at a sampling frequency four times the system reference.

edges to multiple images that seem to jump across the display. As a general rule, motions resulting in slight geometrical distortion or jagged edges can be tolerated with no significant impact on performance, but motions large enough to result in multiple images and/or jumping cannot. Experience with TV and motion pictures indicates that 30 frames per second is sufficient for most cases. However, high-speed maneuvering aircraft or missiles may well require frame rates of 60 Hz or higher to avoid scene motion effects.

2.3.3.3 Correlated Noise. Excess random white noise can be accounted for by a reduction in the effective detector efficiency. Power supply oscillations, clocking and timing pulse feedthroughs, etc., are deterministic, and not random. They may be stationary in time at the output or roll or drift through at a set rate. The effect of this is essentially cosmetic, with little, if any, impact on performance. The tolerable level depends on the spatial extent of this noise

and its rate of motion. Random correlated noise is the real problem, and it has two main sources: detector $1/f$ noise and fixed-pattern noise.

For a staring array, detector $1/f$ noise results in a random spatial pattern correlated in space over the detector angular subtense area, and correlated in time proportional to the $1/f$ corner frequency. If this $1/f$ corner is less than the frame time, there will be essentially no correlation from frame to frame, and the impact is the same as additional white noise. If the $1/f$ corner is appreciably greater than the frame rate, the effect is much worse than white noise, and such an array is not really usable. For a scanning system, the effect is not so great, but the $1/f$ corner requirement is the same. For any raster-line output format, the effect is almost complete correlation along a line and some correlation from line to line. If the $1/f$ corner is less than the frame rate, this noise can be removed by clamping each line to a fixed level. If it is greater than the frame rate, the removal by clamping will be incomplete, and the corresponding line-to-line noise pattern is very annoying to an operator and can cause serious problems in many other information processors. Again, the $1/f$ noise corners in excess of the frame rate generally are not usable for scanning systems either.

Fixed-pattern noise results from imperfect normalization of the detector dc offsets. For staring arrays this is a random spatial pattern fixed in time. It has the same effect as grain noise in a photograph and is a direct factor in effective sensitivity. To achieve detector random-noise limit, fixed-pattern noise must be reduced to at least one-third of the detector noise. This is difficult to do for efficient detectors, with the result that fixed-pattern-noise normalization for a staring array is usually the limiting noise. For scanning arrays, the pattern is fixed in time but varies in the cross-scan direction. Line clamping can significantly reduce this, so the effect here is much less than for staring arrays.

2.3.3.4 Dynamic Range. Dynamic range is defined as the useful peak-to-peak signal swing divided by the rms noise. For an amplifier, for example, this would be the maximum voltage output minus the minimum voltage output, divided by the system noise at this point. Every FLIR component, except perhaps the optics, has an instantaneous, finite, dynamic range of its own, and the total system result is the smallest of these. In the signal processor, this instantaneous value is determined by the gain, and this can be variable. A typical desired value for the total available dynamic range of a FLIR is 1000, or about 10 bits digital. This means that if the rms noise in the system output is 0.1 K, then a target temperature range of 100 K can be accommodated. On the other hand, the dynamic range of the display must be variable down to the point where system noise is clearly visible in order to reach the limit of system/operator performance, and this will typically be a dynamic range of about 10. That is, for a noise of 0.1 K, the display black-to-white transition will correspond to about 1 K. In this situation, many portions of the display will be saturated white, or black, and will contain no information, so we must ensure that the unsaturated portions are where we want them to be. This means that at some point in the processor there must be a node of higher dynamic range and that the display output can select any portion of this.

An additional consideration in this context is called dynamic-range enhancement. Large sections of the IR scene may well vary from one another in average temperature by 10 K or more. Then, by simple gain and level control, we could see detail in either area, but not necessarily at the same time. Several signal-processing schemes, such as level slicing and histogram modification, have been employed successfully to selectively adjust gain and level across the display according to the scene content at each location. This is really information processing, and the interested reader is referred to sources concerned with this topic.

2.3.4 Human Operator Interface

A human viewing any imaging sensor display can be considered as the endpoint information processor for the composite system. Then, as previously stated, if we know the transfer function of any information processor, and its criteria for success, we can calculate the probability of such a processor to perform any given task relative to those criteria. Unfortunately, for a human observer this is a very complicated problem, and the study of this is usually referred to as the psychophysics of vision. To date, no completely accurate model exists—and perhaps never will. Nevertheless, it is possible to incorporate three major characteristics into a simple model that at least gives approximate results for simple images and allows us to determine the system characteristics important for operator performance.

2.3.4.1 A Simple Model for a Human Operator. The three following major characteristics are assumed:

1. A human operator spatially integrates signals, and noise, over the extent of a target of interest in an optimum filter manner.
2. A human operator temporally integrates signals, and noise, over an effective time interval τ_E.
3. The probability of a human operator to detect, recognize, or identify a given object is a monotonically increasing function of the signal-to-noise ratio resulting after the above two integrations.

These assumptions are not specific with respect to the exact nature of the spatial and temporal transfer functions to be used in calculating the effective signal-to-noise ratio, nor is the probability function associated with the third assumption specified. It is in these details that all current theories differ, and the quest for more accuracy drives the evolving theoretical and experimental work in this field. The first assumption implies the simple fact that small objects are harder to see in low-contrast conditions than large objects and certainly corresponds to common experience. The second may be less obvious but can be made plausible by several simple experiments. Stopping a VCR on a single frame clearly shows an increase in displayed noise. Variable time exposure photographs of a noisy CRT display will show more (or less) apparent noise compared to viewing the screen directly and will appear *more or less* equivalent for an exposure time between 0.1 and 0.2 s, depending on the screen brightness. The implication here is that the human operator sets the composite system bandwidth, and not the sensor. In fact, aside from flicker and scene motion effects, operator sensitivity performance is independent of the sensor frame rate as long as it is appreciably greater than 10 or so frames per second.

2.3.4.2 Minimum Resolvable Temperature—MRT. A geometrical target of particular interest is a simple bar pattern of equal-sized bars and spacings. Perhaps surprisingly, there is a great deal of experimental evidence indicating a definite correlation between an operator's ability to detect, recognize, or identify a specific target (car, truck, tank, etc.) and the number of bars and spaces of a bar pattern of total angular dimensions equal to that of the target. Therefore, bar-pattern recognition itself has become the industry standard FLIR system/operator performance measure. Specifically, the system minimum resolvable temperature MRT is defined as the equivalent blackbody temperature difference between the bars and spaces of a standard MRT bar pattern required for an average operator to discern the presence on the display of this target. The standard pattern is four bars and three spaces (seven lines) of height equal to seven times the width of a bar or space (a 7:1 aspect ratio).

To derive an expression for MRT we must assume a specific functional form for the first model assumption. To this end we define an effective signal S to be the integral over one bar minus the integral over the adjacent space. That is, if ΔT_D is the two-dimensional displayed image, $\Delta\phi$ is a bar width, and $7\Delta\phi$ is its height,

$$S(\Delta\phi) = \int_{-7\Delta\phi/2}^{7\Delta\phi/2}\int_{-\Delta\phi/2}^{\Delta\phi/2} \Delta T_D \, dx \, dy - \int_{-7\Delta\phi/2}^{7\Delta\phi/2}\int_{\Delta\phi/2}^{3\Delta\phi/2} \Delta T_D \, dx \, dy \ , \tag{2.81}$$

where we have aligned the bar pattern along x and centered it at the origin. This corresponds to a spatial transfer function given by

$$\mathrm{TF}(f_x,f_y) = (7\Delta\phi^2)\{\mathrm{sinc}(\pi f_x\Delta\phi)[1 - \exp(j2\pi f_x\Delta\phi)]\}\ \mathrm{sinc}(7\pi f_y\Delta\phi) \ . \tag{2.82}$$

Now, we can very closely approximate the displayed system response to the MRT target by its response to a continuous bar pattern of the same spacing, $\Delta\theta$. We also note that since the bars are always seven times longer than their width, the system vertical MTF can be set equal to unity for this purpose. Thus, the displayed MRT pattern is well approximated near its center by

$$\Delta T_D = \frac{1}{2}\left\{1 + \left(\frac{4}{\pi}\right)\sum_{n=0}^{\infty}\left[\frac{(-1)^n}{2n+1}\right]\mathrm{MTF}_s\left(\frac{2n+1}{2\Delta\phi}\right)\cos\left(\pi\frac{x}{\Delta\phi}\right)\right\} \ , \tag{2.83}$$

where MTF_s is the MTF of the entire system. Then, using Eq. (2.81) we obtain

$$S(\Delta\phi) = (7\Delta\phi^2)\left(\frac{8}{\pi^2}\right)\sum_{n=0}^{\infty}\left(\frac{1}{2n+1}\right)^2\mathrm{MTF}_s\left(\frac{2n+1}{2\Delta\phi}\right) \ . \tag{2.84}$$

All terms in Eq. (2.84) for $n \geq 1$ are very small compared to the first for any $\Delta\phi$ of interest, and can be ignored. Therefore, we have, to good approximation,

$$S(\Delta\phi) \cong \left[\left(\frac{56\Delta\phi^2}{\pi^2}\right)\mathrm{MTF}_s\left(\frac{1}{2}\Delta\phi\right)\right]\Delta T \ . \tag{2.85}$$

We next assume that the observer temporal integration can be accounted for by scaling the system noise power spectrum by the ratio of the system frame time τ_F and the eye integration time τ_E. That is,

$$G_{\text{eff}} = \left(\frac{\tau_F}{\tau_E}\right)G \ , \tag{2.86}$$

where G is given by Eq. (2.67). We also note that the effect of Eq. (2.86) is to replace τ_F in Eq. (2.68) by τ_E, giving credence to the previous statement that the system frame time is really unimportant as long as it is small compared to τ_E. Then, with Eq. (2.86), the effective "noise" is

$$N^2(\Delta\phi) = \left(\frac{\tau_F}{\tau_E}\right)G_0\int_{-\infty}^{\infty}\int_{-\infty}^{\infty} a^2(f_x,f_y)\text{TF}^2(f_x,f_y,\Delta\phi)\, df_x\, df_y \ , \tag{2.87}$$

where TF is given by Eq. (2.82), and a^2 is the MTF^2 of all elements following the system noise insertion. We also note that if the system noise sources are not all white, they can be included in a^2.

Using Eq. (2.82) we can write

$$\begin{aligned}\text{TF}^2(f_x,f_y,\Delta\phi) = {} & (14\Delta\phi)^2[\text{sinc}^2(\pi f_x\Delta\phi) - \text{sinc}^2(2\pi f_x\Delta\phi)] \\ & \times \text{sinc}^2(7\pi f_y\Delta\phi) \ .\end{aligned} \tag{2.88}$$

Then, with this and Eq. (2.86),

$$N^2(\Delta\phi) = (14\Delta\phi^2)\left(\frac{\tau_F}{\tau_E}G_0\right)Q \ , \tag{2.89}$$

where

$$Q = (14\Delta\phi^2)\int_{-\infty}^{\infty}\int_{-\infty}^{\infty} a^2(f_x,f_y)\text{TF}^2(f_x,f_y,\Delta\phi)\, df_x\, df_y \ . \tag{2.90}$$

Now, from the third model assumption, MRT is that value of ΔT required to make the effective signal-to-noise ratio equal to some required value, K. Thus, using Eqs. (2.85) and (2.89),

$$\text{MRT}(\Delta\phi) = (0.12K\tau_E^{-1/2})\left(\frac{G_0Q}{\Delta\phi^2}\right)^{1/2}\left[\text{MTF}_s\left(\frac{1}{2\Delta\phi}\right)\right]^{-1} \ , \tag{2.91}$$

where in the above we have set τ_F to the normally standard value of 1/30 s.

In FLIR system design and component trade-off analysis, it is convenient to express MRT in terms of normalized spatial frequency. If we define

$$f_T = \frac{1}{2}\Delta\phi \tag{2.92}$$

and

$$f_0 = \frac{1}{2}\Delta\theta \ , \tag{2.93}$$

then

$$\frac{f_T}{f_0} = \frac{\Delta\theta}{\Delta\phi} \ , \tag{2.94}$$

and Eq. (2.91) becomes

$$\mathrm{MRT}(f_T) = K'\mathrm{NET}^*\left(\frac{f_T}{f_0}\right)\left[\mathrm{MTF}_s\left(\frac{f_T}{f_0}\right)\right]^{-1} Q^{1/2} \ , \tag{2.95}$$

where

$$K' = 0.12K\tau_E^{-1/2} \tag{2.96}$$

and NET* is the previously defined integrated noise figure given by Eq. (2.75) with $\tau_F = 1/30$ s. The simplicity of Eq. (2.95) depends on this choice of NET. If the electrical NET were used in an expression like (2.95), the new factor corresponding to K' would depend on the details of system operation.

The value of K' can be determined by laboratory measurements with the result that

$$\mathrm{MRT}\left(\frac{f_T}{f_0}\right) = 0.7\left(\frac{f_T}{f_0}\right)\left[\frac{\mathrm{NET}^*}{\mathrm{MTF}_s(f_T/f_0)}\right]Q^{1/2} \ . \tag{2.97}$$

This function is plotted in Fig. 2.14 for an NET* of 0.07°C, the system MTF plotted in Fig. 2.10, and Q set equal to unity.

The validity of the particular model used is indicated by the accuracy with which it predicts laboratory measurements. If the factor Q (e.g., 90) is carefully calculated at each target frequency f_T, then Eq. (2.97) gives good results from about 0.5 to 1.5 f_0, but tends to be somewhat large at frequencies above f_0 and low for frequencies below f_0. There is little doubt that the assumed model is too simple to represent a real observer in all circumstances. We also note that Q is equal to unity if $a^2(f_x,f_y)$ is unity over a frequency range much larger than f_T. If the system noise is predominately white and if $a^2(f_x,f_y)$ decreases with frequency, then Q decreases with increasing frequency. Therefore, the factor Q is often conservatively set equal to one in FLIR component trade-off analyses. In the general case, the Q factor is determined by performing the integral (2.90). Figure 2.15 is a plot of the integrand of Eq. (2.90) for three different values of $\Delta\phi$ corresponding to f_T equal to ½ f_0, f_0, and ³⁄₂ f_0. Here, the function $a(f_x,f_y)$ is simply set equal to unity out to 2 f_0 and to zero beyond that.

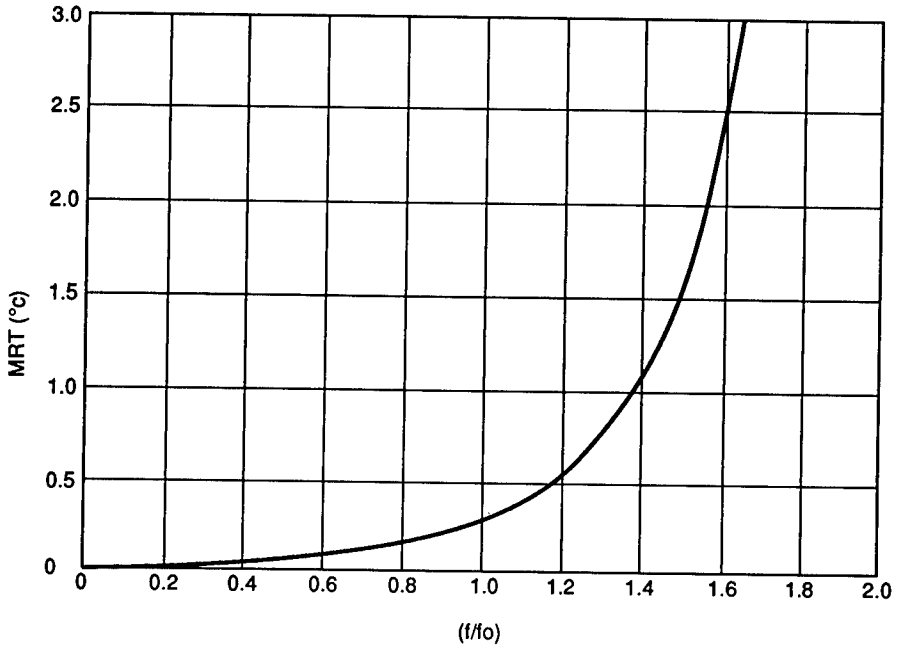

Fig. 2.14 A typical MRT curve for a system with a relative aperture $A_R = 0.7$ and NET* = 0.14°C. MRT tends to infinity as (f/f_0) approaches 2.0.

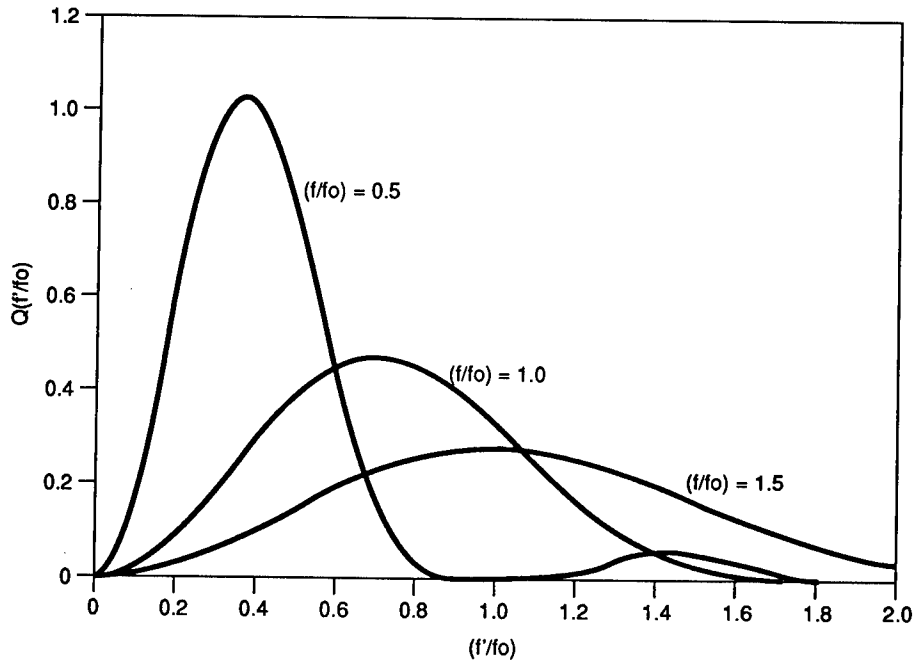

Fig. 2.15 The Q factor in MRT is determined by integrating $Q(f)$ over all frequencies. If $\alpha^2(f)$ is flat to decreasing, Q is a very weak function of the target frequency.

2.4 SYSTEM DESIGN REQUIREMENTS

FLIR system requirements can be grouped into three general categories. The first, which can be referred to as image quality, is related to how well the general appearance of the imagery compares with most user's expectations. The second group, which can be referred to as field performance, is related to the system's ability to provide the information required to perform its intended function. The final category can be called resource cost and includes such factors as size, weight, power, reliability, and the total cost of system ownership. All three categories are interrelated and conflicting, and the essence of good system design is the balancing of these conflicts according to the priority of the requirements.

2.5 IMAGE QUALITY

By its very nature this is obviously a subjective area, and it is actually far easier to describe a poor image in quantitative terms than a good one. We are thus reduced to discussing things we do not want and quantifying positive factors by similarity and experience. A standard "excellent" image would contain a more or less continuous distribution of gray scales from black to white, a total absence of any spurious signals, uniform response with no shading, no discernible random noise, and crisp, clean lines and edges.

The first factor requires the existence of some mode within the system electronics capable of providing large voltage swings compared to the total system noise at that point, i.e., a high dynamic range. This is normally designed to be at least 1000/1. In addition, we must also provide manual, or automatic, gain and level control to select the best section of this signal spectrum for ultimate display. It should be noted that this cannot be done effectively by adjusting the display contrast and brightness controls. These controls must be set so that reference video zero corresponds to solid black, and reference video one corresponds to the maximum useful white. There is thus only one correct setting for these controls, and proper use of the display requires gain and level control of the input signal to the display. In broadcast TV this is done by the broadcast studio in the setup of its transmitted signal, and in the automatic gain control circuitry in the receiver/display. A FLIR must provide this function prior to the display.

Spurious signals and uniformity were previously discussed and there is little to add. Observers are particularly intolerant of lines or spots fixed (or slowly varying) in space or time and unrelated to the underlying scene. This has the appearance of viewing imagery through a dirty window. The degree of this depends on the IR gain setting, and to eliminate it at the highest gain level requires that all such artifacts be reduced to about 1/6 the system noise. Observers are far more tolerant of scene-dependent nonuniformities in IR imagery than in visible scenes, because no one knows, *a priori,* what an IR scene should look like. These errors result from responsivity (gain) variations and show up primarily as fictitious internal structure in extended uniform objects; this is tolerable as long as it is restricted to 10% or so variation from the mean.

The receptors in the human eye are themselves photon counters, so there is always a signal-to-noise ratio associated with viewing a display even if it

is driven by an essentially noise-free signal. This sets the ultimate limit to the size and contrast of visible objects that can be seen. But, when viewing visible scenes directly, we do not perceive imagery getting noisier and noisier as the external illumination goes down. Objects just start to disappear. When viewing a display driven by a noisy source, we definitely perceive this noise, but do so as an irrelevant, masking, signal. The condition then for noise-free imagery is that this noise "signal" be unresolvable to the observer, and this requires a system display drive signal-to-noise ratio of at least 30/1. This depends on both the maximum temperature variation in that portion of the IR scene of interest and the system noise parameter NET*. Therefore, to maximize the probability of providing noise-free imagery under a wide variety of scene temperature variations and atmospheric conditions, the NET* should be as low as practical. This is often in conflict with field performance requirements, which may favor a trade-off that increases NET* to improve resolution. On the other hand, the ability to perceive extended, low-level, terrain features is important for orientation and general utility. As a result, a rule of thumb is to keep NET* less than 0.15°C for short-range (<2 km) applications and less than 0.07°C for longer-range applications.

The perception of image sharpness is directly related to the degree to which the displayed imagery is limited by the MTF of the eye. Even the highest-quality photograph, with thousands of lines per inch, will eventually become blurred if magnified enough. No image can appear sharp unless it is eye limited. Thus, to ensure sharpness one need only to sufficiently reduce the display size or increase the viewing distance. But, this is clearly at the expense of information transfer, for much detail in the imagery is lost. The rule of thumb here is to maintain the system MTF at the reference frequency, $f_0 = \frac{1}{2}\Delta\theta$, to at least 0.25.

2.6 FIELD PERFORMANCE

The fundamental basis of user performance requirements is to be able to see a certain level of detail at a given distance. Usually, this is stated as a need to detect, recognize, or identify certain objects. A security surveillance application may only need to detect the presence of human intruders at a few hundred meters. At the other extreme, an aircraft fire-control system may need to identify a tank as friend or foe at a range of several kilometers. Spatial resolution is clearly a key parameter, but, considering the finite thermal contrast of targets, atmospheric transmission, and the inevitable noise associated with the photon-detection process, system noise is also important. The connection between the two can almost always be made by determining the required MRT function. This task is really one of operational analysis rather than system design and is usually done by specific analyses, extrapolations of similar successful implementations, computer simulations, or combinations of these.

Therefore, to concentrate on system aspects, we assume that our field performance task is to recognize an MRT-type target of temperature ΔT, at a range R, and at a specified atmospheric transmission. We also assume that the atmospheric transmission can be expressed by an effective extinction coefficient β such that the target temperature ΔT_A available to the system is given by

$$\Delta T_A = \Delta T e^{-\beta R} \ . \tag{2.98}$$

Now, since the aspect ratio for an MRT target is 7:1, one bar subtends an angle of

$$\Delta\phi = \frac{S}{7R} \ , \tag{2.99}$$

and the target frequency is

$$f = \frac{1}{2}\Delta\phi = \left(\frac{3.5}{S}\right)R \ . \tag{2.100}$$

Then, defining R_0 by

$$R_0 = \frac{S}{7\Delta\theta} \ , \tag{2.101}$$

we have

$$\frac{f}{f_0} = \frac{\Delta\theta}{\Delta\phi} = \frac{R}{R_0} \ . \tag{2.102}$$

Therefore, since the temperature required to resolve the target is the MRT at the target frequency, it must be that

$$\Delta T e^{-\beta R} = \mathrm{MRT}\left(\frac{R}{R_0}\right) \ . \tag{2.103}$$

Relation (2.103) is the fundamental expression for determining recognition range for a given system. This can be done by simultaneously plotting both sides of Eq. (2.103) as a function of R and noting that the intersection is the value of R that makes them equal; this is graphically represented in Fig. 2.16. We note that the factor translating target frequency to range is R_0. That is, in plotting the system MRT curve, stated in terms of f/f_0, we scale the ordinate to range R by

$$R = R_0\left(\frac{f}{f_0}\right) \tag{2.104}$$

and thus anticipate that R_0 will be a dominant factor in determining recognition range.

The graphical procedure described above is only useful in determining the range performance of a specific system. What is needed for trade-off analyses is a closed expression relating range to system parameters. To this end we note that if $a^2(f)$ is a monotonically decreasing function of f, we can approximate MRT by

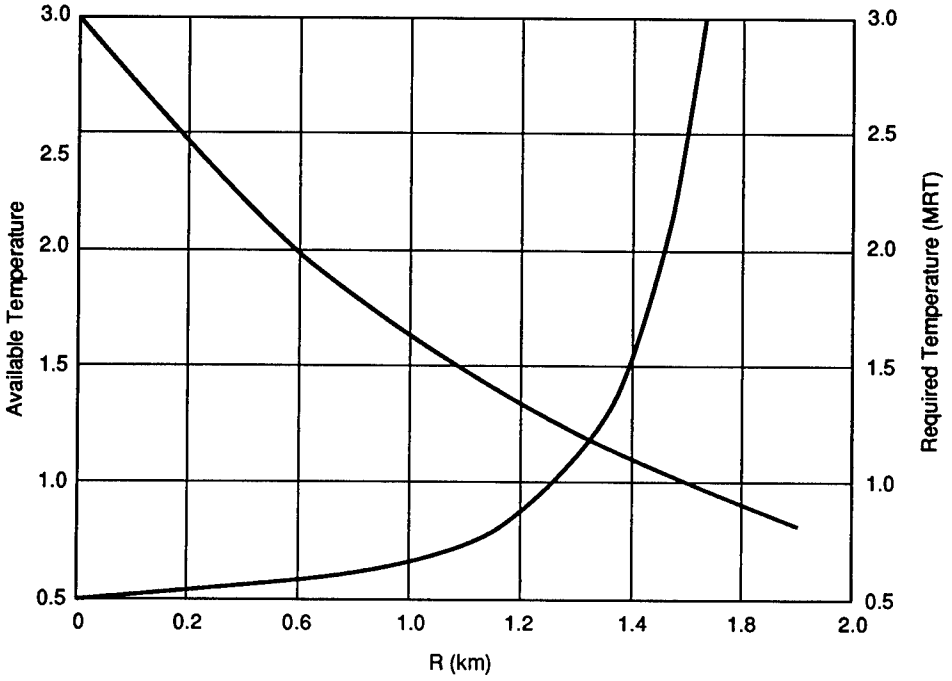

Fig. 2.16 The recognition range of an MRT-type target can be determined by the intersection of the available ΔT and the required ΔT—the system MRT. The MRT curve is shown for a system $A_R = 0.7$ and NET* = 0.14°C. The atmospheric extinction coefficient used is 0.4 km^{-1}.

$$\mathrm{MRT}\left(\frac{R}{R_0}\right) \cong 0.7\mathrm{NET}^*\left(\frac{R}{R_0}\right) \exp\left[\alpha\left(\frac{R}{R_0}\right)^2\right] , \tag{2.105}$$

with

$$\alpha = -\ln \mathrm{MTF}_s(1) . \tag{2.106}$$

Then, defining

$$\gamma = \frac{\Delta T}{0.7\mathrm{NET}^*} \tag{2.107}$$

and using Eq. (2.105) in (2.103), we can write

$$\ln\gamma - \beta R = \ln\left(\frac{R}{R_0}\right) + \alpha\left(\frac{R}{R_0}\right)^2 . \tag{2.108}$$

Then, expanding the logarithm about $R/R_0 = 1$, we have, to two terms,

$$\ln\left(\frac{R}{R_0}\right) \cong \left(\frac{R}{R_0 - 1}\right) - \frac{1}{2}\left(\frac{R}{R_0 - 1}\right)^2 . \tag{2.109}$$

Using (2.109) in Eq. (2.108) and collecting terms,

$$\left(\alpha - \frac{1}{2}\right)\left(\frac{R}{R_0}\right)^2 + 2\left(\frac{R}{R_0}\right) - \left(\frac{3}{2} + \ln\gamma - \beta R\right) = 0 \ , \tag{2.110}$$

which results in

$$\frac{R}{R_0} = \frac{[1 + (\alpha - 1/2)\,(3/2 + \ln\gamma - \beta R)]^{1/2}}{(\alpha - 1/2)} \ . \tag{2.111}$$

Now, since the relative aperture A_R is given by

$$A_R = D_o \Delta\theta \ , \tag{2.112}$$

we can write

$$R_0 = \frac{S}{7\Delta\theta} = \left(\frac{S}{7A_R}\right)D_o \ , \tag{2.113}$$

and, from Eq. (2.111) we have

$$D_o = \left\{\frac{7(\alpha - 1/2)(A_R/S)}{[1 + (\alpha - 1/2)(3/2 + \ln\gamma - \beta R)]^{1/2} - 1}\right\}R \ . \tag{2.114}$$

Equation (2.114) expresses the aperture required to achieve a certain range as a function of the target temperature and size, the atmospheric extinction coefficient β, and the system parameters A_R, NET*, and $\mathrm{MTF}_s(f_0)$. The latter two terms depend on A_R:

$$\mathrm{NET}^* = (\eta_s^{1/2} A_R)^{-1}\mathrm{NET}_0 \ , \tag{2.115}$$

$$\mathrm{MTF}_s(1) = 0.64\left(\frac{4A_R - 1}{4A_R}\right)\mathrm{MTF}_D(1) \ . \tag{2.116}$$

An additional performance factor that must be taken into account is the vertical and horizontal field of view. This depends on the detector array format and the aspect ratio (usually 4/3), and is proportional to $\Delta\theta$. That is,

$$\phi_{x,y} \sim \Delta\theta = \frac{A_R}{D_o} \ . \tag{2.117}$$

Relations (2.114) through (2.117), plus the array information necessary to relate field of view to $\Delta\theta$, are sufficient for almost any system trade-off analysis. From Eq. (2.114) reducing A_R is desirable because this either extends recognition range for a fixed aperture or allows the aperture to be reduced at fixed range. On the other hand, doing so reduces the field of view, increases NET*,

and decreases MTF at f_0. If we adhere to the considerations of image quality (MTF > 0.25 at f_0; NET* ~ 0.1°C) and allow a display MTF of about 0.8, then Eq. (2.116) requires 0.5 as the minimum value for A_R. Also, relative aperture is related to the IR optics ($f/\#$) by

$$(f/\#) = \frac{W_D}{A_R} , \tag{2.118}$$

where W_D is the detector size—usually between 1.0 and 1.5 mils. So, the optics ($f/\#$) decreases with A_R, which is of no consequence except that values less than about 1.5 are difficult to build with good performance. Practically, we can take the maximum value of A_R as being no greater than one.

With this range of A_R (0.5 to 1.0), the value of the term $\alpha - 1/2$ ranges from about 0.46 to 0.89. Also, since A_R varies by a factor of two, we note from Eq. (2.115) that to maintain a constant NET*, $\eta_s^{1/2}$ must increase by a factor of two as A_R goes from 0.5 to 1.0. This means the number of detectors must increase by a factor of four. In addition, the value of NET_0 can be determined by numerical integration, with the result that

$$NET_0 = 3.42 \times 10^{-4} \text{ °C (LWIR)} \tag{2.119}$$

and

$$NET_0 = 1.05 \times 10^{-3} \text{ °C (MWIR)} . \tag{2.120}$$

The ratio of Eq. (2.120) to Eq. (2.119) is about 3, so, to maintain the same NET* at any given A_R requires about nine times as many detectors of equal η_D for MWIR compared to LWIR. This is generally taken to imply that MWIR is not a good choice for general-purpose scanning arrays and is only a realistic candidate for staring-array applications. In this same context it should be noted that the factor of four increase required for LWIR systems as A_R goes from 1.0 to 0.5 is very difficult to do for serial systems. This severely restricts the aperture/range trade-offs often required for long-range applications. We note that for any array format,

$$\eta_s \sim N^{1/2} , \tag{2.121}$$

where N is the total number of detectors. Thus, increasing the number of detectors increases the system efficiency, which in turn allows greater flexibility in system design. This is particularly important for long-range or poor-weather (high-β) applications. Recognition range is a weak function of NET* but a strong function of A_R. This is the primary motivation in increasing the number of detectors—not just to achieve ever-lower values of NET*. Figure 2.17 graphically illustrates this.

2.7 EXAMPLE CALCULATIONS

As an example of the relations introduced in the preceding sections, we calculate some specific values for a given system. We assume a parallel system

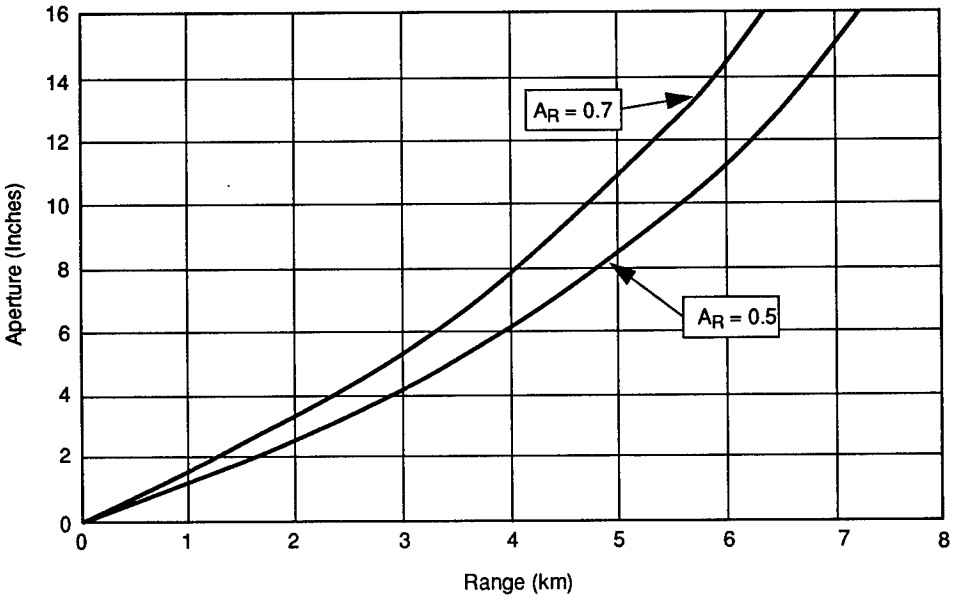

Fig. 2.17 Aperture versus range for recognition of a 2-m MRT target. The aperture required to obtain a given range is a strong function of A_R. In the above, both systems have the same NET* (0.14°C), requiring more detectors for the system with $A_R = 0.5$.

employing a linear detector array of 120 elements aligned vertically and scanned horizontally. The array is interlaced 2:1 to produce an output format of 240 × 320 pixels. The assumed component parameters are given in Table 2.3. Using the values given in Table 2.3, the more pertinent derived parameters are indicated in Table 2.4.

Then,

$$\mathrm{MTF}_{\mathrm{diff}}\left(\frac{f}{f_0}\right) = 1 - \left(\frac{1}{4A_R}\right)\left(\frac{f}{f_0}\right) = 1 - 0.36\left(\frac{f}{f_0}\right), \tag{2.122}$$

Table 2.3 Sample System Component Values

Assumed Component Parameters	Symbol	Value
IR optics aperture	D_o	4 in.
IR optics focal length	fl	11.4 in.
IR optics transmission	τ_o	0.70
IR optics design blur	σ_o	0.058 mrad
Scan efficiency	ε_s	0.70
Cold-shield efficiency	η_{cs}	0.42
Number of detector elements	N	120
Detector element dimension	$w_x w_y$	2.0 mils × 2.0 mils
Detector efficiency	η_D	0.10
Spectral region	λ_1, λ_2	8.0 to 10.0 μm

Table 2.4 Derived System Parameters

Parameter	Relation	Value
$\Delta\theta$	w/fl	0.175 mrad
f_0	$\frac{1}{2}\Delta\theta$	2.86 cycles mrad^{-1}
$(\mathrm{FOV})_y$	$240\Delta\theta$	42.0 mrad
$(\mathrm{FOV})_x$	$320\Delta\theta$	56.0 mrad
A_R	$D_o\Delta\theta$	0.70
η_{cov}	$N\Delta\theta^2/(\mathrm{FOV})_x(\mathrm{FOV})_y$	1.56×10^{-3}
η_s	$\tau_o\varepsilon_s^{1/2}\eta_{\mathrm{cov}}^{1/2}\eta_{\mathrm{cs}}^{1/2}\eta_D^{1/2}$	4.76×10^{-3}
NET_0	[Relation (2.68)]	4.58×10^{-4}°C
G_0	$(\eta_s D_o)^{-2}\mathrm{NET}_0^2$	5.79×10^{-5} °C^2 mrad^2
NET*	$G_0^{1/2}/\Delta\theta$	0.14°C

$$\mathrm{MTF}_{\mathrm{design}}\left(\frac{f}{f_0}\right) = \exp[-\Pi(f\sigma_0)^2] = \exp\left[-0.086\left(\frac{f}{f_0}\right)^2\right], \tag{2.123}$$

$$\mathrm{MTF}_{\mathrm{det}}\left(\frac{f}{f_0}\right) = \mathrm{sinc}\left[\left(\frac{\Pi}{2}\right)\left(\frac{f}{f_0}\right)\right]. \tag{2.124}$$

The product of Eqs. (2.122), (2.123), and (2.124) is shown in Fig. 2.10 labeled as "IR receiver." We next assume that the product of the signal processor and display can be represented by a Gaussian such that the MTF at f_0 is equal to 0.90. That is,

$$\mathrm{MTF}_{\mathrm{display/elec}}\left(\frac{f}{f_0}\right) = \exp\left[-0.10\left(\frac{f}{f_0}\right)^2\right]. \tag{2.125}$$

Equation (2.125) is plotted in Fig. 2.10, labeled "display/elec." The total system MTF, also shown in Fig. 2.10, is then just the product of Eqs. (2.122) through (2.125).

If we ignore the Q factor of Eq. (2.97), we have, for MRT,

$$\mathrm{MRT} = 0.7\left(\frac{f}{f_0}\right)\left[\frac{\mathrm{NET}^*}{\mathrm{MTF}_s(f/f_0)}\right] = 0.098\left[\frac{(f/f_0)}{\mathrm{MTF}_s(f/f_0)}\right]. \tag{2.126}$$

Equation (2.126) is plotted in Fig. 2.14.

Now, for a 2.0-m MRT target, 3°C above ambient, and an atmospheric extinction coefficient of 0.4 km^{-1}, we calculate the following:

$$\alpha = -\ln \mathrm{MTF}_s(1) = -\ln 0.339 = 1.08, \tag{2.127}$$

$$\gamma = \frac{\Delta T}{0.7\ \mathrm{NET}^*} = \frac{3}{0.098} = 30.6; \tag{2.128}$$

then, using (2.127) and (2.128) in (2.114), with $D_o = 4$, and solving for R,

$$R \cong 2.4 \text{ km} . \tag{2.129}$$

If we now allow D_o to vary while maintaining A_R at a constant 0.7, then relation (2.114) becomes

$$D_o = \left\{ \frac{1.42}{[1 + 0.58(4.9 - 0.4R)]^{1/2} - 1} \right\} R , \tag{2.130}$$

and this is plotted in Fig. 2.17 labeled "$A_R = 0.7$."

Bibliography

Biberman, L., Ed., *The Perception of Displayed Information,* Plenum, New York (1973).

Jenkins, F., and H. White, *Fundamentals of Optics,* McGraw-Hill, New York (1957).

Kittel, C., *Elementary Statistical Physics,* John Wiley & Sons, New York (1958).

Linfoot, E., *Fourier Methods in Image Evaluation,* The Focal Press (1964).

Lloyd, M., *Thermal Imaging Systems,* Plenum, New York (1975).

Smith, R., F. Jones, and R. Chasmar, *The Detection and Measurement of Infrared Radiation,* Oxford at the Clarendon Press, Oxford (1957).

Wolfe, W. L., and G. J. Zissis, Eds., *The Infrared Handbook,* Environmental Research Institute of Michigan, Ann Arbor (Revised 1985).

CHAPTER 3

Staring-Sensor Systems

Michael J. Cantella
Massachusetts Institute of Technology
Lincoln Laboratory
Lexington, Massachusetts

CONTENTS

3.1 INTRODUCTION

3.1.1 Types of Staring Focal-Plane Arrays

Staring electro-optical sensors are in very common use and have been designed much like the human eye and photographic camera. The largest commercial and military applications employ TV cameras that operate in the visible spectrum over a very wide range of natural and artificial lighting conditions. Until recently, sensors were constructed mostly with vacuum imaging and scanning tubes.[1–5] Now, a variety of solid-state, staring focal-plane arrays (FPAs) are becoming available to cover the UV, visible, and IR spectral regions.[6–15]

Staring sensors comprise one of two types of configurations that can be used in the design of passive sensors. The two alternatives are presented in Fig. 3.1. A field of view can be covered either (1) sequentially with a small number of detectors and a scanning mechanism or (2) in parallel with a staring mosaic containing a large number of detectors. Historically, the shorter wavelengths have been covered mainly by staring sensors, whereas the longer wavelengths have been covered mainly by scanning sensors. The evolution of this division of spectral coverage has been driven mainly by two physical principles:

1. *Spectral distribution of photon flux.* Photon flux levels from natural backgrounds are generally much lower at shorter wavelengths. The use of staring sensors is desirable because photons imaged by the optics are collected with essentially 100% efficiency owing to complete population of the image plane with detector elements. For many long-wavelength applications, the abundance of photons can permit use of

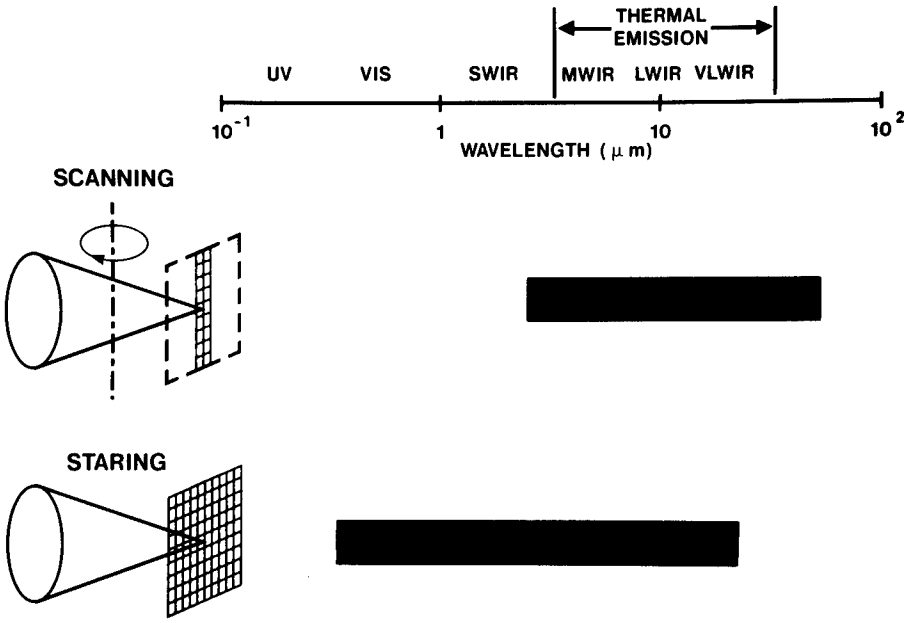

Fig. 3.1 Sensor design alternatives.

scanning arrays that populate only a small fraction of the image and still give adequate performance. Wide-angle coverage can be achieved with relatively simple scanner mechanisms. However, for ultimate sensitivity, the high photon-collection efficiency of staring sensors is required.

2. *FPA producibility and cooling requirement.* Long-wavelength FPAs are more difficult to fabricate and cool adequately than those of short wavelength. This is the direct result of the small energy transitions associated with long wavelengths. FPAs must operate at very low temperatures to minimize dark current, and extreme purity of materials and accuracy of process control are needed for acceptable levels of FPA yield and uniformity. These stringent requirements can limit the practicality of large FPAs, so scanning is mandatory for coverage of large fields of view.

Staring-sensor focal planes collect optical radiation from the optics onto a photon-detecting surface to convert the image to a charge-carrier pattern. This pattern is usually integrated in parallel on a storage surface. Before integration, the photocurrent can first be amplified in an intensifier to provide extremely low-light-level operation. Many devices do not have this prestorage gain, but good sensitivity can still be attained by use of low-noise amplification in the readout process. Readout of almost all staring sensors is accomplished serially. This is an efficient way to access a large number of resolution elements. For further details on construction of staring devices, the reader is referred to the literature.[1,3,5,8–10,14,15]

3.1.2 Staring-Device Performance Summaries

3.1.2.1 Spectral Quantum Efficiency. Figure 3.2 contains typical spectral quantum-efficiency characteristics of various photodetectors. The very long wavelengths are covered by extrinsic-Si materials used mostly in scanning formats for reasons noted previously. At short wavelengths, either vacuum photoemitters or thinned and surface-treated charge-coupled devices (CCDs) have been used mostly in a staring format. In the mid-IR (MWIR) band, available detector types include HgCdTe, InSb, and PtSi and IrSi Schottky-barrier detectors. In addition to the detectors represented in Fig. 3.2, GeSi-heterojunction and GaAs quantum-well detectors recently have been operated successfully in the staring mode.

Final choice of detector material can be derived from trade-offs among coverage format (staring or scanning), FPA producibility, photon flux within the spectral band, sensor integration time, internal noise levels, and cooling requirements.

3.1.2.2 Development Status and Producibility. This chapter pertains to the use of large staring FPAs to achieve high photo-collection efficiency for high-sensitivity coverage of UV, visible, SWIR, MWIR, and LWIR spectral bands. Modern solid-state types of devices are emphasized in this treatment of the subject. Practical implementation of these staring sensors requires selection of FPAs of high producibility.

An important indicator of producibility is the number of industrial firms engaged in the production of FPAs covering UV, visible, and MWIR spectral

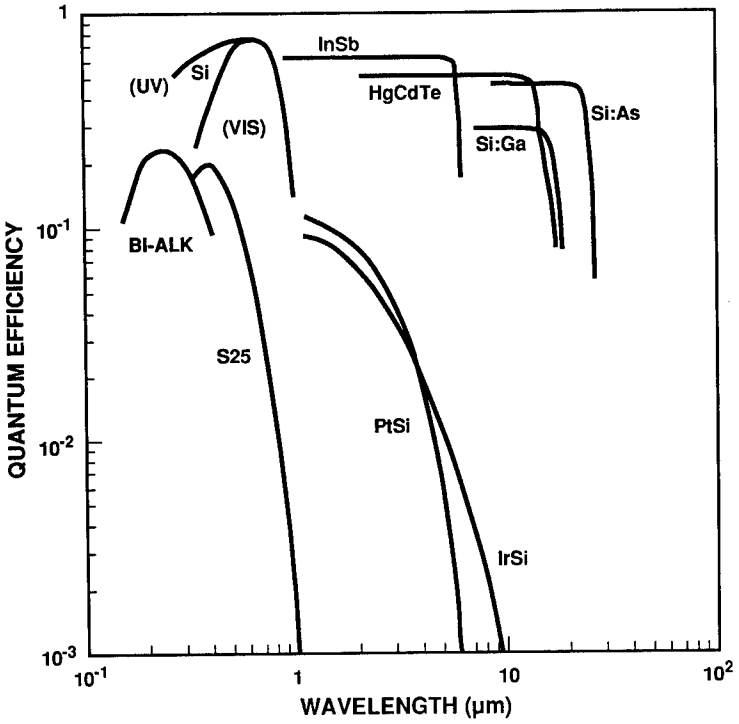

Fig. 3.2 Detector quantum efficiency.

regions. By far, the greatest activity is in Si-CCD FPAs operated in the visible spectrum. This has been fostered by the huge consumer, industrial, and security markets for video cameras and the tremendous technological support provided by the Si semiconductor industry. Arrays of $>10^5$ elements, low-noise performance (<50 rms-electrons), and excellent pixel uniformity (nonuniformity $<1\%$) are readily available at low cost.

Responsivity in the UV spectrum has been demonstrated with a variety of extensions of visible-spectrum CCD technology.[6] While the basic detection/collection technology is still under development, these devices could be moved into production rapidly because the configurations are so similar to visible CCDs.

Schottky-barrier and GeSi-heterojunction FPAs are solid-state photoemissive devices that cover the SWIR, MWIR, and LWIR spectral bands and are another extension of visible-spectrum Si CCD technology.[13,14]

A significant number of industrial organizations are engaged in the fabrication of InSb and HgCdTe staring FPAs.[15,16] This activity is largely an extension of previous scanning-sensor technology. Recent effort has yielded FPAs of high quantum efficiency and quite good uniformity in the 3- to 5-μm band, and progress is being made with HgCdTe to attain the performance and producibility required for 8- to 12-μm applications.

3.1.2.3 Generic Staring-FPA Parameters. To provide a perspective for the reader, basic parameters associated with today's solid-state FPAs[6–8,14–18] are presented in Table 3.1. Rapid progress is being made in the development and

availability of staring FPAs, so the characteristics quoted in Table 3.1 will require updating in the future.

Within the next decade, the availability of very large staring arrays will likely be concentrated in silicon devices covering the UV, visible, and MWIR spectral regions. The most highly developed FPAs are visible CCDs, and arrays as large as 2000×2000 elements have been fabricated for industrial applications.[7] Recently, some of these arrays have been tailored in format and in readout characteristics for space-surveillance applications. Special features include low-noise, multichannel readout, and multiside abutability for fabrication of very large ($>10^9$ pixels) focal planes for wide-angle coverage.[8]

UV CCDs have been under development as an extension of visible-spectrum Si CCD designs. Therefore, total resolution capability can be comparable to visible devices.[6] Most designs treat the illuminated surface of the Si to minimize carrier recombination following photoexcitation. Visible and UV devices have the smallest pixels, and this has evolved from requirements to match optics resolution performance. UV applications require the smallest pixels, but photolithographic technology is likely to limit pixel spacing to a few micrometers.

A variety of Schottky-barrier FPAs of a few hundred elements on a side have been under development for commercial and military applications.[14,17] While currently demonstrated quantum efficiency is relatively low in the thermal-emission band beyond 3 μm, the high uniformity and high photon-collection efficiency afforded by very large staring arrays have permitted demonstration of excellent thermal sensitivity. Fabrication of large Schottky-barrier FPAs has been very practical. Recently, three-side abuttable devices with Schottky-barrier or GeSi-heterojunction detectors have become available for very-wide-angle applications.[18,19]

Table 3.1 Generic Staring-FPA Parameters

SPECTRAL BAND	DET TYPE	FPA TYPE	TYPICAL FPA SIZES	PIXEL SIZES (um)	TEMPORAL NOISE FLOOR (rms-Elect/Pix)	NON-UNIFORMITY (%)	OPERATING TEMP (K)
UV	Si	CCD	400x400	10 to 30	1 to 5	1	260 to 300
VISIBLE	Si	CCD (Single)	488x640 2000x2000	10 to 30	1 to 5	1	260 to 300
		CCD (Buttable)	400x400	10 to 30	1 to 5	1	260 to 300
MWIR	InSb	Hybrid	256x256	40 to 60	80 to 500	4	55 to 80
	HgCdTe	Hybrid	256x256	40 to 60	100 to 1,000	5	60 to 120
	PtSi	Hybrid	512x512	20 to 40	80 to 500	2	55 to 80
	PtSi	CCD (Single)	488x640 400x400	20 to 40	20 to 100	0.25	55 to 80
		CCD (Buttable)	400x400	20 to 40	20 to 100	0.25	55 to 80
LWIR	HgCdTe	Hybrid	256x256	40 to 60	300 to 3,000	20	40 to 80
	IrSi, GeSi-Hetero]'n	CCD (Single)	244x320 400x400	20 to 40	20 to 100	1	30 to 60
		CCD (Buttable)	400x400	20 to 40	20 to 100	1	30 to 60
	BoI, BST	Monolithic, Hybrid	245x328 240x336	50	30,000	20	300

Extremely small pixels are not appropriate for all applications. Because of optics diffraction limits, IR applications require larger pixels. In addition, astronomy and space-surveillance applications require very large optics for photon collection, so large pixels are needed to match the optics. Because of requirements for large pixels, there is an implied need for physically large focal planes to satisfy requirements for total resolution and total field of view. From the viewpoint of FPA fabrication yield, this usually can be achieved best by butting subarrays together.

The internal noise performance of a sensor is important for low-exposure applications. The level needed depends on the background exposure (and noise) associated with the spectral band and with the mode of operation. Historically, intensifier vacuum tubes have had the lowest noise performance (down to a few rms-electrons/pixel). Because these sensors have very high gain (typically $>10{,}000$), dynamic range is somewhat limited compared to solid-state devices. Recently, visible CCDs have been successfully fabricated with internal noise as low as a few rms-electrons/pixel, and very high ($>100{,}000{:}1$) dynamic range is possible.[8] For UV and visible bands, in which backgrounds are low, levels of a few rms-electrons/pixel are needed. Since backgrounds are higher in the MWIR and LWIR bands, levels of a few-hundred rms-electrons/pixel are usually satisfactory.

3.2 ELECTRONIC-IMAGING PERFORMANCE ASSESSMENT METHODOLOGY

3.2.1 General Approach

Electro-optical imaging systems have wide application. Vacuum tube and solid-state devices can be sensitive to spectral radiation ranging from the UV to the far-IR. Sensors can be of the scanning or staring format, and their outputs can either be displayed for interpretation by a human observer or processed for automatic detection, moving target indication, tracking, and pattern recognition. Because of the complexity of design and the diversity of applications for these systems, systematic and accurate analytic methods are needed for sensor performance assessment.

For good utility, a performance model must encompass a wide variety of standards and conventions developed by a large community of experts representing diverse technical interests. Historically, test methods and standards have included periodic and aperiodic bar patterns as well as point sources. Radiation standards have included both absolute and difference levels to simulate various image contrasts. Noise generated within sensors includes fundamental shot noise and various types of temporal and spatial noise. These noise sources may or may not be some function of exposure. Recent progress in staring-FPA technology has provided an opportunity for design of sensor systems of extraordinarily high sensitivity, and proper measurement and representation of spatial fixed-pattern noise has offered a special challenge.

The modeling approach presented here is represented by the block diagram in Fig. 3.3. This model combines sensor exposure, spatial aperture response, and noise performance to obtain a signal-to-noise ratio (SNR). This SNR is formulated for a desired image pattern (point source, aperiodic bar, periodic

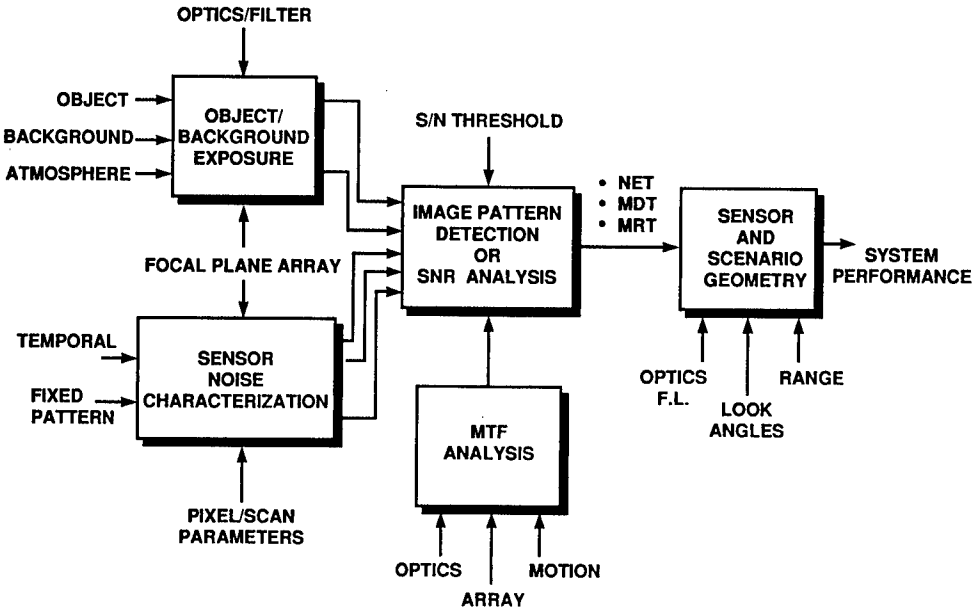

Fig. 3.3 System performance model.

bars, etc.), and an SNR threshold is invoked to represent alternative human and machine performance criteria and standards.[20]

The central block of Fig. 3.3 contains the image-pattern SNR models. These image patterns can be represented in either the space or the frequency domain. The modulation transfer function (MTF)-analysis block supports computation of SNR by appropriate representation of aperture-response functions of optics, FPA, line-of-sight motion, etc. These functions represent line response in the space domain and the corresponding MTF in the spatial-frequency domain. The approach described here, introduced by Schade,[21,22] makes maximum use of space-domain aperture-response functions to provide a direct visualization and interpretation of both performance criteria and computational results. Sensor aperture-response functions can be computed efficiently in the space domain without the use of Fourier integrals. Useful approximations can be formulated to provide a smooth transition between resolved and unresolved image-forming situations, so the model can be applied readily to a broad range of operational conditions, including variable range and/or variable magnification. Experimental techniques based on space-domain representation allow direct assessment of both linear and nonlinear hardware characteristics.

The exposure computational block of Fig. 3.3 represents the combining of all optical-radiation quantities (from objects and backgrounds) with detector responsivity and sensor or eye exposure time to obtain exposures expressed in terms of electrons. Exposure can be normalized to a pixel or a unit area and can pertain to either a scanning or a staring type of sensor. This method of exposure computation permits assessment of sensor signal-readout, dynamic-range, and noise characteristics in terms of fundamental quantities that are independent of spectral band and operating environment. This contributes

greatly to universal application of the model and to the projection of sensor performance to new applications.

The noise computational block of Fig. 3.3 provides mathematical characterization of various types of temporal and fixed-pattern noise. These noise sources may or may not be some function of sensor exposure. Temporal and spatial statistics are represented by appropriate amplitude and spectral characteristics. Noise-equivalent aperture functions are used to formulate mathematical expressions to represent the influence on noise spectrum of sensor temporal and spatial aperture response.

The mathematical function associated with each computational block is described in subsequent portions of Sec. 3.2, and system-application examples are presented in Secs. 3.3 and 3.4.

3.2.2 Signal and Contrast

The electron-density exposure ε associated with either an object or background image at infinity can be expressed by

$$\varepsilon = \frac{\pi T_i F_s}{4e^-(f/\#)^2} \int_{\lambda_1}^{\lambda_2} R_\lambda T_{o\lambda} T_{a\lambda} L_\lambda \, d\lambda \quad (\text{e/m}^2) \ , \tag{3.1}$$

where

$f/\#$ = optics focal ratio
T_i = sensor or eye integration time (s)
F_s = FPA active-area fill factor
e^- = electron charge (C)
λ_1 = lower-wavelength limit (μm)
λ_2 = upper-wavelength limit (μm)
R_λ = sensor spectral responsivity (A W^{-1})
$T_{o\lambda}$ = optics transmission
$T_{a\lambda}$ = atmospheric transmission
L_λ = object or background spectral radiance ($Wm^{-2}sr^{-1}\mu m^{-1}$).

For a graybody, Eq. (3.1) becomes

$$\varepsilon = \frac{\pi c^2 h T_i F_s}{2e^-(f/\#)^2} \int_{\lambda_1}^{\lambda_2} \frac{R_\lambda T_{o\lambda} T_{a\lambda} \epsilon_\lambda \, d\lambda}{\lambda^5[\exp(hc/kT\lambda) - 1]} \quad (\text{e/m}^2) \ , \tag{3.2}$$

where T is the object or background temperature (K), ϵ_λ is the object or background emissivity, h is Planck's constant (J s), k is Boltzmann's constant (J K^{-1}), and c is the velocity of light (m/s). As indicated above, the integration time for accumulation of exposure is that of the sensor if sensor-type quantities are of interest. For assessment of eye-related performance, eye integration time is used if it exceeds the sensor integration time.

This electron-density exposure concept is not confined to a staring FPA, but it can also represent the accumulated exposure collected by a scanning sensor.

By introducing the appropriate numerical constants, Eq. (3.2) becomes

$$\varepsilon = \frac{5.85 \times 10^{26} T_i F_s}{(f/\#)^2} \int_{\lambda_1}^{\lambda_2} \frac{R_\lambda T_{o\lambda} T_{a\lambda} \epsilon_\lambda d\lambda}{\lambda^5 [\exp(14{,}388/\lambda T) - 1]} \quad (\mathrm{e/m^2}) \ . \tag{3.3}$$

The FPA pixel exposure ξ_p is

$$\xi_p = 10^{-6} \varepsilon \Delta^2 \quad (\mathrm{e}) \ , \tag{3.4}$$

where Δ is the mean pixel spacing (mm).

A useful way to express image contrast C is as a ratio of difference-signal to background:

$$C = \frac{|\varepsilon_o - \varepsilon_b|}{\varepsilon_b} \ , \tag{3.5}$$

where ε_o is the object exposure ($\mathrm{e/m^2}$) and ε_b is the background exposure ($\mathrm{e/m^2}$). For IR systems operating in an environment of very small temperature difference between object and background, the background-normalized differential-temperature contrast C_Δ is a useful quantity, which can be computed from

$$C_\Delta = \frac{1}{\varepsilon_b} \frac{d\varepsilon_b}{dT} \quad (\mathrm{K^{-1}}) \ . \tag{3.6}$$

3.2.3 Sensor Noise

3.2.3.1 Noise-Equivalent Aperture Concept. It is very useful to characterize noise sources in terms of parameters that are compatible with measures of cascaded aperture response and with geometric characteristics of image patterns. Noise amplitude in the space domain can be characterized in terms of its power-density spectrum in the spatial-frequency domain $p_n(f)$. This power-density spectrum is the Fourier transform of the autocorrelation function $\phi_n(\Sigma)$, measured in the space domain. Parseval's theorem indicates that the total noise power is conserved.

The concept of noise-equivalent bandwidth was extended and used by Schade[21,22] for representation of aperture response of cascaded elements of an imaging system. These aperture functions are deterministic. Their noise-equivalent bandwidths f_e not only provide a simple means for computation of output noise, but this single measure can be used to establish a useful approximation for MTF for a wide variety of aperture shapes. In the space domain, there is a corresponding noise-equivalent spread factor δ_e. Differences among actual aperture shapes occur at relatively high MTF, where influence on total noise is minimal. For computation of signal from repetitive patterns such as square waves, the exact value of square-wave response is more appropriate.

An example of Fourier-transform pairs for a white-noise source passing through a rectangular aperture function is presented in Fig. 3.4. The noise-

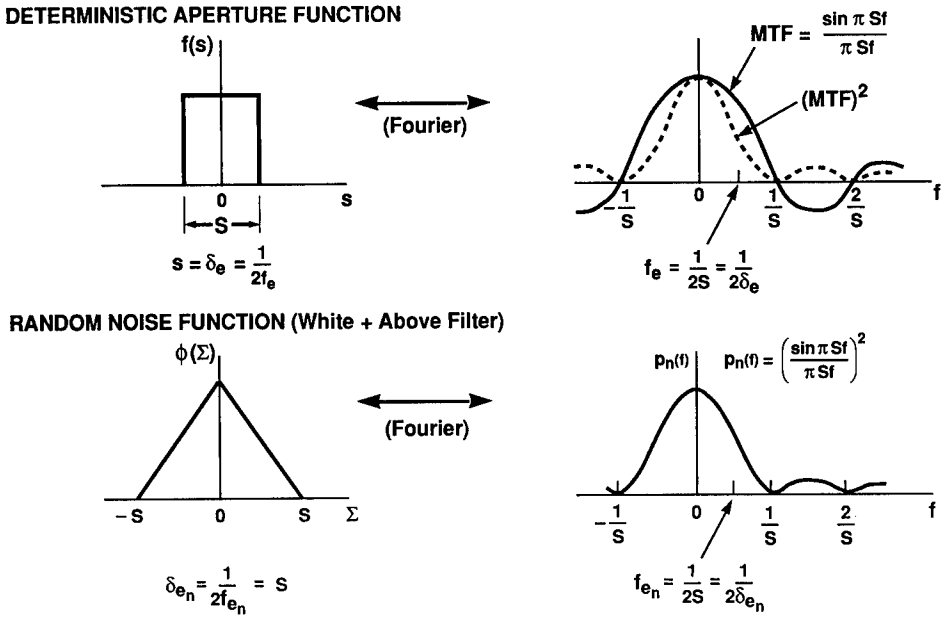

Fig. 3.4 Fourier transform pairs—rectangular aperture functions.

equivalent bandwidths for this and for some other common aperture functions are listed in Table 3.2.

Schade has shown that in the cascading of aperture functions, a good approximation for the total spread factor is

$$\delta_e = (\delta_{e1}^2 + \delta_{e2}^2 + \ldots)^{1/2} , \tag{3.7}$$

and for the corresponding spatial-frequency quantities,

$$\frac{1}{f_e} = \left(\frac{1}{f_{e1}^2} + \frac{1}{f_{e2}^2} + \ldots\right)^{1/2} . \tag{3.8}$$

A sensor can have a point-spread function that is noncircularly symmetric. In this case, the geometric-mean spread factor δ represents a useful approximation and is computed from

$$\delta = (\delta_{ex}\delta_{ey})^{1/2} , \tag{3.9}$$

where δ_{ex} is the spread-factor horizontal component (mm) and δ_{ey} is the spread-factor vertical component (mm). This approximation will be assumed throughout subsequent discussions.

Table 3.2 Noise-Equivalent Spread Factors and Bandwidths

Aperture Shape	Noise-Equivalent Spread Factor δ_e	Noise-Equivalent Bandwidth f_e
Rectangular	S	$1/(2S)$
Round	$0.926d$	$0.540/d$
Gaussian	$2\pi^{1/2}\sigma$	$1/(4\pi^{1/2}\sigma)$
Diffraction-limited optics	$1.79\lambda(f/\#)$	$0.279/[\lambda(f/\#)]$

Table 3.3 Noise Considerations for Sensor Design

Types/Sources
• FPA temporal • FPA spatial • Scene clutter • Aliased scene clutter from sampling
Mathematical Representation
• Exposure dependence • Spatial and temporal characteristics • Image-pattern normalization — Aperiodic bar — Periodic bar — Pixel — Resel — Video

Table 3.4 Exposure-Dependent Noise Classification

Noise Type		Exposure Dependence
Temporal	Quantum	$\propto \sqrt{\text{exp}}$ (quantum)
	Readout	None (additive)
Fixed pattern	Responsivity	$\propto$ exp (multiplicative)
	Dark-level	None (additive)

3.2.3.2 Noise Classifications

3.2.3.2.1 Overview. Sensor design and performance assessment require identification and quantitative representation of noise sources. Table 3.3 summarizes the factors that must be considered. Noise is generated within a sensor and from the optical-radiation environment. Mathematical representation of various noise sources should include functional dependence on exposure and on spatial and temporal characteristics. For maximum utility, noise levels should be normalized to laboratory test standards such as bar patterns and to hardware design elements such as pixel size and video bandwidth.

A simplified categorization of various types of noise sources in terms of temporal and spatial characteristics is presented in Table 3.4. Temporal noise varies frame to frame, whereas fixed-pattern noise does not. Temporal readout noise and dark-level noise are not a function of exposure, and quantum and responsivity noises are different functions of exposure. The proportionality relationships to exposure are indicated in the table.

Temporal and fixed-pattern noise generated in background regions of an image usually determine the noise threshold for both visual imaging and for machine decisions. Therefore, relationships of noise to background exposure will be described in more detail subsequently and used in Sec. 3.2.4 in the formulation of image-pattern SNR. Detailed mechanisms of noise generation within sensing devices are treated in the literature.[10,23–25]

3.2.3.2.2 Temporal Noise

Quantum noise

For a resolved image pattern, quantum-noise variance density n_Q can be computed from

$$n_Q = K\varepsilon_b = \frac{10^6 K \xi_{pb}}{\Delta^2} \quad (\text{e/m}^2) \ , \tag{3.10}$$

where ε_b is the image-plane exposure density (e/m^2), K is the quantum-noise factor, ξ_{pb} is the pixel exposure (e/pixel), and Δ is the pixel spacing (mm). The factor K is a measure of how ideal the photodetection process is, and is derived from performance measurements. For a given exposure, it is the ratio of measured quantum-noise variance to shot-noise variance. For a real detector K is greater than 1 and represents excess noise not accounted for by Poisson statistics. A typical mechanism that gives rise to this departure from the ideal is the presence of gain in the sensor (more than one carrier generated for a photon interaction). For a sensor containing discrete pixels, it can be computed from

$$K = \frac{10^6 N_Q^2}{\varepsilon_b \Delta^2} = \frac{N_Q^2}{\xi_{pb}} \ , \tag{3.11}$$

where N_Q is the measured quantum rms noise (e/pixel).

Additive temporal noise

The origin of additive temporal noise includes the FPA readout amplifier, dark current, and poor charge-transfer efficiency. The additive-temporal-noise variance density n_{AT} can be determined from FPA noise measurements and is computed from

$$n_{AT} = \frac{10^6 N_{AT}^2}{\Delta^2} \quad (\text{e/m}^2) \ , \tag{3.12}$$

where N_{AT} is the measured rms noise (e/pixel).

3.2.3.2.3 Fixed-Pattern Noise

Multiplicative fixed-pattern noise

Fixed-pattern noise does not vary temporally, and can be either independent of or some function of exposure. An important type of fixed-pattern noise is

represented by an rms level that is directly proportional to exposure and is produced by pixel-to-pixel differences in responsivity or gain. It can easily be the dominant noise source, especially under low-contrast conditions. This type of fixed-pattern noise is termed *multiplicative* and is subsequently described mathematically. This mathematical representation applies to (1) all sensors viewing a source of given spectral distribution, and (2) all sensors that have no variation in relative responsivity, regardless of spectral distribution of the source.

If each pixel has a different relative spectral responsivity, fixed-pattern noise will also be a function of the spectral distribution of the source. Typically, this applies to detectors that exhibit variations in cutoff wavelength.[26] Mathematical description of this situation is very complex, and fixed-pattern-noise correction is less effective. This case is not treated here.

Multiplicative fixed-pattern noise can be measured in the laboratory and expressed as an rms noise-modulation factor M:

$$M = \frac{10^3 N_{\mathrm{MFP}}}{\varepsilon_b f_{en} \Delta^2} = \frac{10^{-3} U}{f_{en}} \quad \text{(m)} \ , \tag{3.13}$$

where N_{MFP} is the measured rms multiplicative fixed-pattern noise (e/pixel), f_{en} is the spatial noise-equivalent bandwidth of noise (cycles/mm), and U is the ratio of rms noise to mean exposure. For fixed-pattern noise that is independent from pixel to pixel,

$$f_{en} = \frac{1}{2\Delta} \quad \text{(cycles/mm)} \ . \tag{3.14}$$

Then,

$$M = 2 \times 10^{-3} U\Delta \quad \text{(m)} \ , \tag{3.15}$$

and the fixed-pattern noise-variance density n_{MFP} is

$$n_{\mathrm{MFP}} = \left(\frac{M\varepsilon_b}{2}\right)^2 \quad \text{(e/m}^2\text{)} \ . \tag{3.16}$$

The rms fixed-pattern noise per pixel N_{MFP} can be computed from

$$N_{\mathrm{MFP}} = 10^{-3} (n_{\mathrm{MFP}} \Delta^2)^{1/2} \quad \text{(e/pixel)} \ . \tag{3.17}$$

For cases in which fixed-pattern noise is not independent from pixel to pixel, computation of noise factor M is somewhat more complicated.[20]

Additive fixed-pattern noise

Additive fixed-pattern noise is not dependent on sensor background exposure. A common origin for this type of noise is sensor dark-current exposure. Variations in this exposure can be modeled in the same manner as described above

for multiplicative background-exposure noise. Comparable dark-current-related quantities N_{DFP}, f_{Den}, U_D, M_D, and n_{DFP} can be described identically to those represented in Eqs. (3.10) through (3.17). Dark-current exposure ε_D can be obtained from

$$\varepsilon_D = \frac{J_D T_i}{e^-} \quad (e/m^2) \ , \tag{3.18}$$

where J_D is the dark-current density adjusted for pixel fill factor (A/m^2), T_i is the integration time (s), and e^- = electron charge (C/e). Then, the additive dark-current fixed-pattern-noise variance density ($n_{AFP} = n_{DFP}$) is

$$n_{AFP} = \left(\frac{M_D \varepsilon_D}{2}\right)^2 \quad (e/m^2) \ , \tag{3.19}$$

and the rms fixed-pattern noise N_{AFP} is

$$N_{AFP} = 10^{-3} (n_{AFP} \Delta^2)^{1/2} \quad (e/pixel). \tag{3.20}$$

3.2.3.2.4 Example of Sensor Noise Measurement and Modeling. FPA noise measurements can be made to separate the components into the various temporal and fixed-pattern types described above. All noise and exposure components are referred to the detector plane by dividing the values measured at the output by the gain between the output and the detectors. For intensifier devices, the gain of the intensifier is included. Temporal-noise components are obtained from frame-to-frame variations that occur in individual detector elements (element average of rms temporal fluctuation). Fixed-pattern-noise components are obtained from spatial (element-to-element) variations, subsequent to frame-to-frame temporal averaging (spatial rms fluctuation of temporal mean).

An example of laboratory noise measurements made on an FPA is presented in Fig. 3.5. These measurements are superimposed on theoretical noise calibrations for shot noise and multiplicative fixed-pattern noise. Note that the shot-noise component varies as the square root of the background exposure, and the fixed-pattern-noise components (corresponding to various nonuniformities) vary directly with background exposure.

The fixed-pattern-noise data presented in Fig. 3.5 were obtained by integration of multiple frames of data to average temporal noise down to a negligible value. Then the rms value of the remaining noise was obtained from the pixel samples. This procedure was followed for each value of exposure. At high exposures, the fixed-pattern noise was found to approach the theoretical direct variation with exposure (multiplicative). At low exposures, fixed-pattern noise was found to become independent of exposure (additive).

Temporal-noise data were obtained by observation of frame-to-frame variations from a selected pixel. This procedure avoids pixel-to-pixel variations caused by fixed-pattern noise. At medium and high exposures, the temporal noise is very close to theoretical shot-noise levels, with the displacement representing the square root of the quantum-noise factor K described in Eq. (3.11). At low exposures, temporal noise becomes independent of exposure and represents the additive component.

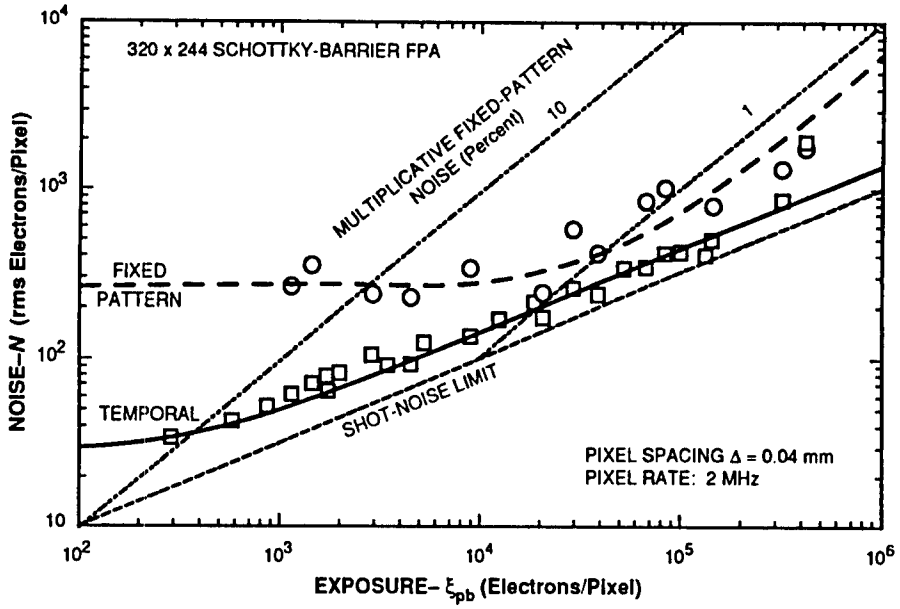

Fig. 3.5 Theoretical and experimental noise.

The noise parameters needed for performance modeling can be derived from Fig. 3.5.

Quantum noise

To obtain the quantum-noise factor K, select an exposure in the quantum-noise-limited region, for example, 10^4 e/pixel. The rms noise is

$$N_Q = 1.3 \times 10^2 \quad \text{(e/pixel)} \ .$$

Then, from Eq. (3.11)

$$K = 1.69 \ ,$$

and, from Eq. (3.10), the quantum-noise variance density is

$$n_Q = 1.69\varepsilon_b \quad \text{(e/m}^2\text{)} \ .$$

Multiplicative fixed-pattern noise

The multiplicative fixed-pattern noise is obtained by using any point on the linearly increasing asymptote of Fig. 3.5. The rms nonuniformity is

$$U = 0.0062 \ .$$

Using Eq. (3.15), the noise-modulation factor is

$$M = 4.96 \times 10^{-7} \quad \text{(m)} \ ,$$

and, from Eq. (3.16), the multiplicative noise variance density is

$$n_{\mathrm{MFP}} = 6.15 \times 10^{-14}\, \varepsilon_b^2 \quad (\mathrm{e/m^2}) \ .$$

Additive fixed-pattern noise

From Fig. 3.5, the rms additive fixed-pattern noise is

$$N_{\mathrm{AFP}} = 2.5 \times 10^2 \quad (\mathrm{e/pixel}) \ ,$$

and, from Eq. (3.19), the additive fixed-pattern-noise density is

$$n_{\mathrm{AFP}} = 3.91 \times 10^{13} \quad (\mathrm{e/m^2}).$$

Additive temporal noise

From Fig. 3.5, the additive temporal rms noise is

$$N_{\mathrm{AT}} = 30 \quad (\mathrm{e/pixel}) \ .$$

From Eq. (3.12), the additive temporal-noise variance density is

$$n_{\mathrm{AT}} = 5.63 \times 10^{11} \quad (\mathrm{e/m^2}) \ .$$

Total noise

The total noise variance density n is

$$\begin{aligned} n &= n_{\mathrm{Q}} + n_{\mathrm{MFP}} + n_{\mathrm{AFP}} + n_{\mathrm{AT}} \quad (\mathrm{e/m^2}) \\ &= 1.21\varepsilon_b + 6.15 \times 10^{-14}\varepsilon_b^2 \\ &\quad + 3.91 \times 10^{13} + 5.63 \times 10^{11} \quad (\mathrm{e/m^2}) \ . \end{aligned} \tag{3.21}$$

3.2.4 Image Pattern Signal-to-Noise Ratio

3.2.4.1 Aperiodic and Periodic Test Patterns. Bar test patterns are convenient for the measurement of performance of electro-optical sensors. Performance criteria can be related to the size, shape, and frequency of the bars and to the signal and noise within the bar areas as defined at the output of the sensor. Bar test patterns are stretched by the finite spatial-frequency bandpass of a sensor, as illustrated in Fig. 3.6 for both aperiodic and periodic bar patterns. For determination of performance, it is assumed that both machine systems and human observers function as a spatial matched filter to provide optimum detection of bar patterns of any size and frequency. The detection threshold is then defined by a bar-pattern signal-to-noise ratio.

3.2.4.1.1 Aperiodic Bar Patterns. Aperiodic patterns provide a useful measure of the detection and/or reproduction of isolated image details. Performance based on this standard has application to image and point-source detection, adaptive-gate tracking, and pattern recognition.

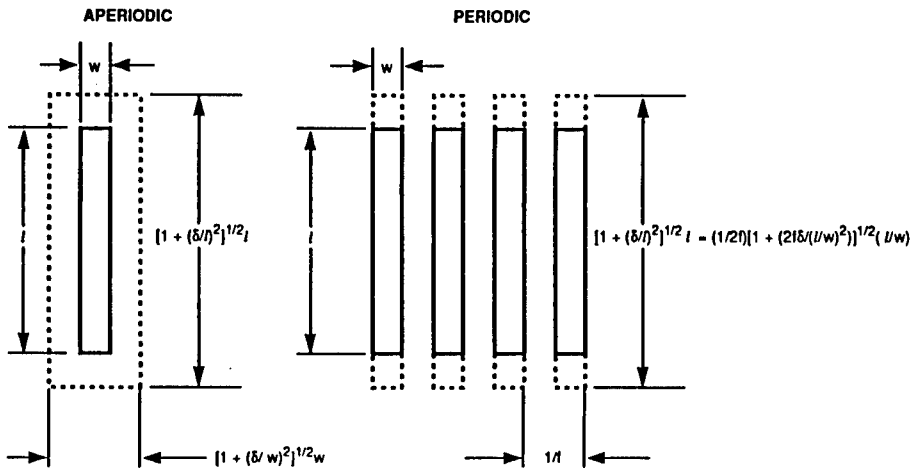

Fig. 3.6 Bar-pattern noise windows.

As indicated in Fig. 3.6, an aperiodic bar is stretched in length l and width w by the finite spatial-frequency response of the imaging system. The noise-equivalent spread-factor methods presented in Sec. 3.2.3.1 can be used with good approximation to determine the degree of stretching of the bar.

The bar signal ξ_B is obtained for the input area of the bar from

$$\xi_B = 10^{-6}\varepsilon_s wl \quad \text{(e/bar)} , \tag{3.22}$$

where ε_s is the signal exposure density (e/m^2), l is the bar length (mm), and w is the bar width (mm). For bar-detection-type applications, the most important component of rms noise is produced by areas of background surrounding the image and is obtained from the noise-equivalent image area A_n from

$$A_n = 10^{-6} wl \left[\left(\frac{1 + \delta^2}{w^2} \right) \left(\frac{1 + \delta^2}{l^2} \right) \right]^{1/2} \quad (\text{m}^2) , \tag{3.23}$$

where δ is the geometric-mean spread factor (mm). Note that Eq. (3.23) is in the form of the product of the input area and a noise-correction factor.

To obtain the noise variance, the noise area A_n is multiplied by the total noise variance density n obtained from Eq. (3.21). The rms noise per bar image is then

$$N_B = 10^{-3} \left[(n_Q + n_{MFP} + n_{AFP} + n_{AT}) wl \times \left(\frac{1 + \delta^2}{w^2} \right)^{1/2} \left(\frac{1 + \delta^2}{l^2} \right)^{1/2} \right]^{1/2} \quad \text{(e/bar)} . \tag{3.24}$$

3.2.4.1.2 Minimum Detectable Temperature. The aperiodic-bar standard used by the IR community is minimum detectable temperature (MDT). This is a plot of the required difference temperature for detection of an isolated bar (usually square) versus the reciprocal of its width.

The bar signal is obtained from

$$\xi_B = 10^{-6} C_\Delta \varepsilon_b w l \Delta T \quad \text{(e/bar)} \ . \tag{3.25}$$

Quantities C_Δ and ε_b are obtained from Eqs. (3.4) and (3.1), respectively. Using Eqs. (3.24) and (3.25) to form an SNR quotient and setting it equal to a threshold T_{SNR}, the difference temperature ΔT becomes the MDT. The final result, expressed as a function of the reciprocal width and length-to-width ratio, is

$$\text{MDT} = \frac{10^3 T_{SNR} w^{-1} \left(n[1+(\delta w^{-1})^2]^{1/2} \left\{ 1 + \left[\frac{\delta w^{-1}}{(l/w)} \right]^2 \right\}^{1/2} \right)^{1/2}}{C_\Delta \varepsilon_b (l/w)^{1/2}} \quad \text{(K)} \ . \tag{3.26}$$

To obtain MDT as a function of angular bar width θ (mrad), measured outside the optics, the following substitution is made in Eq. (3.26):

$$w = 10^{-3} F \theta \quad \text{(mm)} \ . \tag{3.27}$$

3.2.4.1.3 Periodic Bar Patterns. Periodic bar patterns are used to measure spatial-frequency response of electro-optical systems. The modulation transfer function is the sine-wave response, and can be derived with good approximation from measurements made with square-wave patterns of variable spatial frequency. Since modern solid-state FPAs have discrete pixels, bar-pattern frequencies need to be chosen carefully to minimize frequency aliasing due to spatial sampling. The use of slowly moving bar patterns is also helpful for estimation of the modulation envelope, which is obscured by the sampling process. Meaningful bar-pattern modulation magnitude can be ascertained even beyond the Nyquist limit. After the square-wave response is measured, the sine-wave response versus frequency $r(f)$ can be computed from[27]

$$r(f) = \frac{\pi}{4} \left[R(f) + \frac{1}{3} R(3f) - \frac{1}{5} R(5f) + \frac{1}{7} R(7f) \ldots \right] \ , \tag{3.28}$$

where $R(f)$ is the square-wave response.

Alternatively, if the sine-wave response is known, the square-wave response can be computed from

$$R(f) = \frac{4}{\pi} \left[r(f) - \frac{1}{3} r(3f) + \frac{1}{5} r(5f) - \frac{1}{7} r(7f) \ldots \right] \ . \tag{3.29}$$

Periodic bar patterns also are used to measure the maximum bar frequency discernible in a displayed output. This provides a good measure of a systems capability for reproduction of small image details. For visible-spectrum systems, this performance is called resolving power. For TV systems, wedge-shaped patterns have been used to form repetitive bars of variable frequency. Repetitive three-bar groups contained within a square area (bar l/w ratio held constant for any spatial frequency) are used for TV and photographic systems.

3.2.4.1.4 Minimum Resolvable Temperature. The IR community uses repetitive four-bar groups as the standard for measurement of minimum resolvable temperature (MRT). MRT is a plot of the required difference temperature versus spatial frequency. MRT standards include various threshold SNR criteria based on visibility statistics, operator viewing distance, viewing time, fatigue, etc.

Formulation of the SNR expressions for periodic bars requires extension of the methodology presented above for aperiodic bars. The periodic bar geometry was presented in Fig. 3.6. In the periodic direction of the bar group, the difference signal is attenuated by losses in modulation caused by the spatial spread factor of the system. This loss can be approximated by the square-wave response $R(f)$. The width of the bar is not increased in the periodic direction, so noise correction cannot be computed using space-domain techniques. Instead, Schade has shown[21] that the frequency-domain correction factor β is required and can be computed, using the methods described in Sec. 3.2.3.1, from

$$\beta = \frac{f_{ef}}{f} = \frac{1}{f}\int_0^f r^2\, df = \frac{1}{[1+(2f\delta)^2]^{1/2}}\ , \tag{3.30}$$

where f_{ef} is the noise-equivalent bandwidth truncated at f (cycles/mm). Note that $\beta < 1$, and this produces a reduction of noise in the periodic direction to offset partially the reduction in signal represented by losses in square-wave response.

In the aperiodic direction, noise is increased by the spread factor, and this increase can by expressed in terms of the bar spatial frequency.

The minimum resolvable temperature MRT is then

$$\mathrm{MRT} = \frac{\begin{array}{c}2\times 10^3 T_{\mathrm{SNR}} f \\ \times\ (\{(n_{\mathrm{Q}}+n_{\mathrm{MFP}}+n_{\mathrm{AFP}})[1+(2f\delta)^2]^{-1/2}+n_{\mathrm{AT}}\} \\ \times\ \{1+[2f\delta/(l/w)]^2\}^{1/2})^{1/2}\end{array}}{C_{\Delta\varepsilon_b} R(f)(l/w)^{1/2}}\quad (\mathrm{K}) \tag{3.31}$$

Note that this equation assumes that additive temporal noise n_{AT} is introduced after MTF filtering, so the β factor is not applied to that noise component.

To obtain MRT in terms of spatial frequency outside the optics, substitute

$$f = \frac{10^3\phi}{F}\ , \tag{3.32}$$

where ϕ is the angular spatial frequency (cycles/mrad).

The MRT model has been validated repeatedly with experimental measurements. An example showing a comparison between the model and a set of human observations is presented in Fig. 3.7(a) for a Schottky-barrier IR FPA.[20] The measured parameters used in the model are listed in the legend. In order to compare this model with the U.S. Army Night Vision and Electro-Optics Directorate (NVEOD) model,[28] MRT was computed for a hypothetical IR scanning system. The results are presented in Fig. 3.7(b). Excellent agreement was achieved except at the highest spatial frequencies. These results

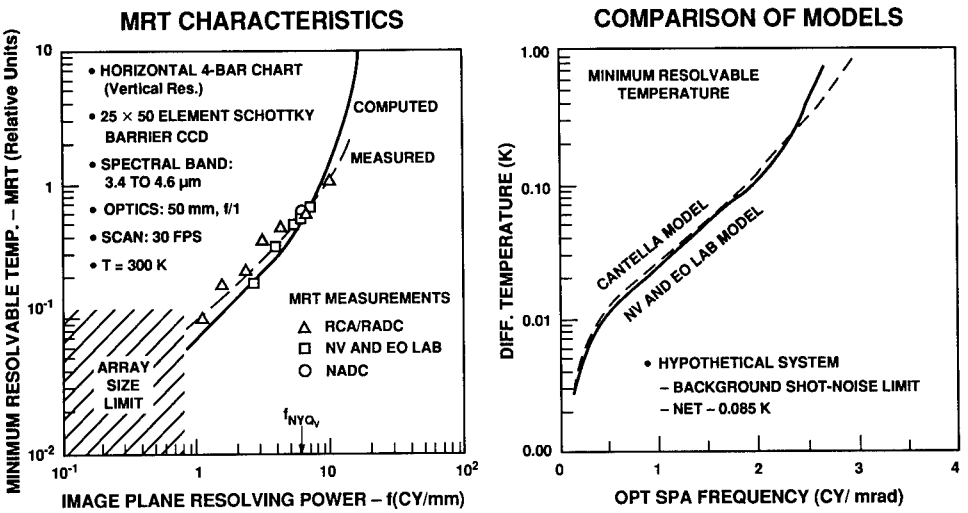

Fig. 3.7 Staring-FPA MRT model validation.

have provided reasonably high confidence for use of this model for staring-system MRT prediction. Additional work is needed for further confirmation.

3.3 TACTICAL IR SYSTEM DESIGN AND PERFORMANCE

3.3.1 Staring-Sensor Design Drivers and Trade-offs

3.3.1.1 IR Radiation Characteristics. The choice of optimum spectral band for IR imaging involves complex trade-offs among target signatures, environmental phenomenology, and hardware design. Figure 3.8 presents photon-flux radiance as a function of wavelength from a 300 K blackbody source. Integration of flux within the atmospheric windows indicates that there is approximately 46 times more flux in the 8- to 12-μm band than in the 3- to 5-μm band. For a quantum-noise-limited sensor and a given image contrast, this yields a sensitivity ratio of $\sqrt{46}$. Historically, this has permitted the design of 8- to 12-μm scanning sensors of excellent sensitivity.

Recently, the availability of high-uniformity staring-FPA sensors has permitted achievement of excellent thermal imagery within the 3- to 5-μm band as well. This is possible because a staring sensor typically has 10,000 times the photon-collection efficiency of a scanning sensor. (Photon-collection efficiency is the ratio of photon flux collected by an FPA to the photon flux incident on the focal-plane area defined by the field of view of the sensor.) As a result, staring FPAs provide high photon exposures, and even detector materials of low quantum efficiency can be used.

Staring sensors operated in the 8- to 12-μm band collect so much flux that quite good imagery can be obtained even with low-responsivity uncooled FPAs. High-quantum-efficiency sensors operated in the 8- to 12-μm band produce very large exposures, so it can be difficult to keep these sensors from saturating. Rapid readout and integration outside the focal plane could theoretically provide extraordinary sensitivity, but this is generally not easy to implement.

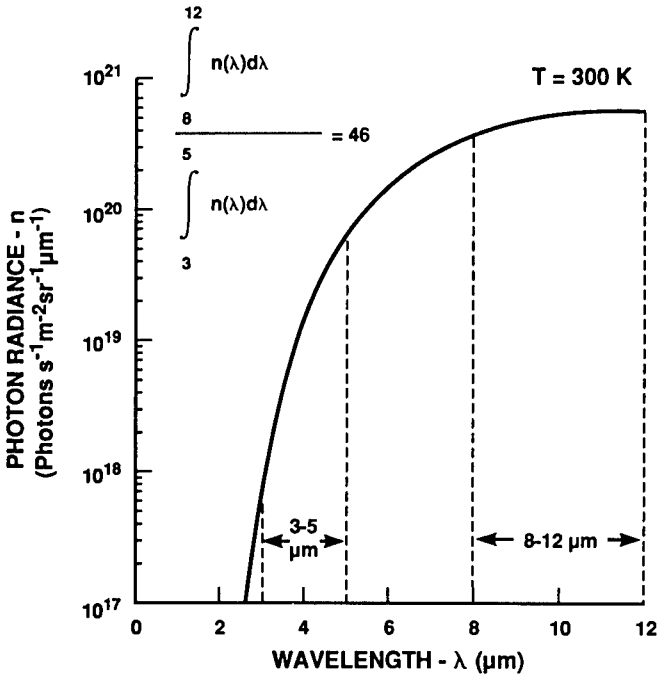

Fig. 3.8 Blackbody photon spectral radiance.

The signal available in each spectral band also depends on the background-normalized radiance contrast C_Δ. Figure 3.9 was derived from blackbody theory and presents the photon contrast versus wavelength for differential changes in temperature. Note that the 3- to 5-μm band is superior to the 8- to 12-μm band by a factor of approximately 2.25, and this factor reduces the advantage of the higher photon flux in the 8- to 12-μm band. The available contrast also determines the requirement for dynamic range in staring sensors.

The background-normalized radiance contrast can also be derived for large temperature differences, with the results presented in Fig. 3.10. For the small differences shown, contrast is consistent with the results presented in Fig. 3.9 obtained by incremental analysis. For large differences, contrast increases more rapidly in the 3- to 5-μm band than in the 8- to 12-μm band. For example, for a 100°C temperature difference, there is six times the contrast in the 3- to 5-μm band. This phenomenon produces expansion of the temperature gray scale in an image.

3.3.1.2 Sensor Exposure, Dynamic Range, and Noise

3.3.1.2.1 Noise-Equivalent Temperature. A useful FPA performance criterion for FPA design is noise-equivalent temperature (NET). NET pertains to resolved IR images and is the difference temperature at which the pixel SNR = 1.

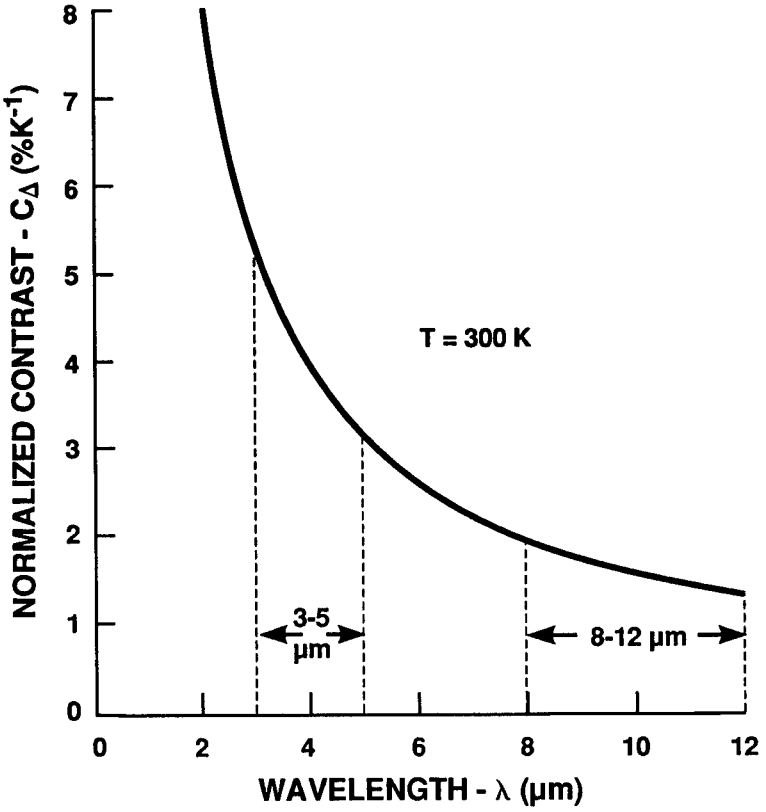

Fig. 3.9 Blackbody differential contrast.

The difference signal ξ_{pd} is obtained by combining Eqs. (3.4) and (3.6):

$$\xi_{pd} = 10^{-6} C_\Delta \varepsilon_b (\Delta T) \Delta^2 \quad \text{(e)} \ . \tag{3.33}$$

The total rms pixel noise N is obtained from the noise variance density n:

$$N = 10^{-3} (n\Delta^2)^{1/2} \quad \text{(e)} \ . \tag{3.34}$$

Forming an SNR quotient and letting SNR = 1 and ΔT = NET, NET is then

$$\text{NET} = \frac{10^3 n^{1/2}}{C_\Delta \varepsilon_b \Delta} \quad \text{(K)} \ . \tag{3.35}$$

Substituting Eq. (3.21),

$$\text{NET} = \frac{10^3 (n_Q + n_{MFP} + n_{FP} + n_{AT})^{1/2}}{C_\Delta \varepsilon_b \Delta} \quad \text{(K)} \ . \tag{3.36}$$

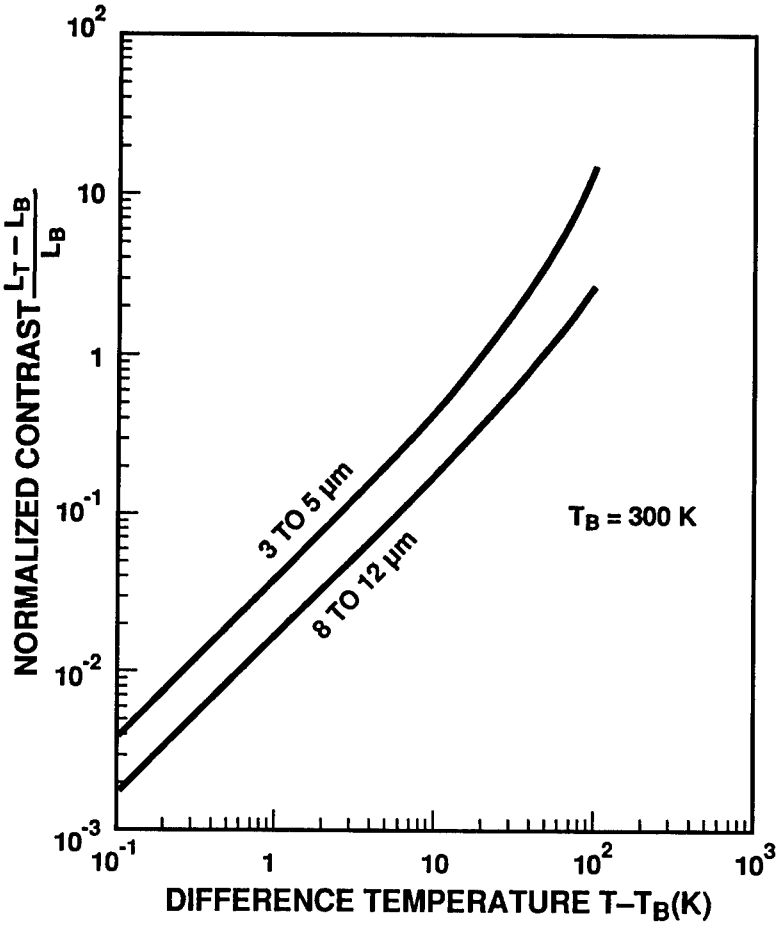

Fig. 3.10 Blackbody difference-temperature contrast.

This is the complete expression. It differs from the current standard for NET, which was derived for single-pixel scanning sensors and contains only temporal noise. This temporal standard (NET_T) is given by

$$NET_T = \frac{10^3(n_Q + n_{AT})^{1/2}}{C_\Delta \varepsilon_b \Delta} \quad (K) \ . \tag{3.37}$$

3.3.1.2.2 FPA Design Requirements Nomogram. For high-sensitivity staring-FPA applications, image contrast is very low, so sensor dynamic range and multiplicative fixed-pattern noise performance are very important. For operation in either the 3- to 5-μm or 8- to 12-μm band, requirements for FPA multiplicative fixed-pattern noise uniformity and charge storage capacity can be derived from sensor NET performance requirements.

If the multiplicative fixed-pattern noise dominates, Eq. (3.36) becomes

$$\mathrm{NET}_{\mathrm{MFP}} = \frac{10^3 n_{\mathrm{MFP}}^{1/2}}{C_\Delta \varepsilon_b \Delta}(\mathrm{K}) \ . \tag{3.38}$$

Substituting Eq. (3.16), combining Eq. (3.15), and solving for the required nonuniformity U yields

$$U = \mathrm{NET}_{\mathrm{MFP}} C_\Delta \ . \tag{3.39}$$

Here, C_Δ has been computed from Eq. (3.6) for a quantum detector viewing a 300 K background. For the 3- to 5-μm band, $C_\Delta = 0.036$, and for the 8- to 12-μm band, $C_\Delta = 0.016$. The required nonuniformity for each band is plotted in the lower section of the nomogram presented in Fig. 3.11.

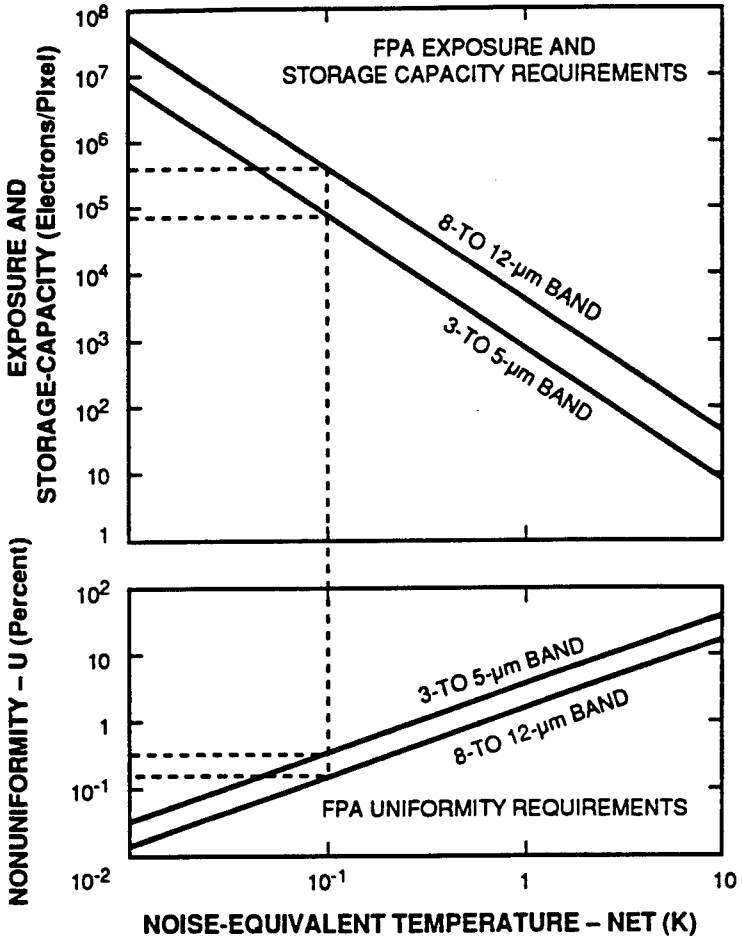

Fig. 3.11 FPA performance requirements for quantum-type detectors.

To satisfy ideal quantum-noise requirements, quantum-noise variance density n_Q, from Eq. (3.10), can be substituted in Eq. (3.36) to obtain quantum NET_Q. The required background pixel exposure ξ_{pb} then becomes

$$\xi_{pb} = \frac{1}{C_\Delta^2 \, NET_Q^2} \quad \text{(e/pixel)} \; . \tag{3.40}$$

This exposure represents the FPA pixel storage requirement, and the relationship is plotted in the upper portion of the nomogram of Fig. 3.11.

The nomogram of Fig. 3.11 is constructed by letting $NET_{MFP} = NET_Q$. A typical design solution is shown for NET = 0.1 K for each of the spectral bands. Note that the requirements for both uniformity and dynamic range are significantly more stringent for the 8- to 12-μm band than for the 3- to 5-μm band.

3.3.1.2.3 Fixed-Pattern Noise Correction. For high-sensitivity performance, most staring IR sensors require fixed-pattern-noise correction.[26,29–32] If the noise is well represented by the additive and multiplicative categories described in Sec. 3.2.3.2.3, then computational methods can provide a high degree of correction over a wide dynamic range. Characterization of fixed-pattern noise is accomplished by recording one or more exposures from a uniform source. A time average of multiple exposures permits reduction of temporal noise so that a good statistical estimate can be obtained. Stored fixed-pattern-noise data corresponding to various exposure levels can then be used for real-time correction.

FPAs in which additive noise dominates can be corrected most easily by straightforward subtraction of the stored reference pattern. This has been termed *single-point,* or *offset,* correction. If the multiplicative component of noise is also important, both additive and multiplicative computations are required. This has been termed *two-point* correction.

Some FPAs exhibit a significant variation in detector cutoff wavelength. The resulting fixed-pattern noise cannot be corrected completely because the noise is a function of the spectral content of the scene and this is not known *a priori.*[26]

3.3.1.3 Optics Resolution. The diffraction limit of optics provides a boundary for system resolution performance and an important relationship to the design of FPA pixel geometry. A useful perspective can be established by use of the noise-equivalent aperture theory presented in Sec. 3.2.3.1.

As an example hardware design criterion, let us assume that the image-plane noise-equivalent spread factor of the optics δ_o is one-half the size of the spread factor of the FPA determined by the mean pixel spacing Δ. This criterion provides good resolution but allows some aliasing due to image sampling. The combined optics/array angular spread factor Ψ is then

$$\Psi = 5^{1/2}\Psi_o \quad \text{(mrad)} \; , \tag{3.41}$$

where Ψ_o is the optics angular spread factor (mrad). For diffraction-limited optics, the required diameter D_o is then

$$D_o = \frac{4.13\lambda}{\Psi} \quad \text{(mm)} \ . \tag{3.42}$$

Plots of this relationship for 4 μm and 10 μm are presented in Fig. 3.12. Superimposed are typical diameters for a missile seeker and a search/track system. It is apparent that the 3- to 5-μm band offers a significant advantage in resolution over that of the 8- to 12-μm band.

3.3.1.4 FPA Pixel Geometry. The pixel spacing of an FPA will determine the optics focal length required in a system. The focal length F is expressed by

$$F = \frac{10^3\Delta}{\Psi_A} \quad \text{(mm)} \ , \tag{3.43}$$

where Ψ_A = pixel instantaneous field of view (mrad). A plot of this relationship is presented in Fig. 3.13, and superimposed are typical design parameters for a missile system and a search/track system. Small pixel spacings permit use of short-focal-length optics, which allows compact packaging of the sensor. This compactness must, however, be traded against sensitivity reduction caused by the smaller optics aperture, and the requirement for reduced optics $f/\#$, which could escalate the difficulty and cost of optics fabrication.

Another related trade-off is sensor field of view (FOV). To achieve wide FOV with good sensitivity and resolution requires FPAs that are physically large. This principle is illustrated in Fig. 3.14 for a typical search/track system designed with 200-mm-diameter, $f/2$ optics. Note that an FOV of more than a

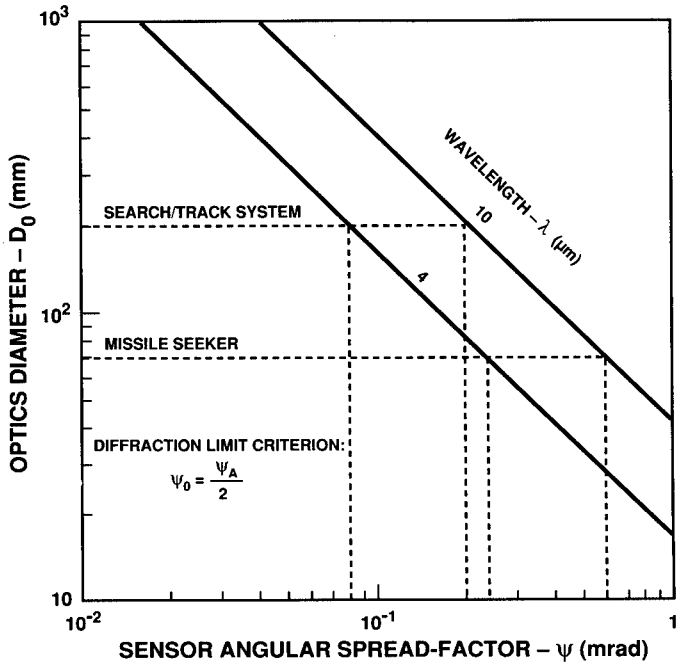

Fig. 3.12 Diffraction-limited optics performance.

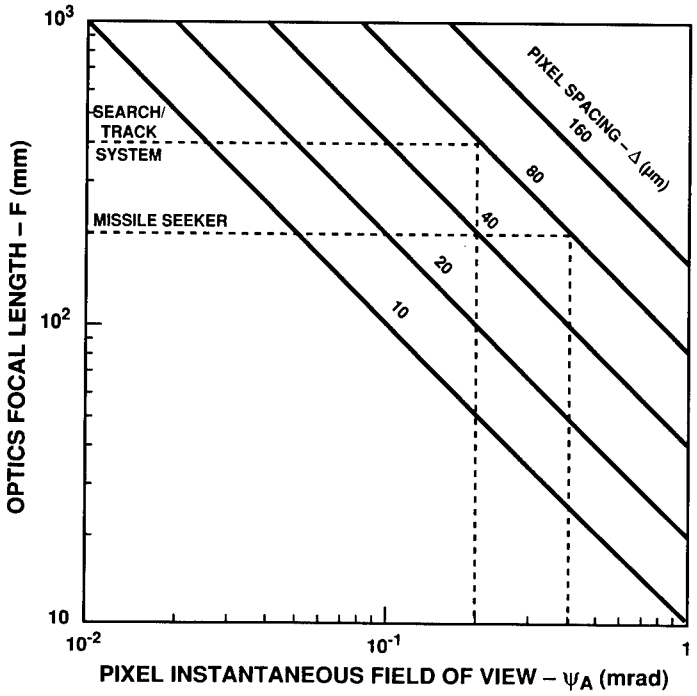

Fig. 3.13 Pixel-spacing requirements.

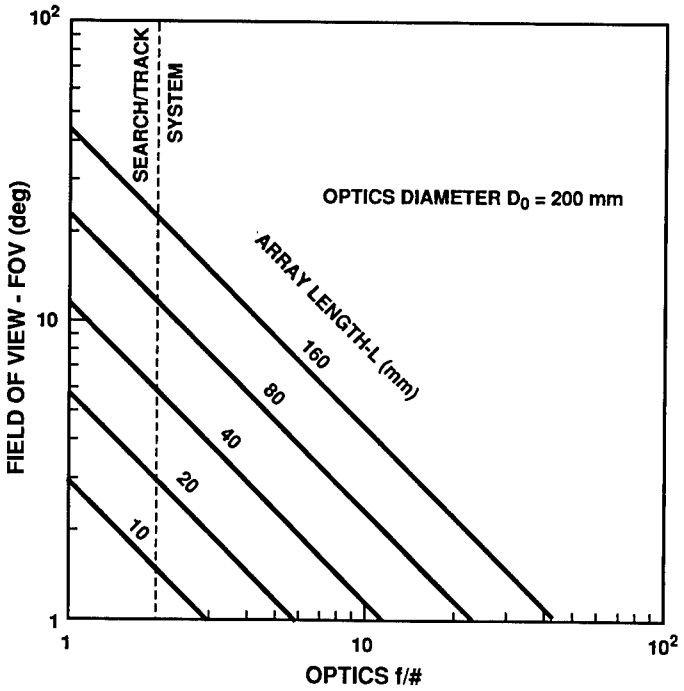

Fig. 3.14 FPA total-length requirements.

few degrees requires tens of millimeters of FPA length. For practical realization of such a staring sensor, the use of a mosaic architecture and/or high-producibility materials such as silicon is implied.

3.3.2 Recognition-Range Prediction Model

Recognition range is an important performance parameter for many sensor systems. Prediction of this quantity requires appropriate use of object signatures, atmospheric attenuation, hardware performance, and human recognition criteria. A useful methodology has been applied to IR sensors by the NVEOD,[28] and an example is presented below of the extension of this approach for use with the staring-sensor model presented in this chapter.

The methodology is depicted in Fig. 3.15. The principal target signature is thermal radiation, which is expressed as a difference temperature defined relative to the adjacent background. This signature is attenuated by atmospheric transmission. For relatively good transmission (i.e., 23-km visibility), the LOWTRAN[33] model or an exponential-attenuation function is appropriate. For poor transmission, high-obscuration models are more appropriate.[34]

Minimum resolvable temperature (MRT), introduced in Sec. 3.2.4.1, is a measure of hardware performance and is a function of optical spatial frequency. MRT can be measured directly by human observers or predicted mathematically.

The use of MRT data for prediction of recognition-range performance requires scaling the optical spatial frequency of the sensor to the angular subtense of the target. This scaling is based on a separate set of human factors

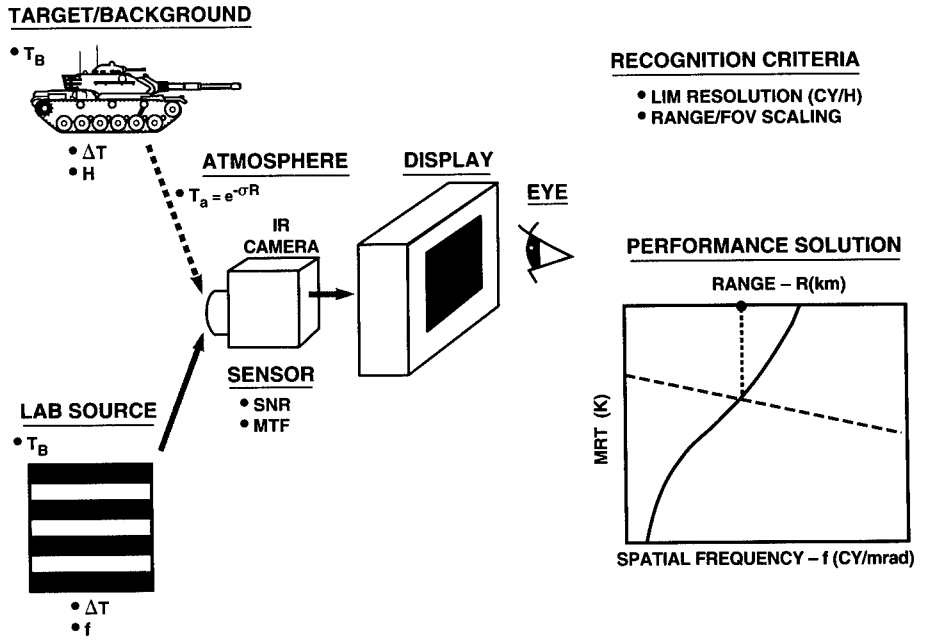

Fig. 3.15 Recognition-range prediction.

experiments involving real targets. A recognition criterion f_{SR} normalized to the target size (usually height) is computed from

$$f_{SR} = \frac{S\phi}{R} \quad \text{(cycles/size)} \ , \tag{3.44}$$

where S is the target size (m), ϕ is the sensor MRT spatial frequency (cycles/mrad), and R is the target range (km). The spatial-frequency scale of a measured or computed MRT characteristic can be scaled to range using a range-scaling factor (k_R) derived from Eq. (3.44):

$$k_R = \frac{\phi}{R} = \frac{f_{SR}}{S} \quad \text{(cycles mrad}^{-1}\text{ km}^{-1}\text{)} \ . \tag{3.45}$$

In the past, considerable success has been achieved by use of the *Johnson criteria* for f_{SR}, developed at NVEOD for nonsampled imaging systems. The recent successful development of image-sampling FPAs has fostered effort currently in progress for updating these criteria. For purposes of illustration, the original Johnson criterion will be used below. While this approach ignores the sampling problem, preliminary tests have shown that reasonably accurate predictions can be made for real objects, especially with multiframe, moving imagery.

The final solution for target recognition range is obtained graphically by overlaying MRT, target differential temperature, and atmospheric transmission versus range, as illustrated in Fig. 3.15. This graphical technique provides an excellent perspective of hardware design trade-offs, performance margins, and operational capability.

3.3.3 Staring IR Viewer Design Example

To illustrate the use of recognition-range model, a design example is presented for an IR Schottky-barrier 320 × 244 staring-FPA sensor.[35,36] This FPA has a 40-μm × 40-μm pixel spacing and 39% fill factor. Noise characteristics are similar to those presented in Fig. 3.5. The optics noise-equivalent spread factor δ_o is one-half the spread factor determined by the FPA pixel spacing Δ, but because of the small fill factor, optics MTF is lower and δ_o is larger than those of the FPA.

The MTFs of these individual components and of the product response of the sensor are presented in Fig. 3.16. Also superimposed on Fig. 3.16 is a noise-equivalent Gaussian approximation for MTF. This is a simpler analytic form and generally yields accurate results, because the sensor is an element in the cascade of imaging elements such as the display, the eye, etc. The central-limit theorem predicts that a cascade of aperture functions of various types and similar size will rapidly converge to a Gaussian form. The use of this form also smoothly truncates the oscillatory response (above the spatial frequencies shown) associated with the $\sin x/x$ type of MTF of the FPA.

An FPA sensor spatially samples an image, and to faithfully reproduce the image, sensor functions of the type shown in Fig. 3.17 are required. The prefilter associated with the optics and FPA would limit the system MTF to the

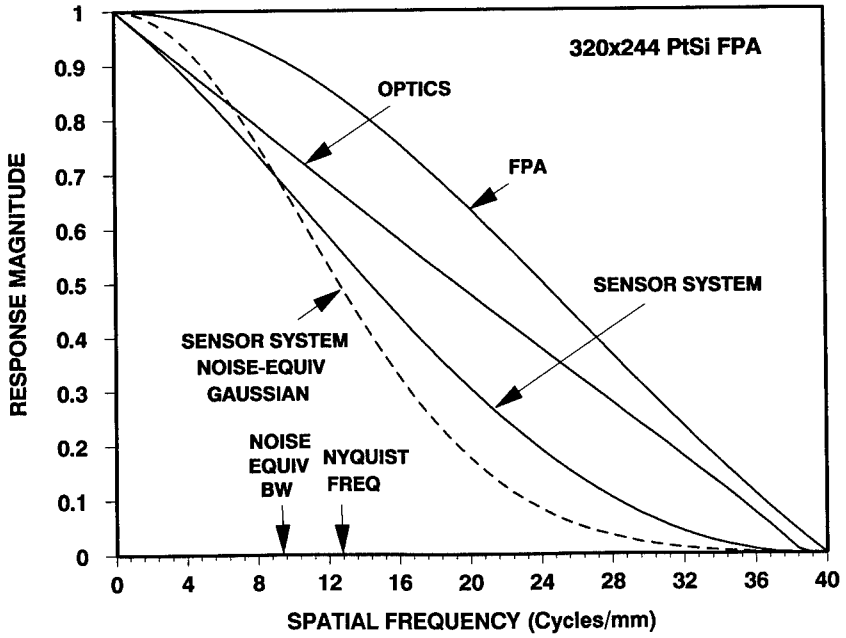

Fig. 3.16 Modulation transfer functions.

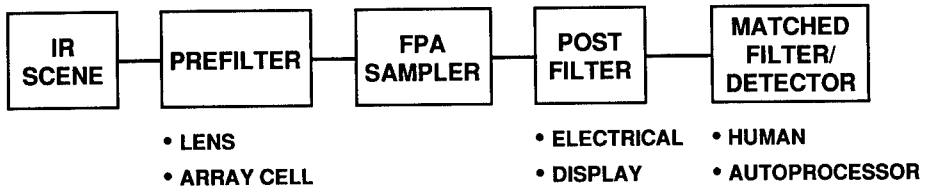

Fig. 3.17 Sampled-image detail detection.

Nyquist frequency, and the postfilter would limit the output bandwidth to this same frequency. To compare this ideal Nyquist design to the design example presented here, the sensor noise-equivalent bandwidth f_e and Nyquist frequencies are also indicated on Fig. 3.16. Note that at the Nyquist frequency, the sensor MTF is high (approximately 55%), which can result in the perception of high image sharpness. This high response also can produce image aliasing, but, in the author's experience, considerable aliasing can be tolerated, and the high image sharpness is generally preferred over the lack of aliasing in a system of lesser MTF, which conforms to Nyquist theory.

The condition of high MTF at the Nyquist frequency has presented a periodic-bar performance measurement and modeling dilemma because the bars will not be reproduced faithfully for spatial frequencies above and often even below the Nyquist frequency. If system response is artificially truncated at the Nyquist frequency, the resulting prediction of object recognition has been observed by the author to greatly underestimate (by a factor of two or more) the measured recognition capability. Additional future work is needed to better quantify these indications; however, the approximation used here is to ignore aliasing in the computation of minimum resolvable temperature and to include in the human performance criteria the image degradation due to aliasing.

A typical set of recognition criteria measured at CNVEO for a Schottky-barrier FPA system is presented in Table 3.5. In terms of pixel sampling, 2.3 Nyquist-frequency cycles/height were required for recognition. The scaling of recognition range to computed MRT (with sampling ignored) resulted in the need for 4.6 cycles/height. The Johnson criterion (for nonsampled sensors) is 3 to 4 cycles/height, only slightly less than the computed value. This suggests that performance is determined more by the MTF (high at the Nyquist frequency) and SNR than by the Nyquist-sampling limit. The slightly higher cycles/height than required by the Johnson criterion is believed to represent a reasonable way, for the time being, to embody degradation due to image aliasing.

Using the methods outlined above and depicted in Fig. 3.15, a sensor can be designed to meet a specified recognition-range performance. Suppose that the following performance is specified:

Recognition range: 3.5 km
Object height: 3.3 m
Object difference-temperature: 1.5 K
Atmospheric extinction coefficient: 0.29/km.

As a design example, computations have been made for a viewer that uses the 320 × 244 Schottky-barrier FPA introduced above. The responsivity of the detectors is characterized by a quantum-efficiency coefficient of 0.24 eV^{-1} and a barrier height of 0.22 eV. Equations for signal, noise, and aperture response were presented in Sec. 3.2. It has been convenient to use a spreadsheet for these computations, and a summary of parameters is presented in Table 3.6. Input quantities are represented by uppercase type, and computed parameters are represented by lowercase type. The spreadsheet provides a convenient way to conduct simulations that permit iteration of the design to achieve the desired level of recognition-range performance. Final entries in the spreadsheet represent the sensor design characteristics.

Table 3.5 FPA Recognition Performance Data

Reciprocal Visual Angle for P(rec) = 0.5 (NVEOD Lab Data) $(rad)^{-1}$	Equivalent Frequency for Tank Height h			
	Array Pitch (pixels/height)	Array Pitch Nyquist Frequency (cycles/height)	Model MRT Frequency (cycles/height)	Johnson Criterion (cycles/height)
135	4.6	2.3	4.8	3 to 4

Part A of Table 3.6 contains geometric quantities associated with the optics and FPA. Characteristics include optics and FPA spread factors and appropriate MTF types used for subsequent MRT computations. Noise-equivalent spread factors are computed for the cascaded combination of these components. Also presented are the overall FPA size and corresponding FOV of the sensor.

The first portion of Part A summarizes the computation of the optics spread factor using the methods described in Sec. 3.2.3.1. The optics spread factor δ_o is computed from the diffraction-limited expression in Table 3.2, and is increased over that value by the aberration factor. FPA pixel spread factors are computed from the active detector area (and other optical and electrical spread factors if present), and the Nyquist frequency is computed from the pixel spacing. Optics and FPA spread factors are combined using Eq. (3.9) to obtain the sensor mean spread factor. Finally, the sensor FOV is computed from the optics focal length and FPA size.

Part B of Table 3.6 contains quantities that pertain to exposure and noise. The spectral limits of integration shown are used in Eq. (3.2) for exposure computations. Object temperature, emissivity, and area are tabulated. FPA noise characteristics cover temporal and fixed-pattern-noise types, and quantities are modeled using the methods described in Sec. 3.2.3.2. Noise variance density is totaled in accordance with Eq. (3.21). The total noise for a resolution element is also computed for the sensor mean spread factor δ defined by Eq. (3.9). Part B is completed with a summary of earth-background exposure computed with Eq. (3.2), normalized contrast computed with Eq. (3.6), and NET computed with Eq. (3.37).

Part C of Table 3.6 contains the quantities associated with computation of MRT for the sensor. Inputs are shown for bar-pattern type and for visual-system integration time and bar-resolution SNR threshold. Sensor exposure and noise quantities are scaled to correspond to human perception quantities. Finally, target temperature, atmospheric transmission, and target size and recognition criteria are introduced to permit scaling of sensor MRT characteristics to recognition-range performance using Eqs. (3.44) and (3.45).

The resulting sensor MRT is presented in Fig. 3.18. Superimposed is the object difference temperature attenuated by the atmosphere. Intersection of these characteristics results in the solution of recognition-range performance.

Also superimposed on Fig. 3.18 is the Nyquist frequency of the sensor. This frequency is below that corresponding to the range performance determined from the nonsampled methodology described above. Exceeding the Nyquist limit can degrade the image, and more research is required to quantify the effect. As indicated previously, the author's experience indicates that, especially for moving, multiframe imagery, the human can tolerate exceeding the Nyquist limit by up to a factor of approximately two without significant loss in performance. It is believed that within this bound, useful results can be obtained from the nonsampled range-prediction methodology.

This performance characterization substantiates the design of a compact staring sensor that can provide the required target-recognition-range performance.

Table 3.6 Tactical IR Sensor Design Parameters

Part A - Optics and Focal-Plane Geometry

OPTICS	
DIAMETER (m):	0.1
FOCAL LENGTH (m):	0.3
Computed f/#:	3.00
WAVELENGTH (μm):	4.3
SPREAD ANGLES	
Diffraction (μRad):	76.970
ABERRATION FACTOR:	2
Total (μRad):	153.94
Computed (arcsec):	31.75
Spread Factor (μm):	46.18
MTF APPROX.-"DIFF","GAUSS":	DIFF
FPA PIXEL SIZE (μm)	
HORIZ. TDI SHIFT:	0
HORIZ. SPACING:	40
VERT. SPACING:	40
HORIZ. BINNING RATIO:	1
VERT. BINNING RATIO:	1
Horiz. Spacing w/Binning:	40.00
Vert. Spacing w/Binning:	40.00
FPA AREA FILL FACTOR:	0.39
Horiz. Size w/Binning:	24.98
Vert. Size w/Binning:	24.98
OPT./CHG. SPREAD (μm):	0
Horiz. Spread Factor (μm):	24.98
Vert. Spread Factor (μm):	24.98
Mean Spread Factor (μm):	24.98
Mean Spread Angle (μRad):	83.27
Mean Spread Angle (arcsec):	17.18
FPA NYQUIST FREQUENCY and MTF TYPE	
Horiz. Nyquist Freq (cy/mm):	12.5
Vert. Nyquist Freq (cy/mm):	12.5
MTF APPROX.-"RECT","GAUSS":	RECT
SENSOR MEAN RESOLUTION	
Spread Factor (μm):	52.51
Noise-Equiv BW (cycles/mm):	9.52E+00
Spread Angle (μRad):	175.03
(arcsec):	36.1
SUB-FPA NO. PIXELS W/O BINNING	
AZ.:	320
EL.:	244
Total:	7.81E+04
Total FPA Length (mm):	
AZ.:	12.8
EL.:	9.76
Diagonal:	16.1
SYSTEM FOV (deg)	
AZ.:	2.44
EL.:	1.86
Diagonal:	3.07

Part B - Exposure and Noise Parameters

INTEG WAVELENGTH LIMIT (μm):	
LOWER:	3.40
UPPER:	4.60
OBJECT SURFACE #1	
TEMPERATURE (K):	320
EMISSIVITY:	0.76
AREA (m^2):	15
Emissivity*Area:	11.4
OPTICS TRANSMISSION:	0.5
SENSOR READ AND INTEGRATION TIMES	
READ FRAME TIME (sec):	3.33E-02
NO. FRAMES OF INTEGRATION	1
Integration Time (sec):	3.33E-02
FPA Fill Factor:	0.39
FPA NOISE PARAMETERS	
QUANTUM NOISE FACTOR:	1.1
MULTIPLICATIVE FIXED PATTERN	
PIXEL NONUNIFORMITY (%):	0.2
Noise Factor (m):	1.60E-07
ADDITIVE (DARK-CURRENT) FIXED PATTERN	
PIXEL DARK I NONUNIF (%):	0.5
Noise Factor (m):	4.00E-07

Table 3.6 *(continued)*

ADDITIVE AMPLIFIER READOUT	
MEAS rms FLOOR (Elect/Pix):	15
MEAS rms@1MHz(Elect/MHz^.5):	15
PRE-NOISE GAIN	1
Channel Pixel Rate (MHz):	2.3424
Floor Var Dens (Elect/m^2):	1.41E+11
Read Rate VarDns(Elect/m^2):	3.29E+11
Tot Read VarDens(Elect/m^2):	4.70E+11
Tot rms (Elect/Binned-Pixel):	27.4
ADDITIVE DARK CURRENT	
MEAS CURRENT DENS (nA/cm^2):	5
Req FPA Operating Temp (K):	79.4
Dark Expos Dens (Elect/m^2):	4.06E+12
Dark Exp (Elect/Binned-Pixel):	6.50E+03
rms Noise Dens (Elect/Pix):	80.6
SENSOR NOISE	
Variance Density (Elect/m^2)	
Backgnd. Photoelectron:	3.35E+13
Mult. Fixed Pattern:	5.93E+12
Additive Fixed-Pattern:	6.60E+11
Additive Temporal:	4.53E+12
Total:	4.46E+13
Sprd Fact rms (Elect/Resel)	
Backgnd. Photoelectron:	3.04E+02
Mult. Fixed Pattern:	1.28E+02
Additive Fixed-Pattern:	4.27E+01
Additive Temporal:	1.12E+02
Total:	3.51E+02
EARTH THERMAL-EXPOSURE, CONTRAST, AND NET	
Earth-Bckgrnd Temperature (K):	300
Bckrnd Exp Density (Elect/m^2):	3.04E+13
Bckrnd Exposure (Elect/Pixel):	4.86E+04
Incr Bckrnd Exp Dens (El/m^2):	3.04E+13
Normalized Contrast (1/K):	4.16E-02
Temporal rms Noise (Elect/Pix):	2.46E+02
Temporal/Pixel NET (K):	0.122

Part C - Minimum Resolvable Temperature Data

BAR-PATTERN l/w RATIO:	7
HUMAN-EYE BAR SNR-THRESHOLD:	2.7
HUMAN-EYE INTEG TIME (s):	0.1
Therm-Exp Norm Contrast (1/K):	0.042
SENSOR EXPOSURE DENSITY (Elect/m^2)	
Thermal Background:	3.04E+13
Difference Signal:	1.26E+12
HUMAN-EYE EXPOSURE DENSITY (Elect/m^2)	
Thermal Background:	9.11E+13
Difference Signal:	3.79E+12
SENSOR NOISE	
Variance Density (Elect/m^2)	
Backgnd. Photoelectron:	3.35E+13
Mult. Fixed Pattern:	5.93E+12
Additive Fixed-Pattern:	6.60E+11
Additive Temporal:	4.53E+12
EYE NOISE	
Variance Density (Elect/m^2)	
Backgnd. Photoelectron:	1.00E+14
Mult. Fixed Pattern:	5.33E+13
Additive Fixed-Pattern:	5.94E+12
Additive Temporal:	1.36E+13
Sensor Noise-Eq Sprd-Fact (μm):	52.5
Sensor Noise-Equiv BW (cy/mm):	9.523
FPA Horiz Nyquist Freq (cy/mm):	12.5
FPA Vert Nyquist Freq (cy/mm):	12.5
TARGET-TEMP/RECOGNITION & RANGE SCALING	
TARGET DIFFERENCE TEMP (K):	1.5
TARGET SIZE (m):	3.3
"JOHNSON" CRITERION (cy/size):	4.8
Required Target-Freq (cy/m):	1.45E+00
Range Scaling Fact(cy/mRad/km):	1.45E+00
ATMOS EXTINCTION COEFF (1/km):	0.29
Sensor Mean Spread-Factor (μm):	52.51
Sensor Mean Spread-Factor (mRad):	1.75E-01
Sensor Noise-Equiv BW (cy/mRad):	2.86E+00
FPA Horiz Nyquist Freq (cy/mRad):	3.75E+00
FPA Vert Nyquist Freq (cy/mRad):	3.75E+00

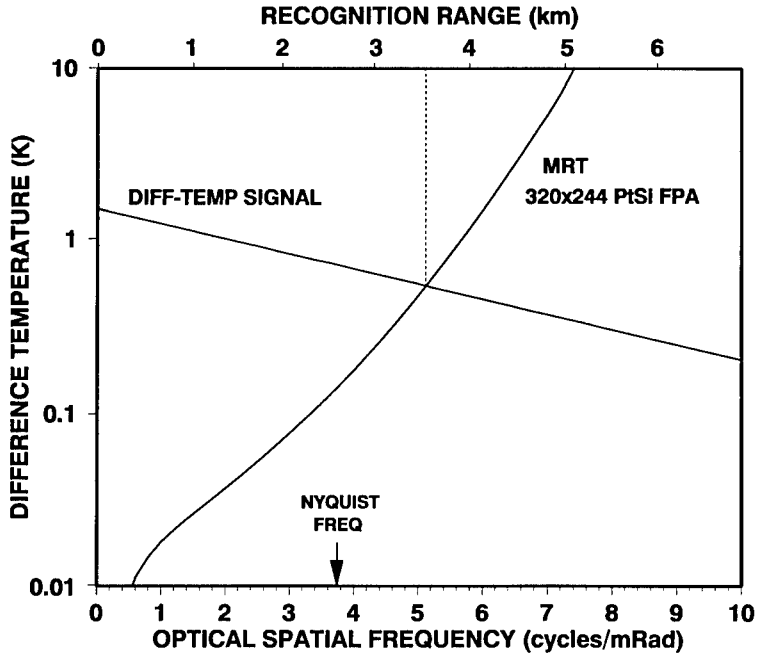

Fig. 3.18 Minimum resolvable temperature.

3.4 SPACE-SURVEILLANCE SENSOR DESIGN AND PERFORMANCE

3.4.1 Staring-Sensor Design Drivers and Trade-offs

3.4.1.1 Design Methodology. Previous sections of this chapter have emphasized the use of staring sensors for acquisition of imagery. Another important class of applications involves the detection and track of distant point-source objects located within a background scene. Space surveillance is one example and will be used to illustrate this type of design and performance-characterization methodology.

Today's electro-optical space-surveillance sensors cover the visible spectrum and are located on the ground. At night, when the weather is clear, these sensors offer outstanding sensitivity for acquisition and track of deep-space objects that are illuminated by sunlight.[37,38] These sensors also can cover low-altitude objects located in the twilight regions but cannot detect objects in the earth's shadow.

There is a need to upgrade current operational space-surveillance systems to attain more extensive and timely coverage of a rapidly expanding population of satellites. Recently, developmental ground-based visible-spectrum sensors

have been used to detect low-altitude objects located on the sun-illuminated (day) side of the earth, but sensitivity performance is restricted by the high level of background caused by sunlight scattered from the atmosphere. Spaceborne systems are not hampered by atmospheric scatter and thus can provide good coverage of sunlit regions. However, earth-shadow regions cannot be accessed by visible sensors since there is no sunlight there.

The IR spectrum offers an opportunity for significant extension of surveillance capability, and spaceborne systems offer the best potential because clouds and atmospheric attenuation and scatter are absent.[39] Thermal-emission and earthshine signatures make the low-altitude earth-shadow region accessible.

The development of spaceborne space-surveillance sensors will provide significant future operational capability. A practical approach for sensor design is a multispectral capability that uses the visible spectrum for most of the space coverage volume and concentrates IR coverage on the low-altitude earth-shadow region.[40] A design example for a visible/IR, multispectral staring sensor is presented below.

The fundamental performance requirements for a space surveillance sensor include sensitivity and coverage. To obtain satisfactory coverage rate, a surveillance fence is set up with a revisit time short enough to assure at least one look at satellites with highest azimuth and elevation angle rates. This revisit time indirectly affects range performance by limiting the photon integration time available for each look.

In the search process, there is uncertainty in the geometry and dynamics associated with satellite motion. This uncertainty is increased if the satellite has maneuver capability, and is bounded by available thrust. A statistical description of this uncertainty can be depicted as an area in range/angle-rate space, and a generic characteristic is presented in Fig. 3.19. Sensor sensitivity can be described in terms of range versus angle rate, and a generic characteristic is shown superimposed on the satellite population. The objective of sensor design is to ensure that the satellite population lies below the sensor performance characteristic.

Computation of sensor sensitivity requires a large number of parameters, as shown in Fig. 3.19. Note that signature components include thermal emission, reflected sunlight (except in the earth-shadow region), and earthshine; background components include sky, telescope, and cold-shield radiation and FPA dark current. The signal and background exposure components are computed using the methods described in Sec. 3.2.2. The performance model of Fig. 3.19 also includes system requirements for angular resolution and for coverage. These parameters are combined appropriately to compute signal and noise.

For a fixed signal-to-noise criterion, sensor static (zero angle rate) range performance R_S can be computed from

$$R_S = \frac{10^{-9/2} F \left[\sum_j (\varepsilon_{sj} A_{\mathrm{OBJ}_j}) \right]^{1/2}}{\delta T_{\mathrm{SNR}}^{1/2} n^{1/4}} \quad \text{(km)} , \tag{3.46}$$

where ε_s is the exposure from each signature component (e/m^2) and A_{OBJ} is the object area corresponding with $\varepsilon_s(m^2)$. Sensor SNR performance is a func-

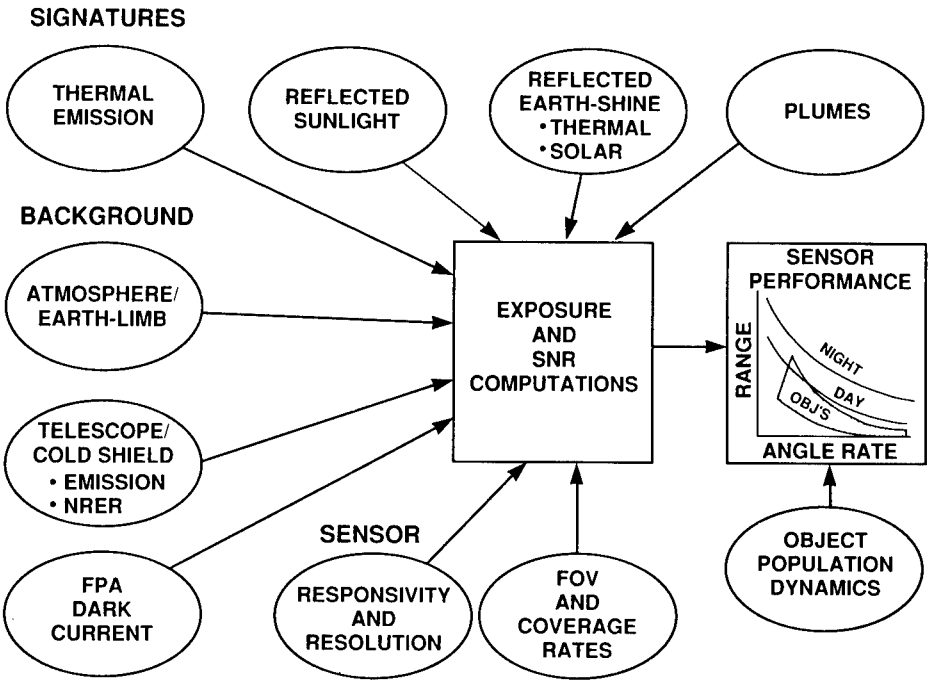

Fig. 3.19 IR sensor sensitivity analysis.

tion of angle rate; it decreases linearly beyond the dwell-in-cell condition (angle rate for object motion of one resolution element). To assess sensor performance, the corresponding range versus angle-rate performance can be compared to the range/angle-rate statistics of space objects of interests.

3.4.1.2 Space Environment IR-Radiation Characteristics. For space-surveillance applications, a variety of emissive and reflective signatures are available in the visible and IR spectra. These include thermal emission, sunlight reflection, earthshine, and earthshine reflection. The ultimate utility of these signatures is set by the effects of background radiation in the following manner.

Space objects appear as point sources of radiation within some background. An ideal sensor will be background quantum-noise limited, so sensor spatial resolution will set a limit on SNR performance. For a given size telescope, ultimate spatial resolution will be determined by diffraction limits, and this is a function of wavelength. Based on these principles, typical signature components have been compiled, and their amplitudes have been normalized to account for wavelength-dependent diffraction-limited resolution used for background rejection. The results are presented in Fig. 3.20.

For graybody temperatures of 300 K or less, signature amplitude peaks at approximately 10 μm (LWIR band) and falls off rapidly in the MWIR band. However, reflected earthshine, especially significant at low orbital altitude,

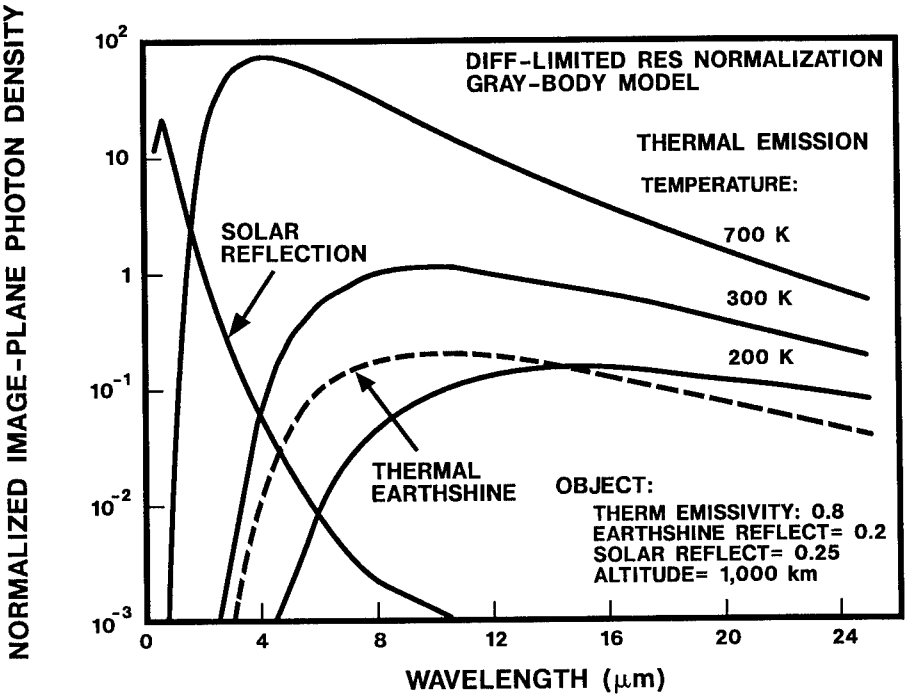

Fig. 3.20 Point source signals.

places a floor on available radiant intensity. Sunlight reflection, if available, can enhance these signatures in the MWIR band. Even though signatures are somewhat lower in the MWIR band than in the LWIR band, good sensitivity can be realized by use of a low-noise staring-format sensor. For higher temperatures, signal increases very substantially in the MWIR band.

The phenomenology associated with the ground-to-space atmosphere is of particular importance for ground-based surveillance sensors. Transmission losses affect the level of signal available, and background noise is produced by radiation from both thermal emission and scatter. Data have been obtained from available measurements and from the USAF Geophysics Laboratory LOWTRAN program.[33] Figure 3.21 contains a summary of important characteristics of both dry and tropical air masses.

Transmission is plotted for elevation angles extending from 15 to 90 deg. Low elevation angles are desirable for maximum coverage from a particular ground site. Note that there is significant degradation in transmission at small elevation angles in the visible band for both air masses. In the LWIR band, transmission is improved in a dry air mass but is essentially unusable in a tropical air mass. The MWIR band maintains good transmission for both air masses.

To achieve high sensitivity, low atmospheric path radiance is also desirable. Path radiance data for day and night conditions also are summarized in Fig. 3.21. (Path radiance varies much less with elevation angle than does transmission,

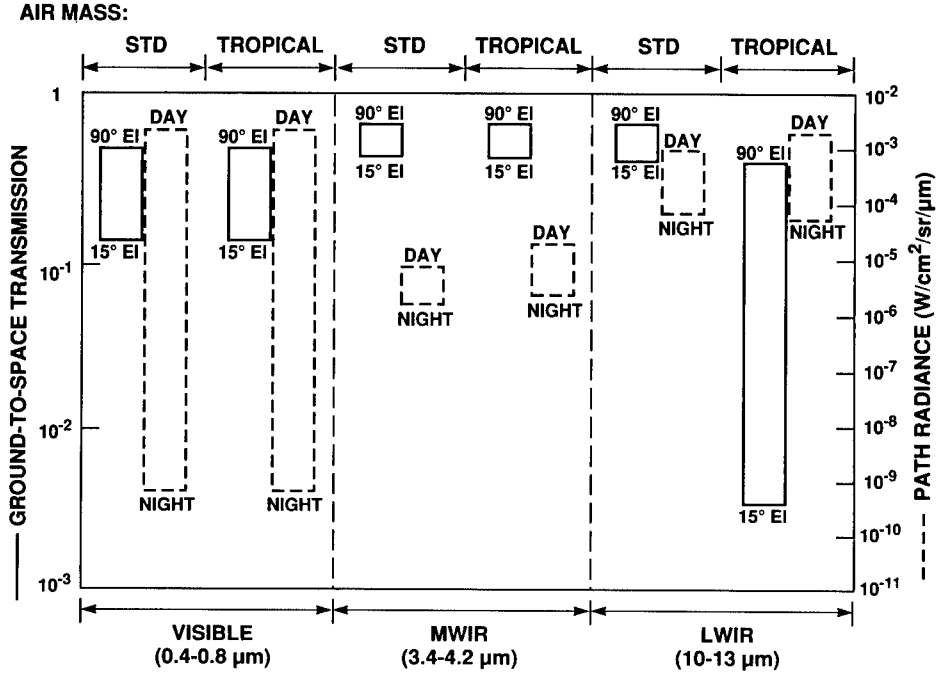

Fig. 3.21 Ground-to-space atmosphere.

so that consideration has been omitted from this discussion.) Note that in the visible band, there is approximately a 10^6:1 increase in path radiance during daylight hours, which results in a substantial loss in sensitivity. In both the MWIR and LWIR bands, there is much less variation between day and night conditions, and the MWIR band exhibits significantly less background than the LWIR band.

The combination of transmission and path-radiance data presented in Fig. 3.21 suggests that the MWIR band has the highest potential for application in ground-based systems where site placement and coverage and day/night operation are of great importance. This environmental advantage needs to be weighed against the availability of signatures in the alternative spectral regions and against achievable sensor SNR performance. Exploitation of the desirable MWIR atmospheric parameters suggests the use of a staring-sensor configuration to attain high SNR through high photon-collection efficiency.

Figure 3.22 presents sky spectral-radiance data applicable to a spaceborne sensor looking at the earth-limb at a 100-km tangent height. These data were obtained from the AFGL (Degges) model.[41,42] Note that there is considerable structure in this background, and the nulls in the MWIR region are especially deep. These nulls represent significant opportunity for high-sensitivity detection of objects and for acquisition of MWIR signature data. Exploitation of these opportunities suggests a staring-sensor format and low-internal-noise performance.

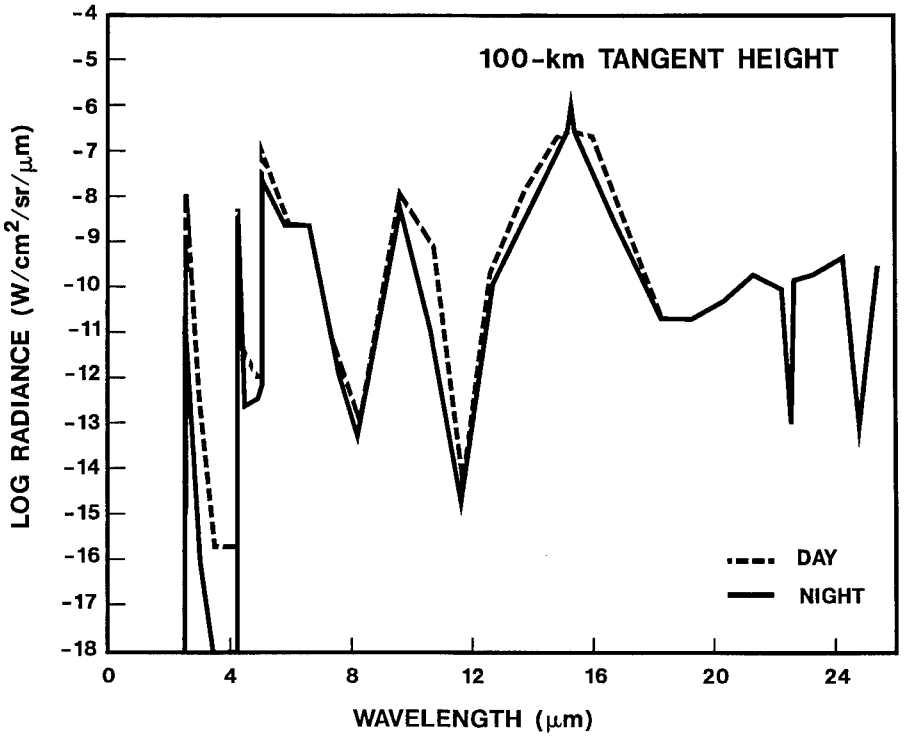

Fig. 3.22 Earth-limb background.

3.4.1.3 Space-Surveillance Sensor Requirements. Table 3.7 lists several special requirements for space-based FPAs. Large formats are needed for simultaneous achievement of high sensitivity, high resolution, and high coverage rate. A practical way to achieve high total resolution is to butt together FPA subarrays to form a large mosaic. To minimize the total number of subarrays, each one should be large, and this implies a high fabrication yield.

Pixel size should match the resolution requirements of a particular functional task. For surveillance, relatively large pixels are needed for

1. wide FOV coverage with relatively high optics *f*/#. (To cover the FOV and to match the required angular resolution, small pixels require the optics focal length to be short, and this yields a low *f*/#.)
2. high sensitivity achieved by the integration (dwell) time matched to the angular velocity of the target. This is particularly important for sensor internal-noise-limited conditions.

For track and closely spaced object (CSO) separation tasks, maximum angular resolution is required, so smaller pixels are needed, consistent with optics resolution, to provide sufficient pixel density to minimize losses in angle accuracy due to spatial sampling.

Because of these differences in the requirements for surveillance and tracking/CSO separation, there is a general need for variable pixel size. This can be achieved by fabricating FPAs of high pixel density (and corresponding high

Table 3.7 Attributes of Space-Sensor FPAs

- Large image-plane format
  - — Large high-yield subarray
  - — Subarray abuttability
  - — Multichannel readout
- Variable pixel size
  - — Large for search
  - — Small for track and close-object resolution
- Low temporal and fixed-pattern noise
- Radiation hardness
- Minimum cryogenic cooling

total number) and then by performing a pixel-binning operation to obtain the larger effective pixel size. This ideally should be accomplished on-chip before the introduction of readout noise.

For high sensitivity in a low-space-background environment, low readout noise must be achieved.[8,39,40] Low fixed-pattern noise is also needed, especially for high-background conditions. It is very difficult to compensate for fixed-pattern noise, particularly the nonadditive type. The demands for signal processing are severe, and calibration methods can only approximate the complexity of the FPA noise characteristics and the spectroradiometric properties of the space environment. Therefore, achievement of high inherent uniformity in the FPA is of utmost importance.

Severe high-energy radiation is likely to be part of a space environment. This radiation can produce spurious noise pulses of high amplitude and produce long-term calibration changes and damage. Shielding is difficult to accomplish, so inherent immunity in the FPA is an important objective. This pertains to both the detector materials and the readout multiplexer.

Sensor dark currents must be reduced to levels compatible with low-level space backgrounds, which requires cryogenic cooling. The longer the wavelength, the lower the temperature. The achievement of low temperatures implies use of a refrigerator of high input power and weight and limited life. These requirements are of particular concern for spaceborne sensors. Therefore, selection of a sensor type and configuration should be influenced heavily by the minimum-cooling attribute. The staring-sensor format can allow minimization of cooling by efficient collection of photons of relatively short wavelength. In this manner, adequate sensitivity can be attained without the long-wavelength, low-temperature burden.

3.4.1.4 Space Surveillance Sensor Design Example

3.4.1.4.1 Design Requirements. An example is presented of the design of a small spaceborne staring sensor that can provide satellite detection with coverage over a wide range of orbital altitudes. The satellite model has two principal elements, a solar panel and a body.

Suppose the sensor requirements are as follows:

Satellite altitude range: 600 to 50,000 km

Coverage rate: 1.5 deg^2/s

Satellite signature components (composite elements)

Object element #1
Temperature: 250 K
Area: 5 m^2
Emissivity: 0.9
Solar reflectivity: 0.3

Object element #2
Temperature: 175 K
Area: 5 m^2
Emissivity: 0.33
Solar reflectivity: 0.9

To accomplish long-range detection of high-altitude objects, the visible spectrum provides the best opportunity because of the stronger signatures presented in Sec. 3.4.1.2. The earth shadow covers very little total volume at high altitudes, so good overall coverage is possible. At lower altitudes, the earth shadow occupies a more significant volume, so an IR sensor is needed. IR signatures are not as strong, but range requirements are reduced. This combination of surveillance geometry and signature availability suggests the use of a multispectral sensor that shares a single telescope of minimum size.[43] Because of photon-collection efficiency, a staring-type sensor is highly desirable.

To illustrate the design and performance-assessment process, a ten-element mosaic of 420 × 420, three-side abuttable CCDs is used for both visible and IR sensors to achieve the required wide-FOV coverage. For the visible sensor, a silicon CCD[8] has been selected, and for the IR sensor, a Schottky-barrier MWIR CCD[19,40] has been selected. CCDs provide low-noise readout, which is compatible with low-space-background exposures. Other IR materials such as InSb and HgCdTe also are candidates for space-surveillance applications. However, low-sky-background performance data are not currently available for use in a design example.

The characteristics of visible CCDs designed for space-surveillance applications have been described in the literature.[8] These devices have very-low-noise performance (approximately six rms-electrons/pixel at 1-MHz pixel rate) and excellent transfer efficiency at low (few electrons/pixel) exposures.

Recently, PtSi and IrSi Schottky-barrier and GeSi-heterojunction CCDs have been under development specifically for space-surveillance applications.[18,19,40,44,45] Presented below is a brief summary of the pertinent characteristics of an advanced PtSi CCD used in this example.

Schottky-barrier quantum efficiency and dark current

Extension of the long-wavelength cutoff of Schottky-barrier devices enhances detection of low-temperature space objects. This wavelength extension is bounded by the requirements for refrigeration needed to reduce dark current to levels compatible with low space backgrounds. As a typical compromise, this design example pertains to an extended-wavelength, 6.7-μm-cutoff, PtSi CCD, with detector spectral quantum efficiency as presented in Fig. 3.2. This detector has a quantum-efficiency factor $C_1 = 0.297\ eV^{-1}$ and a barrier height $\Psi = 0.19$ eV.

Reduction of dark current to space-background levels requires detectors to operate at 65 to 70 K,[19] which can be achieved with a split-Stirling refrigerator of low power and high reliability, suitable for spaceborne sensors.

Schottky-barrier CCD noise and signal-transfer efficiency

Typical measured noise as a function of background exposure was presented in Fig. 3.5 for a 320 × 244-element FPA, and similar characteristics are used in this example.

Just as important as the noise characteristics is the signal transfer efficiency, under conditions of low background exposure and low temperature. At room temperature, CCDs provide excellent transfer efficiency with exposures down to 1 electron/pixel.[8] However, it has been recognized that the operation of CCDs at cryogenic temperatures and low exposure can be hampered by electron trapping.

To study signal trapping, laboratory measurements were made of point-signal transfer efficiency versus background bias versus operating temperature.[19] An example of the results is presented in Fig. 3.23. Superimposed are typical exposures corresponding with earth background and ground-based sky background. These early results were obtained on a CCD designed for high-exposure earth-background applications, and tailoring of the design has been necessary for low sky backgrounds. Improvements have been made in both the design and operation of this type of CCD, and test results are also given in Fig. 3.23.[19] These improvements have yielded excellent surveillance capability and are assumed in this design example.

3.4.1.4.2 Surveillance Sensor Range Performance Prediction. The methodology depicted in Fig. 3.19 is illustrated below. The equations for signal and noise were presented in Sec. 3.2 and pertain to a point source. It has been convenient to use a spreadsheet for these computations, and a summary of parameters is presented in Table 3.8. Input quantities are represented by up-

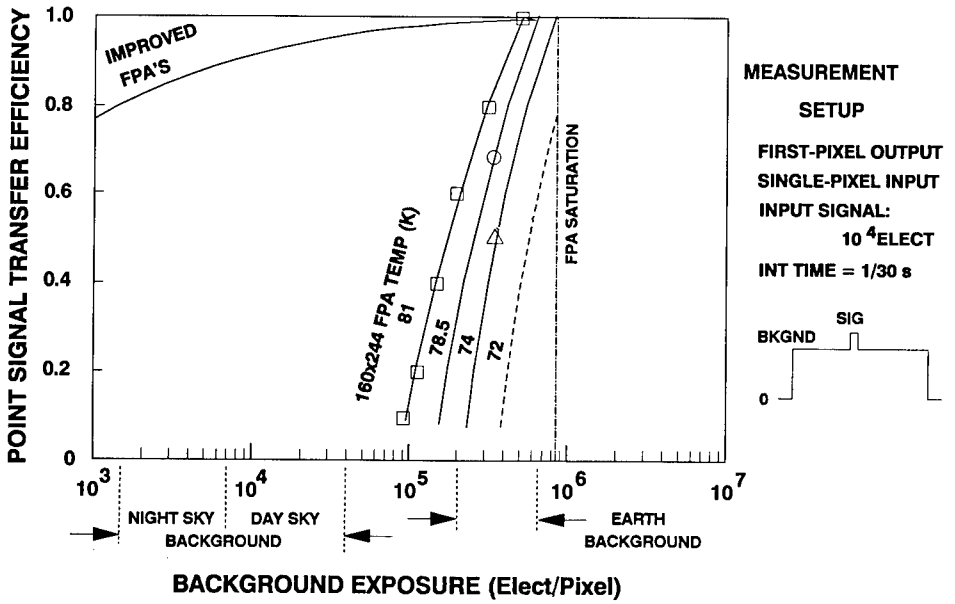

Fig. 3.23 Signal-transfer efficiency for a Schottky-barrier CCD.

Table 3.8 Spaceborne Sensor Design Parameters

Part A - Optics and Focal-Plane Geometry

	VISIBLE	IR-SCHOTTKY
OPTICS		
DIAMETER (m):	0.3	0.3
FOCAL LENGTH (m):	0.9	0.9
Computed f/#:	3	3
WAVELENGTH (μm):	0.55	5.1
SPREAD ANGLES		
Diffraction (μRad):	3.282	30.43
ABERRATION FACTOR:	1.5	1.2
Total (μRad):	4.92	36.52
Computed (arcsec):	1.01	7.53
Spread Factor (μm):	4.43	32.87
FPA PIXEL SIZE (μm)		
HORIZ. TDI SHIFT:	0	0
HORIZ.:	27	27
VERT.:	27	27
HORIZ. BINNING RATIO:	1	4
VERT. BINNING RATIO:	1	4
Horiz. w/Binning:	27	108
Vert. w/Binning:	27	108
OPT./CHG. SPREAD (μm):	0	0
Mean Spread Factor (μm):	27	108
Mean Spread Angle (μRad):	30	120
Mean Spread Angle (arcsec):	6.19	24.75
SENSOR RESOLUTION		
Spread Factor (μm):	27.36	112.89
Spread Angle (μRad):	30.4	125.43
(arcsec):	6.27	25.87
EXPERIMENT RESOLUTION		
ATMOS/LOS SPRD ANGL(arcsec):	2	2
Computed Sprd Angl (μRad):	9.7	9.7
Computed Sprd Fact (μm):	8.73	8.73
Exper. Sprd Angl (arcsec):	6.58	25.95
Sprd Angl (μRad):	31.91	125.8
Sprd Fact (μm):	28.72	113.22
FOOTPRINT @ OPERATING RANGE		
DESIRED OPERATING RNGE (km):	20000	6000
Pixel IFOV Footprint (m):	6.00E+02	7.20E+02
Res El Footprint (m):	6.38E+02	7.55E+02
SUB-FPA NO. PIXELS W/O BINNING		
AZ.:	420	420
EL.:	420	420
Total:	1.76E+05	1.76E+05
TOTAL NO. SUB FPA'S		
AZ.:	10	10
EL.:	1	1
Total:	10	10
Total-FPA No. Pixels w/Binning		
Az.:	4200	1050
El.(Image Region Only):	420	105
Total:	1.76E+06	1.10E+05
Total FPA Length (mm)		
Az.:	113.4	113.4
El.(Image Region Only):	11.34	11.34
Diagonal:	114	114
SYSTEM FOV (deg)		
Az.:	7.21	7.21
El.:	0.72	0.72
Diagonal:	7.25	7.25
FOV FOOTPRINT @ OPERATING RANGE (km)		
Az.:	2520.1	756.0
El.:	251.3	75.4
Diagonal:	2534.1	760.2

Part B - System Coverage and Data-Rates

Integration Time (sec):	5.00E-01	1.50E-01
Dw/Cl Ang Rate (arcsec/sec):	13.2	173
NO. FRAMES PER STARE:	5	5
STEP-SETTLE TIME (sec):	1.00E+00	1.00E+00
FOV Look-Step Time (sec):	3.50E+00	2.62E+00
Read Frame Time (sec):	5.00E-01	1.50E-01
Read Pix Rate w/Stor (MHz):	3.53E+00	7.35E-01
Ave. Pix Rate w/Step (MHz):	2.52E+00	2.10E-01
FPA OUTPUTS		
SELCT NO PARALLEL CHAN/FPA:	1	1
Channel Pixel Rate (MHz):	3.53E-01	7.35E-02
NO. QUANTIZATION BITS:	12	12
Single Fr Mem Req (MBytes):	2.65E+00	1.65E-01
Coverage FOV (sq deg):	5.19E+00	5.19E+00
Coverage Rate (sq deg/sec):	1.48E+00	1.98E+00

(continued)

Table 3.8 *(continued)*

Part C - Exposure and Noise Parameters		
INTEG WAVELENGTH LIMIT (μm):		
LOWER:	0.40	3.00
UPPER:	1.00	12.00
OBJECT SURFACE #1		
TEMPERATURE (K):	250	250
EMISSIVITY:	0.9	0.9
Therm Earthshine Tot Refl:	0.1	0.1
AREA (m^2):	5.00E+00	5.00E+00
Emissivity*Area:	4.5	4.5
OBJECT SURFACE #2		
TEMPERATURE (K):	175	175
EMISSIVITY:	0.33	0.33
Therm Earthshine Tot Refl:	0.67	0.67
AREA (m^2):	4.10E+00	4.10E+00
Emissivity*Area:	1.353	1.353
EARTHSHINE EMISSION TEMP. (K):	300	300
SOLAR TEMPERATURE (K):	5900	5900
SOLAR IRRADIANCE (W/m^2):	1390	1390
SOLAR PHASE-ANGLE (Deg):	45	45
Diff-Sphere Eff Sol Irr (W/m^2):	7.00E+02	7.00E+02
OBJECT SOLAR REFLECTIVITY:	0.1	0.1
EARTH SOLAR REFLECTIVITY:	0.3	0.3
OBJECT IN-BAND RADIANT INTENSITY (W/sr)		
Object Surface #1		
Thermal Emission:	9.67E-19	8.66E+01
Thermal Earthshine:	1.52E-15	2.33E+01
Object Surface #2		
Thermal Emission:	3.77E-30	1.90E+00
Thermal Earthshine:	8.35E-15	1.28E+02
Solar Reflection:	1.21E+02	3.98E+00
Solar Earthshine Reflection:	2.87E+01	9.42E-01
DOES OBJ OCCL SKY BKG? "YES/NO":	YES	YES
ATMOSPHERIC TRANSMISSION:	1	1
THERMAL BACKGROUND PARAMETERS		
MEASURED SPECTRAL RADIANCE (W/m^2/sr/um):		
NIGHT:	2.00E-09	2.00E-06
DAY:	3.00E-08	1.50E-05
WAVELENGTH OF MEAS (μm):	6.10	7.40
SEL"GRAY-B"or"CONST" APPROX:	GRAY-B	GRAY-B
GB APPROX THERM-BKGND TEMP (K):	300	300
Gray-B Approx Thermal-Bkgnd Equiv Emissivity:		
Night:	3.69E-10	2.43E-07
Day:	5.53E-09	1.82E-06
SOLAR BACKGROUND PARAMETERS		
MEASURED SPECTRAL RADIANCE (W/m^2/sr/um):		
NIGHT:	3.00E-07	0.00E+00
DAY:	3.00E-06	0.00E+00
WAVELENGTH OF MEAS (μm):	0.55	2.80
SEL"GRAY-B"or"CONST" APPROX:	GRAY-B	CONST
GB APPROX SOLAR-BKGND TEMP (K):	5900	5900
Gray-B Approx Solar-Bkgnd Equiv Emissivity:		
Night:	1.06E-14	0.00E+00
Day:	1.06E-13	0.00E+00
Solar Background Brightness (Mv/arcsec^2)		
Night:	24.3	ERR
Day:	21.8	ERR
OPTICS NON-REJECTED EARTH RADIANCE (NRER)		
EARTH THERMAL EMISSION		
MEAS RADIANCE (W/m^2/sr/um):	1.00E-06	1.00E-06
WAVELENGTH OF MEAS (μm):	5.00	5.00
Equivalent Emissivity:	3.85E-07	3.85E-07
EARTH SOLAR REFLECTION		
MEAS RADIANCE (W/m^2/sr/μm):	1.00E-03	2.00E-07
WAVELENGTH OF MEAS (μm):	0.55	5.00
Equivalent Emissivity:	3.52E-11	3.30E-12
Brightness (Mv/arcsec^2):	15.5	18.1
Optics Diameter (m):	0.3	0.3
Optics Focal Length (m):	0.9	0.9
Optics f/#:	3	3
OPTICS TRANSMISSION:	0.9	0.9
OPTICS TEMPERATURE (K):		
NIGHT:	120	120
DAY:	130	130
OPT/COLD-SHIELD EQUIV EMISSIV:	0.03	0.03
SENSOR READ AND INTEGRATION TIMES		
READ FRAME TIME (sec):	5.00E-01	1.50E-01
NO. FRAMES OF INTEGRATION	1	1
Integration Time (sec):	5.00E-01	1.50E-01
Dw/Cell Ang Vel (arcsec/sec):	13.2	173
FPA FILL FACTOR:	1	0.5

Table 3.8 *(continued)*

SENSOR EXPOSURES		
SELECT "Quan, Si, PtSi, AdvPtSi, or AdvIrSi":	Si	AdvPtSi
SELECT "DAY" OR "NIGHT"	DAY	NIGHT
Difference Signal Components (Elect/m^2):		
Object Surface #1		
Thermal Emission:	3.33E-03	7.32E+14
Thermal Earthshine:	5.50E+00	4.33E+14
Object Surface #2		
Thermal Emission:	1.48E-14	2.87E+12
Thermal Earthshine:	3.69E+01	2.90E+15
Solar Reflection:	8.75E+17	0.00E+00
Solar Earthshine Reflection:	2.07E+17	0.00E+00
Total Diff Signal (Elect/m^2):		
Object Surface #1:	1.08E+18	1.16E+15
Object Surface #2:	1.08E+18	2.91E+15
Background Components (Elect/m^2):		
Therm Gray-B Radiance Approx	3.85E-07	1.33E+09
Therm Const-Radiance Approx:	1.12E+09	9.13E+09
Therm Bkgnd (Selec'd Approx):	3.85E-07	1.33E+09
Solar Gray-B Radiance Approx:	9.07E+10	0.00E+00
Solar Const-Radiance Approx:	1.12E+11	0.00E+00
Solar Backgnd (Selec'd Approx):	9.07E+10	0.00E+00
Thermal NRER:	2.68E-05	2.11E+09
Solar NRER:	9.07E+12	7.73E+08
Total NRER ("DAY"or"NIGHT"):	9.07E+12	2.11E+09
Optics/Cold-Shield (Night):	0.00E+00	4.99E+08
Optics/Cold-Shield (Day):	4.39E-28	0.00E+00
Optics/Cold-Shield (Selec'd):	4.39E-28	4.99E+08
Total Backgnd (Elect/m^2):	9.16E+12	3.94E+09
Total Backgnd (Elect/Pixel):	6.68E+03	2.87E+00
FPA NOISE PARAMETERS		
QUANTUM NOISE FACTOR:	1.10E+00	1.10E+00
MULTIPLICATIVE FIXED PATTERN		
PIXEL NONUNIFORMITY (%):	1.00E+00	1.00E-01
Noise Factor (m):	5.40E-07	5.40E-08
ADDITIVE AMPLIFIER READOUT		
MEAS rms FLOOR (Elect/Pix):	2	5
MEAS rms@1MHz(Elect/MHz^.5):	6	20
PRE-NOISE GAIN	1	1
Channel Pixel Rate (MHz):	3.53E-01	7.35E-02
Floor Var Dens (Elect/m^2):	5.49E+09	2.14E+09
Read Rate VarDns(Elect/m^2):	1.74E+10	2.52E+09
Tot Read VarDens(Elect/m^2):	2.29E+10	4.66E+09
Tot rms (Elect/Binned-Pixel):	4.1	7.4
ADDITIVE DARK CURRENT		
MEAS CURRENT DENS (nA/cm^2):	0.001	0.0002
Req FPA Operating Temp (K):		48.1
Dark Expos Dens (Elect/m^2):	3.12E+10	9.38E+08
Dark Exp (Elect/Binned-Pixel):	2.28E+01	1.09E+01
rms Noise Dens (Elect/Pix):	4.8	3.3
FPA TOTAL EXPOSURES (El/Pixel)		
Input Pix w/o Bin:	6.70E+03	1.38E+01
Ouput Reg Pix w/V-Bin:	6.70E+03	5.52E+01
Output Node w/H&V-Bin:	6.70E+03	2.21E+02
SENSOR NOISE		
Variance Density (Elect/m^2)		
Backgnd. Photoelectron:	1.01E+13	4.34E+09
Mult. Fixed Pattern:	6.12E+12	1.13E+04
Additive:	5.42E+10	5.60E+09
Total:	1.63E+13	9.94E+09
Sprd Fact rms (Elect/Resel)		
Backgnd. Photoelectron:	9.12E+01	7.46E+00
Mult. Fixed Pattern:	7.10E+01	1.21E-02
Additive:	6.68E+00	8.47E+00
Total:	1.16E+02	1.13E+01
Part D - Range Performance		
DESIRED RESEL OR STREAK SNR:	6.00E+00	6.00E+00
Req Sig (El/Resel or Streak):	6.95E+02	6.77E+01
Req Luminous Intensity (Mv):	15.3	ERR
Static (0-Vel) Range Perf (km):	1.27E+05	1.73E+04
Dwell/Cell Range Perf. (km):	9.01E+04	1.22E+04

percase type, and computed parameters are represented by lowercase type. The spreadsheet provides a convenient way to conduct simulations that permit iteration of the design to achieve the desired level of coverage rate and range versus angle-rate performance. Final entries in the spreadsheet represent the sensor design characteristics.

Part A of Table 3.8 contains geometric quantities associated with the optics and FPA. Characteristics include optics and FPA spread factors. Noise-equivalent spread factors are computed for both individual components and the cascaded combination of these components in accordance with the methodology presented in Sec. 3.2.3.1. Visible and IR sensors are designed to share the optics, and resolution can be selected through pixel binning to match the task (surveillance or track) as well as the range of angle rates anticipated. A binning ratio of one for the visible sensor matches the low angle rates associated with high-altitude search; a binning ratio of four for the MWIR sensor matches the high angle rates associated with low-altitude search. Also presented in Part A are the overall FPA size and corresponding FOV and footprint of the sensor.

Part B of Table 3.8 contains quantities that pertain to system coverage and data rates. For a step-stare sensor, the integration time and resolution determine the dwell-in-cell angle rate (rate for single resolution-element motion), and this quantity has been chosen to match the range versus angle-rate statistics of the satellite population. This sensor uses five frames/stare for determination of point-source motion characteristics for separation of the desired satellites from the star background. These quantities determine data rates and coverages.

Part C of Table 3.8 contains quantities that pertain to exposure and noise. Spectral bandwidths as well as object and background signature components are shown. The space object is modeled as if it consists of two separate segments, and signatures include solar reflection, thermal emission, and reflected earthshine from both thermal emission and solar irradiation. Background components include sky solar and thermal components as well as optics thermal emission and nonrejected earth radiation. All exposures are computed using Eq. (3.1).

The FPA noise characteristics of Part C cover temporal and fixed-pattern noise types, and their numerical values are determined using the methods of Sec. 3.2.3.2. Noise is determined for FPA pixel normalizations initially, and then noise is computed for the sensor mean spread factor (resel) δ, defined by Eq. (3.9). This procedure is compatible with optimum, point-source, matched-filter detection theory.

Part D of Table 3.8 permits introduction of the SNR performance criterion, and range performance is computed for the static (zero angle rate) using Eq. (3.46). The dwell-in-cell range performance is below the static range performance by a factor of $\sqrt{2}$.

A graph of range versus angle rate for the multispectral sensor is presented in Fig. 3.24. As anticipated, sensor performance decreases with angle rate. Superimposed on the graph is a typical statistical population of space objects to be detected in the search task. Note that the MWIR sensor covers the low-altitude region where the earth shadow occupies a large fraction of the surveillance volume. The high-altitude region and the sunlit portion of the low-altitude region are covered very adequately by the visible-band sensor.

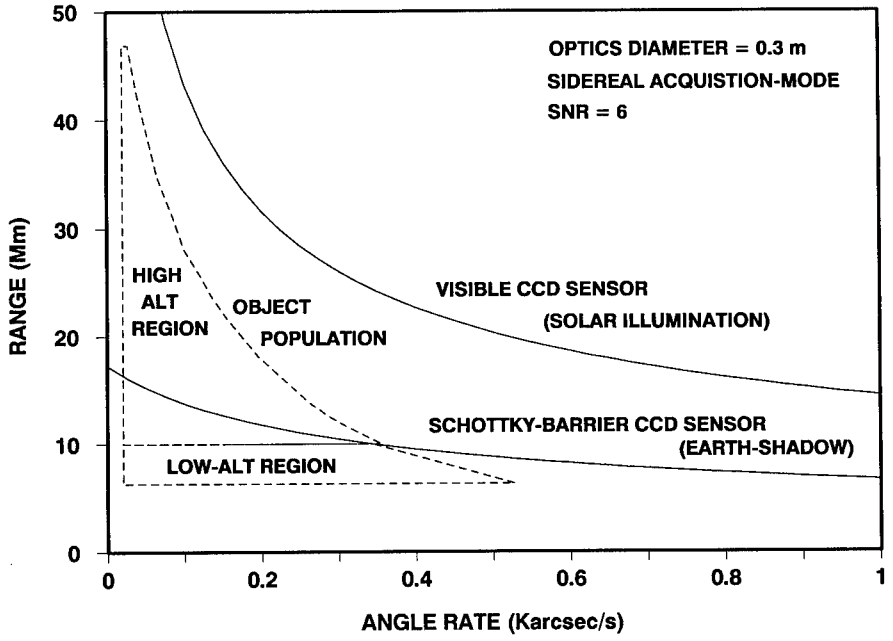

Fig. 3.24 Spaceborne visible/MWIR sensor performance.

This performance characterization substantiates the design of a compact, multispectral staring sensor that can provide the desired coverage and sensitivity for surveillance of both near-earth and deep-space objects.

References

1. L. M. Biberman and S. Nudleman, Eds., *Photoelectronic Imaging Devices, Volume 2, Devices and Their Evaluation,* Plenum, New York (1971).
2. L. M. Biberman, F. A. Rosell, and A. D. Schnitzler, *Low-Light-Level Devices: A Designer's Handbook,* Institute of Defense Analyses (1971).
3. O. H. Schade, "Electron optics and signal readout of high definition return beam vidicon camera," *RCA Rev.* **31**(1), 60–119 (1970).
4. M. J. Cantella, "Application of the high resolution return beam vidicon," *Opt. Eng.* **16**(3), 257–261 (1977).
5. J. A. Hall, "Imaging tubes," Chap. 13 in *The Infrared Handbook,* W. L. Wolfe and G. J. Zissis, Eds., Environmental Research Institute of Michigan, Ann Arbor (1978).
6. R. A. Stern, R. C. Catura, R. Kimble, A. F. Davidson, M. Winzenread, M. M. Blouke, R. Hayes, D. M. Walton, and J. L. Culhane, "Ultraviolet and extreme ultraviolet response of charge-coupled-device detectors," *Opt. Eng.* **26**(9), 875–883 (1987).
7. M. M. Blouke, B. Corrie, D. L. Heidtmann, F. H. Yang, M. Winzenread, M. L. Lust, H. H. Marsh IV, and J. R. Janesick, "Large format, high resolution image sensors," *Opt. Eng.* **26**(9), 837–843 (1987).
8. B. E. Burke, R. W. Mountain, D. C. Harrison, M. W. Bautz, J. P. Doty, G. R. Ricker, and P. J. Daniels, "An abuttable CCD imager for visible and x-ray focal plane arrays," *IEEE Trans. Electron Devices* **38**(5), 1069–1076 (1991).
9. A. J. Steckl, "Charge-coupled devices," Chap. 12 in *The Infrared Handbook,* W. L. Wolfe and G. J. Zissis, Eds., Environmental Research Institute of Michigan, Ann Arbor (1978).

10. H. Elabd, W. F. Kosonocky, and M. J. Cantella, "Solid-state infrared imaging," Chap. 6 in *VLSI Electronics,* N. G. Einspruch, Ed., pp. 228–295, Academic Press, Orlando (1982).
11. R. Balcerak, J. F. Gibson, W. A. Gutierrez, and J. H. Pollard, "Evolution of a new semiconductor product: mercury cadmium telluride focal plane arrays," *Opt. Eng.* **26**(3), 191–200 (1987).
12. M. R. Kruer, D. A. Scribner, and J. M. Killiany, "Infrared focal plane array technology development for Navy applications," *Opt. Eng.* **26**(3), 182–190 (1987).
13. F. D. Shepherd, "Schottky diode based infrared sensors," *Proc. SPIE* **443,** 42–49 (1984).
14. W. F. Kosonocky, "Infrared image sensors with Schottky-barrier detectors," *Proc. SPIE* **869,** 90–106 (1988).
15. P. R. Horton, "Infrared image sensors," *Opt. Eng.* **30**(11), 1649–1663 (1991).
16. K. Vural, "Mercury cadmium telluride short- and medium-wavelength infrared staring focal plane arrays," *Opt. Eng.* **26**(3), 201–208 (1987).
17. W. F. Kosonocky and G. W. Hughes, "High fill factor silicide monolithic arrays," *Proc. SPIE* **782,** 114–120 (1987).
18. B.-Y. Tsaur, C. K. Chen, and S. A. Marino, "Long-wavelength Ge_xSi_{1-x}/Si heterojunction IR detectors and arrays," *Proc. SPIE* **1540,** 580–595 (1991).
19. M. J. Cantella, M. H. Ide, P. J. O'Donnell, and B.-Y. Tsaur, "Application of IR staring arrays to space surveillance," *Proc. SPIE* **1540,** 634–652 (1991).
20. M. J. Cantella, "IR focal plane array system performance modeling," *Proc. SPIE* **327,** 40–58 (1982).
21. O. H. Schade, "An evaluation of photographic image quality and resolving power," *J. SMPTE* **73**(2), 81–119 (1964).
22. O. H. Schade, "Resolving power functions and integrals of high definition television and photographic cameras—a new concept in image evaluation," *RCA Rev.* **32,** 567–609 (1971).
23. R. J. Keyes, *Optical and Infrared Detectors,* Springer-Verlag, New York (1977).
24. T. Limperis and J. Mudar, "Detectors," Chap. 11 in *The Infrared Handbook,* W. L. Wolfe and G. J. Zissis, Eds., Environmental Research Institute of Michigan, Ann Arbor (1978).
25. K. K. Thornber, "Theory of noise in charge-transfer devices," *Bell Syst. Tech. J.* **53**(7), 1211–1261 (1974).
26. J. M. Mooney, F. D. Shepherd, W. S. Ewing, J. E. Murguia, and J. Silverman, "Responsivity nonuniformity limited performance of infrared staring cameras," *Opt. Eng.* **28**(11), 1151–1161 (1989).
27. W. J. Smith, "Optical Design," Chap. 8 in *The Infrared Handbook,* W. L. Wolfe and G. J. Zissis, Eds., Environmental Research Institute of Michigan, Ann Arbor (1978).
28. J. A. Ratches, "Static performance model for thermal imaging systems," *Opt. Eng.* **15**(6), 525–530 (1976).
29. D. A. Scribner, M. R. Kruer, C. J. Gridley, and K. A. Sarkady, "Measurement, characterization, and modeling of noise in staring infrared focal plane arrays," *Proc. SPIE* **782,** 147–160, (1987).
30. D. A. Scribner, K. A. Sarkady, M. R. Kruer, J. Hunt, and J. T. Caulfield, "Adaptive nonuniformity correction for IR focal planes," *Proc. SPIE* **1541,** 100–109 (1991).
31. J. M. Mooney and E. L. Dereniak, "Comparison of the performance limit of Schottky-barrier and standard infrared focal planes," *Opt. Eng.* **26**(3), 223–227 (1987).
32. J. E. Murguia, J. M. Mooney, and W. S. Ewing, "Evaluation of a PtSi infrared camera," *Opt. Eng.* **29**(7), 786–794 (1990).
33. *Atmospheric Transmittance/Radiance: Computer Code LOWTRAN 7,* AEGL-TR-88-0177, Air Force Geophysics Laboratory (1988).
34. R. A. Sutherland, D. W. Hoock, and R. B Gomez, "Objective summary of U.S. Army electro-optical modeling and field testing in an obscuring environment," *Opt. Eng.* **22**(1), 2–19 (1983).
35. W. F. Kosonocky, F. V. Shallcross, T. S. Villani, and J. V. Groppe, "160 × 244 element PtSi Schottky-barrier IR-CCD image sensor," *IEEE Trans. Electron Devices* **ED-32**(8), 1564–1573 (1985).
36. T. S. Villani, W. F. Kosonocky, F. V. Shallcross, J. V. Groppe, G. M. Meray, J. J. O'Neil, and B. J. Exposito, "Construction and performance of a 320 × 244-element IRCCD imager with PtSi SB-Detectors," *Proc. SPIE* **1107,** 9–21 (1989).

37. R. Weber, "The ground-based electro-optical detection of deep-space satellites," *Proc. SPIE* **143,** 59 (1978).
38. R. Weber, "Large-format ebsicon for low light level satellite surveillance," *Opt. Eng.* **(20),** 212 (1981).
39. M. J. Cantella, "Space surveillance with medium-wave infrared sensors," *Lincoln Lab. J.* 1(1), 75–88 (1988).
40. M. J. Cantella, N. C. Davison, C. H. Gylfphe, J. P. Mattia, and B.-Y. Tsaur, "Low-background application of Schottky-barrier IR sensors," *Proc. SPIE* **1071,** 12–30 (1989).
41. A. S. Jursa, *Handbook of Geophysics and the Space Environment,* Air Force Geophysics Laboratory (1985).
42. T. C. Degges and H. J. P. Smith, "A high-altitude infrared radiance model," AFCRL-TR-77-0217, ADA059242 (1977).
43. D. F. Kostishack, "Small satellite sensors for multi-spectral space surveillance," *Proc. SPIE* **1495,** 214–227 (1991).
44. B.-Y. Tsaur, M. M. Weeks, and P. W. Pelligrini, "Pt-Ir Schottky-barrier IR detectors," *IEEE Electron Device Lett.* **9**(2), 100–102 (1988).
45. B.-Y. Tsaur, M. J. McNutt, R. A. Bredthauer, and R. B. Matson, "128 × 128-element Schottky-barrier focal plane arrays for long-wavelength infrared imaging," *IEEE Electron Device Lett.* **10**(8), 361–363 (1989).

CHAPTER 4

Infrared Search and Track Systems

Joseph S. Accetta
Infrared Information Analysis Center
Environmental Research Institute of Michigan
Ann Arbor, Michigan

with contributions by
T. D. Conley
R. Steinberg
J. R. Maxwell
D. Kryskowski
and others

CONTENTS

4.1 INTRODUCTION

The treatment of infrared search and track (IRST) systems in this chapter begins with an introduction to its practical applications in the military domain. IRST issues are separated into major phenomenological influences and "systems" level considerations to aid the subsequent discussion.

The phenomenology typical of targets and backgrounds is treated first with special emphasis on background variations characterized in the spatial-frequency domain resulting from the employment of either staring- or scanning-mode sensors. These are given in the form of classical power spectral density functions that subsequently can be utilized with suitable precautions in system performance estimates. The atmosphere as a source of attenuation and background radiation is introduced and characterized with supporting data also to be used in subsequent calculations. Methods for system performance estimates are then outlined, including a discussion of typical IRST performance metrics.

Signal-processing schemes such as adaptive thresholding and passive ranging also are discussed, concluding with a brief description of some actual IRST hardware implementations.

Generally, the subject is pedagogically approached by asserting that the sine qua non of IRST performance metrics is the probability of detection and false alarm rate and proceeding then to calculate the components of the target and background signal from first principles and in some cases with a considerable number of assumptions. The characteristics of the sensor are parametrically introduced with the ultimate objective of defining signal and noise levels and the range equation often used in discussion of IRST performance. The end result should enable the reader to gain an elementary understanding of the important issues in IRST performance and the physics that influence the problem, as well as a modest ability to estimate the performance of a given system in terms of its major specifications or to synthesize a candidate system to accomplish a specific IRST mission.

The author wishes to acknowledge R. Steinberg, T. D. Conley, J. R. Maxwell, and D. Kryskowski in particular and the many other authors whose mere references hardly give due credit to their major contributions. This chapter is largely a synthesis of many articles written by IRST experts, included in many instances verbatim. As a handbook demands, it is a product of the community that it is intended to serve.

4.1.1 IRST Definition

IRSTs are a functionally defined subset or class of passive military infrared systems whose objective is to reliably detect, locate, and continuously track infrared-emitting objects and targets in the presence of background radiation and other disturbances. As implemented and addressed herein, the domain of IRST is principally confined to unresolved, point-source objects in highly structured backgrounds and at ranges beyond 5 km. The spectral band of interest is 1 to 15 μm, with emphasis on the atmospheric windows of high infrared transmission at 3 to 5 and 8 to 12 μm. This definition does not preclude other infrared systems providing search and track functions. Psychophysical factors are not generally an explicit consideration in IRST since the detection and tracking process is usually automated. Imaging systems, although capable of

providing search and track functions, are relegated to the domain of forward-looking infrared (FLIR) systems, which are treated in Chapter 2 in this volume.

Most of the current research in IRST systems is concentrated in signal processing to extract target tracks from severe clutter. As the signal-to-clutter problem is the dominant theme of IRST research, it is given special emphasis, with many of the details common to IR systems in general relegated to other chapters in this handbook. In some current military environments IRST is considered a serious alternative to radar because of its passive nature and antistealth capability.

4.1.2 IRST Versus FLIR (Gibbons[1])

There are four principal distinctions between a scanning IRST and FLIR:

1. Field of view—The standard FLIR is a relatively small-field-of-view device. Wide-field-of-view FLIRs are not uncommon but are usually low-resolution devices. On the other hand, it is not unusual for an IRST to scan a 360-deg hemisphere in azimuth and perhaps as much as 90 deg in elevation (for an airborne system).
2. Frame time—The typical FLIR is for real-time display to a human observer; thus, it must "frame" at a high rate to avoid image flicker. A typical frame rate would be the standard TV rate of 30 frames per second. The IRST, on the other hand, presents information only to a computer. The frame rate is based on mission considerations; frame times of 1 to 10 s are typical.
3. Number of pixels—The large field of view of an IRST system results in great numbers of pixels per frame. For example, an IRST system with a 360-deg azimuth field and a 50-deg vertical field would, if the sensor had 1/4-mrad resolution, provide 87.7 million pixels per frame. A FLIR might have 480 vertical pixels and perhaps 1000 horizontal pixels, for a total of 480,000 pixels. The IRST thus has approximately 183 times as many pixels per frame as the FLIR. In terms of pixel rate, the comparison is closer. At a frame rate of 1 Hz, an IRST processes 87.7 million pixels per second, 6.1 times the number of pixels (14.4 million) processed by a FLIR at a frame rate of 30 Hz.
4. Signal processing—The FLIR sensor is usually observed by a human (as the postsensor processor); the advent of automated target recognition (ATR) will gradually diminish human intervention. On the other hand, the IRST covers far too many pixels per frame for a human to track. Some form of computer-controlled data processing is used to separate the large number of false targets (clutter) from the true targets.

In general, the FLIR emphasizes a real-time display, with good cosmetic qualities for human interpretation. The IRST emphasizes scanning a large volume of space, with priority on detecting small targets. The IRST usually does not depend on humans to screen false alarms but uses automatic data processing to decide the likelihood of a source being a true target rather than clutter.

4.1.3 IRST System Characteristics (Hirschman[2])

An IRST system consists of a scanning telescope, optical bandpass filters, a detector or detector array, real-time signal-processing electronics, a computer,

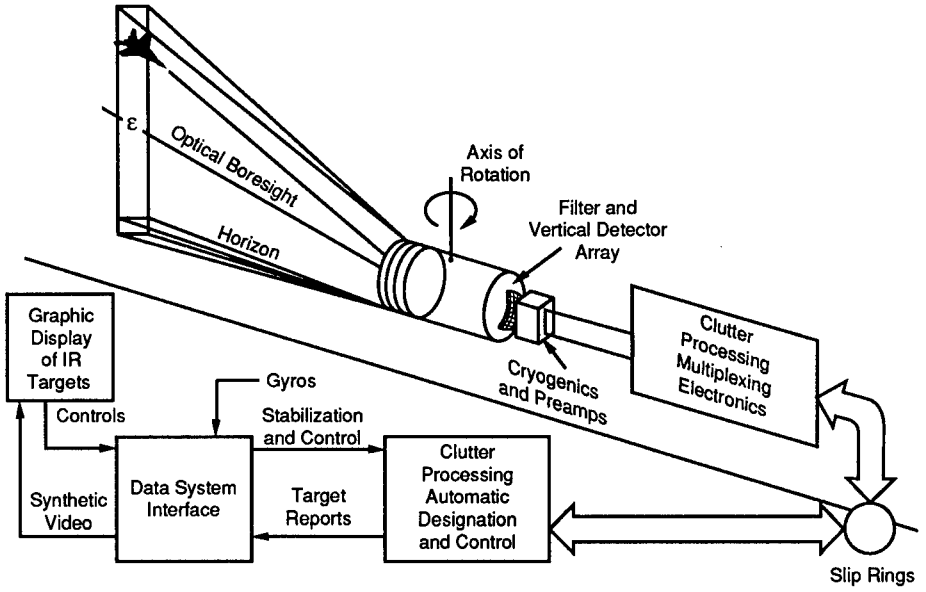

Fig. 4.1 Typical IRST block diagram.

a display, and other output functions. Figure 4.1 shows a block diagram of such a system. There also may be an auxiliary sensor that tracks the contact briefly when cued by the main sensor in order to carry out some functions not suited to the scanner, such as a laser rangefinder or some analysis of the signal that requires a longer dwell time on the target.

The telescope is designed to produce an image, on the focal plane, of the infrared scene about the optical line of sight using the radiation received in all or part of the two regions of infrared transparency (windows) nominally given as 3- to 5-μm and 8- to 12-μm windows. The telescope axis may be slewed continuously in azimuth at a fixed rate moving the image of the infrared scene across the detector array fixed to the focal plane, thus generating video signals in the detectors, or it may stare in one direction continuously.

Typical real-time signal processing performed on the output of the detectors includes amplification, electronic bandpassing, thresholding, and multiplexing to put the parallel video in serial format, but the processing is not limited to these functions.

The computer operates on the threshold exceedances, performing tracking functions and evaluating each established track according to various algorithms to decide whether the signal being tracked is a threat or arises from a clutter source. These decisions, related to precisely defined track coordinates, are the major output of the system and may be represented on a display as symbolic video and electronically routed to user systems.

To optimally select the spectral band for an IRST, it is necessary to take into account the various factors that impact the various bands in the infrared region.[3] A predominant factor is the target signal-to-clutter ratio in each band.

Targets refer collectively to those objects that infrared systems are designed to detect. The source signature of a target is a composite of reflected earthshine, reflected skyshine, reflected sunshine, skin thermal emission, aircraft hot-part emission, and aircraft plume emission.

Earthshine is defined as any radiation from the ground or clouds below the aircraft and includes scattered solar radiation. Skyshine is defined as radiation from the sky or clouds above the aircraft, including any solar scatter from the components. Reflected sunshine is the diffuse and specular components scattered by the airframe of directly illuminating sunlight. Thermal emissions result from the airframe that is heated by the aerodynamic flow of air over the fuselage and by solar radiation. The major "hot parts" are those components in direct contact with the exhaust plume gases. The plume radiation depends strongly on the temperature, composition, and velocity of the exhaust gases.

Along with the target signatures, it is important that the sources and characteristics of the background clutter environment be examined. Against high-altitude targets, the background will consist basically of sky, a few scattered clouds, the horizon, and the sun. In the look-down missions, the sources of clutter are many and are rapidly changing. Typical background clutter for the look-down missions consists of sunlit cloud and cloud edges, the earth, and all the terrain features, either natural or man-made.

4.1.4 IRST Applications

IRST systems have a multitude of applications in both military and civilian domains. Specific applications addressed include airborne or space-based surveillance and tracking of multivarious targets against sky, ground, or sea backgrounds and ground- or ship-based detection of aircraft and missiles in background clutter. More specific military-oriented applications include ship, aircraft, and ground defense against incoming missiles or aircraft, general high-altitude or space-based surveillance/reconnaissance, and early warning of low-altitude air vehicles or missile launches. The general distinguishing features between IRST and other IR systems are high sensitivity, operation at relatively long ranges against mostly aerial point targets, and extensive employment of spatial, temporal, and spectral discrimination signal processing for clutter rejection and attendant reduction in false-alarm rate.

4.1.4.1 Airborne Surveillance (Janakowitz and Raboul[4]). The airborne surveillance role of IRST is principally illustrated by the long-range detection and tracking of incoming intercept aircraft. The high-altitude, high-velocity nature of some of the targets creates a severe time compression problem stressing the need for high-sensitivity systems operating at long ranges. Higher-altitude, faster targets afford a somewhat easier detection problem than the lower-altitude cases because IR radiation from the target is increased and atmospheric attenuation is reduced. Originally providing a "down-look" capability for interceptor aircraft, IRST is now principally used in an air-to-air intercept role, which includes down-look. Thus, the range of possible backgrounds spans clouds through ground clutter in non-coaltitude cases. A typical naval air-to-air scenario is shown in Fig. 4.2. The range of possible threat altitudes spans 500 to 70,000 ft and includes bombers, long-range air-to-surface missiles, and fighter interceptors. IRST functional and performance require-

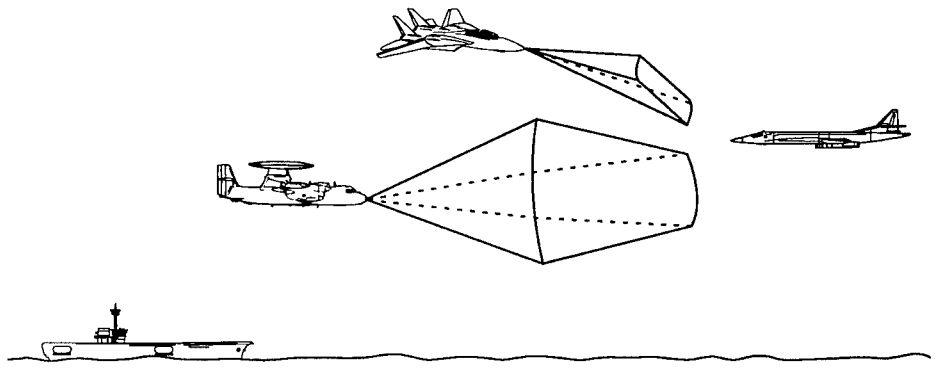

Fig. 4.2 Typical Naval IRST implementation for air-to-air intercept and long-range search roles.[4]

ments are derived from consideration of the operational scenario, threats or targets, environment, and host aircraft capabilities.

The diversity of target speed, size, signature, threat countermeasures, limitations of radar performance in ground clutter, low observable techniques, and the engagement dynamics result in the need for an IRST system in an airborne surveillance role to exhibit the following capabilities:

1. autonomously provide high probability of detection with a low false-alarm rate out to ranges of several hundred miles
2. perform raid cell count (how many attacking aircraft?), multiple threat track while prioritizing scan and threat using possible range and range rate determination
3. provide continuous coverage of the largest practicable defense swath width to minimize aircraft assets required in establishing a line of defense
4. cue radar to the threat in an electronic countermeasure (ECM) environment for missile fire control/guidance, and, when possible, provide range data
5. be reasonably insensitive to host vehicle environment
6. integrate with the host aircraft fire-control systems to improve weapons delivery capability, thereby increasing its operational utility and mission effectiveness
7. not seriously degrade the host vehicle performance
8. be capable of passive estimation of target motion parameters based on IR measurements.

4.1.4.2 Low-Altitude Air-Defense Ground-Based Systems (Keicher and Keyes[5]). Keicher and Keyes[5] considered the acute problem of detection and tracking of aircraft and cruise missiles flying at very low altitudes. Radar systems that attempt to detect and track a low-flying target often encounter problems such as nulls in the antenna pattern caused by interfering backscatter from the earth, false targets generated by multipath transmission, and difficulties in detection of targets with small radar cross sections in the pres-

ence of strong competing radar clutter. While there are techniques that can minimize these detection and tracking problems, active systems often reveal the location of the air-defense system and thus permit the use of air-defense suppression weapons. Since IRST relies upon the passive detection of the infrared energy emitted by aircraft or cruise missiles, they can often complement radar systems by minimizing these problems. Furthermore, these systems have the advantage of being relatively small and low cost.

Typically, IRSTs employ linear vertical arrays of IR detectors that scan in azimuth up through 360 deg. The elevation field of regard can often exceed 70 deg with a field of view of <10 deg. Low-altitude defense systems can use line-of-sight elevation angles of less than 10 deg. Figure 4.3 illustrates an IRST system employed on a tracked vehicle that can launch infrared surface-to-air missiles (SAMs). Similar systems can be employed for shipboard defense.

The targets of interest to IRST sets employed in air-defense systems include low-flying manned aircraft and helicopters, remotely piloted vehicles (RPVs), and cruise missiles. Understanding the characteristics of these targets is important in determining both system design and performance. The range of velocities of targets varies from 30 to 450 m s^{-1}. These targets use various types of propulsion systems, such as piston, turbojet, turbofan, or rocket engines. The infrared "signature" of the target depends on the type of propulsion system, target velocity, spectral emissivity, and reflectivity of the radiating surfaces of the vehicle and the presence of heat exchangers required for cooling electrical or propulsion systems. The spatial distribution of target infrared radiant intensity is usually a strong function of aspect angle. The infrared emission can vary over a range of two orders of magnitude.

One of the most advantageous aspects of an IRST system is its passive operation, allowing covert detection and tracking. It is intrinsically immune to rf location sensors or attack from antiradiation missiles and regarded as

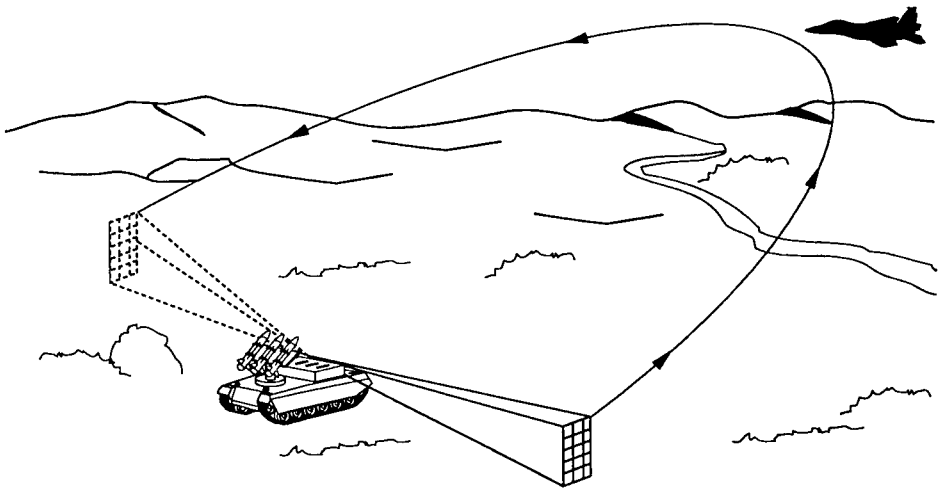

Fig. 4.3 Ground-based infrared search and track system employed with an infrared surface-to-air missile system.[5]

difficult to jam. Another advantage is higher angular resolution. Passive maneuvering can be employed to derive absolute range and range rate in some circumstances (see Sec. 4.5). In addition to the requirements cited above, ground-based systems should be reasonably immune to battlefield smoke and haze.

4.1.4.3 Low-Altitude Air Defense Ship-Based Systems (MacCallum[6]). The principal role of IRST systems on ships is the detection and tracking of incoming antiship missiles. It is essentially passive, using the infrared spectrum, but it may employ an active mode such as laser rangefinder as an adjunct. A typical implementation is a track-while-scan system assigned to a self-defense role.

IRST can be used alone but it would be used more effectively to augment the other shipboard acquisition sensors such as search radar and electronic support measures (ESMs). It would have the greatest utility in the detection and tracking of small, low-flying missiles where radar encounters severe sea clutter and multipath problems. These problems are minimized for the infrared sensor because of the superior resolution of optical systems.

Because of the relatively short time between detection and impact of antiship missiles and the large data rate generated by these high-resolution sensors, it is necessary to have automatic target detection; that is, the sensor must provide the clutter rejection. The principal threats encountered in sea-based systems are missiles launched from aircraft, ships, or submarines with trajectories varying from sea skimming to 45 deg, and incoming supersonic velocities. Band selection in shipboard IRST is generally complex and requires consideration of the marine environment as well as the multiplicity of missile threats utilizing liquid and solid rocket propulsion as well as ramjets. Sea-based systems that have passive detection and track of multiple aircraft and missiles at sufficient range to permit defensive system activation is the primary goal.

Secondary functions include navigation, station keeping, and surface target classification. Size and weight constraints are less critical than in the airborne case. A typical shipboard IRST is shown in Fig. 4.4. The single most difficult

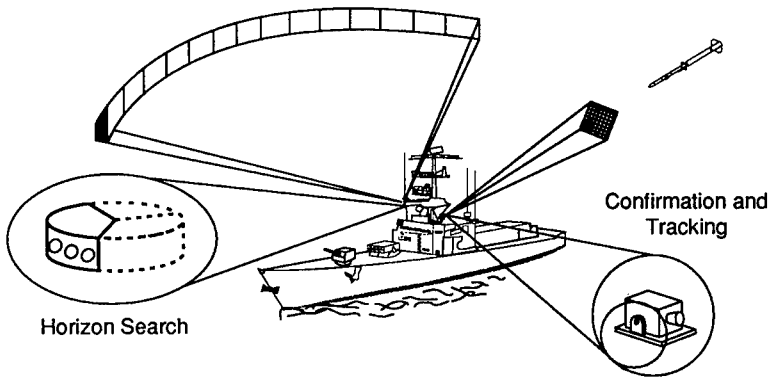

Fig. 4.4 Advanced staring IR sensors for shipboard applications. On the right is a narrow-field-of-view sensor tracking a high-flying missile, and on the left is a sector of a staring IRST performing a horizon search.[6]

problem in sea-based systems is clutter rejection, followed closely by spectral band selection.

Obviously, the selection of a given spectral band will result in different detection ranges for different threats and is doubly complicated by extreme variations in weather and environmental conditions.

A shipboard installation issue is precise stabilization of the IRST optical system and the trade-offs involved. Precise stabilization is needed to make use of the system's inherent resolution for multiple target separation and designation. Large stable platforms provide this level of stabilization, but they are expensive and heavy. Lightweight optical and electronic stabilization techniques have been developed that appear feasible and promising, and recent field test data appear to confirm this promise.

Because of the current approach of one IRST per ship and the complexity of topside equipment, reliability, maintainability, and availability (RMA) and coverage trade-offs must be made as follows:

1. A mast-mounted IRST system provides 360-deg coverage; however, there is no personnel access to the mast because of the motion and electromagnetic environmental hazards. This location implies the requirement for high reliability, electromagnetic interference (EMI) proof enclosures, and remote fault isolation. Another consequence of mast mounting is the exposure of the optical system to intermittent stack gas immersion.
2. A superstructure location for IRST allows the RMA factors to be relaxed somewhat because of its ready accessibility for local fault isolation and repair. However, this accessibility is obtained at the expense of reducing the 360-deg coverage and reducing the optical horizon. The use of more than one sensor head is feasible given sufficiently low cost.

Two generic staring focal-plane array (FPA) sensor concepts for potential use in future naval shipboard sensor applications are shown in Fig. 4.4. The first is a narrow-field-of-view sensor for target confirmation and tracking. It would acquire threats using hand-over data from a search mode IRST, radar, or self-search of a small target volume. In the track mode it could be used for fire control, kill assessment, and raid count. To make the sensor practical it would need to be low in cost as well as small and lightweight to facilitate mounting it high on the ship's mast.

The second concept is for a full staring IRST for horizon coverage, 360 deg in azimuth by approximately 4 deg in elevation. This would exploit recent advances in staring FPAs and optical subsystems. The increases in sensitivity and declaration range make the concept very attractive.

4.1.4.4 Satellite-Based Systems (Spiro and Schlessinger[7]). Satellite-based IRST applications include the detection and tracking of missile plume in the boost phase and the much more difficult task of detection and tracking of air vehicles against the earth background. Although satellite-based early warning systems usually are not regarded as IRSTs, they are included herein for completeness. The problem of detecting targets in clutter at low signal-to-clutter levels is complex. The earth's background with its variety of terrain and cloud types represents an extreme case of clutter, and the detection of dim targets

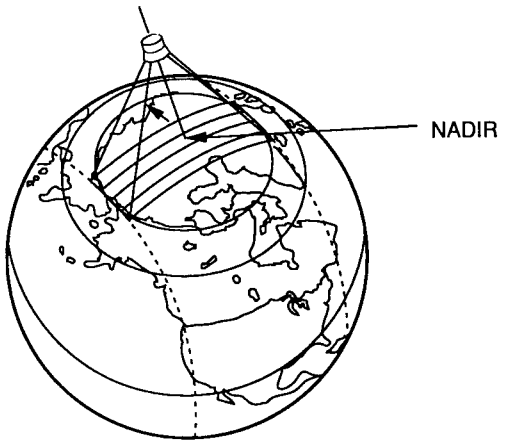

Fig. 4.5 Satellite-based IRST implementation.[7]

within is probably the most stressing IRST problem. A space-based IRST would be expected to provide attack-warning functions.

One of the distinguishing features of IRST down-looking systems over that of military or commercial LANDSAT, SPOT, and other multispectral remote-sensing systems is the existence of elaborate signal-processing techniques to extract dim targets from severe clutter. Generally speaking, it is the motion relative to the clutter of these targets that supports hope of separating them from the background. Space-based IRST systems can use either scanning or staring-FPA implementations, both of which have to be compensated for sensor motion that occurs during the collections in the form of target sensor dynamics, drift, and vibration. These latter effects cause temporal variations in the clutter that must be removed by signal processing. Because of the complex interaction between target, wide range of backgrounds, atmospheric effects, and solar reflection, band selection is complex. Further, the air-vehicle dimensions are such that they could subtend less than one pixel, thereby rendering pixel registration in any multiframe processing technique extremely critical.

Most of the system requirements can be derived from the specification of five quantities: the surveillance area and location (for example, latitude), the frequency of update, the area of the target, and its temperature. The key sensor parameter is the value of the footprint area; the nadir projection of a single detector on the earth. Given the system requirements, this defines the technology requirement. Motion compensation is probably the most significant issue in satellite-based IRST besides clutter discrimination. A satellite-based IRST system is shown in Fig. 4.5. Important IRST requirements in this implementation are light weight and very high reliability.

4.2 PHENOMENOLOGY

4.2.1 Target Signature Phenomenology

The three targets of primary interest to IRST are jet aircraft, helicopters, and missiles. Attendant phenomenologies associated with each as shown in Fig. 4.6 are direct radiation from the exhaust plume, hot engine parts, aerodynamic

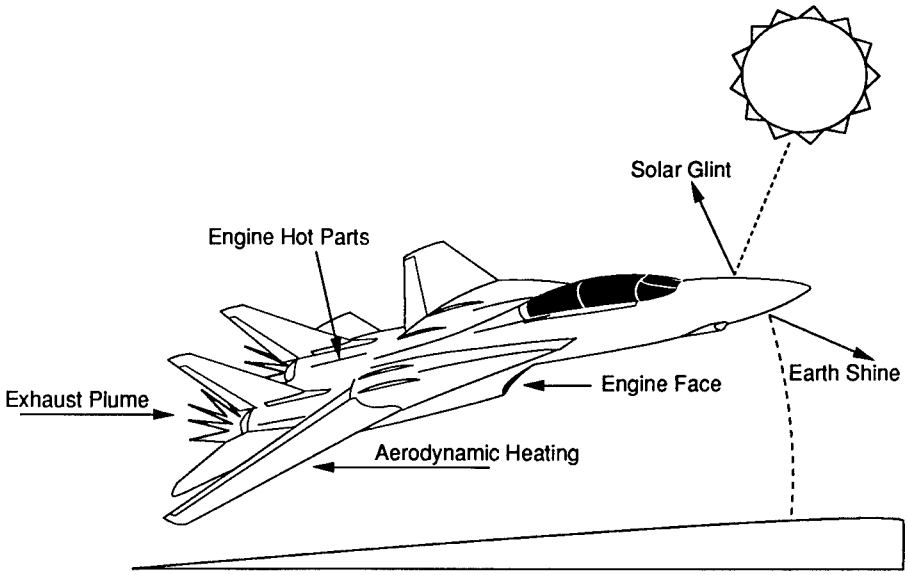

Fig. 4.6 Typical sources of radiation comprising a target signature.

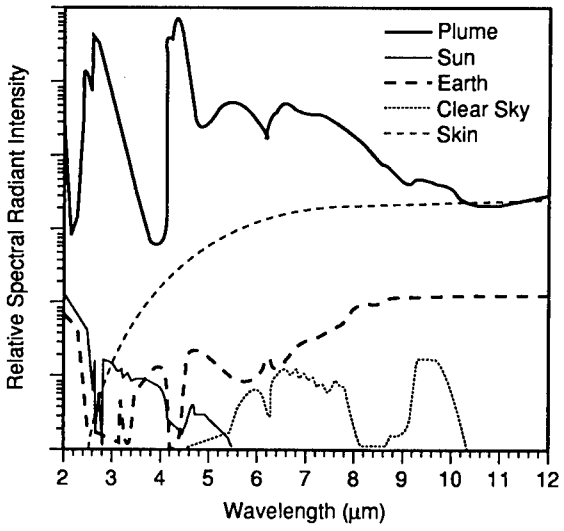

Fig. 4.7 The relative magnitude of typical target signature components versus wavelength for a jet aircraft at 90-deg aspect, M1.2 airspeed.[8]

skin heating, and reflected radiation from terrain, sky, and solar sources. The relative intensity of the respective components shown in Fig. 4.7 depend on the given geometry; however, it should be noted that there is no "typical" signature. The importance of various components is given in Table 4.1. This section consists of approximate quantitative methods for describing this phenomenology.

Table 4.1 Importance of Unobscured Signature Contributors

Band	Tailpipe	Plume	Aero Heating	Solar	Sky	Earthshine
3–5 μm	Yes	No[a]	Yes	Yes	No	Yes
8–12 μm	Yes	No[a]	Yes	No	Yes	Yes

[a]Except in afterburning mode or ramjets/rockets.

Target signatures are extremely complex and are analytically treated with equally complex computer simulations. Measurements are the best source of signature data.

For spatially unresolved targets, the total spectral radiant intensity I_t (w sr^{-1} μm^{-1}) is the quantity of most utility and is expressed as the sum I_t of the individual contributing spectral radiant intensities:

$$I_t(\lambda) = I_p(\lambda) + I_h(\lambda) + I_n(\lambda) + I_s(\lambda) + I_e(\lambda) + I_q(\lambda) \ , \tag{4.1}$$

where I_p, I_h, I_n, I_s, I_e, and I_q represent spectral radiant intensities of the plume, hot engine, cowling and nozzle, reflected solar and earthshine components, and skin aerodynamic heating from various target components, respectively. Occultation signatures are a special case treated in Sec. 4.2.1.13.

The total radiant intensity from the target will be loosely referred to as the IRST target signature. It is highly dependent on atmospheric transmission. As observed at the receiver it is often referred to as the "apparent" target radiant intensity. Section 4.3.5 considers atmosphere attenuation.

In the most general sense, target signature predictions are elaborate affairs with an appreciable amount of first-principles calculations. The optimum choice is to use measured signature data adjusted for environmental differences. The next most efficient choice is to use one of several computer programs for calculating signatures that may also contain rocket or jet plume numerical calculations. The least accurate are estimates made from projected area, assumed reflectance or bidirectional reflectance, stagnation temperature calculations for skin heating, and graybody assumptions for plume emission and some approximation for obscuration of the plume by the airframe. More detailed signature predictions are treated in Volume 4, Chapter 6, of this Handbook. For our present purposes, only the most rudimentary methods for calculating signatures are presented.

In the limit, all infrared signature calculations reduce to dividing the target into elements of area A_i over which the temperature and emissivity (reflectivity) can be assumed constant, estimating these parameters for each element of the object, and then summing the contribution of each element over the total surface. For complicated geometries and processes contributing to the signatures, such as engine plumes, it is necessary to use computer-based numerical methods[a,b] for reasonably accurate answers. A few simple cases are amenable to analytical methods but are correspondingly inaccurate.

In the subsequent sections, each of the components of $I_t(\lambda)$ are discussed.

[a]SPIRITS Signature Code, distributed by Aerodyne Research, Billerica, MA (617/663-9500).

[b]PCNirATAM Signature Code, distributed by ONTAR Corporation, Brookline, MA (617/739-6607).

4.2.1.1 Radiative Signature Components. A general methodology to estimate target signature radiative components is as follows:

1. Divide the object, including the plume, into elements of surface area A_i small enough such that the temperature and emissivity of each can be assumed constant.
2. By reference to the appropriate phenomenology (plume, aerodynamic heating, etc.) deduce the temperature T_i of each surface element A_i and its respective spectral angular emissivity $\varepsilon_i(\lambda, \theta, \phi)$.
3. Calculate the spectral radiant exitance from each surface element A_i using the Planck expression for graybody emission:

$$W_{\lambda i} = \varepsilon_i(\lambda, \theta, \phi) C_1 \lambda^{-5} \left[\exp\left(\frac{C_2}{\lambda T_i}\right) - 1 \right]^{-1} \quad [\text{W cm}^{-2}\ \mu\text{m}^{-1}] \ , \tag{4.2}$$

where

C_1 = 3.7415×10^4 W cm^{-2} μm^4
C_2 = 1.43879×10^4 μm K
$\varepsilon_i(\lambda, \theta, \phi)$ = directional spectral emissivity
λ = wavelength in microns
T_i = temperature of surface element.

4. Determine the projected area of each surface element A_i' in the direction of the observation. For a diffuse Lambertian emitter $\varepsilon(\lambda, \theta, \phi) = \varepsilon(\lambda)$, where $\varepsilon(\lambda)$ is the hemispherical spectral emissivity.
5. Calculate the radiant intensity from each element in the direction of the receiver:

$$I_i(\lambda) = \frac{W_{\lambda i}}{\pi} A_i' \ . \tag{4.3}$$

6. Sum over all target elements:

$$I_T(\lambda) = \sum_i I_i(\lambda) \ . \tag{4.4}$$

4.2.1.2 Reflected Signature Components. These components are treated in Secs. 4.2.1.8 and 4.2.1.9.

4.2.1.3 Jet Engine Signature Approximations. Jet engines can be divided into three classes: turbojets, turbofans, and ramjets. The total infrared emission from jet engines consists of plume, tailpipe, exhaust nozzle, and cowling components, shown in Fig. 4.8. Estimation of this radiation relies on simple graybody approximations. Typical jet engines meet the conditions required for treatment of the exhaust nozzle component as a graybody cavity, thus reducing all jet engine radiation components to treatment by the steps outlined in Sec. 4.2.1.1. The emissivity ε for the nozzle and tailpipe components can be taken to be 0.9 and to be spectrally independent. The exhaust nozzle component temperature T_e is related to a commonly reported engine parameter known as exhaust gas temperature (EGT) read by thermocouple just aft of the turbine. EGT is a function of airspeed and altitude, and varies from 300 to 900°C for

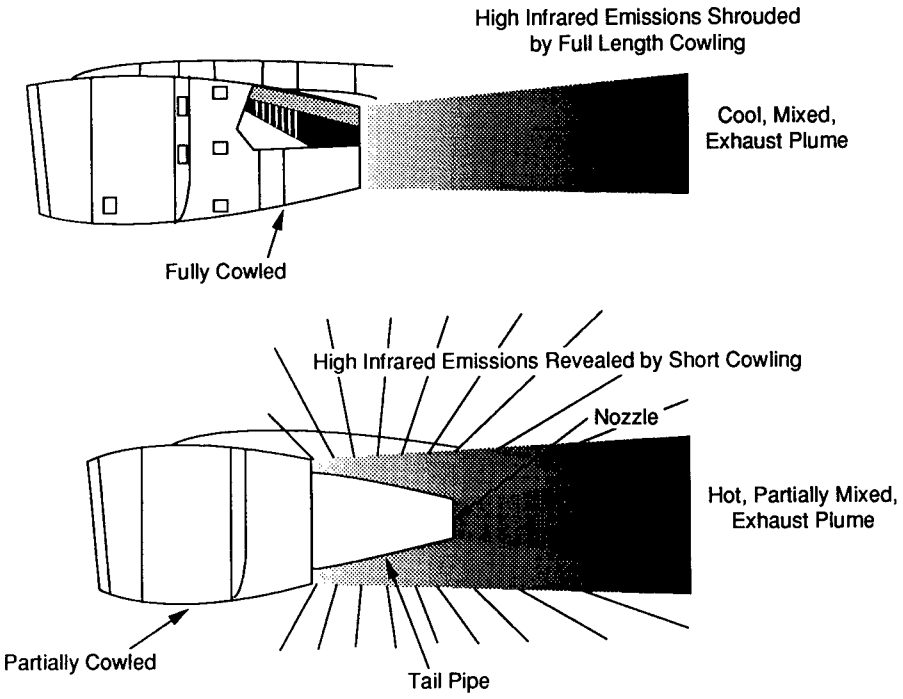

Fig. 4.8 Components of a jet engine radiative signature.[9]

most jet engines. Figure 4.9 gives example variations in EGT as a function of flight conditions. According to Hudson,[8] a rule-of-thumb relationship is

$$T_e \approx 0.85\text{EGT} \quad [°\text{C}] \ . \tag{4.5}$$

At rearward aspects, the exhaust nozzle component dominates the emitted radiation; however, consideration must be given to the possibility of obscuration by the aircraft components.

The other required parameter for this calculation is the area of the nozzle, which must be obtained from manufacturers' engine data. A cautionary note is that in some engines the signature is suppressed by a cowling and due consideration must be given to the effects of this shielding on the side aspect viewing of the tailpipe (see Fig. 4.8). The cowling temperature must be estimated by considering heat transfer from the plume and removal due to free-stream air flow on the exterior.

An additional complication is turbojet versus turbofan engines. The latter run at somewhat lower EGTs because the plume is sheathed by colder gas from the fan. The distribution and the temperature of the plume is markedly different.

Generally, even the most rudimentary estimate of jet-engine radiation requires a knowledge of EGT, nozzle area and the projected areas in the direction of interest, emissivity of the cowling and plume (tailpipe and nozzle $\varepsilon = 0.9$), and temperature of the cowling and plume. Table 4.2 gives selected engine data.

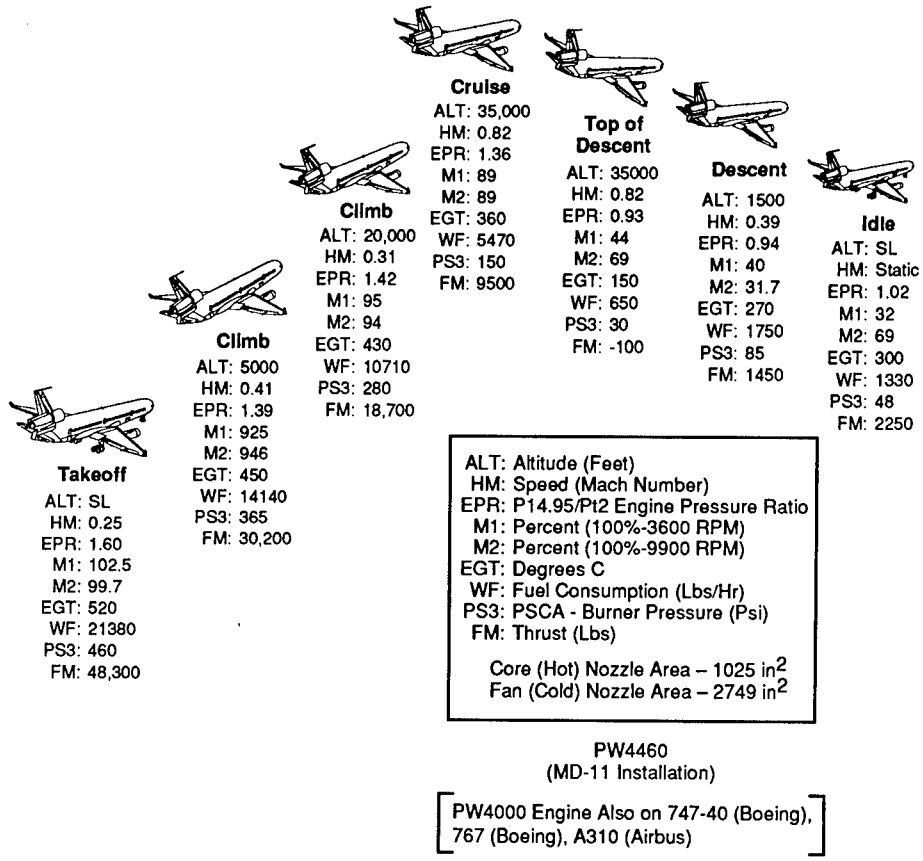

Fig. 4.9 Typical flight cycle.

Example. Calculate the total tailpipe exhaust nozzle radiant intensity from a jet engine with an EGT of 500°C and a nozzle area of 3500 cm^2 from the above, noting that once some idea of the exhaust temperature is acquired, the distinction between turbojets, ramjets, and so forth, is secondary.

In this instance, we resort to Eq. (4.2) for W_λ and integrate overall wavelengths, yielding the familiar Stefan-Boltzmann equation:

$$I_n = \int_0^\infty W_\lambda \, d\lambda = \frac{\varepsilon}{\pi} \sigma T_e^4 \; ; \tag{4.6}$$

thus,

$$I_n = \frac{0.9}{\pi}[5.67 \times 10^{-12}(273 + 0.85 \times 500)^4 3500] = 1.35 \text{ kW sr}^{-1} \; .$$

Table 4.2 Selected Engine Data (from Ref. 9)

PW2000 (Partially Cowled Engine)
PW200 featured on 757 (Boeing), C17 (Douglas-Military Transport) Cruise condition ALT = 35,000 ft MN = 0.78 EPR = 1.25 Thrust = 6500 lbf N1 = 3681 rpm N2 = 10,600 rpm EGT = 580°C Core area (hot) nozzle ≈ 710 in.^{2} (4580 cm^2) Fan area (cold) nozzle ≈ 2088 in.^{2} (13,471 cm^2)
CFM56-2/3 Turbofan
CFM56-2/3 used on 737 and KC-135 aircraft Alt = 35,000 ft MN = 0.75 EPR = 1.25 Thrust = 18,000 lbf at takeoff N1 = 4300 rpm N2 = 13,000 rpm EGT = 510°C (625°C at takeoff) Core area (hot) nozzle ≈ 450 in.^{2} Fan area (cold) nozzle ≈ 1150 in.^{2}
PW 4460
PW 4460 used on MD-11, 747-400, 767, A310 in a partially cowled configuration Alt = 35,000 ft MN = 0.82 EPR = 1.36 Thrust = 9500 lbf N1 = 3200 rpm N2 = 8100 rpm EGT = 360°C Core area (hot) nozzle ≈ 1025 in.^{2} Fan area (cold) nozzle ≈ 2749 in.^{2}

4.2.1.4 Spectral Considerations and Geometry. Generally, tailpipe and plume radiation is significantly stronger in the 3- to 5-μm atmospheric window than in the 8- to 12-μm band. Thus, sensors viewing rearward aspects would likely operate in the 3- to 5-μm band. For forward aspects, tailpipe radiation usually is not directly observable; thus plume, skin emission, and reflected components dominate. In this case 8- to 12-μm bands may offer superior performance; however, a detailed analysis considering all operational requirements must be performed to validate such a choice.

Example. For the previous example, calculate the radiant intensity of the tailpipe in the 3- to 5-μm and 8- to 12-μm band at the source-neglect atmospherics. Assume the spectral emissivity constant at 0.9. Either by explicit integration of Eq. (4.2) over the appropriate limits or from the Infrared Sli-

derule[c] we see that approximately 35% of the total radiation lies within the 3- to 5-μm band and 15% lies within the 8- to 12-μm band:

$$I(3 \text{ to } 5\ \mu\text{m}) = 1.35\ \text{kW sr}^{-1}\ (0.35) = 0.473\ \text{kW sr}^{-1}\ ,$$

$$I(8 \text{ to } 12\ \mu\text{m}) = 1.35\ \text{kW sr}^{-1}\ (0.15) = 0.203\ \text{kW sr}^{-1}\ .$$

4.2.1.5 Ramjets. Tailpipe radiation from ramjets is calculated as in normal turbojets or turbofans. However, since these engines are much simpler, they can run at much higher temperatures. A nominal EGT for ramjets is about 1600°C. Plume radiation can be treated similarly; however, high-speed operation reduces the plume temperature as in conventional turbojets or turbofans.

4.2.1.6 Plume Radiation. The principal combustion products in the plume are carbon dioxide and water vapor, giving rise to characteristic molecular emission bands.[10] The strongest water bands are centered near 2.7 and 6.3 μm, whereas the strongest CO_2 band is centered near 4.3 μm with weaker bands at 2.7 and 15 μm, respectively. The spectral radiance between 4.2 and 4.5 μm is much larger than the water band at 2.7 μm. The so-called red and blue "spikes" at 4 μm are caused by absorption by carbon dioxide in the atmosphere. Although there are also atmospheric absorption bands at these very wavelengths, the plume radiation is temperature broadened such that significant amounts of shifted radiation are transmitted. This absorption effect is more clearly illustrated in Fig. 4.10.

Figure 4.10 is a synthetic spectrum of an unattenuated engine plume emission at a resolution of 0.1 cm^{-1}. Figure 4.10 also gives a spectral plot of the transmittance from space to an altitude of 9 km at the same resolution. When the transmittance affects the plume signal, the resulting red spike, 2220 to 2300 cm^{-1} (4.35 to 4.5 μm), and blue spike, 2380 to 2398 cm^{-1} (4.17 to 4.2 μm), are formed, as shown in Fig. 4.10. This particular calculation was performed to synthesize a T-38 engine, which is rather unique in that an appreciable amount of CO radiation is present. The CO radiation appears in the spectrum between 2100 and 2200 cm^{-1} (4.5 to 4.76 μm), as shown in the figure. Note that the atmospheric absorption carves out the center of the CO_2 emission leaving the blue spike (shorter wavelength) and the red spike (longer wavelength).

Plume radiation is dependent on EGT, Mach number, afterburning, and altitude and viewing aspect. Accurate calculations are extremely complicated; however, we again resort to blackbody approximation with recourse to several rules of thumb regarding the effect of the above factors.

As a simple approximation, at $T = 650$°C, the limits of integration are taken to be 4.3 to 4.55 μm[8] with the emissivity of the gas assumed constant at 0.5 across this band (see Fig. 4.11). Note that the spectral emissivity for gases is generally a function of temperature.

In general, W_λ varies from point to point within the plume because of temperature and emissivity variations, and thus, the radiant existence is itself

[c]The Infrared Sliderule is available from Environmental Research Institute of Michigan (ERIM), Infrared Information and Analysis (IRIA) Center, P.O. Box 134001, Ann Arbor, MI 48113-4001 (313/994-1200, ext. 2215).

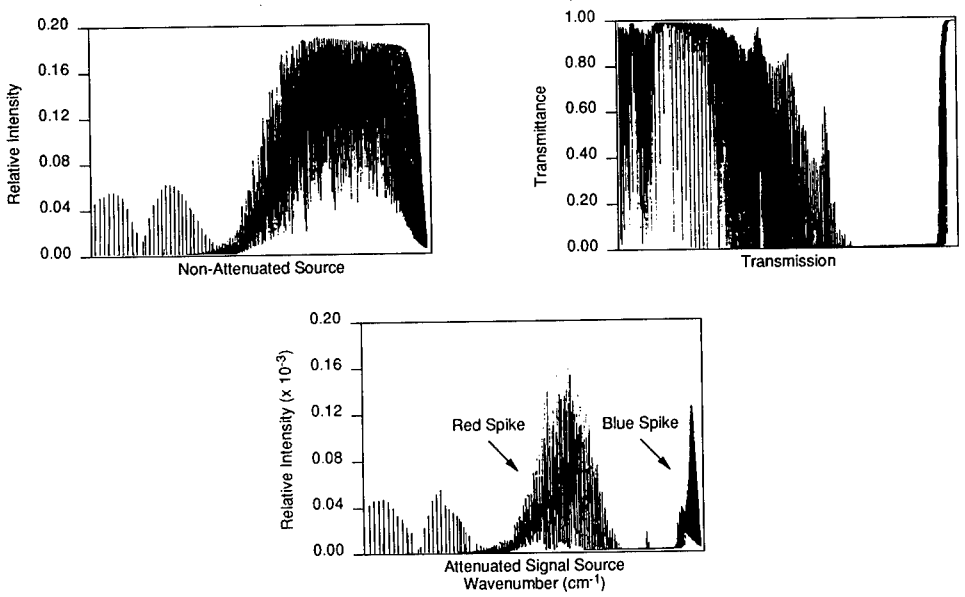

Fig. 4.10 Synthetic spectrum of engine plume at a resolution of 0.01 cm^{-1} showing the formation of the blue and red spike.[10]

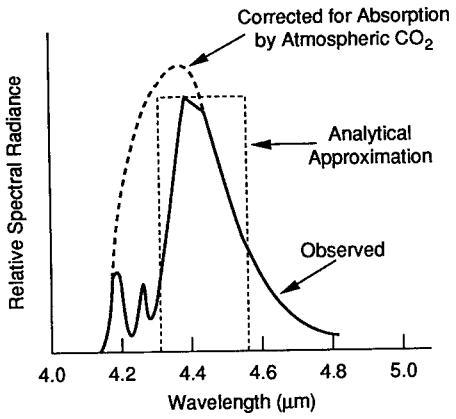

Fig. 4.11 The 4.4-μm emission band of carbon dioxide.[10]

spatially variant. More generally, the radiation from the i'th element of the plume where $W_{\lambda i}$ can be assumed constant is

$$I_i = \frac{Ai}{\pi} \int_{4.3\ \mu m}^{4.55\ \mu m} \varepsilon(\lambda) W_{\lambda i}\, d\lambda \quad [\mathrm{W\ cm^{-2}\ sr^{-1}}] \ . \tag{4.7}$$

Calculation of the radiation from the plume requires some knowledge of the temperature distribution of the gases, which is a function of the flight condition of the aircraft. Figure 4.12 is an example of plume temperature distribution.

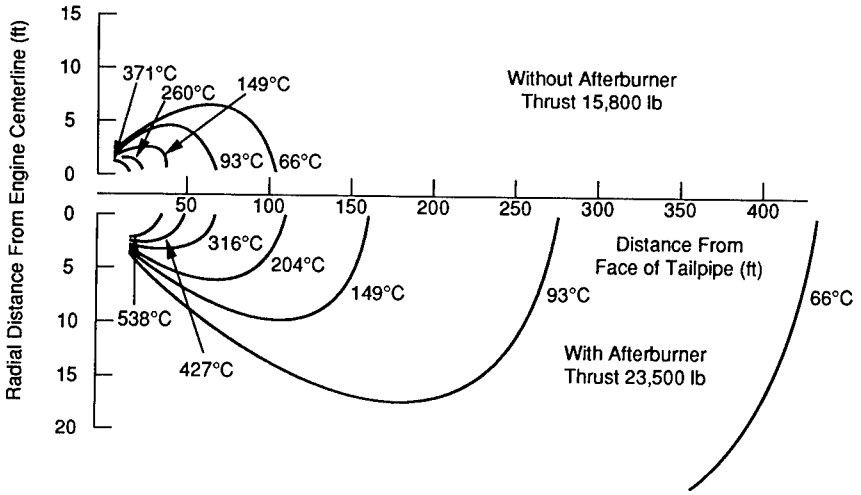

Fig. 4.12 Exhaust temperature contours for the Pratt and Whitney JT4A turbojet engines at maximum sea level thrust with and without afterburner (Courtesy of Pratt and Whitney Aircraft, Division of United Aircraft Corporation, East Hartford, CT).[8]

No presumption of accuracy should be made in the above methods. It is illustrative of the most basic approach and may yield notoriously inaccurate results.

For serious endeavors, one of the numerous currently available signature models[d,e] should be employed.

Afterburning Plume. The afterburning engine consumes about five times the normal fuel and drastically increases thrust. The size of the plume increases substantially at high supersonic speeds. Because of low engine efficiency, the plume temperature may actually decrease. Nevertheless, if the temperature and emissivity can be estimated, the radiance from the plume can be calculated from the above (see Fig. 4.12). At higher temperatures during afterburning, the plume radiation spectra would be expected to broaden and the radiant intensity to increase by two to three orders of magnitude.

4.2.1.7 Rocket Engines. Combustion temperatures ranging from 600 to 4500°C are expected in rocket engines. Engine radiation may be found by the method of Gouffe if the EGT is known. For liquid fueled engines, EGT $\approx$ 2000 K. At high altitudes, rocket plumes are extremely large, and generally the radiance can be estimated by recourse to the previous method if the spatial distribution is known.

4.2.1.8 Aerodynamic Heating. The emission from the target skin[10] can be significant at frontal aspects in the 8- to 12-μm region of the spectrum. This signal component can be written as

$$I_q = L_q(\lambda)\varepsilon(\lambda)A_T \ , \tag{4.8}$$

[d]SPIRITS Signature Code, distributed by Aerodyne Research, Billerica, MA (617/663-9500).
[e]PCNirATAM Signature Code, distributed by ONTAR Corporation, Brookline, MA (617/739-6607).

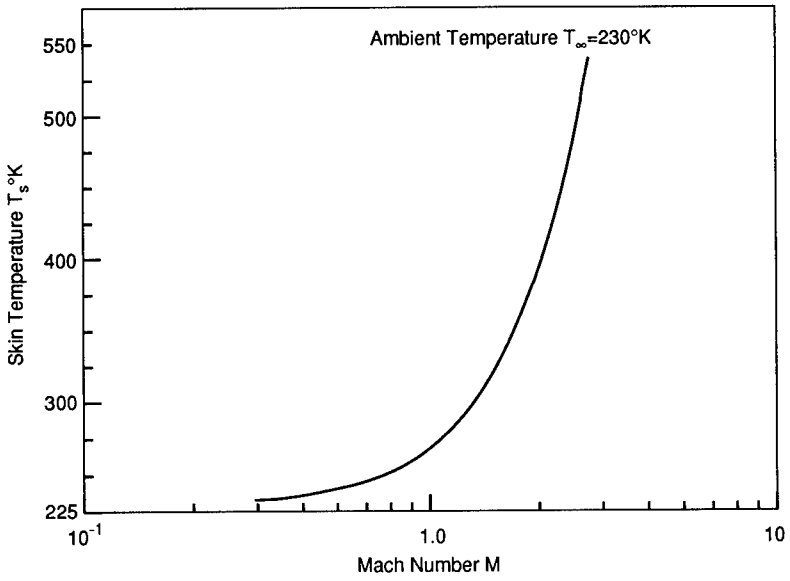

Fig. 4.13 Calculated variation of target skin temperature with Mach number.[10]

where

$L_q(\lambda)$ = radiance from skin
$\varepsilon(\lambda)$ = emissivity
A_T = target surface area.

The skin is aerodynamically heated according to the equation

$$T_s = \left(1 + \frac{\gamma - 1}{2}\beta M^2\right)T_a \ , \tag{4.9}$$

where

T_s = skin temperature
T_a = ambient temperature
γ = ratio of the specific heats of air $\approx$ 1.4 at 25°C
M = Mach number
β = recovery factor (0.75 to 0.98).

Figure 4.13 shows the variation of skin temperature with Mach number for an ambient temperature of 230 K. Thus, for aircraft velocities on the order of $M = 0.7$ (a typical cruise velocity) the skin temperature is approximately 20 K above the ambient air. Figure 4.14 shows actual measured data.

4.2.1.9 Bidirectional Reflectance. Most materials are not Lambertian (totally diffuse) reflectors, and thus their reflective properties depend on the

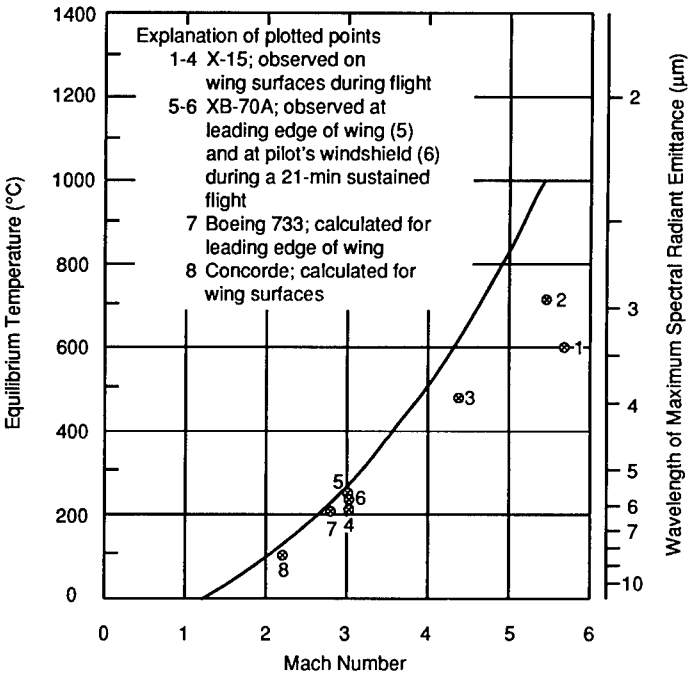

Fig. 4.14 Equilibrium surface temperature caused by aerodynamic heating (for altitudes above 37,000 ft with laminar flow).[8]

direction of radiant incidence and observation point. As shown in Fig. 4.15, the geometry of the measurement is referenced to the surface normal.

A convenient parameter to describe this relationship is the bidirectional reflectance distribution function (BRDF), defined as

$$f_{pp}(\theta_i, \phi_i; \theta_r, \phi_r) = \frac{\delta L_r(\theta_r, \phi_r)}{\delta E_i(\theta_i, \phi_i)} \quad [\mathrm{sr}^{-1}] \ , \tag{4.10}$$

where

L_r = reflected radiance in W m^{-2} sr^{-2} (power per unit projected area per unit solid angle)
E_i = incident irradiance in W m^{-2}
$(\cdot)_{pp}$ = the polarization of the source and receiver, respectively.

Most BRDF measurements usually use plane-wave illumination with a coherent laser source at one or more wavelengths, and thus the raw data exhibit speckle characteristics that can be (and usually are) smoothed, to represent an ensemble average over many samples. Although the shape of the BRDF curve usually is not a strong function of wavelength within a given IR band, its magnitude may be, so the reader is cautioned about extrapolating a BRDF measured at a single wavelength to the entire IRST passband of interest.

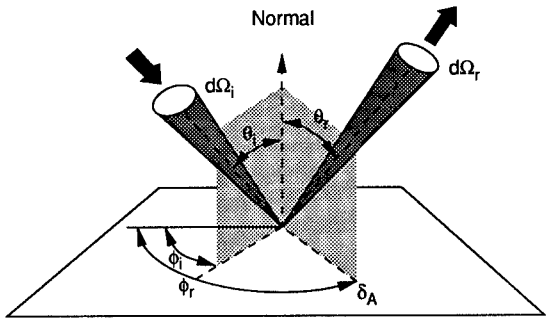

Fig. 4.15 Bidirectional reflectance measurement geometry.

The conveniences of the BRDF parameter are that the reflected flux per unit solid angle (radiant intensity) can be written independent of the specific geometry as

$$I_r = \frac{d\Phi_r}{d\Omega_r} = f\Phi_i \quad [\text{W sr}^{-1}] \ , \tag{4.11}$$

where Φ = flux in watts and the angular dependence notation has been dropped for convenience. The total polarized reflectance is the BRDF integrated over a hemisphere:

$$\rho_{pp} = \int_{hem} f_{pp}\, d\Omega_r' \ , \tag{4.12}$$

where $d\Omega_r' = d\Omega_r \cos\theta$ and the total BRDF (unpolarized) written in terms of its polarized components is

$$f = \frac{f_{vv} + f_{hh} + f_{vh} + f_{hv}}{2} \ . \tag{4.13}$$

As an aside, the conventional radar cross-section definition for a planar incremental target surface element of area A can be written in terms of the BRDF as

$$\sigma_{pp} = 4\pi A f_{pp} \cos\theta_r \cos\theta_i \ . \tag{4.14}$$

For a perfect diffuse (Lambertian) reflector,

$$f_{hh} = f_{vv} = f_{vh} = f_{hv} = \frac{1}{2\pi} \ , \tag{4.15}$$

$$f = \frac{1}{\pi} \ , \tag{4.16}$$

$$\sigma = 4A \cos\theta_r \cos\theta_i \ . \tag{4.17}$$

Under the assumption that multiple scattering between surface elements can be ignored and the scattering fields from different surface elements are uncorrelated, the total cross section of a composite target can be written as the sum of the cross sections of its various components.

4.2.1.10 Natural Sources of Radiation Affecting Target Signatures. Natural sources of radiation affect target signatures by way of reflected solar radiation and earthshine and to a much lesser extent by lunar sources, which should be accounted for in signature calculations. In the general case, targets are complex surfaces and can be treated by dividing the surface into facets of constant total bidirectional reflectance and then summing over all facets comprising the surface. The reflected spectral intensity $I_r(\lambda)$ from a surface facet of area A illuminated by a source of irradiance E is

$$I_r(\lambda) = E_i(\lambda) f(\lambda) A \cos\theta_i \ . \tag{4.18}$$

Thus, for a strictly diffuse surface, $f = \rho/\pi$, where ρ is the hemispherical reflectance of the surface. A strictly specular surface would not yield a return unless the receiver were located at precisely the specular angle. Although it is common to treat surfaces as diffuse, this may lead to large errors. The classical monostatic radar cross section is a commonly used quantity and is defined as

$$\sigma = 4\pi f A \cos\theta_i \ , \tag{4.19}$$

in which case Eq. (4.18) becomes

$$I_r(\lambda) = E_i(\lambda) \frac{\sigma}{4\pi} \ ; \tag{4.20}$$

however, caution is urged here because occasionally the cross section can be defined as

$$\sigma = 2\pi f A \cos\theta_i \ , \tag{4.21}$$

which has become common practice when measuring optical cross section with a laser. In terms of the hemispherical reflectance ρ, the cross section is

$$\sigma = 4\rho A \cos\theta_i \ . \tag{4.22}$$

After the geometrical relationship between each surface element has been defined with respect to the source, the total intensity is the sum over all the surface facets of the target.

Phenomenologically, reflected solar radiation for IRST is only important in the 3- to 5-μm band since there is negligible solar radiation in the 8- to 12-μm band.

4.2.1.11 Earthshine (Conley[10]). Reflected earthshine is a minor component of the total contrast signature for nadir viewing. However, as the view extends toward the horizon and the aspect becomes more side-on, the component increases. The total irradiance from earthshine on a surface element of an aircraft is

$$E_e(\theta,\phi) = \pi L_e \sin^2\frac{\theta}{2} , \tag{4.23}$$

where

θ = angle between zenith and the surface normal [see Fig. 4.16(a)]
E_e = irradiance
L_e = earthshine radiance.

The radiation scattered from the aircraft is calculated as emission from a Lambertian source of area A. Accordingly, the scattered radiant intensity is

$$I_e = \frac{\rho}{\pi} E_e(\theta,\phi)\mathbf{m}\cdot\mathbf{n}\, A , \tag{4.24}$$

where

A = area of source
ρ = reflectivity of surface
$\mathbf{m}$ = direction of scattered radiation
$\mathbf{n}$ = surface normal.

We now assume for a first approximation that an aircraft is an assembly of a cylinder and planes. Referring to Fig. 4.16, the scattered earthshine radiant intensity for the various shapes are as follows:

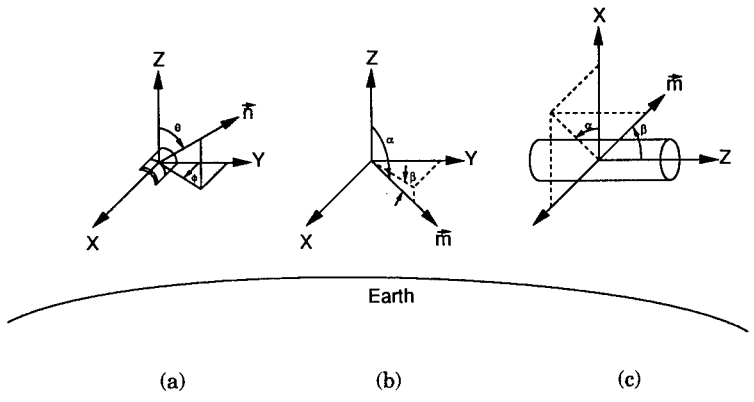

Fig. 4.16 Geometry for calculating earthshine from (a) geometry for the normal of an aircraft surface element, (b) geometry for direction to a sensor for a plane, and (c) geometry for direction to a sensor for a cylinder.

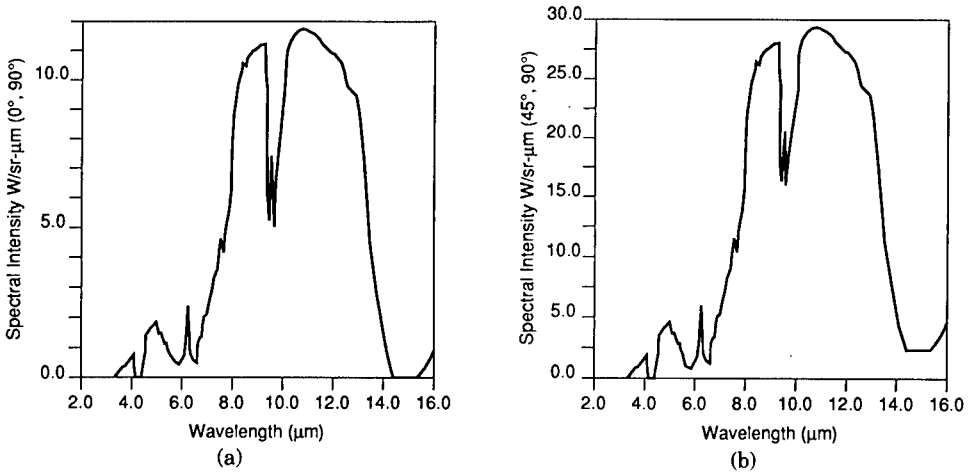

Fig. 4.17 Calculated earthshine for the KC-135 aircraft[10]: (a) broadside aspect, nadir viewing, and (b) broadside aspect, viewing angle 45-deg from nadir.

Plane:

$$I_e(\alpha,\beta) = \frac{\rho}{\pi} L_e A \sin\alpha \sin\beta \ , \tag{4.25}$$

where A = area of the plane.

Cylinder:

$$I_e(\alpha,\beta) = \frac{\rho}{\pi} L_e A \sin\beta \left(1 - \frac{\pi}{4}\cos\alpha\right) \ , \tag{4.26}$$

where A = surface area of cylinder.

The reflectivity ρ and emissivity ε are related; that is, $\rho + \varepsilon = 1$. The reflectivity and emissivity depend on the type of surface and wavelength. Conley[10] calculated scattered earthshine from a KC-135 aircraft. For earthshine, a reflectivity $\rho = 0.1$ was assumed. A broadside aspect angle $\beta = 90$ deg and a viewing angle $\alpha = 0$ and 45 deg off nadir were chosen by way of example. The background radiance was obtained by LOWTRAN. Figure 4.17(a) shows the earthshine component at a nadir viewing angle and Fig. 4.17(b) shows its value at 45 deg from nadir. In general, the calculation shows that earthshine has a peak value of 30 W sr^{-1} μm^{-1} at angles 45 deg off nadir and, depending on the spectral band, may be a significant component of the total target signature.

Table 4.3 Tabular Values of Total Solar Irradiance and Band Average Transmission of Indicated Altitude to Space

Case	(μm) $\Delta\lambda$	Solar Zenith Angle (deg)	Altitude (km)	Total Irradiance (W cm^{-2} μm^{-1})	Average Transmission
1	3–5	0	3	1.56×10^{-3}	0.687
2	3–5	0	10	1.97×10^{-3}	0.865
3	3–5	30	3	1.52×10^{-3}	0.671
4	3–5	30	10	1.96×10^{-3}	0.860
5	3–5	60	3	1.37×10^{-3}	0.601
6	3–5	60	10	1.92×10^{-3}	0.837
7	8–12	0	3	9.94×10^{-5}	0.860
8	8–12	0	10	1.07×10^{-4}	0.920
9	8–12	30	3	9.79×10^{-5}	0.848
10	8–12	30	10	1.06×10^{-4}	0.914
11	8–12	60	3	9.15×10^{-5}	0.797
12	8–12	60	10	1.03×10^{-4}	0.884

4.2.1.12 Solar Reflection (Conley[10]). Expected solar radiation values E_i as calculated by LOWTRAN 7[f] are shown in Table 4.3.

The spectral target irradiance due to reflected sunlight can be obtained by multiplying the solar irradiance at the target by the target differential scattering cross section.[10] Thus,

$$E_s = L_s \Omega_s T \rho \frac{d\sigma}{d\Omega} , \tag{4.27}$$

where

L_s = radiance of sun
Ω_s = solid angle subtended by the sun
T = atmospheric transmittance space to target
ρ = reflectivity of target
$d\sigma/d\Omega$ = differential scattering cross section.

The differential scattering cross section for certain smooth geometric shapes are well defined. However, for complex targets such as aircraft and other dim targets, the differential cross section is difficult to estimate. To convert to differential cross section, the radar cross section must be divided by 4π.

Plane. For a plane surface at normal incidence and an extended source such as the sun, the differential cross section becomes

$$\frac{d\sigma}{d\Omega} = \frac{A}{\Omega_s} , \tag{4.28}$$

[f]A personal computer version of LOWTRAN 7 (designated PCTRAN 7) is commercially available from ONTAR Corporation, 129 University Road, Brookline, MA 02146-4532 (617/739-6607).

where A = area of surface and Ω_s = solid angle subtended by the sun.

Sphere. For a sphere, the well-known differential cross section is

$$\frac{d\sigma}{d\Omega} = \frac{R^2}{4} , \tag{4.29}$$

where R is the radius of sphere.

Ellipsoid. For an ellipsoid viewed at arbitrary angles, the differential cross section is

$$\frac{d\sigma}{d\Omega} = \frac{a^4 b^2}{4(b^2 \cos^2\theta + a^2 \sin^2\theta)^2} , \tag{4.30}$$

where

b = one-half the major axis
a = one-half the minor axis
θ = angle of incidence measured from the major axis.

The fuselage of an aircraft can be approximated by an elongated ellipsoid. Consider a KC-135 aircraft with b = 22 m and a = 2 m illuminated at θ = 30 deg at an altitude of 9 km. The solar specular intensity signal observed from space is shown in Fig. 4.18 assuming a reflectivity of 0.2. As the illumination angle increases to 90 deg, the solar-scattered signal will increase by two orders of magnitude.

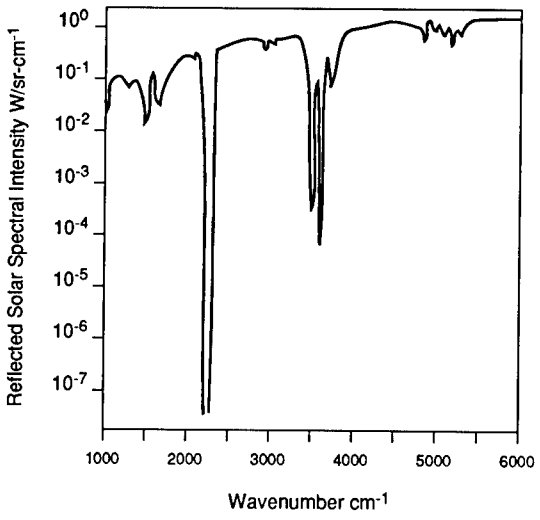

Fig. 4.18 Calculated solar scatter from a KC-125 fuselage illuminated 60-deg from broadside, θ = 30 deg.[10]

Example. Calculate the average reflected solar radiant intensity *as observed from space* from a flat 1 m^2 panel of aluminum with a Lambertian reflectance distribution at 30 deg to the normal at 10 km altitude in the 3- to 5-μm and 8- to 14-μm wavelength bands.

$$I_s = \rho \frac{E_s A}{\pi} T \cos\theta \ , \tag{4.31}$$

where

ρ = average reflectance of aluminum in the band of interest
E_s = the average irradiance within the band
A = area of the plate
T = band average transmission from ground to space
θ = angle of incidence relative to the surface normal.

From Table 4.3 we find the following quantities (we take $\rho \approx 0.8$ in both bands):

$$I_r(3\text{–}5) = \frac{0.8}{\pi} \times 1.96 \times 10^{-3} \times 10^4 \times 0.860 \times 0.866 = 3.72 \text{ W sr}^{-1} \ ,$$

$$I_r(8\text{–}12) = \frac{0.8}{\pi} \times 1.06 \times 10^{-4} \times 10^4 \times 10 \times 0.914 \times 0.866$$

$$= 0.214 \text{ W sr}^{-1} \ .$$

4.2.1.13 Occultation Signal. The occultation signal is the signal generated by a colder target obscuring the warmer background.[10] Consider a space sensor observing the earth. If the normal signal radiant intensity observed by the sensor is due to background, it can be represented as

$$I_B = L_B X^2 \ , \tag{4.32}$$

where

I_B = normal sensor signal
L_B = background radiance (sensor to ground)
X = sensor linear footprint.

An aerospace target appearing in the sensor FOV at a temperature 20 K above the ambient temperature (for example, at an altitude of 9 km its temperature might be 250 K) will obscure the radiance from the warm terrain. Consequently, the signal from the target pixel becomes

$$I_0 = L_B X^2 + A_T(L_T - L_B) \ , \tag{4.33}$$

where A_T is the surface area of target viewed from above and L_T is the target radiance.

The second term is the radiant intensity contrast and can be positive or negative. The dominant signals are the skin emission and obscuration components. In the short-wavelength infrared (SWIR) solar effects are large and

variable. At wavelengths longer than about 5 μm, solar effects diminish. Consequently, the solar component is difficult to calculate and is not suitable for detection of targets from space because of its random nature. Earthshine becomes less important for nadir viewing because only a small fraction of the fuselage will reflect earthshine. Earthshine is more observable when viewed from oblique angles. There is some compensation between target surface emission and earthshine reflection as a surface of high emissivity will have low reflectivity, and vice versa. The plume component for aircraft targets is of little importance except under afterburning conditions. If we define the contrast signal as

$$C = I_{T+B} - I_B \ , \tag{4.34}$$

where I_{T+B} is the radiant intensity of target plus background and I_B is the radiant intensity of background alone, then the contrast can be written as

$$C = A_T(L_T - L_B) \ . \tag{4.35}$$

4.2.1.14 Calculated Aircraft Contrast Signal (Conley[10]). From Eq. (4.35) it can be seen that the contrast depends on the ambient temperature of the air, the velocity of the target, the surface area of the target, and the background radiance.[10] Consequently, it is highly dependent on season of the year, background (terrain, snow, or water), as well as the altitude of the target. Using a LOWTRAN atmospheric model, Eq. (4.35) was used to calculate the contrast signatures of an aircraft target with a surface area of 500 m^2 moving at Mach 0.8. Figure 4.19 shows the contrast signatures during the summer at mid-latitudes at an altitude of 10 km. The signatures below about 5 μm are representative only for nighttime conditions. Note that for these conditions, the contrast is either zero or negative at all wavelengths. In the 4.3- and 15-μm region where the atmosphere is opaque, the contrast is zero for target altitude below about 50 km. In the 2.7- and 6-μm region the contrast is zero at all altitudes below approximately 9 km, where the atmosphere is opaque in these bands. In this case the target is at 10 km, and consequently a small positive contrast and negative spike is present in the band. The remaining portion of the spectrum can be considered window bands or semiwindow bands and are useful bands for space observation of low-altitude targets. For comparison purposes, a low-altitude signature for the same atmospheric model is shown in Fig. 4.20. Here, the target is located at 1-km altitude and the contrast is reversed, becoming positive in the window bands and zero in the opaque bands. An exception occurs near 13 μm, where a small negative contrast occurs. These plots are representative, and the effects of seasons or cloud backgrounds versus terrain versus sky on the contrast spectrum are dramatic.

4.2.2 Background Phenomenology (Suits[11])

Several sources of radiation contribute to the general background that the IRST must deal with. Referred to as clutter, the most severe are clouds in an airborne search role and varying terrain in the case of down-looking systems. The spatio-temporal variation of backgrounds is probably the most critical effect in IRST performance. Specifically to maintain high sensitivity while holding down the false-alarm rate to some acceptable value in the presence of

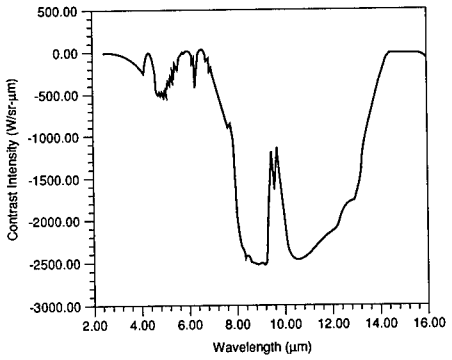

Fig. 4.19 Calculated contrast signature of a 500-m^2 target at an altitude of 10 km observed from space, midlatitude summer conditions, T = 294 K.[10]

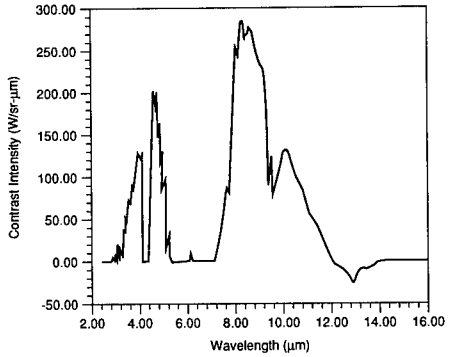

Fig. 4.20 Calculated contrast signature of a 500-m^2 target at an altitude of 1 km observed from space, midlatitude summer conditions, T = 294 K.[10]

high clutter is the major problem in IRST systems. Other sources of background or noise are scattered solar radiation, earth-limb backgrounds, IR stars, and aurora.

This section describes the phenomenology of each of these sources, relegating the actual quantitative use of the data to the sections on system performance. To accomplish this, some of the above sources will be characterized in terms of a power spectral density function (PSD), which subsequently may be used in a statistical description of performance; however, it should be noted that rarely are the PSDs sufficiently well behaved to be employed at face value in performance calculations.

4.2.2.1 Sky Spectral Radiance. Sky-background radiation in the infrared is caused by scattering of the sun's radiation and by emission from atmospheric constituents. Figure 4.21 illustrates the separation of the spectrum into two regions: the solar-scattering region short of 3 μm and the thermal-emission region beyond 4 μm. Solar scattering is represented by reflection from a bright sunlit cloud and, alternatively, by a curve for clear-air scattering. The thermal region is represented by a 300 K blackbody. Figure 4.22 shows blackbody curves for temperatures ranging from 0 to 40°C. This simple model is modified by a number of factors: in the solar region there are absorption bands of water vapor at 0.94, 1.1, 1.4, 1.9, and 2.7 μm, and of carbon dioxide at 2.7 μm. The effect of these bands is shown in Fig. 4.23.

In the thermal region, curves for those bands that have strong absorption (and thus strong emission) will approach the blackbody curve appropriate to the temperature of the atmosphere. Less strongly emitting regions may contribute only a small fraction of the radiation of a blackbody at the temperature of the atmosphere. The bottom curve in Fig. 4.24 is a good example. This zenith measurement, taken from a high, dry location, shows low emission except in the strong band of CO_2 at 15 μm and of H_2O at 6.3 μm. There is also a weak emission peak, due to ozone, at 9.6 μm. The low-level continuum is due to the wings of the strong bands of H_2O and CO_2. The effect of increased humidity

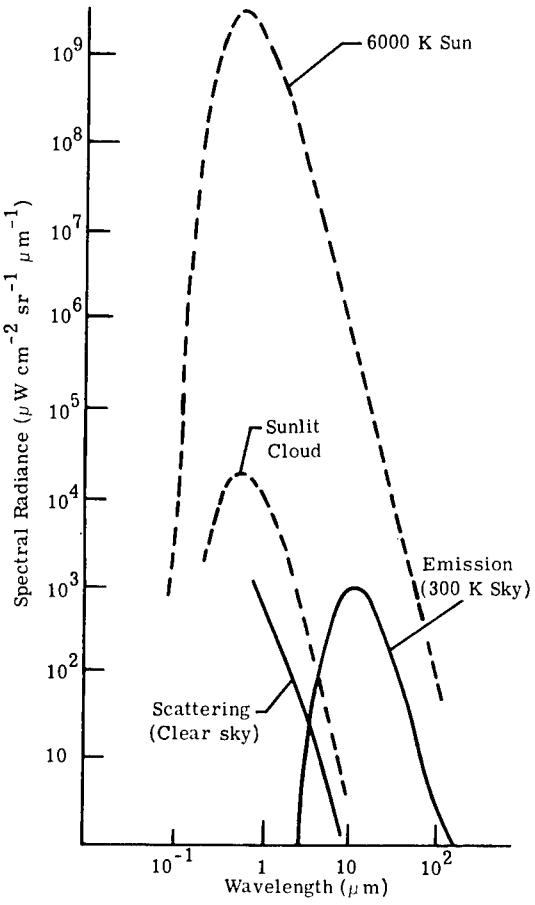

Fig. 4.21 Contributions from scattering and atmospheric emission to background radiation.[11]

and air mass can be seen by comparing the bottom curves of Figs. 4.24 and 4.25. Figure 4.25 shows measurements taken at a humid, sea-level location.

The effect of increasing air mass alone can be seen in both Figs. 4.24 and 4.25 by comparing curves taken from the same altitude at various elevation angles. The emission shows a systematic decrease with increasing elevation angle. The direction of look also has an effect in the solar-scattering region, as seen in Fig. 4.23, where, for a clear sky, the sun's position is fixed and the spectral radiance is plotted for several observer angles.

The position of the sun has a strong effect on the scattered radiation in the solar region, as shown in Fig. 4.26. Here, the observer looks at the zenith. The elevation angle of the sun is varied but has little effect on the radiation in the thermal region. The temperature of the atmosphere, on the other hand, has a strong effect on the radiation in the thermal region but little effect in the solar region.

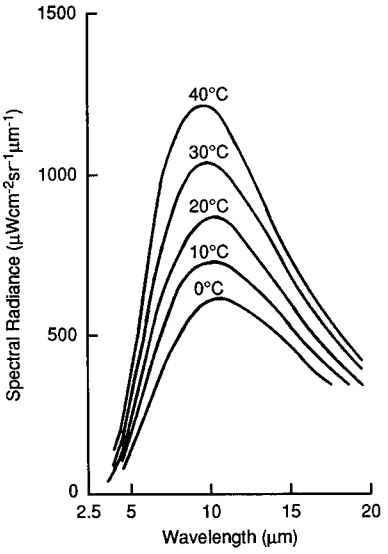

Fig. 4.22 Spectral radiance of a blackbody with a temperature range of 0 to 40°C.[11]

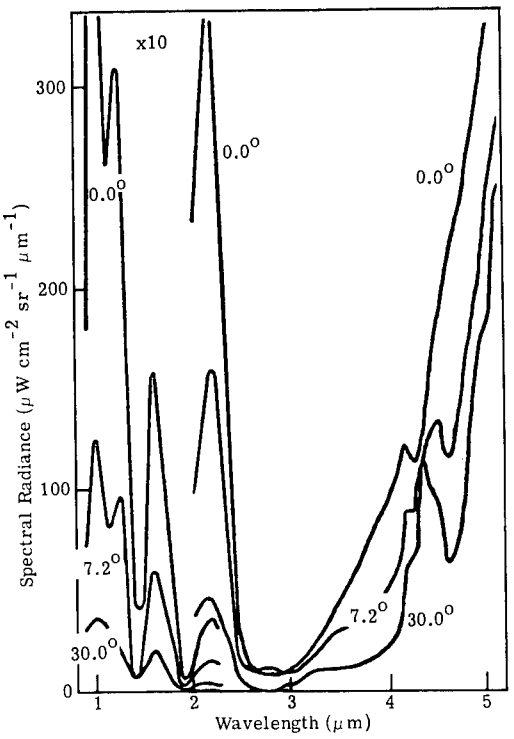

Fig. 4.23 The spectral radiance of a clear daytime sky.[11]

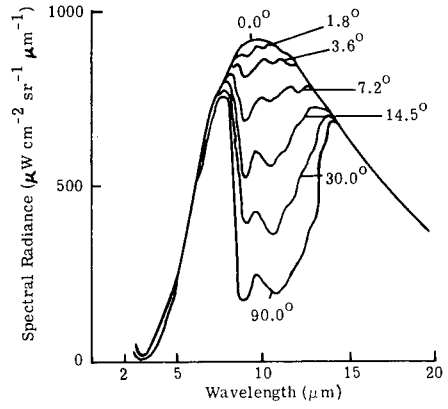

Fig. 4.24 The spectral radiance of a clear nighttime sky for several angles of elevation above the horizon (Elk Park Station, Colorado).[11]

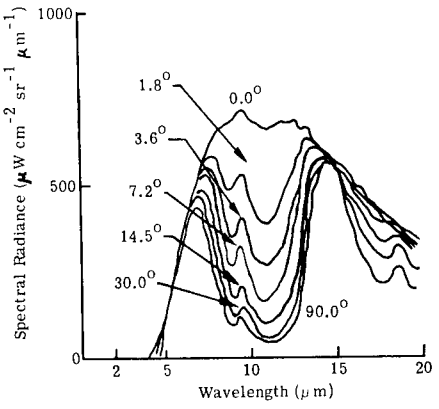

Fig. 4.25 The spectral radiance of a clear nighttime sky for several angles of elevation above the horizon (Elk Park Station, Colorado).[11]

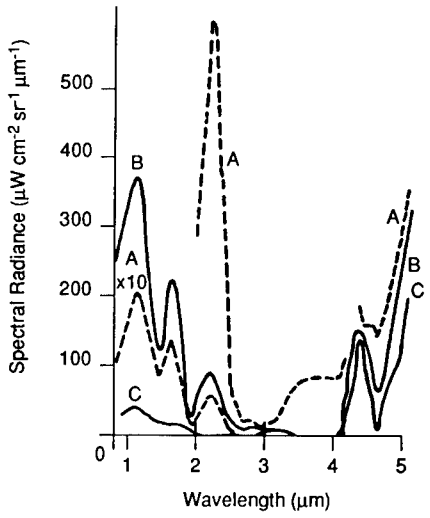

Fig. 4.26 The spectral radiance of a clear zenith sky as a function of the sun position. Curve A = sun elevation 77 deg, temperature 30°C; curve B = sun elevation 41 deg, temperature 25.5°C; curve C = sun elevation 15 deg, temperature 26.5 °C.[11]

4.2.2.2 Cloud Radiance. The presence of clouds will affect both near-infrared solar scattering and thermal-region emission.

Near-infrared radiation exhibits strong forward scattering in clouds. Thus, the relative positions of sun, observer, and cloud cover become especially important. For a heavy, overcast sky, multiple scattering reduces the strong forward-scattering effect.

Thick clouds are good blackbodies. Emission from clouds is in the 8- to 13-μm region and is, of course, dependent on the cloud temperature. Because of the emission and absorption bands of the atmosphere at 6.3 and 15.0 μm, a cloud may not be visible in these regions, and the radiation here is determined by the temperature of the atmosphere. A striking example is given in Fig. 4.27. Here, the atmospheric temperature is +10°C, and the radiation in the emission bands at 6.3 and 15.0 μm approaches a value appropriate to that temperature. The underside of the cloud has a temperature of −10°C, and the radiation in the 8- to 13-μm window approaches that of a blackbody at −10°C.

Figure 4.28 shows the variation of sky radiance as a function of elevation angle. Figure 4.29 shows the variation with respect to variations of ambient air temperature. Figure 4.30 shows seasonal variations.

4.2.2.3 Ground-Level Thermal Irradiance of the Sky. The total thermal irradiance from a clear sky at sea level $E(\text{sky})$ may be estimated from the Idso-Jackson[12] empirical relation using ground-level meteorological absolute air temperature T_a:

$$E(\text{sky}) = \sigma T_a^4\{1 - 0.261 \exp[-7.77 \times 10^{-4}(273 - T_a)^2]\} , \qquad (4.36)$$

where σ is the Boltzmann constant. This relation is primarily for heat-transfer applications. Most of the irradiance is due to emission in the absorption bands

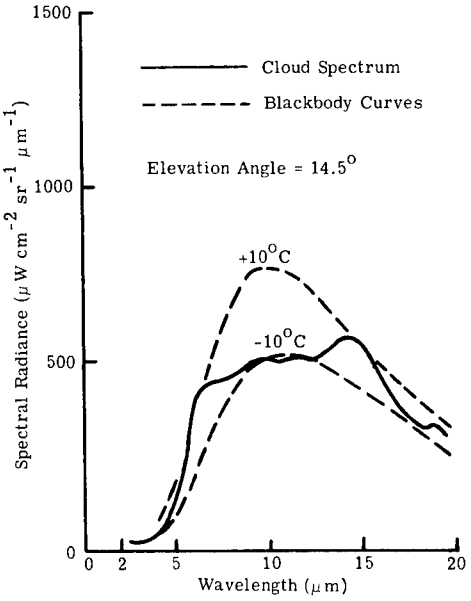

Fig. 4.27 The spectral radiance of the underside of a dark cumulus cloud.[11]

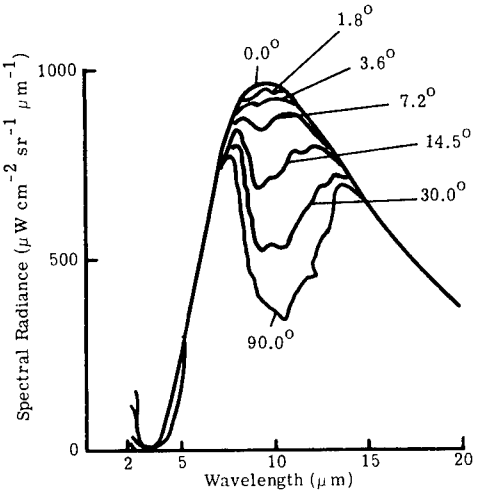

Fig. 4.28 The spectral radiance of sky covered with cirrus clouds at several angles of elevation.[11]

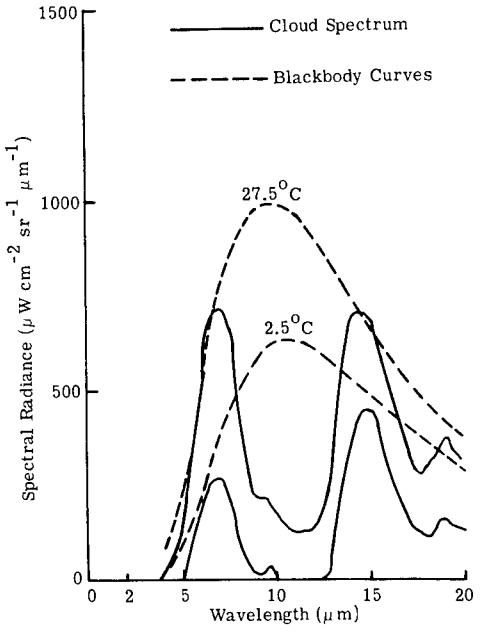

Fig. 4.29 Zenith sky spectral radiance showing the large variation with ambient air temperature.[11]

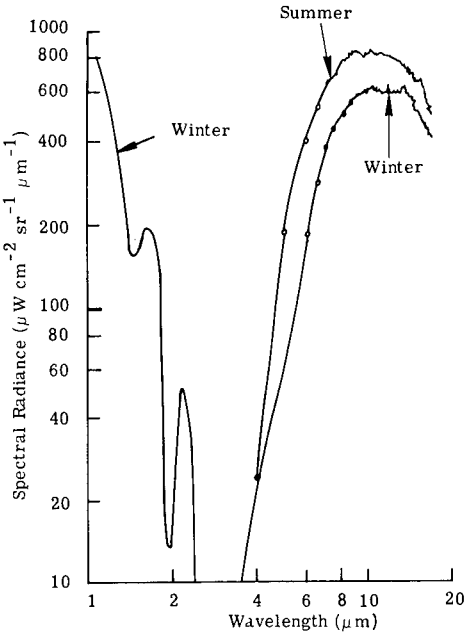

Fig. 4.30 Spectral radiance of overcast skies in the winter and summer.[11]

on either side of the 8- to 14-μm atmospheric window. Consequently, it is not directly useful for calculating the sky reflections from metal plates within the atmospheric window.

4.2.2.4 Radiation from the Earth's Surface. Figure 4.31 shows the comparative spectral radiances of a patch of ground at an airfield observed on a clear night and during the following morning with the sun shining on it.

Figure 4.32 shows the radiance of the night sky just above the horizon and that of the ground at the same angle below the horizon.

The spectra of distant terrain do not always conform to the blackbody characteristics observed in the radiance of nearby terrain. This can be seen in Fig. 4.33, where the upper curve represents the radiance of a city on a plain as viewed from the summit of a mountain at a distance of about 15 miles.

Figure 4.34 shows the diurnal variation in the 10-μm radiance of selected backgrounds on the plains as measured from the summit of Pike's Peak. The line-of-sight distances are forest—30 miles; grassy plains—21 miles; airfield—19 miles; city—15 miles.

Figures 4.35 and 4.36 show seasonal variation over North America exhibiting the likely extremes between sunlit summer and overcast winter terrain for three different solar zenith angles.

The spectral radiance of water bodies is shown in Figs. 4.37 and 4.38. The relative values of spectral reflectance over North America for several natural background materials are presented in Fig. 4.39 in the SWIR and MWIR bands.

Additional data calculated with LOWTRAN are given in Section 4.2.3.2.

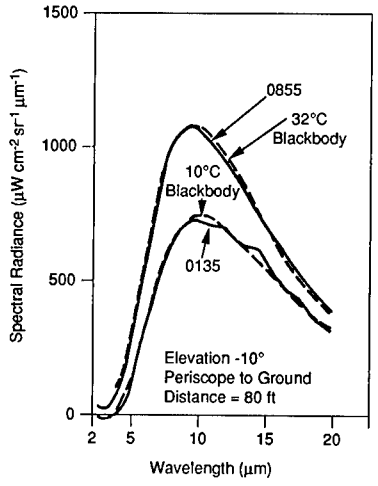

Fig. 4.31 Day and night radiance of grass-covered field (Peterson Field, Colorado).[11]

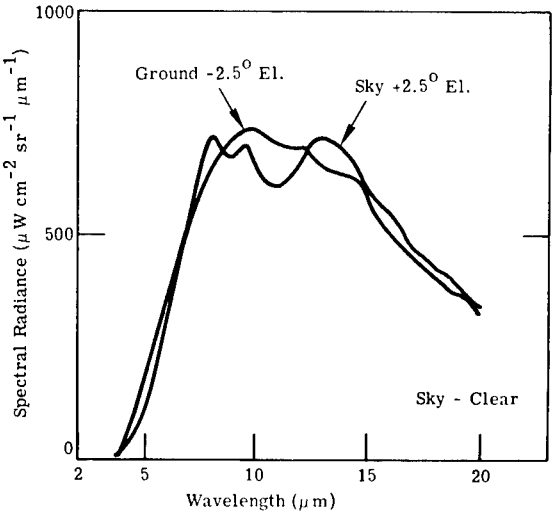

Fig. 4.32 Comparative spectra of the ground and sky near the horizon (Peterson Field, Colorado).[11]

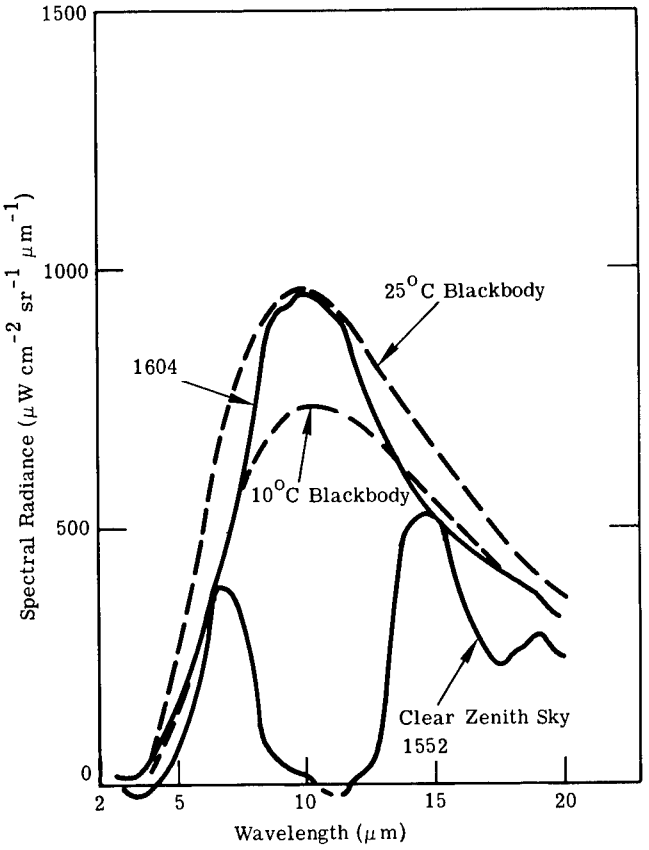

Fig. 4.33 Radiance of an urban area and of clear zenith sky (Colorado Springs from Pikes Peak).[11]

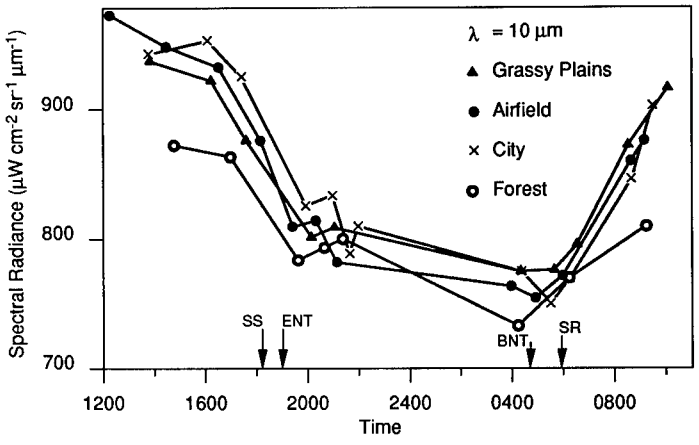

Fig. 4.34 Diurnal variation in the 10-μm radiance of selected backgrounds. SS = sunset; SR = sunrise; ENT = end of nautical twilight; BNT = beginning of nautical twilight.[11]

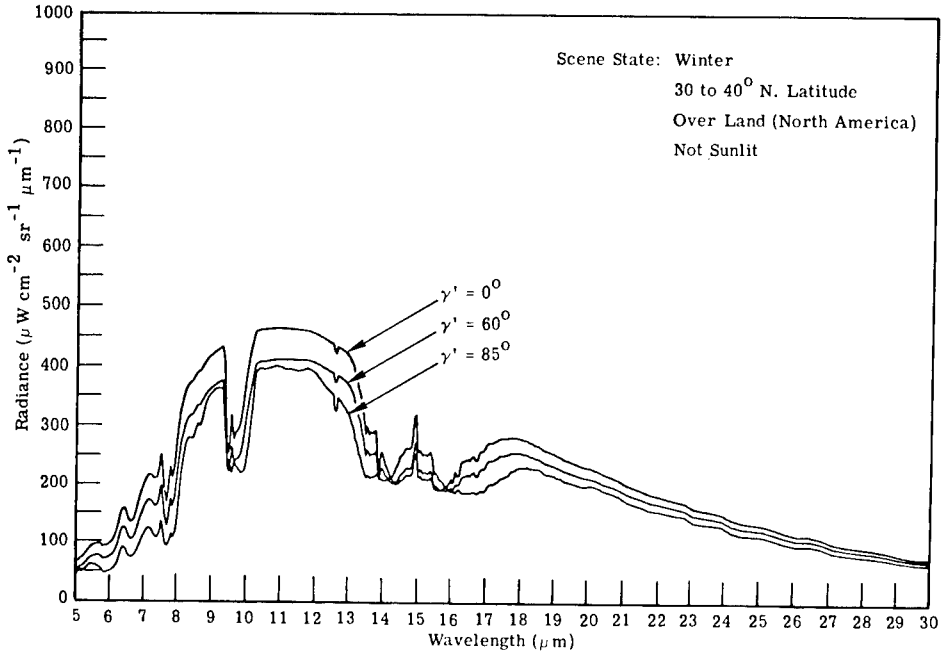

Fig. 4.35 The expected value of spectral radiance for three solar zenith (γ') angles.[11]

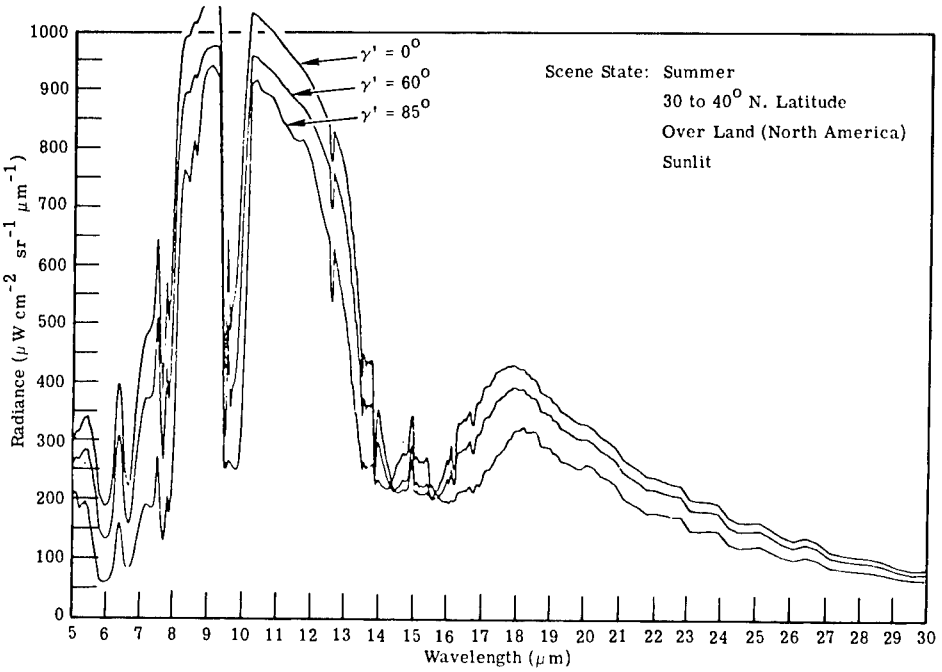

Fig. 4.36 The expected value of spectral radiance for three solar zenith (γ') angles.[11]

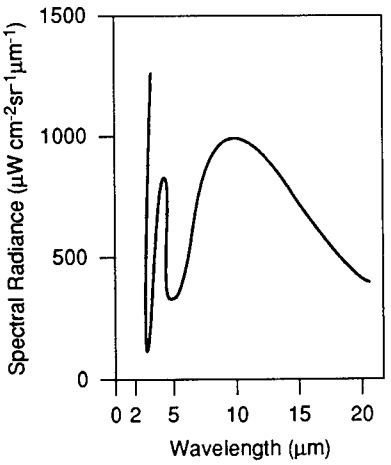

Fig. 4.37 Spectral radiance of the Banana River at Cocoa Beach, Florida.[11]

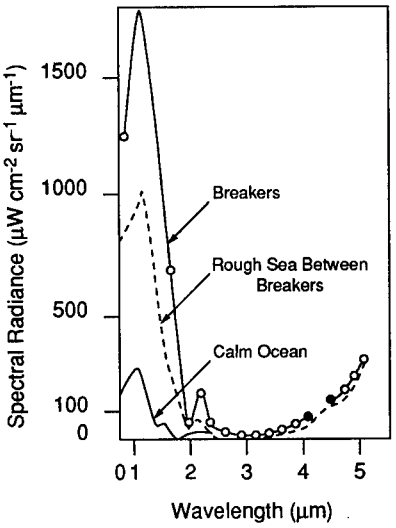

Fig. 4.38 Spectral radiance of the ocean.[11]

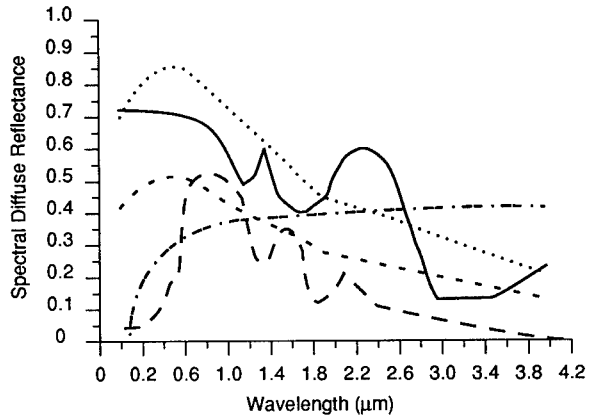

——— Clouds. Data are directional reflectance of a middle layer cloud.

····· Winter Snow and Ice. Data are directional reflectance of dry snow.

- - - - Summer Ice. Data are directional reflectance of summer Arctic ice.

·—·—· Soil and Rocks. Data represent the average value of the bidirectional reflectance, (45°, 0 ,0 ,0), of gravel, wet clay, dry clay, tuff bedrock, and sandy loam.

— — — Vegetation. Data represent the average value of directional reflectance of many types of vegetation (from the ERIM data file).

Fig. 4.39 Spectral diffuse reflectance of earth-atmosphere constituents.[11]

4.2.2.5 Aurora. Aurora is a high-altitude background effect that may represent limiting conditions for limb-view IRST systems. Aurora emission lines occur at 0.92, 1.04, and 1.11 μm. The measured brightnesses are about 6×10^{-8} W cm^{-2} sr^{-1} line^{-1}.

It is difficult to investigate the aurora and airglow beyond 2.0 μm because of absorption and thermal-emission processes in the atmosphere.

The green color of bright aurora is attributed to a 557.7 nm atomic oxygen line; the red color is attributed to an atomic oxygen doublet at 630.0 and 636.4 nm; the bluish purple color is attributed to molecular nitrogen. Combinations of these excitations may result in the visual perception of white and yellow. The photon radiance of aurora range from 10^3 to 10^6 Ry. (Ry is the unit symbol used here for a rayleigh, where 1 Ry corresponds to a photon radiance of $1/4\pi \times 10^6$ photons s^{-1} cm^{-2} sr^{-1}.)

Figure 4.40 shows the auroral spectrum between 0.9 and 1.2 μm. This reproduction was obtained by averaging a number of individual spectra.

High-altitude, rocket-borne spectrometers were used to obtain auroral spectra in 1973.[11] Figures 4.41 and 4.42 show the spectral radiance in the short-wavelength infrared (SWIR) range from 1.6 to 5.6 μm and in the long-wavelength infrared (LWIR) from 7.0 to 23.0 μm. Figure 4.43 shows a profile of spectral radiance at 4.3 μm as a function of altitude. The unit MRy is a megarayleigh.

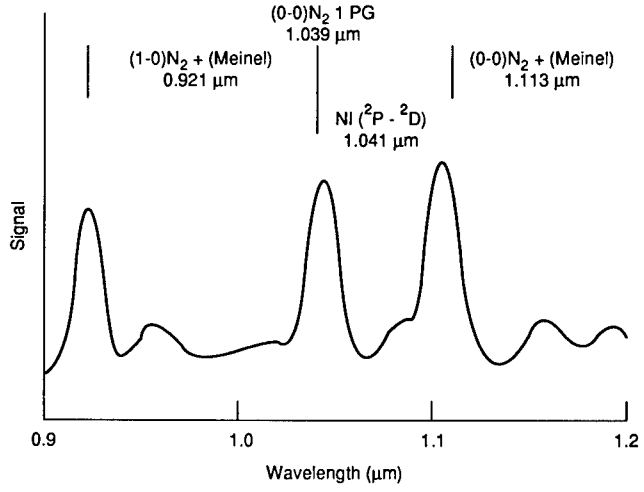

Fig. 4.40 Auroral spectrum, 0.9 to 1.2 μm, obtained with a lead sulfide spectrometer; projected slit width 100 Å.[11]

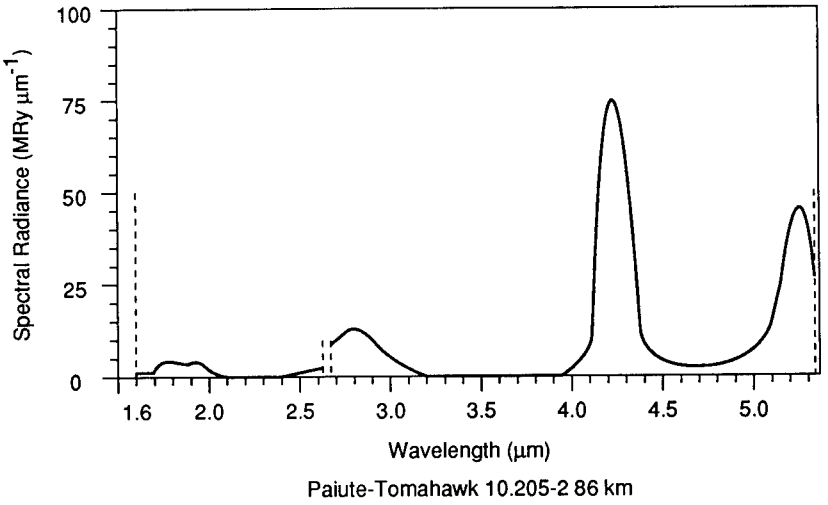

Fig. 4.41 Sample auroral spectral scans from an SWIR spectrometer aboard a Paiute-Tomahawk rocket launched from Poker Flat, Alaska, 24 March 1973. Although uncorrected for actual rocket aspect, the data approximate the zenith radiance.[11]

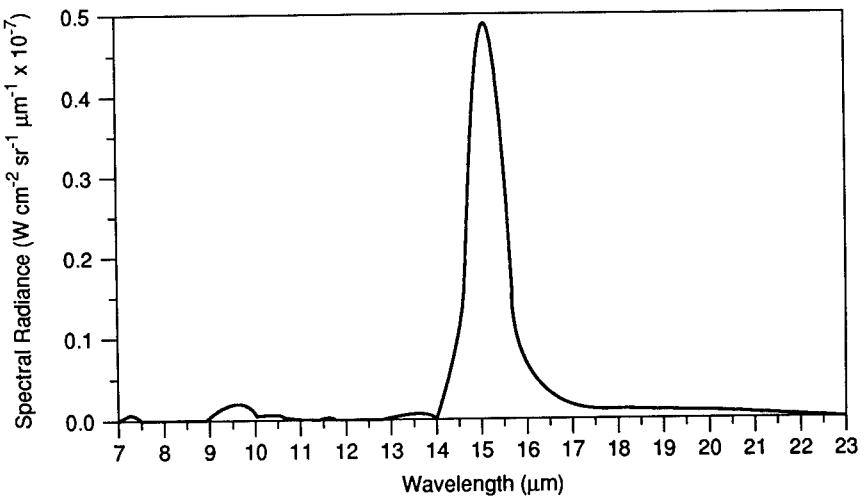

Fig. 4.42 Sample auroral spectrum scan (vertical) from an LWIR spectrometer aboard a Black Brant rocket flown from Poker Flat, Alaska, 22 March 1973. The rocket altitude is 96.9 km on rocket descent.[11]

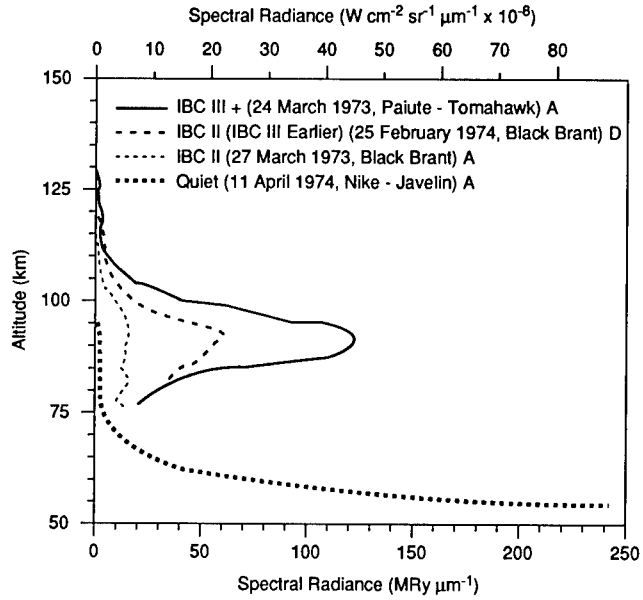

Fig. 4.43 Zenith peak spectral radiance at 4.3 μm measured with SWIR spectrometers flown on four different rockets under various auroral conditions.[11]

4.2.2.6 Night Airglow.[11] Airglow may be defined as the nonthermal radiation emitted by the earth's atmosphere. The exceptions are auroral emission and radiation of a cataclysmic origin, such as lightning and meteor trails.

Night airglow emissions in the infrared are caused by transitions between vibrational states of the OH^- radical. The exact mechanism of excitation is still unclear, but the effect is to release energy from solar radiation stored during the daytime. Airglow occurs at all latitudes.

There is evidence that some of the excitation is

$$H + O_3 \rightarrow OH + O_2$$

$$OH + O \rightarrow O_2 + H \ .$$

Thus, it appears that the distribution of night airglow is related to that of ozone. The measured heights of the airglow range from 70.0 to 90.0 km, which correspond to the location of ozone.

The nightglow increases away from the zenith at approximately secθ. Measurements usually are reported normalized to the zenith.

Variations in airglow radiance during the night seem to be caused by the motion of large patches (airglow cells) with dimensions of about 2500 km, moving with velocities of about 70 m s^{-1}.

Figure 4.44 shows the relative airglow radiance. Airglow emissions caused by OH^- appear as small maxima in the vicinity of 1.6 and 2.15 μm. Although further emission bands are predicted in the range from 2.8 to 4.5 μm, they are thoroughly masked by the thermal emission of the atmosphere. Figure 4.45 shows the nightglow spectrum in the 1- to 2-μm region.

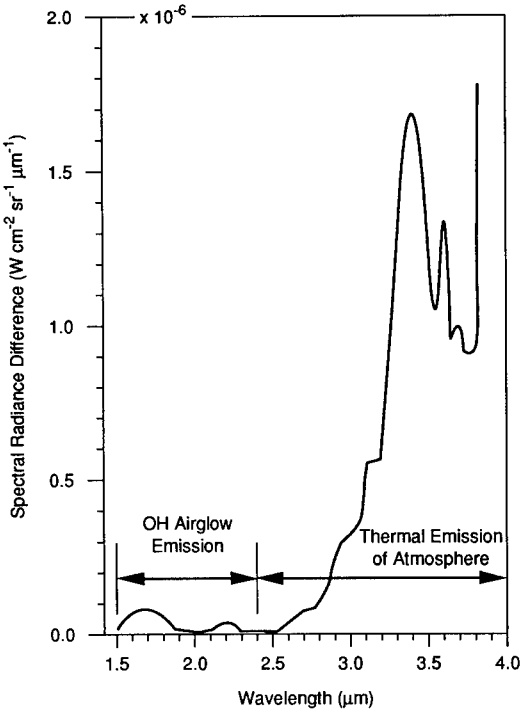

Fig. 4.44 Airglow spectral intensity.[11]

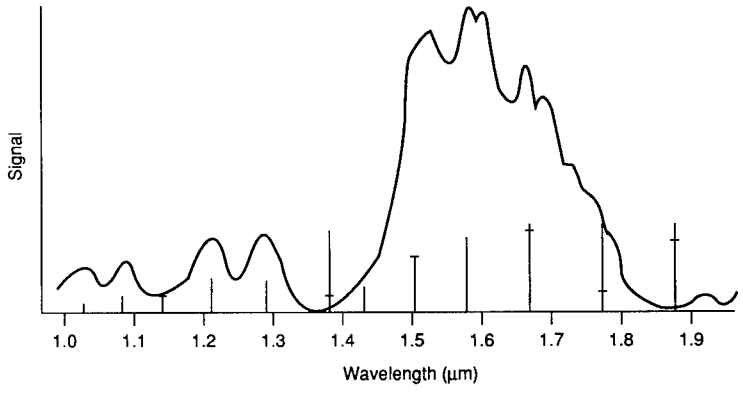

Fig. 4.45 Airglow spectrum, obtained with a scanning spectrometer (projecting slit width 200 Å). The origins and expected intensities of OH bands are shown by vertical lines; the horizontal strokes indicate the reduction due to water vapor.[11]

If one looks straight down from a satellite, the atmospheric spectrum should be very similar to that shown in Figs. 4.44 and 4.45. Note that for the airglow all results are given for the zenith itself rather than for the angles at which observations are usually made.

4.2.2.7 The Sun. The sun is a G-class star with a mean radius of about 695,000 km. The surface temperature is approximately 5900 K by best-fit

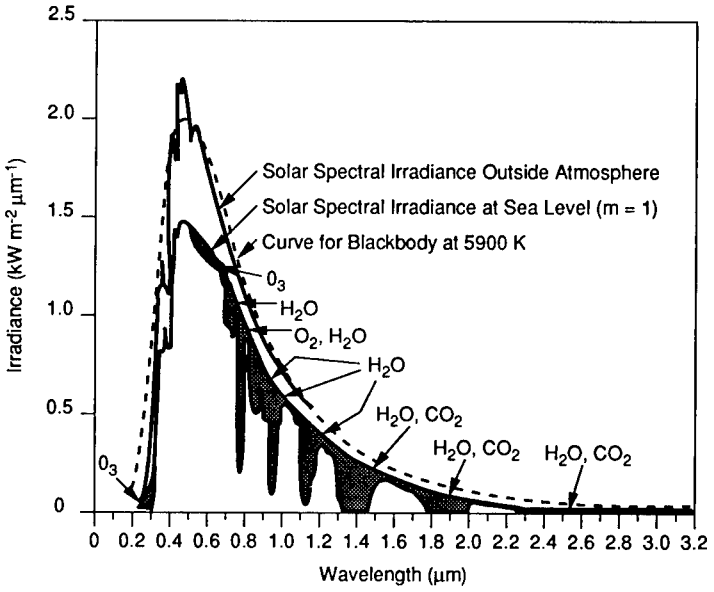

Fig. 4.46 Spectral irradiance distribution curves related to the sun. The shaded areas indicate absorption at sea level due to the atmospheric constituents shown.

blackbody curve, or about 5770 K for the temperature of a blackbody source that is the size and distance of the sun and that would produce an exoatmospheric total irradiance of 1353 W m^{-2} at the earth.

The surface is largely a heated plasma that should radiate very nearly as a blackbody. However, the cooler atomic gases of the solar atmosphere and the large temperature gradient below the surface, coupled with the nonisothermal character of transient surface features, lead to deviations from blackbody radiation.

Figure 4.46 shows the spectral irradiance of exoatmospheric solar radiation, the comparable blackbody spectrum for a temperature of 5900 K, and the approximate solar spectral irradiance at sea level through one atmospheric air mass ($m = 1$).

4.2.2.8 Background Fluctuations (Conley[10]). Target-to-background contrasts will not be constant under actual operating conditions because of the often large variation in background radiance. An instantaneous value of target-to-background contrast will be difficult to predict. Its statistical description will be controlled by the statistics of the background, which vary widely over typical clutter. Generally, a typical IRST background scene is statistically nonstationary.

As indicated previously by emphasis on the probability of detection, the system designer is interested primarily in the probability that a target signal will be larger than the background and in how often the background will resemble a target. The pertinent statistical properties of the background, such as the variance, must be determined. The data can be treated as stationary

over subelements of the scene in some signal-processing schemes. The problem in practice is that to obtain sufficient statistics, one frequently must obtain data from different types of terrain, such as forests, mountains, and so forth. What is done, in practice, is to separate the data into segments, for example, desert, mountains, and so forth. The next step is to filter out the frequencies where insufficient data points are available. Each data segment is processed separately. They can then be averaged to form an ensemble average, for example, of deserts, broken clouds, arctic terrain, and so forth.

The classical treatment of background with stationary statistics usually is given in terms of Wiener spectra or a power spectral density (PSD) function [see Eq. (4.104)]. The variance of the background can be obtained from the PSD; thus, the signal-to-clutter ratio is determinate. Detection thresholds for a given probability of detection and false-alarm rate subsequently can be determined; however, because of the nonstationarity problem this procedure usually leads to unacceptably high false-alarm rates. In subsequent sections we present two important time-varying backgrounds in IRST applications, clouds and terrain. Use of the PSD to derive detection probability in stationary backgrounds is given in Sec. 4.3.7. Treatment of nonstationary backgrounds follows in Sec. 4.4.

4.2.2.9 The Power Spectral Density of Clouds. One important source of temporal background is moving clouds.

Conley[10] considered a broken cloud distribution moving past a staring sensor. If the cloud is opaque, the radiance observed at the sensor represents the radiation from a blackbody at the temperature of the ambient air at the cloud altitude. When the atmosphere is clear, the sensor would observe the warm terrain. To illustrate this situation a hypothetical trace is shown in Fig. 4.47. This illustrates the radiance fluctuations that a downward-looking sensor would observe operating at a wavelength of 9 μm for clouds at 3 or 6 km. It is reasonable to assume that the random arrival of clouds may be modeled as a Poisson process with arrival parameter adjusted for an assumed percentage of cloud cover. For the calculations that follow, a 50% cloud cover is assumed. The effect of a cloud on the measured radiance depends on the wavelength and the altitude, speed, size, and shape of a cloud passing through the field of view. For the present example, a sensor operating at 9-μm viewing terrain with broken clouds at a 6-km altitude was assumed. The idea is to allow clouds to

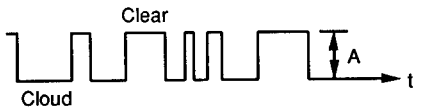

$A = 400 \dfrac{\mu W}{cm^2\ sr\ \mu m}$ for Cloud at 3 km

$A = 200 \dfrac{\mu W}{cm^2\ sr\ \mu m}$ for Cloud at 6 km

Fig. 4.47 Hypothetical radiance trace caused by moving clouds.[10]

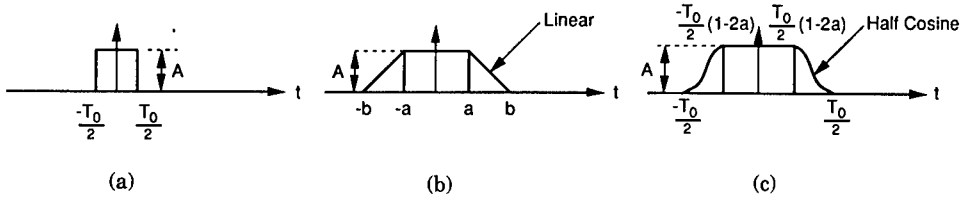

Fig. 4.48 Assumed cloud radiance trace waveform.[10]

enter the field of view, reach a maximum change of radiance, and then exit. The effect of a cloud on the radiance trace was assumed to take one of the forms shown in Fig. 4.48. Obviously, many shapes may be assumed, but it is felt that those shown would be representative of the problem, allowing for an upper limit of fast entry and exit as well as for a smooth entry and exit, thus bounding the probable spectral roll-off that could occur with an actual cloud.

The time required for entry and exit and the duration of time the cloud is within the field of view depend on the size and speed of a cloud. The radiance waveform may be coupled with the Poisson arrival process by convolving the shape with the Poisson impulses. This yields what is commonly called a "shot-noise" process model.

If we denote the cloud shape trace by $h(t)$, the assumed process may be taken as

$$h(t) = \sum_{i=-\infty}^{\infty} h(t - t_i) \ , \tag{4.37}$$

where t_i are the Poisson random time arrivals. The statistical autocovariance function for the process $h(t)$ is obtained by convolving the process with itself, denoted by $R(t)$. Thus,

$$R(T) = \int_{-\infty}^{\infty} h(\alpha)h(t + \alpha)\, d\alpha \ . \tag{4.38}$$

The power spectrum is the Fourier transform of $R(t)$; thus,

$$S(\omega) = |H(\omega)|^2 \ . \tag{4.39}$$

The Fourier transform of $h(t)$ is defined as

$$H(\omega) = \int_{-\infty}^{\infty} h(t) \exp(-j\omega t)\, dt \ . \tag{4.40}$$

For the waveforms of Fig. 4.48(a) through (c), the corresponding $H(\omega)$ are, respectively,

$$H(\omega) = AT_0\left(\frac{\sin\omega T_0/2}{\omega T_0/2}\right) \ , \tag{4.41}$$

$$H(\omega) = \frac{2A}{b - a}\left(\frac{\cos a\omega - \cos b\omega}{\omega^2}\right), \tag{4.42}$$

$$H(\omega) = A\left\{\frac{T_0}{2}(1 - 2\alpha)\frac{\sin[(\omega T_0/2)(1 - 2\alpha)]}{(\omega T_0/2)(1 - 2\alpha)} + \frac{T_0}{2}\frac{\sin(\omega T_0/2)}{\omega T_0/2} - \cos\left(\frac{\alpha\omega T_0}{2}\right) \times \sin\left(\frac{\omega T_0}{2}\right)(1 - \alpha)\left[\frac{2\omega}{\omega^2 - (4\pi^2/4\alpha^2 T_0^2)}\right]\right\}. \tag{4.43}$$

For the results that follow, footprints of 200 m and 1 km were chosen as representative. For the 200-m footprint, cloud sizes of 200 m, 500 m, 1 km, and 5 km were arbitrarily assumed. For the 1-km footprint, cloud sizes of 1 km, 5 km, and 10 km were assumed, and cloud speeds of 10 m s^{-1} and 30 m s^{-1} were chosen. As indicated earlier, a 50% cloud cover was assumed. Cloud size and velocity were evaluated separately for the trapezoidal waveform and cosine trapezoid. The power spectrum for each case was calculated. Selected PSDs are presented in Figs. 4.49 to 4.53 to show the effects of cloud size, speed, and type of waveform. All clouds are assumed to be at 6-km altitude. For clouds at 3 km the results should be divided by 2. Figure 4.49 shows the PSD of the random arrival of 200-m clouds moving at a speed of 10 m s^{-1} assuming a cosine trapezoidal waveform. The first null occurs at approximately 0.05 Hz with a roll-off of approximately $f^{-5.5}$. The same situation is shown in Fig. 4.50, except for a trapezoidal waveform, the first null occurs at approximately the same frequency; however, the roll-off is now changed to $f^{-3.5}$. The effect of an increase in velocity is shown in Fig. 4.51 for the same conditions shown in Fig. 4.50. The velocity of the clouds is now 30 m s^{-1}. The first null has shifted to a higher frequency of approximately 0.15 Hz and the roll-off is now f^{-4}.

The situation for larger footprints is shown in the next two figures. Figure 4.52 shows the PSD of 1-km clouds moving at speeds of 10 m s^{-1} across a 1-km footprint. The first null now occurs at 0.01 Hz with a roll-off of approximately f^{-6}. Figure 4.53 shows the PSD of 10-km clouds moving at speeds of 30 m s^{-1} across a 1-km footprint. The first null occurs at a frequency of approximately 0.002 Hz with a roll-off of f^{-5}.

The rectangular waveform of Fig. 4.48 serves as an upper bound on the high-frequency roll-off rate of f^{-2}. The first null of the spectrum depends on the duration of the pulses $\sim 1/T$. This is consistent with the results shown. Thus, the speed and size of the cloud dictate the bandwidth of the spectrum.

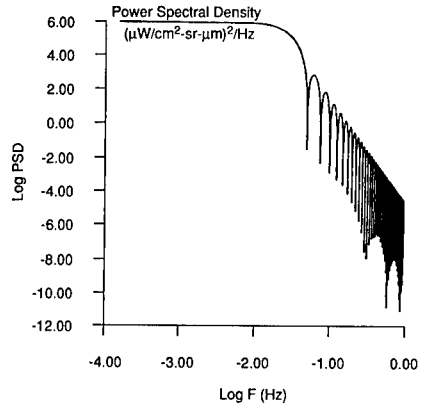

Fig. 4.49 The PSD of 200-m clouds moving at 10 m s^{-1} across a 200-m pixel using a cosine trapezoidal waveform.[10]

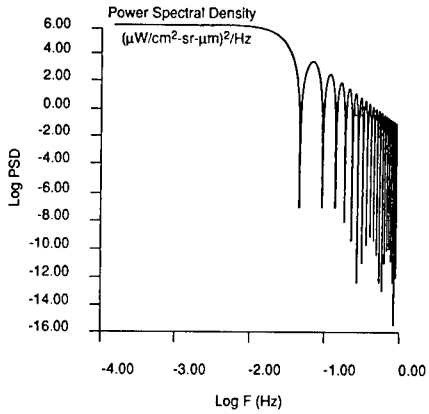

Fig. 4.50 The PSD of 200-m clouds moving at 10 m s^{-1} across a 200-m pixel using a trapezoidal waveform.[10]

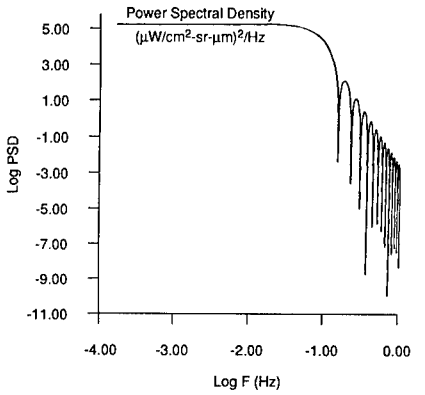

Fig. 4.51 The PSD of 200-m clouds moving at 30 m s^{-1} across a 200-m pixel using a half-cosine waveform.[10]

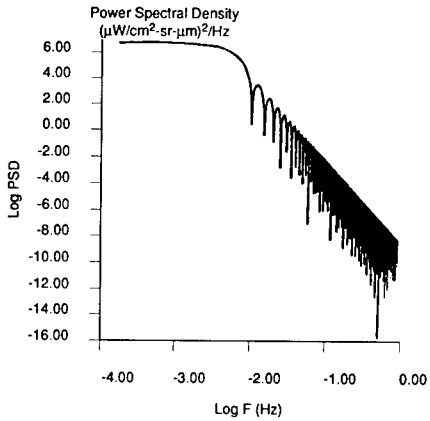

Fig. 4.52 The PSD of 1-km clouds moving at 10 m s^{-1} across a 1-km pixel using a half-cosine waveform.[10]

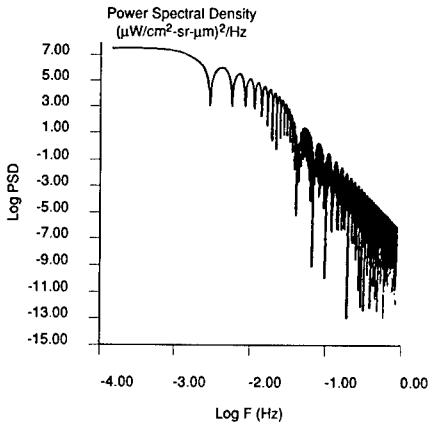

Fig. 4.53 The PSD of 10-km clouds moving at 30 m s^{-1} across a 1-km pixel using a half-cosine waveform.[10]

4.2.2.10 Spatial Structure of Background Radiance. No satisfactory model is available that will predict spatial backgrounds as a function of terrain, wavelength, and so forth. One effective model discussed by Conley[10] is to consider a radiance trace as a random set of two-dimensional pulses whose widths obey Poisson statistics and whose amplitudes obey either Gaussian or Poisson statistics. This is a reasonable assumption since a radiance trace resembles a random telegraph signal and it has long been recognized that "shot noise" and the random telegraph signal obey Poisson statistics. Furthermore, it is expected that daytime SWIR background traces would have amplitudes that obey Gaussian statistics and LWIR amplitudes would obey Poisson statistics. This is because the daytime SWIR backgrounds are governed by both solar scatter and thermal radiance, whereas LWIR traces are governed solely by thermal radiances. Therefore, it is expected that nighttime SWIR backgrounds also would follow Poisson statistics. The general reasoning behind this is the fact that the number of amplitude variations due to thermal radiances is much smaller than that caused by both solar and thermal radiance. For large numbers of variations, Poisson statistics approach Gaussian statistics. There is some experimental evidence supporting this model.[13]

The PSD of the spatial structure can be interpreted in terms of Poisson statistics. The autocovariance function for a random telegraph signal is

$$C(L) = \sigma^2 e^{-\alpha L} \ . \tag{4.44}$$

The Fourier transform of Eq. (4.44) becomes the PSD and is of the form

$$S(\omega) = \frac{\alpha\sigma^2}{\alpha^2 + \omega^2} \ , \tag{4.45}$$

where

ω = spatial frequency
σ^2 = variance of the radiance trace
α = reciprocal of the average pulse width; also reciprocal of the correlation length.

While the output of a sensor may be described in one dimension, such as Eq. (4.45), the terrain itself is described by two dimensions. If we assume isotropy, the two-dimensional spectrum can be obtained from a one-dimensional output. If the one-dimensional spectrum $S(\omega)$ is represented as

$$S(\omega) = C\omega^{-n} \ , \tag{4.46}$$

then the two-dimensional spectrum $F(\omega)$ is

$$F(\omega) = C'\omega^{-(n+1)} \ , \tag{4.47}$$

where

$$\omega = (\omega_x^2 + w_y^2)^{1/2} \ . \tag{4.48}$$

Thus, Eq. (4.45) becomes, for two dimensions,

$$F(\omega_x,\omega_y) = \frac{\alpha\sigma^2}{(\alpha^2 + \omega_x^2 + \omega_y^2)^{3/2}} \cdot \tag{4.49}$$

It can be shown that only a small difference in clutter leakage is obtained if one uses Eq. (4.45) rather than Eq. (4.49). Generally, Eq. (4.45) says that the PSD rolls off at -2 for large spatial frequencies where $\omega^2 \gg \alpha^2$. At very small spatial frequencies where $\omega^2 \ll \alpha^2$ the spectrum is flat.

The spectrum obtained from Eq. (4.45) is similar to the envelope of the spectrum obtained from Eq. (4.41). However, the latter assumes the pulses have fast rise times. For pulses that have slow rise times, we have shown earlier [Eqs. (4.42) and (4.43)] that the spectrum at high frequencies rolls off at -4, or with even larger negative numbers. Consequently, we may expect similar behavior for spatial pulses.

In a real background radiance trace, we would, at times, expect combinations of structure and accordingly combinations of spectra. For example, we may expect spectra to be the sum of Eqs. (4.41) and (4.42). Accordingly, we also may expect spectra with two or more breakpoints or correlation lengths with different roll-off values. Fortunately, we have examples that verify these assumptions. Figure 4.54 represents a smoothed version of the calculated PSD. We notice the spectrum has a constant roll-off of almost -2. According to our model, this means the radiance trace would consist of reasonably sharp rise times but with an average pulse width greater than 25 km. Since the spectrum represents data obtained during a cloudy day, that is not an unreasonable value.

Figure 4.55 shows a Wiener spectrum or PSD of an ocean background that can be represented as the sum of two different spectra with different correlation lengths:

$$S(\omega) = S_1(\omega) + S_2(\omega) \ . \tag{4.50}$$

One correlation length is on the order of 8 km and the second correlation length is on the order of 0.1 km. Figure 4.56 shows a comparison of the model with the data. In the model, it is assumed that a breakpoint occurs at 0.1 cycles km^{-1}.

Figure 4.57 shows a spectrum of extended clouds. We have modeled it as the sum of two distinct spectra. One spectrum rolls off at ω^{-4} and the other at ω^{-2}. We interpret the line trace as consisting of two types of pulses, one with slow rise times with a correlation length of 5.5 km and the second with fast rise times with a correlation length of 1.2 km, as shown in Fig. 4.58. Figure 4.59 shows a comparison of the model with the data. The divergence at the high end of the spectrum is probably due to the overcorrection for the system transfer function in the data.

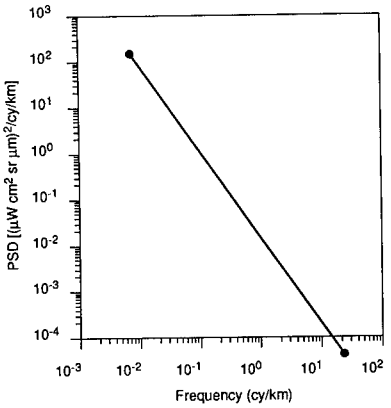

Fig. 4.54 PSD, cloudy day, red spike band.[10]

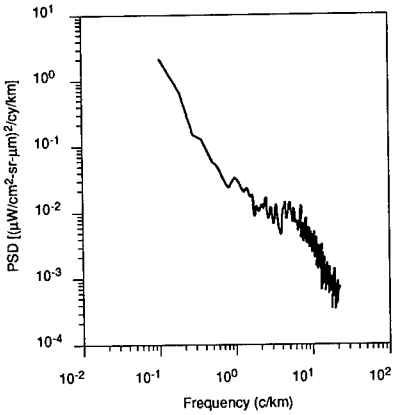

Fig. 4.55 PSD, ocean, blue spike band.[10]

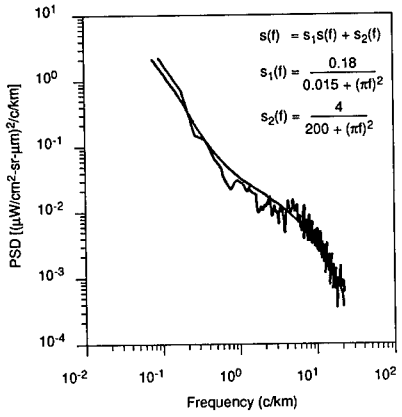

Fig. 4.56 Comparison of model with Fig. 5.55.[10]

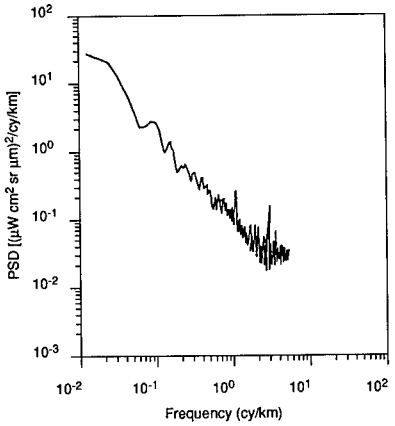

Fig. 4.57 PSD, extended clouds, blue spike band.[10]

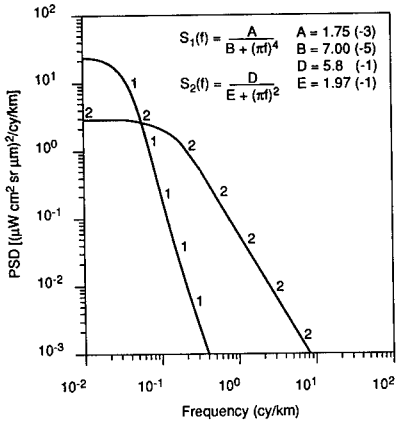

Fig. 4.58 Model-derived spectra.[10]

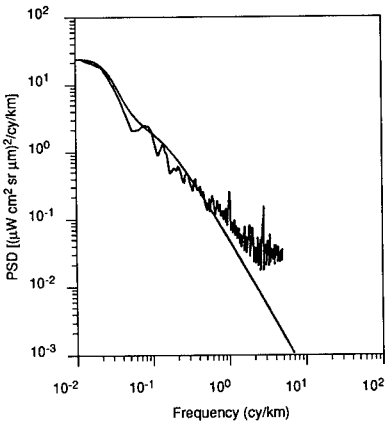

Fig. 4.59 Comparison of model with Fig. 5.57.

4.2.2.11 Measured Terrain PSD Data. The data on the following pages (Figs. 4.60 to 4.97) is presented as a representation of measured background power spectra density functions, including arctic, farm and field, clouds, mountain, ocean and coastline, and urban areas. These data were gathered with the calibrated HICAMP II sensor mounted on NASA U-2 aircraft at a constant altitude of 60,000 ft. PSD data are presented in representative spectral bands in the SWIR 3- to 5-μm band and the LWIR 8- to 12-μm band and are given in terms of "μ flicks" = 10^{-6} W cm^{-2} sr^{-1} μm^{-1}. A correction for the response of the instrument must be made to render these data useful as indicators of the spatial-frequency content of these scenes. The approximate normalized MTFs of the instrument are

$$\text{MTF(SWIR)} = \exp(-1.21 f^2) \tag{4.51}$$

and

$$\text{MTF(LWIR)} = \exp(-1.38 f^2) \ , \tag{4.52}$$

where f is in cycles per milliradian. For f in cycles per kilometer, the constant in the above expression becomes -4.02×10^{-4} and -4.63×10^{-4}, respectively. The instrument's response is relatively constant out to about 20 cycles per kilometer.

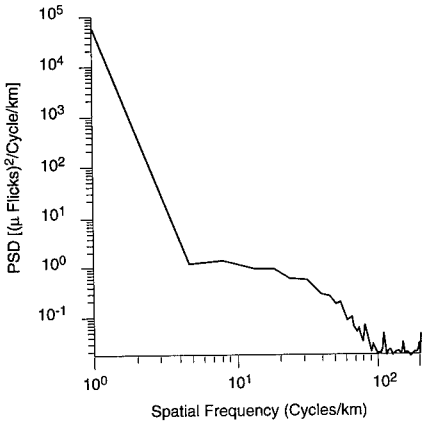

Fig. 4.60 PSD of a relatively featureless Arctic background with snow in the 4.46- to 5.20-μm band (HC393R).

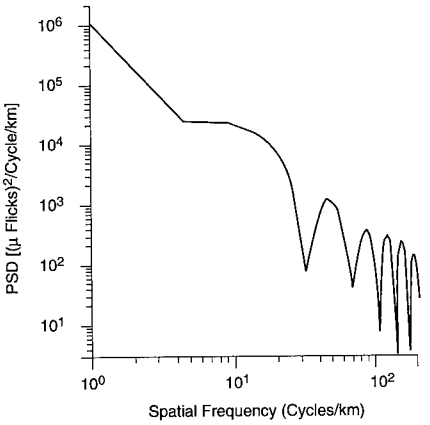

Fig. 4.61 PSD of a relatively featureless Arctic background with snow in the 8.28- to 8.76-μm band. The high-frequency structure is artifact (HC394R).

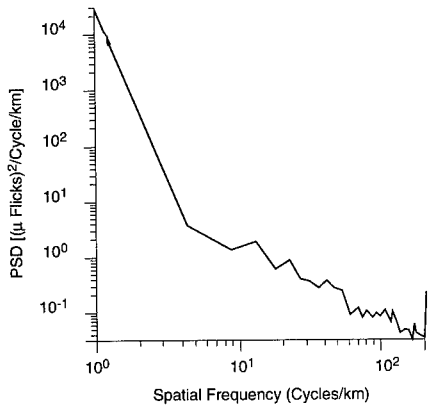

Fig. 4.62 PSD of moderately structured Arctic background with ice and snow in the 4.46- to 5.20-μm band (HC384R).

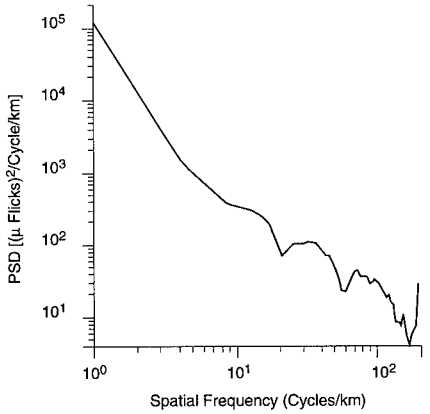

Fig. 4.63 PSD of moderately structured Arctic background with ice and snow in the 8.28- to 8.76-μm band (HC385R).

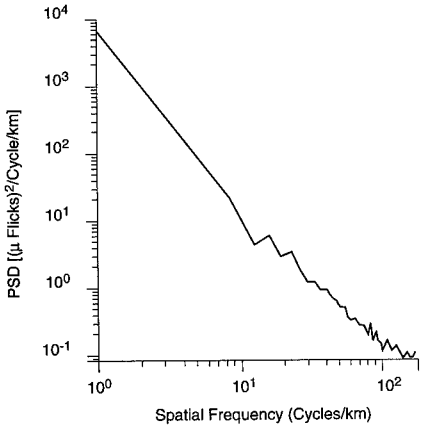

Fig. 4.64 PSD of Arctic background with moderate structure including snow and snow crests in the 4.46- to 5.20-μm band (HC351R).

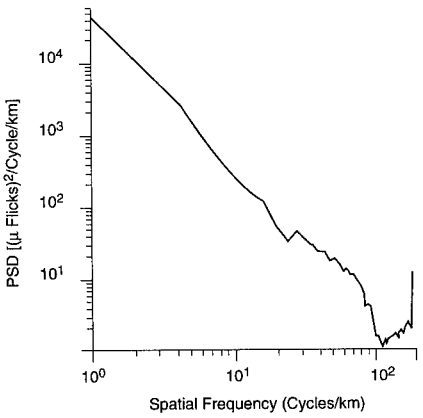

Fig. 4.65 PSD of Arctic background with moderate structure including snow and snow crests in the 7.80- to 13.50-μm band (HC352R).

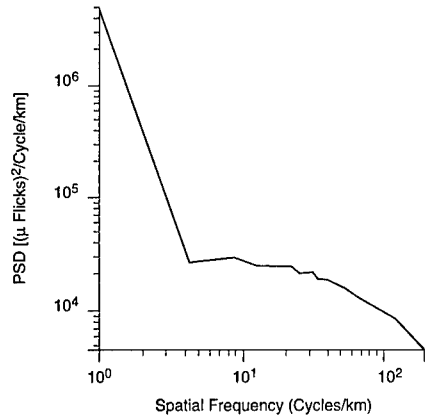

Fig. 4.66 PSD of farm and field terrain at night in the 11.64- to 12.12-μm band (HC426R).

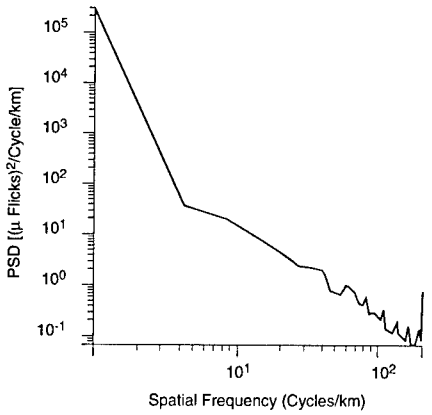

Fig. 4.67 PSD of farm and field terrain at night in the 4.46- to 5.20-μm band (HC425R).

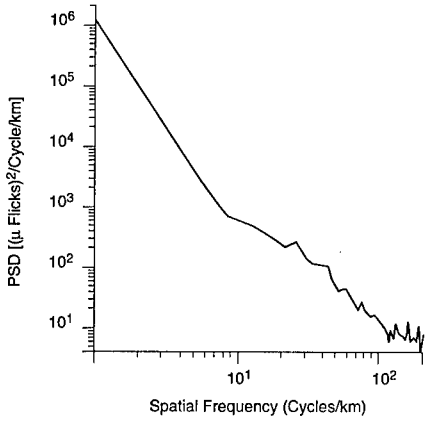

Fig. 4.68 PSD of farmland terrain in the 3.74- to 4.08-μm band (HC441R).

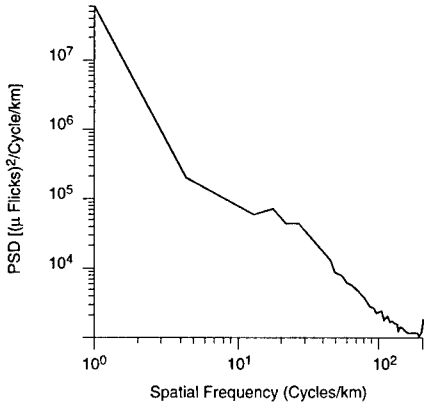

Fig. 4.69 PSD of farmland terrain in the 8.28- to 8.76-μm band (HC442R).

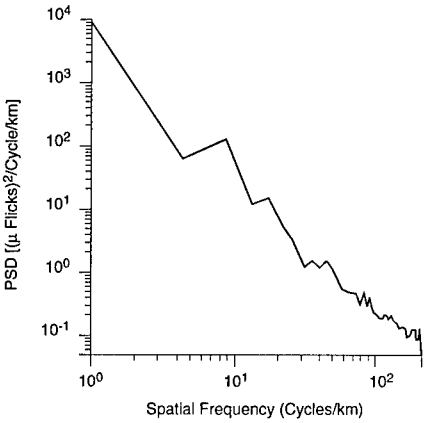

Fig. 4.70 PSD of mountain terrain with some clouds in the 4.46- to 5.20-μm band (HC477R).

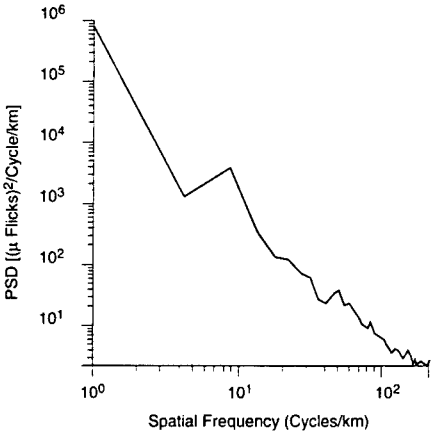

Fig. 4.71 PSD of mountain terrain with some clouds in the 11.64- to 12.12-μm band (HC478R).

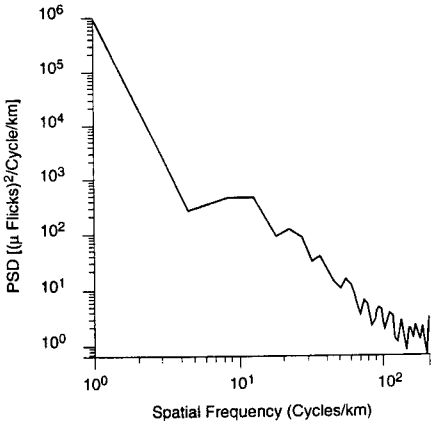

Fig. 4.72 PSD of mountain hills and fields in the 4.46- to 5.20-μm band (HC633R).

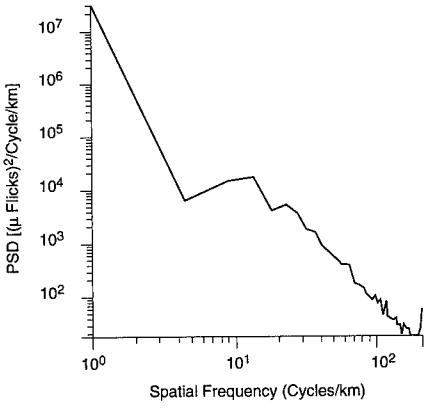

Fig. 4.73 PSD of mountain hills and fields in the 8.28- to 8.76-μm band (HC635R).

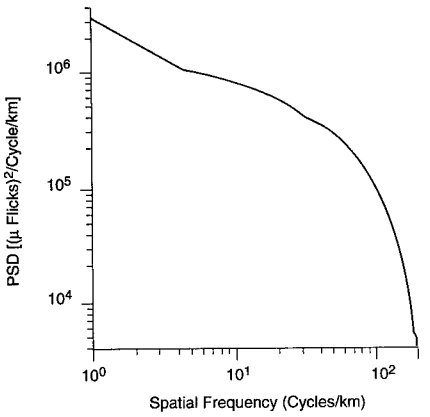

Fig. 4.74 PSD of desert terrain in the 4.56- to 4.78-μm band (HC741R).

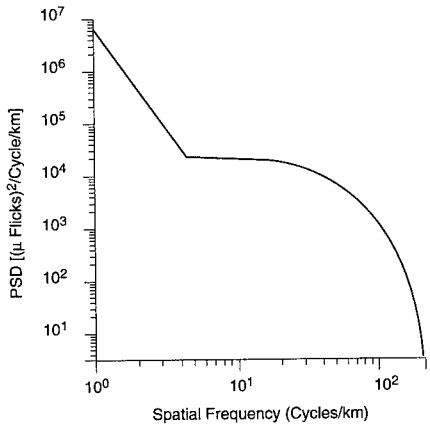

Fig. 4.75 PSD of desert terrain in the 6.68- to 7.28-μm band (HC742R).

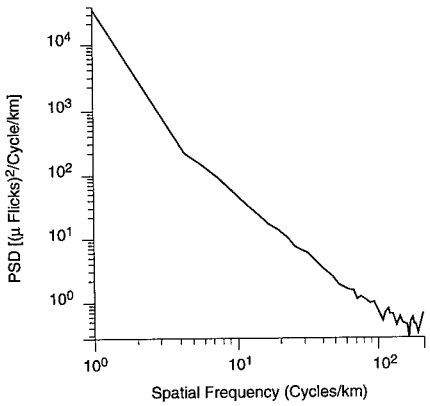

Fig. 4.76 PSD of clear night sky in the 3.74- to 4.08-μm band (HC770R).

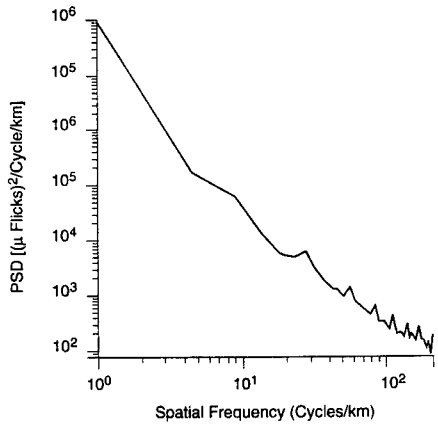

Fig. 4.77 PSD of the clear night sky in the 7.80- to 13.50-μm band (HC771R).

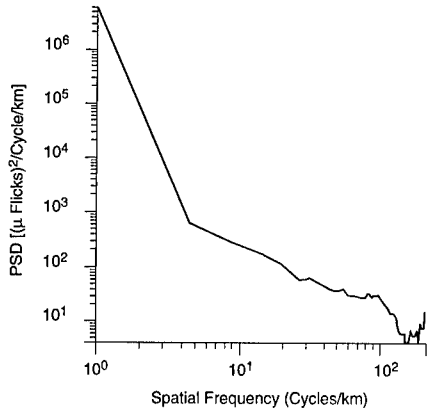

Fig. 4.78 PSD of open ocean in the 8.28- to 8.76-μm band (HC333R).

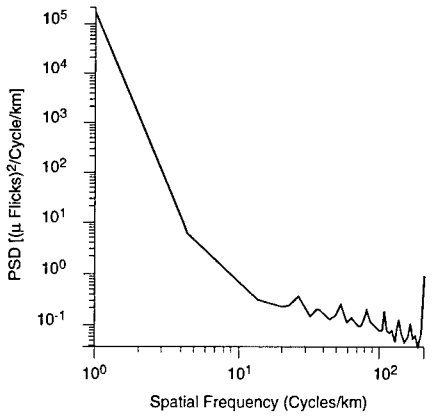

Fig. 4.79 PSD of open ocean in the 4.46- to 5.20-μm band (HC332R).

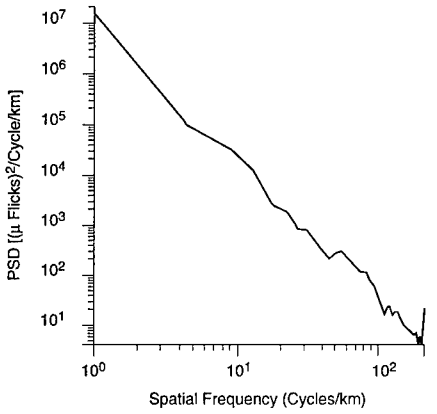

Fig. 4.80 PSD of ocean island coast background in the 8.28- to 8.76-μm band (HC655R).

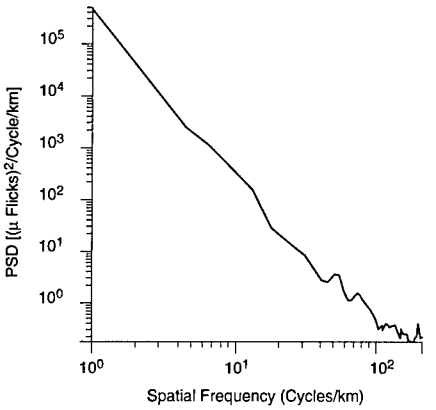

Fig. 4.81 PSD of ocean island coast background in the 4.46- to 5.20-μm band (HC654R).

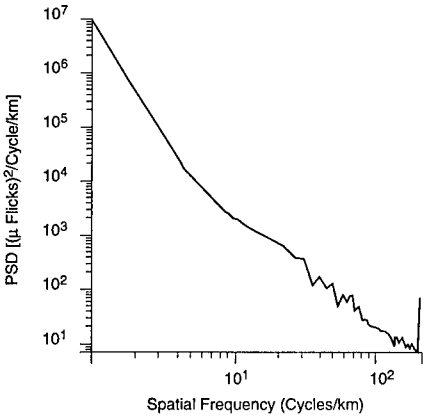

Fig. 4.82 PSD of ocean coastline in the 8.28- to 8.76-μm band (HC506R).

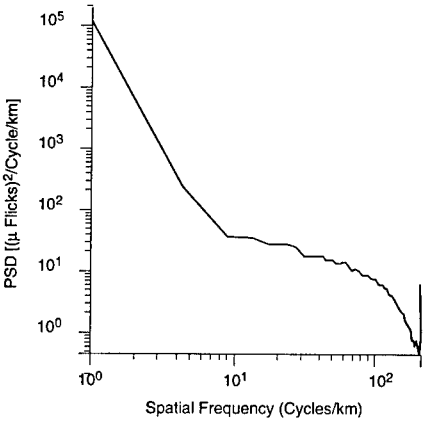

Fig. 4.83 PSD of ocean coastline in the 4.46- to 5.20-μm band (HC505R).

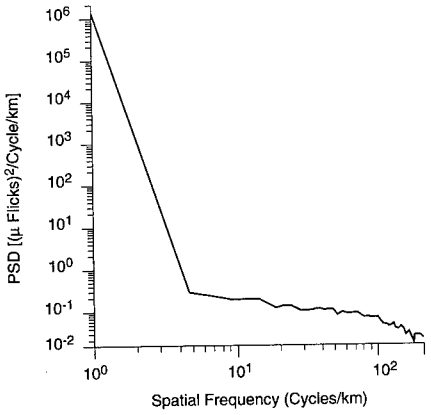

Fig. 4.84 PSD of a uniform cloud background in the 4.46- to 5.20-μm band (HC914R).

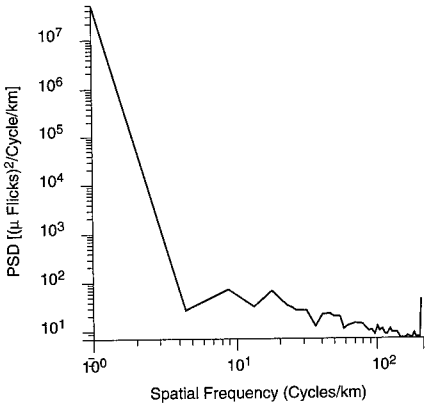

Fig. 4.85 PSD of a uniform cloud background in the 8.28- to 8.76-μm band (HC915R).

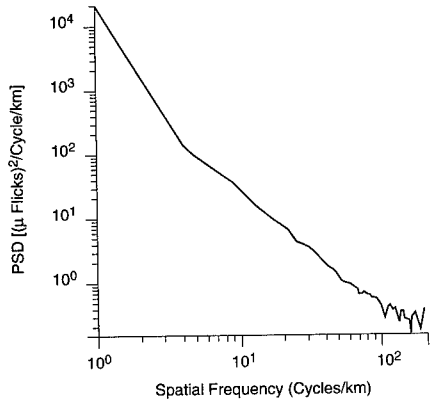

Fig. 4.86 PSD of a clear night sky in the 3.74- to 4.08-μm band (HC770R).

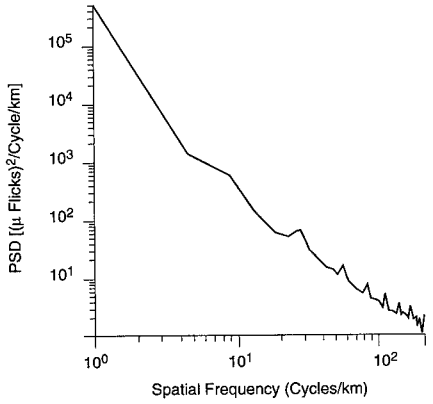

Fig. 4.87 PSD of a clear night sky in the 7.80- to 13.50-μm band (HC771R).

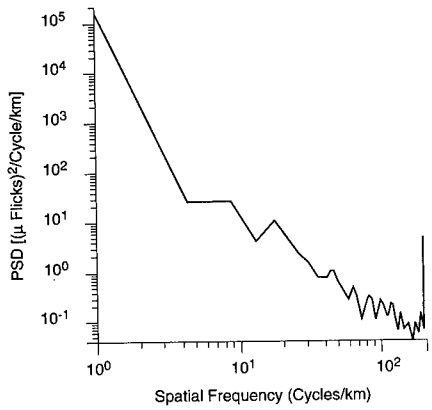

Fig. 4.88 PSD of a multilayer solid cloud cover over the ocean in the 4.46- to 5.20-μm band (HC511R).

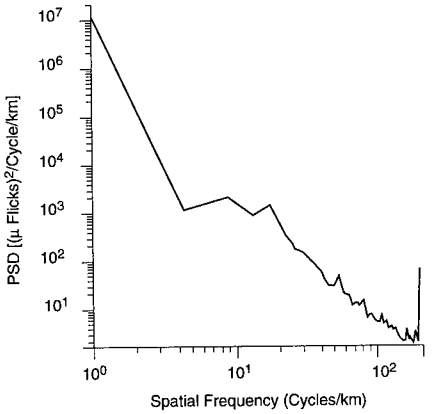

Fig. 4.89 PSD of a multilayer solid cloud cover over the ocean in the 8.28- to 8.76-μm band (HC512R).

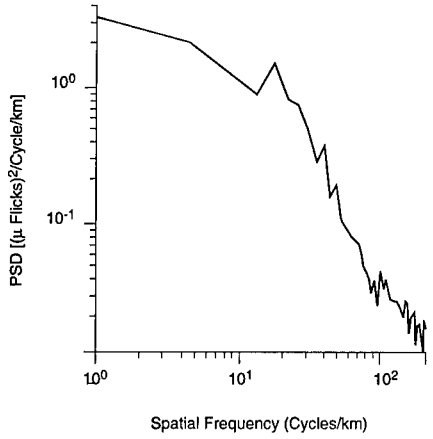

Fig. 4.90 PSD of broken clouds over Arctic terrain in the 4.46- to 5.20-μm band (HC356R).

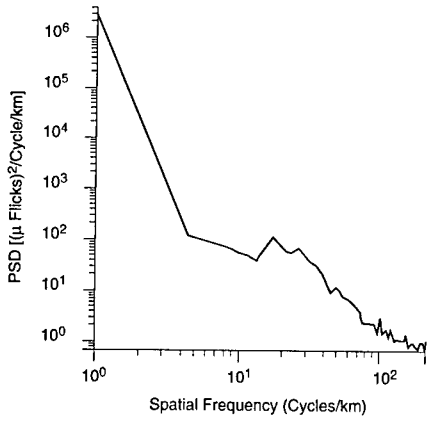

Fig. 4.91 PSD of broken clouds over Arctic terrain in the 7.80- to 13.50-μm band (HC357R).

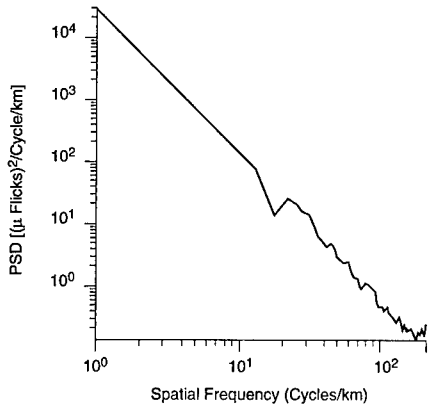

Fig. 4.92 PSD of broken clouds over farm and field background in the 4.46- to 5.20-μm band (HC303R).

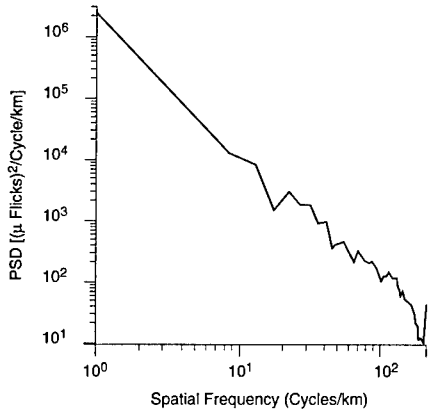

Fig. 4.93 PSD of broken clouds over farm and field background in the 11.64- to 12.12-μm band (HC306R).

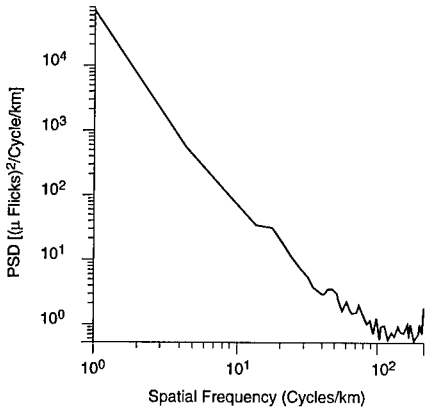

Fig. 4.94 PSD of broken clouds over desert terrain in the 3.74- to 4.08-μm band (HC301R).

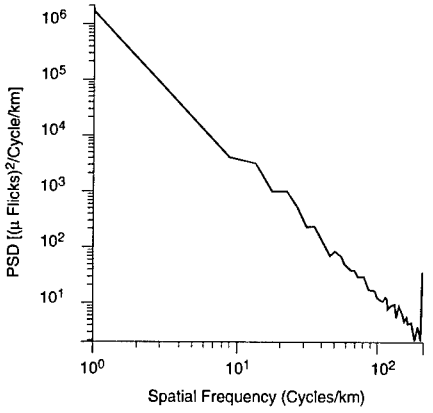

Fig. 4.95 PSD of broken clouds over desert terrain in the 7.88- to 8.80-μm band (HC302R).

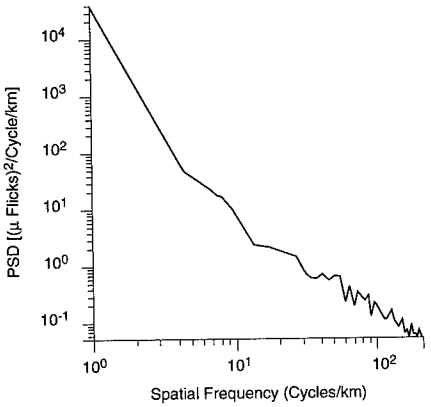

Fig. 4.96 PSD of urban area in the 4.46- to 5.20-μm band (HC652R).

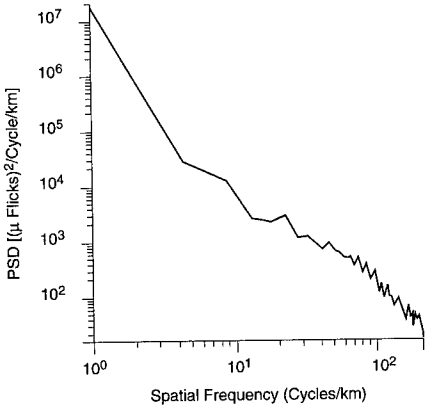

Fig. 4.97 PSD of urban area in the 8.28- to 8.76-μm band (HC653R).

4.2.2.12 Cloud-Cover Transmittance. Clouds in the atmosphere can seriously degrade satellite IR surveillance systems. To define system performance there is an obvious need for a quantitative statistical model defining cloud-cover fractions and length of cloud-free track intervals, and cloud thickness, which is important in thin cloud statistics inasmuch as target attenuation will be a function of cloud thickness.

Calculations for altostratus clouds by Yamamoto et al.[14] yield the spectral transmission curves illustrated in Fig. 4.98. Transmittances for three different cloud thicknesses are given, showing that a 50-m-thick cloud layer transmits less than 10% throughout the infrared. Altostratus are usually found in the 2- to 4-km altitude range in the arctic region. The thickness of these clouds usually is much greater than the 50 m referred to above.

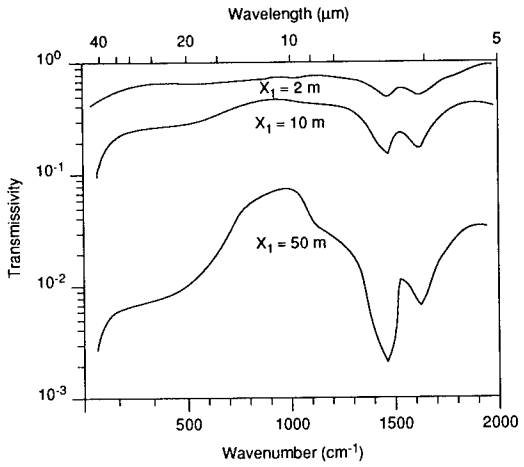

Fig. 4.98 Spectral transmissivity of clouds of various thickness versus wavelength.[12]

The curves in Fig. 4.98 illustrate the fact that the transmission decreases with increasing wavelength beyond the mid-infrared, that is, at wave numbers lower than about 1100 (wavelength >9 μm). An average over the entire mid- and long-wave infrared, illustrated in Fig. 4.99 shows that the transmittance drops to 10% at a thickness of about 30 m.

A review of the literature available on IR properties of clouds indicates that only cirrus clouds, which are composed of ice crystals and are usually thin, with low water-vapor content, are sufficiently transparent for detection of targets underneath. IR transmittance by cirrus clouds is reported by Davis[15] to be approximately a linear function of cloud thickness. The experimental relationship he found is reported in Fig. 4.100. Cirrus clouds are quite thin,

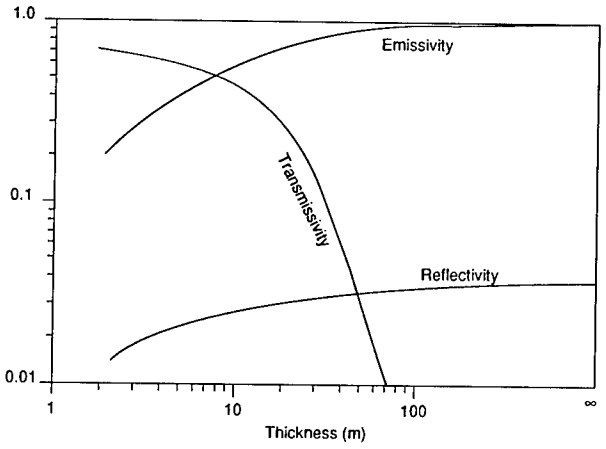

Fig. 4.99 Emissivity, reflectivity, and transmissivity of clouds versus cloud thickness in the spectral region 5 to 50 μm.[13]

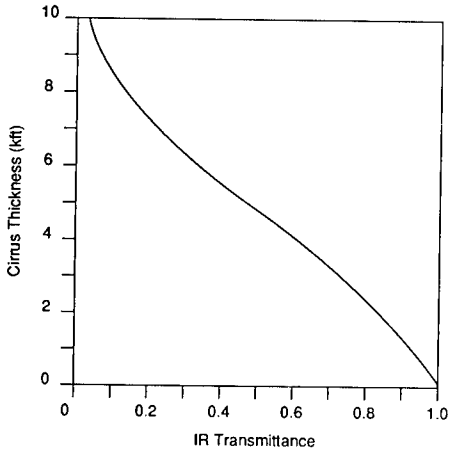

Fig. 4.100 Infrared transmission (10 to 12 μm) versus cirrus cloud thickness, corrected for probable reflections.[15]

averaging 1.2 km in a study by Platt.[16] Thus, IR radiation from a target beneath a cirrus deck would be attenuated to about 60% of its initial level. This may not be a serious problem for an IR surveillance system.

4.2.3 Atmospheric Phenomenology

4.2.3.1 Extinction (Sattinger[17]). The intervening atmosphere between target and receiver is a major source of attenuation of the signal from the target. Its phenomenology involves both molecular absorption and scattering. The calculation of atmospheric extinction is for IRST purposes generally relegated to a widely used computer program known as LOWTRAN, in version 7 at this writing. The details of the physics can be found in Volume 2, Chapter 1, of this handbook. In general, the investigator is obliged to run LOWTRAN or the equivalent for the specific case of interest, especially since IRST systems generally operate over a wide spectral band in which the extinction can vary substantially; thus, the total absorption over the band can involve a rather tedious process of numerical integration. Another complication is non-coaltitude cases. Although inaccurate, the transmission is often treated as a first approximation by Beers law:

$$I = I_0^{-\alpha R} , \tag{4.53}$$

where α is calculated from first principles or measured over some fixed path in inverse units of length.

To deal with these complex phenomena, the Geophysics Directorate at Hanscom Air Force Base, Massachusetts, has developed atmospheric propagation codes that predict transmittance/radiance effects for sensor systems under these varying conditions. The Directorate provides the general community with three major propagation codes: LOWTRAN (low spectral resolution transmission); FASCODE (fast atmospheric signature code); and MODTRAN (moderate spectral resolution transmission), which was developed recently.[g]

Supporting these codes is HITRAN (high-resolution transmission), which is a molecular absorption database. HITRAN is a compilation of spectroscopic parameters from which a wide variety of computer simulation codes are able to calculate and predict the transmission and emission of radiation in the atmosphere. In addition to being a stand-alone database, HITRAN is used as direct input to FASCODE and indirectly to the band-model codes LOWTRAN and MODTRAN.

4.2.3.1.1 LOWTRAN. LOWTRAN is a one-parameter, band-model code that predicts transmittance/radiance for systems with low spectral resolution (20 cm^{-1}). These predictions use algorithms developed at the Geophysics Directorate to calculate the average transmittance value for a given atmospheric path.

[g]FASCODE, MODTRAN, and LOWTRAN tapes can be purchased from National Climatic Data Center, NOAA, Environmental Data Service, Federal Building, Asheville, NC 28801 (704/259-0272). See also footnote in Sec. 4.2.1.12.

LOWTRAN 7, the latest version of the code, was completed early in 1988 and released publicly in February 1989. It expanded the spectral coverage of its predecessor, LOWTRAN 6, to include the region from the near-ultraviolet through the microwave. In terms of revised models and other refinements, LOWTRAN 7 represents a significant increase in sophistication over LOWTRAN 6, which had been issued in 1983.

One of the code's major advantages is its fast computational capability, which makes it suitable for operational use. The modular structure of the code, designed for flexibility, includes options for gaseous or molecular profiles and for large particles in the atmosphere. The latter includes atmospheric aerosols (dust, haze, and smoke) and hydrometeors (fog, clouds, and rain). Because of limitations of the molecular band-model approximation used in LOWTRAN, its accuracy degrades seriously for upper atmospheric regions (above about 40 km). LOWTRAN is used primarily as an aid for tactical systems operating in the lower atmosphere or on the earth's surface. It applies to the classical scenarios for conventional warfare: air strikes, air-to-air missions, and close air support for ground-launched weapons.

A new atmospheric database for use with LOWTRAN presents six reference atmospheres with varied constituents as a function of altitude. It allows a range of climatological choices and provides separate molecular profiles for 13 minor and trace gases. The LOWTRAN code can use extensive knowledge of climate and atmospheric characteristics in various geographic locations, including Europe and the Middle East.

IRST LOWTRAN Extinction Calculations. For the purpose of illustration, the LOWTRAN 7 results for a number of typical cases of interest in IRST scenarios are presented in Figs. 4.101 through 4.124. Data are calculated in the 3- to 5-μm and 8- to 12-μm bands at altitudes of 3 and 10 km for horizontal paths of 100, 200, and 300 km.

Typical input data are shown in Table 4.4. Up-looking cases are given in Figs. 4.125 through 4.140 with input data in Table 4.5. Down-looking cases are given in Figs. 4.141 through 4.148 with input data in Table 4.6.

As of May 1991, DoD agencies and contractors, the National Aeronautics and Space Administration (NASA), and organizations around the world made up a group of over 1000 LOWTRAN 7 users.

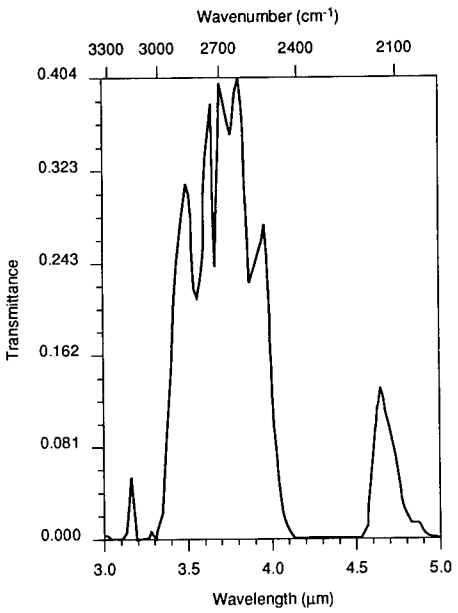

Fig. 4.101 Total horizontal path spectral transmittance in the 3- to 5-μm band at 100-km range, 3-km altitude. 1976 Standard Atmosphere is calculated from LOWTRAN 7. Input conditions are shown in Table 4.4. Average band transmittance = 0.0981.

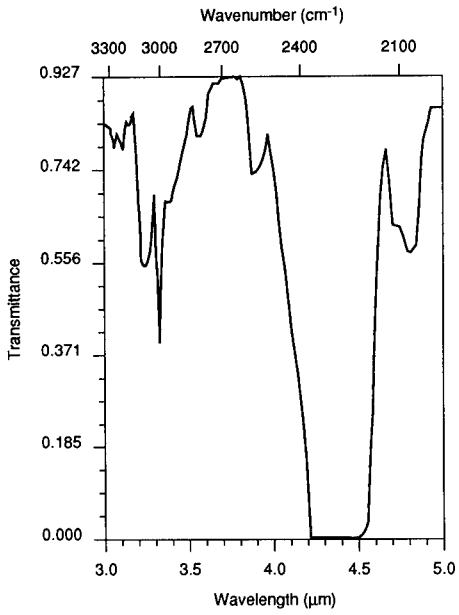

Fig. 4.102 Total horizontal path spectral transmittance in the 3- to 5-μm band at 100-km range, 10-km altitude. 1976 Standard Atmosphere is calculated from LOWTRAN 7. Input conditions are shown in Table 4.4. Average band transmittance = 0.6211.

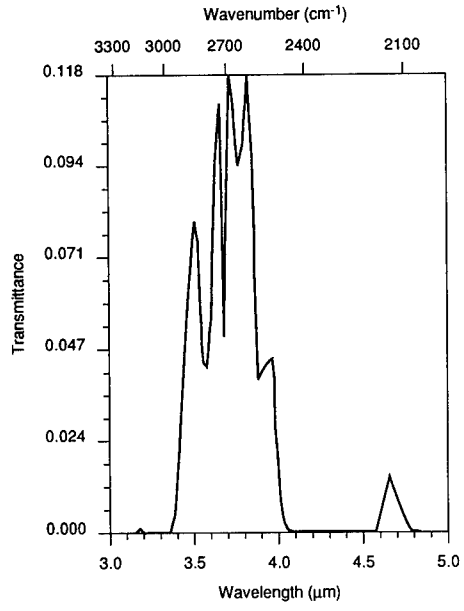

Fig. 4.103 Total horizontal path spectral transmittance in the 3- to 5-μm band at 200-km range, 3-km altitude. 1976 Standard Atmosphere is calculated from LOWTRAN 7. Input conditions are shown in Table 4.4. Average band transmittance = 0.0213.

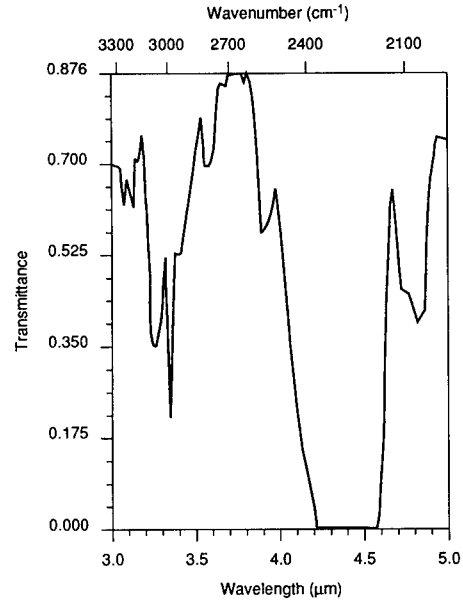

Fig. 4.104 Total horizontal path spectral transmittance in the 3- to 5-μm band at 200-km range, 10-km altitude. 1976 Standard Atmosphere is calculated from LOWTRAN 7. Input conditions are shown in Table 4.4. Average band transmittance = 0.4950.

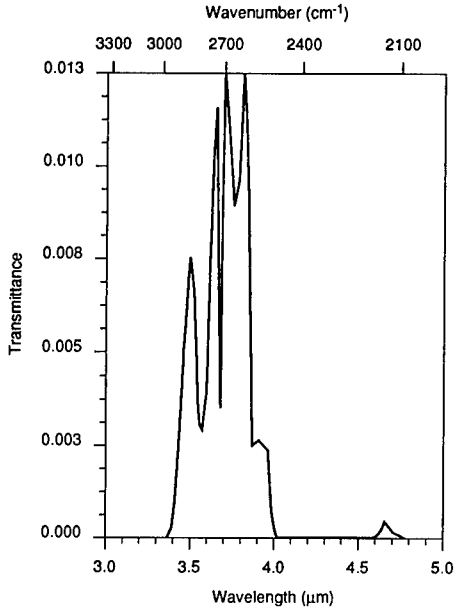

Fig. 4.105 Total horizontal path spectral transmittance in the 3- to 5-μm band at 300-km range, 3-km altitude. 1976 Standard Atmosphere is calculated from LOWTRAN 7. Input conditions are shown in Table 4.4. Average band transmittance = 0.0019.

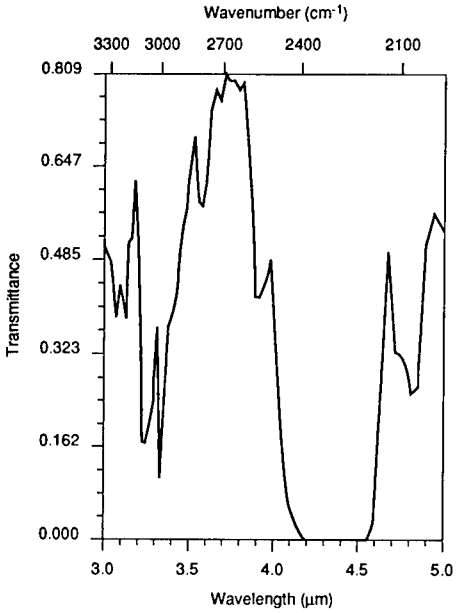

Fig. 4.106 Total horizontal path spectral transmittance in the 3- to 5-μm band at 300-km range, 10-km altitude. 1976 Standard Atmosphere is calculated from LOWTRAN 7. Input conditions are shown in Table 4.4. Average band transmittance = 0.3659.

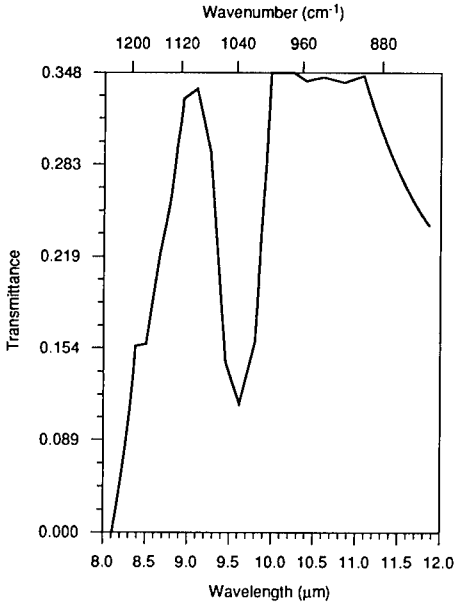

Fig. 4.107 Total horizontal path spectral transmittance in the 8- to 12-μm band at 100-km range, 3-km altitude. 1976 Standard Atmosphere is calculated from LOWTRAN 7. Input conditions are shown in Table 4.4. Average band transmittance = 0.232.

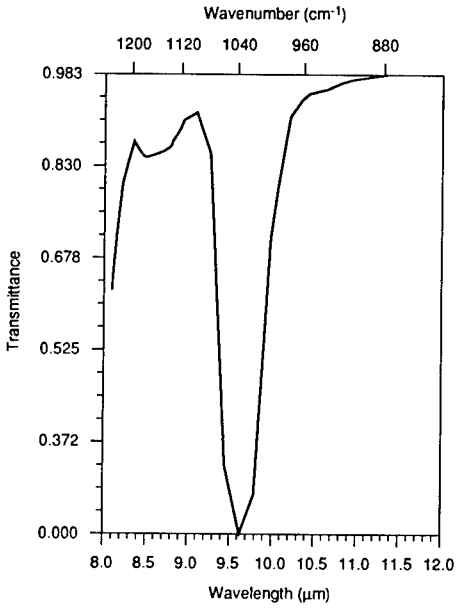

Fig. 4.108 Total horizontal path spectral transmittance in the 8- to 12-μm band at 100-km range, 10-km altitude. 1976 Standard Atmosphere is calculated from LOWTRAN 7. Input conditions are shown in Table 4.4. Average band transmittance = 0.798.

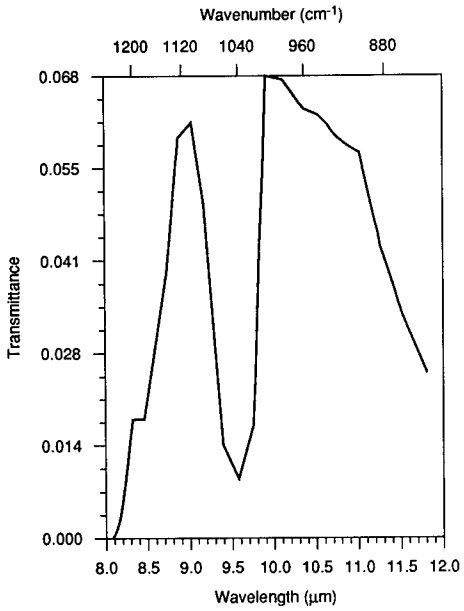

Fig. 4.109 Total horizontal path spectral transmittance in the 8- to 12-μm band at 200-km range, 3-km altitude. 1976 Standard Atmosphere is calculated from LOWTRAN 7. Input conditions are shown in Table 4.4. Average band transmittance = 0.0352.

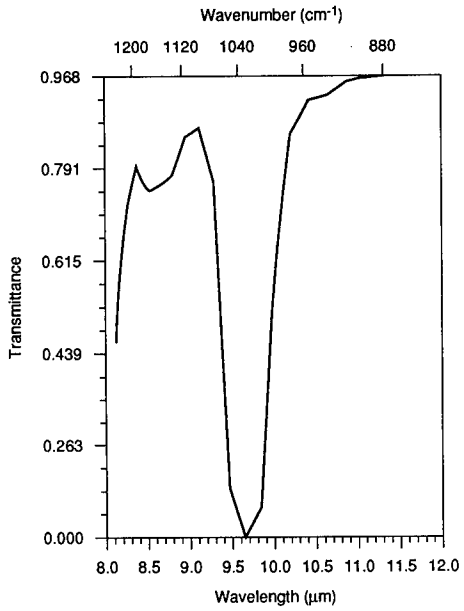

Fig. 4.110 Total horizontal path spectral transmittance in the 8- to 12-μm band at 200-km range, 10-km altitude. 1976 Standard Atmosphere is calculated from LOWTRAN 7. Input conditions are shown in Table 4.4. Average band transmittance = 0.7184.

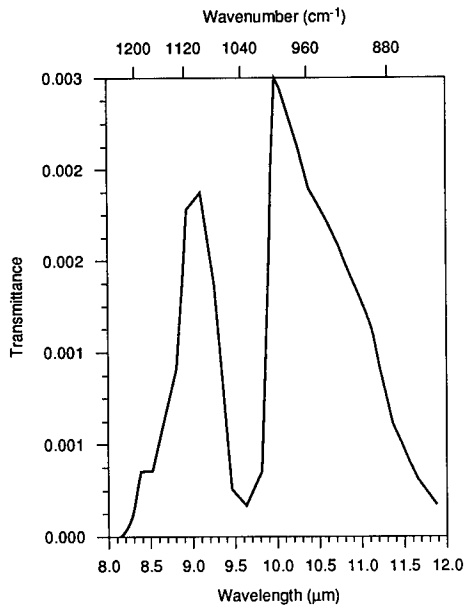

Fig. 4.111 Total horizontal path spectral transmittance in the 8- to 12-μm band at 300-km range, 3-km altitude. 1976 Standard Atmosphere is calculated from LOWTRAN 7. Input conditions are shown in Table 4.4. Average band transmittance = 0.0010.

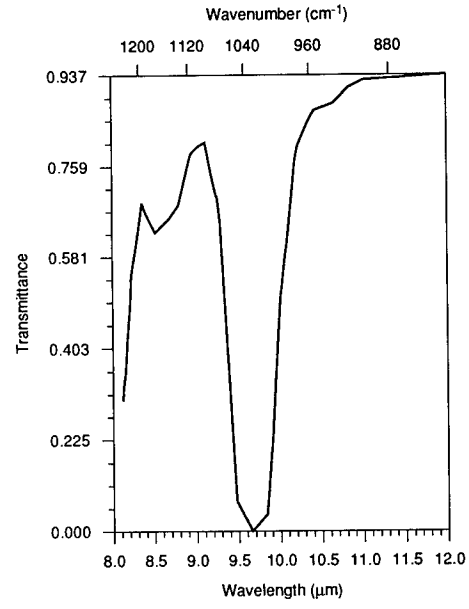

Fig. 4.112 Total horizontal path spectral transmittance in the 8- to 12-μm band at 300-km range, 10-km altitude. 1976 Standard Atmosphere is calculated from LOWTRAN 7. Input conditions are shown in Table 4.4. Average band transmittance = 0.6487.

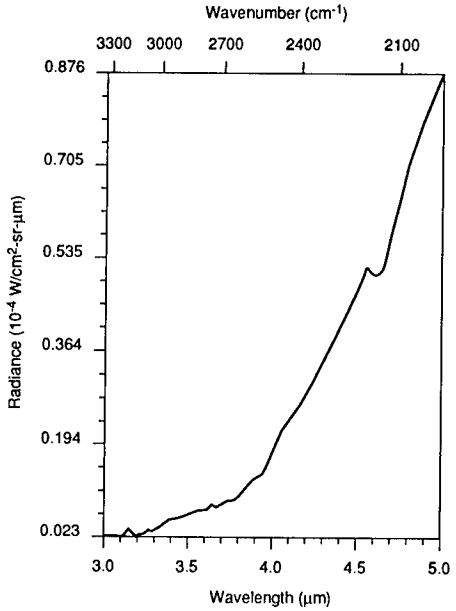

Fig. 4.113 Total horizontal path spectral radiance in the 3- to 5-μm band looking due east at 100-km range, 3-km altitude. 1976 Standard Atmosphere is calculated from LOWTRAN 7. Input conditions are shown in Table 4.4. Average radiance = 5.403×10^{-5} W cm^{-2} sr^{-1} μm^{-1}.

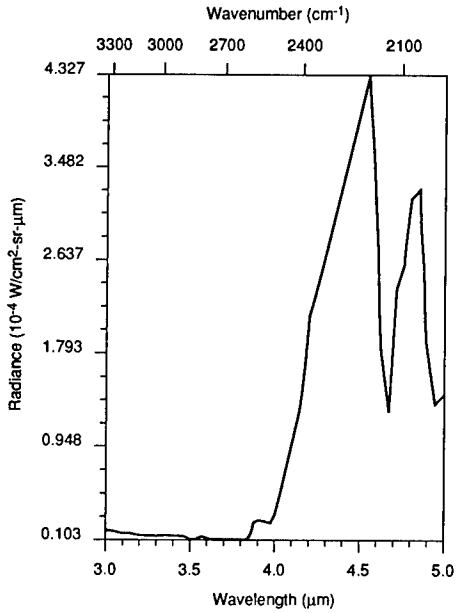

Fig. 4.114 Total horizontal path spectral radiance in the 3- to 5-μm band looking due east at 100-km range, 10-km altitude. 1976 Standard Atmosphere is calculated from LOWTRAN 7. Input conditions are shown in Table 4.4. Average radiance = 2.562×10^{-6} W cm^{-2} sr^{-1} μm^{-1}.

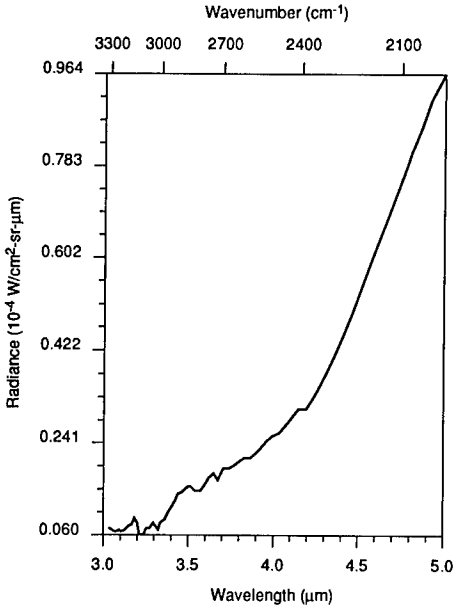

Fig. 4.115 Total horizontal path spectral radiance in the 3- to 5-μm band looking due east at 200-km range, 3-km altitude. 1976 Standard Atmosphere is calculated from LOWTRAN 7. Input conditions are shown in Table 4.4. Average radiance = 6.910×10^{-5} W cm^{-2} sr^{-1} μm^{-1}.

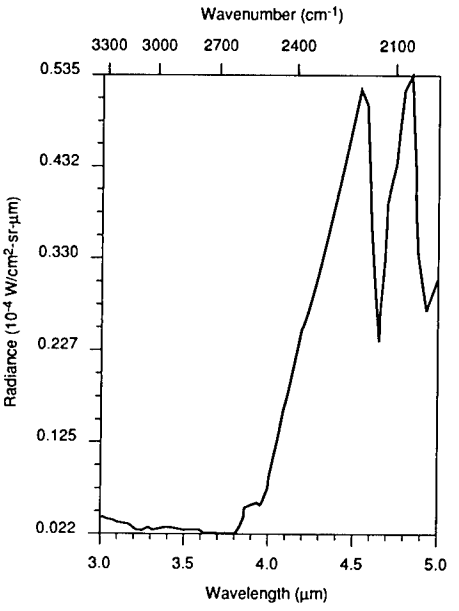

Fig. 4.116 Total horizontal path spectral radiance in the 3- to 5-μm band looking due east at 200-km range, 10-km altitude. 1976 Standard Atmosphere is calculated from LOWTRAN 7. Input conditions are shown in Table 4.4. Average radiance = 3.766×10^{-6} W cm^{-2} sr^{-1} μm^{-1}.

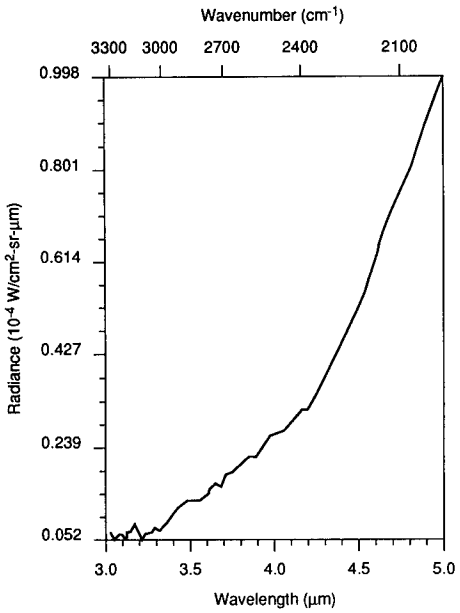

Fig. 4.117 Total horizontal path spectral radiance in the 3- to 5-μm band looking due east at 300-km range, 3-km altitude. 1976 Standard Atmosphere is calculated from LOWTRAN 7. Input conditions are shown in Table 4.4. Average radiance = 6.980×10^{-5} W cm^{-2} sr^{-1} μm^{-1}.

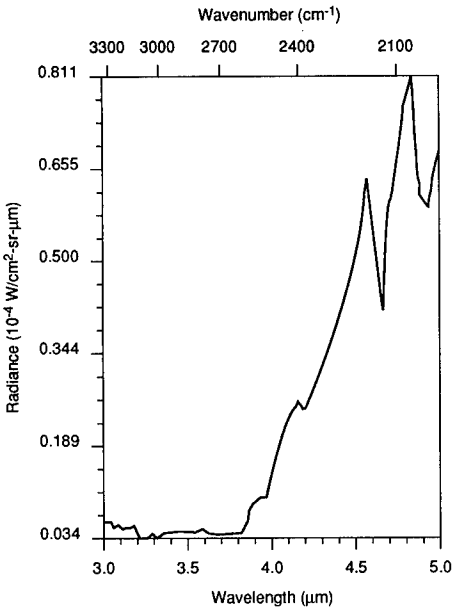

Fig. 4.118 Total horizontal path spectral radiance in the 3- to 5-μm band looking due east at 300-km range, 10-km altitude. 1976 Standard Atmosphere is calculated from LOWTRAN 7. Input conditions are shown in Table 4.4. Average radiance = 5.257×10^{-6} W cm^{-2} sr^{-1} μm^{-1}.

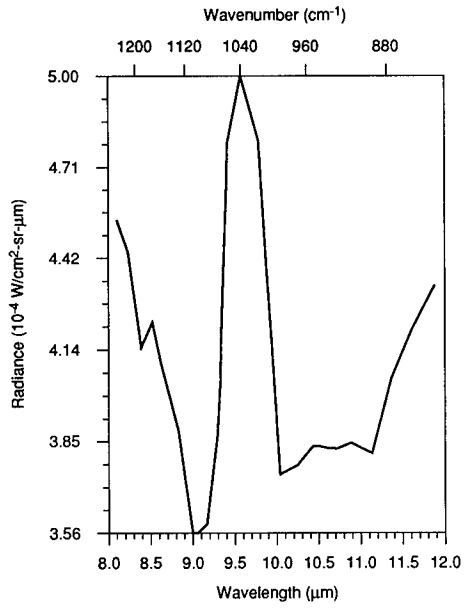

Fig. 4.119 Total horizontal path spectral radiance in the 8- to 12-μm band looking due east at 100-km range, 3-km altitude. 1976 Standard Atmosphere is calculated from LOWTRAN 7. Input conditions are shown in Table 4.4. Average radiance = 1.898×10^{-3} W cm^{-2} sr^{-1} μm^{-1}.

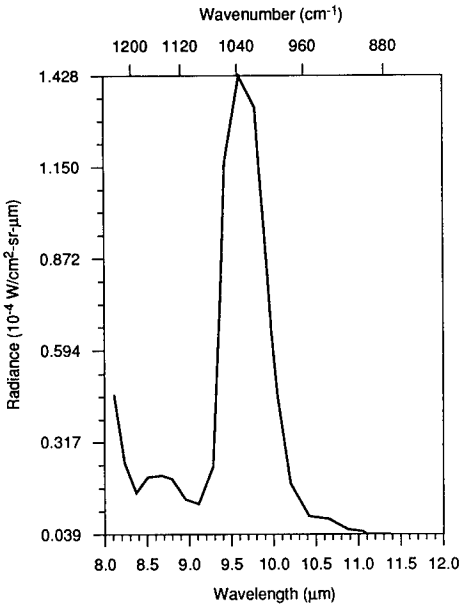

Fig. 4.120 Total horizontal path spectral radiance in the 8- to 12-μm band looking due east at 100-km range, 10-km altitude. 1976 Standard Atmosphere is calculated from LOWTRAN 7. Input conditions are shown in Table 4.4. Average radiance = 1.410×10^{-4} W cm^{-2} sr^{-1} μm^{-1}.

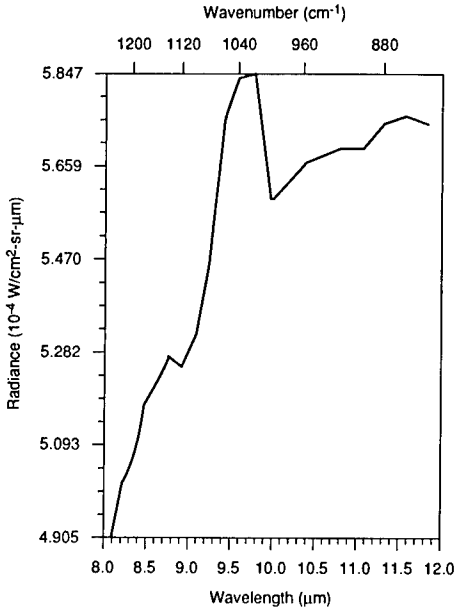

Fig. 4.121 Total horizontal path spectral radiance in the 8- to 12-μm band looking due east at 200-km range, 3-km altitude. 1976 Standard Atmosphere is calculated from LOWTRAN 7. Input conditions are shown in Table 4.4. Average radiance = 2.530×10^{-3} W cm^{-2} sr^{-1} μm^{-1}.

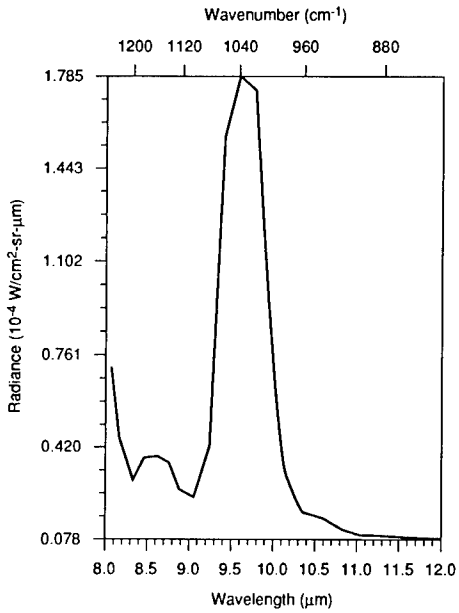

Fig. 4.122 Total horizontal path spectral radiance in the 8- to 12-μm band looking due east at 200-km range, 10-km altitude. 1976 Standard Atmosphere is calculated from LOWTRAN 7. Input conditions are shown in Table 4.4. Average radiance = 2.11×10^{-4} W cm^{-2} sr^{-1} μm^{-1}.

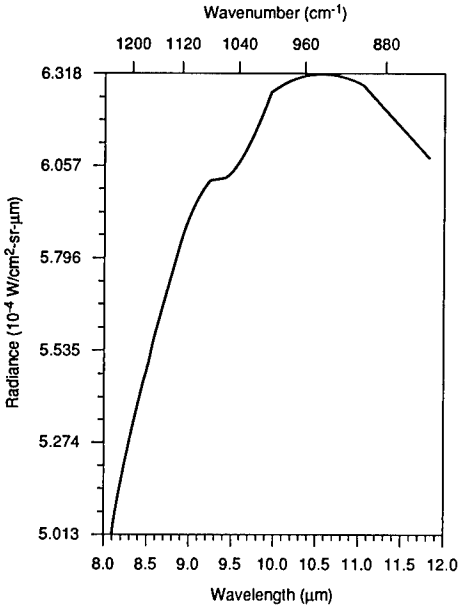

Fig. 4.123 Total horizontal path spectral radiance in the 8- to 12-μm band looking due east at 300-km range, 3-km altitude. 1976 Standard Atmosphere is calculated from LOWTRAN 7. Input conditions are shown in Table 4.4. Average radiance = 2.732×10^{-3} W cm^{-2} sr^{-1} μm^{-1}.

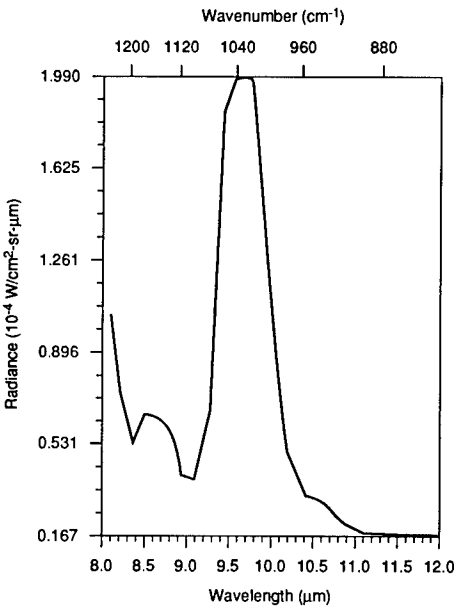

Fig. 4.124 Total horizontal path spectral radiance in the 8- to 12-μm band looking due east at 300-km range, 10-km altitude. 1976 Standard Atmosphere is calculated from LOWTRAN 7. Input conditions are shown in Table 4.4. Average radiance = 2.921×10^{-4} W cm^{-2} sr^{-1} μm^{-1}.

Table 4.4 Typical LOWTRAN 7 Input Data for Horizontal Path IRST Cases

Model atmosphere	1976 U.S. standard
Type of atmospheric path	Slant path
Mode of execution	Radiance with scattering
Executed with multiple scattering	No
Temperature and pressure altitude profile	1976 U.S. standard
Water-vapor altitude profile	1976 U.S. standard
Ozone altitude profile	1976 U.S. standard
Methane altitude profile	1976 U.S. standard
Nitrous oxide altitude profile	1976 U.S. standard
Carbon monoxide altitude profile	1976 U.S. standard
Other gases altitude profile	1976 U.S. standard
Radiosonde data are to be input	No
Output file options	Suppress ATM profiles
Temp at boundary (0.000—T @ first level)	0.000
Surface albedo (0.000—blackbody)	0.000
LOWTRAN 7 Card #1 Screen	
Aerosol model used	Rural—VIS = 23 km
Seasonal modifications to aerosols	Determined by model
Upper atmosphere aerosols (30–100 km)	Background stratospheric
Air-mass character for Navy maritime aerosols	0
Use cloud/rain aerosol extensions	No clouds or rain
Use of Army (VSA) for aerosol extension	No
Surface range for boundary layer	0.000
Wind speed for Navy maritime aerosols	0.000
24-h average wind speed for Navy maritime	0.000
Rain rate (mm h^{-1})	0.000
Ground altitude above sea level (km)	0.000
LOWTRAN 7 Card #2 Screen	
Initial altitude (km)	3.000
Final altitude/tangent height (km)	3.000
Initial zenith angle (deg)	0.000
Path length (km)	0.000
Earth center angle (deg)	0.898
Radius of earth (km) (0.000—default)	0.000
0—short path; 1—long path	0
Initial frequency (wave number)	2000.000
Final frequency (wave number)	3500.000
Frequency increment (wave number)	20.000
LOWTRAN 7 Card #3 and #4 Screen	
Solar/lunar geometry type (0-2)	1.000
Aerosol phase function	MIE generated
Day of the year (91-365)	180.000
Extraterrestrial source	Sun
PARM1—observer latitude/azimuthal angle	40.000
PARM2—observer longitude/sun zenith	105.000
Sun/moon latitude (-90 to 90 deg)	0.000
Sun/moon longitude (0 to 360 deg)	0.000
Greenwich time (decal hours)	19.000
Path azimuth (deg east of north)	0.000
Phase angle of the moon (deg)	0.000
Asymmetry factor	0.000

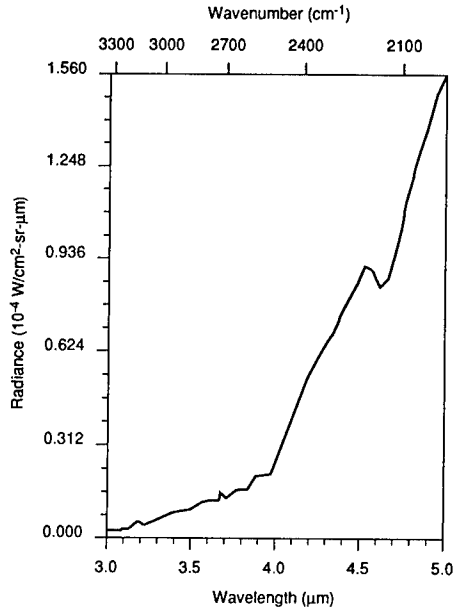

Fig. 4.125 Uplooking scattered path radiance from ground to space in the 3- to 5-μm band. Observer zenith look angle of 85 deg and a solar zenith angle of 0 deg. 1976 Standard Atmosphere is calculated from LOWTRAN 7. Input conditions are shown in Table 4.5. Average band radiance = 9.653×10^{-5} W cm^{-2} sr^{-1} μm^{-1}.

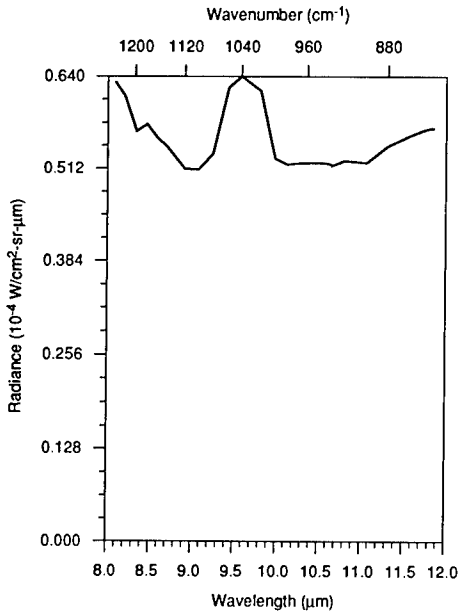

Fig. 4.126 Uplooking scattered path radiance from ground to space in the 8- to 12-μm band. Observer zenith look angle of 85 deg and a solar zenith angle of 0 deg. 1976 Standard Atmosphere is calculated from LOWTRAN 7. Input conditions are shown in Table 4.5. Average band radiance = 6.210×10^{-5} W cm^{-2} sr^{-1} μm^{-1}.

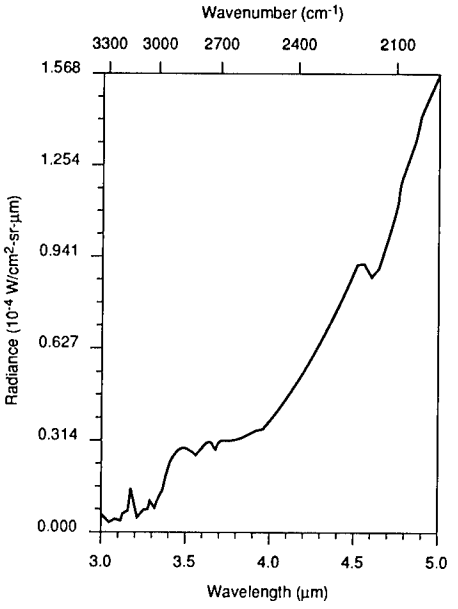

Fig. 4.127 Uplooking scattered path radiance from ground to space in the 3- to 5-μm band. Observer zenith look angle of 85 deg and a solar zenith angle of 45 deg. 1976 Standard Atmosphere is calculated from LOWTRAN 7. Input conditions are shown in Table 4.5. Average band radiance = 1.098×10^{-4} W cm^{-2} sr^{-1} μm^{-1}.

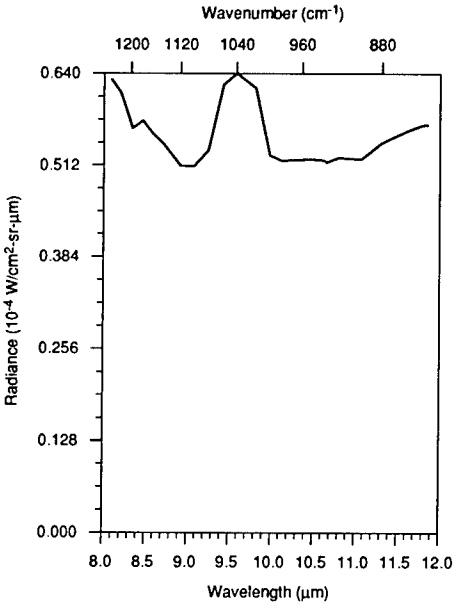

Fig. 4.128 Uplooking scattered path radiance from ground to space in the 8- to 12-μm band. Observer zenith look angle of 85 deg and a solar zenith angle of 45 deg. 1976 Standard Atmosphere is calculated from LOWTRAN 7. Input conditions are shown in Table 4.5. Average band radiance = 7.102×10^{-5} W cm^{-2} sr^{-1} μm^{-1}.

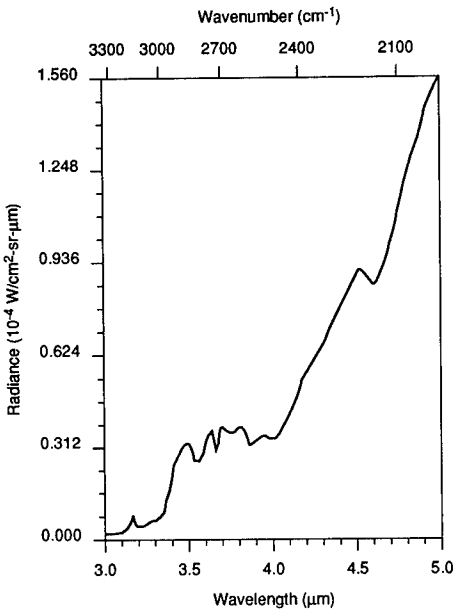

Fig. 4.129 Uplooking scattered path radiance from ground to space in the 3- to 5-μm band. Observer zenith look angle of 85 deg and a solar zenith angle of 85 deg. 1976 Standard Atmosphere is calculated from LOWTRAN 7. Input conditions are shown in Table 4.5. Average band radiance = 1.079×10^{-4} W cm^{-2} sr^{-1} μm^{-1}.

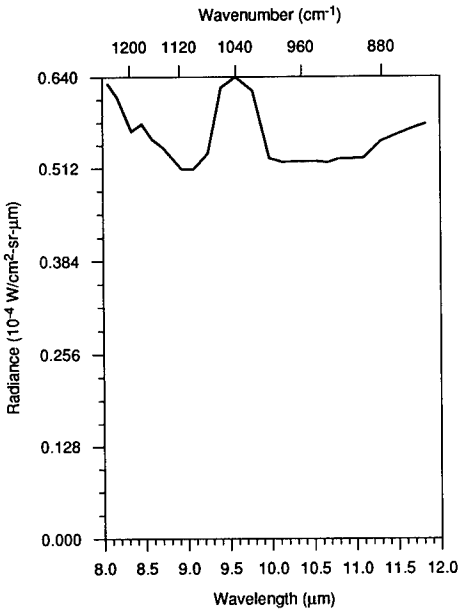

Fig. 4.130 Uplooking scattered path radiance from ground to space in the 8- to 12-μm band. Observer zenith look angle of 85 deg and a solar zenith angle of 85 deg. 1976 Standard Atmosphere is calculated from LOWTRAN 7. Input conditions are shown in Table 4.5. Average band radiance = 5.583×10^{-5} W cm^{-2} sr^{-1} μm^{-1}.

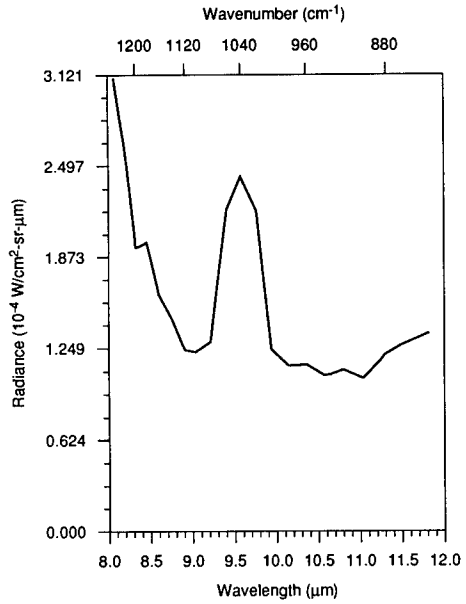

Fig. 4.131 Uplooking scattered path radiance from ground to space in the 3- to 5-μm band. Observer zenith look angle of 30 deg and a solar zenith angle of 0 deg. 1976 Standard Atmosphere is calculated from LOWTRAN 7. Input conditions are shown in Table 4.5. Average band radiance = 5.583×10^{-5} W cm^{-2} sr^{-1} μm^{-1}.

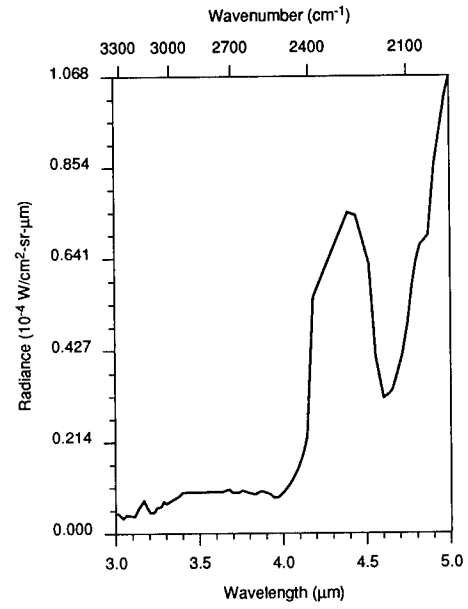

Fig. 4.132 Uplooking scattered path radiance from ground to space in the 8- to 12-μm band. Observer zenith look angle of 30 deg and a solar zenith angle of 0 deg. 1976 Standard Atmosphere is calculated from LOWTRAN 7. Input conditions are shown in Table 4.5. Average band radiance = 7.362×10^{-4} W cm^{-2} sr^{-1} μm^{-1}.

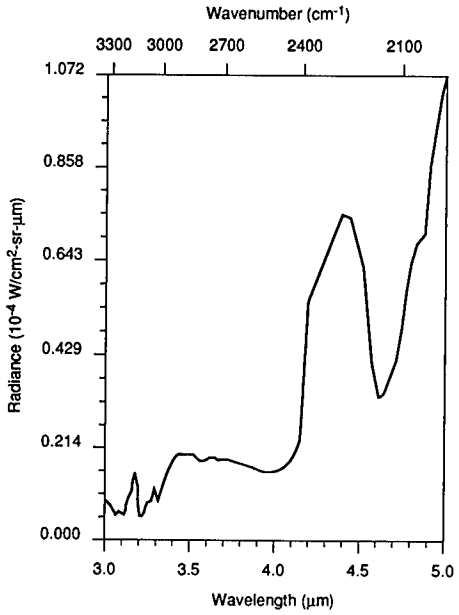

Fig. 4.133 Uplooking scattered path radiance from ground to space in the 3- to 5-μm band. Observer zenith look angle of 30 deg and a solar zenith angle of 45 deg. 1976 Standard Atmosphere is calculated from LOWTRAN 7. Input conditions are shown in Table 4.5. Average band radiance = 2.555×10^{-3} W cm^{-2} sr^{-1} μm^{-1}.

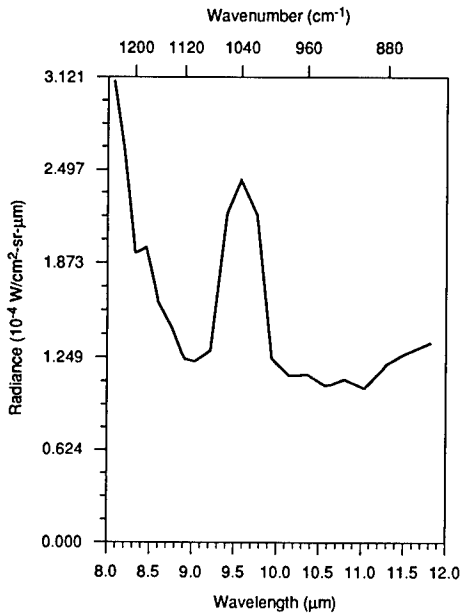

Fig. 4.134 Uplooking scattered path radiance from ground to space in the 8- to 12-μm band. Observer zenith look angle of 30 deg and a solar zenith angle of 45 deg. 1976 Standard Atmosphere is calculated from LOWTRAN 7. Input conditions are shown in Table 4.5. Average band radiance = 7.362×10^{-4} W cm^{-2} sr^{-1} μm^{-1}.

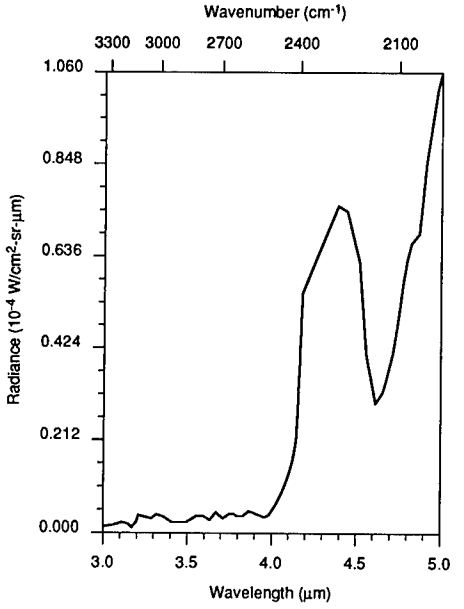

Fig. 4.135 Uplooking scattered path radiance from ground to space in the 3- to 5-μm band. Observer zenith look angle of 30 deg and a solar zenith angle of 85 deg. 1976 Standard Atmosphere is calculated from LOWTRAN 7. Input conditions are shown in Table 4.5. Average band radiance = 2.556×10^{-3} W cm^{-2} sr^{-1} μm^{-1}.

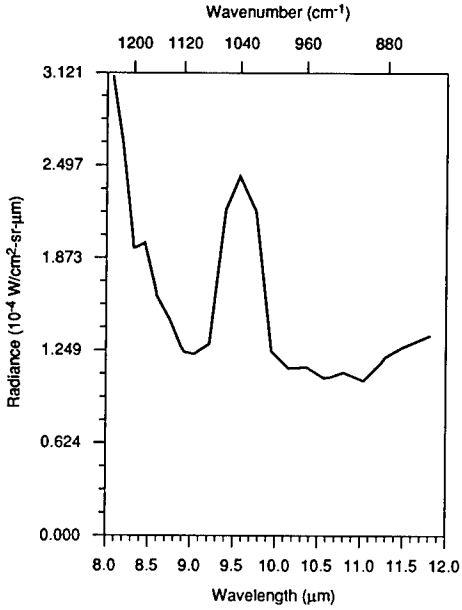

Fig. 4.136 Uplooking scattered path radiance from ground to space in the 8- to 12-μm band. Observer zenith look angle of 30 deg and a solar zenith angle of 85 deg. 1976 Standard Atmosphere is calculated from LOWTRAN 7. Input conditions are shown in Table 4.5. Average band radiance = 7.362×10^{-4} W cm^{-2} sr^{-1} μm^{-1}.

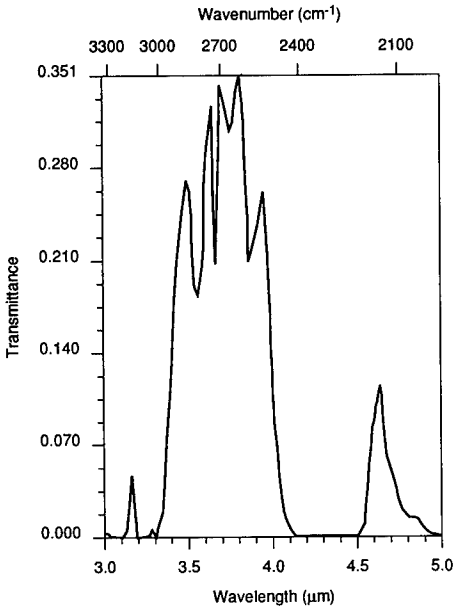

Fig. 4.137 Total uplooking path spectral transmittance to space in the 3- to 5-μm band at a solar zenith angle of 85 deg. 1976 Standard Atmosphere is calculated from LOWTRAN 7. Input conditions are shown in Table 4.5. Average band transmittance = 0.0866.

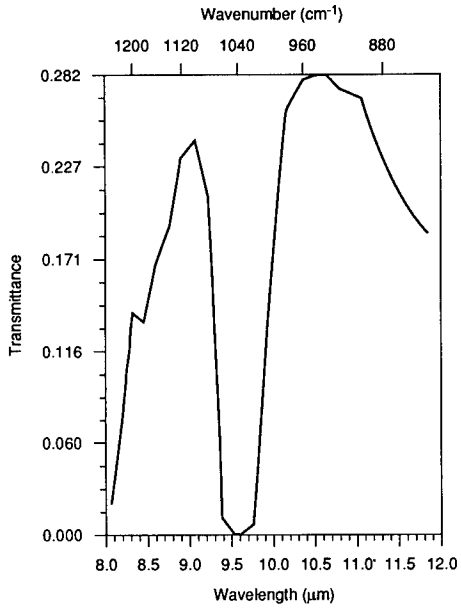

Fig. 4.138 Total uplooking path spectral transmittance to space in the 8- to 12-μm band at a solar zenith angle of 85 deg. 1976 Standard Atmosphere is calculated from LOWTRAN 7. Input conditions are shown in Table 4.5. Average band transmittance = 0.163.

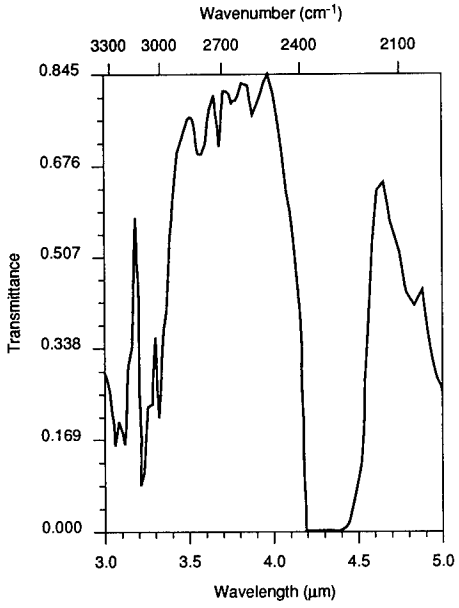

Fig. 4.139 Total uplooking path spectral transmittance to space in the 3- to 5-μm band at a solar zenith angle of 30 deg. 1976 Standard Atmosphere is calculated from LOWTRAN 7. Input conditions are shown in Table 4.5. Average band transmittance = 0.4242.

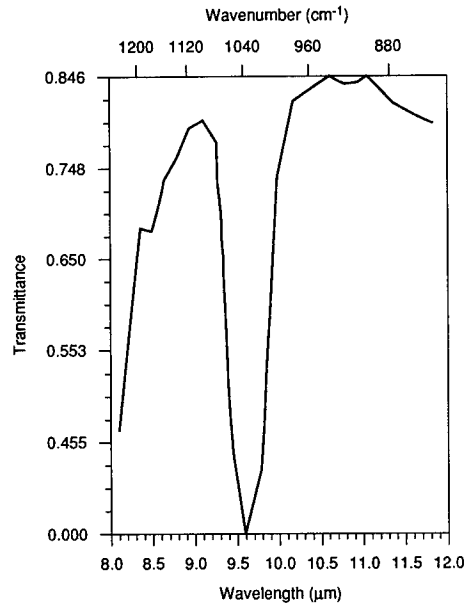

Fig. 4.140 Total uplooking path spectral transmittance to space in the 8- to 12-μm band at a solar zenith angle of 30 deg. 1976 Standard Atmosphere is calculated from LOWTRAN 7. Input conditions are shown in Table 4.5. Average band transmittance = 0.6966.

Table 4.5 Typical LOWTRAN 7 Input Data for Up-Looking IRST Cases

Model atmosphere	1976 U.S. standard
Type of atmospheric path	Slant path to space
Mode of execution	Radiance with scattering
Executed with multiple scattering	No
Temperature and pressure altitude profile	1976 U.S. standard
Water-vapor altitude profile	1976 U.S. standard
Ozone altitude profile	1976 U.S. standard
Methane altitude profile	1976 U.S. standard
Nitrous oxide altitude profile	1976 U.S. standard
Carbon monoxide altitude profile	1976 U.S. standard
Other gases altitude profile	1976 U.S. standard
Radiosonde data are to be input	No
Output file options	Suppress ATM profiles
Temp at boundary (0.000—T @ first level)	0.000
Surface albedo (0.000—blackbody)	0.000
LOWTRAN 7 Card #1 Screen	
Aerosol model used	Rural—VIS = 23 km
Seasonal modifications to aerosols	Determined by model
Upper atmosphere aerosols (30–100 km)	Background stratospheric
Air-mass character for Navy maritime aerosols	0
Use cloud/rain aerosol extensions	No clouds or rain
Use of Army (VSA) for aerosol extension	No
Surface range for boundary layer	0.000
Wind speed for Navy maritime aerosols	0.000
24-h average wind speed for Navy maritime	0.000
Rain rate (mm h^{-1})	0.000
Ground altitude above sea level (km)	0.000
LOWTRAN 7 Card #2 Screen	
Initial altitude (km)	0.000
Final altitude/tangent height (km)	0.000
Initial zenith angle (deg)	85.000
Path length (km)	0.000
Earth center angle (deg)	0.000
Radius of earth (km) (0.000—default)	0.000
0—short path; 1—long path	0
Initial frequency (wave number)	800.000
Final frequency (wave number)	1250.000
Frequency increment (wave number)	20.000
LOWTRAN 7 Card #3 and #4 Screen	
Solar/lunar geometry type (0-2)	0
Aerosol phase function	MIE generated
Day of the year (91-365)	180
Extraterrestrial source	Sun
PARM1—observer latitude/azimuthal angle	40.000
PARM2—observer longitude/sun zenith	105.000
Sun/moon latitude (−90 to 90 deg)	40.000
Sun/moon longitude (0 to 360 deg)	60.000
Greenwich time (decal hours)	0.000
Path azimuth (deg east of north)	0.000
Phase angle of the moon (deg)	0.000
Asymmetry factor	0.000

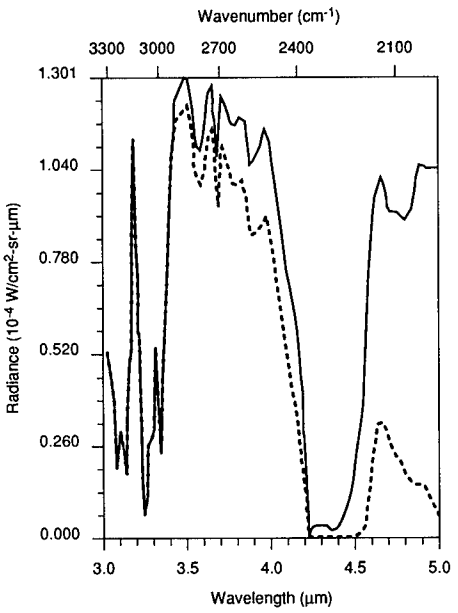

Fig. 4.141 Total downlooking path spectral radiance from space in the 3- to 5-μm band. Solar zenith angle of 0 deg. The dotted line is the contribution from the earth's albedo, ≈ 0.4. Input conditions are shown in Table 4.6. Average band radiance = 1.524×10^{-4} W cm^{-2} sr^{-1} μm^{-1}.

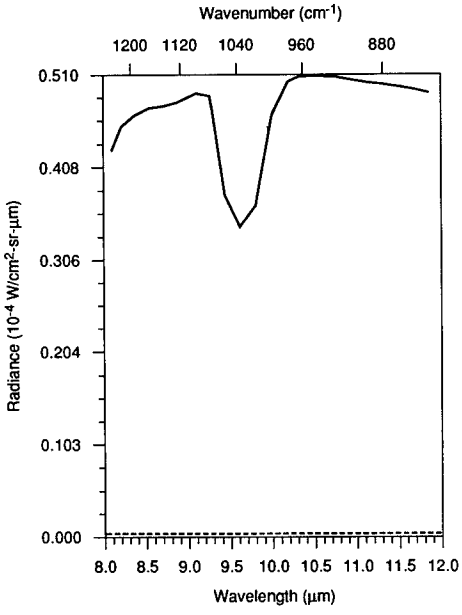

Fig. 4.142 Total downlooking path spectral radiance from space in the 8- to 12-μm band. Solar zenith angle of 0 deg. The dotted line is the contribution from the earth's albedo, ≈ 0.4. Input conditions are shown in Table 4.6. Average band radiance = 2.147×10^{-3} W cm^{-2} sr^{-1} μm^{-1}.

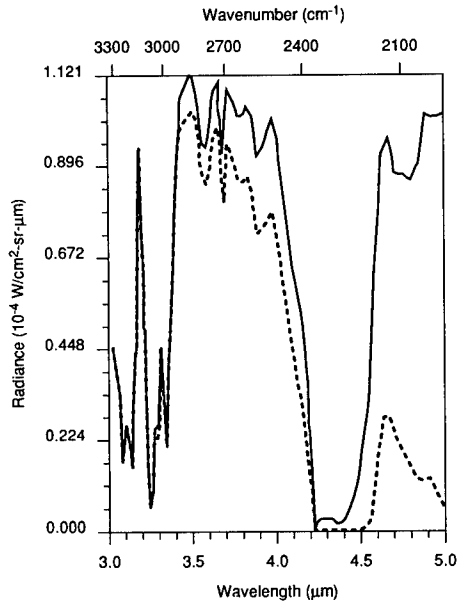

Fig. 4.143 Total downlooking path spectral radiance from space in the 3- to 5-μm band. Solar zenith angle of 30 deg. The dotted line is the contribution from the earth's albedo, ≈ 0.4. Input conditions are shown in Table 4.6. Average band radiance = 1.355×10^{-4} W cm^{-2} sr^{-1} μm^{-1}.

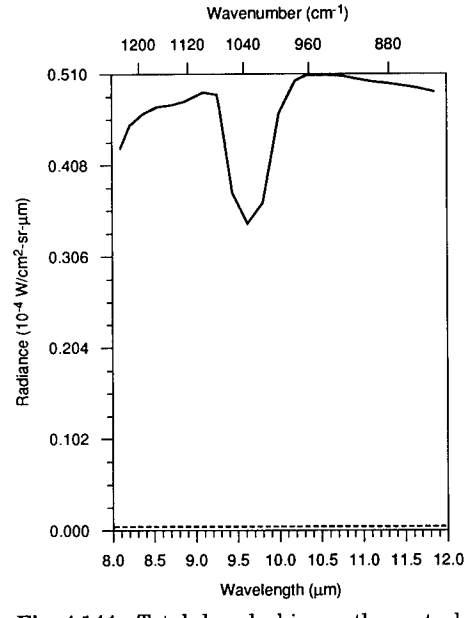

Fig. 4.144 Total downlooking path spectral radiance from space in the 8- to 12-μm band. Solar zenith angle of 30 deg. The dotted line is the contribution from the earth's albedo, ≈ 0.4. Input conditions are shown in Table 4.6. Average band radiance = 2.146×10^{-3} W cm^{-2} sr^{-1} μm^{-1}.

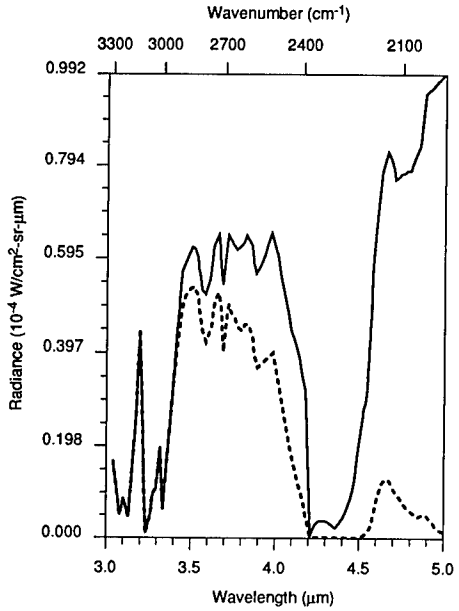

Fig. 4.145 Total downlooking path spectral radiance from space in the 3- to 5-μm band. Solar zenith angle of 60 deg. The dotted line is the contribution from the earth's albedo, ≈ 0.4. Input conditions are shown in Table 4.6. Average band radiance = 9.148×10^{-5} W cm^{-2} sr^{-1} μm^{-1}.

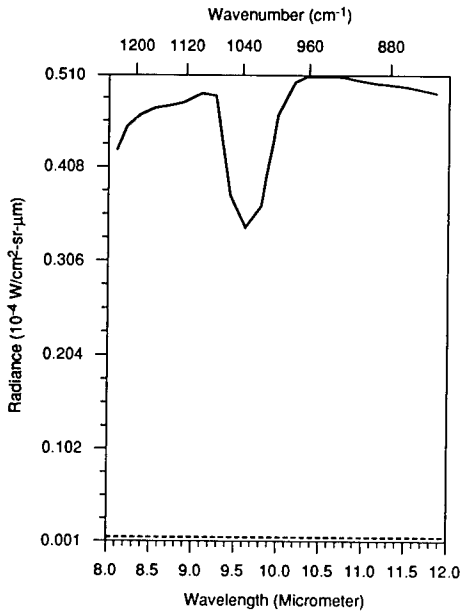

Fig. 4.146 Total downlooking path spectral radiance from space in the 8- to 12-μm band. Solar zenith angle of 60 deg. The dotted line is the contribution from the earth's albedo, ≈ 0.4. Input conditions are shown in Table 4.6. Average band radiance = 2.142×10^{-3} W cm^{-2} sr^{-1} μm^{-1}.

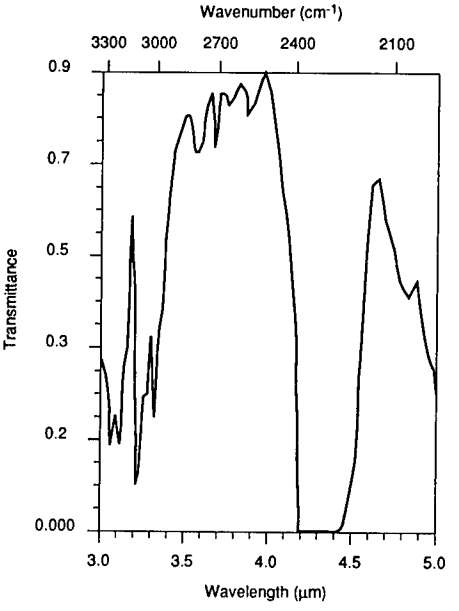

Fig. 4.147 Total downlooking path spectral transmittance from space in the 3- to 5-μm band. 1976 Standard Atmosphere is calculated from LOWTRAN 7. Input conditions are shown in Table 4.6. Average band transmittance = 0.4479.

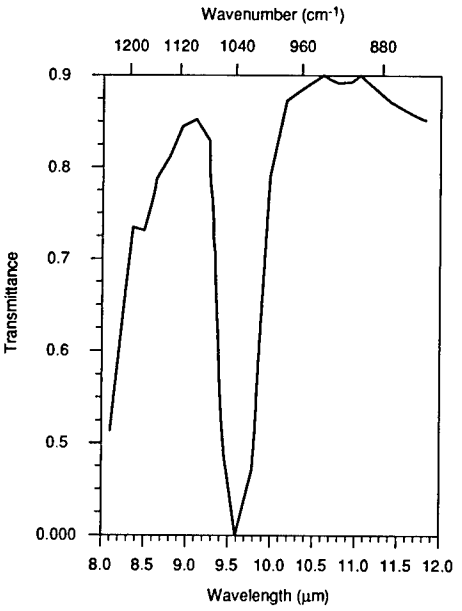

Fig. 4.148 Total downlooking path spectral transmittance from space in the 8- to 12-μm band. 1976 Standard Atmosphere is calculated from LOWTRAN 7. Input conditions are shown in Table 4.6. Average band transmittance = 0.721.

Table 4.6 Typical LOWTRAN 7 Input Data for Down-Looking IRST Cases

Model atmosphere	1976 U.S. standard
Type of atmospheric path	Slant path
Mode of execution	Radiance with scattering
Executed with multiple scattering	No
Temperature and pressure altitude profile	1976 U.S. standard
Water-vapor altitude profile	1976 U.S. standard
Ozone altitude profile	1976 U.S. standard
Methane altitude profile	1976 U.S. standard
Nitrous oxide altitude profile	1976 U.S. standard
Carbon monoxide altitude profile	1976 U.S. standard
Other gases altitude profile	1976 U.S. standard
Radiosonde data are to be input	No
Output file options	Include ATM profiles
Temp at boundary (0.000—T @ first level)	0.000
Surface albedo (0.000—blackbody)	0.400
LOWTRAN 7 Card #1 Screen	
Aerosol model used	Rural—VIS = 23 km
Seasonal modifications to aerosols	Determined by model
Upper atmosphere aerosols (30–100 km)	Background stratospheric
Air-mass character for Navy maritime aerosols	0
Use cloud/rain aerosol extensions	No clouds or rain
Use of Army (VSA) for aerosol extension	No
Surface range for boundary layer	0.000
Wind speed for Navy maritime aerosols	0.000
24-h average wind speed for Navy maritime	0.000
Rain rate (mm h^{-1})	0.000
Ground altitude above sea level (km)	0.000
LOWTRAN 7 Card #2 Screen	
Initial altitude (km)	40.000
Final altitude/tangent height (km)	0.000
Initial zenith angle (deg)	180.000
Path length (km)	0.000
Earth center angle (deg)	0.000
Radius of earth (km) (0.000—default)	0.000
0—short path; 1—long path	0
Initial frequency (wave number)	800.000
Final frequency (wave number)	1250.000
Frequency increment (wave number)	20.000
LOWTRAN 7 Card #3 and #4 Screen	
Solar/lunar geometry type (0-2)	2
Aerosol phase function	MIE generated
Day of the year (91-365)	180
Extraterrestrial source	Sun
PARM1—observer latitude/azimuthal angle	0.000
PARM2—observer longitude/sun zenith	0.000
Sun/moon latitude (−90 to 90 deg)	0.000
Sun/moon longitude (0 to 360 deg)	0.000
Greenwich time (decal hours)	0.000
Path azimuth (deg east of north)	0.000
Phase angle of the moon (deg)	0.000
Asymmetry factor	0.000

4.2.3.1.2 FASCODE. The second major code is FASCODE. The latest version is FASCOD3, which is now in a beta test version. It models calculations of the absorption line shapes for individual atmospheric species by using algorithms created by the scientists of the Geophysics Directorate. Spectral line data for its line-by-line calculations are contained in the HITRAN database, which was compiled at the Directorate. The new edition of this database, HITRAN "91" (issued in March 1991), expands the number of molecular transitions to two-thirds of a million.

Because FASCODE is a physically exact code, it achieves a much higher level of accuracy than LOWTRAN. However, the computer time required to do the complex line-by-line calculations makes it computationally much slower than LOWTRAN. The application for FASCODE is for all systems requiring predictions for high-resolution propagation.

4.2.3.1.3 MODTRAN. MODTRAN is a two-parameter, band-model code covering the same spectral range as LOWTRAN and including all its capabilities. Like LOWTRAN 7, it includes separate band-model parameters for a set of molecules, but they are calculated at a higher resolution (2 cm^{-1} for MODTRAN compared to 20 cm^{-1} for LOWTRAN). MODTRAN therefore requires somewhat more computer time than LOWTRAN.

In contrast to FASCODE, it includes its own spectral database. With the inclusion of both direct and scattered solar radiances, it is appropriate for low atmospheric paths (surface to 30 km) and middle atmospheric paths (30 to 60 km). MODTRAN can also be used (with caution) to model bands for paths above 60 km.

4.2.3.1.4 HITRAN. Beginning in the late 1960s, the Air Force Geophysics Laboratory began developing the HITRAN molecular spectroscopic database in response to the requirement of a detailed knowledge of infrared transmission properties of the atmosphere. The current edition of HITRAN was made public in March 1991, replacing the 1986 edition. HITRAN is the internationally recognized standard for computation and reference of the absorption and radiance properties of the terrestrial atmosphere due to molecular transitions.

HITRAN archives spectral parameters for 30 molecular species and their significant isotopic variants, covering the electromagnetic spectral range from the millimeter through the visible. It contains information on the wave number of relevant transitions, their intensity, air-broadened halfwidths, self-broadened halfwidths, lower-state energies, and temperature-dependent quantities. The discrete transitions number approximately 650,000.

In addition, HITRAN contains a supplemental file of cross-sectional data for molecular species that are not amenable to line-by-line formulation. These include species such as chlorofluorocarbons (CFCs) and heavy oxides of nitrogen. The database has been expanded so that with these new data some quantitative remote-sensing studies can be achieved.

HITRAN is also being extended into the arena of hot gases through an analogous compilation called HITEMP, which is being developed to provide capabilities for hot-gas detection.

In addition to being a stand-alone database, HITRAN is used as direct input to FASCODE and indirect input to the band-model codes, such as LOWTRAN and MODTRAN. In the latter cases, molecular bands are now run in the line-

by-line mode, degraded to the particular resolution of the band model, and then parameterized accordingly.

There are at least 800 users of HITRAN, including DoD agencies and contractors; U.S. government agencies such as NASA, the National Oceanic and Atmospheric Administration (NOAA), and the Environmental Protection Agency (EPA); and universities and commercial enterprises throughout the world.

4.2.3.2 Atmospheric Radiation. The atmosphere itself gives rise to a significant amount of background radiation in the form of natural graybody emission due to molecules being at a finite temperature and to scattered radiation from the sun. In down-looking cases, the earth also reflects radiation from the sun.

In this section, we show graphical data representative of the magnitude of these effects as predicted by LOWTRAN in typical IRST scenarios: horizontal paths to 300 km in Figs. 4.101 to 4.124, up-looking from ground to space in Figs. 4.125 to 4.140, and down-looking from space to ground in Figs. 4.141 to 4.148. The data were calculated from LOWTRAN 7 with typical input parameters shown in Tables 4.4, 4.5, and 4.6.

4.2.3.3 Aerodynamic Influences. Depending on the application, aerodynamic effects can significantly influence IRST system performance. The turbulent properties of the free atmosphere can, under certain conditions, induce angle jitter into the tracking loops. In addition, high-performance airborne platforms introduce additional aero-optical effects by virtue of the laminar and turbulent flow fields in and around the sensor aperture and thermo-optical heating effects that introduce spurious radiation into the field of view.

4.2.3.4 Atmospheric Turbulence. Turbulence induces random variations in the atmosphere's index of refraction (see Volume 2, Chapter 2). The lateral variation in index in-turn produces distorted optical phase fronts giving rise to image motion, distortion, added blur, and irradiance fluctuations. The index of refraction depends on temperature, pressure, humidity, and optical wavelength. In IR applications the temperature dependence is the most important. Quantitative effects of the atmosphere are treated statistically and are characterized by the atmospheric index structure constant $C_n^2(\mathrm{m}^{-2/3})$. Near the ground up to the first temperature inversion, C_n^2 is a very complicated function of wind, solar loading, and terrain. The variation in C_n^2 over the ocean is shown in Fig. 4.149.

For most IRST applications, ground-level turbulence is not a concern; however, the altitude dependence of C_n^2 can be modeled crudely as

$$C_n^2(h) = \begin{cases} \dfrac{1.5 \times 10^{-13}}{h \ \ [\mathrm{m}]} \ \ [\mathrm{m}^{-2/3}] \ , & h < 20 \text{ km} \\ 0 \ , & h > 20 \text{ km (66,000 ft)} \ . \end{cases} \tag{4.54}$$

(There is no accurate means of computing C_n^2.)

Most of the first-order effects of turbulence on IRST performance can be predicted with a knowledge of C_n^2 and certain system parameters as shown in the following sections.

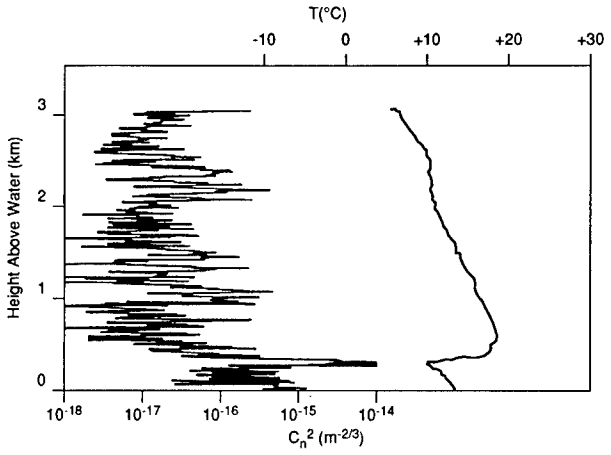

Fig. 4.149 C_n^2 versus altitude for the first 3000 m over the ocean. The local air temperature is shown on the right, with the scale on the upper right. (Note the increase in C_n^2 at the base of the strong temperature inversion.)[11]

Irradiance Fluctuations. The normalized variance of irradiance fluctuation due to turbulence is given as

$$\frac{\sigma^2}{\langle E\rangle^2} = \exp(4\sigma_t^2) - 1 \ , \tag{4.55}$$

where

$$\sigma_t^2 = 0.56\mathrm{k}^{7/6} \int_0^L C_n^2(z)(L - Z)^{5/6}\, dz \ , \tag{4.56}$$

where

$\langle E\rangle$ = average irradiance
L = path length
$k = \dfrac{2\pi}{\lambda}$
σ^2 = variance of irradiance.

For plane waves (long-range IRST) and optical paths parallel to the ground (C_n^2 = constant),

$$\sigma_t^2 = 0.31 C_n^2 k^{7/6} L^{11/6} \ . \tag{4.57}$$

The reader is cautioned that the above is a worst case estimate since receiver aperture averaging has not been explicitly considered.

Image Angular Motion. Image angular motion in the case where irradiance fluctuations are small and plane-wave geometry dominates is given by

$$\langle \alpha_x^2 \rangle = \langle \alpha_y^2 \rangle \simeq 0.975 \left(\frac{1}{k}\right)^2 \frac{[D_\phi(2a)]}{4a^2} , \tag{4.58}$$

where $k = 2\pi/\lambda$, a = radius of the system aperture, and the phase structure function $D_\phi(r)$ is given by

$$D_\phi(2a) = 2.91k^2(2a)^{5/3} \int_0^L C_n^2(z)\, dz , \tag{4.59}$$

where L is the path length.

Example. Calculate the irradiance variance and rms angular motion due to turbulence over a 100-km IRST path assuming a 4-μm center wavelength, $C_n^2 = 10^{-17}$, and an aperture diameter of 0.5 m.

From Eq. (4.57),

$$\sigma_l^2 = 0.31(10^{-17}) \left(\frac{2\pi}{4.0 \times 10^{-6}}\right)^{7/6} (100 \times 10^3)^{11/6} = 0.067 .$$

Equation (4.55) yields

$$\frac{\sigma^2}{\langle E \rangle^2} = \exp(0.067) - 1 = 0.07 .$$

The rms irradiance variation σ is about 0.26 of the mean. Equation (4.59) yields

$$D_\phi(2a) = 2.91 \left(\frac{2\pi}{4.0 \times 10^{-6}}\right)^2 (0.5)^{5/3} \times 10^{-17} \times 100 \times 10^3 = 2.26 .$$

From Eq. (4.58),

$$\langle \alpha_x^2 \rangle = 0.975 \left(\frac{4.0 \times 10^{-6}}{6.28}\right)^2 \left(\frac{2.26}{(0.5)^2}\right) = 3.57 \times 10^{-12} .$$

The rms single-axis motion is $\langle \alpha_x^2 \rangle^{1/2} = 1.9$ μrad.

4.2.3.5 Aero-Mechanical and Aero-Optical Effects. IRST performance can be markedly influenced by aerodynamic effects resulting from operation of high-speed airborne platforms, as shown in Fig. 4.150. Performance of the system can be seriously compromised by poor placement on the platform or disregard of deleterious effects of aero-mechanical and aero-optical phenomena, resulting from high-speed air flow in and around sensor apertures. Aero-mechanical effects result from platform-induced vibration or from thermal loading on sensor components or mounting configuration. Aero-optical effects

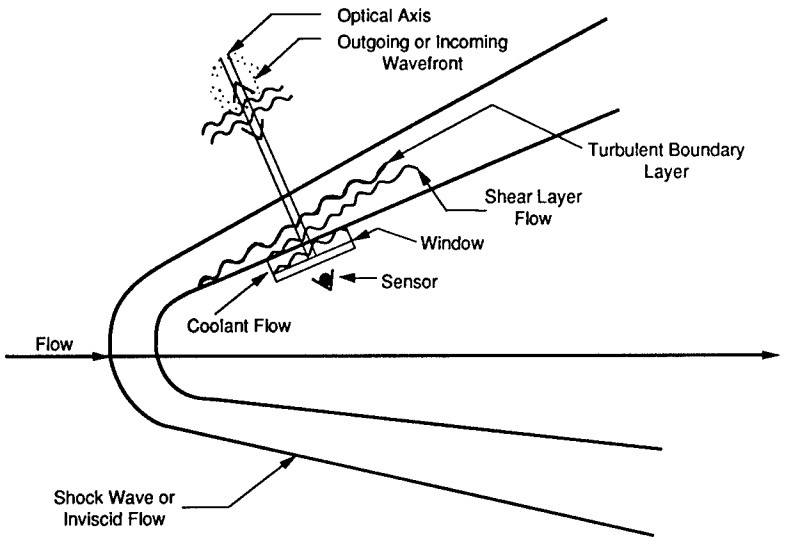

Fig. 4.150 Aero-optical effects.

refer to nonuniform indices of refraction variation, which influence the propagation of optical fields around the aperture.

Table 4.7, taken from Volume 2, Chapter 3, of this handbook, summarizes aero-optical effects. Of particular interest to IRST problems are mechanically induced gimbal jitter, tracking error resulting from aero-optical wave-front tilt, and thermal loading on the sensor window from aerodynamic heating. The designer is urged to consider carefully the potential impact of these effects when using IRST in airborne platforms.

Below Mach 0.3 the (incompressible) flow generally yields small optical distortion. Between Mach 0.3 and ~7.0, the flow fields impress optical aberrations on both incoming and outgoing wave fronts. Additional aberrations arise beyond Mach 7.0 due to ionization and acoustical radiation effects. Optical degradations in these latter two regimes may compromise mission objectives if mitigation procedures are not implemented.

4.3 IRST SYSTEMS PERFORMANCE ANALYSIS

The systems performance model presented here presumes IRST operational requirements that define the target, background areal or volumetric coverage rates, the required spatial-resolution characteristics of the platform be it stationary or moving, the probability of detection or loss of a target of targets with a given false-alarm rate, and the environmental conditions. Given the foregoing, it is possible to derive the major system parameters or combinations thereof and to further select, given weight/size/cost constraints, a final set or sets of parameters that represent realizable designs (see Refs. 7 and 18).

Table 4.7 Aero-Optical Effects in Three Mach Number Regimes*

AO Phenomena	$M < 0.3$	$0.3 < M < 8$	$M > 8$
Boundary layers/ shear layers Mixing layers (e.g., open cavities)	• Incompressible flow regime • Natural AO effects negligible (injection of thermal energy can yield strong optical aberrations) • Calculate properties via classical fluid mechanics	• Compressibility flow regime • Perfect gas law valid • Random flow phase variance $\sigma^2 = 2G^2\int_0^L \langle\rho'^2\rangle \ell_z\, dz,$ $(\ell_z \ll L)$ G = Gladstone-Dale parameter $\langle\rho'^2\rangle$ = fluctuating density variance ℓ_z = flow correlation length along optical axis L = path length through flow field • In weak-aberration regime $(\sigma/\lambda < 1/\pi)$ Strehl $S \propto \exp-(K\sigma)^2$, $K \equiv 2\pi/\lambda$ Resolution loss $\theta_\beta \propto \theta_D/S^{1/2}$ • In strong-aberration regime $(\sigma/\lambda \gg 1/\pi)$ Strehl $S \propto (\ell_z/\sigma)^2$ Resolution loss $\theta_\beta \propto \sigma/\ell_z$ • Nominal aberration compensation bandwidth requirements > 10 kHz • Thermal control of windows may be essential	• Perfect gas law invalid • Chemistry of air important • Ionization/plasma causes beam reflection/ refraction/absorption and radiation effects; longer wavelength degraded more • Radiated sound intensity scales strongly with velocity, probably effects turbulent field • Thermal control of optical windows essential • Flow reradiation effects can contribute significantly to sensor background noise
Inviscid flow/ shocks	• Negligible effects	• Boresite error, defocus • Correctable via low-order adaptive optics unless angle of attack varying rapidly • Phase error scales as $\Delta\phi \propto KG\int_0^L \rho'\, dz$ • Shock strength is function of adiabatic index, Mach number, and shock angle • Flow reradiation energy can cause sensor thermal noise	• Inviscid field strength scales as $\phi \propto \rho' R$ (R = flow-field radius curvature) • Shock-induced ionization/plasma formation degrades wave front

*AO effects can be partitioned into three Mach-number regimes. Below Mach 0.3 the (incompressible) flow generally yields small optical distortion. Between Mach 0.3 and ~8 a host of flow fields impress optical aberrations on both incoming and outgoing wave fronts. Additional aberrations arise beyond Mach 8 owing to ionization and acoustical radiation effects. Optical degradations in these latter two regimes may stifle mission objectives if mitigation procedures are not implemented.

4.3.1 Sensor Search Geometry

A number of search geometries and focal-plane arrays are in wide use in IRST applications. These are categorized as *scanning* and *staring* systems.

In the simple serial *scanning* configuration shown in Fig. 4.151, the detector or detector subarray is projected into the far field by the system optic defining angles $\theta_{x,y}$. The projection defines the instantaneous field of view (IFOV) and corresponding angular resolution of the sensor. The detector subarray projection is scanned over angles $\phi_{x,y}$ defining the field of regard (FOR) (sometimes known as field of view). Scanning the IFOV over the the complete FOR defines a frame and the time to do this as a frame time T_f. Many scanning configurations are possible.

In the case where multiple detectors are used, the number of possible variations in scanning increases considerably. Of particular interest is time-delay integration (TDI), where n detectors are scanned serially across the scene as in Fig. 4.152(b), the output of each detector being suitably delayed such that each resolution element is in effect sensed by n detectors whose outputs are integrated together to yield a net signal-to-noise ratio increase of $\sqrt{n}$.

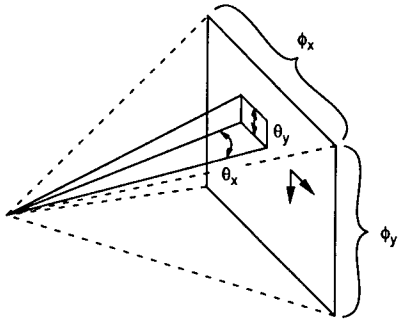

Fig. 4.151 IRST raster scanning configuration.

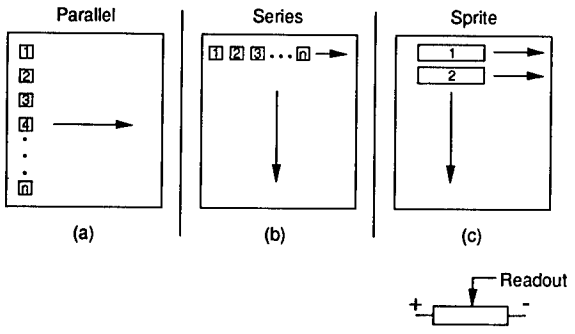

Fig. 4.152 Scanning several detectors over the same source.[7]

Figure 4.152(c) shows a concept called SPRITE, which is much like TDI. In this concept, the delay and addition are effectively carried out within the detector element itself.

In a *staring* system the entire focal-plane array is projected into the far field by the optics, as shown in Fig. 4.153. The angular subtense of the individual detector elements, or pixels, is again defined by $\theta_{x,y}$ and the total subtense of the array by $\phi_{x,y}$. There are always gaps between detectors so that the FOR is not simply the sum of the IFOV of all the detectors. The solid angle generated by the IFOV is given as

$$\alpha = \theta_x \theta_y \ , \tag{4.60}$$

and that generated by the FOR is

$$\Omega = \phi_x \phi_y \ . \tag{4.61}$$

The number of independent resolution elements is approximately $N = \Omega/\alpha$.

A method by which the effective signal-to-noise ratio of a staring array is increased is shown in Fig. 4.154. Referred to as a "step-stare," the detector

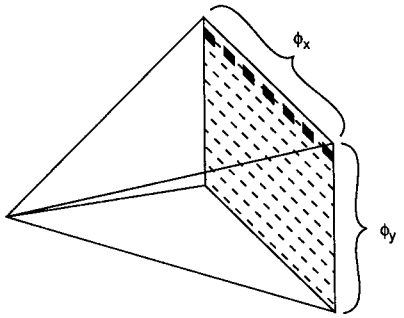

Fig. 4.153 IRST staring configuration.

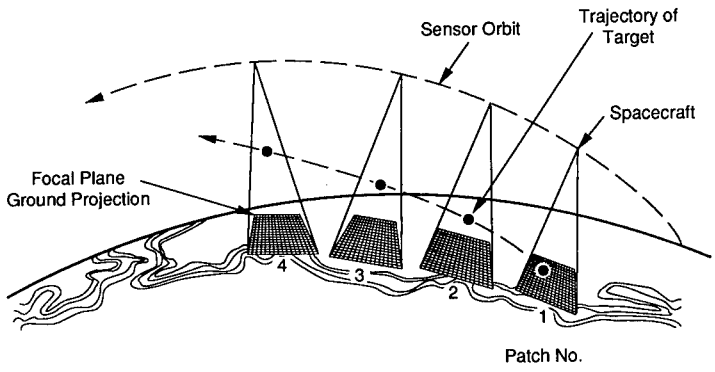

Fig. 4.154 Step-stare scanning example with no overlap.[7]

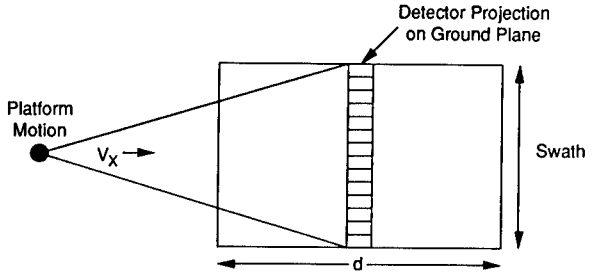

Fig. 4.155 Pushbroom scanning configuration.

array projection is in effect held in place over the target area for a predetermined period of time. In the "pushbroom" configuration shown in Fig. 4.155, the moving platform scans in the motion direction.

4.3.2 Search Volume

The area search rate ($m^2\ s^{-1}$) or angular coverage rate ($sr\ s^{-1}$) may be important IRST performance requirements driven by operational necessity. In a *forward-looking scanning* system (Fig. 4.151) the single-detector angular coverage rate is given by

$$\mathring{\Omega}_c = \theta_y \omega_x \varepsilon_s \ , \tag{4.62}$$

where

ω_x = scanning rates (rad s^{-1}) in the x direction
ε_s = scanning efficiency accounting for overlap, scanning, retrace, and so forth
θ_y = IFOV.

The search volume in a look-ahead geometry is approximately

$$V = \frac{1}{3} R_m^3 \phi_x \phi_y \ , \tag{4.63}$$

where R_m is the maximum detection range.

In a *look-ahead staring* system, the search rate is, in a general way, driven by the detector readout time; thus,

$$\mathring{\Omega} = \frac{\theta_x \theta_y}{t_{ro}} \ , \tag{4.64}$$

where N is the total number of detectors and t_{ro} is the readout time of an individual detector without overlap.

In a *look-down staring* system on a moving platform, the area coverage rate is given by

$$\mathring{A} = h\phi_y V_x \ , \tag{4.65}$$

where

h = platform altitude
V_x = platform velocity in the x direction
ϕ_y = FOR_y.

For a linear array of n detectors in the y direction, an important condition on the validity of Eq. (4.65) is

$$t_{\text{ro}}\sqrt{N} \ll \frac{\theta_x h}{V_x} \ , \tag{4.66}$$

where

t_{ro} = detector readout time
N = total number of detectors
h = altitude of the platform.

This represents a condition that the time to read out a line of detectors transverse to the platform motion is small relative to measuring the time a pixel projected on the ground moves across a reference point. If this is not true, then there are gaps in the coverage and the coverage rate expressed by Eq. (4.65) is fictitious.

For a *look-down scanning* system the approximate coverage rate is given by

$$\mathring{A} = h\phi_y V_x \varepsilon_s \ , \tag{4.67}$$

but the condition on platform velocity and scan rates is now

$$\frac{2\phi_x}{\omega_x} = \frac{kh\theta_x}{V_x} \ . \tag{4.68}$$

This ensures pixel overlap from scan to scan to avoid gaps in coverage. Typically $k \approx 1/2$.

There are more general cases where the geometry is such that the sensor is looking down a "squint" angle β of 20 to 30 deg for which the expressions for coverage rates are more complex.

The projected area on the ground for the configuration shown in Fig. 4.156 for a $\phi \times \phi$ FOR is

$$A = h^2\left[\frac{\sin\phi \tan\left(\frac{\phi}{2}\right)}{\cos^2\xi \sin\psi}\right]\left(1 + \frac{\sin\theta}{\sin\psi}\right) \ , \tag{4.69}$$

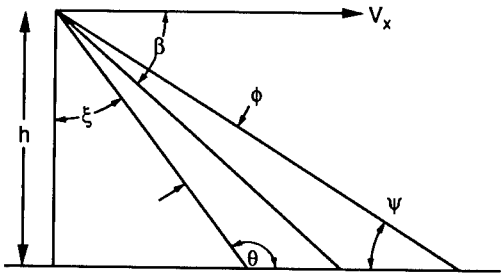

Fig. 4.156 Geometry definition parameters for projected area on ground plane.

where

$$\xi = \frac{\pi}{2} - \left(\beta + \frac{\phi_y}{2}\right) , \tag{4.70}$$

$$\psi = \beta - \frac{\phi_y}{} , \quad \theta = \frac{\pi}{} + \xi . \tag{4.71}$$

In the case of a platform moving with a forward velocity, scanning in the direction parallel to the direction of motion could be done with the forward motion of the platform, as shown in Fig. 4.155. This is known as "pushbroom" scanning; thus, a frame time would be given as

$$T = \frac{d}{V_x} . \tag{4.72}$$

4.3.3 System Bandwidth Requirements

The electrical bandwidth of the system is derived by a consideration of response of the detector to a step-function target input, the bandwidth being approximately inverse to the duration the target spends within a pixel, or resolution element. This interval is known as dwell time; thus,

$$\Delta\nu = \frac{K}{t_d} , \tag{4.73}$$

where $\Delta\nu$ = bandwidth and $K \approx 0.5$ to 3 depending on the application.[18]

In a scanning system, t_d is defined by the scanning characteristics. The number of independent resolution elements is

$$N_r = \frac{\Omega}{\alpha} , \tag{4.74}$$

where Ω = FOR and α = IFOV.

The detector dwell time t_d is the time required for a point target to move across a resolution element; thus,

$$t_d = \frac{\theta_x}{\omega_x} . \tag{4.75}$$

In a staring array, the dwell time is determined by the time it takes for a target to move across the pixel:

$$t_d = \frac{R \sin\theta_x}{V_x} \approx \frac{R\theta_x}{V_x} , \tag{4.76}$$

where V_x is the target velocity and $R\theta_x$ is the linear extent of the pixel at range R.

A "frame" time can be defined as

$$t_f = \frac{t_d N_r}{\varepsilon_s} , \tag{4.77}$$

where t_f is the actual time it takes to scan an entire field of regard, including scanning inefficiencies and detector overlap. This efficiency could range from 0.25 to 0.75 depending on the waveform used and the detector redundancy.

4.3.4 Angular Resolution and Aperture

The angular resolution required of the IRST system is driven by operational considerations. One target diameter at the maximum detection range would seem to be the lowest practical limit on required system spatial resolution; thus,

$$\theta_{x,y}(\text{TGT}) = \frac{D_t}{R_{\max}} , \tag{4.78}$$

where D_t is the target diameter and $R_{\max}$ is the maximum detection range. The system aperture diameter and optical aberrations determine the *obtainable* system resolution. Diffraction limits the resolution to

$$\theta_{x,y}(\text{DIFF}) = 2.44 \frac{\lambda_{\max}}{D_s} N_d , \tag{4.79}$$

where

$\lambda_{\max}$ = system cutoff wavelength
D_s = system aperture diameter
N_d = factor > 1 expressing effect of optical aberrations.

Given the required spatial resolution, the sizing of the collection aperture is subject to several constraints. Sensitivity considerations in Sec. 4.3.6 will demand a certain minimum aperture size that must be consistent with the condition

$$\theta_{x,y}(\text{TGT}) \geq \theta_{x,y}(\text{DIFF}) \ , \tag{4.80}$$

as determined through Eq. (4.79) and the minimum spatial resolution as determined through Eq. (4.78) or specified independently. We choose the largest aperture diameter that simultaneously satisfies the foregoing conditions, being mindful of the following practical limitation:

$$f/\# = \frac{f}{D_s} \gtrsim 1 \ . \tag{4.81}$$

The steps in the procedure are as follows:

1. Ascertain system spatial resolution $\theta_{x,y}(\text{TGT})$.
2. Derive the minimum aperture $D_{\min}$ required for system sensitivity from Sec. 4.3.6.
3. Substitute $D_{\min}$ in Eq. (4.79).
4. See that Eq. (4.80) is satisfied. If not, choose a larger aperture given by

$$D_s = \frac{2.44\ \lambda_{\max} N_d}{\theta_{x,y}(\text{TGT})} \ . \tag{4.82}$$

For maximum sensitivity, the detector size should be matched to the spot size on the focal plane. Given that the system aperture has been determined by appeal to the considerations in the previous section, then the approximate detector size is given as

$$d_0 = \theta_{x,y} fl \tag{4.83}$$

where fl = effective focal length of the system optics.

Due to fabrication difficulties, a lower limit for the effective focal length can be estimated from the constraint

$$\frac{fl}{D_s} = f/\# \gtrsim 1 \ , \tag{4.84}$$

where $f/\#$ = numerical aperture of the optical system.

In multiple-detector systems as in staring arrays, detector elements cannot be made infinitely close together. To ensure that the target image on the focal plane does not fall between detectors, the detector spacing should be less than about one-half detector width for complete coverage.

4.3.5 System Sensitivity (Seyrafi[18])

IRST performance is typically background limited (denoted as BLIP). A point-source target with total spectral radiant intensity $I_t(\lambda)$ defined in Sec. 4.2.1 at range R from a sensor produces irradiance $E_T(\lambda)$ at the sensor aperture of

$$E_T(\lambda) = \frac{I_t(\lambda) T_a(\lambda)}{R^2} \ , \tag{4.85}$$

where $T_a(\lambda)$ is the spectral transmission of the intervening medium.

The noise equivalent flux density (NEFD), also known as the noise equivalent irradiance (NEI), is a convenient unit and is defined as that irradiance yielding a signal-to-noise ratio = 1. In the case of background-limited IRST systems, NEFD is a function of the background irradiance and is given by

$$\text{NEFD} = \left[\frac{4(f/\#)(\alpha\Delta\nu)^{1/2}}{\pi K_e D_0}\right]\left[\frac{\int_{\Delta\lambda} E_T(\lambda)\, d\lambda}{\int_{\Delta\lambda} T_o(\lambda)E_T(\lambda)D^*_{\text{BLIP}}(\lambda)\, d\lambda}\right], \tag{4.86}$$

where

$f/\#$ = f/D_0, where f is the effective focal length of the optics
α = solid angle generated by the field of view (FOV) of the optics
$\Delta\nu$ = electrical bandwidth
K_e = electrical efficiency of the temporal filter
D_0 = aperture diameter
$\Delta\lambda$ = spectral bandpass of interest
$T_o(\lambda)$ = spectral transmission of the optics
$D^*_{\text{BLIP}}(\lambda)$ = the spectral background-limited detectivity of the detector element.

The preceding equation was derived under the assumption that the response of the detector is temporal frequency independent and that the input filter response is also frequency independent with transfer function K_e ranging from $\sim$0.7 to 0.9. The signal-to-noise ratio is given as

$$\text{S/N} = \frac{\int_{\Delta\lambda} E_T(\lambda)\, d\lambda}{\text{NEFD}}. \tag{4.87}$$

If the signal from N independent detectors is integrated as in TDI, for example, then

$$(\text{S/N})_i = (\text{S/N})\sqrt{N}, \tag{4.88}$$

or

$$\text{NEFD}_i = \frac{\text{NEFD}}{\sqrt{N}}. \tag{4.89}$$

For SPRITE detectors the equivalent N is

$$N = 2\tau\frac{\left[1 - \exp\left(\frac{-t_d}{\tau}\right)\right]}{d_0/V}, \tag{4.90}$$

where

τ = minority carrier lifetime
t_d = transit time of the carriers through the material = L/v, where L = detector length and v = charge velocity
V = μE, where μ = mobility and E = field
d_0 = detector width.

For SPRITE detectors

$$D^*(\lambda) = \frac{1}{h\nu}\left(\frac{\eta\tau V_s}{2\phi_B w}\right)^{1/2}\left[1 - \exp\left(\frac{L}{V_s\tau}\right)\right]^{1/2} , \tag{4.91}$$

where

$h\nu$ = photon energy
η = quantum efficiency
τ = minority carrier recombination time
V_s = scan speed
w = detector width
L = detector length
ϕ_B = background flux.

The detectivity D^*_{BLIP} is further defined as

$$D^*_{\text{BLIP}} = \frac{\lambda}{hc}\left[\frac{\eta(\lambda)}{\phi_q}\right]^{1/2} \quad \text{(for photovoltaics)} , \tag{4.92}$$

$$D^*_{\text{BLIP}} = \frac{\lambda}{2hc}\left[\frac{\eta(\lambda)}{\phi_q}\right]^{1/2} \quad \text{(for photoconductors)} , \tag{4.93}$$

where

$\eta(\lambda)$ = spectral quantum efficiency
h = 6.63×10^{-34} J s
c = 3×10^8 m s^{-1}.

The photon flux is

$$\phi_q = L_q(\lambda)\Omega A T_o(\lambda) = \frac{\pi L_q(\lambda) A T_o(\lambda)}{4(f/\#)^2} , \tag{4.94}$$

where Ω = specified FOR or can be estimated by

$$\Omega \approx \frac{\pi D_0^2}{D_0^2 + 4f^2} \approx \frac{\pi D_0^2}{4f^2} = \frac{\pi}{4(f/\#)^2} , \tag{4.95}$$

where

$$A = \frac{\pi D_0^2}{4} , \tag{4.96}$$

$$L_q(\lambda) = \frac{L_{BB}(\lambda)}{hc} , \tag{4.97}$$

where $L_{BB}(\lambda)$ is the background radiance.

Given background irradiance $E_{BB}(\lambda)$, then

$$\phi_q = E_{BB}(\lambda)\left(\frac{\lambda}{hc}\right)\left(\frac{\pi D_0^2}{4}\right)T_o(\lambda) . \tag{4.98}$$

Substitution of Eq. (4.93) in Eq. (4.86) yields

$$\text{NEFD} = \frac{4(f/\#)\alpha d(\Delta f)^{1/2}\int_{\Delta\lambda} E_t(\lambda)L_q(\lambda)T_o(\lambda)\,d\lambda}{\frac{\pi K_e^{1/2}}{hc}\int_{\Delta\lambda} T_o(\lambda)E_t(\lambda)[\eta(\lambda)]^{1/2}\,d\lambda} \tag{4.99}$$

for a *photoconductor*.

If $T_o(\lambda)$, $L_q(\lambda)$, and $\eta(\lambda)$ are reasonably constant, or represented by their averages over the bandpass of interest, the above equation becomes

$$\text{NEFD} = \frac{4(f/\#)\alpha_d}{K_e}\left(\frac{L_q\Delta f}{\pi T_o N}\right)^{1/2}\frac{\int_{\Delta\lambda} E_t(\lambda)\,d\lambda}{\int_{\Delta\lambda}\frac{\lambda}{hc}E_t(\lambda)\,d\lambda} . \tag{4.100}$$

If we assume some average or constant $E_t(\lambda)$, then

$$\text{NEFD} \approx \frac{8(f/\#)\alpha_d}{K_e}\left(\frac{L_q\Delta f}{\pi T_o N}\right)^{1/2}\frac{hc}{\Delta\lambda} . \tag{4.101}$$

For a detector operated in the photovoltaic mode,

$$\text{NEFD}_{pv} = \frac{\text{NEFD}_{pc}}{2} . \tag{4.102}$$

Similar expressions for detector of postprocessing noise-limited system can be found in Ref. 18.

4.3.6 Range Equation

With a specified NEFD and S/N, the maximum range at which a target can be detected is

$$R_{\max} = \left[\frac{\int_{\Delta\lambda} I_t(\lambda)T_a(\lambda)\,d\lambda}{\text{NEFD}}\right]^{1/2} , \tag{4.103}$$

which, in the general case, is solved iteratively.

4.3.7 Clutter Noise (Conley[10])

Clutter noise is a dominant mechanism in the performance of IRST systems. It arises from variations in the background radiance induced by scanning a spatially varying scene or by sensor motion in a frame as in the case of a staring array. Clutter rejection is thus a dominant theme in IRST signal processors. Given a background power spectral density function or Wiener spectrum $S(f)$ in units of $(\mathrm{W\ m^{-2}\ sr^{-1}})^2$ (cycles per unit space)$^{-1}$ at the aperture and a sensor modulation transfer function $\mathrm{MTF}(f)$ both assumed to be of average quantity over a given spectral band, the rms clutter intensity can be computed as

$$\sigma_c = x^2\left[\int_{-\infty}^{\infty} |\mathrm{MTF}(f)|^2 S(f)\, df\right]^{1/2} \quad [\mathrm{W\ sr^{-1}}] \ , \tag{4.104}$$

where x is the "footprint" subtended at the range of interest; $x^2 \approx R^2\Omega$.

$\mathrm{MTF}(f)$ is the sensor modulation transfer function:

$$\mathrm{MTF}(f) = O(f)D(f)F(f) \ , \tag{4.105}$$

where

O = transfer function of the optics
D = transfer function of the detector
F = transfer function of the electrical filter.

The rms noise current is then

$$i_n = \sigma_c R\Omega T_o \ , \tag{4.106}$$

where R = detector responsivity in A W^{-1} and T_o = transmission of the optics.

The transformation from scanning or sensor motion to spatial frequency is given by

$$\nu = fV \ , \tag{4.107}$$

where

ν = temporal frequency
f = spatial frequency
V = velocity of relative motion.

Thus,

$$S(f) = S\left(\frac{\nu}{V}\right) \ . \tag{4.108}$$

To minimize the clutter noise, $\mathrm{MTF}(f)$ is chosen judiciously with minimal compromise of the target signal, by choice of an electrical filter with appropriate

bandpass characteristics, as in Fig. 4.162. The design of these filters is of considerable importance.

The "fundamental" frequency of interest is $f_0 = 1/t_d$ and the bandwidth is some multiple thereof that captures the maximum target response

$$\Delta\nu = \frac{k}{t_d} , \tag{4.109}$$

where $k \simeq 0.5$ for detection systems. To translate these values to the spatial domain,

$$f_0 = \frac{\nu_0}{V} , \tag{4.110}$$

and

$$\Delta f_0 = \frac{\Delta\nu}{V} . \tag{4.111}$$

In the case of a scanner,

$$t_d = \frac{x}{V_s} , \tag{4.112}$$

where V_s is the scanning velocity and x is the linear subtense of the scan at the range of the target $= \alpha R$.

The corresponding spatial frequency of interest is

$$f_0 = \frac{\nu_0}{V_s} = \frac{1}{t_d V_s} = \frac{1}{x} , \tag{4.113}$$

and the bandwidth is

$$\Delta f = \frac{\Delta\nu_0}{V_s} = \frac{K}{t_d V_s} = \frac{K}{x} . \tag{4.114}$$

For a staring system with drift velocity V_d,

$$t_d = \frac{x}{V_d} , \tag{4.115}$$

where x is the linear subtense of a pixel at target range.

If the starer is not drifting but the target is moving with velocity V_t, then

$$t_d = \frac{x}{V_t} \tag{4.116}$$

and again $f_0 = 1/x$ and $\Delta f = K/x$.

If the starer is drifting and the target is moving, then

$$f_0 = \frac{1}{x}\left(\frac{V_t}{V_d}\right) , \quad \Delta f = \frac{K}{x}\left(\frac{V_t}{V_d}\right) . \tag{4.117}$$

Jitter noise can be treated by using the jitter transfer function in the spatial domain.

Example. Suppose the scene can be characterized by a PSD of $S(f) = Cf^{-\gamma}$, where $\gamma > 1$ and $\text{MTF}(f) = 1$ within Δf and $= 0$ otherwise; then

$$\sigma_c^2 = x^2 \int_{\Delta f} S(f)|\text{MTF}(f)|^2 \, df \approx x^2 S(f_0)\Delta f , \tag{4.118}$$

where f_0 is the center spatial frequency of interest.

For a scanning system,

$$f_0 = \frac{1}{x} , \quad \Delta f = \frac{K}{x} , \tag{4.119}$$

and

$$\sigma_c^2 = x^2\left(\frac{1}{x}\right)^{-\gamma}\left(\frac{K}{x}\right) = xCK\left(\frac{1}{x}\right)^{-\gamma} . \tag{4.120}$$

Example. Suppose $S(f) = 133\, f^{-1.2}$ and the transfer function for a circular aperture is

$$A(f) = \frac{2}{\pi}\left\{\cos^{-1}\frac{xf}{2.44} - \frac{xf}{2.44}\left[1 - \left(\frac{xf}{2.44}\right)^2\right]^{1/2}\right\} . \tag{4.121}$$

The detector transfer function is

$$D(f) = \frac{\sin \pi f x}{\pi f x} , \tag{4.122}$$

and the filter transfer function corresponding to a second-order differencing filter is

$$F(\nu) = \frac{\sin \pi \nu t_d}{\pi \nu t_d}(\sin^2 \pi \nu t_d) . \tag{4.123}$$

In the spatial domain the electrical filter transforms to

$$F(f) = \frac{\sin \pi f V_s t_d}{\pi f V_s t_d}(\sin^2 \pi f V_s t_d) . \tag{4.124}$$

Figure 4.157 shows the rms clutter radiance and radiant intensity as a function of cloud diameter with scan (or drift) velocity as a parameter.

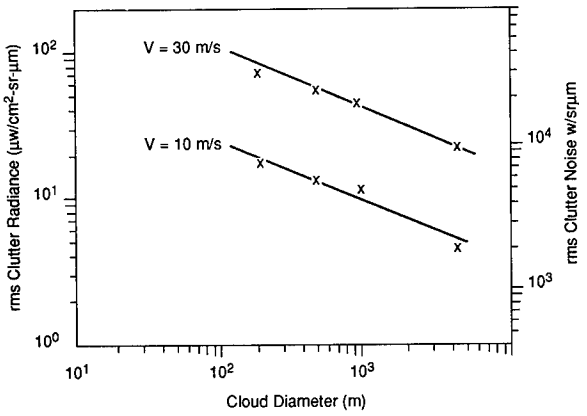

Fig. 4.157 Temporal clutter noise from clouds for a 200-m footprint.

4.3.8 Signal-to-Clutter Ratio (Conley[10])

A convenient figure of merit often used in IRST design is signal-to-clutter ratio, defined as

$$S/C = \frac{\int_{-\infty}^{\infty} T(f)\mathrm{MTF}(f)\, df}{x\left[\int_{-\infty}^{\infty} |\mathrm{MTF}(f)|^2 S(f)\, df\right]^{1/2}}, \tag{4.125}$$

where $T(f)$ is the target spectrum. For a point target, $T(f) = K$, $T(x) = K\delta(x)$, and $S(f)$ = clutter spectrum.

Optimization of signal-to-clutter ratio in a given background does not necessarily lead to maximum system sensitivity, that is, the ability to detect faint targets at long ranges. In practical IRST systems design there is a considered trade-off to be made with regard to maximizing signal-to-noise ratio for maximum target detection range or maximizing signal-to-clutter ratio for minimum false-alarm rates in structured backgrounds.

4.3.9 Starer Versus Scanner Clutter Performance

Spiro and Schlessinger[7] give the following expression for starer versus scanner clutter rejection performance:

$$\left(\frac{D_{\mathrm{st}}}{D_{\mathrm{sc}}}\right)^2 = \left(\frac{d_{\mathrm{st}}}{d_{\mathrm{sc}}}\right)\left(\frac{t_{\mathrm{sc}}}{t_{\mathrm{st}}}\frac{N_{\mathrm{sc}}}{N_{\mathrm{st}}}\right)^{1/2}\left(\frac{D^*_{\mathrm{sc}}}{D^*_{\mathrm{st}}}\right), \tag{4.126}$$

where

D_{st} = starer aperture diameter
D_{sc} = scanner aperture diameter
d = detector size
t = dwell time
N = number of TDI stages
D^* = specific detectivity of the detectors.

4.3.10 Probability of Detection and False-Alarm Rate

This topic is covered in considerable detail in Sec. 4.4. The approach to IRST system design often begins with a statement regarding the single scan or frame probability of detection P_d (given a certain target, background, environmental condition, etc.) *and* the maximum tolerable false-alarm rate (FAR) (given the absence of a target under the same condition). As stated previously, a detection is defined as a signal exceedance of a predetermined threshold. Given a certain noise characteristic, this threshold defines a false-alarm rate. Thus, P_d and FAR are related, and the specification of both uniquely determines the signal-to-noise ratio required of the system.

The IRST detection problem treated in this section consists of characterizing a target detection as a rectangular pulse immersed in white noise and passed through a matched filter, as shown in Fig. 4.158. The pulse duration will be taken to be the dwell time t_d defined previously, and the matched filter will have a bandwidth $\Delta\nu = 1/2t_d$.

The output rms noise current is

$$i_n = \left(\frac{w}{2T}\right)^{1/2} , \tag{4.127}$$

where w is the single-sided power spectral density of the input white noise (A^2Hz^{-1}). The classical expression for the average false-alarm rate is

$$\overline{\text{FAR}} = \frac{1}{2\sqrt{3}t_d} \exp\left[-\left(\frac{i_t^2}{2i_n^2}\right)\right] , \tag{4.128}$$

where i_t is the threshold current setting.

The probability of detection is approximately

$$P_d \approx \frac{1}{2}\left[1 + \text{erf}\left(\frac{i_s - i_t}{\sqrt{2}i_n}\right)\right] , \tag{4.129}$$

where i_s is the peak signal current. Note that P_d can be written as

$$P_d \approx \frac{1}{2}\left\{1 + \text{erf}\left[\frac{1}{\sqrt{2}}\left(\text{S/N} - \frac{i_t}{i_n}\right)\right]\right\} . \tag{4.130}$$

So, given i_n, the specified $\overline{\text{FAR}}$ determines i_t; *and* given P_d, i_t, and i_n, the S/N also is determined. The relationship between these quantities is graphically illustrated in Figs. 4.159 and 4.160.

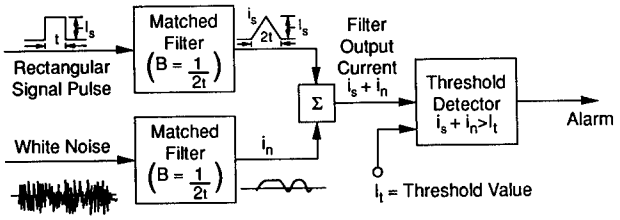

Fig. 4.158 Description of threshold detection process.

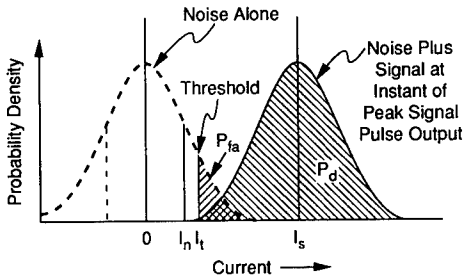

Fig. 4.159 Graphical relations between probability of detection P_d, probability of false alarm P_{fa}, and current threshold I_t, where I_n and I_s are the noise and signal currents, respectively.

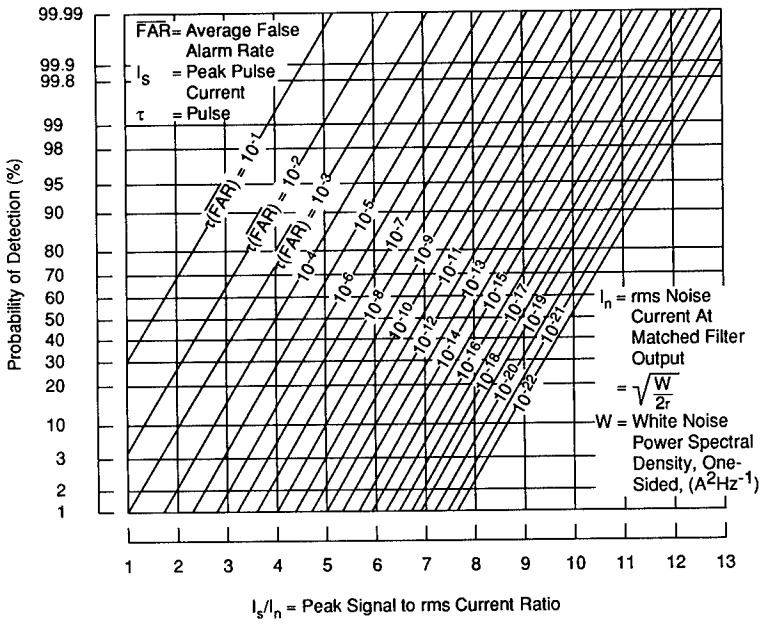

Fig. 4.160 Probability of detecting a rectangular pulse in white noise.[19]

4.4 IRST SIGNAL PROCESSING

The principal IRST technical challenges are tracking subpixel targets in moving clutter and additive noise and with a bipolar format, allowing targets to be above or below the immediate background level. In general, targets may exhibit both positive and negative contrasts with respect to the background.

Discrimination is the process of differentiating between target and (false target) background clutter. In IRST systems discrimination may be implemented through differences in signal amplitude or frequency, received IR spectrum, motion, or spatial characteristics. Differences can be detected in ways ranging from simple thresholding to sophisticated space-time correlations. All are generally employed in modern IRSTs.

Electrical filters are employed for two principal reasons: to filter unwanted random electrical noise arising from various sources within the focal plane and signal processors, and to filter components of the background clutter signal, as shown in Fig. 4.161. The literature on filter implementation is voluminous. The filters required in IRST systems depend on detailed considerations of target and background clutter characteristics and on focal-plane architecture. Reference 7 discusses several specific filter implementations in IRST systems. Finally, recursive filters may be employed in the tracking function to minimize the error in the predicted target trajectory.

The objective of the signal processor in the IRST system is the reliable determination of the presence of a target within the field of view in a highly structured background and the corresponding establishment of tracks. These backgrounds can give rise to false targets or false alarms, thus characterizing detection as background structure limited (BSL). This is distinct from BLIP, which refers to average background irradiance levels. The classic Neyman-Pearson criterion[20] applies to IRST: maximizing the probability of detection, given a tolerable false-alarm rate, is a powerful optimization criterion frequently used in IRST performance analysis.

4.4.1 Signal-Processing Algorithms (Maxwell and Kryskowski[21])

Significant technological advances have been made in the past ten years, particularly in the development of detector arrays and digital signal-processing electronics, that are being included in advanced IRSTs. These advances potentially give them high sensitivity, high resolution, long detection ranges for surveillance as well as fire control, and high clutter suppression capability for high P_d and low PFA.

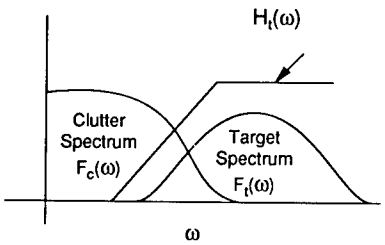

Fig. 4.161 The employment of a high-pass filter to increase the clutter-to-noise ratio.

The conventional way of thinking about an IRST is that it is an IR imaging device that provides a sequence of images in time. The simplest processing involves detection of the (unresolved) targets in each frame on the basis of its contrast. This is the process referred to as spatial processing. Spatial processing is a technique for estimating the background scene in the absence of a target so that the presence of a target can be inferred by excess contrast. In general, the target has some angular velocity relative to the background, and detections from the same target in a sequence of frames can be correlated to form a track. This processing is temporal processing but will be referred to as track-file processing. It is also referred to as velocity filtering. The combination of spatial processing and track-file processing is a "detect-before-track" type of algorithm. The spatial filtering and track-file algorithms are being used in systems today.

It is also very useful to view the sequence of images generated in time by the IRST as a three-dimensional data set. Signal-processing algorithms have been developed that use all of the data in the process of detecting the target. These algorithms use both the two-dimensional spatial characteristics and the third-dimensional temporal characteristic of the target to detect the target. Such an algorithm is a "track-before-detect" type algorithm in which there is no separable signal-processing component identifiable as track-file processing. These algorithms are in the class of advanced algorithms for long-range IRSTs requiring a very high degree of clutter suppression.

The multiband terminology will be used in reference to MWIR IRSTs employing several bands between 3 and 5.5 μm. Typically, three bands are used to discriminate between solar reflections, ambient backgrounds, and plumes. The basis for discrimination against clutter is that the solar reflections give a large response in the shortest band, the ambient backgrounds are comparable in all three bands, and the target gives a strong response in the longest band.

The multispectral terminology will be used in reference to the utilization of subbands within either or both of the MWIR and LWIR windows. The processing is similar to, and in principle the same as, that for the multiband algorithms, but the motivation is more driven by the power of signal processing with multiple bands and by the desire to obtain large clutter suppression with highly correlated background data that can be obtained simultaneously and in registration.

The polarization approach to clutter suppression is based on the difference in the polarization characteristics in the thermal IR from targets and from backgrounds. The phenomenology is different but the signal processing is very similar to the multispectral processing for two or three bands. The same advantages accrue from simultaneous collection and from attendant ease of registration.

It should be recognized that track-file processing could be included with multiband, multispectral, and polarization processing, and in fact a $(2N + 1)$-dimensional signal-processing algorithm could be envisioned consisting of the two spatial dimensions, N (spectral or polarization) bands of data, and one temporal dimension as a fully advanced track-before-detect algorithm.

4.4.1.1 Spatial Processing. Current and near-term IRSTs generally are configured with linear detector arrays. One-dimensional filtering implies a filtering of the temporal output of each detector as it scans from pixel to pixel

with an analog electronic filter, or a digital spatial filtering of each scan of each detector across the scene.

A large number of one-dimensional analog electronic filters are possible. All have a high-pass characteristic to pass the high-frequency content of an unresolved target and to block much of the low-frequency variation from the background clutter. Spatial filtering is frequently limited to one dimension for its simplicity and because it can be implemented with analog hardware. However, the designer may be constrained to one-dimensional processing because of uncontrollable nonuniformities across the array. Although the processing is one-dimensional, some two-dimensional processing can be effected (at least most easily conceptually) with digital hardware by eliminating clusters of detections in a single frame of imagery that cannot correspond to an unresolved target.

Two-dimensional processing provides significantly more clutter suppression, but this requires both digital hardware and reasonably high-quality arrays such that corrections can be made for detector nonuniformities.

A variety of one-dimensional and two-dimensional spatial filters have been utilized in target detection and clutter suppression studies. These include linear (high-pass) filters, differentiators, nonlinear filters such as the sub-median filter (median and subtract), filters optimized to the target signal such as the LMS filter, and linear matched filters (Wiener filters).

A generic IRST signal processor based on spatial filtering and track-file processing is shown in Fig. 4.162(a). Spatial filtering (or analog electronic

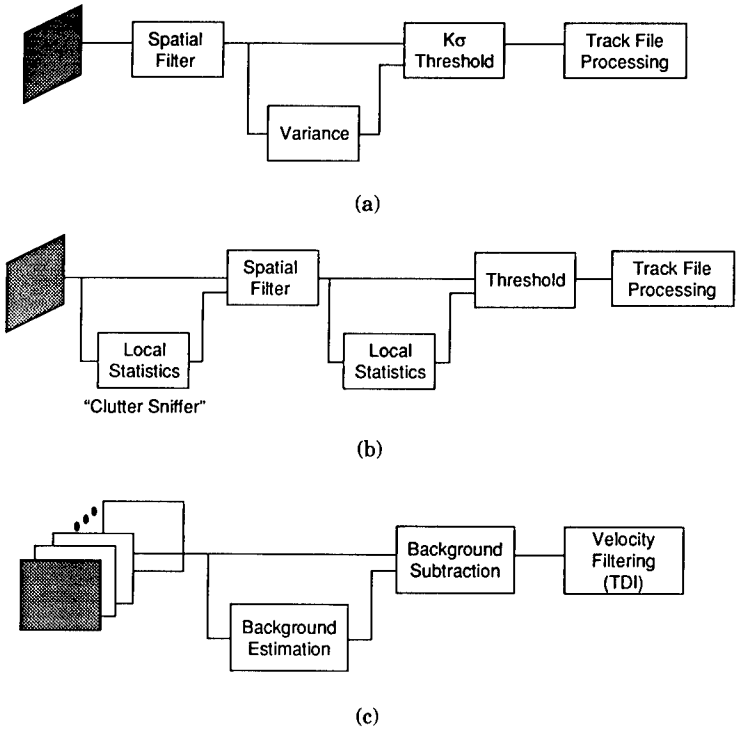

Fig. 4.162 Basic functions of a signal processor (after Ref. 7): (a) Constant false-alarm rate processor, (b) adaptive processor, and (c) space-time processor.

filtering) is the first step. Thresholding is the second step. The third step is track-file processing. The threshold is not generally a fixed threshold but is determined on the basis of the scene clutter level to maintain a more or less constant false-alarm rate (CFAR). This CFAR operation can be implemented with analog circuitry. Feedback varies the gain of a variable-gain amplifier, by averaging the "clutter" over a time that is comparable to a scan time, so that a fixed threshold later in the processing passes false alarms at a fixed rate that can be adjusted by the operator.

With digital-processing hardware it is advantageous and straightforward to use a much smaller window and to determine the clutter level locally. This does a much more effective job of obtaining CFAR performance across boundaries of regions of high clutter and regions of low clutter. The technique or processing step for determining the clutter level locally is usually referred to as the background normalizer. The background normalizer function is sometimes contained in a type of filtering referred to as double-gated filtering, wherein a decision about a pixel in the center of the window is made on the basis of the statistics of the data in a window about the center pixel.

Figure 4.162(b) shows the generic form of a more advanced spatial processor. This configuration is referred to as an adaptive processor and includes a "clutter sniffer" and a filter whose characteristics can be set by the output of the clutter sniffer, or a "filter bank" such that an appropriate filter can be selected for the clutter at hand. The background normalizer may be based on local variance or some other parameters determined by the clutter sniffer statistics in the local window to best maintain a CFAR.

4.4.1.2 Temporal Processing. Temporal processing is track-file processing for this discussion, and it generally follows the spatial processing described above. Simple track-file processing can be done by an observer and a display, or detections from sequential frames of data can be stored in digital memory and processed. These processors generally take the form of requiring several (e.g., two) detections in sequential frames within a small spatial window to initiate a track, and M detections in N frames in appropriately sized and positioned windows to detect and maintain a track. The digital track-file processor is generally limited in the number of track initiations and tracks that it can maintain, so that the performance of the spatial-processing detection algorithm is critical. The general form of this processor is shown in Fig. 4.162(c).

4.4.1.3 Spatial-Temporal Processing. It is convenient to view the data from an IRST as a stack of images in x, y, and t. The dimensions of the image stack are i, j, and k. In its simplest form the images are all the same in each frame. That is, the scene has not changed over the time period for collection of k frames of data, and the images in all frames are spatially registered. Under these conditions a sequence of $k - 1$ frames of data, formed by a frame-differencing operation between sequential frames of data, removes all of the background data from the static scene (except, in principle, detector noise times root two), leaving only a residual from the moving target. The residual from the moving target appears at a different spatial coordinate in each of the difference frames, and this constitutes the "target track." It is straightforward to threshold each difference frame and to do an M/N track-file processing.

There are many variations on the above theme, as will be pointed out. However, it is important to note that the potential degree of clutter suppression that is obtainable from frame differencing is much higher than from the one-dimensional and two-dimensional spatial processing described in the previous section. This is because spatial processing removes the low-frequency clutter from the scene that is unlike the target, but it does not remove that spatial-frequency content that is similar to that of the target. Even the best linear matched spatial filters are limited in their clutter suppression capability under ideal conditions of stationary Gaussian clutter. However, frame differencing (for static scenes and well-registered data) in principle removes all of the clutter.

The general form of the space-time processing algorithm is shown in Fig. 4.162(c). In the frame-differencing algorithm just described, the estimate of the background at time t is the scene at time $t - 1$. Under the assumed ideal conditions, the estimate is perfect except for the pixel(s) containing the target. A better estimate of the background might be made by averaging all of the images in the image stack. If the number of images is large (>10), the noise in the background estimate will be reduced by the square root of the number of scenes averaged, and the effect of the target on any one pixel will be diluted by a factor equal to the number of frames.

It has been suggested that the difference frames be thresholded and that track-file processing follow. This is equivalent to a binary time delay and integrate algorithm (TDI), and some improvement can be made by performing the TDI before thresholding. This is velocity filtering and may involve extensive computing for low-contrast targets.

A number of system considerations must be taken into account for the space-time processing to be fully effective. These considerations are

1. registration of images in the image stack
2. uniformity of detectors in the array
3. sampling in both space and time
4. target dynamics
5. scene dynamics
6. target contrast.

A main requirement for the simple frame-differencing type algorithms to remove the background clutter is that the frames be registered. The pointing stability that can be attained with today's IRSTs that employ spatial processing and track-file processing provides sufficient stability for the temporal processing required for track-file processing (perhaps stability to one or a few pixels). However, for frame-to-frame-differencing type temporal-processing algorithms, accuracies to the order of 1% of a pixel are necessary, and this cannot be achieved by stabilization alone. For an airborne IRST the platform is moving relative to a three-dimensional background, and the background is at varying range. The result is parallax-induced scene motion in the image plane of the IRST.

Hence, a crucial component of an IRST space-time processing algorithm is an algorithm to bring a time sequence of images into registration. There are a number of algorithmic approaches that have been developed for this purpose. The simplest of these uses an image-to-image correlation to determine the

displacement of one image with respect to the other and then resamples the second onto the grid of the first. Another approach operates on the sequence of difference images and forms an estimate of the displacement based on the scene gradients estimated from one or the other of the two images used to form the difference. Then the second image is resampled to the grid of the first. This is known as the gradient estimation (GEM) method. Another method, known as a subspace projection (SSP), considers the time-sampled data from each pixel a k- (k images) dimensional vector. The k vectors from all of the pixels span only a limited volume of the k-dimensional space because of constraints on the image displacements in the temporal stack of images. By projecting out the principal components in this k space it becomes possible to remove much of the motion between frames of data.

The development of the two-dimensional focal plane has provided much of the impetus for space-time processing for several reasons. In part it is because of the increased sensitivity achievable with more detectors, but it is also because the dimensionality of the image registration problem is very much constrained by the rigid focal plane. Much of the motion is of the form of an image displacement from one image to the next. Sensor motion also may introduce some rotation, and motions due to parallax likely will be uniform locally but not globally.

More robust registration algorithms are required to handle the parallax-induced motions. Under some conditions it may be sufficient to window the data and use one of the above registration algorithms locally. More sophisticated algorithms may segment the scene into components with common motion, perhaps radiometrically or by spatial processing and texture or other image-processing techniques. However, in principle it takes knowledge of the range to each pixel in the image, along with knowledge of the platform motion, to determine the motion of each pixel on the focal plane (required for resampling, registration, and background subtraction). There is current interest in developing algorithms that determine the range to each pixel in the scene from the data itself. These techniques are based on the concept of optical flow (all scene features move radially away from the velocity vector of the sensor platform) and are sometimes referred to as video moving target indicator (video MTI) algorithms.

Another registration technique involves Fourier transforms and phase correlation. This technique appears to provide a much sharper correlation peak than that obtained by correlating the original amplitude images.

4.4.1.4 Uniformity of Detectors in the Array. Some form of image registration is required for IRST space-time processing. Registration is a two-step process involving displacement estimation and resampling. The accuracy of the resampling is determined by noise in the images. In the resampling process nonuniformity of response between detectors contributes to the inaccuracy of the resampling process in the same way as detector noise. Most of the IR systems today are limited by clutter, and performance is seldom achieved that is limited by system sensitivity. The potential for space-time processing to achieve a very high degree of clutter suppression affords the opportunity to build higher-sensitivity systems and to achieve sensitivity-limited performance. However, it is no small matter to reduce the pattern noise (due to

detector-to-detector nonuniformities) to the sensitivity of the individual detectors. Responsivity variations (gains), offsets, nonuniform cooling, and $1/f$ noise all contribute to nonuniformities in response that have to be corrected over the array containing large numbers of detectors.

4.4.1.5 Sampling in Both Space and Time. Target motion relative to any background motion is the key to space-time processing. It is necessary to sample temporally at twice the single-pixel crossing time to avoid temporal aliasing effects that are manifest as time-varying target intensity effects. Spatial sampling is also very important in that the aliasing caused by any undersampling appears as noise in the resampling step of the registration algorithm. If linear arrays are used to generate the IRST images, it is desirable to use staggered arrays to avoid aliasing as well as multiple columns of detectors for TDI and increased sensitivity. The use of full two-dimensional arrays may necessitate a higher temporal sampling rate and some form of known fractional pixel displacement to avoid spatial aliasing.

4.4.1.6 Target Dynamics. The discussion of space-time processing thus far has centered on clutter suppression. For the IRST scenario the target rates of angular motion may be very small, and this implies long observation times. It is likely that advanced pointing and stabilization systems will be required to take full advantage of the opportunity afforded by today's focal-plane arrays and high sensitivity.

4.4.1.7 Scene Dynamics. Cloud scenes are dynamic rather than static scenes. An understanding of the dynamics of backgrounds, and especially clouds, is important to the specific design parameters and performance characteristics of an airborne IRST employing space-time processing. A good understanding of the dynamic characteristics of backgrounds is a requirement, and a variety of image-processing techniques are applicable to this problem.

4.4.1.8 Target Contrast. A frame-to-frame difference algorithm has been developed wherein the difference frames were thresholded for both positive and negative exceedances. The positive exceedances were "ANDed," the negative exceedances were "ANDed," and the results were "ORed" before track-file processing. Both positive and negative contrast targets contributed equally to the track-file processing algorithm. However, there is valuable information in the time-varying contrast as the target moves from one pixel to the next. Such a varying contrast can exist even for a target with a zero-average contrast by virtue of background obscuration. Spatial-temporal algorithms based on the contrast variation caused by the spatial variation of the background clutter currently are being evaluated for potential use in advanced systems.

The above issues of registration, array uniformity, sampling, target and scene dynamics, and target contrast impact all forms of space-time processing algorithms. The above discussion has focused on frame-differencing type algorithms, but there are a variety of other forms that accomplish the same type of result that may have a quite different implementation. Some of these involve IIR processing or Fourier transforming the spatial dimensions of the image stack, while others involve a full three-dimensional Fourier transform. Yet another implementation involves tailoring a three-dimensional filter in the

two spatial dimensions and one temporal dimension, and the velocity filtering is implicit in the nature of the temporal dimension of the filter.

4.4.1.9 Multiband Processing. Multiband systems in the MWIR have been used to reduce false-alarm rates in IRSTs as well as various tail warning systems. Sometimes the band that is sensitive to solar reflection is referred to as a guard band. The phenomenology behind the band selection is straightforward. For example, a three-band MWIR system might have one band between 3 and 4 μm, another a redspike band beyond 4.5 μm, and a third in between. Specular solar reflections clearly affect the short band most significantly, targets of interest affect the redspike band, and ambient graybody backgrounds affect all bands more or less equally. One simple processing scheme involves forming two ratios from the three bands by normalizing the short and long bands by the graybody band and discriminating targets from solar reflections based on the amplitudes of the band ratios. A similar band-ratioing technique has been established in geological remote sensing for detecting various soil compositions using three spectral bands in the LWIR based on known spectral emissivity differences. This is equivalent to the more general processing technique of treating the three band radiances from each pixel as a three-dimensional vector partitioning the three-dimensional space into target and nontarget regions.

Multiband IR systems also have been considered for applications in which the targets may appear in any of a variety of conditions. For example, high-altitude targets may be above most of the water vapor in the atmosphere. In this case an absorption band might be useful as a means of providing a uniform low-clutter background. On the other hand, a good window band would be necessary for situations with the target at low altitude.

4.4.1.10 Multispectral Processing. There is significant current interest in applying multispectral sensing techniques to the long-range IRST problem. One of the compelling motivations for considering a multispectral approach is that it is possible to collect data in several spectral bands nearly simultaneously and in near spatial registration. Near simultaneous collection avoids the parallax problems that make the registration associated with space-time processing difficult and complex, and the remaining registration problems are determined by the sensor and can be characterized and easily corrected.

Multispectral remote sensing is a mature technology that has been developed over the last 25 years and is widely used in the NASA airborne and satellite remote-sensing community. Much of the analysis has been based on statistical decision theory. However, most of the applications have been with spectral bands in the reflective portion of the spectrum (0.4 to 2.6 μm). An exception is the multispectral remote sensing done in the LWIR by the geological remote-sensing community.

It is only recently that thermal IR multispectral techniques have been seriously considered for IRST applications. Part of the recent interest arises from the fact that the signal processing required is very amenable to the theoretical treatments of classical signal processing. Although the multispectral techniques derived from statistical decision theory and signal-processing theory are the same, the emphases have been somewhat different in the reflective and thermal multispectral regimes. In the reflective regime there is consid-

erable variability because of the variable solar illumination, sun and view-angle effects, atmospheric scattering, etc. The emphasis has been to correct the data for these variations before processing. In the thermal infrared it is temperature variations that cause a large variability that tends to mask spectral variations caused by the emissivity differences that are of interest in discriminating targets from backgrounds. Different techniques are required to remove the effects of temperature from the data, and the band ratioing was mostly an ad-hoc and empirical technique.

Classical signal processing suggests that the N-spectral channels of data from each pixel be treated as an N-dimensional vector and that the likelihood ratio be used to discriminate between targets and backgrounds. The formalism is well known (and the same as that used for the statistically based multispectral processing in the reflective portion of the spectrum); however, the assumption is usually made that the data are multivariate Gaussian, which is not the case. One approach that has taken favor is to filter the data from each spectral channel with a high-pass spatial filter. This removes much of the scene inhomogeneity and tends to "Gaussianize" the data. The likelihood-ratio processing is then a matter of estimating the spectral noise covariance matrix and thresholding the log likelihood ratio.

Another technique (more directly like that used in the reflective multispectral regime) is to perform a principal component analysis on the N-dimensional multispectral data. In the thermal region of the spectrum there tends to be one principal component much larger than all the others. This principal component direction is associated with variations in temperature, and the others are associated with variations in spectral emissivity. The temperature variations can be removed (to a very large degree) by projecting the N-dimensional data onto an $(N - 1)$-dimensional subspace and removing the principal component direction. Temperature variations are the cause of much of the inhomogeneity, and the result of projection operation is to effectively "Gaussianize" the data. This technique is analogous to the well-known linear Fisher discriminant technique for two-dimensional data designed for application to non-Gaussian data.

Current efforts to apply multispectral techniques to the IRST problem have focused on the LWIR; however, there is no reason not to include the MWIR and the well-established phenomenological attributes of targets in the MWIR. There is little spectral emissivity data on targets and backgrounds, so that data must be acquired to assess the effectiveness of the multispectral approach. The potential payoff could be large by virtue of avoiding the registration processing required for space-time processing. At the same time it should be noted that the clutter-suppression potential for the multispectral techniques are likely to be limited by the spectral variations in emissivity created by nature and the differences between these and the targets of interest. It should be possible to counter spectral differences that may occur in targets today. On the other hand, the limit to the degree of clutter suppression attainable by space-time processing is limited by system sensitivity and by the accuracy of the registration algorithm, something that is under the control (and imagination) of the designer and is very difficult to countermeasure.

4.4.1.11 Polarization Processing. Polarization in the thermal IR arises from polarized emission. Many man-made target surfaces are smooth relative to 5

or 10 μm, whereas many natural materials are correspondingly rough. Most paints are smooth in the IR and are dielectric. Metals also tend to be smooth. They tend to be specular reflectors with polarized reflectances well described by the Fresnel equations. The polarized emittances are thus complementary to the Fresnel polarized reflectances (by the Kirchoff relation $R = 1 - E$). Polarization is a function of target surface geometry and view angle from the sensor to the target. Shallow view angles to horizontal target surfaces provide maximum polarization, so polarization is a candidate for clutter suppression for the IRST.

Typical polarizations from target surfaces are about 5% and many backgrounds are polarized at less than 1%. This suggests that an immediate factor of 5 in clutter suppression can be obtained just by sensing polarized radiance in the IRST. The sensor design considerations for a polarized sensor are very similar to those for a multispectral sensor with only two or three channels. A 5% polarization is comparable to the spectral contrast associated with a 5% change in spectral emissivity in one spectral band. A 5% polarized radiance is also comparable to the pixel-to-pixel spatial variation of unpolarized radiance that constitutes clutter in typical scenes.

The best IRST application of polarization is likely to be for targets against cloud and terrain backgrounds (as opposed to blue sky), where the unpolarized contrasts are low and the clutter is high. As with the multispectral IRST, the ultimate clutter suppression is dictated by nature rather than by the sensor/algorithm/processor designer, and more data are needed to assess the clutter-suppression potential for polarization.

4.4.2 Threshold Receivers: Detection

The treatment presented here closely follows an extensive treatment by Steinberg,[22] which begins with a discussion of elementary concepts in the detection of targets in uniform backgrounds and proceeds to more general cases of nonstationary background statistics and adaptive-threshold processors. In contrast to the Wiener spectrum approach,[18] as discussed in Secs. 4.2.2.10, 4.3.8, and 4.3.9, the methodology presumes an arbitrary but deterministic background input. A statistical description of a specific processor performance within a certain class of backgrounds can be accomplished via Monte Carlo techniques.

4.4.2.1 Probability of Detection and False-Alarm Rate. Detection and false alarms represent exceedances of a threshold by the signal and noise, respectively. Analytical treatment of these events is conventionally a statistical "level-crossing" problem,[23] the probability of detection P_d is functionally defined as the probability that the system threshold will be exceeded in some time interval given hypothesis H_1 (a target present).

Similarly, the probability of false alarms P_{fa} is the probability that the system threshold will be exceeded given hypotheses H_0 (a target absent). Thus,

$$P_d = \int_{t_s} \mathring{M}_a(t)\, dt\} H_1 \ , \tag{4.131}$$

$$P_{\text{fa}} = \int_{t_s} \mathring{M}_a(t)\, dt\} H_0 \ , \tag{4.132}$$

where $\mathring{M}_a(t)$ is the level or threshold-crossing rate. The assumption implicit in Eq. (4.131) is that the likelihood of two or more target-induced crossings in interval t is small and that background-induced crossing during t in Eq. (4.132) can be ignored. To ground the above expression in system terms, t_s will be defined as a scan or frame time; thus, P_d and P_{fa} are single scan or frame probabilities. The false-alarm rate is thus

$$\text{FAR} = \frac{P_{\text{fa}}}{t_s} = \dot{M}_a \ . \tag{4.133}$$

4.4.2.2 Sensor Output Current or Voltage Statistics. Given a *uniform scene*, the average sensor output current M_y is shot-noise limited and is given as

$$M_y = H(0)M_x \ , \tag{4.134}$$

where M_x is the average detector noise current (from shot noise) and $H(0)$ is the filter transfer function at zero frequency. The variance in the current and its derivative [assuming $H(\nu) = 1$] is

$$\sigma_y^2 = 2eM_x\int_0^\infty |H(\nu)|^2 \, d\nu = 2eM_x\Delta\nu \ , \tag{4.135}$$

$$\sigma_{\dot{y}}^2 = (2\pi\nu)^2\sigma_y^2 \ , \tag{4.136}$$

where

$\Delta\nu$ = noise bandwidth of $H(\nu) = \int_0^\infty |H(\nu)|^2 \, d\nu$
M_x = $L_B\Omega A T_o R$, where L_B is the scene radiance at the aperture, Ω is the field of view of the sensor, A is the area of the aperture, T_o is the transmission of the optics, and R is the current responsivity of the detector.

Given a *nonuniform scene*, the average detector current and variance is somewhat more complex and is given as

$$M_x = K_o R\int \text{MTF}(f)H_d(f)E(f)\exp(i2\pi f\,\bar{v}t)\, df \ , \tag{4.137}$$

where

K_o = $\pi T_o/(2f/\#)^2$
T_o = optics transmission
f = spatial frequency
MTF = modulation transfer function of the optics
$H_d(f)$ = spatial transfer function of the detector
$E(f)$ = Fourier transform of the scene irradiance distribution
$\bar{v}$ = focal-plane scanning velocity.

The variance of the current is written by reference to the scene power spectral density defined in Secs. 4.3.8 and 4.3.9:

$$\sigma_y^2 = \left[2\int_0^\infty S(f)\,df\right]\Omega A T_o R \ . \tag{4.138}$$

4.4.2.3 Level-Crossing Statistics. Given a differentiable stochastic process $X(t)$, the level-crossing rate is[25]

$$\mathring{M}_a = f_x(a)E\{|\mathring{X}(t)||X(t) = a|\} \ , \tag{4.139}$$

where $f_x(a)$ is the probability density function of the process $X(t)$ with derivative $\mathring{X}(t)$ evaluated at level A, and E is the expectation operator.

As expected, the two principal difficulties with the above expressions are the determination of f_x and the evaluation of the expectation integrals.

Example. Given a Gaussian zero mean stationary process $X(t)$ with autocorrelation $R(t)$, the level-crossing rate is

$$\mathring{M}_a = \frac{1}{\pi}\left(\frac{-R''(0)}{R(0)}\right)^{1/2} \exp\left[\frac{-a^2}{2R(0)}\right] \ , \tag{4.140}$$

$$(\mathring{M}_a)^2 = \frac{1}{\pi^2}\frac{\displaystyle\int_{-\infty}^{\infty}\omega^2 s(\omega)\,d(\omega)}{\displaystyle\int_{-\infty}^{\infty}S(\omega)\,d(\omega)} \exp\left[\frac{-a^2}{R(0)}\right] \ , \tag{4.141}$$

where $S(\omega)$ is the power spectral density of the process $X(t)$ with autocorrelation $R(t)$.

For an ideal low-pass filter where $S(\omega) = 0$ for $|\omega| > \omega_{co}$,

$$\mathring{M}_a = \frac{\omega_{co}}{\sqrt{3}\pi} \exp\left[\frac{-a^2}{2R(0)}\right] \ . \tag{4.142}$$

4.4.2.4 Generalized Adaptive-Threshold Processor Architecture (Steinberg[22]). Consider a generalized processor to which a question is posed: does the signal exceed the threshold given H_1, where we have allowed for a threshold level that is itself derivable from the input signal and a nonstationary Gaussian background? This is known as an adaptive-threshold processor.

In terms of the above quantities, a complicated but exact expression for the mean crossing rate is

$$\overline{\mathring{M}}_a = \left[\frac{\sigma_{\dot{y}}(t)}{\sigma_y(t)}\right](1 - r^2)^{1/2}\phi(\mu)[\phi(p) + p_1\Phi(p)] \ , \tag{4.143}$$

where

$$\phi(X) = \frac{1}{\sqrt{2\pi}} \exp\left(\frac{-X^2}{2}\right) \ , \tag{4.144}$$

$$\Phi(X) = \int_{-\infty}^{X} \phi(X)\, dX \ , \tag{4.145}$$

$$p = [\sigma_{\mathring{y}}(1 - r^2)^{1/2}]^{-1}[M_{\mathring{y}}(t) + r\mu\sigma_{\mathring{y}} - \mathring{y}_0\, U(\mathring{y}_0)] \ , \tag{4.146}$$

$$p = \begin{cases} p_0, \mathring{y}_0 < 0 \\ p_1, \mathring{y}_0 > 0 \end{cases} , \tag{4.147}$$

$$U(\mathring{y}_0) = \begin{cases} 0, \mathring{y}_0 \le 0 \\ 1, y_0 > 0 \end{cases} , \quad r = \frac{\mathring{\sigma}_y(t)}{\sigma_{\mathring{y}}(t)} \ , \tag{4.148}$$

$$\mu = \frac{y_0 - M_y(t)}{\sigma_y(t)} \ , \tag{4.149}$$

and where

$$M_y(t) = h(t)*M_x(t) \ , \tag{4.150}$$

$$M_{\mathring{y}}(t) = \mathring{h}(t)*M_x(t) \ , \tag{4.151}$$

$$\sigma_y^2(t) = \langle y_0(t) - M_y(t)\rangle = qh^2(t)*\langle I(t)\rangle \ , \tag{4.152}$$

$$\sigma_{\mathring{y}}^2(t) = \langle \mathring{y}_0(t) - M_{\mathring{y}}(t)\rangle = q[\mathring{h}(t)]^2*\langle I(t)\rangle \ , \tag{4.153}$$

where

$y_0, \mathring{y}_0$ = threshold and threshold derivative
$y(t)$ = postdetection detector current
$h(t)$ = filter impulse response function
q = electronic charge
$*$ = convolution operator.

Steinberg[22] shows that the assumption for nonstationary Gaussian statistics for the filtered output current is justifiable for typical sensor parameters and background radiances.

Example. Consider the case of uniform scenes and constant thresholds. It follows that

$$M_{\mathring{y}}(t) = \sigma_y(t) = \mathring{y}_0 = 0 \text{ and } r = 0 \ , \tag{4.154}$$

so that

$$\dot{M}_a = \frac{\sigma_{\mathring{y}}(t)}{\sigma_y(t)} \frac{1}{\sqrt{2\pi}} \phi(\mu) \ . \tag{4.155}$$

This expression is equivalent to Eq. (4.142) and Rice's original expression for P_d appropriate for zero mean Gaussian noise sources since

$$\mathring{M}_a = \frac{\sigma_{\dot{y}}(t)}{\sigma_y(t)} \frac{1}{\sqrt{2\pi}} \left[\frac{1}{\sqrt{2\pi}} \exp\left(\frac{-\mu^2}{2} \right) \right] , \tag{4.156}$$

where

$$\mu = \frac{y_0}{\sigma_y(t)} , \tag{4.157}$$

so

$$\mathring{M}_a = \frac{\sigma_{\dot{y}}(t)}{\sigma_y(t)} \frac{1}{2\pi} \exp\left(\frac{-y_0^2}{2\sigma_y^2} \right) , \tag{4.158}$$

$$\sigma_{\dot{y}}(t)^2 = -R''(0), \quad \sigma_y(t)^2 = R(0) , \tag{4.159}$$

$$a = y_0 . \tag{4.160}$$

This expression is one-half the crossing rate of Eq. (4.142) because we are only considering positive-going crossings.

Example. Consider a simple adaptive-threshold receiver, as shown in Fig. 4.163, where $H_1(f) = \exp(-i2\pi f\tau_d)$, and τ_d introduces a delay. In this case the threshold current statistics become

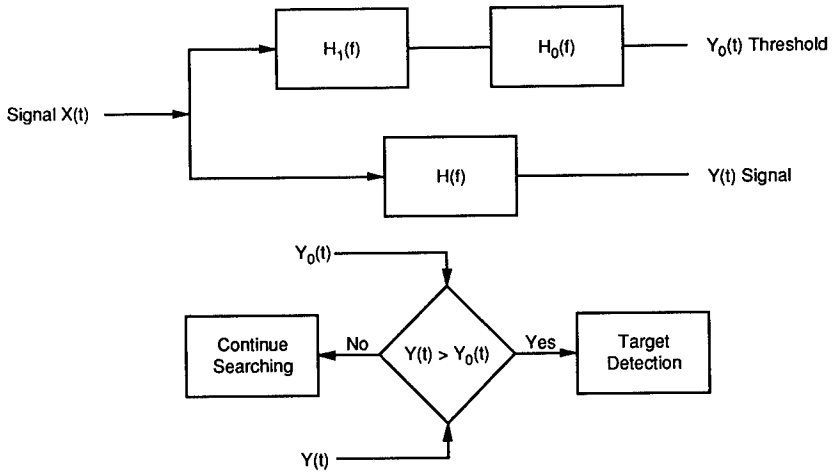

Fig. 4.163 A simple adaptive-threshold processor.

$$M_{y0}(t) = Kh_0(t - \tau_d)*M_x(t) \ , \tag{4.161}$$

$$M_{\mathring{y}0}(t) = \mathring{M}_{y0}(t) \ , \tag{4.162}$$

$$\sigma^2_{y0}(t) = kh^2_0(t - \tau_d)*M_x(t) \ , \tag{4.163}$$

$$\sigma^2_{\mathring{y}0}(t) = K[\mathring{h}_0(t - \tau_d)]^2*M_x(t) \ . \tag{4.164}$$

An approximation to Eq. (4.143) is given as

$$\mathring{M}_a(t) \approx \mathring{M}_{a0}(t) \exp\left[\frac{-\mu^2(t)}{2}\right] \ , \tag{4.165}$$

where

$$M_{a0}(t) = \frac{1}{2\pi}\left[\frac{\sigma^2_{\mathring{y}} + \sigma^2_{\mathring{y}0}}{\sigma^2_y + \sigma^2_{y0}}\right]^{1/2} \ , \tag{4.166}$$

$$\mu^2(t) = \frac{(M_{y0} - M_y)^2}{\sigma^2_y + \sigma^2_{y0}} \ . \tag{4.167}$$

When $M_x(t)$ is slowly varying with respect to $h(t)$, $\mathring{M}_{a0}(t) = \mathring{M}_{a0}$, so that Eq. (4.131) becomes

$$P_d = \mathring{M}_{a0}\int_0^{T_s} \exp\left[\frac{-\mu^2(t)}{2}\right] dt \ . \tag{4.168}$$

Example. For a *fixed-threshold* processor,

$$\sigma_{y0} = \sigma_{\mathring{y}0} = 0 \ , \quad M_{y0} = y_0 \ ; \tag{4.169}$$

thus,

$$\mathring{M}_a(t) = \frac{1}{2\pi}\frac{\sigma_{\mathring{y}}}{\sigma_y} \exp\left[\frac{-\mu^2(t)}{2}\right] \ , \tag{4.170}$$

$$\mu(t) = \frac{y_0 - M_y}{\sigma_y} \ , \tag{4.171}$$

where y_0 is the fixed-threshold current value.

When $M_x(t)$ is slowly varying compared to $h(t)$,

$$\mathring{M}_{a0} = \left[\frac{1}{\Delta\nu}\int_0^\infty \nu^2|H(\nu)|^2 \, df\right]^{1/2} = (\Delta\nu)_{\text{rms}} \ . \tag{4.172}$$

In a *uniform background* Eq. (4.166) becomes

$$P_d = (\Delta\nu)_{\text{rms}} \exp\left[\frac{-\mu^2(t)}{2}\right] T_f \ , \tag{4.173}$$

where T_f is frame time as defined previously. This again is Rice's expression, which expresses the probability of detection of a fixed-threshold processor in a perfectly uniform background.

4.4.2.5 Adaptive-Threshold versus Fixed-Threshold Processors. As shown in Fig. 4.164, a fixed-threshold (FT) processor suffers a false alarm whenever the peak clutter amplitude exceeds the threshold, whereas the peak target amplitude is less than threshold. The performance is background structure limited (BSL). Quantum noise is insignificant. Given a properly chosen filter transfer function, most background crossings can be eliminated, as shown in Fig. 4.165, using an adaptive threshold. In this instance the IRST is quantum noise limited, a preferable mode of operation.

Example. Uniform Scenes of Known Brightness. Adaptive-threshold (AT) performance is superior to FT only when the background scene is nonuniform. The AT false-alarm rate is greater than the FT rate in scenes of uniform and known brightness.

A uniform background false-alarm penalty FAP is defined as

$$\text{FAP} \triangleq 10 \log\left(\frac{\text{FAR}_{\text{AT}}}{\text{FAR}_{\text{FT}}}\right) \quad [db] \ , \tag{4.174}$$

given equal target detection sensitivities.

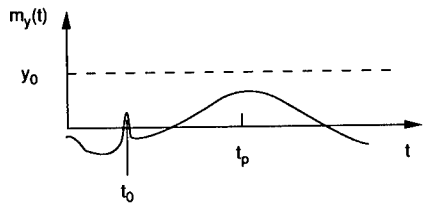

Fig. 4.164 A critical shortcoming of fixed-threshold processing. The slowly varying maximum centered at t_p has its origin in the nonuniform background scene. The narrower peak at t_0 is due to a target. The likelihood of a false alarm grows rapidly as the threshold level y_0 is reduced. There is no way for the constant-threshold processor to detect the target peak at t_0 without also incurring a false alarm arising from the clutter peak centered at t_p. A plot of the threshold-crossing rate $m_i(t)$ corresponding to this figure would show that the probability of a threshold crossing, and hence a false alarm, is far greater at time t_p than at any other time, since t_p is a time of closest approach.

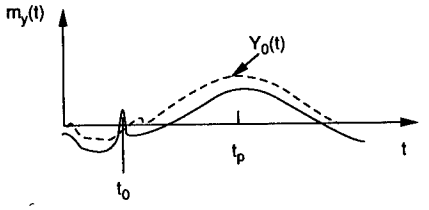

Fig. 4.165 An important advantage of adaptive-threshold processing. The mean current $m_y(t)$ is the same as for Fig. 4.164. The adaptive threshold $Y_0(t)$ accurately tracks the slowly varying background signal but not the more rapidly varying target signal. Thus, target detection is assured, and the probability of a false alarm is kept acceptably small. As contrasted with the situation of Fig. 4.164, the probability of a false alarm is now no greater in the neighborhood of time t_p than at any other time.

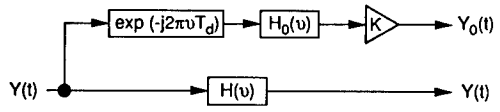

Fig. 4.166 A simple adaptive-threshold scheme. The transfer function $\exp(-j2\pi\nu T_d)$ introduces a delay of T_d seconds, ensuring decorrelation of the random processes $Y(t)$ and $Y_0(t)$.

Example. The FAP of the simple adaptive-threshold scheme shown in Fig. 4.166 where $H_1(t)$ is defined as

$$H_1(t) = \exp(-i2\pi\nu\tau_d) \tag{4.175}$$

is given as

$$\text{FAP} = 2.17\left(\frac{\alpha}{1+\alpha}\right)\left[\frac{M_{y0} - M_y}{\sigma_y}\right]^2 + 5\log_{10}[1 - \alpha(1-\alpha)] , \tag{4.176}$$

where

$$\alpha = \frac{\Delta\nu_0}{\Delta\nu} \tag{4.177}$$

corresponding to $H(\nu)$ and $H_0(\nu)$. Suppose

$$\frac{M_{y0} - M_y}{\sigma_y} = 5 \quad \text{and} \quad \alpha = \frac{1}{2} ;$$

then

$$\text{FAP} = 17.46 \text{ db} ,$$

a considerable degradation in performance.

4.4.2.6 TDI Compensation for FAP (Spiro and Schlessinger[7]). In the case of time delay integration employing N stages as described in Sec. 4.3.1, it can be shown that

$$\text{FAP}_{\text{TDI}} = \left(\frac{1 + \alpha - N}{\alpha}\right)\text{FAP} ; \tag{4.178}$$

thus, the FAP can be decreased by using TDI in uniform scenes. Alternatively, the FAR can be held constant with increasing N by making $\mu(t) \propto 1/N^{1/2}$. IRST performance improves monotonically as the number of TDI stages. Since the noise variance increases with scene radiance, bright scenes occasion decreased target detection sensitivity and/or increased false-alarm rate. TDI effectively diminishes the variance and lowers the FAR.

4.4.2.7 Constant False-Alarm-Rate Receiver (CFAR). The signal processor in an adaptive-threshold receiver establishes the threshold level as some function of the input signal by definition. A simple version of this scheme is shown in Fig. 4.167, whereby the threshold was established by a simple time delay and scaling transfer function. Alternatively, we can regard the generation of $y_0(t)$ as an estimation process where the mean video signal and quantum-noise estimation are components of the total estimate, as shown in Fig. 4.168. Thus,

$$y_0(t) = \hat{M}_y(t) + K\hat{\sigma}_y(t) \ , \tag{4.179}$$

where $\hat{M}_y$ and $\hat{\sigma}_y$ are estimates of M_y and σ_y, respectively. It follows from Eqs. (4.167) and (4.179) that

$$\mu(t) = K\left(\frac{M_{\hat{\sigma}y}}{\sigma_y^2 + \sigma_{\hat{y}}^2}\right) + \frac{M_{\hat{m}y} - M_y}{\sigma_y^2 + \sigma_{\hat{y}}^2} \ . \tag{4.180}$$

Generally, the IRST scenario renders the video processor the more dominant consideration, and hence the quantum-noise estimator will be disregarded.

The condition $\mu(t) \approx K$ with no target present is equivalent to the threshold crossing rate being independent of time. By definition this is a CFAR processor. In this case Eq. (4.168) becomes

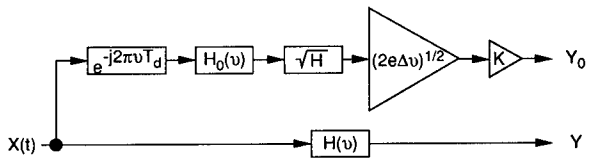

Fig. 4.167 Candidate processor structure that achieves constant-false-alarm-rate (CFAR) performance against all spatially uniform scenes regardless of brightness. Realization of $H_0(\nu)$ requires either true dc response or dc restoration. Comparing this figure with Fig. 4.166 shows that the mean video has been estimated as having a zero value. A unique feature of this processor is that the expected value of σ_y is equal to the rms value of $Y(t)$.

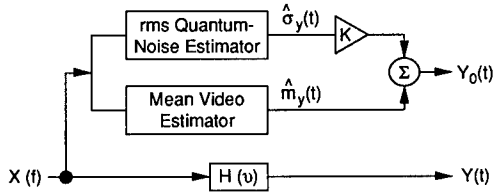

Fig. 4.168 Generic structure of the signal processors considered in this section. The expected value and rms value of the video signal $Y(t)$ are denoted as $m_y(t)$ and $\sigma_y(t)$, respectively. The signals $\hat{m}_y(t)$ and $\hat{\sigma}_y(t)$ are estimates for $m_y(t)$ and $\sigma_y(t)$. The adaptive-threshold constant K is the gain of an ideal amplifier. A target's presence is declared (rightly or wrongly) whenever the video signal $Y(t)$ exceeds the threshold signal $Y_0(t)$.

$$P_{\text{fa}} = (\text{FAR})\, T_f = \mathring{M}_{j0} \exp\left(\frac{-K^2}{2}\right) T_f \ , \tag{4.181}$$

where $K = (y_0 - M_y)/\sigma_y$.

The CFAR processor is a nonrealizable ideal. The estimation process is never perfect.

Example: FT Processor in Uniform Scenes of Unknown Brightness. Assume $H(0) = 0$; thus,

$$\text{FAR} = (\Delta\nu)_{\text{rms}} \exp\left[-\frac{1}{2}\left(\frac{y_0}{\sigma_y}\right)^2 \right] . \tag{4.182}$$

The current variance is proportional to scene radiance from Eq. (4.135):

$$\sigma_y^2 = \text{cM}_x \ . \tag{4.183}$$

Suppose we choose $y_0 = 8$, $\sigma_{\text{yc}} = 8(CM_{\text{xc}})^{1/2}$, where M_{xc} is the radiance of the scene used to initially calibrate the IRST and σ_{yc}^2 is the corresponding variance; then

$$\text{FAR} = \text{FAR}_c \exp\left[32\frac{(M_x - M_{\text{xc}})}{M_x} \right] , \tag{4.184}$$

where FAR_c = calibration value:

$$\text{FAR}_c = (\Delta\nu)_{\text{rms}} \exp(-32) \ . \tag{4.185}$$

If M_x increases by 20%, then $M_x = 1.2M_{\text{xc}}$ and the false-alarm rate increases by a factor of 200.

Example: AT Processor in Uniform Scenes of Unknown Brightness. For the processing structure shown in Fig. 4.167,

$$\sigma_{yy0}^2 = \sigma_y^2(1 + \alpha) \ , \tag{4.186}$$

$$\sigma_{\mathring{y}\mathring{y}0}^2 \approx \sigma_{\mathring{y}}^2(1 + \alpha^3) \ , \tag{4.187}$$

where α is defined by Eq. (4.177) and

$$\sigma_{yy0}^2 = \sigma_y^2 + \sigma_{y0}^2 \ , \tag{4.188}$$

$$\text{FAR} = (\Delta\nu)_{\text{rms}}\left(\frac{1 + \alpha^3}{1 + \alpha}\right)^{1/2} \exp\left\{\frac{-1}{2(1 + \alpha)}\left[\frac{M_{y0} - M_y}{\sigma_y}\right]^2\right\} . \tag{4.189}$$

Given $H(f)$ is bandpass such that $H(0) = 0$, then $M_y = 0$ from Eq. (4.134) and $M_x = H_0(f) = H_0(0) = 1$, $M_{y0} = KH_0(0)$, $M_x = KM_x$, and

$$\left[\frac{M_{y0} - M_y}{\sigma_y}\right]^2 = K^2\left[\frac{M_x^2}{2\Delta\nu M_x}\right] . \tag{4.190}$$

So the exponential argument in Eq. (4.189) is proportional to scene radiance, and thus the FAR of the AT processor as in the FT processor strongly depends on scene brightness. The architecture shown in Fig. 4.168 remedies that problem. Thus,

$$Y_0(t) = K\hat{\sigma}_y(t) \quad \text{and} \quad M_{\hat{y}}(t) = 0 . \tag{4.191}$$

It follows that

$$\mu(t) = K\left(\frac{M_{\hat{\sigma}y}}{\sigma_{yy0}}\right) , \tag{4.192}$$

where σ_{yy0} is defined by Eq. (4.188).

It can be shown that

$$M_{\hat{\sigma}y} = \sigma_y \text{ (unbiased)} , \tag{4.193}$$

$$\sigma_{yy0}^2 = \sigma_y^2\left[1 + K^2\left(\frac{\sigma_{\hat{\sigma}y}}{\sigma_{yy0}}\right)\right] . \tag{4.194}$$

Steinberg[22] shows that

$$\frac{M_{\hat{\sigma}y}}{\sigma_{yy0}} \approx 1 ; \tag{4.195}$$

thus,

$$\mu(t) \approx K , \tag{4.196}$$

$$\text{FAR} = (\Delta\nu)_{\text{rms}} \exp\left(\frac{-K^2}{2}\right) . \tag{4.197}$$

Thus, the false-alarm rate is independent of the brightness level in this case. Although the $Y(t)$ and $Y_0(t)$ were both assumed Gaussian random variables, the square-root device ensures that $Y_0(t)$ is not. However, Steinberg[22] shows that a more rigorous treatment of this problem under the conditions herein would not yield significantly different results.

4.4.2.8 Slowly Varying Structured Backgrounds. Qualitatively, a slowly varying background is defined such that all objects in the field of view are much larger than a single pixel in extent. The time variations of $M_x(t)$ are slow compared to $h(t)$. $M_x(t)$ is not "target-like." In the case where $H(\nu)$ = bandpass limited, $H(0) = 0$, and $H'(0) = 0$, using a three-term Taylor expansion for $M_x(t)$ it can be shown that

$$M_y(t) \cong \frac{1}{8\pi^2} H''(0)\ddot{M}_x(t) \ . \tag{4.198}$$

From Eq. (4.135),

$$\sigma_y^2(t) \cong 2e\Delta\nu M_x(t) \ , \tag{4.199}$$

and, as previously stated,

$$M_{\hat{\sigma}y} = \sigma_y(t) \ ; \tag{4.200}$$

thus,

$$M_{y0}(t) \cong k m_{\hat{\sigma}y}(t) \cong K(2e\Delta\nu)^{1/2} M_x^{1/2}(t) \ . \tag{4.201}$$

4.4.3 Discrimination

4.4.3.1 Spectral Discrimination (Williams[24]). This consideration in IRST design on target and background phenomenology was first discussed in Sec. 4.2. Certain spectral differences between the expected target and background may naturally occur that aid the discrimination process. A more detailed discussion begins with a presentation of spectral contrast in the form of spectral irradiance examples, for various backgrounds and hypothetical targets, shown in Fig. 4.169. It may be possible to select two spectral bands below and above the CO_2 "notch." The ratio of energy between these two bands (defined as the *color ratio*) will be consistently different, for example, a sunlit cloud compared with the threat. The two requisites in this procedure are (1) selection of two bands where the target variation is minimum and the background is maximum (or vice versa) and (2) sufficient dynamic range in the system to enable the first requisite.

The color ratio of the two chosen bands for a sunlit cloud is shown in Fig. 4.170. Four conclusions can be drawn.

1. For the indicated spectral bands the color ratio stays relatively constant over a four-to-one variation in visibility and a ten-to-one variation in range. This implies that spectral discrimination may not need to be adaptive and does not require weather or range data inputs.
2. The dynamic range of the system must be about 35 to 40 dB in irradiance (70 to 80 dB in video signal processing) to successfully process the spectral information.
3. The color ratio for sunlit clouds is less than one-tenth of the color ratio for the hypothetical threat. This means that spectral discrimination can be extremely effective against sunglint clutter without significantly decreasing the threat detection.
4. The color ratio for nonsolar ground clutter (from a shoreline, for example) is not significantly different from the color ratio for the threat. Spatial and temporal processing must be used in conjunction with spectral processing to reject the entire range of clutter inputs.

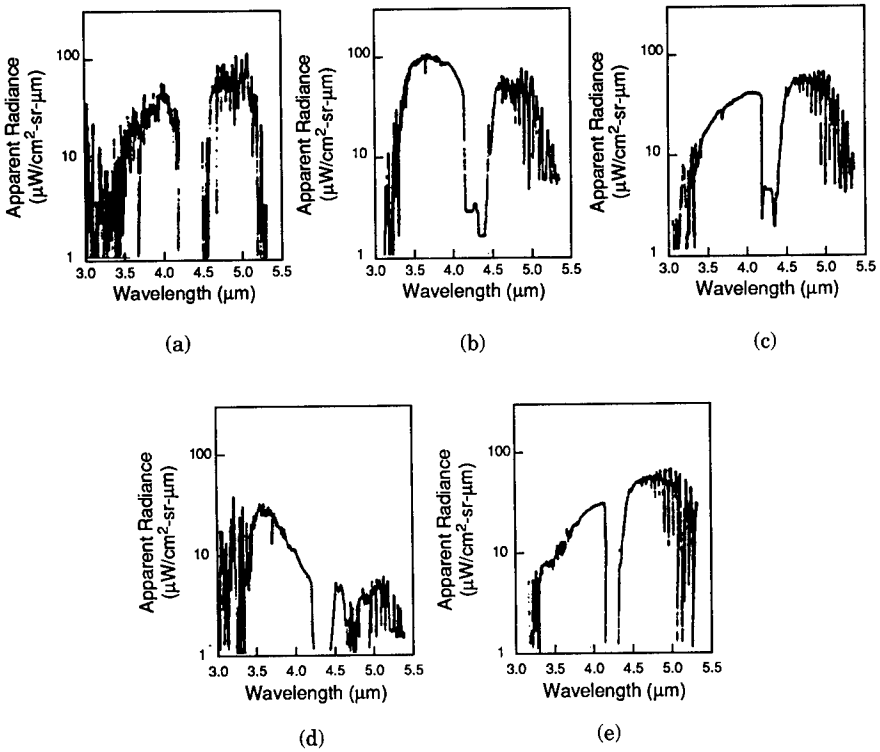

Fig. 4.169 Spectral contrast signatures for various materials[24]: (a) hypothetical threat, (b) sunlit cloud against blue sky, (c) dirt against foliage, (d) sunlight or water, and (e) sunlit rock against fog.

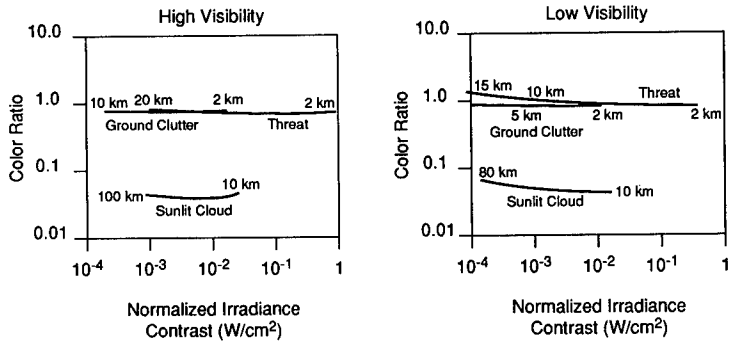

Fig. 4.170 Color ratio versus contrast and range (two-color system) for a hypothetical threat and sunlit cloud.[24]

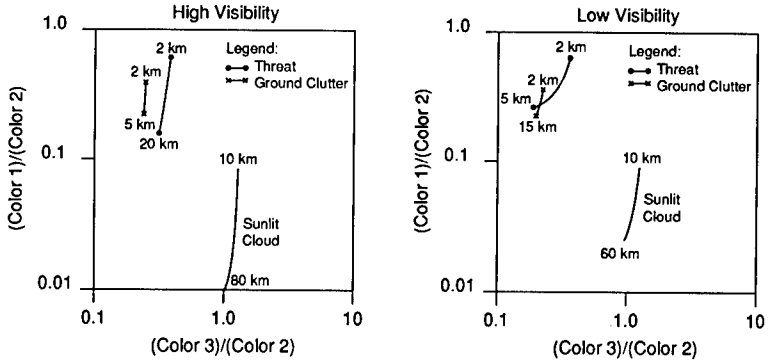

Fig. 4.171 Color ratio versus contrast and range (three-color system).[24] Compare with Fig. 4.170.

This process can be extended to three-color or N-color discriminants with an attendant increase in complexity, as shown in Fig. 4.171; the background source was ground clutter, which was not effectively discriminated against, as shown in the previous two-color-system example. Note that a modest improvement in ground-clutter discrimination was obtained. This technique is equivalent to classic multispectral remote sensing.

4.4.3.2 Spatial Discrimination (Williams[24]). The usefulness of spatial discrimination is shown in Fig. 4.172. In the upper left of the figure, the hypothetical threat is in a benign environment and no clutter discrimination is necessary. In the lower left, the same signal is viewed against earth background. A spatial filter matched to the width of a point source impulse response

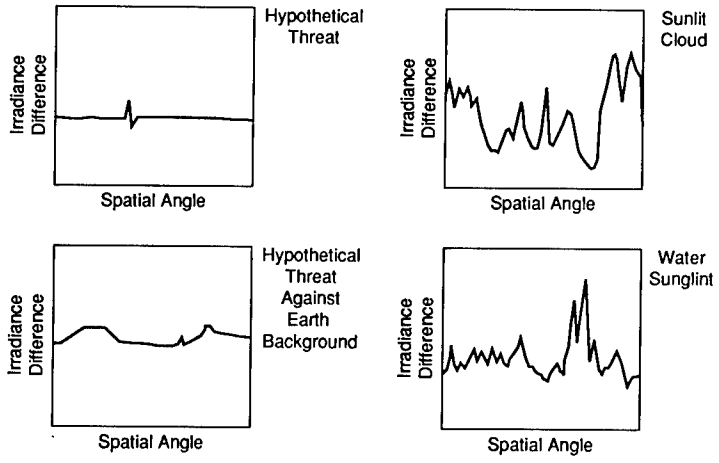

Fig. 4.172 Spatial discrimination.[24]

will be very effective against the gentle (low-frequency) hump to the left of the threat and moderately effective against the more pronounced hump to the right of the impulse. In light clutter regions, spatial discrimination is quite effective.

The two traces on the right of the figure illustrate one of the major problem areas for spatial discrimination. Bright sunlit objects can have numerous point-like characteristics resulting in many false alarms if no other discrimination techniques are used. However, even in heavy clutter, spatial discrimination can serve as a useful prefilter to select only point-like objects for further processing. The dynamic range and linearity of the spatial processor must be adequate to pass the characteristics used in such processing. No hypothetical threat is present in either of the two right-hand traces in Fig. 4.172.

4.4.3.3 Temporal Discrimination. This discriminant is based on the differing temporal characteristics of the target versus background, for example, as a function of range closure where the target signal amplitude is increasing rapidly and the background is substantially constant. This difference can be accentuated by observation of the temporal variation in two or more spectral bands.

4.4.3.4 Motion Discrimination. One of the most effective discriminants in IRST is motion of the target relative to the background. Ideally, a moving target of subpixel dimensions and intensity can be detected by background subtraction techniques whereby successive "frames" in memory are subtracted, leaving only the target signal or variants thereof. Multiple differencing is also extensively employed. This process is known as multiple-stage transversal filtering or n'th-order differencing. In practice, this procedure is complicated by frame-to-frame registration problems arising from sensor jitter and by the correlation of time of the background clutter influenced by motion parallax and other natural effects.

When attempting frame-to-frame differencing, pixel "smear" may occur because of relative motion between platform and target scene during the finite time required to create a frame. Jannsens[25] estimated the allowable smear rates with the following expression:

$$V_s \approx 0.2(k_0 X)^{-0.25}\left(\frac{\sigma}{\overline{L}}\right) A_T^{0.5} X^{-1} V_T \ , \tag{4.202}$$

where

V_s = smear velocity
k_0 = correlation length of background PSD fit to a -2 asymtotic slope
σ = standard deviation of the background radiance
$\overline{L}$ = average background radiance
A_T = target area
X^2 = nadir footprint area
V_T = target velocity.

Differencing Filters. Casasent[26] considered a number of algorithms for target motion discrimination as follows:

First differencing is given by

$$D_k(X) = \frac{I_k(X) - I_{k-1}(X)}{2} , \tag{4.203}$$

where D_k is the difference signal at coordinate X after the k'th frame and I_k is the intensity of a pixel in the k'th frame. The transfer function is

$$H_1(\omega_s) = \frac{1 - \exp(-j\omega_s \Delta x)}{2} , \tag{4.204}$$

where

ω_s = spatial frequency
$\Delta x = v\Delta t$
v = relative velocity
Δt = sampling interval or frame time.

The magnitude response is

$$|H_1(\omega_s)| = \left(\frac{1 - \cos w_s \Delta x}{2}\right)^{1/2} . \tag{4.205}$$

Second differencing is calculated by

$$D_k(x) = \frac{1}{2} I_k(x) + I_{k-1}(x) - \frac{1}{2} I_{k-2}(x) , \tag{4.206}$$

with transfer function

$$H_2(\omega_s) = -\frac{1}{2} + \exp(-j\omega_s \Delta x) - \frac{1}{2} \exp(-j2\omega_s \Delta x) \tag{4.207}$$

and

$$|H_2(\omega_s)| = \left[\frac{1}{2}(3 - 4\cos\omega_s \Delta x + \cos 2\omega_s \Delta x)\right]^{1/2} . \tag{4.208}$$

Triple differencing is calculated by

$$D_k(x) = I_k(x) - 3I_{k-1}(x) + 3I_{k-2}(x) - I_{k-3} . \tag{4.209}$$

Linear interpolated differencing is given by

$$D_k(x) = I_{k-1}(x) - \hat{I}_k(x) , \tag{4.210}$$

where

$$\hat{I}_k(x) = (1 - \Delta\hat{B})I_k(x) + \Delta\hat{B}I_{k-1}(x) \tag{4.211}$$

and $\Delta\hat{B}$ is the estimated subpixel shift between two image frames. The term $\Delta\hat{B}$ is estimated by the cross-correlation of two image frames, for example, $I_k(x)$ and $I_{k-1}(x)$. The correlation surface is searched for the peak value. A second-order polynomial, for example, is then fitted to the correlation values near the peak. The coefficients of the polynomial can be used to estimate the subpixel shift. The transfer function is given by

$$H_3(\omega_s) = [1 + \Delta\hat{B}(\cos\omega_s - 1) - \cos(\omega_s\Delta\hat{B})] + j[\sin(\omega_s\Delta\hat{B}) - \Delta\hat{B}\sin\omega_s] . \tag{4.212}$$

A target that moves more than $\Delta\hat{B}$ will not be suppressed by the linear interpolated method. Parabolic interpolated differencing is given by

$$I_k(x) = \frac{\Delta\hat{B}(\Delta\hat{B} + 1)}{2}I_{k-1}(x) + (1 - \Delta\hat{B}^2)I_k(x) + \frac{\Delta\hat{B}(\Delta\hat{B} - 1)}{2}I_{k+1}(x) , \tag{4.213}$$

and the transfer function is given by

$$\begin{aligned} H_4(\omega_s) = {} & [1 + \Delta\hat{B}^2(\cos\omega_s - 1) - \cos(\omega_s\Delta\hat{B})] \\ & + j[\sin(\omega_s\Delta\hat{B}) - \Delta\hat{B}\sin\omega_s] , \end{aligned} \tag{4.214}$$

where again $\Delta\hat{B}$ is estimated by the cross-correlation of two image frames.

4.4.3.5 Spatial Filtering (Casasent[26]). In this method, originally proposed by Wang,[27] only one image frame at a time is considered and the background has highly correlated adjacent pixels, whereas the target pixels exhibit less spatial correlation. This can be used to design an optimal spatial filter that yields minimum mean-square error. This is achieved by estimating an average 3×3 covariance matrix estimated for each image snapshot and using this to solve for nine coefficients that are used in a 3×3 filter mask. While this is mathematically elegant, it has a few practical drawbacks. First, this method requires the estimation of the covariance matrix, which can be quite time consuming and is not easily amenable to optical implementation. Second, this method requires the specification of a desired vector before the filter coefficients are obtained. Specifying the desired vector requires that we know whether or not the target is in the region of interest. This is not always feasible. Finally, this method does not make use of the temporal information at all. It ignores the fact that the targets move faster than the background.

4.4.3.6 Spatial Differencing (Casasent[26]). This method[28] considers 3×3 windows centered at the same point in successive image frames. The center pixel value from the current frame is subtracted from the nine pixel values of

the same window in the previous frame. The output of this algorithm is the magnitude of the smallest of these nine differences. Because of the sorting operation inherent in this, it is a nonlinear operation. In that sense, this algorithm is very different than the previous five.

To understand how this method works, we note that the targets move faster than the backgrounds. Thus, if the 3×3 observation window does not contain the target, there should be little difference between successive frames, yielding very small values for the difference. On the other hand, if the window in one frame contains a target, it is probably not seen in the same window in the next frame. Simple subtraction will not eliminate this target. While this method is attractive because of its robustness to small amounts of noise, it also has two drawbacks. First, because of the nonlinear ranking operation needed, an optical implementation is difficult. The second problem is that targets that do not move by more than one pixel between frames (essentially those that do not move out of the window) will be suppressed by this algorithm.

4.4.4 Tracking Algorithms (Spiro and Schlessinger[7])

In IRST, detection is defined as the exceedance of a fixed or variable threshold (sometimes called *threshold exceedance*). After filtering a frame, pixels that meet the detection criteria in all frames form the basis of the data by which the characteristics and validity of that particular target are deduced (called *track processing*). Generally, conclusions drawn depend on certain *a priori* assertions regarding the expected behavior of a particular class of targets. IRST targets are usually expected to form long persistent linear streaks from which deductions can be made concerning target dynamics, such as speed and heading, relative to the sensor platform. Given the motion of the sensor, target motion can be translated into earth-fixed coordinates. The following algorithms are used with transversal filters with one or more stages of frame-to-frame differencing.

4.4.4.1 Multidifference Algorithms (Spiro and Schlessinger[7]). These algorithms use bipolar thresholds set at the same absolute level and frame differencing. It is clear that, from the previous discussion on frame differencing and phasing, bipolar signals are generated irrespective of the ultimate nature of target phenomenology, be it occultation or emission signatures. Positive and negative exceedances are collected in separate virtual pixel memory locations that are subsequently "ANDed" together in composite memory for streak processing. As a target moves from pixel to pixel, each virtual pixel will generate both positive and negative exceedances, as shown in Fig. 4.173. Generally,

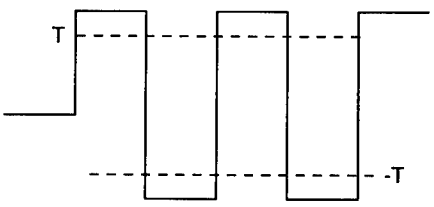

Fig. 4.173 Positive and negative exceedances created by first-order differencing as a target moves from pixel to pixel.[7]

clutter does not generate both positive and negative exceedance; thus, significant reduction in clutter can be obtained. The streak can be processed further by subjecting it to length, velocity, and linearity testing.

4.4.4.2 Multithreshold Algorithms (Spiro and Schlessinger[7]). These algorithms are based on multiple-threshold-level exceedances using a pattern of expected amplitudes for a fixed number of frames. Note that a perfectly phased target generates a 4-pixel pattern for third-order differencing that can be subjected to a test involving multiple thresholds.

The multithreshold for third-order differencing (assuming perfect registration) is

$$I_k \leqslant -I_t \cap I_{k+1} \geqslant 3I_t \cap I_{k+2} \leqslant -3I_t \cap I_{k+3} \geqslant I_t \ , \tag{4.215}$$

where I_t is the threshold and $\cap$ denotes "AND." The satisfaction of the above condition defines a target hit.

Simulation studies accounting for noise and other imperfect conditions have shown that each pixel must pass the following tests in four successive frames:

Positive contrast targets:

$$I_k > 0.33I_t \cap I_{k+1} < -I_t \cap I_{k+2} > I_t \cap I_t > 0 \ , \tag{4.216}$$

$$I_k > 0.33I_t \cap I_{k+1} < -I_t \cap I_{k+2} > 0 \cap I_t > 0 \ , \tag{4.217}$$

$$I_k > 0.33I_t \cap I_{k+1} > 0 \cap I_{k+2} < -I_t \cap I_{k+3} > I_t \ . \tag{4.218}$$

Negative contrast targets:

$$I_k < -0.33I_t \cap I_{k+1} > I_t \cap I_{k+2} < -I_t \cap I_{k+3} < 0 \ , \tag{4.219}$$

$$I_k < -0.33I_t \cap I_{k+1} > I_t \cap I_{k+2} < 0 \cap I_{k+3} < -I_t \ , \tag{4.220}$$

$$I_k < -0.33I_t \cap I_{k+1} < 0 \cap I_{k+3} > 1 \cap I_{k+3} < -I_t \ . \tag{4.221}$$

The bipolar virtual memory output passing the above tests are then "ORed" together to form a composite memory for streak processing. The streak again can be subjected to other tests of length, linearity, or velocity. A deficiency of this tracker is that time monotonicity is lost.

4.4.4.3 Linear-Tracker Algorithm (Spiro and Schlessinger[7]). The linear-tracker (Fig. 4.174) algorithm may have special features peculiar to a given problem, but in general the concept is to test each new "hit" (threshold exceedance) with the information obtained from past history. Initialization of the track starts by taking the points that have passed threshold tests and placing a "search box" around the point. The extent of the search box is usually a function of expected target speed and position uncertainties and frame time. As a new "hit" arrives, it is tested to determine if it lies within the search box. Based on two associated hits, a new search box of smaller extent can be erected in a preferred direction. The algorithm can be implemented with either

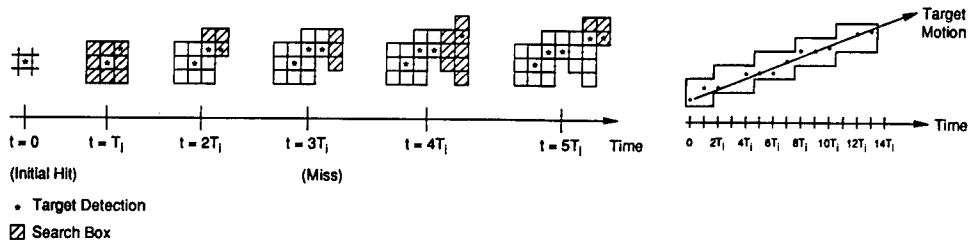

Fig. 4.174 Linear tracker algorithm target track is deduced by exceedances in search boxes predetermined by past target motion.[7]

a no-miss rule or a one-or-more-miss rule. The tracking function is usually implemented in a general-purpose computer where track files are maintained, initiated, or dropped, depending on the rules that are established. Further refinements can be added by further demanding that the collected track points pass a linearity test.

4.4.4.4 Advanced Processing Techniques. The IRST signal-processing techniques discussed herein are elementary. The literature[29–31] abounds with advanced techniques using sophisticated statistical decision methods to detect and track targets in cluttered backgrounds, including three-dimensional and four-dimensional spatio-temporal processing, track before detect, and velocity filtering. The reader is referred to the above references for extensive discussion of advanced techniques.

4.5 PASSIVE LOCATION AND RANGING (Ruben and Michalowicz[32])

Unlike radar, an IRST must derive range velocity and position by passive means from sequential azimuth and elevation measurements relative to the observer. In the general case both observer and target are in motion. Passive location for an IRST is essentially a dynamic triangulation process with the additional complexities of errors in azimuth and elevation measurement and certain maneuvers required of the observer to minimize errors in derived range.

4.5.1 Fixed Target

The geometry of passive location on a fixed target is shown in Fig. 4.175. Note that observer motion with constant velocity along $\bar{v}_1$ generates a triangle from which two successive azimuth/elevation measurements can be made at times t_1 and t_2.

If the measurements were errorless, only two would be required; however, each measurement has a finite error denoted by the dotted lines in the figure. The intersection of these cones defines a region of uncertainty R, and an estimate of the error in range is denoted by δR. This error may be minimized by making a number of successive measurements and resorting to least-square fits, for example, minimizing the error between the estimated range and the true range.

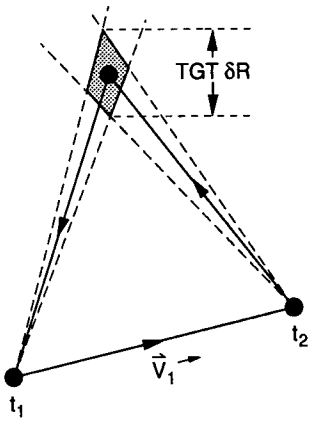

Fig. 4.175 Passive location geometry for a fixed target.[32]

4.5.1.1 Line-of-Sight Statistics. Given the position x, y, z and true bearing θ and ϕ of a target relative to an observer at the origin, the unit vector of the line of sight to the target is

$$\hat{n} = \hat{i}\cos\theta\cos\phi + \hat{j}\sin\theta\cos\phi + \hat{k}\sin\phi = (a,b,c) \ , \tag{4.222}$$

with

$$\tan\theta = \frac{y}{x} \ , \quad \sin\phi = \frac{z}{r} \ , \quad r^2 = x^2 + y^2 + z^2 \ . \tag{4.223}$$

Given that the bearing measurements are Gaussian random variables with variance σ^2, the mean and variance of the components of the unit vector $\hat{\mathbf{n}}$ can be written as

$$E(a) \approx \cos\theta\cos\phi\left(1 - \frac{\sigma^2}{2}\right)^2 \ , \tag{4.224}$$

$$\sigma_a^2 \approx \sigma^2(\cos^2\theta\sin^2\phi + \sin^2\theta\cos^2\phi) \ , \tag{4.225}$$

$$E(b) \approx \sin\theta\cos\phi\left(1 - \frac{\sigma^2}{2}\right)^2 \ , \tag{4.226}$$

$$\sigma_b^2 \approx \sigma^2(\cos^2\theta\cos^2\phi + \sin^2\theta\sin^2\phi) \ , \tag{4.227}$$

$$E(c) \approx \sin\phi\left(1 - \frac{\sigma^2}{2}\right)^2 \ , \tag{4.228}$$

$$\sigma_c^2 \approx \sigma^2 \cos^2\phi \ , \tag{4.229}$$

where E is the expectation operator and $\sigma^2 \ll 1$. A value of 0 for any of the above variances is an artifact resulting from truncation of higher order terms. Also,

$$\text{covariance } (a,b) = \sigma^2 \cos\theta \sin\theta(1 - 2\cos^2\phi) \ , \tag{4.230}$$

$$\text{covariance } (a,c) = \sigma^2 \cos\theta \cos\phi \sin\phi \ , \tag{4.231}$$

$$\text{covariance } (b,c) = -\sigma^2 \sin\theta \cos\phi \sin\phi \ . \tag{4.232}$$

4.5.1.2 Least-Squares Range Estimator. The methodology relies on n sets of bearing measurements with $2n$ components (azimuth and altitude). The k'th set of bearings is denoted by $\theta(k)$ and $\phi(k)$, and the assumed errorless locations from which these measurements are made are $x(k), y(k), z(k)$. A least-squares estimate function for $k > 1$ is given as

$$S = \sum_k \left\{ \theta(k) - \arctan\left[\frac{y - y(k)}{x - x(k)}\right] \right\}^2 + \sum_k \left\{ \phi(k) - \arcsin\left[\frac{z - z(k)}{r(k)}\right] \right\}^2 \ , \tag{4.233}$$

where $r(k) = [x - x(k)]^2 + [y - y(k)]^2 + [z - z(k)]^2$. The objective is to choose x,y,z to minimize S, providing a best estimate of position in the least-squares sense.

An example of this procedure is shown in Fig. 4.176. As expected, the estimates that provide the largest number of bearings yield the better estimates of target location.

Rubin and Michalowicz[32] conclude from a number of simulations on least squares estimates of position of a stationary target that (1) the most reliable estimates come from targets that are well off axis, (2) for short tracks, reliability is determined more by the direction of the target than by its range, (3) for longer tracks, the situation reverses, and (4) after about 30 s in the conditions shown in Fig. 4.176, the standard deviation is a few percent or less of the true range of target, independent of the target direction and range.

4.5.1.3 Azimuth-Only Estimates. An estimate that lends itself to closed-form solutions and provides a reasonably good result in using only azimuth information is

$$S = \sum_k \{[y - y(k)] - g(k)[x - x(k)]\}^2 \ , \tag{4.234}$$

where $g(k)$ is $\tan\theta(k)$, which leads to the expressions

$$x = \frac{\bar{y}\sum_k g(k) - \bar{g}\sum_k g(k)y(k) + \sum_k g^2(k)x(k)}{\sum_k g^2(k) - \bar{g}\sum_k g(k)} \ , \tag{4.235}$$

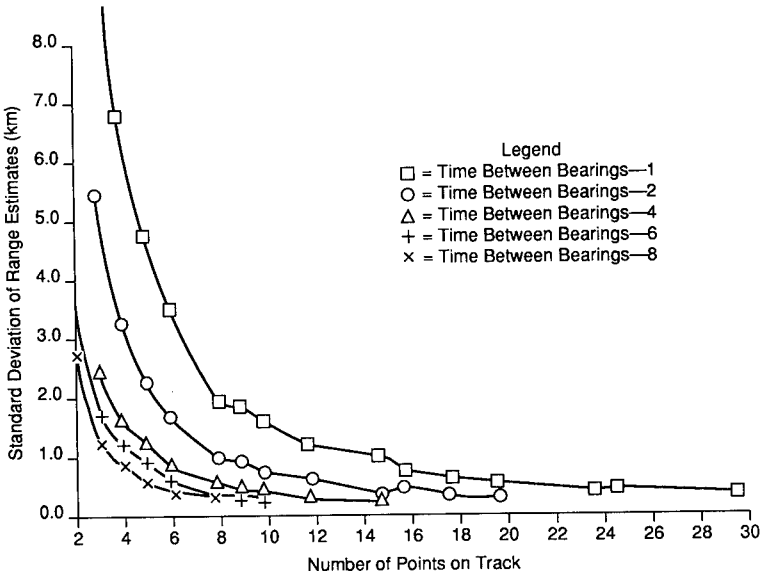

Fig. 4.176 Track error versus number of measurements for various times between measurements. Least-square fit to fixed target standard deviation of range versus points on track, 100 samples per point, $\sigma = 0.000333$, target coordinates: (50, 50, 2), $R = 70.7$ km, $a = 0$ ($V_x = 0.16$, $V_y = 0$, $V_z = 0$) nm s^{-1}.[32]

$$y = \bar{y} + x\bar{g} - \frac{1}{N}g(k)x(k) \ , \tag{4.236}$$

where

$$\bar{y} = \frac{1}{N}\sum_k y(k) \ , \tag{4.237}$$

$$\bar{g} = \frac{1}{N}\sum_k g(k) \ , \tag{4.238}$$

$$z = \tan\phi(0)(x^2 + y^2)^{1/2} \ , \tag{4.239}$$

where $\theta(0)$ is the elevation angle observed at time = 0.

The preceding procedure matches the accuracy of estimates using only bearing information; however, it should be noted that it produces biased underestimates of range and does not apply in the general moving target case where the target changes altitude.

4.5.2 Constant-Velocity Targets

The procedures for estimating range of a moving target at velocity V are the same as for a fixed target except for the number of parameters to be estimated. An expression for least-squares range estimation is

$$S = \sum_k \tan\theta(k) - \arctan\left[\frac{y + (k-1)V_y - y(k)}{x + (k-1)V_x - x(k)}\right] + \sum_k \tan\phi(k) - \arcsin\left[\frac{z + (k-1)V_z - z(k)}{r(k)}\right] . \quad (4.240)$$

Again, the objective is to find a set of x,y,z,V_x,V_y,V_z that minimizes S, where

$$r^2(k) = [x + (k-1)V_x - x(k)]^2 + [y + (k-1)V_y - y(k)]^2 + [z + (k-1)V_z - z(k)]^2 . \quad (4.241)$$

In the case where both observer and target are moving, ambiguities can arise, as illustrated in Fig. 4.177.

The observer moving along vector **O** measures three line-of-sight angles at times t_1,t_2,t_3 of a target moving along **T**. By triangulation these measurements yield virtual positions P_1 and P_2 with little relation to actual target position.

In addition, a target moving along vector **T′** would yield an identical set of line-of-sight angles and virtual positions. In general, there is no unique solution for the target position for a constant velocity observer, so the observer must accelerate to achieve unique convergence in the least-squares sense.

An example of observer acceleration is shown in Fig. 4.178 with various conditions shown. The curves show considerable complexity, and monotonic

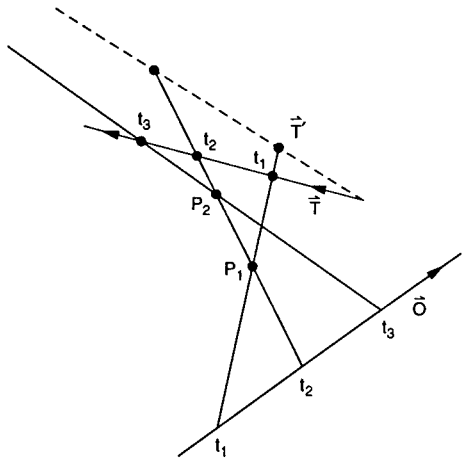

Fig. 4.177 Ambiguities in position created by a moving target.

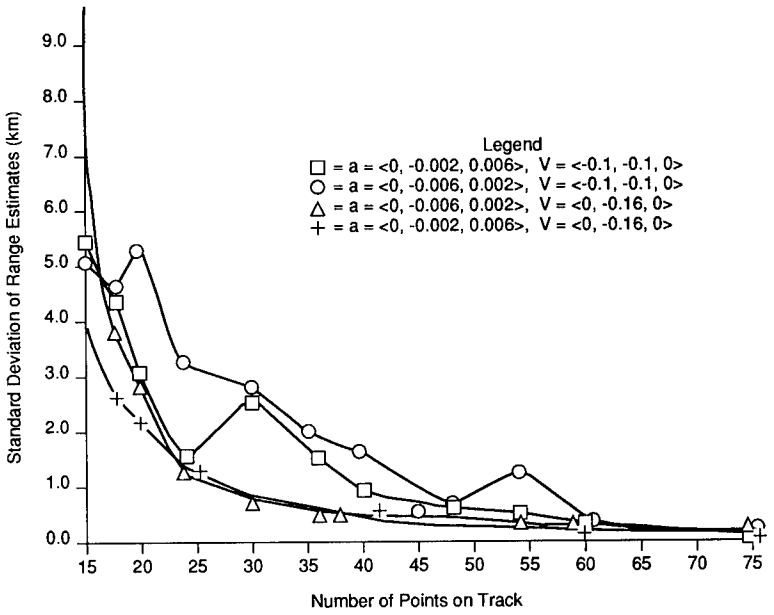

Fig. 4.178 Track error versus number of measurements for various velocity vectors. Least-square fit to fixed target standard deviation of range versus points on track. 100 samples per point, initial observer $V_0 = \langle 0.16, 0, 0 \rangle$ nm s^{-1}, target coordinates (50, 10, 1) km, R = 51.0 km.[32]

convergence is not always observed. In practice, a sequence of maneuvers by the observation platform is used to define acceleration and thus achieve unique convergence.

4.6 IRST OPERATIONAL SYSTEMS

4.6.1 Air Surveillance

IRST systems were employed in the 1960s and 1970s on both U.S. Navy and U.S. Air Force fighter aircraft. Technology limitations on systems of that era, including inadequate range and high false-alarm rates, led to eventual abandonment. Since 1981, a resurgence of interest by the U.S. Navy and Air Force has taken place, culminating in the scheduled deployment of an IRST system on the F-14D U.S. Navy fighter aircraft, where Navy F-14Ds will use the IRST in an outer air battle fleet defense role. At this writing the U.S. Air Force has not committed to an IRST system for the F-15 or ATF.

F-14D IRST. IRST midwave (MW) and longwave (LW) systems built by General Electric have undergone extensive flight-test evaluation at the U.S. Navy's Pacific Missile Test Center, Pt. Mugu, California, as part of the F-14 IRST Full Scale Development (FSD) Program. Flight-test results on a modified F-14A test aircraft meet or exceed performance specifications for the F-14D aircraft. Both the MW and LW IRST systems have demonstrated performance at op-

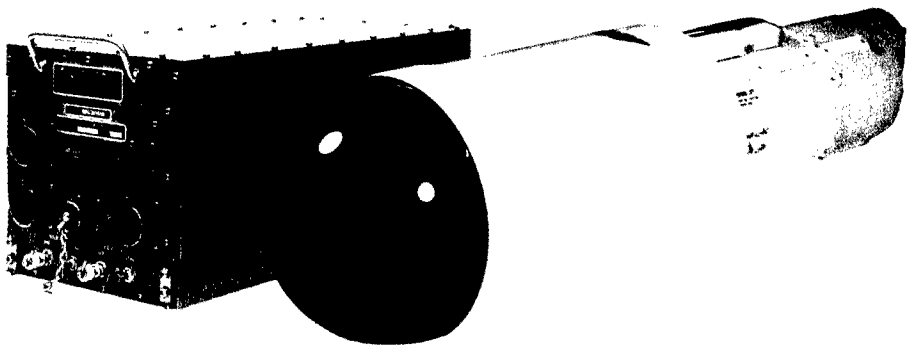

Fig. 4.179 F-14D IRST sensor head and processor.

erationally significant ranges. In addition, the IRST system's imaging capability was recently demonstrated in flight test, and further system enhancements are planned. The IRST entered limited production in April 1990.

The F-14D IRST is a passive sensor subsystem that searches and detects all thermal targets within its field of view and IR spectral band. Using a series of sophisticated filter techniques and software algorithms, candidate detections are processed, background clutter is rejected, and real targets are declared and displayed to the aircrew. The IRST functions in six separate modes similar in operation to the APG-71 tactical air intercept radar. Both azimuth and elevation scan volumes are selectable and separately controlled by the aircrew.

The GE F-14D IRST consists of two units: a sensor head and a controller-processor, shown in Fig. 4.179. The sensor head, mounted in a chin pod, contains the optics and detector assembly. A three-axis inertially stabilized gimbal allows the system to accurately search multiple scan volumes, either automatically or under manual pilot control.

Required signal and data processing are performed in the air-cooled controller-processor.

The F-14D will be the first production U.S. fighter in 25 years to be IRST equipped. Operating as a stand-alone primary sensor or together with the APG-71 radar and/or the television camera system (TCS), the IRST makes the F-14D offensive sensor suite the most advanced of any U.S. or NATO fighter aircraft.

4.6.2 Shipboard IRST

An example of a shipboard IRST installation was a joint U.S./Canadian effort resulting in a trial installation aboard the Canadian *Algonquin* (DDH-283), as shown in Fig. 4.180. The scanner assembly, which contains the telescope, detector dewar, cryogenics, preamps, and the adaptive-threshold processor (background normalizer), rotates at 30 rpm on an electric three-axis stable platform. The signals are brought below decks via slip rings to the data conditioner unit, which formats them for processing and display.

The target energy is filtered, detected, amplified, and passed to the background normalizer, which is an adaptive-threshold device that outputs a nearly

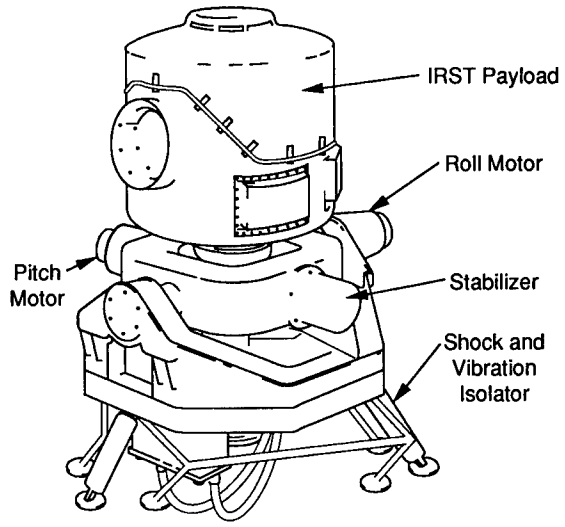

Fig. 4.180 IRST stabilized platform on HMCS *Algonquin*.

constant false-alarm rate, as discussed in Sec. 4.4. The CFAR signal is processed in the shipboard computer to separate residual false alarm. The adaptive threshold is derived from sampling a window 2 deg × 2 deg about the target cell.

The postdetection processor has three functions: (1) it establishes a track on detections that exhibit a degree of scan-to-scan correlation, (2) it tests each established track for target and clutter properties, and (3) it outputs target declarations.

4.6.3 Future Activities

The IRST is expected to play a larger role in military sensor suites as increased performance is progressively demonstrated in both sensitivity for long-range detection and clutter suppression for reduced false-alarm rates. Specifically, with the advent of "stealth" technology, which reduces the effectiveness of conventional radar, the IRST will play an increasingly important role in all the military domains relying on surveillance for military superiority.

References

1. R. C. Gibbons, Texas Instruments, Dallas, TX, private communication 190566 (March 1987).
2. A. Hirschman, "Signal processing for clutter rejection in infrared search and track systems," in *Proc. 12th Annual Asilomar Conference on Circuits and Systems Computing*, pp. 609–612 (1978).
3. W. R. Moore, M. Spector, and V. Best, "Infrared search and track system development," in *Proc. AIAA/Institute of Electrical and Electronics Engineers (IEEE) 6th Digital Avionics Systems Conference*, pp. 65–67 (1984).
4. G. Janakowitz and M. Raboul, ITT Avionics Division, Nutley, NJ, private communication 185153 (Feb. 1982).
5. W. E. Keicher and R. J. Keyes, MIT Lincoln Laboratory, Cambridge, MA, private communication 182719 (April 1979).

6. J. M. MacCallum, Naval Research Laboratory, private communication 181744 (Aug. 1977).
7. I. J. Spiro and M. Schlessinger, *Infrared Technology Fundamentals,* Marcel Dekker, New York (1989).
8. R. D. Hudson, Jr., *Infrared Systems Engineering,* John Wiley & Sons, New York (1969).
9. B. Papayoti, McDonnell Douglas Corporation, private communication (1991).
10. T. D. Conley, Air Force Geophysics Laboratory, private communication 216517 (March 1980).
11. G. H. Suits, "Natural sources," Chap. 3 in *The Infrared Handbook,* W. L. Wolf and G. J. Zissis, Eds., Environmental Research Institute of Michigan, Ann Arbor, MI (Revised 1985).
12. S. B. Idso and R. D. Jackson, "Thermal radiation from the atmosphere," *Journal of Geophysical Research* **74,** 5397 (1969).
13. Y. Itakura, S. Tsutsumi, and T. Takagi, "Statistical properties of the background noise for the atmospheric windows in the intermediate infrared region," *Infrared Physics* **14**(1), 17–29 (1974).
14. G. Yamamoto, M. Tanaka, and S. Asano, *Journal of Atmospheric Science* **27,** 282 (1970).
15. P. A. Davis, *Journal of Applied Meteorology* **10,** 1314 (1971).
16. C. M. R. Platt, *Journal of Atmospheric Science* **30,** 1191 (1973).
17. I. Sattinger, *Spectral Reflections* **21**(4), ERIM (Sept. 1991).
18. K. Seyrafi, *Electro-Optical Systems Design,* Electro-Optical Research Company, Los Angeles, CA (1985).
19. *The RCA Electro-Optics Handbook,* Technical Series EOH-10, Harrison, NJ (1968).
20. M. I. Skolnik, *Introduction to Radar Systems,* McGraw-Hill, New York (1980).
21. J. R. Maxwell and D. Kryskowski, ERIM, private communication (Jan. 1991).
22. R. A. Steinberg, "Passive infrared surveillance: new methods of analysis," Memorandum Report 4078, Naval Research Laboratory, DTIC, Washington, DC (Sep. 1979).
23. A. Papoulis, *Probability, Random Variables, and Stochastic Processes,* 2nd ed., McGraw-Hill, New York (1984).
24. L. A. Williams, Jr., "Spectral discrimination for long range search/track infrared systems," in *Proceedings of the SPIE* **292,** 225–231 (1981).
25. T. J. Jannsens, Aerospace Corporation, El Segundo, CA, private communication 182719 (May 1979).
26. D. Casasent, V. Kumar, and Y. L. Lin, "Subpixel target detection and tracking," *Proceedings of the SPIE* **726,** 206–220 (1986).
27. C. D. Wang, "Adaptive spatial/temporal/spectral for background clutter suppression and target detection," *Optical Engineering* **21**(6), 1033–1038 (1982).
28. T. J. Patterson, D. M. Chabries, and R. W. Christiansen, "Image processing for target detection using data from a staring mosaic IR sensor in geosynchronous orbit," *Optical Engineering* **25**(1), 166–172 (1986).
29. *Signal and Data Processing of Small Targets 1989,* O. E. Drummond, Ed., *Proceedings of the SPIE* **1096** (1989).
30. *Signal and Data Processing of Small Targets 1990,* O. E. Drummond, Ed., *Proceedings of the SPIE* **1305** (1990).
31. *Signal and Data Processing of Small Targets 1991,* O. E. Drummond, Ed., *Proceedings of the SPIE* **1481** (1991).
32. R. Ruben and J. Michalowicz, "Bearings only air-to-air ranging," Memorandum Report 6046, Naval Research Laboratory, DTIC, Washington, DC (July 1988).

Index